

IntechOpen

Heat Transfer Studies and Applications

Edited by Salim Newaz Kazi



HEAT TRANSFER STUDIES AND APPLICATIONS

Edited by **Salim Newaz Kazi**

Heat Transfer Studies and Applications

<http://dx.doi.org/10.5772/58727>

Edited by Salim Newaz Kazi

Contributors

Mauro Ravagnani, Muhammad Musaddique Ali Rafique, Kewei Song, Alberto E. Quintero, Marcos Vera, Panagiotis Sismanis, Masood Khan, Asif Munir, Azeem Shahzad, Hideo Kawahara, Heinz Herwig, Rodolphe Heyd, Jan Marian Taler, Pawel Oclór, Dawid Taler, Marzena Nowak, Mikhail Tokar, Jong-Taek Oh, Salim Newaz Kazi, M. M. Awad, Ahmet Selim Dalkilic, Somchai Wongwises

© The Editor(s) and the Author(s) 2015

The moral rights of the and the author(s) have been asserted.

All rights to the book as a whole are reserved by INTECH. The book as a whole (compilation) cannot be reproduced, distributed or used for commercial or non-commercial purposes without INTECH's written permission.

Enquiries concerning the use of the book should be directed to INTECH rights and permissions department (permissions@intechopen.com).

Violations are liable to prosecution under the governing Copyright Law.



Individual chapters of this publication are distributed under the terms of the Creative Commons Attribution 3.0 Unported License which permits commercial use, distribution and reproduction of the individual chapters, provided the original author(s) and source publication are appropriately acknowledged. If so indicated, certain images may not be included under the Creative Commons license. In such cases users will need to obtain permission from the license holder to reproduce the material. More details and guidelines concerning content reuse and adaptation can be found at <http://www.intechopen.com/copyright-policy.html>.

Notice

Statements and opinions expressed in the chapters are those of the individual contributors and not necessarily those of the editors or publisher. No responsibility is accepted for the accuracy of information contained in the published chapters. The publisher assumes no responsibility for any damage or injury to persons or property arising out of the use of any materials, instructions, methods or ideas contained in the book.

First published in Croatia, 2015 by INTECH d.o.o.

eBook (PDF) Published by IN TECH d.o.o.

Place and year of publication of eBook (PDF): Rijeka, 2019.

IntechOpen is the global imprint of IN TECH d.o.o.

Printed in Croatia

Legal deposit, Croatia: National and University Library in Zagreb

Additional hard and PDF copies can be obtained from orders@intechopen.com

Heat Transfer Studies and Applications

Edited by Salim Newaz Kazi

p. cm.

ISBN 978-953-51-2146-6

eBook (PDF) ISBN 978-953-51-6381-7

We are IntechOpen, the world's leading publisher of Open Access books Built by scientists, for scientists

3,800+

Open access books available

116,000+

International authors and editors

120M+

Downloads

151

Countries delivered to

Our authors are among the
Top 1%

most cited scientists

12.2%

Contributors from top 500 universities



WEB OF SCIENCE™

Selection of our books indexed in the Book Citation Index
in Web of Science™ Core Collection (BKCI)

Interested in publishing with us?
Contact book.department@intechopen.com

Numbers displayed above are based on latest data collected.
For more information visit www.intechopen.com



Meet the editor



Salim Newaz Kazi has eighteen years engineering service experience in petrochemical industries. He was the head of engineering and construction of a chemical plant for two years. He has the academic background with B.Sc. in Engineering (Mechanical), M.Sc. in Mechanical Engineering and PhD in Chemical and Materials Engineering. Dr. Kazi has 85 technical papers published in national and international journals and conference proceedings. He has also worked as a part time consultant in a consulting team for gas pipelines layout and installation, gas drilling environment management, etc. At present he is working as an academic in the Department of Mechanical Engineering, Faculty of Engineering, University of Malaya, Kuala Lumpur, Malaysia, supervising/co – supervising 16 PhD and 3 Masters Theses. He has completed supervision of 4 PhD and 10 Masters Theses.

Contents

Preface XI

Section 1 General Aspects of Heat Transfer 1

Chapter 1 **Wall Conduction Effects in Laminar Counterflow Parallel-Plate Heat Exchangers with Small-Scale Wall Corrugations 3**

Marcos Vera and Alberto E. Quintero

Chapter 2 **Interaction of Longitudinal Vortices and the Effect on Fluid Flow and Heat Transfer 33**

Kewei Song

Chapter 3 **A Critical Review on Condensation Pressure Drop in Microchannels and Minichannels 53**

Mohamed M. Awad, Ahmet Selim Dalkiliç and Somchai Wongwises

Chapter 4 **Pressure Drop and Heat Transfer during a Two-phase Flow Vaporization of Propane in Horizontal Smooth Minichannels 103**

Jong-Taek Oh, Kwang-II Choi and Nguyen-Ba Chien

Chapter 5 **Effect of Depth Length on Mixing in a Double-Diffusive Convection Two-Layer System 129**

Hideo Kawahara

Chapter 6 **Heat Transfer and Entropy 143**

Heinz Herwig and Christoph Redecker

Section 2 Analytical and Experimental Investigation 163

Chapter 7 **Modeling and Design of Plate Heat Exchanger 165**

Fábio A.S. Mota, E.P. Carvalho and Mauro A.S.S. Ravagnani

- Chapter 8 **Modelling of Global Heat Transfer by Local Cooling in Fusion Plasmas 201**
Mikhail Tokar
- Chapter 9 **Modeling and Simulation of Heat Transfer Phenomena 225**
Muhammad Musaddique Ali Rafique
- Chapter 10 **Computer-Aided Determination of the Air-Side Heat Transfer Coefficient and Thermal Contact Resistance for a Fin-and-Tube Heat Exchanger 259**
Jan Taler, Paweł Ocioń, Dawid Taler and Marzena Nowak-Ocioń
- Section 3 Heat Transfer Enhancement 293**
- Chapter 11 **Heat Transfer and Nanofluid Flow Through Different Geometries 295**
S.N. Kazi and Hussein Togun
- Chapter 12 **Evaluation of Solidification Times for Medium and High Carbon Steels Based upon Heat Transfer and Solidification Phenomena in the Continuous Casting of Blooms 315**
Panagiotis Sismanis
- Chapter 13 **Convective Heat Transfer to Sisko Fluid over a Nonlinear Radially Stretching Sheet 341**
Masood Khan, Asif Munir and Azeem Shahzad
- Section 4 Heat Transfer Applications 365**
- Chapter 14 **Resistive Electrothermal Sensors, Mechanism of Operation and Modelling 367**
Heyd Rodolphe

Preface

The book "Heat Transfer Studies and Applications" is a collection of knowledge on different aspects of heat transfer, research based results, reviews and studies on applications. Basic principles of heat transfer in different avenues, such as vortices effect on heat transfer, studies on heat exchangers, convection phenomena, conduction heat transfer, analysis of heat transfer and entropy are systematically presented.

Two phase flow is a complex phenomenon and it is extensively observed in chemical and process industries. In depth description along with mechanisms and modeling are highlighted here. Separation flow is being studied for a long time and still under intensive investigation for exploring mechanism and applications. Here it is being incorporated with data and analysis.

A series of theoretical and numerical studies has been incorporated in this book. Theoretical framework for analyzing the boundary layer flow and heat transfer with viscous dissipation to sisko fluid has been formulated. Numerical analysis of heat transfer and thermal contact resistances on tubular heat exchanger, nonlinear heat transfer in thermally developing pipe flow, cooling in fusion plasma, mixing phenomena along with optimization of heat exchangers are presented.

Currently, researchers are deeply engaged in development of sensors for numerous applications. Study on sensors development has been incorporated. Practical applications of heat transfer in different utility fields are incorporated. Also, analytical studies on different models for metals, validation of theoretical and experimental data are highlighted. Intensive investigations are going on to enhance heat transfer. Some of the approaches are presented in this volume.

Though this work was an addition to my prescheduled academic work load, it was very enjoyable. I would like to thank my students for their patience in getting slow responses from me. And lastly, I would like to thank my wife Nilufa and son Mehrab for their sacrifice in daily life during this work.

Salim Newaz Kazi

Department of Mechanical Engineering,
Faculty of Engineering, University of Malaya,
Kuala Lumpur, Malaysia

General Aspects of Heat Transfer

Wall Conduction Effects in Laminar Counterflow Parallel-Plate Heat Exchangers with Small-Scale Wall Corrugations

Marcos Vera and Alberto E. Quintero

Additional information is available at the end of the chapter

<http://dx.doi.org/10.5772/60550>

1. Introduction

Parallel-plate heat exchangers are widely used in chemical, pharmaceutical, food processing, and many other industrial applications. More recently, they have also found application in a variety of emerging branches of thermal engineering. They are currently used in miniaturized reaction systems involving heterogeneously catalyzed gas-phase reactions [1], in thermoelectric generators that convert low-grade thermal energy into electrical power [2, 3], and in thermoacoustic engines [4]. In addition, they are a key component of many cryogenic systems [5,6,7].

Progress in the analysis of parallel-plate heat exchangers has been significant in the last decades due to their simple geometry and well established flow conditions [8]. In particular, the analysis of the steady-state laminar heat transfer between different streams coupled through compatibility conditions at the boundaries constitutes the so-called conjugated Graetz problem. Under certain simplifying assumptions, i.e., constant property fluids and fully developed laminar flow, the problem becomes linear and is amenable to an elegant solution based on eigenfunction expansions, which in counterflow systems involves sets of positive and negative eigenfunctions associated with sets of positive and negative eigenvalues [9,10,11,12].

It is well known that the use of corrugated plates is a suitable method for increasing the thermal performance of heat exchangers and provide higher compactness [13]. In many practical applications the flow is turbulent, and the corrugated surface has a significant effect on the enhancement of heat transfer rates. Because of the presence of highly unsteady recirculation zones, the heat transfer coefficients obtained with corrugated walls are higher than those with flat plates. However, the pressure drop is also significantly higher.

In some other cases the Reynolds number remains small due to the small dimensions of the system, hence laminar flow conditions prevail. In this case the corrugation troughs exhibit low-velocity swirling cells [14] that are both weak and steady. As a result, the convective heat enhancement process is poor and the effect on heat exchanger performance is much smaller. For certain corrugation shapes and/or flow conditions no enhancement of the heat transfer rate may even occur [15]. Thus, even if the heat transfer surface between the wall and the fluid is increased, the global heat transfer effectiveness may not overcome that of a flat wall channel of comparable size [16]. This difficulty has motivated a considerable amount of work on methods to increase the rates of heat and mass transfer in compact heat exchangers operated in the laminar flow regime.

Durmuş et al. [17] demonstrated that under laminar flow conditions the heat exchanged by a plate heat exchanger with a corrugated sinusoidal surface is higher than for other geometries (flat plate and asterisk plate), although corrugated plate heat exchangers exhibit also higher pressure drops. Specifically, the pressure drop in corrugated channels is higher than in flat channels of the same external size. Therefore, a trade-off exists between the heat gained and the pressure drop, because increasing the heat exchanger efficiency leads to smaller system dimensions, which reduces production costs, whereas larger pressure drops result in increased operating costs.

The aim of this work is to extend recent analyses of laminar counterflow parallel-plate heat exchangers [12,18,19] to quantify the effect of small scale wall corrugations. In particular, the amplitude and wavelength of the corrugations will be assumed to be comparable to each other, but small compared to the channel half-widths. Although such separation of scales hardly occurs in practical devices, it enables the problem to be solved by a multi-scale asymptotic approach similar to that proposed by Woollard et al. [20] for mass transfer in channels with small-scale wall corrugations. In this case the problem exhibits two main asymptotic regions: a bulk flow region where the walls appear flat at leading order, and a wall region where there is a full interaction between convection and conduction in the fluids, coupled by transverse and longitudinal conduction in the (thin) corrugated wall.

The multi-scale asymptotic analysis proceeds in two steps:

- On the large (i.e., bulk flow) scale, a theoretical study of laminar counterflow parallel-plate heat exchangers [19] provides the temperature field as an infinite series of eigenfunctions associated with sets of positive and negative eigenvalues. The analysis, which ignores the effects of axial conduction both in the fluids and in the plates, is used to construct an approximate two-term solution that incorporates the effect of higher order eigenfunctions through apparent temperature offsets introduced at the inlet/outlet sections [12]. The approximate solution yields an accurate description of the temperature field away from the thermal entrance regions, thereby enabling simplified expressions for the wall and fluid temperatures, local Nusselt numbers, and overall heat-transfer coefficient in terms of the wall thermal resistance.
- On the small (i.e., wall corrugation) scale, the shear-induced flow of two Newtonian fluids that exchange heat through a thin corrugated wall is studied numerically, retaining both transverse and longitudinal conduction effects in the heat conducting wall. The analysis shows that far from the wall the effect of the corrugations is equivalent to that of a thickened

virtual plane surface with partial slip along the corrugations [21,22]. This virtual plane wall exhibits an apparent thermal resistance that incorporates i) the intrinsic thermal resistance of the corrugated wall, ii) an additional resistance due to the apparent wall thickening, and iii) a negative contribution associated with the heat-transfer enhancement induced by the corrugations (due to the enlarged heat exchange surface area and, when the wall conductivity is larger than those of the fluids, also to the longitudinal heat conduction along the wall). Apparent wall thicknesses and thermal resistances will be presented here for the reference case of sinusoidal corrugations.

Evaluating the approximate solution of the bulk flow model presented in Section 2 with the apparent thermal resistance derived from the wall corrugation model of Section 3, a physically sound multi-scale description of laminar counterflow parallel-plate heat exchangers with small-scale wall corrugations is proposed in Section 4. Illustrative results are presented in Section 5, and some conclusions are drawn in Section 6.

2. Bulk flow model

In this section we analyze the heat exchange process between two constant-property fluids flowing through a multilayered counterflow parallel-plate heat exchanger composed by a relatively large number of channels. A detailed account of this problem can be found elsewhere [19], but we shall summarize here its main aspects for completeness of the presentation. The flow channels are separated by flat plates of finite thickness, δ_w , and thermal conductivity, k_w . The heat conducting plates allow the exchange of heat through a section of length L . Figure 1 shows a sketch of the theoretical configuration under study, showing the coordinate system, the velocity profiles, the boundary conditions, and the physical properties of fluids $i = 1, 2$ (namely, fluid density, ρ_i , heat capacity, c_i , and thermal conductivity, k_i).

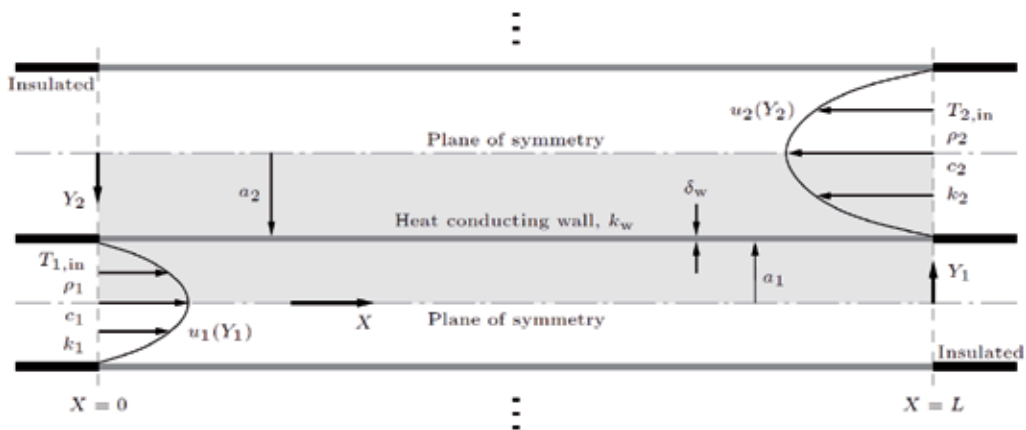


Figure 1. Unitary cell of the idealized counterflow parallel-plate heat exchanger considered in the bulk flow model, showing the coordinate system, the velocity profiles, the inlet conditions, and the physical properties of fluids 1 and 2. A heat conducting wall, of finite thickness, δ_w and thermal conductivity, k_w , separates both fluids. The domain under study is shaded gray.

The Reynolds numbers, $Re_i = 2a_i V_i / \nu_i$, based on the channel half-width, a_i , average flow velocity, V_i , and kinematic viscosity, ν_i , of fluid i , are assumed to be sufficiently small for the flows to remain laminar and steady [23]. The Prandtl numbers, $Pr_i = \nu_i / \alpha_i$, based on the thermal diffusivity, $\alpha_i = k_i / (\rho_i c_i)$, of fluid i , are also assumed to be moderately large compared to unity, a good approximation for most non-metallic liquids in applications. In this case, the thermal entry length is large compared to the hydrodynamic entry length, and the flow can be assumed to be a fully developed Poiseuille flow independent of the temperature field, $u_i(Y_i) = \pm(3/2)V_i[1 - (Y_i/a_i)^2]$, where the + (−) sign holds for fluid 1 (2). As a result, we shall assume that the Peclet numbers of the flow in the channels, $Pe_i = Re_i Pr_i = 2a_i V_i / \alpha_i$, are both large compared to unity. Then, axial heat conduction can be neglected in both fluids in first approximation, and we can assume that the inlet temperature of fluid i is uniform and equal to $T_{i,in}$.

To write the problem in non-dimensional form, we introduce the dimensionless axial and transverse coordinates $\xi = X / (Pe_1 a_1)$ and $y_i = Y_i / a_i$, and the normalized temperature $\theta_i = (T_i - T_{1,in}) / (T_{2,in} - T_{1,in})$. Then, under the assumptions stated above, the energy equation reduces, in first approximation, to a balance between axial convection and transverse conduction

$$\begin{aligned} \frac{3}{4}(1-y_1^2)\frac{\partial\theta_1}{\partial\xi} &= \frac{\partial^2\theta_1}{\partial y_1^2} \\ -m\frac{3}{4}(1-y_2^2)\frac{\partial\theta_2}{\partial\xi} &= \frac{\partial^2\theta_2}{\partial y_2^2} \end{aligned} \quad \text{in } 0 < \xi < \xi_L, \quad 0 < y_i < 1. \quad (1)$$

These equations are to be integrated with adiabatic boundary conditions at the channel symmetry planes

$$\frac{\partial\theta_1}{\partial y_1} = \frac{\partial\theta_2}{\partial y_2} = 0 \quad \text{at } 0 < \xi < \xi_L, \quad y_i = 0, \quad (2)$$

the condition of continuity of wall-normal heat fluxes at the heat conducting wall

$$\begin{aligned} \theta_2 - \theta_1 &= \frac{1}{\kappa_w} \frac{\partial\theta_1}{\partial y_1} = \frac{\nu(\xi)}{\kappa_w} \\ \frac{\partial\theta_1}{\partial y_1} &= -k \frac{\partial\theta_2}{\partial y_2} \equiv \nu(\xi) \end{aligned} \quad \text{at } 0 < \xi < \xi_L, \quad y_i = 1, \quad (3)$$

and the inlet conditions

$$\begin{aligned} \theta_1 &= \theta_{1,in} = 0 \quad \text{at } \xi = 0, \quad 0 \leq y_1 < 1, \\ \theta_2 &= \theta_{2,in} = 1 \quad \text{at } \xi = \xi_L, \quad 0 \leq y_2 < 1. \end{aligned} \quad (4)$$

It should be noted that in writing the compatibility condition at the heat conducting wall (3) we have ignored the effect of axial conduction in the wall, which constitutes a good approximation provided the dimensionless wall thickness δ_w/a_1 remains sufficiently small [19].

The solution to the problem stated above provides the temperature field, $\theta_i(\xi, y_i)$, for given values of the parameters

$$m = \frac{a_2 Pe_2}{a_1 Pe_1}, \quad k = \frac{a_1 k_2}{a_2 k_1}, \quad \kappa_w = \frac{a_1 k_w}{\delta_w k_1}, \quad \text{and} \quad \xi_L = \frac{L}{a_1 Pe_1}. \quad (5)$$

It also provides the local heat-transfer rate from fluid 2 to fluid 1, $\nu(\xi)$, the interfacial wall-fluid temperature distributions, $\theta_{wi}(\xi) \equiv \theta_i(\xi, 1)$, the local wall temperature jump, $\theta_{w2}(\xi) - \theta_{w1}(\xi) = \nu(\xi)/\kappa_w$, and the outlet temperature profiles, $\theta_{1,out}(y_1) = \theta_1(\xi_L, y_1)$ and $\theta_{2,out}(y_2) = \theta_2(0, y_2)$. Another interesting result is the spatial distribution of the bulk (or mixing-cup) temperatures

$$\theta_{mi}(\xi) = \int_0^1 \frac{3}{2} (1 - y_i^2) \theta_i(\xi, y_i) dy_i \quad (6)$$

which represent the uniform temperature that would eventually be attained by fluid i if it was allowed to evolve adiabatically downstream of a certain section ξ . This includes, in particular, the values of the outlet bulk temperatures of both streams, $\theta_{m1}(\xi_L) \equiv \theta_{m1,out}$ and $\theta_{m2}(0) \equiv \theta_{m2,out} = 1 - \theta_{m1,out}/(mk)$, which are closely related to the heat exchanger effectiveness [12].

It is interesting to note that the inverse of κ_w which appears explicitly in Eq. (3) represents the dimensionless wall thermal resistance, $1/\kappa_w = (\delta_w/a_1)/(k_w/k_1)$, defined as the ratio of the dimensionless wall thickness, δ_w/a_1 , to the dimensionless heat conductivity, k_w/k_1 ; the dimensionless wall temperature jump being proportional to $1/\kappa_w$. Note also that the product of m and k represents the ratio of heat capacity flow rates, $mk = (2a_2 V_2 \rho_2 c_2)/(2a_1 V_1 \rho_1 c_1)$, which will hereafter be assumed, without loss of generality, to be greater than one, so that fluid 1 has the lowest heat capacity flow rate [12].

Following standard practice, the solution of the problem can be expanded as an infinite series of eigenfunctions of the form [19]

$$\theta_i(\xi, y_i) = A + \sum_{n=-\infty}^{+\infty} C_n e^{-\lambda_n \xi} g_{n,i}(y_i) \quad (7)$$

where the eigenfunctions are given by

$$g_{n,i}(y_i) = \left(1 \mp \frac{g'_{n,1}(1)}{2\kappa_w} \right) f_{n,i}(y_i), \quad g'_{n,1}(1) = \frac{f'_{n,1}(1)}{1 + \frac{1}{2\kappa_w} f'_{n,1}(1)} \quad (8)$$

with the $- (+)$ sign corresponding to fluid 1 (2), and the eigenvalues are determined by the eigencondition

$$f'_{n,1}(1; \lambda_n) + k f'_{n,2}(1; m, \lambda_n) \left[1 + \frac{f'_{n,1}(1; \lambda_n)}{\kappa_w} \right] = 0. \quad (9)$$

In the above expressions, $f_{n,i}(y_i)$ represent the eigenfunctions of the thermally thin wall limit $\kappa_w \rightarrow \infty$ (or $1/\kappa_w \rightarrow 0$) which can be expressed in terms of Whittaker functions as shown by Vera & Liñán [12]. These written can be derived analytically and evaluated at $y_i = 1$ to give the derivative of the eigenfunctions at the heat conducting wall

$$f'_{n,i}(1) = -\frac{1}{2} + 2 \left[\kappa_{n,i} + \frac{2\sqrt{\pi} \left(\frac{3}{4} + \kappa_{n,i} \right) M_{\kappa_{n,i}+1, \frac{1}{4}}(4\kappa_{n,i}) - \Gamma\left(\frac{1}{4} - \kappa_{n,i}\right) W_{\kappa_{n,i}+1, \frac{1}{4}}(4\kappa_{n,i})}{2\sqrt{\pi} M_{\kappa_{n,i}, \frac{1}{4}}(4\kappa_{n,i}) + \Gamma\left(\frac{1}{4} - \kappa_{n,i}\right) W_{\kappa_{n,i}, \frac{1}{4}}(4\kappa_{n,i})} \right], \quad (10)$$

where $\kappa_{n,1} = \sqrt{3\lambda_n}/8$, $\kappa_{n,2} = i\sqrt{3m\lambda_n}/8$, $\Gamma(z)$ is the complex Gamma function and i is the imaginary unit. Using this expression in Eq. (9) it is possible to compute the eigenvalues λ_n for given values of m , k , and κ_w .

As pointed out by Nunge and Gill [9], the exact solution to the problem stated in Eqs. (1) – (4) involves an infinite set of linear equations for the coefficients A and C_n involved in the series expansion (7), which must be truncated to a finite number of terms in order to get an approximate numerical solution. An alternative approach, initially proposed by Vera and Liñán [12] in the thermally thin wall limit and recently extended by Quintero et al. [19] to the case of non-zero wall thermal resistance, proceeds by constructing an approximate two-term solution that retains only the first two eigenvalues (0 and λ_0) but still incorporates the effect of higher order terms through apparent temperature offsets Δ_i at the inlet section of fluid i . This leads to analytic expressions for the outlet bulk temperatures of the form

$$\begin{aligned} \theta_{m1,out} &\cong \Delta_1 + (1 - \Delta_1 - \Delta_2) \left[\frac{1 - e^{-\lambda_0 \xi_L}}{1 - (mk)^{-1} e^{-\lambda_0 \xi_L}} \right] + mk \Delta_2 \\ \theta_{m2,out} &\cong \Delta_1 + (1 - \Delta_1 - \Delta_2) \left[\frac{1 - (mk)^{-1}}{1 - (mk)^{-1} e^{-\lambda_0 \xi_L}} \right] + (mk)^{-1} \Delta_1 \end{aligned} \quad (11)$$

where Δ_i represents the inlet bulk temperature offset of fluid i associated with the neglected higher-order eigenfunctions at both ends of the heat exchanger, given by

$$\Delta_1 = \left[\frac{1 - (mk)^{-1}}{1 - (mk)^{-1} e^{-\lambda_0 \xi_L}} \right] \frac{\Delta_1^{[0]}}{2}, \quad \Delta_2 = (mk)^{-1} \left[1 - \frac{1 - e^{-\lambda_0 \xi_L}}{1 - (mk)^{-1} e^{-\lambda_0 \xi_L}} \right] \frac{\Delta_1^{[0]}}{2} \quad (12)$$

with

$$\Delta_1^{[0]} = \frac{2(1 + mk)g_{0,1}'^2(1) + mk \left[\Omega_0^- - \frac{g_{0,1}'(1)\Omega_0^+}{2\kappa_w} \right] \lambda_0^2}{8g_{0,1}'^2(1) + (1 + mk) \left[\Omega_0^- - \frac{g_{0,1}'(1)\Omega_0^+}{2\kappa_w} \right] \lambda_0^2}. \quad (13)$$

For given values of m , k , κ_w and ξ_L , the above expressions provide closed-form approximate expressions for the outlet bulk temperatures of both streams in terms of the computed values of λ_0 , $g'_{0,1}(1)$, and

$$\Omega_0^\pm = \frac{\partial}{\partial \lambda_0} \left[g'_{0,1}(1; \lambda_0) \pm kg'_{0,2}(1; m, \lambda_0) \right], \quad (14)$$

which are to be obtained numerically from Eqs. (8) – (10). As shown by Quintero et al. [19], the approximate two-term solution provides accurate representations for the temperature field away from the thermal entrance regions, thereby enabling simplified expressions for the wall and bulk temperature distributions, local Nusselt numbers, and overall heat-transfer coefficient.

Figure 2 shows the variation of the outlet bulk temperature of fluid 1, $\theta_{m1,out}$, with the dimensionless wall thermal resistance, $1/\kappa_w$, for increasing values of the heat exchanger length, $\xi_L = [0.125, 0.25, 0.5, 1, 2]$. As previously discussed, although m and k take different values in the left and right plots, in both cases $mk = (\dot{m}_2 c_2) / (\dot{m}_1 c_1) > 1$, so that $\theta_{m1,out}$ coincides by definition with the heat exchanger effectiveness.

The model results indicate that the heat exchanger effectiveness increases monotonously with the dimensionless heat exchanger length, ξ_L , and decreases with the wall thermal resistance, $1/\kappa_w$. The results presented in Figure 2 were obtained from the numerical integration of Eqs. (1) – (4) (solid lines) and from the approximate two-term solution presented above (symbols). As can be seen, the agreement is excellent even for the shortest heat exchangers under study, with errors below 1% for $\xi_L \geq 0.25$ [19]. This demonstrates that the approximate two-term solution constitutes a fast evaluation tool that could be readily used for the optimization of heat exchanger performance.

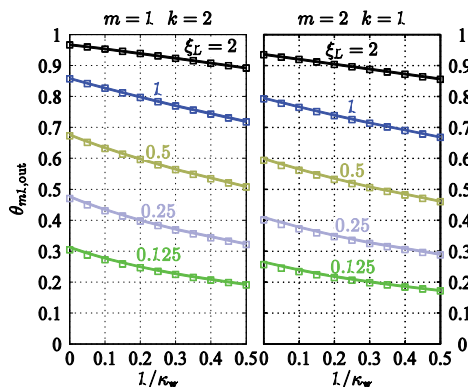


Figure 2. Variation of the outlet bulk temperature of fluid 1 with the wall thermal resistance $1/\kappa_w$ for several heat exchanger lengths ξ_L corresponding to $m = 1, k = 2$ (left) and $m = 2, k = 1$ (right), as obtained from the numerical integration of Eqs. (1) – (4) (solid lines) and from the approximate two-term solution (symbols).

The aim of the following sections is to extend the present analysis to the study of laminar counterflow heat exchangers with small-scale wall corrugations. It will be shown that when the corrugation wavelength and amplitude are small compared to the channel half-widths, the effect of the corrugated wall on the bulk flow is similar to that of a thickened virtual plane surface with an apparent thermal resistance that has to be obtained numerically. We shall begin in Section 3 investigating the local conjugate heat-transfer problem that provides this apparent thermal resistance for a fixed wall design, characterized by its shape, thickness, and thermal conductivity, and specified values of the Reynolds and Prandtl numbers of both streams. The

analysis will provide the apparent values of the dimensionless parameters m^* , k^* , κ_w^* , and ξ_L^* that should be used in the bulk flow model to incorporate the effect of small-scale wall corrugations and evaluate the corresponding changes in heat exchanger performance.

3. Wall corrugation model

In this section, we analyze the incompressible two-dimensional shear-induced flow of two constant property fluids $i = 1, 2$, that exchange heat through a thin corrugated wall. The wall thickness, δ_w , is assumed to be small compared to the corrugation wavelength, λ , so that the dimensionless wall thickness, $\Delta_w = \delta_w / \lambda \ll 1$, emerges naturally as a small parameter. In addition, the Reynolds numbers of the shear flows at both sides of the wall, $Re_{\tau_i} = \rho_i \lambda^2 \tau_i / \mu_i^2$, based on the shear stress far from the wall, τ_i , the corrugation wavelength, λ , and the fluid density, ρ_i and viscosity, μ_i of fluid i , are also assumed to be sufficiently small for the flows to remain laminar and steady.

The mathematical formulation of the problem can be written in non-dimensional form using the corrugation wavelength λ as appropriate length scale. The resulting Cartesian dimensionless coordinates (x, y, z) are shown in Figure 3. The wall geometry is assumed to be a periodic function of the x -coordinate, while the y -coordinate is defined normal to the mean plane of the corrugated wall pointing from fluid 1 to fluid 2. The z -coordinate is perpendicular to the x - y plane shown in the figure.

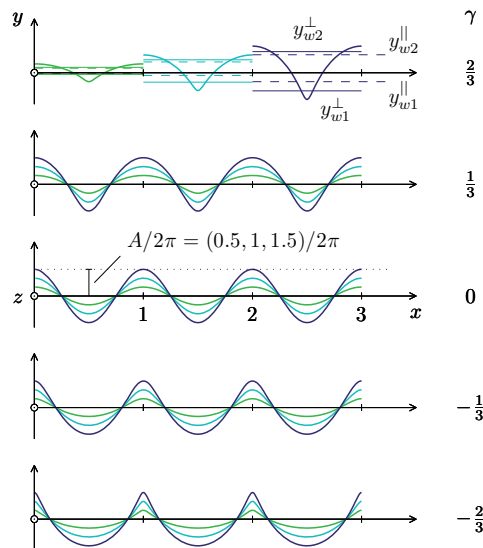


Figure 3. Schematic representation of the wall geometry defined by the functions $x_w(\alpha)$ and $y_w(\alpha)$ given by Eq. (15). The upper plot illustrates the apparent wall position for Stokes flow (i.e., $Re=0$) parallel (y_{wi}^{\parallel} , dashed lines) and transverse (y_{wi}^{\perp} , solid lines) to the corrugations for the three corrugation amplitudes $A/2\pi = [0.5, 1, 1.5]/2\pi$ considered in the figure.

For illustrative purposes, we define the corrugation shape using the parametric representation

$$x = x_w(\alpha) = \frac{\alpha + \gamma \sin(\alpha)}{2\pi}, \quad y = y_w(\alpha) = \frac{A}{2\pi} \cos(\alpha), \quad \alpha \in \mathbb{R}, \quad (15)$$

adopted from [24]. Here, $A \geq 0$ measures the amplitude of the corrugations, $A/2\pi$ being an effective amplitude-to-wavelength ratio, and $-1 \leq \gamma \leq 1$ represents a suitable scallop parameter. As previously discussed, we further assume that the dimensionless wall thickness is small, $\Delta_w \ll 1$, as often occurs in the applications. The surface thus defined is periodic and symmetric with respect to x , with the x -axis located midway between the highest and lowest points of the corrugations, and with values of $y_w(\alpha)$ ranging between $\pm A/2\pi$. The parameter γ has a strong influence on the corrugation shape. Thus, for $\gamma = 0$ the surface adopts a wavy (i.e., sinusoidal) shape devoid of any irregularities, whereas for $0 < |\gamma| < 1$ it develops a scalloped geometry that becomes more and more pronounced for increasing values of $|\gamma|$, with downward (upward) cusps appearing in the surface as $\gamma \rightarrow 1$ (-1). Note that the amplitude parameter A also represents the maximum slope of the sinusoidal surface $y_w = (A/2\pi)\cos(2\pi x)$ obtained for $\gamma = 0$.

The velocity of fluid i is measured with the characteristic shear velocity $\lambda\tau_i/\mu_i$ to give the dimensionless velocity field $\mathbf{u} = (u, v, w)$. The variations in pressure with respect to its unperturbed value far from the wall are scaled in fluid i with the corresponding shear stress, τ_i , to give the dimensionless pressure, p . Finally, the characteristic temperature $q\lambda/k_1$, based on the corrugation wavelength, λ , the heat conductivity of fluid 1, k_1 , and the overall heat flux, q , transferred from fluid 2 to fluid 1, is used to define the dimensionless temperature T . Note that the thermal coupling through the heat conducting wall enforces the use of a common temperature scale for both fluids.

Assuming that the pressure, velocity, and temperature fields are translation invariant along the z -axis, the continuity, momentum, and energy conservation equations take the form

$$\begin{aligned} \frac{\partial u}{\partial x} + \frac{\partial v}{\partial y} &= 0 \\ \text{Re}_{\tau_i} \left(u \frac{\partial u}{\partial x} + v \frac{\partial u}{\partial y} \right) &= -\frac{\partial p}{\partial x} + \frac{\partial^2 u}{\partial x^2} + \frac{\partial^2 u}{\partial y^2} \\ \text{Re}_{\tau_i} \left(u \frac{\partial v}{\partial x} + v \frac{\partial v}{\partial y} \right) &= -\frac{\partial p}{\partial y} + \frac{\partial^2 v}{\partial x^2} + \frac{\partial^2 v}{\partial y^2} \\ \text{Re}_{\tau_i} \left(u \frac{\partial w}{\partial x} + v \frac{\partial w}{\partial y} \right) &= \frac{\partial^2 w}{\partial x^2} + \frac{\partial^2 w}{\partial y^2} \\ \text{Re}_{\tau_i} \text{Pr}_i \left(u \frac{\partial T}{\partial x} + v \frac{\partial T}{\partial y} \right) &= \frac{\partial^2 T}{\partial x^2} + \frac{\partial^2 T}{\partial y^2} \end{aligned} \quad (16)$$

where viscous dissipation has been neglected in the energy balance and $\text{Pr}_i = \nu_i/\alpha_i = \mu_i/(k_i/c_i)$ denotes again the Prandtl number of fluid i . The above equations must be integrated in the periodic domain $0 < x < 1$ for fluids 1 and 2, located, respectively, below ($-\infty < y < y_w$) and above

($y_w^+ < y < \infty$) the wall. Hereafter we shall use y_w to denote the wall position, y_w^\pm representing the lower (-) and upper (+) wall surfaces.

As boundary conditions we impose periodicity at $x=0$ and 1, the no-slip boundary condition at the wall

$$y = y_w : \quad u = v = w = 0, \quad (17)$$

and a uniform shear flow far from the wall

$$y \gg 1: \quad \frac{\partial u}{\partial y} = \sin \theta_2, \quad v = 0, \quad \frac{\partial w}{\partial y} = \cos \theta_2, \quad p = 0, \quad (18)$$

$$-y \gg 1: \quad \frac{\partial u}{\partial y} = -\sin \theta_1, \quad v = 0, \quad \frac{\partial w}{\partial y} = -\cos \theta_1, \quad p = 0. \quad (19)$$

In the far field boundary conditions θ_i denotes the angle of misalignment between the wall corrugations and the uniform shear imposed on fluid i far from the wall. So that $\theta_i=0, \pi$, and $\theta_i = \pm\pi/2$ correspond, respectively, to flows parallel ($u = v = p = 0$) and transverse ($w = 0$) to the corrugations, with $\theta_2 = \theta_1$ and $\theta_2 = \theta_1 + \pi$ corresponding, respectively, to co-current and counter-current flow arrangements.

We also impose the overall heat flux transferred by conduction from fluid 2 to fluid 1 by specifying a uniform temperature gradient in fluid 2 far from the wall

$$y \gg 1: \quad \frac{\partial T}{\partial y} = K^{-1}, \quad (20)$$

where $K = k_2/k_1$ denotes the fluid-to-fluid heat conductivity ratio, whereas in fluid 1 we impose a linear temperature profile of the form

$$-y \gg 1: \quad T = y. \quad (21)$$

Note that, due to the invariance of the problem under arbitrary shifts in temperature, we can always add a constant to the temperature distribution of fluid 1 so as to set its apparent value at the mean plane ($y = 0$) of the corrugated wall equal to zero.

In the thin wall limit considered here, $\Delta_w \ll 1$, the jump conditions for the temperature and the wall-normal heat fluxes at the heat conducting wall can be written as

$$y = y_w : \begin{cases} T_w^+ - T_w^- = \frac{\Delta_w}{K_w} \left[\frac{v_w^+ + v_w^-}{2} + \mathcal{O}(\Delta_w^2) \right] \\ v_w^+ - v_w^- = -\Delta_w K_w \left[\frac{1}{2} \left(\frac{d^2 T_w^+}{ds^2} + \frac{d^2 T_w^-}{ds^2} \right) + \mathcal{O}(\Delta_w^2) \right] \end{cases} \quad (22)$$

where $T_w^\pm = T(x_w(\alpha), y_w^\pm(\alpha))$ denotes the temperature at the upper (+) and lower (-) wall surfaces, and

$$v_w^+ = K \frac{\partial T(x_w(\alpha), y_w^+(\alpha))}{\partial n}, \quad v_w^- = \frac{\partial T(x_w(\alpha), y_w^-(\alpha))}{\partial n} \quad (23)$$

are the local wall-normal heat fluxes transferred by conduction from fluid 2 to the wall, and from the wall to fluid 1, respectively. In the above expressions, n represents the local wall-normal coordinate pointing from fluid 1 to fluid 2, and s is the arc-length coordinate measured along the wall, defined by

$$ds = \sqrt{x_w'^2(\alpha) + y_w'^2(\alpha)} d\alpha. \quad (24)$$

In addition to the dimensionless wall thickness, Δ_w , the jump conditions (22) involve the wall-to-fluid heat conductivity ratio, $K_w = k_w/k_1$, as an additional dimensionless parameter; the wall temperature difference being proportional to Δ_w/K_w , whereas the jump in wall-normal heat fluxes is proportional to $\Delta_w K_w$. As a result, in the formal limit $\Delta_w \rightarrow 0$ both Δ_w and K_w disappear from the formulation and the jump conditions (22) reduce to the continuity of temperatures, $T_w^+ = T_w^-$, and wall-normal heat fluxes, $v_w^+ = v_w^-$.

Inspection of the mathematical problem stated above shows that the steady conjugate heat transfer between two shear-induced flows separated by a corrugated wall can be characterized by the Reynolds and Prandtl numbers of the two fluid streams, Re_{τ_i} and Pr_i , the fluid-to-fluid and wall-to-fluid heat conductivity ratios, $K = k_2/k_1$ and $K_w = k_w/k_1$, the dimensionless wall thickness, $\Delta_w = \delta_w/\lambda \ll 1$, the angles of misalignment between the imposed shear and the direction of the corrugations, θ_i , and the dimensionless wall geometry, determined here by the parameters A and γ . Thus, for a fixed wall geometry the solution of the problem depends on the nine dimensionless parameters: Re_{τ_1} , Re_{τ_2} , Pr_1 , Pr_2 , K , K_w , Δ_w , θ_1 , and θ_2 .

In addition to the velocity, pressure, and temperature fields, the solution of the problem determines the virtual no-slip plane wall location for the flows parallel (y_{wi}^{\parallel}) and transverse (y_{wi}^{\perp}) to the corrugations

$$\begin{aligned} y_{w2}^{\parallel} &= \lim_{y \rightarrow \infty} \left(y - \frac{w}{\cos \theta_2} \right), & y_{w2}^{\perp} &= \lim_{y \rightarrow \infty} \left(y - \frac{u}{\sin \theta_2} \right), \\ y_{w1}^{\parallel} &= \lim_{y \rightarrow -\infty} \left(y + \frac{w}{\cos \theta_1} \right), & y_{w1}^{\perp} &= \lim_{y \rightarrow -\infty} \left(y + \frac{u}{\sin \theta_1} \right), \end{aligned} \quad (25)$$

as well as the apparent temperature jump at $y = 0$

$$\Delta T = \lim_{y \rightarrow \infty} (T - K^{-1}y). \quad (26)$$

The conjugate heat transfer problem stated in Eqs. (16) – (22) can be solved numerically using standard finite-difference or finite-volume methods. A closer inspection reveals that the transverse flow problem (u, v, p) is uncoupled from the longitudinal flow (w) and thermal (T) problems, so that it can be integrated first; the resulting velocity field being required to evaluate the convective terms in the equations for w and T . Since the transverse flow field is two-

dimensional, a vorticity-streamfunction formulation was adopted for the numerical integration, thereby avoiding the determination of the pressure field, which is not required here. Fourth-order finite differences were used for the spatial discretization, resulting in a five-point explicit scheme. An algebraic non-orthogonal coordinate transformation was previously employed to map the complex fluid domain onto a square computational domain with uniform grid spacing, thereby enabling a simple treatment of the wall curvilinear boundaries. The far field boundary conditions (18) – (21) were imposed sufficiently far from the wall to ensure the independence of the solution on the size of the numerical domain. The solution was then marched in pseudo-time until a converged (i.e., steady) solution was obtained. A grid independence study was carried out to ensure at least 4 significant digits in the reported values of y_{wi}^{\parallel} , y_{wi}^{\perp} and ΔT .

Although the formulation presented above is of great generality, the large number of parameters involved makes unfeasible a thorough parametric study. As a result, the analysis will be restricted here to the case of two-dimensional counter-current flows, $\theta_2 = -\theta_1 = \pi/2$, transverse to sinusoidal corrugations, $\gamma = 0$. Figure 4 presents illustrative results for $Pr_i = 5$, $K = 2$, $K_w = 0.1$, $\Delta_w = 0.1$, $A = 1$, and different values of $Re_{ci} = [32, 128, 512]$. As can be seen, the flow exhibits the typical low-velocity recirculation regions within the corrugation troughs, which grow spatially with the Reynolds number. The presence of this quasi-stagnant fluid in the vicinity of the wall modifies the overall wall thermal resistance, thereby changing the effectiveness of the heat exchange process in a way that is to be determined below.

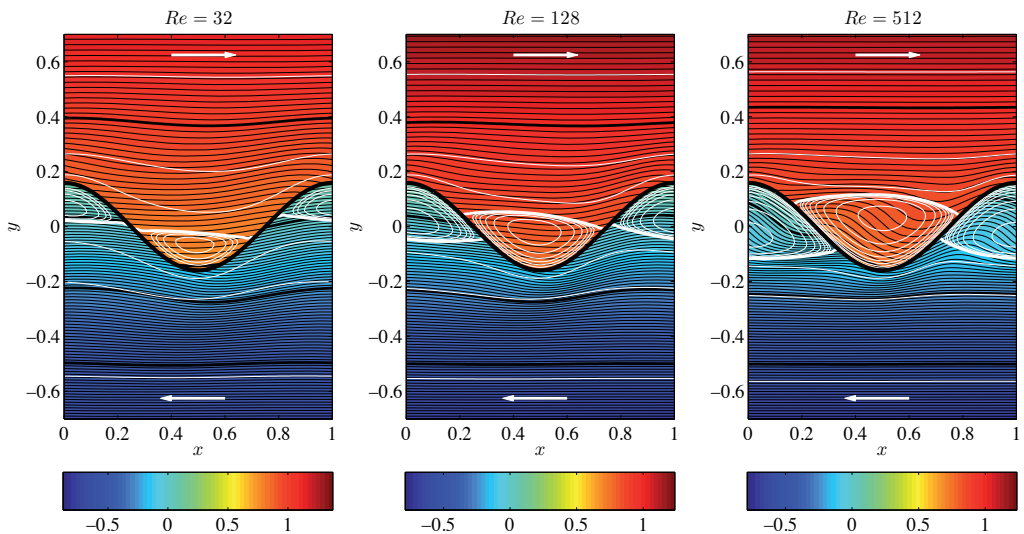


Figure 4. Streamlines (white contours) obtained for $A = 1$, $\gamma = 0$, $\theta_2 = -\theta_1 = \pi/2$, and $Re_{ci} = [32, 128, 512]$, and temperature field (black contours and colored background; see colorbars for the color scale) corresponding to $Pr_i = 5$, $K = 2$, $K_w = 0.1$, and $\Delta_w = 0.1$. The parameters defining the thickened virtual plane surface, obtained from the three simulations shown in the figure, are $y_{w2}^{\perp} = -y_{w1}^{\perp} = [0.1032, 0.1084, 0.1167]$ and $\Delta T = [0.8092, 0.8081, 0.7688]$.

Figure 5 top shows the effect of the Reynolds number on the virtual no-slip plane wall location for flow transverse to the corrugations, y_{wi}^{\perp} , given by Eq. (25). As can be seen, the growth of

the recirculation regions observed in Figure 4 results in an apparent thickening of the virtual plane wall for increasing values of Re_{τ_i} . On the other hand, for decreasing Re_{τ_i} the value of y_{wi}^\perp approaches the asymptotic (i.e., Stokes-flow) limit provided by the semi-analytical solution of Luchini et al. [25], recalculated here as an additional check of the accuracy of the numerical method. Figure 5 (bottom) shows the influence of the Reynolds number Re_{τ_i} on the apparent temperature jump ΔT at $y = 0$, defined by Eq. (26). As can be seen, for low wall conductivities ΔT takes positive values due to the correspondingly large wall thermal resistance. However, for high wall conductivities ΔT becomes negative due to the effect of longitudinal heat conduction along the wall, which provides an efficient way of transferring heat from the corrugation crests to the troughs, making the wall to behave as an effective thermal shortcut. This mechanism, which is absent for $K_w \ll 1$, becomes dominant for $K_w \gg 1$, leading to the negative values of ΔT reported in the last plot of Figure 5. It is also interesting to note that although ΔT tends to decrease for increasing values of Re_{τ_i} due to the enhancement of heat transfer by convection, in poorly conductive walls this trend is partially reversed for Re_{τ_i} in the range 100 – 200, when the downstream stagnation points of the swirling cells that develop at each side of the wall come closer to each other; see, e.g, Figure 4.

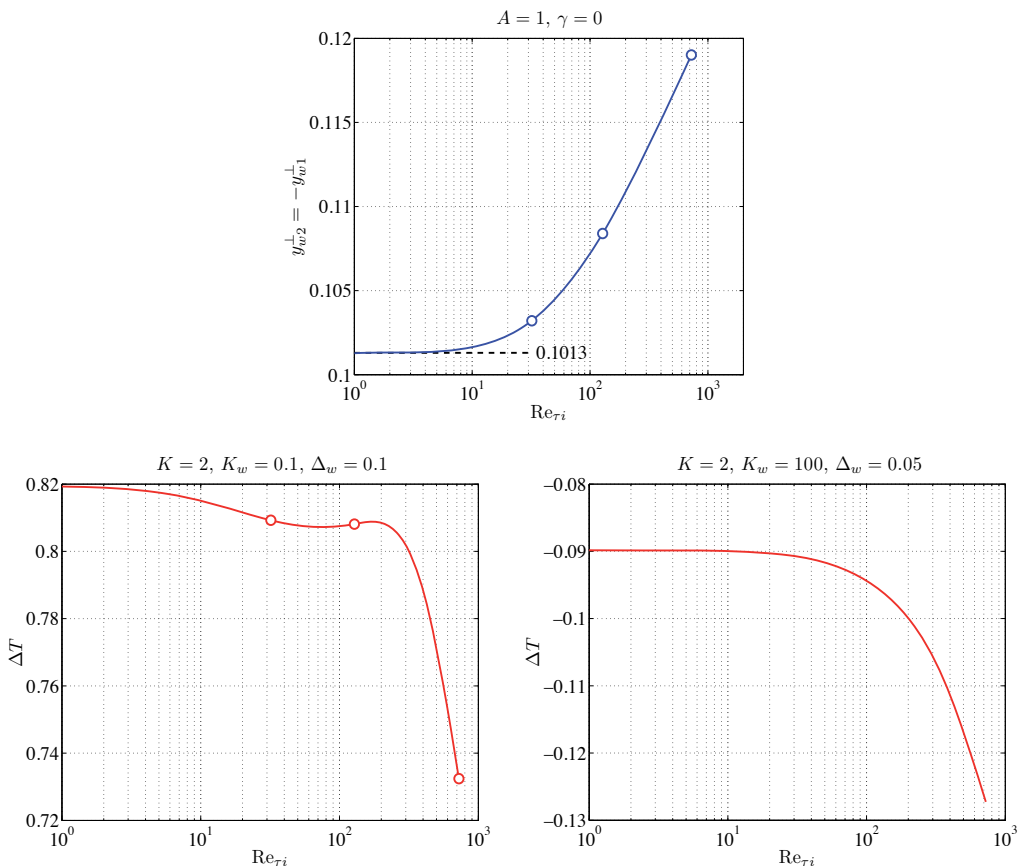


Figure 5. Top: Variation with the Reynolds number of the apparent plane wall location for flow transverse to the corrugations obtained numerically for $A = 1, \gamma = 0$. Bottom: Variation with the Reynolds number of the normalized apparent

wall temperature jump ΔT for values of $Pr_i = 5$, K , K_w and Δ_w representative of low (left) and high (right) conductive walls. The open symbols indicate values obtained from the simulations of Figure 4.

4. Combined multi-scale model

The virtual plane wall concept introduced in Section 3 can be used in numerical simulations of corrugated-plate, or -tube, heat exchangers to account for the effect of small-scale wall corrugations in a computationally effective way. According to the results presented above, the corrugated wall behaves as a virtual plane wall of apparent thickness

$$\Delta_w^* = y_{w2}^\perp + \Delta_w - y_{w1}^\perp > \Delta_w, \quad (27)$$

with an apparent wall temperature jump

$$\Delta T^* = K^{-1} y_{w2}^\perp + \Delta T - y_{w1}^\perp > \Delta T. \quad (28)$$

This virtual wall separates two fluid channels of apparent half-widths

$$a_i^* = a_i - \lambda |y_{w,i}^\perp| = a_i \left(1 - \frac{\lambda}{a_i} |y_{w,i}^\perp| \right) < a_i, \quad (29)$$

smaller than the average channel half-widths, a_i , as a result of the apparent wall displacement introduced by the corrugations, which effectively reduces the hydraulic diameter of the channels. From here on, all apparent quantities obtained from the application of the virtual plane wall concept will be denoted by a superscript asterisk (*).

Note that the dimensionless corrugation wavelength, $\Lambda_i = \lambda/a_i$, appearing explicitly in Eq. (29) must be small compared to unity for the present multi-scale asymptotic analysis to hold. Otherwise the flow perturbations induced by the corrugations would significantly alter the flow in the channels, which will no longer resemble a planar Poiseuille flow, as assumed in Section 2.

Using Eq. (29) to evaluate the apparent channel half-widths, we obtain the apparent value of parameter

$$k^* = \frac{k_2 a_1^*}{k_1 a_2^*} = \frac{k_2 a_1}{k_1 a_2} \left(\frac{a_1^* / a_1}{a_2^* / a_2} \right) = k \frac{\left(1 - \frac{\lambda}{a_1} |y_{w,1}^\perp| \right)}{\left(1 - \frac{\lambda}{a_2} |y_{w,2}^\perp| \right)}. \quad (30)$$

The apparent value of $\kappa_w^* = (k_w / \delta_w)^* (a_1^* / k_1)$ can be determined from the dimensional apparent wall temperature jump $(q\lambda / k_1) \Delta T^*$, where ΔT^* is given by Eq. (28) in terms of the computed

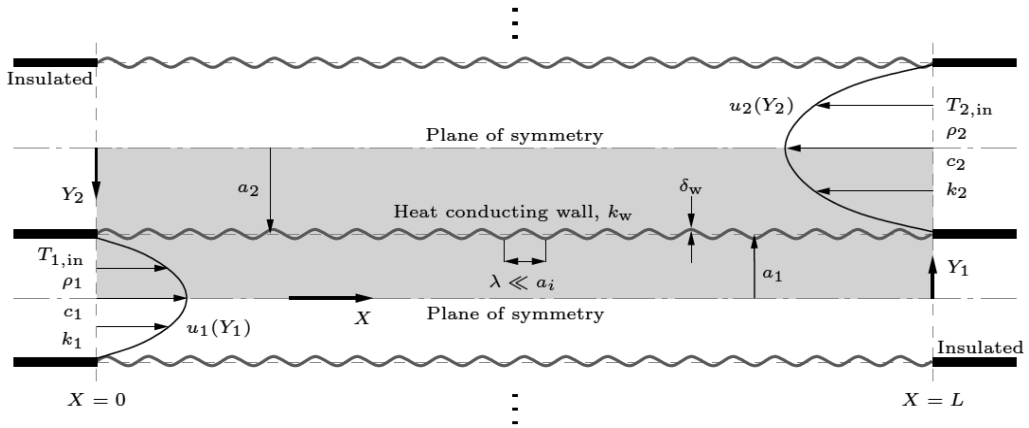


Figure 6. A corrugated heat conducting wall of finite thickness, δ_w and thermal conductivity, k_w separates the channels of fluids 1 and 2 with average half-widths a_1 and a_2 , respectively. The wall corrugation amplitude and wavelength are both assumed to be small compared to a_i .

values of $y_{w,i}^\perp$ and ΔT . Multiplying the apparent wall temperature jump by $(k_w/\delta_w)^* = \kappa_w^*(k_1/a_1^*)$ we should recover the overall heat flux transferred by conduction from fluid 2 to fluid 1, i.e., $q = (q\lambda/k_1)\Delta T^* \kappa_w^*(k_1/a_1^*)$, whence solving for κ_w^* we get

$$\kappa_w^* = \frac{a_1^*}{\lambda \Delta T^*} = \frac{a_1}{\lambda \Delta T^*} \left(1 - \frac{\lambda}{a_1} |y_{w,1}^\perp| \right) = \underbrace{\left(\frac{a_1 k_w}{\delta_w k_1} \right)}_{\kappa_w} \underbrace{\left(\frac{\delta_w k_1}{\lambda k_w} \right)}_{\Delta_w/K_w} \frac{1}{\Delta T^*} \left(1 - \frac{\lambda}{a_1} |y_{w,1}^\perp| \right) = \frac{\kappa_w}{\Delta T} \left(1 - \frac{\lambda}{a_1} |y_{w,1}^\perp| \right). \quad (31)$$

In the above expression we have expressed κ_w^* in terms of the normalized apparent wall temperature jump

$$\overline{\Delta T} = \frac{\Delta T^*}{\Delta_w / K_w} \quad (32)$$

a quantity defined so that it tends to unity as the amplitude of the corrugations tends to zero ($A \rightarrow 0$). In this limiting case, when $y_{w,1}^\perp$ also tends to zero, Eq. (31) reduces to $\kappa_w^* = \kappa_w \equiv (k_w/\delta_w)(a_1/k_1)$, and the original expression for κ_w given in Eq. (5) for a flat wall of finite thickness, δ_w , and thermal conductivity, k_w , is recovered. Note also that, by definition, the values of κ_w , K_w , $\Delta_w \ll 1$, and $\Lambda \ll 1$ verify the following relation

$$\kappa_w = \frac{a_1 k_w}{\delta_w k_1} = \frac{a_1 \lambda k_w}{\lambda \delta_w k_1} = \frac{K_w}{\Lambda \Delta_w} \quad (33)$$

which provides κ_w explicitly in terms of K_w , Δ_w , and Λ .

Figure 7 shows the influence of the Reynolds number, Re_{ti} on the normalized apparent wall temperature jump, $\overline{\Delta T}$, for the same values of K , K_w and Δ_w considered in Figure 5. As can be seen, for low-conductive walls $\overline{\Delta T}$ remains slightly below unity regardless of the Reynolds number. In this case, the relatively high conductivity of the recirculating fluids combined with the higher surface area of the corrugated wall results in a smaller apparent wall temperature jump as compared to the originally flat wall. On the other hand, for high-conductive walls $\overline{\Delta T}$ takes values well above unity, indicating that in this case the presence of low-conductive recirculating fluids within the corrugation troughs significantly increases the apparent wall temperature jump. In both cases, $\overline{\Delta T}$ exhibits a non-monotonous behavior with Re_{ti} that ends in an abrupt reduction for Reynolds numbers Re_{ti} above 300 or so.

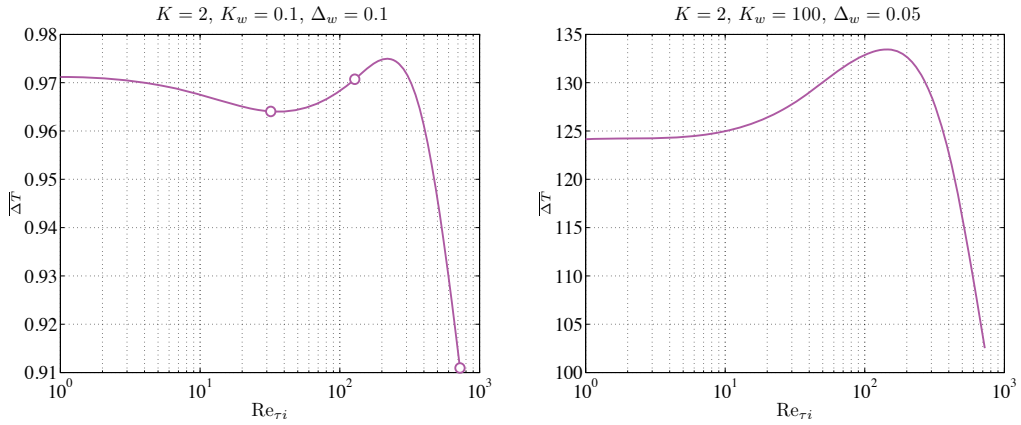


Figure 7. Variation with the Reynolds number of the normalized apparent wall temperature jump $\overline{\Delta T}$ for values of $Pr_i = 5$, K , K_w and Δ_w representative of low (left) and high (right) conductive walls. The open symbols correspond to results obtained from the simulations of Figure 4.

For the plane Poiseuille flow considered in this work, the wall shear stress is given by $\tau_i = 3\mu_i V_i / a_i$, which upon substitution in the expression for Re_{ti} yields the relation

$$Re_{ti} = \frac{\rho_i \lambda^2 \tau_i}{\mu_i} = \frac{3}{2} \left(\frac{\lambda}{a_i} \right)^2 \frac{2\rho_i V_i a_i}{\mu_i} = \frac{3}{2} \Lambda_i^2 Re_i, \quad (34)$$

stating that the ratio between the Reynolds numbers Re_{ti} and Re_i equals 3/2 times the square of the dimensionless wall corrugation wavelength, $\Lambda_i = \lambda/a_i \ll 1$. Since in plane Poiseuille flow finite-amplitude disturbances are known to drive transition to turbulence at Reynolds numbers as low as $Re_{i,crit} \cong 1330$ [23], the above expression severely limits the maximum value of Re_{ti} compatible with steady laminar flow in the channels. Thus, for the moderately large value of Λ_i considered below ($\Lambda_i = 0.25 \ll 1$) the maximum allowable value of Re_{ti} turns out to

be 125. From the results shown in Figure 7, it is clear that below this critical Reynolds number the normalized wall temperature jump $\overline{\Delta T}$ remains almost constant, with convective effects accounting only for small variations of $\overline{\Delta T}$ of order 1% for $K_w = 0.1$ and 7% for $K_w = 100$. Thus, to get a first idea of the effect of the corrugations on the performance of the heat exchanger we may simply evaluate κ_w^* using Eq. (31) with the value of $\overline{\Delta T}$ corresponding to $Re_{ti} = 0$.

To quantify this effect, let us consider the ratio between the overall heat transfer rate, $\dot{m}c_1(T_{m1,out} - T_{1,in})$, and the mechanical power required to drive the flow, characterized here by the pumping power, $\Delta P_1 Q_1$, delivered to fluid 1. Normalizing this ratio with that of a flat-wall heat exchanger, we introduce the overall augmentation heat-transfer number

$$R_a = \frac{\left[\frac{\dot{m}_1 c_1 (T_{m1,out} - T_{1,in})}{\Delta P_1 Q_1} \right]_{\text{corr}}}{\left[\frac{\dot{m}_1 c_1 (T_{m1,out} - T_{1,in})}{\Delta P_1 Q_1} \right]_{\text{flat}}}, \quad (35)$$

where $T_{m1,out}$ denotes the outlet bulk temperature of fluid 1. As previously discussed, this temperature is closely related to the heat exchanger effectiveness, $\varepsilon = (T_{m1,out} - T_{1,in}) / (T_{2,in} - T_{1,in})$, when fluid 1 has the smallest heat capacity flow rate. For the plane Poiseuille flow considered in this work the pressure drop, ΔP_i , the volume flow rate, Q_i , and the mass flow rate, \dot{m}_i , are given respectively by

$$\Delta P_i = \frac{3\mu_i V_i}{a_i^2} L, \quad Q_i = 2a_i V_i, \quad \dot{m}_i = \rho_i Q_i. \quad (36)$$

Using these expressions in Eq. (35), the overall augmentation heat-transfer number can be expressed as

$$R_a = \left(\frac{a_1^*}{a_1} \right)^2 \frac{V_1}{V_1^*} \frac{\varepsilon^*}{\varepsilon}. \quad (37)$$

A thorough optimization of the heat exchange process requires also comparison of the entropy generation rates achieved with corrugated and flat walls. As a first attempt to use the entropy minimization method [26,27,28] for the thermodynamic optimization of corrugated-wall heat exchangers, we introduce the augmentation entropy generation number

$$N_a = \frac{\dot{S}_{\text{corr}}}{\dot{S}_{\text{flat}}} = \frac{\left(\frac{\dot{S}}{\dot{m}_1 c_1} \right)_{\text{corr}} \left(\dot{m}_1 c_1 \right)_{\text{corr}}}{\left(\frac{\dot{S}}{\dot{m}_1 c_1} \right)_{\text{flat}} \left(\dot{m}_1 c_1 \right)_{\text{flat}}} = \frac{\left(\frac{\dot{S}}{\dot{m}_1 c_1} \right)_{\text{corr}} \left(\frac{Q_1^*}{Q_1} \right)}{\left(\frac{\dot{S}}{\dot{m}_1 c_1} \right)_{\text{flat}} \left(\frac{Q_1}{Q_1} \right)} = \frac{\left(\frac{\dot{S}}{\dot{m}_1 c_1} \right)_{\text{corr}} \left(\frac{a_1^* V_1^*}{a_1 V_1} \right)}{\left(\frac{\dot{S}}{\dot{m}_1 c_1} \right)_{\text{flat}} \left(\frac{a_1 V_1}{a_1 V_1} \right)} \quad (38)$$

defined as the ratio of the entropy generation rates with corrugated and flat plates. In the above expression $\dot{S}/\dot{m}_1 c_1$ denotes the dimensionless entropy generation rate, which is approximated by

$$\begin{aligned} \frac{\dot{S}}{\dot{m}_1 c_1} &\cong \frac{\dot{S}_1 + \dot{S}_2}{\dot{m}_1 c_1} \cong \ln \frac{T_{m1,out}}{T_{1,in}} + \frac{\overbrace{\dot{m}_2 c_2}^{mk}}{\dot{m}_1 c_1} \ln \frac{T_{m2,out}}{T_{2,in}} = \ln \left[\frac{T_{m1,out}}{T_{1,in}} \left(\frac{T_{m2,out}}{T_{2,in}} \right)^{mk} \right] \\ &= \ln \left[\left(1 + \varepsilon \frac{\Delta T}{T_{1,in}} \right) \left(\frac{1}{1 + \Delta T/T_{1,in}} \right)^{mk} \left(1 + \left(1 - \frac{\varepsilon}{mk} \right) \frac{\Delta T}{T_{1,in}} \right)^{mk} \right], \end{aligned} \quad (39)$$

where entropy changes associated with viscous dissipation (i.e., pressure drop irreversibility) and heat conduction in the wall have both been neglected. These changes should be retained in a detailed second-law analysis of heat exchanger performance, which is not to be pursued in this work, as they may be critical for the thermodynamic optimization of the heat transfer equipment [29]. It should be noted that the evaluation of the dimensionless entropy generation rate requires the introduction of the dimensionless temperature difference $\Delta T/T_{1,in} = (T_{2,in} - T_{1,in})/T_{1,in}$ or, alternatively, the temperature ratio $T_{2,in}/T_{1,in} = \Delta T/T_{1,in} + 1$, as an additional parameter of the problem.

Combining Eqs. (38) and (39), we obtain the final expression for the augmentation entropy generation number

$$N_a = \frac{\ln \left[\left(1 + \varepsilon^* \frac{\Delta T}{T_{1,in}} \right) \left(\frac{1}{1 + \Delta T/T_{1,in}} \right)^{m^* k^*} \left(1 + \left(1 - \frac{\varepsilon^*}{m^* k^*} \right) \frac{\Delta T}{T_{1,in}} \right)^{m^* k^*} \right]}{\ln \left[\left(1 + \varepsilon \frac{\Delta T}{T_{1,in}} \right) \left(\frac{1}{1 + \Delta T/T_{1,in}} \right)^{mk} \left(1 + \left(1 - \frac{\varepsilon}{mk} \right) \frac{\Delta T}{T_{1,in}} \right)^{mk} \right]} \left(\frac{a_1^* V_1^*}{a_1 V_1} \right). \quad (40)$$

The remaining two apparent parameters of the bulk flow model, i.e., m^* and ξ_{L^*} , involve by definition the Peclet numbers of the fluid streams. To evaluate their apparent values we must therefore specify the apparent Peclet numbers, Pe_i^* , in the heat exchanger with corrugated walls. To this end, we shall consider three different flow constraints, namely: i) constant flow rate, ii) constant pumping power, and iii) constant pressure drop.

i. Constant flow rate

To ensure that the volume flow rate $Q_i = 2a_i V_i$ of fluid i is the same with flat and corrugated walls, the average flow velocity V_i^* must grow to compensate for the reduction of the channel half-width

$$V_i^* a_i^* = V_i a_i \Rightarrow V_i^* = V_i \frac{a_i}{a_i^*} = V_i \left(1 - \frac{\lambda}{a_i} |y_{w,i}^\perp| \right)^{-1} \quad (41)$$

In this case, the apparent value of Pe_i , defined with the apparent velocities and channel half-widths, remains unchanged

$$Pe_i^* = \frac{2a_i^* V_i^*}{\alpha_i} = \frac{2a_i V_i}{\alpha_i} = Pe_i, \quad (42)$$

while the apparent values of m and ξ_L are given by

$$m^* = \frac{Pe_2^* a_2^*}{Pe_1^* a_1^*} = \frac{Pe_2 a_2}{Pe_1 a_1} \left(\frac{a_2^* / a_2}{a_1^* / a_1} \right) = m \frac{\left(1 - \frac{\lambda}{a_2} |y_{w,2}^\perp| \right)}{\left(1 - \frac{\lambda}{a_1} |y_{w,1}^\perp| \right)} \Rightarrow m^* k^* = mk, \quad (43)$$

$$\xi_L^* = \frac{L}{a_1^* Pe_1^*} = \frac{L}{a_1 Pe_1} \left(\frac{a_1}{a_1^*} \right) = \xi_L \left(1 - \frac{\lambda}{a_1} |y_{w,1}^\perp| \right)^{-1} \quad (44)$$

Using (29) and (41) in (37), the overall augmentation heat-transfer parameter takes the form

$$R_a = \left(1 - \frac{\lambda}{a_1} |y_{w,1}^\perp| \right)^3 \frac{\varepsilon^*}{\varepsilon} \quad (45)$$

ii. Constant pumping power

The pumping power is equal to the product of the volume flow rate, $2a_i V_i$, by the pressure drop, $3\mu_i L V_i / a_i^2$. To ensure that the pumping power remains the same with flat and corrugated walls, the average flow velocity V_i^* of fluid i must satisfy the condition

$$\frac{V_i^{*2}}{a_i^*} = \frac{V_i^2}{a_i} \Rightarrow V_i^* = V_i \left(\frac{a_i^*}{a_i} \right)^{\frac{1}{2}} = V_i \left(1 - \frac{\lambda}{a_i} |y_{w,i}^\perp| \right)^{\frac{1}{2}} \quad (46)$$

In this case, the apparent values of Pe_i , m , and ξ_L are given by

$$Pe_i^* = \frac{2a_i^* V_i^*}{\alpha_i} = \frac{2a_i V_i}{\alpha_i} \left(\frac{a_i^* V_i^*}{a_i V_i} \right) = Pe_i \left(1 - \frac{\lambda}{a_i} |y_{w,i}^\perp| \right)^{\frac{3}{2}}, \quad (47)$$

$$m^* = m \left[\frac{1 - \frac{\lambda}{a_2} |y_{w,2}^\perp|}{1 - \frac{\lambda}{a_1} |y_{w,1}^\perp|} \right]^{\frac{5}{2}} \Rightarrow m^* k^* = mk \left[\frac{1 - \frac{\lambda}{a_2} |y_{w,2}^\perp|}{1 - \frac{\lambda}{a_1} |y_{w,1}^\perp|} \right]^{\frac{3}{2}}, \quad (48)$$

$$\xi_L^* = \xi_L \left(1 - \frac{\lambda}{a_1} |y_{w,1}^\perp| \right)^{-\frac{5}{2}}, \quad (49)$$

and, using (29) and (46) in (37), the overall augmentation heat-transfer number takes the form

$$R_a = \left(1 - \frac{\lambda}{a_1} |y_{w,1}^\perp| \right)^{\frac{3}{2}} \frac{\varepsilon^*}{\varepsilon}. \quad (50)$$

iii. Constant pressure drop

To ensure that pressure drop $\Delta P_i = 3\mu_i L V_i / a_i^2$ of fluid i remains the same with flat and corrugated walls, the apparent average flow velocity V_i^* of fluid i must satisfy the condition

$$\frac{V_i^*}{a_i^{*2}} = \frac{V_i}{a_i^2} \Rightarrow V_i^* = V_i \left(\frac{a_i^*}{a_i} \right)^2 = V_i \left(1 - \frac{\lambda}{a_i} |y_{w,i}^\perp| \right)^2. \quad (51)$$

In this case, the apparent values of Pe_i , m , and ξ_L are given by

$$Pe_i^* = Pe_i \left(1 - \frac{\lambda}{a_i} |y_{w,i}^\perp| \right)^3, \quad (52)$$

$$m^* = m \left[\frac{1 - \frac{\lambda}{a_2} |y_{w,2}^\perp|}{1 - \frac{\lambda}{a_1} |y_{w,1}^\perp|} \right]^4 \Rightarrow m^* k^* = mk \left[\frac{1 - \frac{\lambda}{a_2} |y_{w,2}^\perp|}{1 - \frac{\lambda}{a_1} |y_{w,1}^\perp|} \right]^3, \quad (53)$$

$$\xi_L^* = \xi_L \left(1 - \frac{\lambda}{a_1} |y_{w,1}^\perp| \right)^{-4}, \tag{54}$$

and, using (29) and (51) in (37), the overall augmentation heat-transfer number takes the form

$$R_a = \frac{\varepsilon^*}{\varepsilon}. \tag{55}$$

The expressions derived above provide the apparent values m^* , k^* , κ_w^* , and ξ_L^* in terms of the parameters of the bulk flow model m , k , κ_w , and ξ_L corresponding to a flat heat exchanger, and of the numerically computed values of $y_{w,i}^\perp$ and $\overline{\Delta T}$. These apparent values can then be used in the expressions of the bulk flow model provided in Section 2 to determine the outlet bulk temperature of fluid 1, which provides, in particular, the heat exchanger effectiveness $\varepsilon^* = \theta_{m1,out}(m^*, k^*, \kappa_w^*, \xi_L^*)$ needed to evaluate R_a and N_a . Analytic expressions for N_a can be easily derived from Eq. (40) by substituting the values of $a_1^* V_1^* / a_1 V = Pe_1^* / Pe_1$ and $m^* k^*$ reported in each case, but they have been omitted here for brevity.

5. Results and discussion

In this work we shall restrict our attention to the case of flow transverse ($|\theta_i| = \pi/2$) to sinusoidal corrugations ($\gamma=0$, $y_{w,2}^\perp = -y_{w,1}^\perp$) with equal channel half-widths ($a1=a2$). The analysis of other flow configurations is left for future work. Due to the geometrical symmetries of the problem, the apparent channel half-width can be expressed as

$$a_i^* = a_i - \lambda |y_{w,i}^\perp| = a_i \left(1 - \Lambda |y_{w,i}^\perp| \right) \tag{56}$$

in terms of the single small parameter $\Lambda = \lambda / a_1 = \lambda / a_2 \ll 1$ representing the dimensionless corrugation wavelength. In this case, the expressions for m^* , k^* , κ_w^* , and ξ_L^* , as well as those for the heat-transfer and entropy augmentation numbers R_a and N_w reduce to those given in Table 1.

Table 2 shows the variation of κ_w^* with the dimensionless corrugation amplitude, $A/2\pi$, the dimensionless wall thickness, Δ_w , and the wall-to-fluid and fluid-to-fluid heat conductivity ratios, K_w and K . The results are presented in terms of the ratio $\kappa_w^* / \kappa_w = (1 - \Lambda |y_{w,1}^\perp|) / \overline{\Delta T}$, with κ_w^* expressed as percentage of its reference value $\kappa_w = (k_w / \delta_w)(a_1 / k_1)$ for a flat wall of finite thickness, δ_w , and thermal conductivity, k_w . Different wall designs and conductivity ratios are

Constant flow rate (n = 0)	Constant pumping power (n = 3/2)	Constant pressure drop (n = 3)
	$m^* = m \left(= \frac{Pe_2}{Pe_1} \right)$	
	$k^* = k \left(= \frac{k_2}{k_1} \equiv K \right)$	
	$\kappa_w^* = \kappa_w (1 - \Lambda y_{w,1}^\perp) \frac{1}{\Delta T}$ with $\kappa_w = \frac{K_w}{\Lambda \Delta_w}$	
	$\xi_L^* = \xi_L (1 - \Lambda y_{w,1}^\perp)^{-(n+1)}$	
	$R_a = (1 - \Lambda y_{w,1}^\perp)^{3-n} \frac{\varepsilon^*}{\varepsilon}$	
	$N_a = \frac{\ln \left[\left(1 + \varepsilon^* \frac{\Delta T}{T_{1,in}} \right) \left(\frac{1}{1 + \Delta T / T_{1,in}} \right)^{mk} \left(1 + \left(1 - \frac{\varepsilon^*}{mk} \right) \frac{\Delta T}{T_{1,in}} \right)^{mk} \right]}{\ln \left[\left(1 + \varepsilon \frac{\Delta T}{T_{1,in}} \right) \left(\frac{1}{1 + \Delta T / T_{1,in}} \right)^{mk} \left(1 + \left(1 - \frac{\varepsilon}{mk} \right) \frac{\Delta T}{T_{1,in}} \right)^{mk} \right]} (1 - \Lambda y_{w,1}^\perp)^n$	

Table 1. Expressions determining the apparent values of m^* , k^* , κ_w^* , and ξ_L^* to be used in the bulk flow model to evaluate the effect of the wall corrugations in the case of flow transverse ($|\theta_i| = \pi/2$) to sinusoidal corrugations ($\gamma = 0$, $y_{w,2}^\perp = -y_{w,1}^\perp$) with equal channel half-widths ($a_1 = a_2$). Also given are the expressions for the heat-transfer and entropy augmentation numbers R_a and N_a .

considered, ranging from low to moderate amplitudes and from low- to high-conductive materials. For these and all subsequent calculations, the dimensionless corrugation wavelength has been set equal to $\Lambda = \lambda / a_i = 0.25 \ll 1$.

The results shown in Table 2 indicate that the effect of the corrugations is almost invariably to reduce the apparent wall conductivity κ_w^* (i.e., to increase the wall thermal resistance $1 / \kappa_w^*$). This effect is accentuated for highly conductive walls ($\Delta_w \ll 1$, $K_w \gg 1$) with moderately large corrugation amplitudes ($A \sim 1$), when the quasi-stagnant low-conductive recirculating flow established in the corrugation troughs acts as an effective barrier to heat transfer. By contrast, for poorly conductive walls ($\Delta_w = 0.1$, $K_w \ll 1$) the recirculating fluids have significantly larger conductivity than the wall itself and the wall thermal resistance remains virtually unaffected, showing a small reduction as the corrugation amplitude is increased.

Table 3 shows the effect of the dimensionless corrugation amplitude, $A/2\pi$, on the apparent dimensionless heat-exchanger length ξ_L^* . The results are presented in terms of the ratio ξ_L^* / ξ_L and also as percentage increment of the flat wall value ξ_L for the three cases under study. As can be seen, the presence of the corrugations always increases the apparent dimensionless heat-exchanger length $\xi_L^* = L / a_1^* Pe_1^*$ due to the simultaneous reduction of a_1^* and Pe_1^* (except in the case of constant flow rate), with larger increments corresponding to larger corrugation amplitudes under the constraint of constant pressure drop.

κ_w^* / κ_w		$A = 0.25$			$A = 0.5$			$A = 1$			
		K			K			K			
		0.5	1	2	0.5	1	2	0.5	1	2	
$\Delta_w = 0.1$	K_w	100	6.6%	9.5%	12.2%	2.1%	3.1%	4.0%	0.9%	1.3%	1.7%
		10	38.0%	46.5%	52.8%	15.3%	20.2%	24.5%	6.4%	8.6%	10.6%
		1	82.0%	86.6%	89.9%	56.3%	64.6%	71.5%	30.6%	38.0%	46.0%
		0.1	98.6%	99.4%	99.9%	95.2%	98.0%	99.8%	87.5%	95.2%	100.3%
$\Delta_w = 0.05$	K_w	100	3.3%	4.8%	6.2%	1.0%	1.5%	1.9%	0.4%	0.6%	0.8%
		10	21.7%	27.7%	33.1%	7.4%	9.9%	12.4%	2.8%	3.8%	4.8%
		1	67.4%	74.5%	80.2%	36.8%	45.0%	53.2%	16.4%	21.4%	27.6%
		0.1	95.9%	97.5%	98.5%	87.0%	91.8%	95.0%	69.4%	79.3%	87.1%
$\Delta_w = 0.025$	K_w	100	1.6%	2.4%	3.0%	0.5%	0.7%	0.9%	0.2%	0.3%	0.4%
		10	11.0%	14.5%	18.2%	3.4%	4.6%	5.9%	1.2%	1.6%	2.1%
		1	49.5%	58.1%	65.9%	21.6%	27.9%	35.2%	8.4%	11.3%	15.4%
		0.1	91.2%	94.0%	95.9%	74.4%	81.6%	86.8%	49.3%	59.6%	69.1%

Table 2. Variation of the normalized ratio $\kappa_w^* / \kappa_w = (1 - \Lambda |y_{w,1}^\perp|) / \overline{\Delta T}$ (expressed as %) with the dimensionless corrugation amplitude, $A/2\pi$, the dimensionless wall thicknesses, Δ_w , and the fluid-to-fluid and wall-to-fluid conductivity ratios, K and K_w , for fixed values of $\gamma = 0$, $Pr_i = 5$, $Re_i = 0$, and $\Lambda = 0.25$. The apparent wall positions corresponding to $A = [0.25, 0.5, 1]$ are $y_{w2}^\perp = -y_{w1}^\perp = [0.0095, 0.0339, 0.1013]$.

$\xi_L^* / \xi_L = [1 - (\lambda/a_1) y_{w,1}^\perp]^{-(n+1)}$	$A = 0,25$		$A = 0,5$		$A = 1$	
i) Constant flow rate ($n = 0$)	1,0024	+0,24%	1,0091	+0,91%	1,0270	+2,70%
ii) Constant pumping power ($n = 3/2$)	1,0060	+0,60%	1,0230	+2,30%	1,0690	+6,90%
iii) Constant pressure drop ($n = 3$)	1,0096	+0,96%	1,0370	+3,70%	1,1126	+11,26%

Table 3. Variation of the ratio ξ_L^* / ξ_L (expressed both in absolute value and in percentage change) with the dimensionless corrugation amplitude, A , for the three cases under consideration.

As previously discussed, use of the computed values of κ_w^* and ξ_L^* as input parameters for the bulk flow model yields the effectiveness ϵ^* of the corrugated wall heat exchanger for given values of m , k , κ_w ($= K_w / \Lambda \Delta_w$), ξ_L , Λ , Re_{ti} ($= 1.5 \Lambda^2 Re_i$), Pr_i , A , Δ_w , K_w , and K ($= k$). This procedure allows to evaluate the augmentation heat transfer and entropy generation numbers, R_a and N_a , thereby providing a methodology that could be used to optimize the heat exchanger performance from both an energy and/or an entropy (i.e., energy devaluation [30]) point of view.

Table 4 shows preliminary results corresponding to corrugated walls with different parameter sets. The results indicate that in most situations the corrugations increase the heat exchanger effectiveness $\varepsilon^*/\varepsilon > 1$, although the overall heat transfer rate is reduced due to the significant reduction in volume flow rate, making $\varepsilon^*Q_1/(\varepsilon Q_1)_{flat} < 1$. It is interesting to note that the augmentation heat transfer parameter R_a is smaller than one with constant flow rate, but grows above unity when the flow rate is reduced (e.g., constant pumping power or constant pressure drop). Note also that the improvement in R_a is accompanied by a reduction in entropy generation rate N_a , which is almost unaffected ($N_a \cong 1$) under constant flow rate, but takes values smaller than unity for constant pumping power ($N_a \cong 0.95$) and constant pressure drop ($N_a \cong 0.9$) conditions. These results confirm the ability of the multi-scale asymptotic analysis developed here to provide useful estimations of the heat exchanger performance. This method could therefore be used in future work to perform a thermodynamic optimization of the heat exchanger in terms of the different parameters involved in the model.

(a) Ref. Case	Flat wall	Corrugated wall - $A = 1, Re_{ci} = 0, K_w = 0.1$		
ε_{flat}	0.7831	Constant flow rate	Constant pumping power	Constant pressure drop
$m \& m^*$	1		1	
$k \& k^*$	2		2	
$\kappa_w \& \kappa_w^*$	4		4.0141	
$\xi_L \& \xi_L^*$	1	1.0260	1.0662	1.1081
Q_1/Q_{1flat}	1	1.0000	0.9623	0.9259
$\varepsilon^*/\varepsilon_{flat}$	1	1.0090	1.0219	1.0346
$\varepsilon Q_1/(\varepsilon Q_1)_{flat}$	1	1.0090	0.9833	0.9580
$\Delta P_1 Q_1/(\Delta P_1 Q_1)_{flat}$	1	1.0800	1.0000	0.9259
R_a	1	0.9343 (-6.57%)	0.9833 (-1.67 %)	1.0346 (+3.46%)
N_a	1	0.9961 (-0.39%)	0.9528 (-4.72%)	0.9109 (-8.91 %)
(b) Effect of K_w	Flat wall	Corrugated wall - $A = 1, Re_{ci} = 0, K_w = 10$		
ε_{flat}	0.8562	Constant flow rate	Constant pumping power	Constant pressure drop
$m \& m^*$	1		1	
$k \& k^*$	2		2	
$\kappa_w \& \kappa_w^*$	400		42.4926	
$\xi_L \& \xi_L^*$	1	1.0260	1.0662	1.1081
Q_1/Q_{1flat}	1	1.0000	0.9623	0.9259

$\varepsilon^*/\varepsilon_{flat}$	1	0.9992	1.0091	1.0187
$\varepsilon Q_1/(\varepsilon Q_1)_{flat}$	1	0.9992	0.9710	0.9432
$\Delta P_1 Q_1/(\Delta P_1 Q_1)_{flat}$	1	1.0800	1.0000	0.9259
R_a	1	0.9252 (-7.48%)	0.9710 (-2.90%)	1.0187 (+1.87%)
N_a	1	1.0006 (+0.06%)	0.9553 (-4.47%)	0.9117 (-8.83%)
(c) Effect of K_w	Flat wall	Corrugated wall - $A = 1, Re_{ci} = 0, K_w = 100$		
ε_{flat}	0.8569	Constant flow rate	Constant pumping power	Constant pressure drop
$m \& m^*$	1	1		
$k \& k^*$	2	2		
$\kappa_w \& \kappa_w^*$	4000	66.4740		
$\xi_L \& \xi_L^*$	1	1.0260	1.0662	1.1081
Q_1/Q_{1flat}	1	1.0000	0.9623	0.9259
$\varepsilon^*/\varepsilon_{flat}$	1	1.0014	1.0111	1.0207
$\varepsilon Q_1/(\varepsilon Q_1)_{flat}$	1	1.0014	0.9729	0.9451
$\Delta P_1 Q_1/(\Delta P_1 Q_1)_{flat}$	1	1.0800	1.0000	0.9259
R_a	1	0.9272 (-7.28%)	0.9729 (-2.71%)	1.0207 (+2.07%)
N_a	1	0.9989 (-0.11%)	0.9535 (-4.65%)	0.9101 (-8.99%)
(d) Effect of A	Flat wall	Corrugated wall - $A = 0.5, Re_{ci} = 0, K_w = 0.1$		
ε_{flat}	0.7831	Constant flow rate	Constant pumping power	Constant pressure drop
$m \& m^*$	1	1		
$k \& k^*$	2	2		
$\kappa_w \& \kappa_w^*$	4	4.2081		
$\xi_L \& \xi_L^*$	1	1.0085	1.0215	1.0346
Q_1/Q_{1flat}	1	1.0000	0.9873	0.9748
$\varepsilon^*/\varepsilon_{flat}$	1	1.0073	1.0116	1.0159
$\varepsilon Q_1/(\varepsilon Q_1)_{flat}$	1	1.0073	0.9988	0.9903
$\Delta P_1 Q_1/(\Delta P_1 Q_1)_{flat}$	1	1.0259	1.0000	0.9748
R_a	1	0.9819 (-1.81%)	0.9988 (-0.12 %)	1.0159 (+1.59%)
N_a	1	0.9969 (-0.31%)	0.9823 (-1.77%)	0.9679 (-3.21 %)
(e) Effect of A	Flat wall	Corrugated wall - $A = 1.5, Re_{ci} = 0, K_w = 0.1$		

ε_{flat}	0.7831	Constant flow rate	Constant pumping power	Constant pressure drop
$m \& m^*$	1		1	
$k \& k^*$	2		2	
$\kappa_w \& \kappa_w^*$	4		5.5132	
$\xi_L \& \xi_L^*$	1	1.0459	1.1187	1.1966
Q_1/Q_{1flat}	1	1.0000	0.9349	0.8741
$\varepsilon^*/\varepsilon_{flat}$	1	1.0395	1.0607	1.0810
$\varepsilon Q_1/(\varepsilon Q_1)_{flat}$	1	1.0395	0.9917	0.9449
$\Delta P_1 Q_1/(\Delta P_1 Q_1)_{flat}$	1	1.1441	1.0000	0.8741
R_a	1	0.9086 (-9.14%)	0.9917 (-0.83 %)	1.0810 (+8.10%)
N_a	1	0.9813 (-1.87%)	0.9063 (-9.37%)	0.8363 (-16.37 %)
(f) Effect of Re_{ci}	Flat wall	Corrugated wall - $A = 1, Re_{ci} = 64, K_w = 0.1$		
ε_{flat}	0.7831	Constant flow rate	Constant pumping power	Constant pressure drop
$m \& m^*$	1		1	
$k \& k^*$	2		2	
$\kappa_w \& \kappa_w^*$	4		4.0351	
$\xi_L \& \xi_L^*$	1	1.0270	1.0690	1.1126
Q_1/Q_{1flat}	1	1.0000	0.9608	0.9231
$\varepsilon^*/\varepsilon_{flat}$	1	1.0098	1.0232	1.0363
$\varepsilon Q_1/(\varepsilon Q_1)_{flat}$	1	1.0098	0.9831	0.9566
$\Delta P_1 Q_1/(\Delta P_1 Q_1)_{flat}$	1	1.0833	1.0000	0.9231
R_a	1	0.9321 (-6.79%)	0.9831 (-1.69 %)	1.0363 (+3.63%)
N_a	1	0.9957 (-0.43%)	0.9507 (-4.93%)	0.9073 (-9.27 %)

Table 4. (a)(b)(c): Influence of the wall-to-fluid heat conductivity ratio, $K_w = [0.1, 10, 100]$; (d)(a)(e): influence of the dimensionless corrugation amplitude, $A = [0.5, 1, 1.5]$; and (a)(f): influence of the Reynolds number, $Re_{ci} = [0, 64]$, on the performance of laminar counterflow parallel-plate heat exchangers with small scale-wall corrugations. In all reported cases $Pr_i = 5, \Lambda = 0.25, \Delta_w = 0.1,$ and $K = 2.$

6. Conclusion

Laminar counterflow parallel-plate heat exchangers with small-scale wall corrugations have been studied theoretically and numerically following a multi-scale asymptotic approach. The

analysis assumes that the corrugation wavelength and amplitude are comparable to each other but are much smaller than the channel half-width. In this case, the problem exhibits two main asymptotic regions: a bulk flow region where the walls appear flat at leading order, and where axial heat conduction can be neglected in first approximation provided the Peclet numbers are large enough, and a near-wall region where a full interaction exists between heat convection and conduction in the fluids, coupled by transverse and longitudinal conduction in the thin corrugated wall.

In the bulk flow region, an approximated semi-analytical two-term solution based on eigenfunction expansions provides accurate predictions of the outlet fluid temperatures in terms of the bulk parameters m , k , κ_w , and ξ_L .

The heat transfer process in the near wall region is investigated numerically by specifying the overall heat flux transverse to the wall and calculating the apparent wall temperature jump seen by the outer bulk flow. The numerical solution, based on a boundary fitted finite difference method, involves the parameters Re_{τ} , Pr_{τ} , K , K_w , Δ_w , θ_i , as well as the corrugation shape, defined here by A and γ . The analysis shows that, far from the wall, the effect of the corrugations is similar to that of a thickened virtual plane surface with an appropriately defined apparent thermal resistance.

Although for sufficiently large Reynolds numbers the flow in the channels and past the corrugations is known to become unstable and undergo transition to a self-sustained oscillatory and later turbulent regime [31,32] resulting in enhanced heat transfer rates, this study has focused on the role of the wall corrugations on the overall heat transfer process before this transition occurs.

The effect of the corrugations is incorporated into the bulk flow model defining apparent values of the bulk flow parameters m^* , k^* , κ_w^* and ξ_L^* in terms of those of the originally flat wall. Three different constraints have been considered for the determination of the apparent parameters: i) constant flow rate, ii) constant pumping power, and iii) constant pressure drop. The results, restricted to the case of sinusoidal wall geometries ($\gamma = 0$) with equal channel half-widths ($a_1 = a_2$) show that the most relevant parameter determining the effect of the corrugations is the wall thermal conductivity K_w . For highly conductive (e.g., metallic) walls, the addition of the corrugations always leads to a reduced wall conductivity κ_w^* (or an increased wall thermal resistance, $1/\kappa_w^*$). On the other hand, for poorly conductive (e.g., polymeric) walls, the addition of the corrugations may lead to a slightly larger apparent wall conductivity κ_w^* (or a smaller wall thermal resistance) under certain flow conditions, particularly for relatively thick walls and large corrugation amplitudes.

The aim of this work has been to introduce the methodology followed by the multi-scale asymptotic analysis and to present preliminary calculations that illustrate the type of results that can be obtained with the most simple geometry and flow conditions. Corrugations of different shapes, involving for instance scalloped geometries, $\gamma \neq 0$, with different channel half widths, $a_1 \neq a_2$, remain underexplored and warrant future work.

Acknowledgements

This work was supported by Project ENE2011-24574 of Spanish *Ministerio de Economía y Competitividad*.

Author details

Marcos Vera and Alberto E. Quintero

*Address all correspondence to: marcos.vera@uc3m.es

Department of Thermal and Fluids Engineering, Universidad Carlos III de Madrid, Leganés, Spain

References

- [1] Hardt S, Ehrfeld W, Hessel V. Strategies for size reduction of microreactors by heat transfer enhancement effects. *Chem. Eng. Commun.* 2003;(190): 540-559.
- [2] Esarte J, Min G, Rowe DM. Modelling heat exchangers for thermoelectric generators. *J. Power Sources.* 2001;(93): 72-76.
- [3] Yu J, Zhao H. A numerical model for thermoelectric generator with the parallel-plate heat exchanger. *J. Power Sources.* 2007;(172): 428-434.
- [4] Wakeland RS, Keoliana RM. Effectiveness of parallel-plate heat exchangers in thermoacoustic devices. *J. Acoust. Soc. Am.* 2004;(115): 2873-2886.
- [5] Marquardt ED, Radebaugh R. Compact high effectiveness parallel plate heat exchangers. In Ross Jr. RG, editor. *Cryocoolers 12*. R.G. Ross Jr. ed.: Kluwer Academic/Plenum Publishers; 2003. 507-516.
- [6] Nellis GF. A heat exchanger model that includes axial conduction, parasitic heat loads, and property variations. In *Cryogenics* 43.; 2003. 523-538.
- [7] Radebaugh R. Microscale heat transfer at low temperatures. In Kakaç S, Vasiliev LL, Bayazitoğlu Y, Yener Y, editors. *Microscale Heat Transfer Fundamentals and Applications*.: Springer Netherlands 93-124.
- [8] Shah RK, London AL. *Laminar Flow Forced Convection in Ducts: A Source Book for Compact Heat Exchanger Analytical Data: A Source Book for Compact Heat Exchanger Analytical Data*. New York: Academic Press; 1978.

- [9] Nunge RJ, Gill WN. Analysis of heat or mass transfer in some countercurrent flows. *Int. J. Heat Mass Tran.* 1965; 8(6): 873-886.
- [10] Nunge RJ, Gill WN. An analytical study of laminar counterflow double-pipe heat exchangers. *A. I. Ch. E. Journal.* 1966; 12(2): 279-289.
- [11] Papoutsakis E, Ramkrishna D. Conjugated Graetz problems - II: Fluid-fluid problems. *Chem. Eng. Sci.* 1981; 36(8): 1393-1399.
- [12] Vera M, Liñan A. Laminar counterflow parallel-plate heat exchangers: Exact and approximate solutions. *Int. J. Heat Mass Tran.* 2010; 36(8): 1393-1399.
- [13] Webb RL, Kim NH. Principles of enhanced heat transfer. New York: Taylor & Francis; 1994.
- [14] Moffatt HK. Viscous and resistive eddies near a sharp corner. *Journal of Fluid Mechanics.* 1964; 18(1): 1-18.
- [15] Sunden B, Trollheden S. Periodic laminar flow and heat transfer in a corrugated two-dimensional channel. *Int. Commun. Heat Mass.* 1989; 16(2): 215-225.
- [16] Fabbri G. Heat transfer optimization in corrugated wall channels. *International Journal of Heat and Mass Transfer.* 2000; 43: 4299-4310.
- [17] Durmuş A, Benli H, Kurtbaş İ, Gül H. Investigation of heat transfer and pressure drop in plate heat exchangers having different surface profiles. *International Journal of Heat and Mass Transfer.* 2009; 52: 1451-1457.
- [18] Vera M, Liñan A. Exact solution for the conjugate fluid-fluid problem in the thermal entrance region of laminar counterflow heat exchangers. *International Journal of Heat and Mass Transfer.* 2011; 54(1): 490-499.
- [19] Quintero AE, Vera M, Rivero-de-Aguilar B. Wall conduction effects in laminar counterflow parallel-plate heat exchangers. *International Journal of Heat and Mass Transfer.* 2014; 70: 939-953.
- [20] Woollard HF, Billingham J, Jensen OE, Lian G. A multi-scale model for solute transport in a wavy-walled channel. *J. Eng. Math.* 2009; 64(1): 25-48.
- [21] Hocking LM. A moving fluid interface on a rough surface. *J. Fluid Mech.* 1976; 76(4): 801-817.
- [22] Wang CY. Drag due to a striated boundary in slow Couette flow. *Phys. Fluids.* 1978; 21: 697-698.
- [23] Orszag SA, Kells LC. Transition to turbulence in plane Poiseuille and plane Couette flow. *J. Fluid Mech.* 1980; 96(1): 159-205.
- [24] Richardson S. On the no-slip boundary condition. *Journal of Fluid Mechanics.* 1973; 59(04): 707-719.

- [25] Luccini P, Manzo F, Pozzi A. Resistance of a grooved surface to parallel flow and cross-flow. *J Fluid Mech.* 1991; 228: 87-109.
- [26] Bejan A. General criterion for rating heat-exchanger performance. *International Journal of Heat and Mass Transfer.* 1978; 21: 655-658.
- [27] Bejan A. Entropy generation minimization: The new thermodynamics of finite-size devices and finite-time processes. *Journal of Applied Physics.* 1996; 79(3): 1191-1218.
- [28] Bejan A. Entropy generation minimization: The method of thermodynamic optimization of finite-size systems and finite-time processes. Boca Raton: CRC Press; 1996.
- [29] Bejan A. Second law analysis in heat transfer. 1980; 5(8): 720-732.
- [30] Wenterodt T, Herwig H. The entropic potential concept: a new way to look at energy transfer operations. *entropy.* 2014; 16: 2071-2084.
- [31] Stone K, Vanka SP. Numerical study of developing flow and heat transfer in a wavy passage. *Journal of Fluids Engineering (Transactions of ASME).* 1999; 121(4): 713-719.
- [32] Hossain MZ, Sadrul Islam AKM. Numerical Investigation of fluid flow and heat transfer characteristics in sine, triangular and arc-shaped channels. *Thermal Science.* 2007; 11(1): 17-26.

Interaction of Longitudinal Vortices and the Effect on Fluid Flow and Heat Transfer

Kewei Song

Additional information is available at the end of the chapter

<http://dx.doi.org/10.5772/60007>

1. Introduction

Developing and innovating new techniques to enhance the heat transfer of a new compact heat exchanger is not only useful but also necessary for energy saving. The flow with longitudinal velocity components is an important phenomenon in fluid dynamics and heat transfer. Longitudinal vortices are generated by flow separation along the side edges of the vortex generators (VGs) due to the pressure differences between the upstream and the downstream sides and are perpendicular to the main flow direction. A description of the typical vortices structure formed by a delta winglet VG is given in some publications [1, 2]. There is a main vortex that is formed as a result of the flow separating in the tip of the half-delta wing and rolling up due to the lower pressure in the back side of the VG. Then there is a corner vortex that is horseshoe-like vortex formed in the corner between the front side of the VG and the fin. Finally, there is an induced secondary vortex formed in the corner between the back side of the wing and the fin as a result of the redirection of the near wall flow caused by the lower pressure behind the generator.

The longitudinal vortices can potentially enhance heat transfer with small pressure loss penalty and a better heat transfer effect than that of latitudinal vortices. The longitudinal vortices can cause bulk fluid mixing, boundary-layer modification, flow destabilization, and thereby enhance convective heat transfer. Setting protrusions that can generate longitudinal vortices on the fin surface is a promising technique to enhance the airside heat transfer. There are many protrusions that can generate longitudinal vortices. Vortex generators (VGs) are among the most popular actuators for the fin-side heat transfer enhancement. The winglet VG is capable of enhancing heat transfer with less increase in pressure penalty compared to other type of protrusions. A thorough review of the progress made in the application of longitudinal VGs is performed in reference [3].

In order to obtain a better heat transfer performance, researchers always try to punch lots of VGs out of the fin surface. However, the increasing number of VGs is not necessarily linked with the rise in heat transfer performance augmentation. This is because the vortices not only change the boundary layer structure but also interact with each other when they meet in the flow channel and the interaction of vortices affects the intensity of vortices and their effect on heat transfer enhancement. Experimental and numerical studies focusing on the interactions between vortices and boundary layers have been carried out in references [4–6]. The experimental investigation about the interaction between vortices and the boundary layers indicated that in the region where two neighboring vortices induced flow toward the heat transfer surface, local heat transfer was locally enhanced. Conversely, in the regions where neighboring vortices induced outflow departs the heat transfer surface, the local heat transfer was decreased. Close proximity of other vortices strongly affects the spreading of the vorticity. The heat transfer modification produced by the vortex was strongly dependent on vortex interaction. These previous works have shown that the strength of the vortices interaction with the wall is strongly dependent on the arrangement of vortices in the array. However, seldom works consider the interaction of longitudinal vortices and their effect on heat transfer. The effect of interaction of longitudinal vortices generated by winglet VGs on heat transfer enhancement of a flat tube bank fin heat exchanger was qualitatively analyzed in reference [7]. The quantitative study of the interaction of longitudinal vortices was seldom reported due to the lack of parameter that can define the intensity of longitudinal vortices. A nondimensional parameter Se was defined for the intensity of secondary flow in reference [8]. The parameter Se provides a powerful tool for the quantitative study of the interaction between longitudinal vortices. By using Se , quantitative studies about the interaction of longitudinal vortices generated by VGs mounted on the fin surfaces of flat tube bank fin heat exchanger were carried out in references [9, 10].

In this chapter, the nondimensional parameter Se that can be used for the description of the intensity of the longitudinal vortices is introduced first, then the interaction of counterrotating longitudinal vortices generated by VGs is quantitatively studied, and the effect of interaction on the intensity of vortices and heat transfer are discussed in detail by using the nondimensional parameter Se .

2. Physical model

As stated above, the longitudinal vortices can provide good performance for fluid flow and heat transfer enhancement. As the intensity of the longitudinal vortices decreases along the main flow direction, in order to obtain a high intensity of longitudinal vortices in the flow field, lots of VGs are always protruded into the flow field. Different arrangements of VGs will generate longitudinal vortices with different intensity and different rotating directions. These vortices with different rotating directions will inevitably meet and interact with each other when they are flowing downward. The interaction between these vortices affects not only the intensity of the vortices but also the heat transfer enhancement of the longitudinal vortices.

For the plate-fin heat exchangers, there are many rows of VGs, and interaction between these vortices generated by different VGs will be a common physics phenomenon. This chapter focuses on the interaction between two counterrotating longitudinal vortices with different transversal pitches.

The physical model is shown in Figure 1. The flow channel is formed by two plain fins. Two winglet VGs with a certain longitudinal pitch are mounted on the bottom fin surface. The VGs are mounted around the longitudinal center line of the channel and the longitudinal pitch b is fixed to $3.5H$, where $H = 2 \text{ mm}$ is the height of the flow channel. The height of the VGs is $h = 0.7H$, and the length of the base is $l = 2h$. The attack angle of VG is $\theta = 35^\circ$. The first VG is placed $5H$ away from the inlet. The width and the length of the channel are $S = 7H$ and $L = 22H$, respectively. The transversal pitches of the VGs and the ratio of transversal pitch to the projected length of the base of VGs are summarized in Table 1. When the value of c changes from c_1 to c_8 , there are two different arrangement relationships between the VGs. The schematic view and the front view of the two different arrangements of the VGs are shown in Figure 1(b) and (c), respectively. For convenience, the front VG is named as VG1 and the latter is named as VG2. Figure 2 shows the longitudinal vortices in the cross section for different arrangements of VGs.

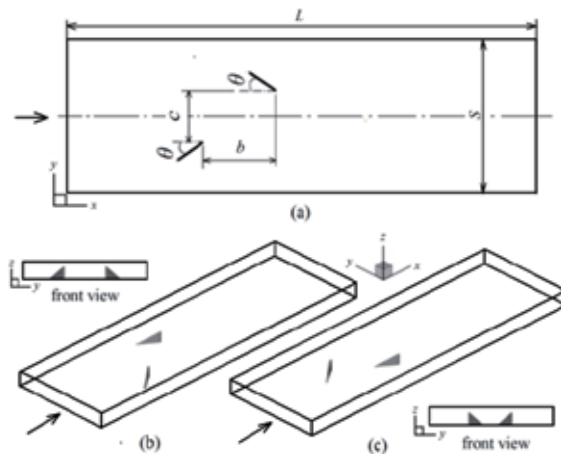


Figure 1. Schematic view of the physical model.

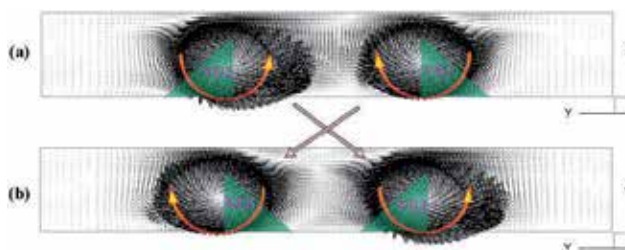


Figure 2. Relationship between the arrangement of VGs and the longitudinal vortices.

Pitch no.	c1	c2	c3	c4	c5	c6	c7	c8
<i>c</i> (mm)	4.818	3.212	1.606	0.0	1.606	3.212	4.818	6.424
<i>c/(l sinθ)</i>	3	2	1	0	1	2	3	4

Table 1. Transversal pitches of VGs

3. Governing equations and boundary condition

In the case of the heat exchangers, the fin spacing is small and the flow in gas side is usually laminar. With this application in mind, the delta winglet VG in a laminar developing flow is considered in the present investigation. In such case, the compact forms of governing equations in physical space are as follows:

Continuity equation

$$\frac{\partial}{\partial x_i}(\rho u_i) = 0 \quad (1)$$

Momentum equations

$$\frac{\partial}{\partial x_i}(\rho u_i u_k) = \frac{\partial}{\partial x_i} \left(\mu \frac{\partial u_k}{\partial x_i} \right) - \frac{\partial p}{\partial x_k} \quad (k = 1, 2, 3) \quad (2)$$

Energy equation

$$\frac{\partial}{\partial x_i}(\rho c_p u_i T) = \frac{\partial}{\partial x_i} \left(\lambda \frac{\partial T}{\partial x_i} \right) \quad (3)$$

For developing flow, the boundary conditions at the inlet surface are given as follows:

$$u(x, y, z)|_{\text{inlet}} = u_{\text{in}}, \quad v(x, y, z)|_{\text{inlet}} = 0, \quad w(x, y, z)|_{\text{inlet}} = 0, \quad T(x, y, z)|_{\text{inlet}} = T_{\text{in}} \quad (4)$$

At the outlet surface

$$\frac{\partial}{\partial x} u(x, y, z) = 0, \quad \frac{\partial}{\partial x} v(x, y, z) = 0, \quad \frac{\partial}{\partial x} w(x, y, z) = 0, \quad \frac{\partial}{\partial x} T(x, y, z) = 0 \quad (5)$$

At the symmetric surfaces

$$v(x, y, z) = 0, \frac{\partial}{\partial y} u(x, y, z) = 0, \frac{\partial}{\partial y} w(x, y, z) = 0, \frac{\partial}{\partial y} T(x, y, z) = 0 \quad (6)$$

At the solid surfaces, constant temperature and no-slip condition for velocity are applied as follows:

$$u(x, y, z) = 0, v(x, y, z) = 0, w(x, y, z) = 0, T = T_w \quad (7)$$

The Reynolds number is

$$Re = \rho \cdot u_m \cdot d_h / \mu \quad (8)$$

The local Nusselt number is determined by

$$Nu_{local} = -d_h \frac{\partial T}{\partial n} / (T_w - T_{bulk}) \quad (9)$$

T_{bulk} is the cross-sectional averaged temperature:

$$T_{bulk} = \frac{\int_A T dA}{A} \quad (10)$$

The span-averaged Nu_s is obtained by averaging Nu_{local} over the span strip fin surfaces at position x :

$$Nu_s(x) = \int_0^S Nu_{local}(x, y) dy / \left(\int_0^S dy \right) \quad (11)$$

The overall average Nu is obtained by averaging Nu_{local} over the entire fin surfaces:

$$Nu = \frac{\iint_A Nu_{local} dA}{\iint_A dA} \quad (12)$$

4. Parameter for the intensity of longitudinal vortices

If the main flow direction is along the x -axis, the secondary flow is the flow in the cross section normal to x -axis. Thus, secondary flow relates to the velocity components' gradients in the cross section: $\partial w/\partial y - \partial v/\partial z$. The vorticity component along the main flow direction represents the angle velocity of flow that rotates around the axis having the direction along the main flow.

According to reference [8], the product of the absolute vorticity flux and the hydraulic diameter is the characteristic velocity of secondary flow, as follows:

$$U_s = d_h J_{ABS}^n \quad (13)$$

U_s is the characteristic velocity of secondary flow, d_h is the hydraulic diameter, and J_{ABS}^n is the absolute vorticity flux in normal direction of the cross section. In references [11, 12], J_{ABS}^n is written as follows:

$$J_{ABS}^n = \frac{1}{A(x)} \iint_{A(x)} |\omega^n| dA \quad (14)$$

where A is the cross-sectional area, and ω^n is the component of ω normal to the cross section.

Based on the study of J_{ABS}^n , a nondimensional parameter Se is defined for the intensity of secondary flow in reference [8]. Se is defined as follows:

$$Se = \frac{\rho d_h U_s}{\mu} \quad (15)$$

Se has the same form as the definition of Re , but the physical meaning is quite different. Se represents the ratio of inertial force to viscous force, which are induced by the secondary flow. Re represents the ratio of inertial force to viscous force, which are induced by the main flow. The cross-sectional average value of Se at position x is a local average intensity of secondary flow in a small volume:

$$Se_s(x) = \frac{\rho d_h^2}{\mu} \iint_{A(x)} |\omega^n| dA / \iint_{A(x)} dA \quad (16)$$

The volume-averaged value of Se is obtained by integrating the local value of Se over the total flow field:

$$Se = \frac{\rho d_h^2}{\mu} \iiint_V |\omega^n| dV / \iiint_V dV \quad (17)$$

5. Numerical method

The simulation domain in physical space (x, y, z) coordinates is transformed into a rectangular parallelepiped in the computational space (ξ, η, ζ) coordinates. The governing equations and

boundary conditions are transformed into the computational space and discretized by the control volume method in a collocated grid system. The power scheme is used to discretize the convective terms, while the central difference scheme is employed to discretize the diffusion terms. The SIMPLE algorithm is used to obtain the numerical solution of continuity and momentum equations.

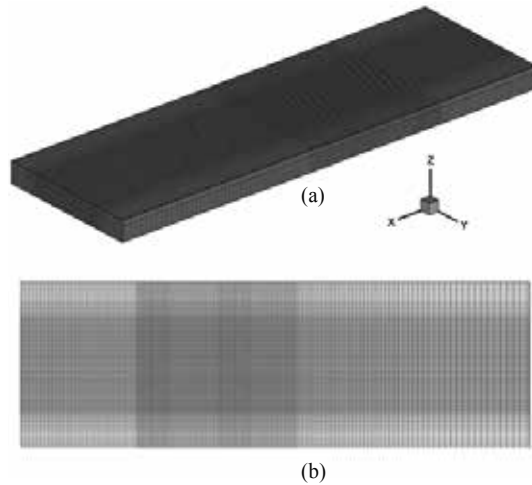


Figure 3. Grid system used for the simulation domain, (a) schematic view of the three-dimensional grid, (b) grid in the x - y plane.

A typical structured grid system used in the present study is shown in Figure 3. Figure 3(a) shows the schematic view of the three-dimensional grid system, and Figure 3(b) is the grid in x - y plane. In the region where VGs are mounted, in order to keep the shape of the VG, fine and uniform grids are needed in each direction and the grid in each direction must keep a proportional interval in the region. In the numerical investigations about the application of VGs, most of the VGs are idealized as of zero thickness. In the present study, the VGs with finite thickness are considered to render the computations more realistic. Grid-independent performance is carried out at three different grid systems with the numbers of the fine grid twice the coarse grid in each coordinate direction, as shown in Table 2. The differences of the grid independent of Nu and f are less than 1% for the studied three grid systems. Considering the mesh quality and the occupation of computer resources, all the results are obtained using the grid size of $194 \times 142 \times 32$.

Grid ($x \times y \times z$)	Nu	f
$134 \times 98 \times 22$	6.6418	0.0580
$194 \times 142 \times 32$	6.6073	0.0578
$258 \times 190 \times 44$	6.6291	0.0582

Table 2. Grid independence

6. Results and discussion

The generation of longitudinal vortices and the subsequent disruption of thermal boundary layers are the prime movers of heat transfer augmentation. Thus, the flow field attracts special attention. In order to show the development of the flow field, eight cross sections are selected as shown in Figure 4, the locations of these selected sections are summarized in Table 3.

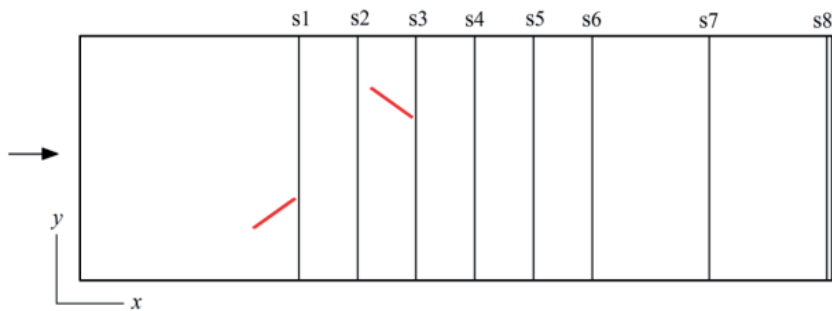


Figure 4. The selected cross-sections.

Cross section	s1	s2	s3	s4	s5	s6	s7	s8
x/L	0.291	0.368	0.448	0.525	0.602	0.682	0.836	0.993

Table 3. Cross-sectional positions

6.1. Effect of interaction of longitudinal vortices on the flow field

The velocity vectors on the cross sections for transversal pitch c_2 and c_6 with $Re = 1800$ are shown in Figures 5 and 6, respectively. When fluid passes through the VGs, strong longitudinal vortices with counterrotating directions are generated. The vortices that have clockwise rotating directions on cross sections s1 to s8 are generated by the first VG, and the vortices that have anticlockwise rotating directions on cross sections s3 to s8 are generated by the second VG. Comparing the vortices on different cross sections, the intensity of the longitudinal vortices decreases gradually downward.

Figures 5 and 6 correspond to the arrangements of Figure 1(b) and (c), respectively. By comparing the flow field structure in Figures 5 and 6, one can find that the flow field structures in the common region between the vortices are different. In Figure 5, the fluid in the common region is directed away from the bottom fin surface and forms a common flow-up flow field structure. However, in Figure 6, the fluid in the common region is directed toward the bottom fin surface and forms a common flow-down flow field structure.

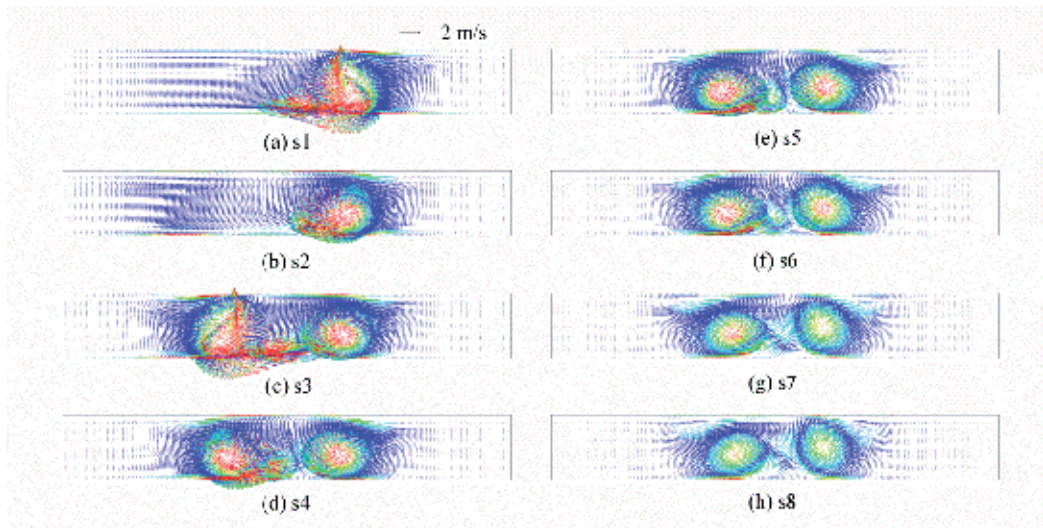


Figure 5. Velocity vectors on the cross sections for transversal pitch $c = c2$.

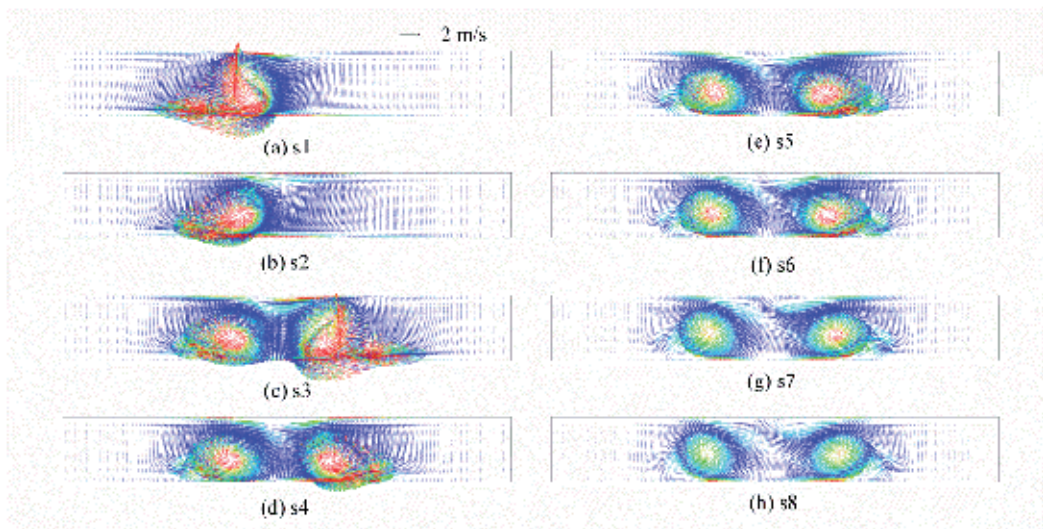


Figure 6. Velocity vectors on the cross sections for transversal pitch $c = c6$.

The velocity vectors on the cross section $s6$ with $Re = 1800$ are shown in Figure 7 for different values of c . There are two vortices with counterrotating directions on each cross section. The stronger one with anticlockwise rotating direction is generated by the second VG, and the weaker one with clockwise rotating direction is generated by the first VG. When the value of c changes from $c1$ to $c4$, the centers of the vortices move toward the centre of the channel and the distance between the vortices decreases. The interaction between these two counterrotating

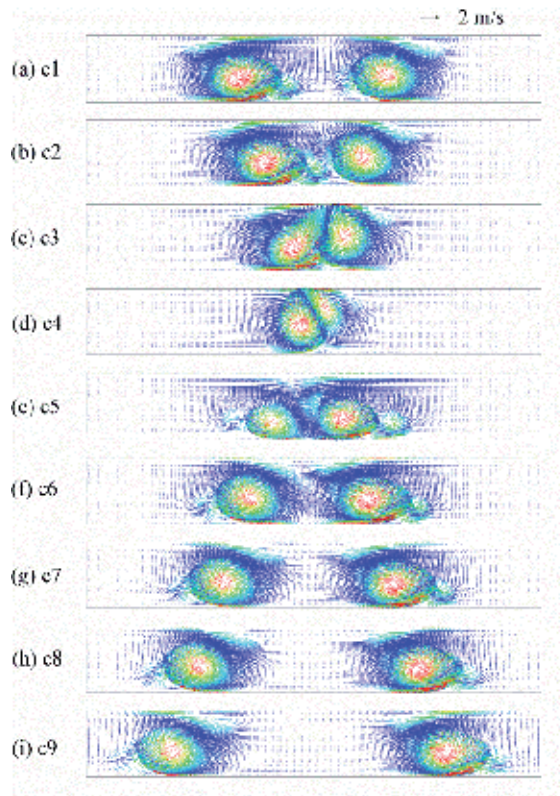


Figure 7. Velocity vectors on the cross sections for different values of c .

vortices increases with decreasing transversal pitch. When the transversal pitch between the VGs is c_4 , the most serious interaction takes place, and the intensity of the vortices becomes weaker. The counterrotating vortices separate from each other when the transversal pitch of VGs changes from c_4 to c_8 . The interaction between the counterrotating vortices decreases, and the intensity of these vortices increases with increasing transversal pitch of VGs. When the counterrotating vortices are located closer to each other, common flow region becomes distinct between the vortices. When the fluid in the common flow region is directed toward the top fin surface, the vortex, especially the weaker one, is directed away from the bottom fin surface. On the contrary, the vortices can be kept at the position close to the bottom fin surface when the fluid in the common flow region is directed toward the bottom fin surface.

6.2. Effect of interaction of longitudinal vortices on Se_s

The parameter Se relates to the intensity of the longitudinal vortices generated by the VGs, and the intensity of these vortices is affected by the interaction between them. Thus, the distribution curve of the span-averaged value of Se along the flow direction can reflect the interaction between the counterrotating longitudinal vortices for different transversal pitches of the VGs.

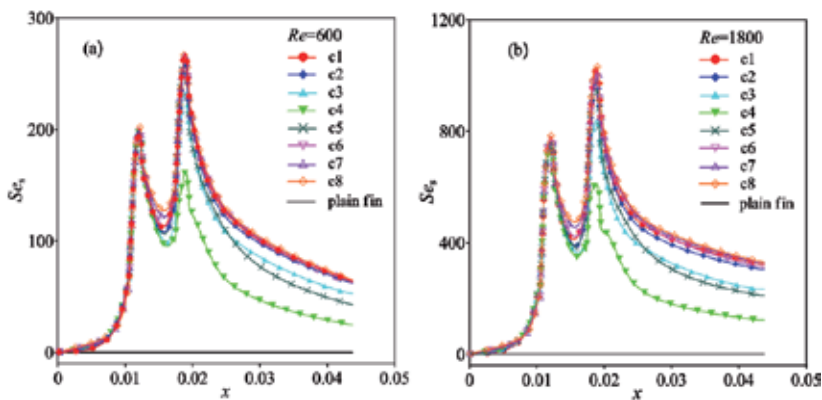


Figure 8. Distribution of Se_s along flow direction.

The distribution of the span-averaged values of Se_s for the range of c are presented in Figure 8 at $Re = 600$ and 1800 . For the flow in the channel formed by plain fin, the fluid flows smoothly and the flow is an irrotational flow; therefore, the vorticity of the irrotational flow is zero. When VGs are added into the fluid, longitudinal vortices are generated by the VGs, and the vorticity of the flow is not zero. The intensity of the vortices changes according to the change of the interaction between the counterrotating longitudinal vortices for different transverse pitches of VGs. In the entrance of the channel, the fluid flows in at a uniform velocity, and the intensity of the vortices is zero. In the region between the entrance and the first VG, the fluid changes flow direction gradually, and the span-averaged value of Se_s also increases gradually from the entrance and then increases rapidly when the fluid passes through the first VG. A peak value of Se_s is obtained at the trailing end of the first VG. Then the value of Se_s decreases rapidly behind the first VG and reaches a peak minimum value in the region between the first and the second VGs. When the fluid passes through the second VG, the value of Se_s increases rapidly and reaches the second peak value at the trailing end of the second VG. Se_s first decreases rapidly just behind the second VG and then becomes smooth till the end of the simulation domain. In the region before the first VG, the distributions of Se_s are nearly the same for all the cases with different transversal pitches. In the region behind the first VG, the distributions of Se_s are different for different values of c due to the interaction between the longitudinal vortices. Evident difference between the distributions of Se_s can be found when the counterrotating longitudinal vortices locate closer to each other. The values of Se_s for the studied cases c3, c4, and c5 are obviously smaller than that for other cases. For the other cases, the interaction between the vortices is weaker, and the differences of Se_s are small. When the transversal pitch of VGs is c4, the interaction between the counterrotating longitudinal vortices is the most serious, and the value of Se_s is also the smallest. The peak value of Se_s for c4 at the trailing end of the second VG is obviously smaller than the first peak value at the trailing end of the first VG due to the serious interaction between the counterrotating vortices. For the other cases of c , the second peak value of Se_s around the second VG is greater than the first peak value of Se_s around the first VG; the intensity of the vortices increases although interaction also takes place between the counterrotating longitudinal vortices.

6.3. Effect of interaction on Nu_s

Figure 9 shows the distributions of the span-averaged values of Nu_s at $Re = 600$ and 1800 for different values of c . The value of Nu_s for plain fin without VGs is also shown in the figure for comparison. The span-averaged values of Nu_s are obviously enhanced by the longitudinal vortices generated by the VGs mounted in the channel. In the entrance of the channel, the fluid flows in at a uniform velocity, the boundary layer starts to develop, and the value of Nu_s gets the largest value. Then Nu_s decreases rapidly apart from the entrance till the region where the first VG mounted. When the fluid flows around the first VG, Nu_s increases and reaches a peak level at the trailing end of the first VG. Then Nu_s starts to decrease downstream and gets the peak minimum value in the region ahead of the second VG. Nu_s starts to increase in the region where the second VG is mounted and reaches another peak value at the trailing end of the second VG. In the region behind the second VG, owing to the attenuation of vortices, the span-averaged Nu_s decreases rapidly in the beginning and then smoothly till the outlet of the channel. The distributions of Nu_s in the region between the entrance and the second VG are nearly the same for all the cases because the intensity of vortices in this region is not affected by the interaction of counterrotating longitudinal vortices. In the region after the second VG, owing to the interaction between the counterrotating vortices, the differences between the distributions of Nu_s are quite evident, especially for the cases c3, c4, and c5. As the interaction of longitudinal vortices for c4 is the most serious, the decreasing intensity of the vortices weakens the heat transfer performance of the vortices, and the span-averaged Nu_s is the smallest. The peak value of Nu_s at the trailing end of the second VG for c4 is smaller than the peak value at the trailing end of the first VG, but the peak value of Nu_s for c6 is larger than the peak value at the trailing end of the first VG. This means that the interaction between the counterrotating vortices may enhance the heat transfer or decrease the heat transfer.

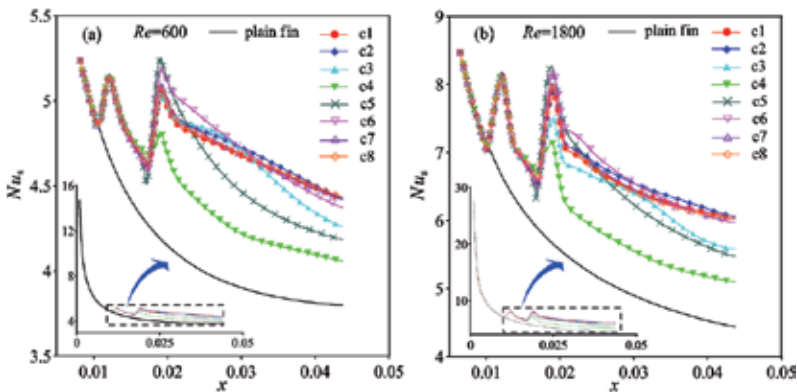


Figure 9. Distribution of Nu_s along flow direction.

The local span-averaged Nu_s for the case c6 is the largest in the region around the second VG. However, the intensity of the longitudinal vortices for the case c6 is not the largest. The reason maybe that a common flow region formed between the VGs and the fluid in the common flow region is directed downwash toward the bottom surface on which the VGs are mounted on, as shown in Figure 6. The heat transfer is locally enhanced benefiting from the local thinning of the thermal boundary layer in the common flow down region. Experimental investigation in reference [4] presents the same conclusion that the heat transfer is locally enhanced in the

region where two neighboring vortices impose a flow toward the surface. Therefore, the interaction of longitudinal vortices does not necessarily decrease the heat transfer performance. The heat transfer performance depends not only on the intensity of the vortices but also on the flow field structure of the vortices.

6.4. Effect of interaction on average values of Se , Nu , and f

The average value of Se over the entire flow and the average value of Nu over the entire area included in the heat transfer are of great interest as they are directly linked to the intensity of longitudinal vortices in the channel and to the amount of total heat transfer. The distributions of Se and Nu for the range of c as a function of Re are presented in Figure 10 (a) and (b), respectively. The values of Se and Nu for the plain fin are also shown for comparison. Both the values of Se and Nu increase monotonically with the increase of Re . The differences between these values also increase with increasing Re , and the differences of Se and Nu for different values of c are quite different. For different values of c , the lowest values of Se and Nu are both obtained for $c = c_4$. The values of Se and Nu for c_3 and c_5 are nearly the same, and both are larger than that for $c = c_5$. For the other cases of c , the values of Se and Nu are larger than that for c_3 , c_4 , and c_5 , but the differences between the values of Se and Nu are very small. Figure 10(c) shows the distributions of friction factor for the range of c studied in this chapter, and the differences between the values of f are quite small. Thus, the interaction between vortices has a very small effect on the friction factor.

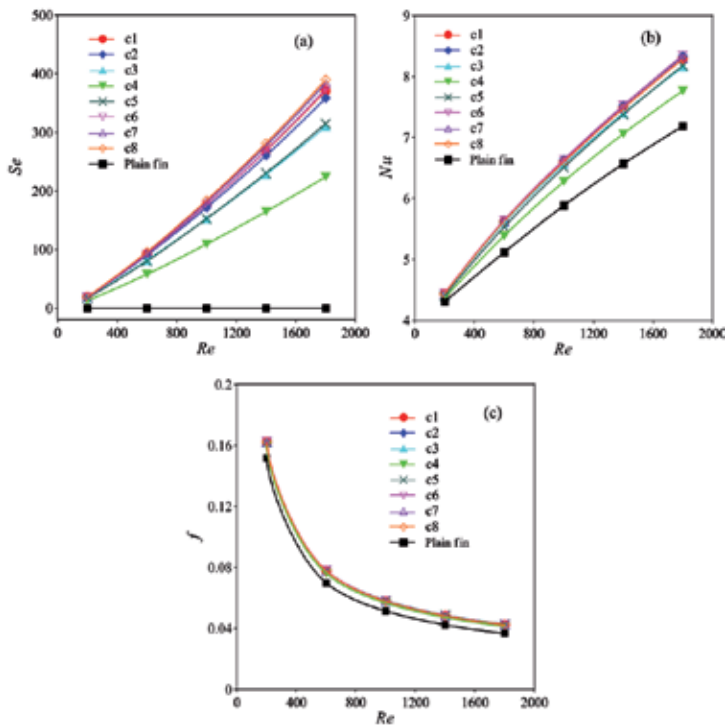


Figure 10. Distribution of Se , Nu , and f for the range of c as a function of Re .

6.5. Effect of interaction on Se/Se_{ref} and Nu/Nu_{ref}

In order to study the effect (in percentage) of the interaction of the counterrotating longitudinal vortices on Se and Nu , the values of Se and Nu for $c1$ are selected as the reference values, then the ratios of Se/Se_{ref} and Nu/Nu_{ref} mean the percentage of Se and Nu compared with the reference values. The distributions of Se/Se_{ref} and Nu/Nu_{ref} as a function of the distance between the VGs are presented in Figure 11 for Re ranging from 200 to 1800. As expected, when values of transversal pitch between the VGs are $c = c3, c4$, and $c5$, the values of Se/Se_{ref} are obviously smaller than those of other configurations, and the ratio of Se/Se_{ref} reaches a peak minimum value at $c = c4$. For other values of c , the differences of Se/Se_{ref} are very small. When the flow in the region between the counterrotating longitudinal vortices is imposed toward the bottom fin surface, the value of Se/Se_{ref} is a little larger than that when a common flow up region between the counterrotating longitudinal vortices is formed.

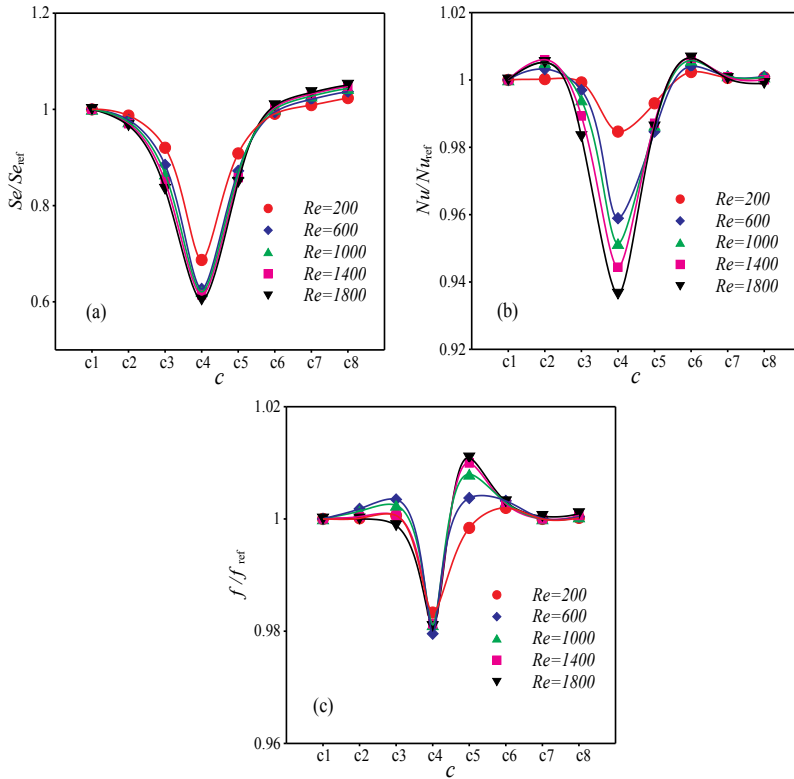


Figure 11. Distributions of Se/Se_{ref} and Nu/Nu_{ref} as a function of c .

The distributions of Nu/Nu_{ref} are much similar to the distributions of Se/Se_{ref} ; the values of Nu/Nu_{ref} also reach the minimum values at $c = c4$. However, the decreasing percentages of Se are not consistent with that of Nu ; the maximum decreasing percentage of Se is about 40%, but it is only about 6% for Nu . The ratio of Nu/Nu_{ref} reaches the peak values at $c = c2$ and $c6$, respectively. This is because when $c = c2$ and $c6$, the interaction between the longitudinal

vortices is relatively small, and the common flow region formed between the VGs is conducive to heat transfer. When $c = c_6$, the fluid in the common flow region is directed downwash toward the bottom fin surface on which the VGs are mounted, and the common flow region imposes fluid toward the top fin surface when $c = c_2$. The fin heat transfer performance is locally enhanced owing to the induced flow in the common flow region. When the distance of c is too large, the common flow region between the vortices will disappear, but when the distance is too small, the intensity of vortices will decrease rapidly due to the interaction between the vortices. Therefore, an optimal arrangement of VGs exists for obtaining a good heat transfer performance of the fin surface mounted with VGs.

6.6. Effect of interaction on JF and JF/JF_{ref}

The surface goodness factor JF under same pump power is more suitable for engineering application and is commonly used as the criteria for evaluating the good performance of heat transfer exchangers or heat transfer surfaces. Figure 12(a) shows the distribution of JF for different values of c as a function of Re. JF increases with increasing Re. When $c = c_3, c_4$, and c_5 , for which there has obvious interaction between the counterrotating longitudinal vortices, the value of JF is obviously smaller than the other cases. When $c = c_4$, the value of JF is the smallest due to the most serious interaction of the counterrotating longitudinal vortices. Figure 12(b) indicates the effect of interaction of longitudinal vortices on the ratio of JF/JF_{ref} for different Re as a function of c . The value of JF for $c = c_1$ is selected as the reference. The distribution of JF/JF_{ref} is similar to the distribution of Nu/Nu_{ref} shown in Figure 11(b). When the transversal pitch between the VGs are $c = c_3, c_4$, and c_5 , the values of JF/JF_{ref} are obviously smaller than the other cases, and the ratio of JF/JF_{ref} decreases with increasing Re. JF/JF_{ref} gets the minimum value at $c = c_4$, and JF is about 5.8% smaller than the reference value at $Re = 1600$. When $c = c_2$ and c_6 , JF/JF_{ref} is greater than 1 and reaches the peak values. Thus, the best heat transfer performance can be obtained at $c = c_2$ and c_6 , for which the distance between the VGs is about twice the projected length of the base length of VGs, that is, $c/(l \sin \theta) = 2.0$.

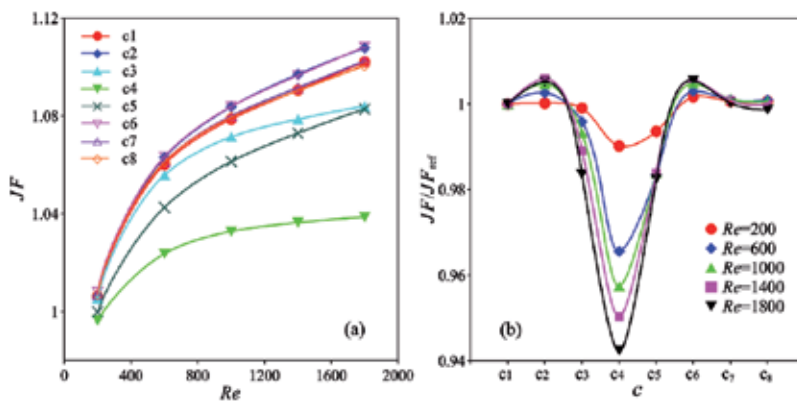


Figure 12. Distributions of JF as a function of Re and JF/JF_{ref} as a function of c .

7. Conclusions

The interaction of two counterrotating longitudinal vortices generated by VGs mounted on the bottom of a channel formed by two neighboring fins and the effect of interaction of counterrotating longitudinal vortices on the intensity of vortices and heat transfer are quantitatively studied using the numerical method. The following conclusions were derived:

- i. The strength of the interaction between the counterrotating vortices is strongly dependent on the transversal pitches between the vortices. The distribution of Se_s does not only reflect the changing of the intensity of the longitudinal vortices in the flow channel but also reflect the interaction between the longitudinal vortices.
- ii. The interaction between the counterrotating longitudinal vortices does not necessarily decrease the intensity of the vortices. When the counterrotating vortices partially interact with each other, the intensity of the vortices can also be increased. When the counterrotating vortices fully interact with each other, the intensity of the vortices decreases seriously.
- iii. The interaction between counterrotating vortices does not necessarily decrease the heat transfer performance of the longitudinal vortices. The heat transfer performance depends on not only the intensity of the vortices but also the structure of the vortices. The common flow region formed between the counterrotating longitudinal vortices is beneficial for the heat transfer enhancement.
- iv. Due to the interactions of counterrotating longitudinal vortices and their effect on heat transfer enhancement, an optimum arrangement of VGs exists for obtaining a better heat transfer performance. When the distance between the VGs is twice the projected length of the base of VGs, the best heat transfer performance can be obtained.

Nomenclature

A ; surface area involved in heat transfer or cross-sectional area (m^2)

$A(x)$; cross-sectional area at position x (m^2)

b ; longitudinal pitch between VGs (m)

c ; transverse pitch between VGs (m)

c_p ; specific heat capacity ($J/(kg\ K)$)

d_h ; hydraulic diameter, characteristic length (m)

f ; friction factor

h ; height of winglet-type VGs (m) or heat transfer coefficient ($W/(m^2\ K)$)

H ; fin spacing (m)

J^n ; vorticity flux in the normal direction of the cross section (1/s)

l ; base length of VG (m)

L ; streamwise length of the simulation domain (m)

n ; direction normal to the cross section

Nu ; Nusselt number: $Nu = h d_h / \lambda$

p ; Pressure loss (Pa)

Re ; Reynolds number: $Re = \rho u_m d_h / \mu$

S ; width of the simulation domain

Se ; secondary flow intensity

T ; temperature (K)

U_s ; characteristic velocity of secondary flow (m/s)

u_m ; maximum average velocity of air (m/s)

u, v, w ; components of velocity vector (m/s)

x, y, z ; coordinates

Greeks

θ ; attack angle of VG ($^\circ$)

λ ; heat conductivity (W/(m K))

μ ; viscosity (kg/(m s))

ρ ; density (kg/m³)

ω ; vorticity (1/s)

Subscripts

ABS; absolute value

bulk; bulk temperature on the cross section

local; local value

s; span-averaged or cross-sectional average value

w; fin surface

Acknowledgements

This work was supported by the National Natural Science Foundation of China (grant nos. 51376086 and 51366008) and the Gansu Provincial Foundation for Distinguished Young Scholars (grant no. 145RJDA324).

Author details

Kewei Song

Address all correspondence to: songkw@mail.lzjtu.cn

School of Mechanical Engineering, Lanzhou Jiaotong University, Lanzhou, Gansu, China

References

- [1] Torri K, Nishino K, Nakayama K. Mechanism of heat transfer augmentation by longitudinal vortices in a flat plate boundary layer. *Proceedings of the Tenth International Heat Transfer Conference, Brighton, 1994*; 6 123–128.
- [2] Biswas G, Torii K, Fujii D, Nishino K. Numerical and experimental determination of flow structure and heat transfer effects of longitudinal vortices in a channel flow. *International Journal of Heat and Mass Transfer* 1996; 38 3441–3445.
- [3] Jacobi, AM, Shah RK. Heat transfer surface enhancement through the use of longitudinal vortices: a review of recent progress. *Experimental Thermal and Fluid Science* 1995; 11 295–309.
- [4] Kataoka K, Doi H, Komai T. Heat mass transfer in Taylor vortex flow with constant axial flow rates. *International Journal of Heat and Mass Transfer* 1977; 20 57–63.
- [5] Pauley WR And Eaton JK. The effect of embedded longitudinal vortex arrays on turbulent boundary layer heat transfer. *Journal of Heat Transfer* 1994; 116(4) 871–879.
- [6] Kim WJ, Patel VC. Influence of streamwise curvature on longitudinal vortices embedded in turbulent boundary layers. *Computers and Fluids* 1994; 23(5) 647–673.
- [7] Zhu ChL, Hua L, Sun DL, Wang LB and Zhang YH. Numerical study of interactions of vortices generated by vortex generators and their effects on heat transfer enhancement. *Numerical Heat Transfer, Part A* 2006; 50 345–360.
- [8] Song KW, Wang LB. The effectiveness of secondary flow produced by vortex generators mounted on both surfaces of the fin to enhance heat transfer in a flat tube bank fin heat exchanger. *ASME Journal of Heat Transfer* 2013; 135: 041902.

- [9] Song KW, Wang LB. Interaction of vortices and the augmentation of heat transfer in a flat tube bank fin heat exchanger by vortex generators. *The 4th Asian Symposium on Computational Heat Transfer and Fluid Flow*, 2013: 91–101, Hong Kong, China.
- [10] Song KW. Numerical research on interaction of longitudinal vortices and the characteristics of fluid flow and heat transfer in the flow channel of exchanger. PhD thesis. Lanzhou Jiaotong University, China; 2014.
- [11] Song, KW, Wang, LB. Relationship between heat transfer intensity and absolute vorticity flux intensity in flat tube bank fin channels with vortex generators. *Progress in Computational Fluid Dynamics* 2008; 8 (7–8) 496–502.
- [12] Chang LM, Wang LB, Song KW. Numerical study of the relationship between heat transfer enhancement and absolute vorticity flux along main flow direction in a channel formed by a flat tube bank fin with vortex generators. *International Journal of Heat and Mass Transfer* 2009; 52 1794–1801.

A Critical Review on Condensation Pressure Drop in Microchannels and Minichannels

Mohamed M. Awad, Ahmet Selim Dalkılıç and Somchai Wongwises

Additional information is available at the end of the chapter

<http://dx.doi.org/10.5772/60965>

1. Introduction

Condensation in microscales has applications in a wide variety of advanced microthermal devices. For instance, condensation in microscales is widely used in small devices like air-cooled condensers for the air-conditioning and automotive industry, in heat pipes, thermosyphons and other applications for system thermal control. Microchannel condensers are being used to increase heat transfer performance to reduce component size and improve energy efficiency. After 2000s, experimental data became available in open literature in condensation of different refrigerants in small hydraulic diameter microchannels.

This chapter is a continuation of the authors' previous work about a critical review on condensation heat transfer in microchannels and minichannels [1]. The current chapter consists of four sections: Introduction, Literature Review, Recommendations for Future Studies, Summary and Conclusions. The authors used the same style in writing their recent paper about condensation heat transfer in microchannels and minichannels [1].

In the present chapter, the authors use the microchannels and minichannels classification proposed by Kandlikar [2]. According to his classification, the following can be used: for microchannels, $d_h = 10\text{-}200\ \mu\text{m}$; for mini-channels, $d_h = 200\ \mu\text{m}\text{-}3\ \text{mm}$. In comparison, conventional channels have hydraulic diameters (d_h) $\geq 3\ \text{mm}$. Therefore, the present chapter covered channels have hydraulic diameters (d_h) in the range $10\ \mu\text{m} \leq d_h < 3\ \text{mm}$ according to the Kandlikar classification [2].

In macroscale, the gravitational forces are more important than the shear and surface tension forces, and the opposite occurs when the diameter is smaller. Also, Wang and Rose [3] cited another important influence in non-circular microchannel condensation: the viscosity in transverse flow.

Majority of the correlations proposed to predict the frictional pressure gradient during condensation in microscales are based on modifications from the Lockhart and Martinelli [4], Chisholm [5] and Friedel [6] correlations, which were proposed for conventional diameters, and their results show large deviations compared with the experimental data of Dalkilic and Wongwises [7].

2. Literature review

Koyama et al. [8] investigated experimentally the local characteristics of heat transfer and pressure drop for pure refrigerant R134a condensation in two kinds of 865 mm long multi-port extruded tubes having eight channels in hydraulic diameter of 1.11 mm and 19 channels in hydraulic diameter of 0.80 mm. The researchers measured the pressure drop through small pressure measuring ports at an interval of 191 mm. They measured the local heat transfer rate in effective cooling length in every subsection of 75 mm using heat flux sensors. They found that the experimental data of frictional pressure drop agreed with the correlation of Mishima and Hibiki [9], while the correlations of Chisholm and Laird [10], Soliman et al. [11], and Haraguchi et al. [12] overpredicted.

Garimella [13] presented an overview of using the flow visualization in micro- and mini-channel geometries to develop the pressure drop and heat transfer models during condensation of refrigerants. The researcher recorded condensation flow mechanisms for round, rectangular, and square tubes for mass flux (G) of 150 kg/(m².s) and 750 kg/(m².s) and $0 < x < 1$ with hydraulic diameters (d_h) in the range of 1-5 mm using unique experimental techniques that permitted flow visualization during the condensation process. He documented the influence of miniaturization on the flow regime transitions and channel shape. He categorized the flow mechanisms into four various flow regimes: dispersed flow, intermittent flow, wavy flow, and annular flow. The four various flow regimes were further subdivided into many flow patterns within every regime. He observed that the annular and intermittent flow regimes became larger as the tube hydraulic diameter (d_h) was decreased, and at the expense of the wavy flow regime. These maps and transition lines could be used to predict the flow pattern or regime that would be established for a given tube geometry, mass flux (G), and mass quality (x). He used these pressure drop measurements, together with observed flow mechanisms, to develop experimentally validated models for pressure drop during condensation in every of these flow regimes for different circular and noncircular channels with $0.4 < d_h < 5$ mm. His flow regime-based models yield substantially better pressure drop predictions than the traditionally used correlations that were primarily based on air-water flows for large diameter tubes.

Garimella et al. [14] presented a multiple flow-regime model of refrigerant R134a in horizontal microchannels for pressure drop during condensation. The researchers used five circular channels ranging in hydraulic diameter (d_h) from 0.5 mm to 4.91 mm to measure two-phase pressure drops. For every tube under consideration, they took first pressure drop measurements for five various refrigerant mass fluxes (G) between 150 kg/(m².s) and 750 kg/(m².s) over the entire range of mass qualities from 100% vapor ($x = 1$) to 100% liquid ($x = 0$). In order to

assign the applicable flow regime to the data points, they used results from previous work by the author on condensation flow mechanisms in microchannel geometries. They modified and combined pressure drop models for intermittent [15, 16] and annular [17] flow reported earlier by the authors to develop a comprehensive model that addressed the entire progression of the condensation process from the vapor phase to the liquid phase. Their model was based on the R134a flow regime transition criteria and pressure drop data observed by Coleman and Garimella [18-20]. Their model considered the intermittent only, intermittent/discrete wavy annular transition, and annular only flow. The intermittent flow model considered the unit cell. This unit cell consisted of a single vapor bubble and a single liquid slug. For every unit cell, the pressure drop contributions of the liquid slug, vapor bubble, and film/slug transition region were summed together to arrive at the total pressure drop. Therefore, the pressure drop in the intermittent flow regime could be represented as follows:

$$\frac{\Delta P}{L} = \left(\frac{dP}{dz} \right)_{\text{film bubble}} \left(\frac{L_{\text{bubble}}}{L_{\text{unit cell}}} \right) + \left(\frac{dP}{dz} \right)_{\text{slug}} \left(\frac{L_{\text{slug}}}{L_{\text{unit cell}}} \right) + \Delta P_{\text{transition}} \left(\frac{N_{\text{unit cell}}}{L} \right) \quad (1)$$

It can be seen that the frictional gradient in the bubble and film region are independently calculated and then related to the total pressure drop by the relative length of the bubble and slug compared to the total unit cell. Also, the pressure drop associated with the acceleration/ deceleration of the liquid phase around the fore and aft regions of the vapor bubble is considered. The total number of unit cells per tube length ($N_{\text{unit cell}}/L$) establishes the total pressure drop contribution of the transitions. Solution of the above equation requires knowledge of the slug frequency that is empirically correlated as follows:

$$N_{UC} \left(\frac{d_h}{L_{tube}} \right) = \left(\frac{d_h}{L_{UC}} \right) = 1.573 (\text{Re}_{\text{slug}})^{-0.507} \quad (2)$$

Garimella et al. [14] correlated Eq. (2) with pressure drop data from the intermittent and discrete wave flow region [15, 16]. The researchers used data from both flow regimes because as the flow transitions from the intermittent to discrete wavy flow, the vapor bubbles were replaced by stratified well-defined liquid/vapor layers. Therefore, within the discrete wavy flow regime between the pure intermittent and pure annular flow regime, the number of unit cells approached zero. This construct of the intermittent/discrete wavy/annular transition allowed the use of the empirical relation in Eq. (2) in a consistent manner.

For pressure drop in annular flow, Garimella et al. [14] used in their model the following assumptions: (1) steady flow, (2) equal pressure gradients in the liquid and vapor core, (3) uniform liquid-film thickness, and (4) no liquid entrainment in the vapor core. Therefore, the resulting equation for annular pressure drop could be represented as follows:

$$\frac{\Delta P}{L} = \frac{2 f_i \rho_g U_g^2}{d_i} \quad (3)$$

Equation (3) could be written in terms of the more convenient tube diameter (d) through the use of Baroczy [21] void fraction model

$$\frac{\Delta P}{L} = \frac{2 f_i G^2 x^2}{\rho_g \alpha^{2.5} d} \quad (4)$$

The ratio of this interfacial friction factor (f_i) obtained from the experimental data to the corresponding liquid phase Fanning friction factor (f_l) computed using the Churchill [22] equation was then computed and correlated in terms of the Lockhart-Martinelli parameter (X) and the liquid phase Reynolds number (Re_l) as follows:

$$\frac{f_i}{f_l} = aXRe_l + bRe_l + cX \quad (5)$$

$$X = \left[\frac{(dP/dz)_l}{(dP/dz)_g} \right]^{1/2} \quad (6)$$

$$Re_l = \frac{Gd(1-x)}{(1+\sqrt{\alpha})\mu_l} \quad (7)$$

It should be noted that the liquid phase Reynolds number (Re_l) was defined in Eq. (7) in terms of the annular flow area occupied by the liquid phase. Also, the liquid phase Reynolds number (Re_l) would be used to compute the liquid phase pressure drop in the Lockhart-Martinelli parameter (X) in Eq. (6). Similarly, the gas phase Reynolds number required (Re_g) for the calculation of the gas phase pressure drop through the gas core in the Lockhart-Martinelli parameter (X) in Eq. (6) was calculated as follows:

$$Re_g = \frac{Gdx}{\mu_g \sqrt{\alpha}} \quad (8)$$

The various correlation constants (a , b , and c in Eq. (5)) were obtained for 249 points in the laminar ($Re_l < 2200$) and 24 points in the turbulent ($Re_l > 3400$) regions, with an appropriate interpolation scheme for 11 points in the transition regime using the observed trends of the friction factor ratio (f_i/f_l). Their model predicted 88% of these data points to within $\pm 20\%$.

Garimella et al. [14] made many improvements to their preliminary model, even though it was able to successfully predict pressure drop in the annular flow regime for a wide range of circular tubes. Also, the researchers extended the applicability of their model to the mist- and disperse-flow regions through the use of the surface tension parameter (ψ). This non-dimensional parameter (ψ), which accounts for the surface tension effects was introduced by Lee and Lee [23]:

$$\psi = \frac{U_l \mu_l}{\sigma} = \frac{G(1-x)\mu_l}{\rho_l(1-\alpha)} \quad (9)$$

Garimella et al. [14] correlated the ratio of the interfacial friction factor to the liquid phase friction factor (f_i/f_l) in terms of the Lockhart-Martinelli parameter (X), liquid phase Reynolds number (Re_l), and the surface tension parameter (ψ) as follows:

$$\frac{f_i}{f_1} = AX^a Re_i^b \psi^c \quad (10)$$

Garimella et al. [14] computed the Fanning friction factors (f_i and f_g) required for the individual phase pressure drops in the Lockhart-Martinelli parameter (X) using $f=16/Re$ for $Re < 2100$ and the Blasius expression $f = 0.079Re^{-0.25}$ for $Re > 3400$. It should be noted that the Churchill [22] friction factor was used for these single phase pressure drops in the previous paper by Garimella et al. [17]; however, the former expressions were found to yield a better fit to the data in this study. The values for the constant A and the exponents a , b , and c were a function of the liquid film flow regime (Re_l) (laminar or turbulent) and the tube geometry. Regression analysis on data grouped into two regions based on the liquid phase Reynolds number (Re_l) yielded the following values for the respective parameters in Eq. (10):

$A = 1.308 \times 10^{-3}$; $a = 0.427$, $b = 0.930$; $c = -0.121$ for laminar region ($Re_l < 2100$).

$A = 25.64$; $a = 0.532$, $b = -0.327$; $c = 0.021$ for turbulent region ($Re_l > 3400$).

They used an interpolation technique for liquid film Reynolds numbers in the transition region ($2100 < Re_l < 3400$) to determine the pressure drop.

Garimella et al. [14] recommended interpolation between the two models for data points determined to be in transition between intermittent/discrete and annular flow. The researchers developed empirical transition criteria from intermittent to other flow regimes from the flow visualization studies of Coleman [24]. These criteria were the model transition criteria for transition from intermittent to other flow regimes. The transition quality from intermittent to other flow regimes was predicted by the following transition criteria, where the mass flux (G) has units of $kg/(m^2.s)$.

$$x \leq \frac{a}{G + b} \quad (11)$$

The geometry-dependent constants a and b were functions of hydraulic diameter (d_h , in mm) given as follows:

$$a = 69.57 + 22.60 \exp(0.259d_h) \quad (12)$$

$$b = -59.99 + 176.8 \exp(0.383d_h) \quad (13)$$

Their combined model accurately predicted condensation pressure drops in the annular, disperse wave, mist, discrete wave, and intermittent flow regimes. They found that their resulting model predicted 82% of the data within $\pm 20\%$.

Hau and Koyama [25] investigated experimentally the local characteristics of heat transfer and pressure drop for carbon dioxide (CO_2) condensation in a multi-port extruded aluminum test section, which had 10 circular channels each with 1.31 mm inner diameter. The researchers performed their measurements for the inlet temperature (T) of CO_2 from 21.63 to 31.33°C, pressure (P) ranged from 6.48 to 7.3 MPa, mass flux (G) from 123.2 to 315.2 $kg/(m^2.s)$, vapor

quality (x) from 0 to 1, and heat flux (q) from 1.10 to 8.12 kW/m². They found that heat transfer coefficient in the two-phase region was higher than that in the single-phase, mass flux had important influence on condensation heat transfer characteristics, and pressure drop was very small along the test section. The influences of vapor quality on the heat transfer coefficients were not evident because of the large scattering of data. Also, they compared their experimental data with previous correlations and observed large discrepancies. Therefore, the existing model failed to predict their experimental data.

Cavallini et al. [26] reviewed published experimental work focusing on condensation flow regimes, pressure drop, and heat transfer in minichannels. New experimental data were available with low pressure (R236ea), medium (R134a) and high pressure (R410A) refrigerants in minichannels of different cross section geometry and with hydraulic diameters (d_h) ranging from 0.4 to 3 mm. The researchers presented a literature review to discuss flow regimes transitions because of the flow regimes effect on pressure drop and heat transfer. They compared the available experimental heat transfer coefficients and frictional pressure gradients with semi empirical and theoretical models developed for conventional channels and with models specifically created for minichannels.

Chowdhury et al. [27] presented an on-going experimental study of condensation pressure drop and heat transfer of refrigerant R134a in a single rectangular microchannel of hydraulic diameter (d_h) = 0.7 mm and high aspect ratio (AR) = 7. Their data would help explore the condensation phenomenon in microchannels that was necessary in the design and development of small-scale heat exchangers and other compact cooling systems. They used the mass fluxes (G) of 130 and 200 kg/(m².s) and the inlet vapor qualities (x_i) range was between 20% and 80% in their study. The researchers maintained the microchannel outlet conditions at close to thermodynamic saturated liquid state through a careful experimental procedure. They compared the data recorded trends to that found in recent literature on similar dimension tubes.

Garimella [28] reviewed a large number of the existing studies on mini- to microchannel condensation covering the flow pattern, pressure drop, void fraction, and heat transfer prediction methods. The researcher presented the available relevant information on pressure drops in condensing flows through relatively small channels and primarily adiabatic flows through microchannels in tabular form. Also, he compared different techniques for predicting the frictional pressure gradient during condensation of refrigerant R-134a flowing through a 1 mm diameter tube, at a mean quality of 0.5, at a mass flux of 300 kg/(m².s), and a pressure of 1500 kPa. He showed graphically a comparison of the pressure drops predicted by these different techniques. He found that the predicted pressure drops varied considerably, from 4.8 to 32.3 kPa. He attributed this large variation to the considerably various two-phase multipliers developed by the different investigators. He recommended choosing a model that was based on the geometry, fluid and operating conditions similar to those of interest for a given application.

Agarwal and Garimella [29] presented a multiple flow-regime model for pressure drop during condensation of refrigerant R134a in horizontal microchannels. The researchers considered in their study condensation pressure drops measured in two circular and six noncircular channels

with hydraulic diameter (d_h) = 0.42 -0.8 mm. For every tube under consideration, they took pressure drop measurements for five various refrigerant mass fluxes (G) between 150 kg/(m².s) and 750 kg/(m².s) over the entire range of qualities from 100% vapor ($x = 1$) to 100% liquid ($x = 0$). In order to assign the applicable flow regime to the data points, they used results from previous work by the authors on condensation flow mechanisms in microchannel geometries. For example, Garimella et al. [14] reported a comprehensive model for circular tubes that addressed the progression of the condensation process from the vapor phase to the liquid phase by modifying and combining the pressure drop models for intermittent [15, 16] and annular [17] flows reported earlier by them. Like the previous work on circular channels, they presented new condensation pressure drop data on six noncircular channels over the same flow conditions. Similar to the multiple flow-regime mode developed earlier by Garimella et al. [14] for circular microchannels, they developed a multiple flow-regime model for these new cross sections. Their combined model accurately predicted condensation pressure drops in the intermittent, disperse-wave, mist, discrete-wave, and annular flow regimes for both circular and noncircular microchannels of similar hydraulic diameters. In addition, they addressed overlap and transition regions between the respective regimes to yield relatively smooth transitions between the predicted pressure drops. They found that their resulting model predicted 80% of the data within $\pm 25\%$. Moreover, they demonstrated the influence of tube shape on pressure drop.

Cavallini et al. [30] presented a model for calculation of the frictional pressure gradient during condensation or adiabatic liquid-gas flow inside minichannels with different surface roughness. The researchers used new experimental frictional pressure gradient data associated to single-phase flow and adiabatic two-phase flow of R134a inside a single horizontal mini tube with rough wall in their modelling to account for the effects of surface roughness. It was a Friedel [6] based model and it took into account fluid properties, tube diameter, mass flux, vapor quality, reduced pressure, entrainment ratio and surface roughness. With respect to the flow pattern prediction capability, they built for shear dominated flow regimes inside pipes, thus, annular, annular-mist and mist flow were here predicted. However, they extended the suggested procedure to the intermittent flow in minichannels and applied it also with success to horizontal macro tubes. Cavallini et al. [30] suggested the following equations to calculate the frictional pressure gradient during adiabatic flow or during condensation, when the dimensionless gas velocity (Jg) 2.5

$$\left(\frac{dP}{dz}\right)_f = \phi_{lo}^2 \left(\frac{dP}{dz}\right)_{f,lo} = \phi_{lo}^2 \frac{2f_{lo} G^2}{\rho_l d_h} \quad (14)$$

$$f_{lo} = 0.046 Re_{lo}^{-0.2} = 0.046 \left(\frac{Gd_h}{\mu_l}\right)^{-0.2} \quad \text{for any } Re_{lo} \quad (15)$$

The friction factor from Eq. (15) refers to surfaces with negligible surface roughness.

$$\phi_{lo}^2 = Z + 3.595 \cdot F \cdot H \cdot (1 - E)^W \quad (16)$$

$$W = 1.398P_r = 1.398 \frac{P}{P_{cr}} \quad (17)$$

$$Z = (1 - x)^2 + x^2 \left(\frac{\rho_l}{\rho_g} \right) \left(\frac{\mu_g}{\mu_l} \right)^{0.2} \quad (18)$$

$$F = x^{0.9525} (1 - x)^{0.414} \quad (19)$$

$$H = \left(\frac{\rho_l}{\rho_g} \right)^{1.132} \left(\frac{\mu_g}{\mu_l} \right)^{0.44} \left(1 - \frac{\mu_g}{\mu_l} \right)^{3.542} \quad (20)$$

The entrainment ratio (E) in Eq. (16) must be calculated as suggested by Paleev and Filippovich [31]:

$$E = 0.015 + 0.44 \cdot \log \left[\left(\frac{\rho_{gc}}{\rho_l} \right) \left(\frac{\mu_l j_g}{\sigma} \right)^2 10^4 \right] \quad (21)$$

if $E \geq 0.95$, $E = 0.95$
if $E \leq 0$, $E = 0$

where the homogeneous gas core density (ρ_{gc}) was given by

$$\rho_{gc} = \left(\frac{x + (1 - x)E}{\frac{x}{\rho_g} + \frac{(1 - x)E}{\rho_l}} \right) \quad (22)$$

$$\rho_{gc} \approx \rho_g \left(1 + \frac{(1 - x)E}{x} \right) \text{ for } \rho_l \gg \rho_g$$

This model, presented above, for the frictional pressure gradient could be extended to lower vapor qualities and mass fluxes when the dimensionless gas velocity (Jg) 2.5, with the constraint to take the higher value between $(dP/dz)_f$ from Eqs. (14)-(22) and the all-liquid frictional pressure gradient $(dP/dz)_{f_{lo}}$ for the considered channel geometry Eqs. (23)-(25)

$$\left(\frac{dP}{dz}\right)_{f,lo} = \frac{2f_{lo}G^2}{\rho_l d_h} \quad (23)$$

$$\begin{aligned} \text{for } Re_{lo} > 2000, \quad f_{lo} &= 0.046 [Gd_h/\mu_1]^{0.2} \\ \text{for } Re_{lo} < 2000, \quad f_{lo} &= C/[Gd_h/\mu_1] \end{aligned} \quad (24)$$

$$C = 16 \text{ for the circular section and } C = 14.3 \text{ for the square section} \quad (25)$$

Cavallini et al. [32] had set up a new test apparatus for heat transfer and fluid flow studies in single minichannels during the condensation and adiabatic flow of R134a and R32 in a single circular section minitube with a much higher surface roughness. The researchers presented new experimental frictional pressure gradient data, relative to single-phase flow and adiabatic two-phase flow of R134a and R32 inside a single horizontal minitube, The test tube was a commercial copper tube with an inner diameter of 0.96 mm and a length of 228.5 mm. The uncertainty associated to the diameter was equal to ± 0.02 mm. The arithmetical mean deviation of the assessed profile (Ra) of the inner surface was $Ra = 1.3 \mu\text{m}$, the maximum height of profile Rz was $10 \mu\text{m}$. Because of high values of Ra and Rz , surface roughness was not negligible. They compared successfully the new all-liquid and all-vapor data against predictions of single-phase flow models. Also, they compared the two-phase flow data against a model previously developed by Cavallini et al. [30] for adiabatic flow or flow during condensation of halogenated refrigerants inside smooth minichannels. They discussed surface roughness effects on the liquid-vapor flow. In this respect, they modified the friction factor in the proposed model previously developed by Cavallini et al. [30] to take into consideration also effects due to wall roughness. The all-liquid friction factor (f_{lo}) of the model of Cavallini et al. [30] was corrected in the following way:

$$f_{lo} = 0.046 Re_{lo}^{0.2} + 0.7 \cdot RR = 0.046 \left(\frac{Gd_h}{\mu_1}\right)^{-0.2} + 0.7 \cdot RR \quad \text{for } RR < 0.0027 \quad (26)$$

The above friction factor (f_{lo}) was in good agreement with the Churchill curve [22] in the range $3000 Re_{lo}$ 6000.

Park and Hrnjak [33] investigated the carbon dioxide (CO_2) flow condensation heat transfer coefficients and pressure drop in multi-port microchannels made of aluminum having a hydraulic diameter (d_h) of 0.89 mm at low temperatures in horizontal flow conditions. The researchers performed their measurements at mass fluxes (G) from 200 to 800 $\text{kg}/(\text{m}^2 \cdot \text{s})$, saturation temperatures (T_s) of -15 and -25°C, and wall subcooling temperatures from 2 to 4°C. They predicted the flow patterns for experimental conditions using the Akbar et al. [34] and

the Breber et al. [35] flow pattern maps before investigating pressure drop and heat transfer. These flow pattern maps demonstrated that the flow patterns were intermittent flow patterns could occur at low and medium vapor qualities for the mass fluxes of $200 \text{ kg}/(\text{m}^2 \cdot \text{s})$, and annular flow patterns in most of flow conditions. Many correlations such as the Thome et al. [36] model could predict the heat transfer coefficients within acceptable error range. Many correlations such as the Mishima and Hibiki model [37] could predict their measured pressure drop relatively well.

Agarwal and Garimella [38] measured condensation heat transfer coefficients and pressure drops for refrigerant R134a flowing through rectangular microchannels with hydraulic diameters (d_h) ranging from $100 \mu\text{m}$ to $200 \mu\text{m}$ in small quality increments. These microchannels were fabricated on a copper substrate by electroforming copper onto a mask patterned by X-ray lithography and sealed by diffusion bonding. The researchers measured heat transfer coefficients for $0 < \text{mass quality } (x) < 1$ for mass fluxes (G) ranging from $200 \text{ kg}/(\text{m}^2 \cdot \text{s})$ to $800 \text{ kg}/(\text{m}^2 \cdot \text{s})$ at several different saturation temperatures. They conducted conjugate heat transfer analyses in conjunction with local pressure drop profiles to obtain accurate driving temperature differences and heat transfer coefficients. They illustrated the influences of mass flux, mass quality, and saturation temperature on condensation heat transfer coefficients and pressure drops through their experiments.

Song et al. [39] reported preliminary results from a new research program for making accurate pressure drop and heat transfer measurements during condensation in microchannels. The researchers used a dummy test section with identical channel and header geometry to that to be used in the main test program. While measuring the vapor flow rate and total heat transfer rate based on coolant measurements, they took the opportunity to make accurate pressure drop measurements. They obtained data for steam and FC72. In addition, they presented approximate comparisons with available pressure drop calculation methods.

Keinath and Garimella [40] investigated R404a condensation in channels diameter of $0.5\text{-}3 \text{ mm}$. The researchers obtained quantitative information on flow mechanisms using image analysis techniques on high speed video. They conducted experiments on condensing R404a at vapor qualities (x) of 0.05 to 0.95 at mass fluxes (G) ranging from 200 to $800 \text{ kg}/(\text{m}^2 \cdot \text{s})$. They conducted the experiments at the high pressures representative of actual operation of air-conditioning and refrigeration equipment. Also, they measured pressure drops as a function of operating conditions and geometry during the flow visualization experiments. Quantitative image analysis enabled detailed computation of void fraction and vapor bubble parameters like diameter, length, frequency, and velocity with a high degree of repeatability and with low uncertainties. They documented the effect of operating conditions on the flow patterns, void fractions, and vapor bubble parameters for saturation temperatures (T_s) = $30\text{-}60^\circ\text{C}$. The resulting void fraction models provided closure for heat transfer and pressure drop models that had thus far not been possible in the reported works in the literature.

Fronk and Garimella [41] measured pressure drops and heat transfer coefficients during carbon dioxide (CO_2) condensation in small quality increments in microchannels of $100 < d_h < 200 \mu\text{m}$. The researchers measured heat transfer coefficients for $0 < \text{mass quality } (x) < 1$ for mass flux (G) = $600 \text{ kg}/(\text{m}^2 \cdot \text{s})$ and multiple saturation temperatures. They presented preliminary

results for a $300 \times 100 \mu\text{m}$ (15 channels) test section. They used these data to evaluate the applicability of correlations developed for larger hydraulic diameters and different fluids for predicting pressure drops and heat transfer coefficients during carbon dioxide (CO_2) condensation.

Kuo and Pan [42] investigated experimentally condensation of steam in rectangular microchannels with uniform and converging cross-sections and a mean hydraulic diameter (d_h) of $135 \mu\text{m}$. The researchers determined the flow patterns, condensation heat transfer coefficient, and two-phase flow pressure drop. They found that heat transfer coefficient was higher for the microchannels with the uniform cross-section design than those with the converging cross-section under condensation in the mist/annular flow regimes, although the latter worked best for draining two-phase fluids composed of liquid water and uncondensed steam, which was consistent with the result of their previous study [43]. Using their experimental results, they developed dimensionless correlations of a two-phase frictional multiplier for the microchannels with both types of cross-section designs and condensation heat transfer for the mist and annular flow regions. Their experimental data agreed well with the obtained correlations, with the maximum mean absolute errors of 6.0% for the condensation heat transfer and 6.4% for the two-phase frictional multiplier.

Goss et al. [44] investigated experimentally the local heat transfer coefficient and pressure drop during the convective condensation of R-134a inside eight round ($d = 0.8 \text{ mm}$) horizontal and parallel microchannels over a mass flux range of $57 < G < 125 \text{ kg}/(\text{m}^2 \cdot \text{s})$ and pressure range of $6.8 < P < 11.2 \text{ bar}$. The researchers compared their experimental results with correlations and semi-empirical models described in the literature. For the pressure drop, they tested five correlations and that proposed by Zhang and Webb [45] gave the best results, with a deviation of 30%.

Keinath and Garimella [46] used the Garimella et al. [14] model on pressure drop data for R404A in circular tubes with diameter ranging from 0.5 mm to 3.0 mm. The researchers found that this model tended to overpredict the data. They observed the poorest agreement for the 3-mm tube data. They surmised that at $d = 3 \text{ mm}$, the various flow regime arising from the significantly higher reduced pressures encountered with R404A compared to R134a accounted for the difference. Also, Andresen [47] found that the Garimella et al. [14] model overpredicted data for R410A at high reduced pressures ($P_r = 0.8$ to 0.9) for tubes with diameter from 0.76 mm to 3.05 mm. Therefore, while the underlying mechanisms in the model appeared to be sound, further work was required to extend the applicability of the model to very high reduced pressures and somewhat larger diameters than for which the model was developed. Moreover, it could be seen that the annular flow pressure drop using the void fraction model of Baroczy [21] (Eq. (4)) was inversely proportional to the void fraction to the 2.5 power ($a^{2.5}$). This shows the importance of developing void fraction models specifically for condensation of refrigerants in small-diameter channels.

Bohdal et al. [48] investigated experimentally the two-phase pressure drop of the environmentally friendly refrigerant R134a (an R12 substitute) during its condensation in pipe minichannels with internal diameter (d_i) = 0.1-3.3 mm in compact condensers. Pipe minichannels could be used in the construction of compact refrigeration condensers. These were

channels with a circular section that in the condensation process of refrigerants intensify the heat transfer process while guaranteeing a high degree of structural compactness. The researchers established local and average pressure drops in the whole range of mass quality (x) = 0-1. They illustrated the effect of the mass quality and mass flux on pressure drop. They compared their results of experimental investigations to the results of calculation according to correlations proposed by other authors. They obtained many experimental results in this range, with was essential to make their owns correlation. They found that the pressure drop in two-phase flow during condensation of refrigerant R134a was dependent on: the agent type, process parameters and the structure of two-phase flow. In the literature, there were no generalized maps of structures for two-phase flow of refrigerants that significantly limited the choice of an appropriate correlation in the design of compact condensers. Therefore, they obtained systematic experimental studies of condensing refrigerant R134a in smooth pipe minichannels (stainless steel) with an inside diameter (d_i) = 0.31-3.3 mm. Their database included measurements of average and local values of pressure drop in pipe minichannels within the range of parameters: saturation temperature (T_s) = 30-40°C, mass quality (x) = 0-1, and refrigerant mass flux (G) = 0-1200 kg/(m².s). They used their database to develop their own correlation for determination of pressure drop under these conditions.

Bohdal et al. [49] presented the results of experimental investigations of heat transfer and pressure drop during R134a and R404A condensation in pipe minichannels with internal diameters (d_i) = 0.31-3.30 mm. Their results concerned investigations of the pressure drop and the local heat transfer coefficient in single mini-channels. The researchers found that the values of the pressure drop and the local heat transfer coefficient in the above mentioned minichannels were higher for R134a than R404A. Also, they compared their results with calculations according to the correlations proposed by other authors. They showed that a pressure drop during the condensation of the R134a and R404A refrigerants was described in a satisfactory manner with Friedel [6] and Garimella [13] correlations.

Bohdal et al. [50] investigated experimentally the pressure drop during R134a, R404a and R407C condensation in pipe minichannels with internal diameter (d_i) of 0.31-3.30 mm. Their results concerned investigations of the local and mean pressure drop in single minichannels. The researchers compared the experimental investigations results with the calculations according to the correlations proposed by other authors. They found that a pressure drop during the refrigerants condensation was described in a satisfactory manner with Friedel [6] and Garimella [13] correlations. They proposed their own correlation for calculation of local pressure drop during condensation in single minichannels using their experimental investigations in the range of two-phase flow structures: annular and annular-stratified for the following parameters: refrigerant mass flux (G) = 0-1300 kg/(m².s), mass quality (x) = 0-1, and saturation temperature (T_{sat}) = 20-50°C. Their pressure drop correlation was

$$\left(\frac{dP}{dz}\right)_f = \left(\frac{dP}{dz}\right)_{f,lo} \left[0.003 \left(\frac{P_{sat}}{P_{cr}}\right)^{-4.722} E^{-0.992} + 143.74 \left(\frac{F^{0.671} H^{-0.019}}{We^{0.308}}\right) \right] \quad (27)$$

$$E = (1 - x)^2 + x^2 \left(\frac{\rho_l}{\rho_g} \right) \left(\frac{f_{go}}{f_{lo}} \right) \quad (28)$$

$$F = x^{0.98} (1 - x)^{0.24} \quad (29)$$

$$H = \left(\frac{\rho_l}{\rho_g} \right)^{0.91} \left(\frac{\mu_g}{\mu_l} \right)^{0.19} \left(1 - \frac{\mu_g}{\mu_l} \right)^{0.7} \quad (30)$$

$$We = \frac{G^2 d}{\sigma \rho_g} \quad (31)$$

The friction coefficients f_{lo} and f_{go} for Eq. (28) were determined for a single-phase flow for the liquid and gaseous phases respectively, from the Baroczy dependence [21] of the following form:

$$f_x = 8 \left[\left(\frac{8}{Re_x} \right)^{12} + \left\{ 2.457 \ln \left[\left(\frac{Re_x}{7} \right)^{0.9} \right]^{16} + \left(\frac{37530}{Re_x} \right)^{16} \right\}^{-1.5} \right]^{1/12} \quad (32)$$

where the lower index $x = go$ was applied in the case of the calculation of f_{go} and $x = lo$ for f_{lo} . The same denotations applied to Reynolds' numbers: Re_{lo} and Re_{go} . They found that the results of the experimental tests and calculations from Eq. (27) fell within the compatibility range of $\pm 25\%$.

Alshqirate et al. [51] obtained the experimental results of the pressure drop and convection heat transfer coefficient during condensation and evaporation of CO₂ at various operating conditions for flow inside micropipes of 0.6, 1.0, and 1.6 mm internal diameter. The Reynolds number (Re_d) range was between 2000 and 15000. The researchers used the dimensional analysis technique to develop correlations for pressure drops and Nusselt numbers. They assumed that the pressure drop of any gas during condensation (ΔP_{cond}) was dependent on the following dimensional variables: the micropipe internal diameter (d_i); the micropipe condenser length (L); micropipe condenser inlet pressure ($P_{in,cond}$); the mean velocity (U_m); and the mean value of the density (ρ_m) and the dynamic viscosity (μ_m). They obtained a general formula for the non-dimensional pressure drop during condensation. Solving for carbon dioxide (CO₂) data generated by their experimental work using the Multiple Linear Regression Method would give the following correlation:

$$\frac{\Delta P_{cond}}{P_{in,cond}} = 1.56 * \left[\left(\frac{1}{Eu * Re_d} \right)^{0.27} \left(\frac{L}{d_i} \right)^{0.14} \right] \quad (33)$$

$$Eu = \frac{P_{in,cond}}{U_m^2 \rho_m} \quad (34)$$

$$Re_d = \frac{\rho_m d_i U_m}{\mu_m} \quad (35)$$

It should be noted that the mean values of the properties were defined by liquid and gas properties. For example

$$\rho_m = \frac{\rho_l + \rho_g}{2} \quad (36)$$

$$\mu_m = \frac{\mu_l + \mu_g}{2} \quad (37)$$

Alshqirate et al. [51] carried out a comparison between experimental and correlated results. The results showed that for the condensation process, the bias errors were 0.4% and 5.25% for Nusselt number and pressure drops respectively. Consequently, Average Standard Deviation (ASD) values reached 4.62% and 17.94% for both respectively. On the other hand, the Nusselt number error for the evaporation process was 3.8% with an ASD of 4.14%. Their correlations could be used in calculating heat transfer coefficients and pressure drops for phase change flows in mini and micro tubes. Also, their correlations could help to enhance design calculations of evaporators, condensers and heat exchangers.

Kim and Mudawar [52] examined the heat transfer characteristics and pressure drop of annular condensation in rectangular micro-channels with three-sided cooling walls. The researchers proposed a theoretical control-volume-based model using the assumptions of smooth interface between the vapor core and annular liquid film, and uniform film thickness around the channel's circumference. They applied mass and momentum conservation to control volumes encompassing the vapor core and the liquid film separately. They compared their model predictions with experimental heat transfer and pressure drop data for annular condensation of FC-72 along $1 \times 1 \text{ mm}^2$ parallel channels. The data spanned FC-72 saturation temperatures (T_s) of 57.8-62.3°C, mass fluxes (G) of 248-367 kg/(m².s), mass qualities (x) of 0.23-1.0, and water mass flow rates of 3-6 g/s. Also, they compared the data to predictions of previous separated flow mini/micro-channel and macro-channel correlations. Their new model accurately

captured the heat transfer coefficient and pressure drop data in both magnitude and trend, evidenced by mean absolute error values of 9.3% and 3.6%, respectively.

In their first part of a two-part study, Kim et al. [53] performed experiments to investigate FC-72 condensation along parallel, square micro-channels with a length (L) of 29.9 cm and a hydraulic diameter (d_h) of 1 mm that were formed in the top surface of a solid copper plate. The operating conditions included FC-72 saturation temperatures (T_s) of 57.2-62.3°C, FC-72 mass fluxes (G) of 68-367 kg/(m².s), and water mass flow rates of 3-6 g/s. The researchers identified five distinct flow regimes: smooth-annular, wavy-annular, transition, slug, and bubbly using high-speed video imaging and photomicrographic techniques, with the smooth-annular and wavy-annular regimes being most prevalent. They presented a detailed pressure model that included all pressure drop components across the micro-channel. They examined various sub-models for the frictional and accelerational pressure gradients using the homogenous equilibrium model (with various two-phase friction factor relations) as well as previous macro-channel and mini/micro-channel separated flow correlations. The homogenous flow model provided far more accurate predictions of pressure drop than the separated flow models. They achieved better predictions with those for adiabatic and mini/micro-channels than those for flow boiling and macro-channels among the separated flow models.

Rose and Wang [54] investigated the annular laminar flow pressure drop, or more precisely pressure gradient, during condensation in microchannels. The annular laminar flow was the only flow regime permitting wholly theoretical solution without having recourse to experimental data. The researchers obtained solutions and made comparisons with empirical formulae for void fraction (needed to calculate the momentum pressure gradient) when obtaining the friction pressure gradient from experimentally measured or "total" pressure gradient. They restricted to date calculations and comparisons to one fluid (R134a), one channel section and one flow condition. They found that earlier approximate models for estimating void fraction agreed quite well with the theoretical annular flow solutions. However, there was significant difference between momentum pressure gradients obtained from approximate models used in the earlier investigations and that given by the theoretical annular flow solution that was (numerically) higher than all of them. The annular flow solution indicated that the momentum pressure gradient was not small in comparison with the friction pressure gradient. The friction pressure gradient in the annular flow case was appreciably smaller than given by the earlier correlations.

Fronk and Garimella [55] investigated experimentally pressure drop and heat transfer during Ammonia condensation in a single circular tube of $d = 1.435$ mm. The researchers chose Ammonia (NH₃) as a working fluid because of its use in thermal systems was attractive due to its favorable transport properties, high latent heat, zero global warming potential (GWP), and zero ozone depletion (ODP) as well as there were few data on ammonia condensation at the microscale while there was a growing body of research on conventional refrigerants condensation (i.e., R134a, R404A, etc.) in microchannels. Ammonia has significantly different fluid properties than synthetic HFC and HCFC refrigerants. For instance, ammonia has an enthalpy of vaporization 7.2 times and a surface tension 3.2 times greater than those of R134a at $T_s = 60^\circ\text{C}$. As a result, models validated with data for synthetic refrigerants might not predict

ammonia condensation with sufficient accuracy. They determined two-phase frictional pressure gradient and condensation heat transfer coefficient at multiple saturation temperatures (corresponding to $P_r = 0.10-0.23$), mass fluxes (G) of 75 and 150 kg/(m².s), and in small quality increments ($\Delta x \sim 15-25\%$) from 0 to 1. They discussed trends in pressure drops and heat transfer coefficients and used the results to assess the applicability of models developed for both macro and microscale geometries for predicting the ammonia condensation. The dependence of heat transfer and pressure drop on mass quality and mass flux was as expected. However, they found that existing models were not able to predict accurately the results. The coupled influences of ammonia properties and microscale geometry were outside the applicable range of most condensation pressure drop and heat transfer models. Additional reliable data pressure drop and heat transfer for smaller tube diameters and with working fluids like ammonia were necessary. These results would enable the development of models, which allow better prediction of condensation over a wider range of working fluids, hydraulic diameters, and operating conditions.

Charun [56] investigated experimentally the heat transfer and pressure drop during the R404A condensation in 1.4-3.30 mm stainless steel pipe minichannels. The researcher provided a review of the present state of knowledge concerning the R404A condensation in conventional channels and in small-diameter channels. He found that there were few prior publications concerning this issue. The test setup is described as well as the results of the experimental tests. He discussed the dependence of the heat transfer coefficient and the pressure drop of the R404A on the minichannel diameter (d), the mass flux (G), and mass quality (x). The pressure drop during the R404A condensation was satisfactorily described by the Friedel [6] and Garimella [13] correlations.

Previous correlations and models for the pressure drop prediction in adiabatic and condensing mini/micro-channel flows had been validated for only a few working fluids and relatively narrow ranges of relevant parameters. Therefore, Kim and Mudawar [57] developed a universal approach for the prediction of pressure drop in adiabatic and condensing mini/micro-channel flows that was capable of tackling many fluids with drastically various thermophysical properties and very broad ranges of all geometrical and flow parameters of practical interest. The researchers amassed a new consolidated database of 7115 frictional pressure gradient data points for both adiabatic and condensing mini/micro-channel flows from 36 sources to achieve this goal. The database consisted of 17 working fluids (air/CO₂/N₂-water mixtures, N₂-ethanol mixture, R12, R22, R134a, R236ea, R245fa, R404A, R410A, R407C, propane, methane, ammonia, CO₂, and water), hydraulic diameters (d_h) from 0.0695 to 6.22 mm, mass fluxes (G) from 4.0 to 8528 kg/(m².s), flow qualities (x) from 0 to 1, liquid-only Reynolds numbers (Re_{lo}) from 3.9 to 89,798, and reduced pressures (P_r) from 0.0052 to 0.91. They showed that, while a few prior models and correlations provided fair predictions of the consolidated database, their predictive accuracy was highly compromised for certain subsets of the database. They proposed a universal approach to predict two-phase frictional pressure drop by incorporating appropriate dimensionless relations in a separated flow model to account for both small channel size and various combinations of liquid and vapor states. Their

new pressure drop correlation for mini/micro-channels in both single- and multichannel configurations was

$$\left(\frac{dP}{dz}\right)_f = \left(\frac{dP}{dz}\right)_l \phi_l^2 \quad (38)$$

$$\phi_l^2 = 1 + \frac{C}{X} + \frac{1}{X^2} \quad (39)$$

$$X^2 = \frac{(dP/dz)_l}{(dP/dz)_g} \quad (40)$$

$$\left(\frac{dP}{dz}\right)_l = \frac{2f_l G^2 (1-x)^2}{\rho_l d_h} \quad (41)$$

$$\left(\frac{dP}{dz}\right)_g = \frac{2f_g G^2 x^2}{\rho_g d_h} \quad (42)$$

$$f_k = \frac{16}{\text{Re}_k} \quad \text{Re}_k < 2000 \quad (43)$$

$$f_k = \frac{0.079}{\text{Re}_k^{0.25}} \quad 2000 \leq \text{Re}_k < 20000 \quad (44)$$

$$f_k = \frac{0.046}{\text{Re}_k^{0.2}} \quad \text{Re}_k \geq 20000 \quad (45)$$

For laminar flow forced convection in rectangular ducts, the Shah and London relation [58] can be used. This relation can be written as a function of the aspect ratio (AR) as follows:

$$f_k \text{Re}_k = 24(1 - 1.3553AR + 1.9467AR^2 - 1.7012AR^3 + 0.9564AR^4 - 0.2537AR^5) \quad (46)$$

where subscript k denotes l or g for liquid and vapor phases, respectively.

In Eq. (46), $AR = 0$ is the case of parallel plates and $f_k Re_k = 24$ in that case while $AR = 1$ is the case of square shape and $f_k Re_k = 14.23$ in that case.

$$Re_l = \frac{G(1-x)d_h}{\mu_l} \quad (47)$$

$$Re_g = \frac{Gx d_h}{\mu_g} \quad (48)$$

The different correlations for C for different laminar and turbulent liquid and vapor flow states were

For turbulent liquid-turbulent vapor flow ($Re_l > 2000$ and $Re_g > 2000$)

$$C = 0.39 Re_{lo}^{0.03} Su_{go}^{0.10} \left(\frac{\rho_l}{\rho_g} \right)^{0.35} \quad (49)$$

For turbulent liquid-turbulent vapor flow ($Re_l > 2000$ and $Re_g > 2000$)

$$C = 8.7 \times 10^{-4} Re_{lo}^{0.17} Su_{go}^{0.50} \left(\frac{\rho_l}{\rho_g} \right)^{0.14} \quad (50)$$

For laminar liquid-turbulent vapor flow ($Re_l < 2000$ and $Re_g > 2000$)

$$C = 0.0015 Re_{lo}^{0.59} Su_{go}^{0.19} \left(\frac{\rho_l}{\rho_g} \right)^{0.36} \quad (51)$$

For laminar liquid-laminar vapor flow ($Re_l < 2000$ and $Re_g < 2000$)

$$C = 3.5 \times 10^{-5} Re_{lo}^{0.44} Su_{go}^{0.50} \left(\frac{\rho_l}{\rho_g} \right)^{0.48} \quad (52)$$

In the equations of the parameter (C), the Reynolds number for all flow as liquid (Re_{lo}), and the Suratman number for all flow as vapor (Su_{go}) were defined as

$$\text{Re}_{lo} = \frac{Gd_h}{\mu_l} \quad (53)$$

$$\text{Su}_{go} = \frac{\rho_g \sigma d_h}{\mu_g^2} \quad (54)$$

Kim and Mudawar [57] showed their new two-phase frictional pressure drop correlation predicted the entire 7115 experimental mini/micro-channel database quite accurately, with Mean Absolute Error (MAE) values of 26.3%, 22.4%, 26.8%, and 21.1% for the laminar-laminar (vv), laminar-turbulent (vt), turbulent-laminar (tv), turbulent-turbulent (tt) flow regimes, respectively. These low values of MAE could be attributed to the large database (7115 data points) upon which it was based. Also, their approach was capable of tackling single and multiple channels as well as situations involving significant flow deceleration due to condensation.

Zhang et al. [59] investigated experimentally condensation pressure drop and heat transfer of R22, R410A and R407C in two single round stainless steel tubes with $d = 1.088$ mm and 1.289 mm. The researchers measured two phase pressure drop and condensation heat transfer coefficients at the saturation temperatures of 30°C and 40°C. The vapor quality (x) varied from 0.1 to 0.9 and the mass flux (G) varied from 300 to 600 kg/(m².s). They investigated the influences of vapor quality and mass flux and their results indicated that condensation heat transfer coefficients increased with vapor quality and mass flux, increasing faster in the high vapor quality region. Two phase pressure drop and condensation heat transfer coefficients of R22 and R407C were equivalent but both higher than those of R410A. As a substitute for R22, R410A had more advantages than R407C in view of the characteristics of pressure drop and condensation heat transfer.

Mikielewicz et al. [60] presented a general method for calculation of two-phase flow pressure drop in flow boiling and flow condensation because flow boiling and flow condensation were often regarded as two opposite or symmetrical phenomena, however their description with a single correlation had yet to be suggested. This task was a little easier in the case of flow boiling/flow condensation in minichannels in comparison to the case of flow boiling/flow condensation in conventional size tubes (diameters greater than 3 mm). This was because they were dealing with two major structures of two-phase flow, namely bubbly flow and annular flow in conventional size tubes while they were dealing with the annular flow structure only in minichannels where the bubble generation/collapse was not present. The difficulty in devising a general method for pressure drop calculations, applicable to both flow condensation and flow boiling, lay in the fact that the non-adiabatic effects were excluded into the present in literature models. In case of bubbly flow the applied heat flux effect was not encountered, similarly the heat flux effect in annular flow was excluded.

The key feature of their method was the approach to model the modification of interface shear stresses in flow boiling and flow condensation due to mass flux and heat flux on interface. In case of annular flow structure incorporation of the so called "blowing parameter" that

differentiated these two modes of heat transfer, was considered. The researchers devoted that effect to a correct mass flux modeling on interface. The differences in shear stress between vapor phase and liquid phase was generally a function of non-adiabatic effect. Correct modeling of that heat flux enabled to predict a thinner liquid film thickness in boiling and thicker in condensations at otherwise exactly the same flow conditions. That was a major reason why that up to date approaches, considering the issue of flow boiling and flow condensation as symmetric, were failing in successful predictions. In case of bubbly flow structure the applied heat flux effect was considered. Therefore, a modified form of the two-phase flow multiplier was obtained, in which the non-adiabatic effect was clearly pronounced. They made comparisons with some well established experimental data from literature for many fluids. These data would be carefully scrutinized to extract the applied heat flux effect. Preliminary calculations showed a satisfactory consistency of their model with experimental data. Also, they made comparisons with well established empirical correlations for calculations of heat transfer coefficient. Their calculations showed that their method presented above was universal and could be used to predict heat transfer in flow boiling and flow condensation for various halogeneous refrigerants and other fluids. They mentioned that their model could be suggested for a wider use amongst engineers, but further validation with experimental data would add value to its robustness.

Son and Oh [61] investigated experimentally the condensation pressure drop characteristics for pure refrigerants R22, R134a, and a binary refrigerant mixture R410A without lubricating oil in a single circular microtube. Their test section consisted of 1220 mm length with horizontal copper tube of 3.38 mm outer diameter and 1.77 mm inner diameter. The researchers conducted their experiments at refrigerant mass flux (G) of 450-1050 kg/(m².s), and saturation temperature (T_s) of 40°C. For the same mass flux, they found that the condensation pressure drop of R134a was higher than that of R22 and R410A. They compared their experimental data against 14 two-phase pressure drop correlations. They presented a new pressure drop model that was based on a superposition model for refrigerants condensing in the single circular tube. They related the experimental pressure drop during condensation inside the single circular tube to mass flux, inner diameter and thermophysical properties such as surface tension, density and viscosity. Therefore, they developed the Chisholm factor (C) as a function of the two-phase Weber number (We_{tp}), and two-phase Reynolds number (Re_{tp}). Their correlation was

$$C = \left(\phi^2 - 1 - \frac{1}{X^2} \right) X = 2485 We_{tp}^{0.407} Re_{tp}^{0.34} \quad (55)$$

$$We_{tp} = \frac{G^2 d}{\sigma \rho_{tp}} \quad (56)$$

$$Re_{tp} = \frac{Gd}{\mu_{tp}} \quad (57)$$

$$\rho_{tp} = \left[\frac{x}{\rho_g} + \frac{(1-x)}{\rho_l} \right]^{-1} \quad (58)$$

$$\mu_{tp} = \left[\frac{x}{\mu_g} + \frac{(1-x)}{\mu_l} \right]^{-1} \quad (59)$$

Based on their experimental database and using a regression method with 108 data points,, their correlation provided a mean deviation of 2.31% and an average deviation of -8.7%.

Zhang et al. [62] presented the heat transfer characteristics of CO₂ condensation in a mini-channel condenser. The condenser consisted of seven tubes in parallel whose inner diameter was 0.9 mm that were thermally connected to two aluminium base-plates by using thermal glue. They obtained the CO₂ condensation heat transfer coefficients, ranging from 1700 to 4500 W/(m².K) at saturation temperatures ranging from -5°C to 15°C, with average vapor qualities from 0.2 to 0.8, and, mass fluxes of 180, 360 and 540 kg/(m².s), respectively. Also, they found that the measured pressure drop over the condenser increased with the vapor quality and the mass flux, but decreased with the saturation temperature.

Garimella and Fronk [63] conducted a systematic series of experiments on condensation flow regimes, heat transfer, and pressure drop using innovative visualization and measurement techniques for condensation of synthetic and natural refrigerants and their azeotropic and zeotropic mixtures through micro-channels with a wide range of diameters (0.1 < d_h < 5 mm), shapes, and operating conditions. These experiments resulted in flow-regime-based pressure drop and heat transfer models with very good predictive capabilities for such micro-channel geometries.

Wang and Rose [64] investigated pressure drop and heat transfer during laminar annular flow condensation in micro-channels. The annular laminar condensate flow permitted wholly theoretical solution without recourse to empirical input. Channel geometry, flow parameters and tube wall temperatures, local pressure gradient, and local heat transfer-coefficient could be calculated as well as local quality and void fraction for laminar annular flow condensation in micro-channels and for specified fluid. The researchers outlined the theory in this article, and discussed recent developments. They summarized and compared results for pressure drop and heat transfer for laminar annular flow condensation in micro-channels with experimental data. They found that correlations of experimental data for both pressure drop and heat transfer could only be expected to have validity for fluids and conditions close to those used when obtaining the data on which the correlations were based. They found that the results for pressure gradient given by the annular laminar flow model were generally lower than those given by the correlations.

Liu et al. [65] presented experimental data for pressure drop and heat transfer during R152a condensation in square and circular microchannels with hydraulic diameters (d_h) of 0.952 mm

and 1.152 mm, respectively. Saturation temperatures (T_s) were 40°C and 50°C with vapor mass qualities (x) varying from 0.1 to 0.9 and mass fluxes (G) from 200 to 800 kg/(m².s). The researchers investigated effects of vapor mass quality, mass flux, and channel geometry on pressure drop and heat transfer. They found that pressure gradients and heat transfer coefficients during condensation decreased with increasing saturation temperature while increased with increasing vapor mass quality and mass flux both in square and circular microchannels. Channel geometry had little influence on two-phase pressure gradients. They used three pressure drop correlations based on experimental data of R134a in microchannels to predict experimental data. These three pressure drop correlations were correlations of Koyama et al. [8], Agarwal and Garimella [29], and Cavallini et al. [30]. They found that Koyama et al. [8] underestimated the data for both square and circular microchannels while Agarwal and Garimella [29] overestimated the data for the square microchannel. Predictions of Cavallini et al. [30] showed large root-mean-square errors for data in both square and circular microchannels.

Wang et al. [66] calculated the frictional pressure gradient for the laminar annular flow condensation in microchannels. The laminar annular flow was the only flow regime permitting theoretical solution without having recourse to experimental data. The researchers made comparisons with correlations using experimental data for R134a. The correlations were different somewhat among themselves with the highest to lowest predicted friction pressure gradient ratio typically around 1.4 and nearer to 1 at high quality. The frictional pressure gradients given by the laminar annular flow solutions were lower than the correlations at lower quality and in fair agreement with the correlations at high quality. The frictional pressure gradient could not be directly observed and its evaluation from measurements required the nondissipative momentum or acceleration pressure gradient estimation. Methods used to estimate the nondissipative pressure gradient required void fraction and quality together with equations that related these and whose accuracy was difficult to quantify. Void fraction and quality could be readily found from the laminar annular flow solutions. They found significant differences between these and values from approximate equations.

Heo et al. [67] investigated the CO₂ condensation pressure drop and heat transfer coefficient in a multiport microchannel with a hydraulic diameter (d_h) of 1.5 mm with variation of the condensation temperature (T) from -5 to 5°C and of the mass flux (G) from 400 to 1000 kg/(m².s). The researchers found that the pressure drop and heat transfer coefficient increased with the increase of mass flux and the decrease of condensation temperature. The gradient of the pressure drop with respect to vapor quality (x) was significant with the mass flux (G) increase. For the pressure drop, they found that the Mishima and Hibiki model [37] showed mean deviation of 29.1%.

Ganapathy et al. [68] presented a numerical model for the simulation of fluid flow characteristics and condensation heat transfer in a single microchannel. The researchers based their model on the volume of fluid approach that governed the hydrodynamics of the two-phase flow. They governed the condensation characteristics using the phenomena physics and excluded any empirical expressions in the formulation. They modified the conventional governing equations for conservation of volume fraction and energy to include source terms,

which accounted for the mass transfer at the liquid–vapor interface and the associated release of latent heat, respectively. They modeled a microchannel having characteristic dimension of 100 μm using a two-dimensional computational domain. The working fluid was R134a and the channel wall was maintained at a constant heat flux (q) ranging from 200 to 800 kW/m^2 . The vapor mass flux (G_g) at the channel inlet ranged from 245 to 615 $\text{kg}/(\text{m}^2\cdot\text{s})$. They assessed the predictive accuracy of their numerical model by comparing the Nusselt number and two-phase frictional pressure drop with available empirical correlations in the literature. They obtained a reasonably good agreement for both parameters with a mean absolute error (MAE) of 8.1% for two-phase frictional pressure drop against a recent universal predictive approach by Kim and Mudawar [57], and 16.6% for Nusselt number against the Dobson and Chato correlation [69].

Heo et al. [70] presented comparison of condensation pressure drop and heat transfer of carbon dioxide (CO_2) in three various microchannels. The channels were rectangular, and the numbers of ports were 7, 19, and 23. The hydraulic diameters (d_h) were 1.5, 0.68, and 0.78 mm for the 7, 19, and 23 ports, respectively. The mass flux (G) range was from 400 to 800 $\text{kg}/(\text{m}^2\cdot\text{s})$, and the test temperature ranged from -5 to 5°C . The researchers found that the highest pressure drop in the microchannel of 23 ports too. The Mishima and Hibiki model [37] had a mean deviation of $\pm 30.1\%$ for the frictional pressure drop.

Murphy [71] investigated heat transfer and pressure drop during condensation of propane (R290) flowing through minichannels because condensation studies of hydrocarbons are important for applications in the petrochemical industry. For accurate design of heat transfer equipment for use in hydrocarbon processing, insights into the mechanisms of propane condensation are required. The researcher designed and fabricated an experimental facility to measure the frictional pressure drop and heat transfer coefficients during condensation of propane in vertical plain tubes with an inner diameter of 1.93 mm. He took measurements across the vapor-liquid dome in nominal quality increments of 0.25 for two saturation temperatures (47°C and 74°C) and four mass flux conditions (75-150 $\text{kg}/(\text{m}^2\cdot\text{s})$). He compared the data to the predictions of relevant correlations in the literature. Also, he used the data from his study to develop models for the frictional pressure drop and heat transfer coefficient based on the measurements and the underlying condensation mechanisms.

Mikielewicz et al. [72] presented investigations of flow condensation with the use of the HFE7100 and HFE 7000 as a working fluids and their own condensation model inside tubes with account of non-adiabatic effects. Their model would be confronted with their own data for a new fluid HFE7000 and HFE 7100. One of the objectives of their study was to add data of HFE7100 and HFE7000 for minichannels because of the lack in published studies. This data was greatly interesting because of the very various thermo physical properties of such fluids compared to other substances commonly tested in minichannels. Another reason for understanding the behavior of two phase flow of the working fluids HFE7100 and HFE7000 was due to increased concerns of ozone depletion (ODP) and GWP (global warming potential), as increased knowledge of the performance of this fluids might contribute to HCFC and HFC refrigerants and might use in many other perspective ecological application like organic Rankine cycles. The researchers used a 2.23 mm circular vertical minichannel to measured both

two-phase pressure losses of the fluids HFE7100 and HFE7000. They found satisfactory consistency of discussed model with their own experimental data for condensation. Their presented model could be suggested for a wider use amongst engineers, but further validation with experimental data would add value to its robustness.

Sakamatapan and Wongwises [73] continued the authors' previous work on the condensation of R134a flowing inside a multiport minichannel [74]. The researchers investigated experimentally the pressure drop's characteristics during condensation for R134a flowing inside a multiport minichannel. Two kinds of multiport minichannels having 14 channels, one with a hydraulic diameter (d_h) of 1.1 mm and another with 8 channels with a hydraulic diameter (d_h) of 1.2 mm, were designed as a counter flow tube in a tube heat exchanger. They observed the pressure drop characteristics under mass flux (G) range of 345-685 kg/(m².s), heat flux (q) of 15-25 kW/m², and saturation temperature (T_{sat}) of 35-45°C. They found that the total pressure drop was dominated by the frictional pressure drop. The frictional pressure gradient increased with the augmentation of mass flux and vapor quality, but the increase of the saturation temperature and channel size led to the frictional pressure gradient decrease. On the other hand, the heat flux had an insignificant influence on the frictional pressure gradient. They conducted the miniscale correlations to predict the frictional pressure gradient, and found that only the multiport minichannel correlations gave a reasonable result. Using the equivalent Reynolds number (Re_{eq}) concept, they proposed a new two-phase friction factor correlation to predict the frictional pressure gradient during condensation. Their correlation was

$$f_{tp} = 6977 Re_{eq}^{-0.337} x^{-0.031} \left(\frac{\rho_l}{\rho_g} \right)^{6.510} \left(\frac{\mu_l}{\mu_g} \right)^{-11.883} \quad (60)$$

$$Re_{tp} = \frac{G_{tp} d}{\mu_l} \quad (61)$$

$$G_{tp} = G \left[(1-x) + x \sqrt{\frac{\rho_l}{\rho_g}} \right] \quad (62)$$

López-Belchí et al. [75] studied condensing two-phase flow pressure drop inside a minichannel tube with 1.16 mm inner hydraulic diameter with R1234yf, R134a and R32. According to the available data, most of the models checked capture the trend correctly. The researchers observed the pressure drop characteristics under mass flux (G) range of 350-940 kg/(m².s), and saturation temperature (T_{sat}) of 20-55°C. They analyzed experimental data to show the effect of saturation temperature, mass fluxes, vapor quality and fluid properties in pressure drop. Finally, they presented a new correlation model with a mean absolute relative deviation (MARD) value of 8.32% reducing the best correlation MARD by more than 34%. The equations of their model are given below.

$$\left(\frac{dP}{dz}\right)_{tp} = \phi_l^2 \left(\frac{dP}{dz}\right)_l \quad (63)$$

$$\phi_l^2 = 1 + \frac{C}{X} + \frac{1}{X^2} \quad (64)$$

$$X^2 = \frac{(dP/dz)_l}{(dP/dz)_g} \quad (65)$$

$$\left(\frac{dP}{dz}\right)_l = \frac{2f_l G^2 (1-x)^2}{\rho_l d} \quad (66)$$

$$\left(\frac{dP}{dz}\right)_g = \frac{2f_g G^2 x^2}{\rho_g d} \quad (67)$$

$$f_k = \frac{16}{\text{Re}_k} \quad \text{Re}_k < 2000 \quad (68)$$

$$f_k = \frac{1}{16} \left[\log \left(\frac{150.39}{\text{Re}_k^{0.98865}} - \frac{152.66}{\text{Re}_k} \right) \right]^{-2} \quad \text{Re}_k \geq 3000 \quad (69)$$

$$f_k = 0.25(1.1525\text{Re}_k + 895) \cdot 10^{-5} \quad 2000 \leq \text{Re}_k < 3000 \quad (70)$$

where subscript k denotes l or g for liquid and vapor phases, respectively.

$$\text{Re}_l = \frac{G(1-x)d}{\mu_l} \quad (71)$$

$$\text{Re}_g = \frac{Gxd}{\mu_g} \quad (72)$$

Eq. (69) for the friction factor in turbulent region was confirmed by Fang et al. [76, 77] and Brkic [78] to be the most accurate single-phase friction factor equation flow in smooth tubes.

Eq. (70) for the transition zone was obtained by linear interpolation (Xu and Fang [79]).

The correlation for C was adjusted for best fitting experimental data.

$$C = 4.6468 \cdot 10^{-6} \left(\frac{P_{sat}}{P_{cr}} \right)^{5.5866} Re_1^{0.4387} \left(\frac{\rho_l}{\rho_g} \right)^{5.7189} X^{0.4243} \quad (73)$$

The experimental tests developed covered the range of, $P_{red} = 0.183-0.603$, $Re_l = 528-8200$, $\rho_l/\rho_g = 7.03-32.92$, $X = 0.05-2.53$ in a multi-port mini-channel tube with square ports and a hydraulic diameter of 1.16 mm.

Thome and Cioncolini [80] presented unified modeling suite convective boiling and condensation for annular flow in macro- and micro-channels. The researchers presented first unified suite of methods, illustrating in particular, the most recent updates. The annular flow suite included models to predict the entrained liquid fraction, void fraction, the wall shear stress and pressure gradient, and a turbulence model for momentum and heat transfer inside the annular liquid film. In particular, the turbulence model allowed prediction of the local liquid film thicknesses and the local heat transfer coefficients during convective evaporation and condensation. The benefit of a unified modeling suite was that all the included prediction methods were consistently formulated and were proven to work well together, and provided a platform for continued advancement based on the other models in the suite. The annular flow in convective condensation was established almost immediately at the channel inlet and persisted over most of the condensation process until the condensate flooded the channel.

Mikielewicz et al. [81] presented experimental investigations on pressure drop during the condensation in flow of HFE7000 in vertical minichannel of 2.23 mm inner diameter. The researchers scrutinized a new working fluid HFE7000, which had a strongly differing properties in comparison to the other fluids that were commonly used for studies in the minichannels. They observed the pressure drop characteristics under mass flux (G) range of 240-850 kg/(m².s), heat flux (q) of 47.2-368.7 kW/m², and saturation temperature (T_{sat}) of 35-93°C over the mass quality (x) range of 0-1. They compared their experimental results with the in-house developed model for two-phase flow pressure drop with inclusion of non-adiabatic effects. The comparisons results showed satisfactory agreement.

Kim and Mudawar [82] presented a review of databases and predictive methods for pressure drop in adiabatic, condensing and boiling mini/micro-channel flows. Their study addressed the limited validity of most published methods to a few working fluids and narrow ranges of operating conditions by discussing the development of two consolidated mini/micro-channel databases. The first database was for adiabatic and condensing flows, and consisted of 7115 frictional pressure gradient data points from 36 sources, and the second database for boiling flow, and consisted of 2378 data points from 16 sources. These researchers used these consolidated databases to assess the accuracy of previous models and correlations as well as to

develop 'universal' correlations, which were applicable to a large number of fluids and very broad ranges of operating conditions.

Illán-Gómez et al. [83] studied condensing two-phase flow pressure drop gradient and heat transfer coefficient (HTC) inside a mini-channel multiport tube with R1234yf and R134a. The researchers used many models available in the literature to compare predictions of these two fluids. They analyzed experimental data to get the effect of saturation temperature, mass flux, vapor quality and fluid properties. HTC values of R1234yf seemed to be lower than R134a under similar conditions. They proposed a readjusted HTC model. Also, two-phase flow pressure drops were lower in the case of the new refrigerant R1234yf.

Ramírez-Rivera et al. [84] measured experimentally two-phase flow pressure drop of R134a and R32 in condensation and evaporation fluid flow in a multiport extruded aluminium tube (MPEs) with $d_h = 0.715$ and 1.16 mm. Their experimental conditions range was: mass flux (G) 200-1229 kg/(m².s), saturation temperatures (T_s) (5, 7.5, 12.5, 30, 35, 40, 45, 50, 55)°C, heat flux (q) 2.55-70 kW/m². The researchers developed two experimental facilities at the Technical University of Cartagena, Spain to study boiling and condensing flow phenomena. They compared their experimental data with some well-known correlations that were developed for macro/mini-channel tubes. Classic macro-channel correlations such as Friedel [6] and Müller-Steinhagen and Heck [85] predicted satisfactorily well their experimental pressure drop data. However, the Souza and Pimenta correlation [86] estimated their experimental pressure gradient data very well with multiport tubes of $d_h = 1.16$ mm, but failed to predict their experimental data in the tube of $d_h = 0.715$ mm with R134a and R32. Also, they tested seven correlations specially developed for mini/micro-channels. They found that Cavallini et al. [26] and Zhang and Webb [45] predicted with reasonable accuracy their experimental two-phase flow pressure drop data.

Goss et al. [87] investigated experimentally the pressure drop during the convective condensation of R-134a inside eight round ($d = 0.77$ mm) horizontal and parallel microchannels. The researchers quantified all pressure drop contributions, including the ones related to expansion, contraction, flow direction change, acceleration, and friction, for microchannel arrangement. Their test conditions included the mass flux (G), vapor quality (x), heat flux (q), and pressure (P), ranging from 230 to 445 kg/(m².s), 0.55 to 1, 17 to 53 kW/m², and 7.3 to 9.7 bar, respectively. The frictional pressure drop roughly was corresponding to 95% of the net pressure drop. They evaluated the effect of temperature, heat flux, and mass flux on the pressure drop. Their results showed that the pressure drop increased with an increase in mass flux (G) and a decrease in saturation temperature (T_s), whereas it is not affected as much by the heat flux (q). They compared their experimental results with correlations and semi-empirical models described in the literature. Correlations based upon the adiabatic two-phase flows within bore pipes could reasonably predict the pressure drop for condensing microchannel flows. The Cavallini et al. model [26] presented the best prediction performance.

Table 1 presents a summary of the aforementioned previous studies on condensation pressure drop in microchannels and minichannels.

Author	D	Fluids	Orientation/ Conditions	Range/ Applicability	Techniques, Basis, Observations
Koyama et al. [8]	1.114 mm (8 channels) 0.807 mm (19 channels)	R-134a	Horizontal	$G = 100-700 \text{ kg}/(\text{m}^2 \cdot \text{s})$ $x = 0-100\%$	The experimental data of frictional pressure drop agreed with the correlation of Mishima and Hibiki [9], while the correlations of Chisholm and Laird [10], Soliman et al. [11], and Haraguchi et al. [12], overpredicted.
Garimella [13]	0.4-4.91 mm	R-134a	Horizontal	$G = 150-750 \text{ kg}/(\text{m}^2 \cdot \text{s})$ $x = 0-100\%$	His flow regime-based models yield substantially better pressure drop predictions than the traditionally used correlations that were primarily based on air-water flows for large diameter tubes.
Garimella et al. [14]	0.5-4.91 mm	R-134a	Horizontal Considering the intermittent only, intermittent/discrete wavy annular transition, and annular only flow	$G = 150-750 \text{ kg}/(\text{m}^2 \cdot \text{s})$ $x = 0-100\%$	Presenting a multiple flow-regime model for pressure drop during condensation.
Hau and Koyama [25]	1.31 mm	CO ₂	Horizontal	$P = 6.48-7.3 \text{ MPa}$ $T_{inlet} = 21.63-31.33^\circ\text{C}$ $q = 1.10-8.12 \text{ kW}/\text{m}^2$ $G = 123.2-315.2 \text{ kg}/(\text{m}^2 \cdot \text{s})$ $x = 0-100\%$	The pressure drop was very small along the test section. The existing model failed to predict the experimental data.
Cavallini et al. [26]	0.4-3 mm	high pressure (R410A), medium (R134a) and low pressure (R236ea)	Horizontal		No model is able to predict the frictional pressure gradient of the high pressure fluid R410A, several models accurately predict the medium pressure fluid R134a and a few satisfactorily estimate

Author	D	Fluids	Orientation/ Conditions	Range/ Applicability	Techniques, Basis, Observations
					the low pressure refrigerant R236ea.
Chowdhury et al. [27]	0.7 mm	R-134a	Horizontal	AR = 7 $T_{sat} = 30^{\circ}\text{C}$ $x = 20\text{-}80\%$ $G = 130, 200 \text{ kg}/(\text{m}^2.\text{s})$	A unique process for fabrication of the microchannel involving milling and electroplating steps was adopted to maintain the channel geometry close to design values.
Garimella [28]	1 mm	R-134a		$G = 300 \text{ kg}/(\text{m}^2.\text{s})$ $x = 50\%$ $P = 1500 \text{ kPa}$	Comparing different techniques for predicting the pressure drop during condensation.
Agarwal and Garimella [29]	0.42- 0.8 mm	R-134a	Horizontal	$G = 150\text{-}750 \text{ kg}/(\text{m}^2.\text{s})$ $x = 0\text{-}100\%$	Their resulting model predicted 80% of the data within $\pm 25\%$. The tube shape effect on pressure drop was demonstrated.
Cavallini et al. [30]	0.96 mm	R134a	Horizontal		Presenting a model for calculation of the frictional pressure gradient during condensation or adiabatic liquid-gas flow inside minichannels with different surface roughness.
Cavallini et al. [32]	0.96 mm	R134a and R32	Horizontal		Presenting modification of the friction factor in the proposed model previously developed by Cavallini et al. [30] to take into consideration also effects due to wall roughness.
Park and Hrnjak [33]	0.89 mm	CO ₂	Horizontal	$T_{sat} = -15, -25^{\circ}\text{C}$ $G = 200\text{-}800 \text{ kg}/(\text{m}^2.\text{s})$	Many correlations could predict their measured values of pressure drop relatively well such as the

Author	D	Fluids	Orientation/ Conditions	Range/ Applicability	Techniques, Basis, Observations
					Mishima and Hibiki model [37].
Agarwal and Garimella [38]	100-200 μm	R134a	Horizontal	$G = 200\text{-}800 \text{ kg}/(\text{m}^2\cdot\text{s})$ $x = 0\text{-}100\%$ $T_{sat} = 30, 40, 50, 60^\circ\text{C}$	The pressure drop increased with increasing vapor quality, increasing mass flux and decreasing saturation temperature.
Song et al. [39]	1.5 mm x 1.0 mm	FC72 and steam	Horizontal	$q = 130\text{-}170 \text{ kW}/\text{m}^2$ for steam $q = 10\text{-}30 \text{ kW}/\text{m}^2$ for FC72	Presenting preliminary results from a new research program for making accurate heat transfer and pressure drop measurements during condensation in microchannels.
Keinath and Garimella [40]	0.5-3 mm	R404a	Horizontal	$G = 200\text{-}800 \text{ kg}/(\text{m}^2\cdot\text{s})$ $x = 5\text{-}95\%$ $T_{sat} = 30\text{-}60^\circ\text{C}$	Presenting a novel and accurate methodology for the quantitative investigation of two-phase flow regimes and flow parameters during condensation in minichannels.
Fronk and Garimella [41]	100-200 μm	CO_2	Horizontal	$G = 600 \text{ kg}/(\text{m}^2\cdot\text{s})$ $x = 0\text{-}100\%$ $T_{sat} = 15, 20^\circ\text{C}$	Using the collected data to evaluate the applicability of correlations developed for larger hydraulic diameters and various fluids for predicting condensation heat transfer and pressure drop of CO_2 .
Kuo and Pan [42]	135 μm	steam	Horizontal	$2.10 \times 10^{-6}\text{-}9.11 \times 10^{-6} \text{ kg}/\text{s}$ for the uniform cross-section microchannel $2.10 \times 10^{-6}\text{-}5.93 \times 10^{-6} \text{ kg}/\text{s}$ for the converging microchannel	Their experimental data agreed well with the obtained correlations, with the maximum mean absolute errors of 6.4% for the two-phase frictional multiplier.

Author	D	Fluids	Orientation/ Conditions	Range/ Applicability	Techniques, Basis, Observations
Goss et al. [44]	0.8 mm	R134a	Horizontal	$G = 57\text{-}125 \text{ kg}/(\text{m}^2\cdot\text{s})$ $P = 6.8\text{-}11.2 \text{ bar}$	The pressure drop correlation proposed by Zang and Webb [45] gave the best results, with a deviation of 30%.
Keinath and Garimella [46]	0.5-3.0 mm	R404A			The Garimella et al. [14] model tends to overpredict the pressure drop data. The poorest agreement is for the 3-mm tube data.
Bohdal et al. [48]	0.1-3.30 mm	R134a	Horizontal	$G = 0\text{-}1200 \text{ kg}/(\text{m}^2\cdot\text{s})$ $x = 0\text{-}100\%$ $T_{sat} = 30\text{-}40^\circ\text{C}$	The pressure drop in two-phase flow during R134a condensation is dependent on: the agent type, process parameters and the structure of two-phase flow.
Bohdal et al. [49]	0.31-3.30 mm	R134a and R404A	Horizontal	$G = 100\text{-}1300 \text{ kg}/(\text{m}^2\cdot\text{s})$ $x = 0\text{-}100\%$ $T_{sat} = 20\text{-}40^\circ\text{C}$	The pressure drop during the condensation of the R134a and R404A refrigerants is described in a satisfactory manner with Friedel [6] and Garimella [13] correlations.
Bohdal et al. [50]	0.31-3.30 mm	R134a, R404a and R407C	Horizontal	$G = 0\text{-}1300 \text{ kg}/(\text{m}^2\cdot\text{s})$ $x = 0\text{-}100\%$ $T_{sat} = 20\text{-}50^\circ\text{C}$	The pressure drop during the condensation of the R134a, R404a and R407C refrigerants is described in a satisfactory manner with Friedel [6] and Garimella [13] correlations.
Alshqirate et al. [51]	0.6, 1.0, and 1.6 mm	CO ₂		$Re_d = 2000\text{-}15000$	Using the dimensional analysis technique to develop correlations for Nusselt numbers and pressure drops.
Kim and Mudawar [52]	1 mm	FC-72 and water (counter flow)	Horizontal	For FC-72, $G = 248\text{-}367 \text{ kg}/(\text{m}^2\cdot\text{s})$ $T_{sat} = 57.8\text{-}62.3^\circ\text{C}$ $x = 23\text{-}100\%$	Their new model accurately captured the pressure drop and heat transfer coefficient data in both magnitude and

Author	D	Fluids	Orientation/ Conditions	Range/ Applicability	Techniques, Basis, Observations
				For water, mass flow rate = 3-6 g/s	trend, evidenced by mean absolute error values of 3.6% and 9.3%, respectively.
Kim et al. [53]	1 mm	FC-72 and water (counter flow)	Horizontal	For FC-72, $G = 248-367 \text{ kg}/(\text{m}^2.\text{s})$ $T_{sat} = 57.2-62.3^\circ\text{C}$ $q = 4.3-32.1 \text{ kW}/\text{m}^2$ For water, $G = 69-138 \text{ kg}/(\text{m}^2.\text{s})$	The homogenous flow model provides far more accurate predictions of pressure drop than the separated flow models. Among the separated flow models, Kim et al. [53] achieve better predictions with those for adiabatic and mini/micro-channels than those for flow boiling and macro-channels.
Rose and Wang [54]		R134a	laminar annular flow		The momentum pressure gradient is not small in comparison with the friction pressure gradient. The friction pressure gradient in the annular flow case is appreciably smaller than given by the earlier correlations.
Fronk and Garimella [55]	1.435 mm	Ammonia (NH_3)	Horizontal	$G = 75-150 \text{ kg}/(\text{m}^2.\text{s})$ $T_{sat} = 30, 40, 50, 60^\circ\text{C}$ (corresponding to P_r , $= 0.10-0.23$)	The coupled influences of ammonia properties and microscale geometry were outside the applicable range of most condensation pressure drop and heat transfer models. Additional reliable data pressure drop and heat transfer for smaller tube diameters and with working fluids like ammonia were necessary.
Charun [56]	1.4, 1.6, 1.94, 2.3 and 3.3 mm	R404A	Horizontal	$G = 97-902 \text{ kg}/(\text{m}^2.\text{s})$ $x = 0-100\%$	The pressure drop during the R404A refrigerant condensation is satisfactorily described by the Friedel [6]

Author	D	Fluids	Orientation/ Conditions	Range/ Applicability	Techniques, Basis, Observations
					and Garimella [13] correlations.
Kim and Mudawar [57]	0.0695- 6.22 mm	17 various working fluids (air/CO ₂ /N ₂ -water mixtures, N ₂ -ethanol mixture, R12, R22, R134a, R236ea, R245fa, R404A, R410A, R407C, propane, methane, ammonia, CO ₂ , and water)		G = 4.0-8528 kg/(m ² .s) Re _{lo} = 3.9-89798 x = 0-100% P _r = 0.0052-0.91	Proposing a new universal approach to predict two-phase frictional pressure drop for adiabatic and condensing mini/micro-channel flows.
Zhang et al. [59]	1.088 and 1.289 mm	R22, R410A and R407C	Horizontal	G = 300-600 kg/(m ² .s) T _{sat} = 30, 40 °C x = 10-90%	Two phase pressure drop and condensation heat transfer coefficients of R22 and R407C are equivalent but both higher than those of R410A. R410A as a substitute for R22, has more advantages than R407C in view of the characteristics of condensation pressure drop and heat transfer.
Mikielewicz et al. [60]					Presenting a general method for calculation of two-phase flow pressure drop in flow boiling and flow condensation because flow boiling and flow condensation are often regarded as two opposite or symmetrical phenomena, however their description with a single correlation have yet to be suggested.

Author	D	Fluids	Orientation/ Conditions	Range/ Applicability	Techniques, Basis, Observations
Son and Oh [61]	1.77 mm	R22, R134a and R410A		$G = 450-1050 \text{ kg}/(\text{m}^2.\text{s})$ $T_{sat} = 40^\circ\text{C}$	The condensation pressure drop of R134a is higher than that of R22 and R410A for the same mass flux. Presenting a new pressure drop model where the Chisholm factor (C) is a function of the two-phase Weber number (We_{tp}), and two-phase Reynolds number (Re_{tp}).
Zhang et al. [62]	0.9 mm	CO ₂		$T_{sat} = -5-15^\circ\text{C}$ $G = 180, 360 \text{ and } 540 \text{ kg}/(\text{m}^2.\text{s})$ $x = 20-80\%$	The measured pressure drop over the condenser increases with the mass flux and the vapor quality, but decreases with the saturation temperature.
Garimella and Fronk [63]	$0.1 < d_h < 5 \text{ mm}$	synthetic and natural refrigerants and their azeotropic and zeotropic mixtures			These experiments resulted in flow-regime-based heat transfer and pressure drop models with very good predictive capabilities for such micro-channel geometries.
Wang and Rose [64]		R134a, ammonia (NH ₃)	laminar annular flow		Results for pressure gradient given by the annular laminar flow model are generally lower than those given by the correlations.
Liu et al. [65]	1.152 mm (circular) 0.952 mm (square)	R152a	Horizontal	$T_{sat} = 40-50^\circ\text{C}$ $G = 200-800 \text{ kg}/(\text{m}^2.\text{s})$ $x = 10-90\%$	Channel geometry has little effect on frictional pressure gradients. Koyama et al. [8] underestimates the square and circular microchannels data while Agarwal and Garimella [29] overestimate the square microchannel data. Predictions of Cavallini et al. [30] show

Author	D	Fluids	Orientation/ Conditions	Range/ Applicability	Techniques, Basis, Observations
					large root-mean-square errors for data in both square and circular microchannels.
Wang et al. [66]		R134a	laminar annular flow		The frictional pressure gradients given by the laminar annular flow solutions are in fair agreement with the correlations at high quality and lower than the correlations at lower quality.
Heo et al. [67]	1.5 mm	CO ₂	Horizontal	$G = 400\text{-}1000 \text{ kg}/(\text{m}^2\cdot\text{s})$ $T_{sat} = -5\text{-}5 \text{ }^\circ\text{C}$	The Mishima and Hibiki model [37] showed mean deviation of 29.1%.
Ganapathy et al. [68]	100 μm	R134a	constant heat flux	$G_g = 245\text{-}615 \text{ kg}/(\text{m}^2\cdot\text{s})$ $q = 200\text{-}800 \text{ kW}/\text{m}^2$	Using the volume of fluid approach. The mean absolute error (MAE) is 8.1% for two-phase frictional pressure drop against a recent universal predictive approach by Kim and Mudawar [57].
Heo et al. [70]	1.5, 0.78, and 0.68 mm for the 7, 23, and 19 ports	CO ₂	Horizontal	$G = 400\text{-}800 \text{ kg}/(\text{m}^2\cdot\text{s})$ $T_{sat} = -5\text{-}5 \text{ }^\circ\text{C}$	The Mishima and Hibiki model [37] has a mean deviation of $\pm 30.1\%$ for the frictional pressure drop.
Murphy [71]	1.93 mm	Propane (R290)	Vertical	$T_{sat} = 47^\circ\text{C}$ and 74°C $G = 75\text{-}150 \text{ kg}/(\text{m}^2\cdot\text{s})$	The results and the corresponding correlations contribute to the understanding of condensation of hydrocarbon.
Mikielewicz et al. [72]	2.23 mm	HFE7000 and HFE7100	Vertical		Satisfactory consistency of discussed model with their own experimental data for condensation has been found.

Author	<i>D</i>	Fluids	Orientation/ Conditions	Range/ Applicability	Techniques, Basis, Observations
					The presented model can be suggested for a wider use amongst engineers, but further validation with experimental data would add value to its robustness.
Sakamatapan and Wongwises [73]	1.1 mm (14 channels), 1.2 mm (8 channels)	R134a	Horizontal	$G = 345\text{--}685 \text{ kg}/(\text{m}^2\cdot\text{s})$ $q = 15\text{--}25 \text{ kW}/\text{m}^2$ $T_{sat} = 35\text{--}45^\circ\text{C}$	Proposing a new two-phase friction factor correlation using the equivalent Reynolds number (Re_{eq}) concept to predict the frictional pressure gradient during condensation.
López-Belchí et al. [75]	1.16 mm	R1234yf, R134a and R32	Horizontal	$G = 350\text{--}940 \text{ kg}/(\text{m}^2\cdot\text{s})$ $T_{sat} = 20\text{--}55^\circ\text{C}$	Presenting a new correlation model with a mean absolute relative deviation (MARD) value of 8.32% reducing the best correlation MARD by more than 34%.
Thome and Cioncolini [80]			Annular flow		Presenting unified modeling suite for annular flow, convective boiling and condensation in macro- and micro-channels.
Mikielewicz et al. [81]	2.23 mm	HFE7000	Vertical	$G = 240\text{--}850 \text{ kg}/(\text{m}^2\cdot\text{s})$ $q = 47.2\text{--}368.7 \text{ kW}/\text{m}^2$ $T_{sat} = 35\text{--}93^\circ\text{C}$ $x = 0\text{--}100\%$	The comparisons of the experimental results with the in-house developed model for two-phase flow pressure drop with inclusion of non-adiabatic effects show satisfactory agreement.
Kim and Mudawar [82]					Presenting a review of databases and predictive methods for pressure drop in adiabatic, condensing and boiling mini/micro-channel flows.

Author	D	Fluids	Orientation/ Conditions	Range/ Applicability	Techniques, Basis, Observations
Illán-Gómez et al. [83]	1.16 mm	R1234yf, and R134a	Horizontal	$G = 350\text{-}940 \text{ kg}/(\text{m}^2\cdot\text{s})$ $T_{sat} = 20\text{-}55^\circ\text{C}$ $q = 4.37\text{-}20.52 \text{ kW}/\text{m}^2$ for R1234yf $q = 5.08\text{-}20.75 \text{ kW}/\text{m}^2$ for R134a $x = 12\text{-}87\%$ for R1234yf $x = 13\text{-}89\%$ for R134a	Pressure drop for R1234yf is by 5-7% lower than for R134a. The existing models are able to predict frictional pressure drop reasonably well.
Ramírez-Rivera et al. [84]	0.715 and 1.16 mm	R134a and R32	Horizontal	For condensing flow multiport tubes of $d_i = 1.16$ mm, but fails to predict the experimental data in the tube of $d_i = 0.715$ mm with R134a and R32. $G = 200\text{-}800 \text{ kg}/(\text{m}^2\cdot\text{s})$ $T_{sat} = 30, 35, 40, 45, 50, 55^\circ\text{C}$ $q = 2.55\text{-}70 \text{ kW}/\text{m}^2$	Friedel [6] and Müller-Steinhagen and Heck [85] predict satisfactorily well the experimental pressure drop data. The Souza and Pimenta correlation [86] estimates the experimental pressure gradient data very well with The Cavallini et al. model [26] presents the best prediction performance. Cavallini et al. [26] and Zhang and Webb [45] predicted with reasonable accuracy the experimental two-phase flow pressure drop data.
Goss et al. [87]	0.77 mm	R134a	Horizontal	$G = 230\text{-}445 \text{ kg}/(\text{m}^2\cdot\text{s})$ $x = 55\text{-}100\%$ $q = 17\text{-}53 \text{ kW}/\text{m}^2$ $P = 7.3$ to 9.7 bar	The pressure drop increases with an increase in (G) and a decrease in saturation temperature (T_s), whereas it is not influenced as much by the heat flux (q).

Table 1. Summary of previous studies on condensation pressure drop in microchannels and minichannels

3. Recommendations for future studies

Finally, recommendations for future studies will be given. These new points can be expected to be the research focus in the coming years. Studying the condensation pressure drop in microscales can be done using:

1. The experiments with new kinds of non-circular shapes like trapezoidal, elliptical,..., etc. To the best of the authors' knowledge, the study of condensation pressure drop in microscales of elliptic cross-section is not yet tackled in literature. Only recently a new interest has been devoted to the elliptical cross-section, produced by mechanical fabrication in metallic microchannels for practical applications in MEMS. Also, the experimental study of the condensation pressure drop in microscales can be done with using various triangular cross sections such as right isosceles triangular.
2. The experiments with new kinds of environmentally friendly refrigerants such as HDR-14, which is low global warming fluid for replacement of R245fa. The GWP is an index used to compare the potential of gases to produce a greenhouse effect and the reference is CO₂ with a value of 1. HDR-14 has a global warming potential (GWP) of only 7, much lower than the value of 930 of R245fa (both considering a period time horizon of 100 years). Also, HDR-14 has a much lower atmospheric life time (0.1 year) in comparison with the atmospheric life time of R245fa (7.6 years).
3. The experiments with oil in the refrigerant loop (refrigerant/lubricant mixture) at various concentrations. For example, Akhavan-Behabadi et al. [88] utilized polyolester oil (POE) as the lubricant in R600a/POE mixture to study experimentally the heat transfer characteristics of flow condensation.
4. The experiments with new types of working fluids such as refrigerant/lubricant/nanoparticles mixture. For example, Akhavan-Behabadi et al. [88] used R600a/ polyolester oil (POE)/CuO nano-refrigerant to study experimentally the heat transfer characteristics of flow condensation. Nano-refrigerant is a type of nanofluid where a refrigerant is used as the base fluid [89]. Recently, Dalkılıç and co-workers [90, 91] presented a review paper on nanorefrigerants.
5. The experiments with new types of refrigerant blends. For instance, new refrigerant blends, like R-417A, are becoming very important due to the possibility of using them in R-22 systems with only minor changes (drop-in refrigerants) [92]. R-417A is the composition with mass fractions of 46.6% R-125, 50% R-134a, and 3.4% R-600. Also, we can carry out the experiments with new kinds of refrigerant blends like R1234yf and R1234ze(E) as constituents as well as blends of old refrigerants with Hydro-Fluoro-Olefin (HFO) refrigerants. These blends can be azeotropic blends or zeotropic blends like zeotropic mixture R32/R1234ze(E). R32 (CH₂F₂) is flammable and has for this reason not been used pure.
6. Similar to recent work on condensation in macroscales at microgravity conditions [93, 94], studies on condensation pressure drop in microscales at microgravity conditions can

be done. These studies will be important because future manned space missions will be expected to greatly increase the space vehicle's weight, size, and heat dissipation requirements. An effective means to reducing both weight and size is replacing single-phase thermal management systems with two-phase counterparts that capitalize upon both sensible and latent heat of the coolant rather than sensible heat alone. This shift is expected to yield orders of magnitude enhancements in condensation heat transfer coefficients. A major challenge to this shift is the reliable tools lack for accurate prediction of heat transfer coefficient and two-phase pressure drop in reduced gravity.

4. Summary and conclusions

This paper provides a comprehensive, up-to-date review in a chronological order on the research progress made on condensation pressure drop in microscales. Also, studies on condensation pressure drop in microscales are summarized in a table. At the end, some suggestions for future work are presented. Therefore, the present study can not only be used as the starting point for the researcher interested in condensation pressure drop in microscales, but it also includes recommendations for future studies on condensation pressure drop in microscales.

Nomenclature

a ; constant, Eq. (5)

a ; geometry-dependent constant, Eq. (12)

a ; exponent, Eq. (10)

A ; constant, Eq. (10)

AR ; aspect ratio (-)

b ; constant, Eq. (5)

b ; geometry-dependent constant, Eq. (13)

b ; exponent, Eq. (10)

c ; constant, Eq. (5)

c ; exponent, Eq. (10)

C ; coefficient in Lockhart-Martinelli parameter (-)

C_p ; specific heat, J/(kg.K)

d ; diameter, m

E ; entrainment ratio, Eq. (21)

E ; parameter, Eq. (28)

Eu ; Euler number (-)

f ; Fanning friction factor (-)

F ; parameter, Eq. (19)

F ; parameter, Eq. (29)

G ; mass flux, kg/(m².s)

H ; parameter, Eq. (20)

H ; parameter, Eq. (30)

J_g ; dimensionless gas velocity = $xG/[gd_h\rho_g(\rho_l-\rho_g)]^{0.5}$

L ; channel length, m

N ; total number of unit cells

P ; pressure, Pa

Ra ; arithmetical mean deviation of the assessed profile (according to ISO 4287: 1997), μm

Rz ; maximum height of profile (according to ISO 4287: 1997), μm

Re ; Reynolds number (-)

RR ; relative roughness of the tube, Eq. (26)

Su ; Suratman number (-)

T ; temperature, °C

U ; velocity, m/s

W ; parameter, Eq. (17)

We ; Weber number (-)

x ; mass quality (-)

X ; Lockhart-Martinelli parameter (-)

Z ; parameter, Eq. (18)

Greek Symbols

α ; void fraction (-)

Δ ; difference

ϕ^2 ; two-phase frictional multiplier (-)

μ ; dynamic viscosity, kg/m.s

ρ ; density, kg/m³

σ ; surface tension, N/m

ψ ; dimensionless surface tension term (-)

Subscripts

bubble; bubble

cond; condenser

cr; critical

d; diameter

eq; equivalent

g; gas

gc ; gas core

go ; gas phase with total mass flow rate

h ; hydraulic

i; inner

in; inlet

l; liquid

lo ; liquid phase with total mass flow rate

m; mean

sat; saturation

slug ; slug

transition transition

tube; tube

UC; unit cell

unit cell unit cell

tp; two-phase

Acknowledgements

Professor Ahmet Selim Dalkilic wishes to thank King Mongkut's University of Technology Thonburi (KMUTT) for providing him with a Post-doctoral fellowship. Professor Somchai Wongwises wishes to thank the "Research Chair Grant" National Science and Technology

Development Agency, the Thailand Research Fund and the National Research University Project for the support.

Author details

Mohamed M. Awad^{1*}, Ahmet Selim Dalkiliç² and Somchai Wongwises³

*Address all correspondence to: m_m_awad@mans.edu.eg

1 Mechanical Power Engineering Department, Faculty of Engineering, Mansoura University, Mansoura, Egypt

2 Heat and Thermodynamics Division, Department of Mechanical Engineering, Yildiz Technical University (YTU), Yildiz, Besiktas, Istanbul, Turkey

3 Fluid Mechanics, Thermal Engineering and Multiphase Flow Research Lab. (FUTURE), Department of Mechanical Engineering, Faculty of Engineering, King Mongkut's University of Technology Thonburi (KMUTT), Bangmod, Bangkok, Thailand

References

- [1] Awad, M. M., Dalkilic, A. S., Wongwises, S. A Critical Review on Condensation Heat Transfer in Microchannels and Minichannels. The Special Issue on: Nanoscale Heat and Mass Transport and Applications in Energy and Medicine, ASME Journal of Nanotechnology in Engineering and Medicine 2014; 5 (1), Article No. (010801), doi: 10.1115/1.4028092.
- [2] Kandlikar S. G. Microchannels and minichannels - History, terminology, classification and current research needs. Proceedings of ASME 1st International Conference on Microchannels and Minichannels (ICMM2003), ICMM2003-1000, April 24-25, 2003, Rochester, New York, USA, 2003.
- [3] Wang, H. S., Rose, J. W. Theory of Heat Transfer During Condensation in Microchannels. International Journal of Heat and Mass Transfer 2011; 54 (11-12) 2525-2534.
- [4] Lockhart, R. W., Martinelli, R. C. Proposed Correlation of Data for Isothermal Two-Phase, Two-Component Flow in Pipes. Chemical Engineering Progress Symposium Series 1949; 45 (1) 39-48.
- [5] Chisholm, D. Pressure Gradients due to Friction during the Flow of Evaporating Two-Phase Mixtures in Smooth Tubes and Channels. International Journal of Heat and Mass Transfer 1973; 16 (2) 347-358.

- [6] Friedel, L. Improved frictional pressure drop correlations for horizontal and vertical two-phase pipe flow. European Two Phase Flow Group Meeting, Paper E2, June 5-8, 1979, Ispra, Italy, 1979.
- [7] Dalkilic, A. S., Wongwises, S. Intensive Literature Review of Condensation inside Smooth and Enhanced Tubes. *International Journal of Heat and Mass Transfer* 2009; 52 (15-16) 3409-3426.
- [8] Koyama, S., Kuwahara, K., Nakashita, K., Yamamoto, K. An Experimental Study on Condensation of Refrigerant R134a in a Multi-Port Extruded Tube. *International Journal of Refrigeration* 2003; 24 (4) 425-432.
- [9] Mishima, K., Hibiki, T. Effect of Inner Diameter on Some Characteristics of Air-Water Two-Phase Flows in Capillary Tubes. *Trans JSME (B)* 1995; 61 (589) 99-106.
- [10] Chisholm, D., Laird, A. D. K. Two-Phase Flow in Rough Tubes. *Trans. ASME* 1958; 80 (2) 227-286.
- [11] Soliman, M., Schuster, J. R., Berenson, P. J. A General Heat Transfer Correlation for Annular Flow Condensation. *Trans. ASME, Ser C* 1968; 90 (2) 267-276.
- [12] Haraguchi, H., Koyama, S., Fujii, T. Condensation of Refrigerants HCFC22, HFC134a and HCFC123 in a Horizontal Smooth Tube (1st Report, Proposal of Empirical Expressions for the Local Frictional Pressure Drop). *Trans. JSME (B)* 1994; 60 (574) 239-244.
- [13] Garimella, S. Condensation Flow Mechanisms in Microchannels: Basis for Pressure Drop and Heat Transfer Models. *Heat Transfer Engineering* 2004; 25 (3) 104-116. Also presented at Proceedings of ASME 2003 1st International Conference on Microchannels and Minichannels (ICMM2003), ICMM2003-1020, pp. 181-192, April 24-25, 2003, Rochester, New York, USA.
- [14] Garimella, S., Agarwal, A., Killion, J. D., Condensation Pressure Drop in Circular Microchannels. *Heat Transfer Engineering* 2005; 26 (3) 1-8. Also presented at Proceedings of ASME 2004 2nd International Conference on Microchannels and Minichannels (ICMM2004), ICMM2004-2393, pp. 649-656, June 17-19, 2004, Rochester, New York, USA.
- [15] Garimella, S., Killion, J. D., Coleman, J. W. An Experimentally Validated Model for Two-Phase Pressure Drop in the Intermittent Flow Regime for Circular Microchannels. *ASME Journal of Fluids Engineering* 2002; 124 (1) 205-214.
- [16] Garimella, S., Killion, J. D., Coleman, J. W. An Experimentally Validated Model for Two-Phase Pressure Drop in the Intermittent Flow Regime for Noncircular Microchannels. *ASME Journal of Fluids Engineering* 2003; 125 (5) 887-894.
- [17] Garimella, S., Agarwal, A., Coleman, J. W. Two-phase pressure drops in the annular flow regime in circular microchannels. 21st IIR International Congress of Refrigera-

- tion, International Institute of Refrigeration, ICR0360, August 17-22, 2003, Washington, DC, USA, 2003.
- [18] Coleman, J. W., Garimella, S. Visualization of refrigerant two-phase flow during condensation. 34th National Heat Transfer Conference, August 20-23, 2000, Pittsburgh, PA, USA, 2000.
- [19] Coleman, J. W., Garimella, S. Two-phase flow regime transitions in microchannel tube :The effect of hydraulic diameter. ASME Heat Transfer Division, Vol. HTD 366-4, pp. 71-83, 2000.
- [20] Coleman, J. W., Garimella, S. Two-Phase Flow Regimes in Round, Square and Rectangular Tubes During Condensation of Refrigerant R134a. International Journal of Refrigeration 2003; 26 (1) 117-128.
- [21] Baroczy, C. J. Correlation of Liquid Fraction in Two-Phase Flow with Applications to Liquid Metals. Chemical Engineering Progress Symposium Series 1965; 61 (57) 179-191.
- [22] Churchill, S. W. Friction Factor Equation Spans all Fluid Flow Regimes. Chemical Engineering 1977; 84 (24) 91-92.
- [23] Lee, H. J., Lee, S. Y. Pressure Drop Correlations for Two-Phase Flow within Horizontal Rectangular Channels with Small Heights. International Journal of Multiphase Flow 2001; 27 (5) 783-796.
- [24] Coleman JW. Flow visualization and pressure drop for refrigerant phase change and air-water flow in small hydraulic diameter geometries. Iowa State University, Ames, IA, USA, pp. 334, 2000.
- [25] Hai, X., Koyama, S. An Experimental Study of Carbon Dioxide Condensation in Mini Channels. Journal of Thermal Science 2004; 13 (4) 358-365.
- [26] Cavallini, A., Doretti, L., Matkovic, M., Rossetto, L. Update on Condensation Heat Transfer and Pressure Drop inside Minichannels. Heat Transfer Engineering 2006; 27 (4) 104-116. Also presented at Proceedings of ASME 3rd International Conference on Microchannels and Minichannels (ICMM2005), ICMM2005-75081, June 13-15, 2005, Toronto, Ontario, Canada, 2005.
- [27] Chowdhury, S., Al-hajri, E., Dessiatoun, S., Shooshtari, A., Ohadi, M. An experimental study of condensation heat transfer and pressure drop in a single high aspect ratio micro-channel for refrigerant R134a, Proceedings of the 4th International Conference on Nanochannels, Microchannels and Minichannels (ICNMM2006), Vol. A, pp. 147-154, ICNMM2006-96211, June 19-21, 2006, Limerick, Ireland, 2006.
- [28] Garimella, S. Condensation in Minichannels and Microchannels. In: Kandlikar, S. G., Garimella, S., Li, D., Colin, S., King, M., (Eds.), Heat Transfer and Fluid Flow in Minichannels and Microchannels. Elsevier Publications, Oxford, UK, 2006.

- [29] Agarwal, A., Garimella, S. Modeling of Pressure Drop During Condensation in Circular and Noncircular Microchannels. *ASME Journal of Fluids Engineering* 2009; 131 (1), Article No. (011302). Also presented at Proceedings of ASME 2006 International Mechanical Engineering Congress and Exposition (IMECE2006), IMECE2006-14672, Heat Transfer, Volume 3/Heat Transfer/K16 Committee: Heat Transfer in Electronic Equipment, pp. 199-206, November 5-10, 2006, Chicago, Illinois, USA.
- [30] Cavallini, A., Del Col, D., Matkovic, M., Rossetto, L. Frictional Pressure Drop during Vapour-Liquid Flow in Minichannels: Modelling and Experimental Evaluation. *International Journal of Heat and Fluid Flow* 2009; 30 (1) 131-139.
- [31] Paleev, I. I., Filippovich, B. S. Phenomena of Liquid Transfer in Two-Phase Dispersed Annular Flow. *International Journal of Heat and Mass Transfer* 1966; 9 (10), 1089-1093.
- [32] Cavallini, A., Del Col, D., Matkovic, M., Rossetto, L. Pressure Drop during Two-Phase Flow of R134a and R32 in a Single Minichannel. *ASME Journal of Heat Transfer* 2009; 131 (3), Article No. (033107).
- [33] Park, C. Y., Hrnjak, P. S. CO₂ Flow Condensation Heat Transfer and Pressure Drop in Multi-Port Microchannels at Low Temperatures. *International Journal of Refrigeration* 2009; 32 (6) 1129-1139.
- [34] Akbar, M. K., Plummer, D. A., Ghiaasiaan, S. M. On Gas-Liquid Two-Phase Flow Regimes in Microchannels. *International Journal of Multiphase Flow* 2003; 29 (5) 855-865.
- [35] Breber, G., Palen, J. W., Taborek, J. Prediction of Horizontal Tubeside Condensation of Pure Components Using Flow Regime Criteria. *ASME Journal of Heat Transfer* 1980; 102 (3) 471-476.
- [36] Thome, J. R., El Hajal, J., Cavallini, A. Condensation in Horizontal Tubes, Part 2: New Heat Transfer Model Based on Flow Regimes. *International Journal of Heat and Mass Transfer* 2003; 46 (18) 3365-3387.
- [37] Mishima, K., Hibiki, T. Some Characteristics of Air-Water Two-Phase Flow in Small Diameter Vertical Tubes. *International Journal of Multiphase Flow* 1996; 22 (4) 703-712.
- [38] Agarwal, A., Garimella, S. Representative Results for Condensation Measurements at Hydraulic Diameters ~100 Microns. *ASME Journal of Heat Transfer* 2010; 132 (4), Article No. (041010). Also presented at Proceedings of ASME 2007 International Mechanical Engineering Congress and Exposition (IMECE2007), IMECE2007-43749, Volume 8: Heat Transfer, Fluid Flows, and Thermal Systems, Parts A and B/Heat Transfer, Fluid Flows, and Thermal Systems/ Symposium on Gas-Liquid and Phase-Change Flows at Macro- and Micro-Scales, pp. 1667-1681, November 11-15, 2007, Seattle, Washington, USA.

- [39] Song, T. Y., Yu, G. X., Ma, X. H., Rose, J. W., Wang, H. S. Pressure drop during condensation in microchannels. Proceedings of the ASME 2010 3rd Joint US-European Fluids Engineering Summer Meeting and 8th International Conference on Nanochannels, Microchannels, and Minichannels (FEDSM-ICNMM2010), FEDSM-ICNMM2010-30230, August 1-5, 2010, Montreal, Canada, 2010.
- [40] Keinath, B. L., Garimella, S. Bubble and film dynamics during condensation of refrigerants in minichannels, Proceedings of 2010 14th International Heat Transfer Conference (IHTC14), IHTC14-22697, Volume 2/Condensation, pp. 177-186, August 8-13, 2010, Washington, DC, USA, 2010.
- [41] Fronk, B. M., Garimella, S. Measurement of heat transfer and pressure drop during condensation of carbon dioxide in microscale geometries. Proceedings of 2010 14th International Heat Transfer Conference (IHTC14), IHTC14-22987, Volume 2/Condensation, pp. 235-243, August 8-13, 2010, Washington, DC, USA, 2010.
- [42] Kuo, C. Y., Pan, C. Two-Phase Flow Pressure Drop and Heat Transfer During Condensation in Microchannels with Uniform and Converging Cross-Sections. Journal of Micromechanics and Microengineering 2010; 20 (9), Article No. (095001).
- [43] Kuo, C. Y., Pan, C. The Effect of Cross-Section Design of Rectangular Microchannels on Convective Steam Condensation. Journal of Micromechanics and Microengineering 2010; 19 (3), Article No. (035017).
- [44] Goss Jr., G., Macarini, S. F., Passos, J. C. Heat transfer and pressure drop during condensation of R-134A inside parallel microchannels. Proceedings of ASME/JSME 2011 8th Thermal Engineering Joint Conference (AJTEC 2011), AJTEC2011-44551, March 13-17, 2011, Honolulu, Hawaii, USA, 2011.
- [45] Zhang M., Webb, R. L. Correlation of Two-Phase Friction for Refrigerants in Small-Diameter Tubes. Experimental Thermal and Fluid Science 2001; 25 (3-4), 131-139.
- [46] Keinath, B. L., Garimella, S. Void fraction and pressure drop during condensation of refrigerants in minichannels. 6th International Berlin Workshop on Transport Phenomena with Moving Boundaries, Berlin, Germany, 2011.
- [47] Andresen UC. Supercritical gas cooling and near-critical-pressure condensation of refrigerant blends in microchannels. Ph. D. Thesis, Georgia Institute of Technology, Atlanta, GA, 2006.
- [48] Bohdal, T., Charun, H., Sikora, M. Pressure drop during the condensation of R134a refrigerant in pipe minichannels. Proceedings of 6th International Conference on Transport Phenomena in Multiphase Systems, (Poniewski, M. E., Alabrudziński S. (Eds.), pp. 233-240, June 28-July 02, 2011, Ryn, Poland, 2011.
- [49] Bohdal, T., Charun, H., Sikora, M. Comparative Investigations of the Condensation of R134a and R404A Refrigerants in Pipe Minichannels. International Journal of Heat and Mass Transfer 2011; 54 (9-10) 1963-1974.

- [50] Bohdal, T., Charun, H., Sikora, M. Pressure Drop During Condensation of Refrigerants in Pipe Minichannels. *Archives of Thermodynamics* 2012; 33 (1) 87-106.
- [51] Alshqirate, A. A. Z. S., Tarawneh, M., Hammad, M., Dimensional Analysis and Empirical Correlations for Heat Transfer and Pressure Drop in Condensation and Evaporation Processes of Flow inside Micropipes: Case Study with Carbon Dioxide (CO₂). *Journal of the Brazilian Society of Mechanical Sciences and Engineering* 2012; 34 (1) 89-96.
- [52] Kim, S. M., Mudawar, I. Theoretical Model for Annular Flow Condensation in Rectangular Micro-Channels. *International Journal of Heat and Mass Transfer* 2012; 55 (4) 958-970.
- [53] Kim, S. -M., Kim, J., Mudawar, I. Flow Condensation in Parallel Micro-Channels - Part 1: Experimental Results and Assessment of Pressure Drop Correlations. *International Journal of Heat and Mass Transfer* 2012; 55 (4) 971-983.
- [54] Rose, J. W., Wang, H. Pressure drop during condensation in microchannels. *ASME 3rd Micro/Nanoscale Heat and Mass Transfer International Conference (MNHMT2012), Track 4: Nano/Microscale Boiling and Condensation Heat Transfer, Session: 4-4 Two-Phase Flow and Phase-Change Heat Transfer in Microchannels, MNHMT2012-75187, March 3-6, 2012, Atlanta, GA, 2012.*
- [55] Fronk, B. M., Garimella, S. Heat transfer and pressure drop during condensation of ammonia in microchannels. *ASME 3rd Micro/Nanoscale Heat and Mass Transfer International Conference (MNHMT2012), Track 4: Nano/Microscale Boiling and Condensation Heat Transfer, Session: 4-4 Two-Phase Flow and Phase-Change Heat Transfer in Microchannels, MNHMT2012-75265, March 3-6, 2012, Atlanta, GA, 2012.*
- [56] Charun, H. Thermal and Flow Characteristics of the condensation of R404A Refrigerant in Pipe Minichannels. *International Journal of Heat and Mass Transfer* 2012; 55 (9-10) 2692-2701.
- [57] Kim, S. -M., Mudawar, I. Universal Approach to Predicting Two-Phase Frictional Pressure Drop for Adiabatic and Condensing Mini/Micro-Channel Flows. *International Journal of Heat and Mass Transfer* 2012; 55 (11-12) 3246-3261.
- [58] Shah RK, London AL. *Advances in Heat Transfer, Suppl. 1, Laminar Forced Flow Convection in Ducts*, New York: Academic Press, 1978.
- [59] Zhang, H. -Y., Li, J. -M., Liu, N., Wang, B. -X. Experimental Investigation of Condensation Heat Transfer and Pressure Drop of R22, R410A and R407C in Mini-Tubes. *International Journal of Heat and Mass Transfer* 2012; 55 (13-14) 3522-3532.
- [60] Mikielwicz, D., Andrzejczyk, R., Wajs, J., Mikielwicz, J. A general method for calculation of two-phase flow pressure drop in flow boiling and flow condensation. *8th ECI International Conference on Boiling and Condensation Heat Transfer*, June 3-7,

- 2012, Ecole Polytechnique Fédérale de Lausanne (EPFL), Lausanne, Switzerland, 2012.
- [61] Son, C. -H., Oh, H. -K., Condensation Pressure Drop of R22, R134a and R410A in a Single Circular Microtube. *Heat and Mass Transfer* 2012; 48 (8), 1437-1450.
- [62] Zhang, Z., Weng, Z. L., Li, T. X., Huang, Z. C., Sun, X. H., He, Z. H., van Es, J., Pauw, A., Laudi, E., Battiston, R. CO₂ Condensation Heat Transfer Coefficient and Pressure Drop in a Mini-Channel Space Condenser. *Experimental Thermal and Fluid Science* 2013; 44, 356-363.
- [63] Garimella, S., Fronk, B. M. Single- and Multi-Constituent Condensation of Fluids and Mixtures with Varying Properties in Micro-Channels. 2013; 26 (2-3) 129-168: Special Issue: ECI Eighth International Conference on Boiling and Condensation Heat Transfer, June 3-7, 2012, Ecole Polytechnique Fédérale de Lausanne (EPFL), Lausanne, Switzerland.
- [64] Wang, H. S., Rose, J. W. Heat Transfer and Pressure Drop during Laminar Annular Flow Condensation in Micro-Channels. *Experimental Heat Transfer* 2013; 26 (2-3) 247-265: Special Issue: ECI Eighth International Conference on Boiling and Condensation Heat Transfer, June 3-7, 2012, Ecole Polytechnique Fédérale de Lausanne (EPFL), Lausanne, Switzerland.
- [65] Liu, N., Li, J. M., Sun, J., Wang, H. S. Heat Transfer and Pressure Drop during Condensation of R152a in Circular and Square Microchannels. *Experimental Thermal and Fluid Science* 2013; 47, 60-67.
- [66] Wang, H. S., Sun, J., Rose, J. W. Pressure Drop During Condensation in Microchannels. *ASME Journal of Heat Transfer* 2013; 135 (9), Article No. (091602).
- [67] Heo, J., Park, H., Yun, R. Condensation Heat Transfer and Pressure Drop Characteristics of CO₂ in a Microchannel. *International Journal of Refrigeration* 2013; 36 (6), 1657-1668.
- [68] Ganapathy, H., Shooshtari, A., Choo, K., Dessiatoun, S., Alshehhi, M., Ohadi, M. Volume of Fluid-Based Numerical Modeling of Condensation Heat Transfer and Fluid Flow Characteristics in Microchannels. *International Journal of Heat and Mass Transfer* 2013; 65, 62-72.
- [69] Dobson, M. K., Chato, J. C. Condensation in Smooth Horizontal Tubes. *ASME Journal of Heat Transfer* 1998; 120 (1) 193-213.
- [70] Heo, J., Park, H., Yun, R. Comparison of Condensation Heat Transfer and Pressure Drop of CO₂ in Rectangular Microchannels. *International Journal of Heat and Mass Transfer* 2013; 65, 719-726.
- [71] Murphy DL. Condensation heat transfer and pressure drop of propane in vertical minichannels, M. Sc. Thesis, Georgia Institute of Technology, Atlanta, GA, 2014.

- [72] Mikielwicz, D., Andrzejczyk, R., Mikielwicz, J. Pressure drop of HFE7000 and HFE7100 in flow condensation in minichannels with account of non-adiabatic effects. 101 Eurotherm Seminar "Transport Phenomena in Multiphase Systems" (HEAT2014), June 30-July 3, 2014, Cracow, Poland, 2014.
- [73] Sakamatapan, K., Wongwises, S. Pressure Drop During Condensation of R134a Flowing inside a Multiport Minichannel. *International Journal of Heat and Mass Transfer* 2014; 75, 31-39.
- [74] Sakamatapan, K., Kaew-On, J., Dalkilic, A. S., Mahian, O., Wongwises, S. Condensation Heat Transfer Characteristics of R-134a Flowing inside the Multiport Minichannels. *International Journal of Heat and Mass Transfer*, 2013; 64, 976-985.
- [75] López-Belchí, A., Illán-Gómez, F., Vera-García, F., García-Cascales, J. R. Experimental Condensing Two-Phase Frictional Pressure Drop inside Mini-Channels. Comparisons and New Model Development. *International Journal of Heat and Mass Transfer* 2014, 75, 581-591.
- [76] Fang, X., Xu, Y., Zhou, Z. New Correlations of Single-Phase Friction Factor for Turbulent Pipe Flow and Evaluation of Existing Single-Phase Friction Factor Correlations. *Nuclear Engineering and Design* 2011; 241, 897-902.
- [77] Fang, X., Zhang, H., Xu, Y., Su, X. Evaluation of Using Two-Phase Frictional Pressure Drop Correlations for Normal Gravity to Microgravity and Reduced Gravity. *Advances in Space Research* 2012; 49, 351-364.
- [78] Brkic, D. New Explicit Correlations for Turbulent Flow Friction Factor. *Nuclear Engineering and Design* 2011; 241, 4055-4059.
- [79] Xu, Y., Fang, X. A New Correlation of Two-Phase Frictional Pressure Drop for Condensing Flow in Pipes. *Nuclear Engineering and Design* 2013; 263, 87-96.
- [80] Thome, J. R., Cioncolini, A. Unified modeling suite for two-phase flow, convective boiling and condensation in macro- and micro-channels. *Proceedings of the Fourth Micro & Nano Flows Conference (MNF2014)*, 7-10 September 2014, University College London (UCL), London, UK, 2014.
- [81] Mikielwicz, D., Klugmann, M., Andrzejczyk, R., Wajs J. Experimental investigations on pressure drop during the condensation in flow of HFE7000 in vertical minichannel. *Proceeding of 15th International Conference on Heat Transfer and Renewable Sources of Energy (HTRSE2014)*, 10-13 September 2014, Szczecin – Międzyzdroje, Poland, 2014.
- [82] Kim, S.-M., Mudawar, I. Review of Databases and Predictive Methods for Pressure Drop in Adiabatic, Condensing and Boiling Mini/Micro-Channel Flows. *International Journal of Heat and Mass Transfer* 2014; 77, 74-97.
- [83] Illán-Gómez, F., López-Belchí, A., García-Cascales, J. R., Vera-García, F. Experimental Two-Phase Heat Transfer Coefficient and Frictional Pressure Drop inside Mini-Chan-

- nels During Condensation with R1234yf and R134a. *International Journal of Refrigeration* 2015; 51, 12-23.
- [84] Ramírez-Rivera, F., López-Belchí, A., Vera-García, F., García-Cascales, J. R., Illán-Gómez, F. Two Phase Flow Pressure Drop in Multiport Mini-Channel Tubes Using R134a and R32 As Working Fluids. *International Journal of Thermal Sciences* 2015; 92, 17-33.
- [85] Müller-Steinhagen, H., Heck, K. A Simple Friction Pressure Drop Correlation for Two Phase Flow in Pipes. *Chemical Engineering and Processing* 1986; 20 (6), 297-308.
- [86] Souza, A. L., Pimenta, M. M. Prediction of pressure drop during horizontal two-phase flow of pure and mixed refrigerants. *ASME Conference Cavitation and Multi-Phase Flow, HTD*, Vol. 210, pp. 161-171, South Carolina, U. S. A, 1995.
- [87] Goss Jr., G., Oliveira, J. L. G., Passos, J. C. Pressure Drop During Condensation of R-134a inside Parallel Microchannels. *International Journal of Refrigeration* 2015; doi: 10.1016/j.ijrefrig.2015.04.005.
- [88] Akhavan-Behabadi, M. A., Sadoughi, M. K., Darzi, M., Fakoor-Pakdaman, M. Experimental Study on Heat Transfer Characteristics of R600a/POE/CuO Nano-Refrigerant Flow Condensation. *Experimental Thermal and Fluid Science* 2015; 66, 46-52.
- [89] Wang, K., Ding, G., Jiang, W. Development of nanorefrigerant and its rudiment property. *Proceedings of 8th International Symposium on Fluid Control, Measurement and Visualization*, Chengdu, China, 2005.
- [90] Dalkılıç, A. S., Aktas, M., Cebi, A., Çelen, A., Mahian, O., Wongwises, S. A focus on the literature review of nanorefrigerants. *Proceedings of the ASME 2014 4th Joint US-European Fluids Engineering Division Summer Meeting and 12th International Conference on Nanochannels, Microchannels, and Minichannels (FEDSM2014)*, Paper No. FEDSM2014-21058, 3-7 August, 2014, Chicago, Illinois, USA.
- [91] Çelen, A., Cebi, A., Aktas, M., Mahian, O., Dalkılıç, A. S., Wongwises, S. A Review of Nanorefrigerants: Flow Characteristics and Applications. *International Journal of Refrigeration* 2014; 44, 125-140.
- [92] Pardiñas, Á. Á., Fernández-Seara, J., Piñeiro-Pontevedra, C., Bastos, S. Experimental Determination of the Boiling Heat Transfer Coefficients of R-134a and R-417A on a Smooth Copper Tube. *Heat Transfer Engineering* 2014; 35 (16-17), 1427-1434. Also presented at the 9th International Conference on Heat Transfer, Fluid Mechanics, and Thermodynamics (HEFAT2012), July 16-18, 2012, Malta.
- [93] Lee, H., Mudawar, I., Hasan, M. M. Experimental and Theoretical Investigation of Annular Flow Condensation in Microgravity. *International Journal of Heat and Mass Transfer* 2013; 61, 293-309.
- [94] Lee, H., Park, I., Konishi, C., Mudawar, I., May, R. I., Juergens, J. R., Wagner, J. D., Hall, N. R., Nahra, H. K., Hasan, M. M., Mackey, J. R. Experimental Investigation of Flow Condensation in Microgravity. *ASME Journal of Heat Transfer* 2014; 136 (2), Article No. (021502).

Pressure Drop and Heat Transfer during a Two-phase Flow Vaporization of Propane in Horizontal Smooth Minichannels

Jong-Taek Oh, Kwang-Il Choi and Nguyen-Ba Chien

Additional information is available at the end of the chapter

<http://dx.doi.org/10.5772/60813>

1. Introduction

Nowadays, the ozone depletion and global warming potential of commonly used refrigerant have been considered as a major environmental matter. The next generation of refrigerants is obliged, not only to be environment friendly, but also to provide high efficiency [1]. Therefore, considerable attention has been focused on the application of natural refrigerant. However, safety issues have been established, such as special demands or suitable applications for refrigerants which include high working pressure, flammability, or toxicity.

Propane is a natural refrigerant that has no ODP and low GWP. It is also a non-toxic chemical and has a suitable thermodynamics and a transport property which are almost similar with those of HFC refrigerant. Other advantages of propane include compatibility with most materials used in HFC equipment and miscibility with commonly used compressor lubricant. The HFC systems such as R22 one can use propane without major changes. Nonetheless, propane has a high flammability that meets the safety demands of refrigerants in design and operation. It means that the propane refrigeration systems should work with minimum refrigerant charges and zero refrigerant leakage.

The question now is: "Could the refrigeration systems avoid leakage?" The answer comes from the difference between the design and the actual, which is a challenge. Mobile air conditioning and commercial refrigerant systems are two types of those that have the largest amount of leakage. The estimated leakage rates of these systems are 7% and 15-20% of the total charges, respectively [2]. Although the leakage percentage improves every year through the development of technology, it is still high and could not possibly reach the ideal case in the near future. The fact clearly shows that the designs of propane systems currently need a decrease in the

amount of refrigerant charges to as minimal as possible. And one of the best solutions at present is the decrease in the size of the heat exchanger. Compact heat exchangers using minichannels and microchannels have more efficient heat transfer performance than conventional types, due to their higher heat transfer area per refrigerant volume. Given that, the systems could reduce the refrigerant charges but still keep the coefficient of performance. However, since various researches observed the many differences of heat transfer and pressure drop of refrigerants in the mini/microchannels and conventional channels [3, 4]. The studies on these characteristics of propane in mini/microchannels and valuable information will be provided for researchers in related fields.

In fact, in the past few decades, numerous interesting researches were published in literature such as the studies of [5-9]. Nevertheless, the following chapter does not attempt to review all the available literature but those most focused on the particular heat exchanger design only or the consideration on the heat transfer and pressure drop separately. The intention is to rather present a basis on heat transfer and pressure drop of propane in minichannels, simultaneously under the variation of mass fluxes, heat fluxes, saturated temperature, and tube diameter. The phenomenon will be explained thoroughly by its mechanism that shows some differences observed in the conventional channel. Furthermore, the development of heat transfer coefficient and pressure drop correlations are demonstrated. The content is believed to bring up the general understanding, as well as useful information on heat exchanger designs to the readers.

2. Experimental apparatus and data reduction

2.1. Experimental model

The schematic diagram of experimental apparatus is depicted in Fig. 1. The facilities were built by Choi et al. [6]. Looking inside, the model mainly comprises the condensing unit, sub-cooler, receiver, pump, mass flow meter, preheater, and test section. The closed refrigeration cycle starts from the receiver. The liquid refrigerant was, at first, pumped by a magnetic gear pump. Then, it was passed through a Coriolis mass flow meter. Before entering the test section, the mass quality of the refrigerant was adjusted by the preheater. At the test section, it was evaporated by applying heat from an AC transformer. The vapor refrigerant at the outlet of the test section was condensed by the condenser and then the liquid refrigerant comes back to the receiver. In this model, the flow rate of the refrigerant can be acquired by controlling the frequency of the gear pump. The photograph of the apparatus is presented in Fig. 2.

The test section was made of stainless steel smooth tube with inner diameters of 1.5mm and 3.0 mm and heated lengths of 1000mm and 2000 mm, respectively. The temperatures of the outside surface of the test section were measured at the top, on both sides, and at the bottom each at 100mm axial intervals from the inlet to the outlet. In this model, Choi et al. [6] used the T-type thermocouples with the outside diameter of 0.1mm. To measure the local pressure in the test section, two pressure gauges were set up at the inlet and outlet. Another differential pressure was used to estimate the exact pressure drop during the evaporation in the test tube. Two sight glasses with the same inner diameter as the test section were installed to visualize

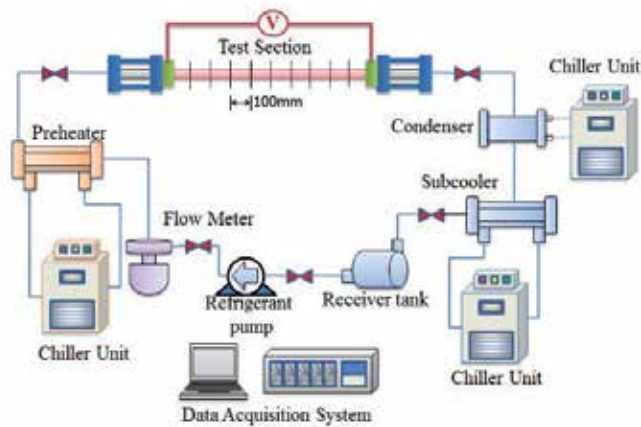


Figure 1. The schematic of apparatus



Figure 2. The Photograph of apparatus

the flow. After all, the test sections and the other components were well isolated by rubber and foams to reduce the effect of the environment. The details of the test section are depicted in Fig. 3.

One of the most important parts in this testing model is to test the heat balance on a test tube. The total electric power was calculated by the root mean square values of electric voltage and current. The heat balance procedure was taken with each tube. The results were then corrected by using logarithmic regression method. The final deviation of electric power was within 5%. The estimated uncertainties of other parameters were also evaluated with the confidence of 95%. The summary is shown in table 1. The testing conditions in study of Choi et al. [6] were also illustrated in table 2. All the properties of refrigerant were queried from REFPROP. 8.

2.2. Data reduction

2.2.1. Pressure drop

The total pressure drop of saturated refrigerants comes from the variation of kinetic energy, potential energy, and the friction of the two-phase flow on the wall. In horizontal tubes, the potential energy can be neglected, thus, the total pressure drop is the sum of the momentum pressure drop and the frictional pressure drop. Assuming that the pressure drop linearly increases with the tube length, the saturation pressure at the starting point of saturation regime is interpolated from the measured pressure and the calculated subcooled length. The experimental two phase frictional pressure drop can be determined as follows:

$$\left(-\frac{dp}{dz}F\right) = \left(-\frac{dp}{dz}\right) - \left(-\frac{dp}{dz}a\right) \quad (1)$$

The refrigerant is evaporated from liquid at the saturation temperature to vapor-liquid mixture at mass quality x with a linear change of test distance over the tube length. Hence, the momentum pressure drop can be calculated with following equation:

$$\left(-\frac{dp}{dz}a\right) = G^2 \frac{d}{dz} \left(\frac{x^2}{\alpha\rho_g} + \frac{(1-x)^2}{(1-\alpha)\rho_f} \right) \quad (2)$$

Choi et al. [6] compared various void fraction models including the ones proposed by Steiner [10], CISE [11], and Chisholm [12] with the homogeneous model and their experimental data. The correlation proposed by CISE shows the best agreement with the homogeneous model, while Steiner's correlation shows the best prediction for the experimental data as shown in Fig. 4. Therefore, the void fraction in their study is obtained from the Steiner [10] void fraction as follows:

$$\alpha = \frac{x}{\rho_g} \left[(1 + 0.12(1-x)) \left(\frac{x}{\rho_g} + \frac{1-x}{\rho_f} \right) + \frac{1.18(1-x) [g\sigma(\rho_f - \rho_g)]^{0.25}}{G\rho_f^{0.5}} \right]^{-1} \quad (3)$$

The friction factor was determined from the measured pressure drop for a given mass flux by using the Fanning equation,

$$f_p = \frac{D_p}{2G^2} \left(-\frac{dp}{dz}F \right) \quad (4)$$

where the average density is calculated with the following equation:

$$\bar{\rho} = \alpha\rho_g + (1 - \alpha)\rho_f \tag{5}$$

The two phase frictional multiplier, ϕ_{fo}^2 is determined by dividing the calculated frictional two-phase pressure drop to the pressure drop of the liquid flow assuming the total flow to be liquid. The equation is defined as:

$$\phi_{fo}^2 = \left(-\frac{dp}{dz} F \right)_{tp} / \left(-\frac{dp}{dz} F \right)_{fo} = \left(-\frac{dp}{dz} F \right)_{tp} / \left(\frac{2f_{fo}G^2}{D\rho_f} \right) \tag{6}$$

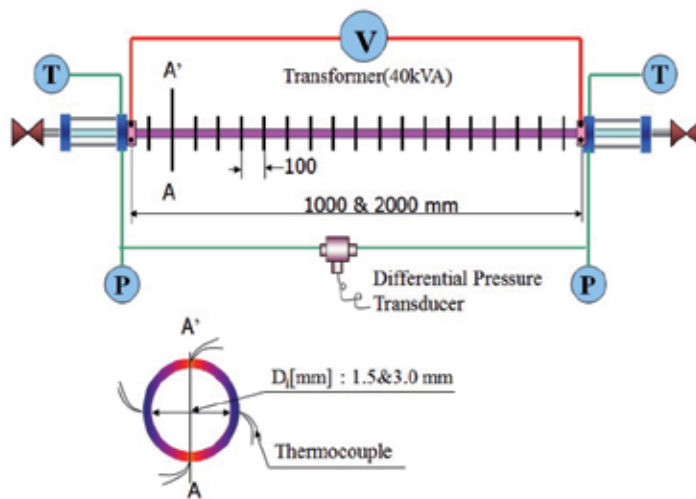


Figure 3. The schematic of test sections

Test section	Horizontal stainless steel circular smooth small tubes
Quality	Up to 1.0
Working refrigerant	Propane
Inlet diameter (mm)	1.5 and 3.0
Tube length (mm)	1000 and 2000
Mass flux (kg m ⁻² s ⁻²)	50-400
Heat flux(KW m ⁻²)	5-20
Inlet T _{sat} (°C)	0, 5, 10

Table 1. Experimental Conditions

Parameter	Uncertainty at a 95% confidence level
Thermocouples (°C)	±0.62
P (kPa)	±2.5
G (%)	±5.89
q (%)	±2.54
x (%)	±6.21
h (%)	±6.89

Table 2. Summary of the estimated uncertainty

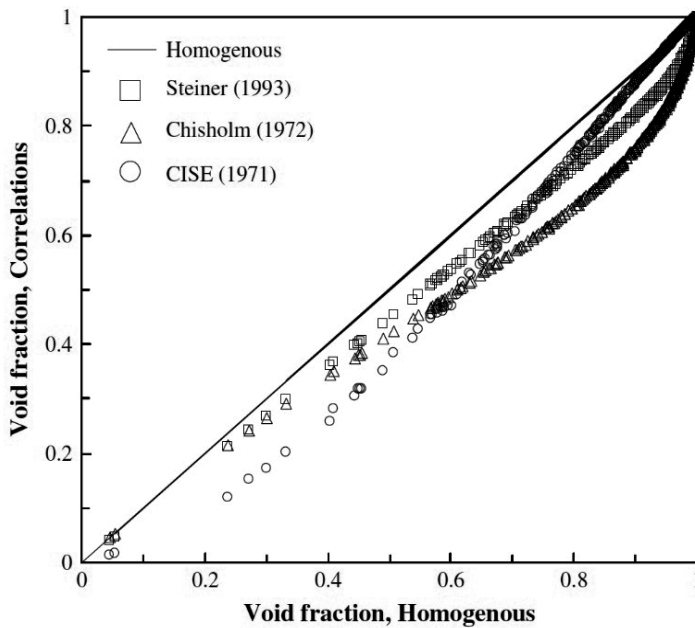


Figure 4. Void fraction comparison between the homogenous model and the existing correlations

2.2.2. Heat transfer coefficient

Choi et al. [6] determined the inside tube wall temperature, T_{wi} , by the average inside temperature of the top, both right and left sides, and bottom wall temperatures. As demonstrated in the apparatus module, the heat was applied on test tubes through uniform current, and the local temperature was evaluated at the cross section where there is an attached the thermocouple, hence, the inside wall temperatures at each point could be determined by using steady state one-dimensional radial conduction heat transfer through the wall with internal heat generation. The quality, x , at the measurement location, z , was determined based on the thermodynamic properties.

$$x = \frac{i - i_g}{i_{fg}} \quad (7)$$

In fact, the refrigerant flow was not completely saturated at the inlet of the test section. The flow becomes totally saturated after a short initial length of tube when the heat, which is called a subcooled length, was applied. Therefore, to ensure the accuracy of data reduction, the subcooled length is calculated using the following equation:

$$z_{sc} = L \frac{i_f - i_{fi}}{\Delta i} = L \frac{i_f - i_{fi}}{(Q/W)} \quad (8)$$

The outlet mass quality was then determined using the following equation:

$$x_o = \frac{\Delta i + i_{fg} - i_f}{i_{fg}} \quad (9)$$

3. Results and discussion

3.1. Two-phase flow pressure drop

The study of Choi et al. [6] showed that mass flux, heat flux, inner tube, and saturation temperature all have affected the two-phase flow pressure drop of propane in minichannels. The effect of mass flux on the pressure drop is shown in Fig. 5. It can be seen that the mass flux has a strong influence on the pressure drop. As described above, the two-phase pressure drop is mainly caused by the frictional and acceleration pressure drop. The increase in the mass flux results in a higher flow velocity, which increases both of the two components and, therefore, increases the pressure drop. The similar trends were reported in the studies [13-17]. The strong effect of heat flux on the pressure drop is also described in Fig. 5. An increase in the heat flux causes a higher vaporization. The average vapor quality and flow velocity of higher heat flux conditions increase faster than those of lower ones, and lead to the increase of the pressure drop when the heat flux increases. The results were in well agreement with the study of Zhao et al. [13]. In addition, Fig. 5 illustrates the effect of the tube diameter on the pressure drop. The comparison of the pressure gradient with the inner diameter of 1.5 and 3.0 mm shows that it is higher in smaller diameter. This phenomenon can be explained by saying that the wall shear stress is higher in smaller tubes, which results in both higher frictional and acceleration pressure drop. The effect of saturation temperature on the pressure drop is also observed in Fig. 5. The pressure gradient is higher at a lower saturation temperature. The physical properties are believed to be the reason for this phenomenon. The liquid density and the viscosity of propane increase when the saturation temperature decreases. Hence, at the constant mass flux conditions, the liquid velocity becomes lower, while the vapor velocity is higher. This means the pressure drop increases during evaporation as the saturation temperature decrease.

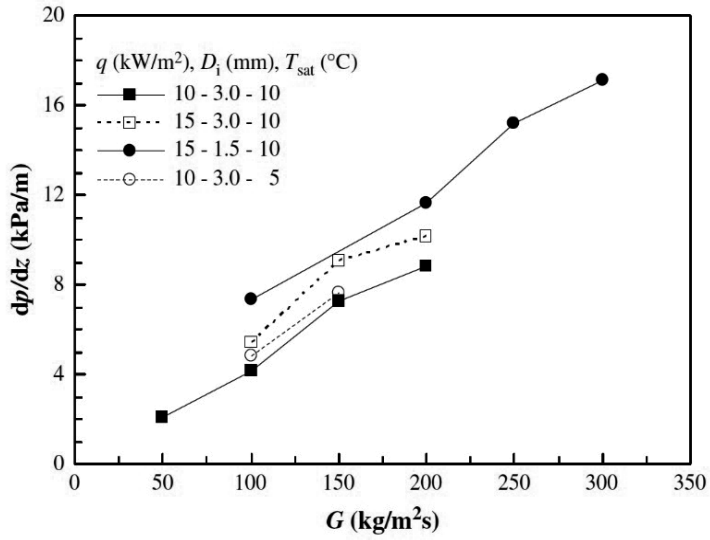


Figure 5. The effect of mass flux, heat flux, inner tube diameter and saturation temperature on the pressure drop

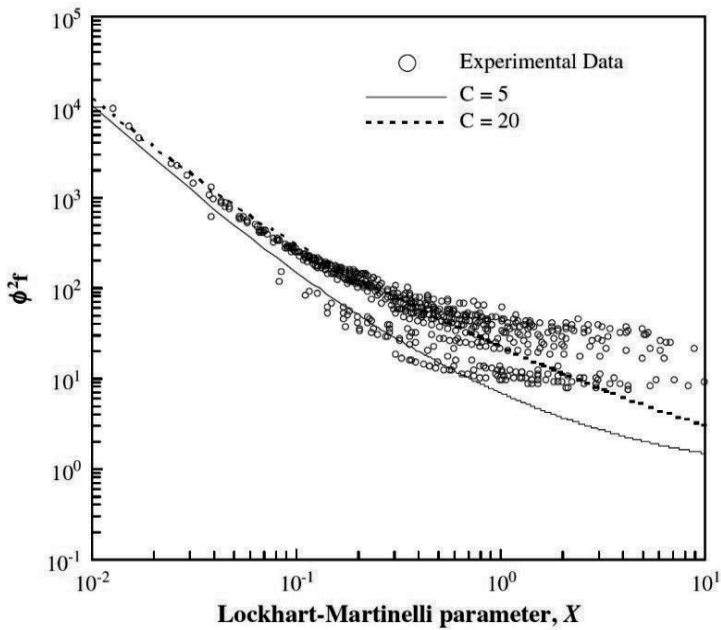


Figure 6. Variation of the two-phase frictional multiplier data with the Lockhart-Martinelli parameter

The comparison of the two-phase frictional multiplier data with the value was predicted from the Lockhart Martinelli correlation with C factors equal to 5 and 20. The value of factor Cs was evaluated follow the study of Chisholm [18]. As shown in figure 6, the presented data is distributed in all regimes: under the baseline C = 5, upper the baseline C = 20, and between the two baselines. That means the flow characteristics include laminar, co-current laminar-turbulent, and turbulent flows were observed in the data.

In order to validate the experimental data, the frictional pressure drop of propane was compared with the 13 existing correlations [19 – 31] as shown in Table 3. Among them, the correlations of Mishima and Hibiki [19], Friedel [20] and Chang et al. [21] showed the best prediction with the experimental data. Mishima and Hibiki [19] proposed the frictional pressure drop for air-water in the vertical tube with an inner diameter of 1 to 4 mm, based on the Chisholm’s equation. Before that time, using a large database, the model developed by Friedel [20] can be used to predict the frictional pressure drop in both the horizontal and vertical upward flow. The correlation of Chang et al. [21] was developed with the data of R410A and air-water in a 5mm smooth tube. Other correlations, including 4 homogenous models proposed, showed large mean deviations.

Pressure drop correlations	Deviation (%)	
	Mean	Average
Mishima and Hibiki [19]	35.37	-25.08
Friedel [20]	38.79	-21.91
Chang et al. [21]	38.86	-21.99
Cicchitti et al. [22]-homogeneous	48.67	-40.27
Beattie and Whalley [23]-homogeneous	54.68	-51.69
McAdams [24]-homogenous	56.07	-53.73
Dukler et al. [25]-homogeneous	58.75	-57.32
Lockhart and Martinelli [26]	41.36	3.46
Chisholm [27]	45.24	18.00
Zhang and Webb [28]	46.82	7.58
Chen et al. [29]	63.67	-63.60
Kawahara et al. [30]	73.04	-72.92
Tran et al. [31]	77.99	35.60

Table 3. Deviation of the pressure drop comparison between the present data and the previous correlations.

Lockhart and Martinelli [26]	$\phi_f^2 = 1 - \frac{C}{X_H} + \frac{1}{X_H^2};$ $X_H = \left(\frac{1-x}{x}\right)^{0.9} \left(\frac{\rho_g}{\rho_f}\right)^{0.5} \left(\frac{\mu_f}{\mu_g}\right)^{0.1}; C_{turbulent-turbulent} = 20$																					
Friedel [20]	$\phi_{fo}^2 = \left(\frac{1-x}{x}\right)^2 [(\rho_f f_{go}) / (\rho_g f_{fo})] + 3.24 A_2 A_3 F r^{-0.045} W e^{-0.035}$ $A_2 = x^{0.78} (1-x)^{0.224}$ $A_3 = \left(\frac{\rho_f}{\rho_g}\right)^{0.91} \left(\frac{\mu_f}{\mu_g}\right)^{0.19} \left[1 - \left(\frac{\mu_f}{\mu_g}\right)\right]^{0.7}$																					
Chisholm [27]	$\phi_{fo}^2 = 1 + (\Gamma^2 - 1) [B x^{0.875} (1-x)^{0.875} + x^{0.175}]$ $\Gamma^2 = \left(\frac{dp}{dz}\right)_{go} / \left(\frac{dp}{dz}\right)_{fo}$ <table border="1"> <thead> <tr> <th>Γ</th> <th>G ($kg\ m^{-2}\ s^{-1}$)</th> <th>B</th> </tr> </thead> <tbody> <tr> <td></td> <td>≤ 500</td> <td>4.8</td> </tr> <tr> <td>≤ 9.5</td> <td>$500 < G < 1900$</td> <td>$2400 / G$</td> </tr> <tr> <td></td> <td>$G \geq 1900$</td> <td>$55 / G^{0.5}$</td> </tr> <tr> <td>$9.5 < \Gamma < 28$</td> <td>≤ 600</td> <td>$520 / (\Gamma G^{0.5})$</td> </tr> <tr> <td></td> <td>> 600</td> <td>$21 / \Gamma$</td> </tr> <tr> <td>≥ 28</td> <td>-</td> <td>$\Gamma^2 G^{0.5}$</td> </tr> </tbody> </table>	Γ	G ($kg\ m^{-2}\ s^{-1}$)	B		≤ 500	4.8	≤ 9.5	$500 < G < 1900$	$2400 / G$		$G \geq 1900$	$55 / G^{0.5}$	$9.5 < \Gamma < 28$	≤ 600	$520 / (\Gamma G^{0.5})$		> 600	$21 / \Gamma$	≥ 28	-	$\Gamma^2 G^{0.5}$
Γ	G ($kg\ m^{-2}\ s^{-1}$)	B																				
	≤ 500	4.8																				
≤ 9.5	$500 < G < 1900$	$2400 / G$																				
	$G \geq 1900$	$55 / G^{0.5}$																				
$9.5 < \Gamma < 28$	≤ 600	$520 / (\Gamma G^{0.5})$																				
	> 600	$21 / \Gamma$																				
≥ 28	-	$\Gamma^2 G^{0.5}$																				
Mishima and Hibiki [19]	$\phi_f^2 = 1 - \frac{C}{X_H} + \frac{1}{X_H^2}$ $X = \left(-\frac{dp}{dz} F\right)_f / \left(-\frac{dp}{dz} F\right)_g$ $C = 21(1 - e^{-319 \times 10^{-6}})$																					
Tran et al. [31]	$\phi_{fo}^2 = 1 + (4.3\Gamma^2 - 1)(N_{conf} x^{0.875} + x^{1.75})$ $\Gamma^2 = \left(\frac{dp}{dz}\right)_{go} / \left(\frac{dp}{dz}\right)_{fo}; N_{conf} = \left[\frac{\alpha}{8(\rho_f - \rho_g)}\right]^{0.5}$																					
Zhang and Webb [28]	$\phi_{fo}^2 = (1-x)^2 + 2.87x^2 \left(\frac{P}{P_c}\right)^{-1} + 1.68x^{0.8}(1-x)^{0.25} \left(\frac{P}{P_c}\right)^{-1.64}$																					

Table 4. Summary of some correlations of two-phase flow pressure drops.

3.2. Heat transfer coefficient

The mass flux, heat flux, inner tube, and saturation temperature also have affected the two-phase flow boiling heat transfer coefficient of propane in the minichannels. Fig. 7 shows the effect of mass flux on heat transfer coefficient. No significant effect of mass flux on the heat transfer coefficient was observed in the low quality region. This phenomenon indicates that the nucleate boiling heat transfer is predominant. The similar tendency of nucleate boiling was performed in numerous studies by Kew and Cornwell [32], Lazarek and Black [33], Wambsganss et al. [34], Tran et al. [35], and Bao et al. [36], those that used small tubes. The dominant of nucleate boiling heat transfer occurred due to the effect of small channels and the physical properties of the refrigerant. The heat transfer coefficient is higher with higher heat flux at high quality regime since the development of convective boiling heat transfer. The trend also depicts that the drop of heat transfer coefficient appears sooner in higher mass flux. The flow pattern develops faster in the smaller tube and higher mass flux, which lead to the occurrence of dry patches at lower quality.

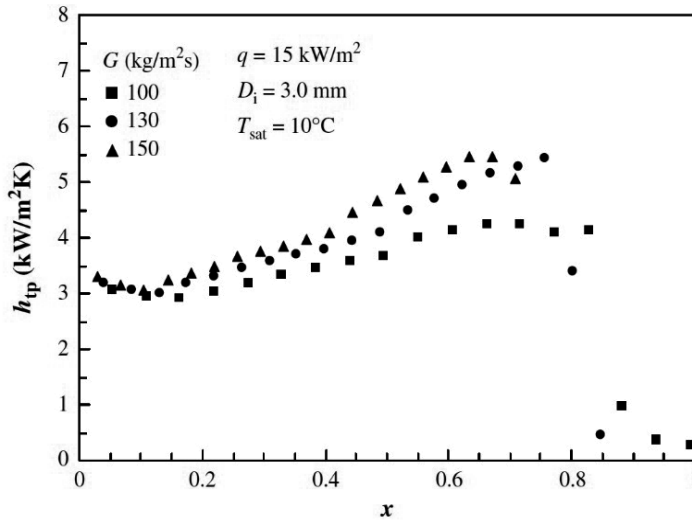


Figure 7. The effect of mass flux on heat transfer coefficient

The influence of heat flux on the heat transfer coefficient is illustrated in Fig. 8. The strong effect of heat flux is observed at a low quality regime. It means that the nucleate boiling heat transfer contribution is dominant. When the vapor quality increases, the nucleate boiling heat transfer is suppressed. Therefore, the effect of heat flux becomes limited. The heat transfer coefficient increases continuously in high quality regime, but no difference is found in given conditions. It shows that the convective boiling heat transfer contribution is predominant in this regime.

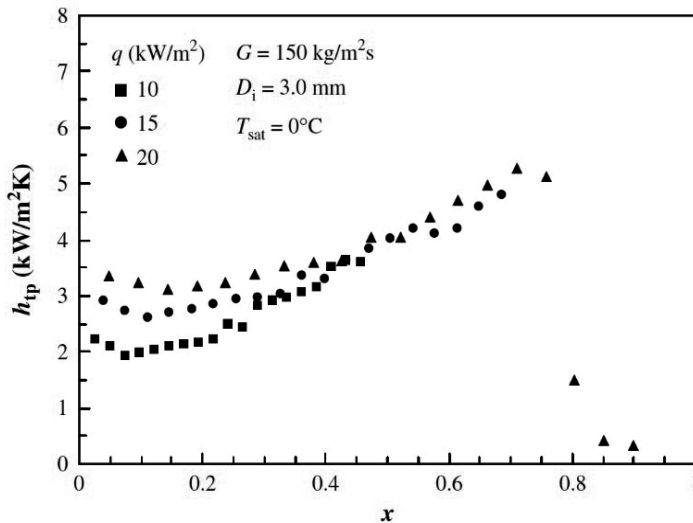


Figure 8. The effect of heat flux on heat transfer coefficient

Fig. 9 shows the effect of a tube diameter on the heat transfer coefficient of propane. The heat transfer coefficient is higher in a smaller tube diameter at a low quality regime. It can be explained that the nucleate boiling is more active when the tube diameter decreases. In addition, the heat transfer performance is higher in smaller tubes at given conditions due to the increase in contact surface per refrigerant volume.

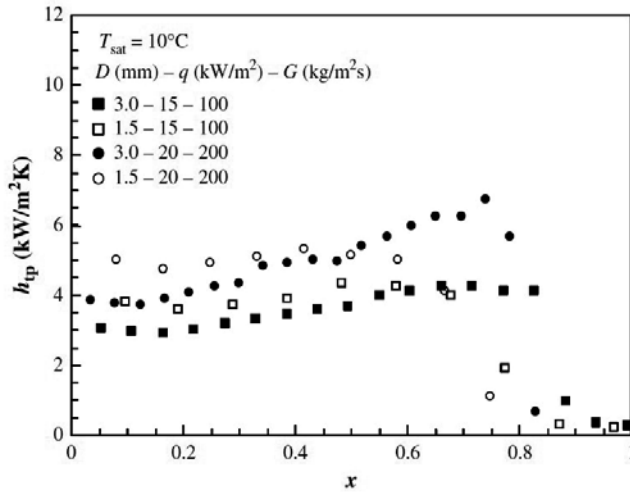


Figure 9. The effect of inner tube diameter on heat transfer coefficient

Fig. 10 illustrates the effect of saturation temperature on the heat transfer coefficient. The increase in saturation temperature leads to the increase in heat transfer coefficient. The reason is that the surface tension is lower and the saturation temperature is higher when the saturation pressure increases. Hence, the heat transfer coefficient is higher when it is considered during the vapor formation in the boiling process.

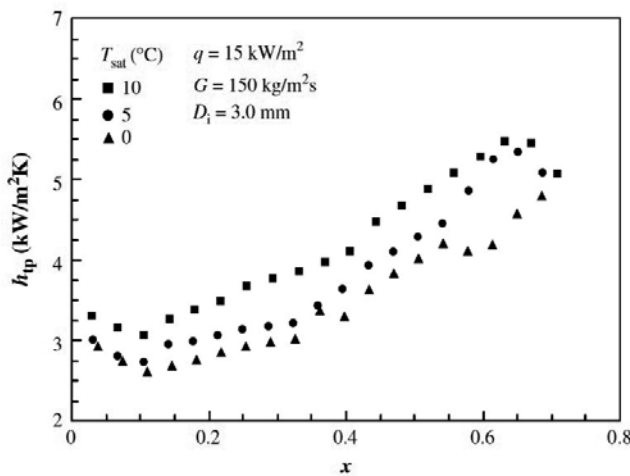


Figure 10. The effect of saturation temperature on heat transfer coefficient

4. Development of new correlations

4.1. Pressure drop correlation

The accuracy of predicting two-phase flow pressure drops in heat exchanger devices is quite important in the design and performance optimization of refrigeration systems. For a simple example, if the predicting method shows a higher value compared to the real value, the material design will cost higher. While, on the other hand, if the predicting value is lower than the real value, the performance of the design system would not reach the estimated values. In addition, the comparison of experimental pressure drops of propane and existing correlations described above showed high deviations. Hence, a more precise pressure drop correlation was proposed by Choi et al [6]. The new correlation was developed based on the method of Lockhart and Martinelli [26]. The pressure drop model of Lockhart and Martinelli [26] is defined in the basis pressure drop of three terms including the liquid phase, vapor phase, and the interaction between two phases. The ideal can be expressed in the following equation:

$$\left(-\frac{dp}{dz}F\right)_p = \left(-\frac{dp}{dz}F\right)_f + C \left[\left(-\frac{dp}{dz}F\right)_f \left(-\frac{dp}{dz}F\right)_g \right]^{1/2} + \left(-\frac{dp}{dz}F\right)_g \quad (10)$$

The two-phase frictional multiplier based on the pressure gradient for the liquid alone flow, ϕ_f^2 , is calculated by dividing Eq.(10) by the liquid phase pressure drop, as is shown in Eq. (11).

$$\phi_f^2 = \frac{\left(-\frac{dp}{dz}F\right)_p}{\left(-\frac{dp}{dz}F\right)_f} = 1 + C \left[\frac{\left(-\frac{dp}{dz}F\right)_g}{\left(-\frac{dp}{dz}F\right)_f} \right]^{1/2} + \frac{\left(-\frac{dp}{dz}F\right)_g}{\left(-\frac{dp}{dz}F\right)_f} = 1 + \frac{C}{X} + \frac{1}{X^2} \quad (11)$$

The Martinelli parameter, X , is defined by the following equation:

$$X = \left[\frac{\left(-\frac{dp}{dz}F\right)_f}{\left(-\frac{dp}{dz}F\right)_g} \right]^{1/2} = \left[\frac{2f_f G^2 (1-x)^2 \rho_g / D}{2f_g G^2 x^2 \rho_f / D} \right]^{1/2} = \left(\frac{f_f}{f_g} \right)^{1/2} \left(\frac{1-x}{x} \right) \left(\frac{\rho_g}{\rho_f} \right)^{1/2} \quad (12)$$

The friction factor in Eq. (12) was determined by the flow conditions: laminar (for $Re < 1000$), $f = 16Re^{-1}$, or turbulent (for $Re > 2000$), $f = 0.079Re^{-0.25}$. For the transition regime, the frictional factor was calculated by interpolating the equations of two regimes.

As discussed in the section above, the experimental result showed that the pressure drop is a function of mass flux, inner tube diameter, surface tension, density, and viscosity. Therefore

Choi et al. [6] proposed the factor C in Eq. (11) as a function of the two-phase Weber number, We_{tp} , and the two-phase Reynolds number, Re_{tp} . A new factor C was developed using the regression method, as shown in Eq. (13).

$$C = \left(\phi_f^2 - 1 - \frac{1}{X^2} \right) X = 1732.953 \times Re_{tp}^{-0.323} We_{tp}^{-0.24} \quad (13)$$

Fig. 11 illustrates the two-phase frictional multiplier comparison between the propane experimental data and the prediction with the new correlation proposed by Choi et al. [6]. The comparison shows a mean deviation of 10.84% and an average deviation of 1.08%.

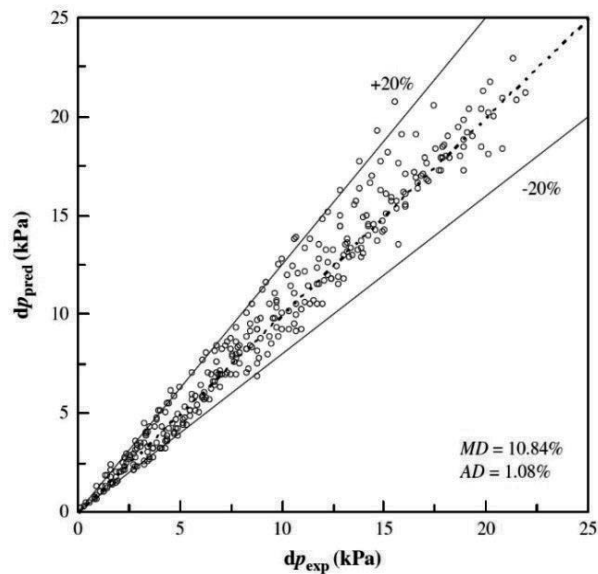


Figure 11. Comparison of the experimental and predicted pressure drop using the new developed correlation

4.2. Heat transfer coefficient correlation

Choi et al. [6] have compared the experimental heat transfer coefficients of propane with the nine correlations for boiling heat transfer coefficient, as shown in tables 5 and 6. The Shah [37] and Tran et al. [35] correlations provided the better prediction among the other presented correlations. The correlation developed by Shah [37] used a large databank from 19 independent studies with various fluids. The correlation can be used to predict the heat transfer coefficient in both horizontal and vertical tubes. However, this correlation was developed for conventional tubes. Tran et al. [35] proposed a nucleation-dominant form of heat transfer coefficient correlation based on the data of R-12 and R-113 in small circular and rectangular channels. Other correlations include the ones proposed by Jung et al. [38], Gungor and

Winterton [39], Takamatsu et al. [40], and Kandlikar and Steinke [41], where the mean deviation is around 30%. The Gungor–Winterton’s correlation [39] was a modification of the superposition model; it was developed using some fluids in several small and conventional channels with various test conditions. The correlations proposed by Wattelet et al. [42] and Chen [43] showed a large mean deviation, since both of them were developed for large tube diameters. The correlation proposed by Zhang et al. [44] used the data of some working fluids without any hydrocarbon, hence, couldn’t predict the present data well. The above comparisons showed the need of developing a more accurate heat transfer coefficient correlations. Based on the one proposed by Chen [43], Choi et al. [6] developed a new correlation for the two-phase flow boiling of propane. He noted that the correlation only used the experimental data prior to the dry-out.

It is well known that the flow boiling heat transfer is mainly governed by the following two important mechanisms: nucleate boiling and forced convective evaporation. The basic form is described by Chen [43] as follows:

$$h_{tp} = F \cdot h_{conv} + h_{nb} \cdot S \tag{14}$$

The convective component was also presented by a Dittus-Boelter type equation.

$$h_{fo} = 0.023 \left[\frac{G(1-x)D}{\mu_f} \right]^{0.8} \left[\frac{\mu_f c_p}{k_f} \right]^{0.4} \frac{k_f}{D} \tag{15}$$

Heat transfer coefficient correlations	Deviation (%)	
	Mean	Average
Chen [43]	50.82	18.74
Gungor and Winterton [39]	28.44	23.78
Shah [37]	19.21	3.55
Takamatsu et al. [40]	32.69	32.15
Wattelet et al. [42]	48.28	48.28
Tran et al. [35]	21.18	-6.15
Kandlikar and Steinke [41]	33.84	24.41
Zhang et al. [44]	79.21	77.89
Jung et al. [38]	26.05	23.38

Table 5. Deviation of the heat transfer coefficient comparison between the present data and the previous correlations.

Chen [43]	$h_{tp} = S.h_{nb} + F.h_{lo}; \text{where } S = fn(\text{Re}_{tp}); F = fn(X_{tt})$ $h_{nb} = 0.00122 \left[\frac{k_f^{0.79} c_{pf}^{0.45} \rho_f^{0.49}}{\sigma^{0.5} \mu_f^{0.29} i_{fg}^{0.24} \rho_g^{0.24}} \right] \Delta T_e^{0.24} \Delta p_e^{0.75}; h_{lo} = 0.023 \left[\frac{G(1-x)D}{\mu_f} \right]^{0.8} \left[\frac{\mu_f c_p}{k_f} \right]^{0.4} \frac{k_f}{D}$
Gungor and Winterton [39]	$h_{tp} = E_{new} \times h_l$ $E_{new} = 1 + 3000Bo^{0.86} + 1.12 \left(\frac{x}{1-x} \right)^{0.75} \left(\frac{\rho_l}{\rho_v} \right)^{0.41}$ <p>If the tube is horizontal and the Froude number (Fr_l) is less than 0.05 then E should be multiplied by the factor $E_2 = Fr_l^{(0.1-2Fr_l)}$</p>
Shah [37]	$\psi = \frac{h_{TP}}{h_f}; Co = \left(\frac{1}{x-1} \right)^{0.8} \left(\frac{\rho_g}{\rho_f} \right)^{0.5}; Bo = \frac{q}{Gh_{fg}}; Fr_f = \frac{G^2}{\rho_f^2 g D}$ $h_l = 0.023 \text{Re}_f^{0.8} \text{Pr}_f^{0.4} \left(\frac{k_f}{D_f} \right)$
Jung et al. [38]	$h_{tp} = S.h_{sA} + F.h_{lo}$ $h_{sA} = 207 \frac{k_1}{bd} \left(\frac{qbd}{k_1 T_{sat}} \right)^{0.745} \left(\frac{\rho_g}{\rho_f} \right)^{0.581} \text{Pr}_f^{0.533};$ $h_l = 0.023 \text{Re}_f^{0.8} \text{Pr}_f^{0.4} \left(\frac{k_f}{D_f} \right)$ $bd = 0.0146 \left(\frac{35\pi}{180} \right) \left[\frac{2\sigma}{g(\rho_f - \rho_g)} \right]^{0.5}$ $S = 4048 X_{tt}^{1.22} Bo^{1.13} \text{ for } X_{tt} < 1$ $F = 2.37 \left(0.29 + \frac{1}{X_{tt}} \right)^{0.85}$
Wattelet et al. [42]	$h_{tp} = [h_{nb}^n + h_{cb}^n]^{1/n}; n = 2.5$ $h_{nb} = 55 p_r^{0.12} (-0.4343 \ln p_r)^{-0.55} M^{-0.5} q^{0.67}$ $h_{cb} = 0.023 \text{Re}_f^{0.8} \text{Pr}_f^{0.4} \left(\frac{k_f}{D_f} \right) \times F \times R$ <p>$F = fn(X_{tt}); \text{ and } S = fn(\text{Re}_{tp})$</p>
Tran et al. [35]	$h = (8.4 \times 10^{-5}) (Bo^2 W e_f)^{0.3} \left(\frac{\rho_f}{\rho_g} \right)^{-0.4}$
Kandlikar and Steinke [41]	$\frac{h_{tp}}{h_f} = D_1 Co^{D_2} \left(\frac{1 \times 0.8}{-} \right) fn(Fr_{fo}) + D_3 Bo^{D_4} \left(\frac{1 \times 0.8}{-} \right) Fr$ <p>$fn(Fr_{fo}) = 1$</p>
Zhang et al. [44]	$h_{tp} = S.h_{nb} + F.h_{sp}$ $h_{nb} = 0.00122 \left[\frac{k_f^{0.79} c_{pf}^{0.45} \rho_f^{0.49}}{\sigma^{0.5} \mu_f^{0.29} i_{fg}^{0.24} \rho_g^{0.24}} \right] \Delta T_e^{0.24} \Delta p_e^{0.75}$ <p>$h_{sp} = \text{MAX}(h_{\text{Dittus-Boelter}})$ if $\text{Re}_f < 2300$; $h_{sp} = (h_{\text{Dittus-Boelter}})$ if $\text{Re}_f \geq 2300$</p> <p>$S = fn(\text{Re}_f); F = fn(\phi_f)$</p>

$$\begin{aligned}
 h_{tp} &= F \cdot h_{lo} + S \cdot h_{pb} \\
 h_{lo} &= 0.0116 \text{Re}_{lo}^{0.89} \text{Pr}_l^{0.4} \frac{k_l}{D_i} \\
 F &= \begin{matrix} (12) \\ -X_{tt}^{-0.88} \end{matrix} \\
 \text{Takamatsu et al.} & \quad h_{pb} = \left[405 C_1 k_l \left(\frac{g(\rho_l - \rho_v)}{2\sigma} \right)^{0.5} \left(\frac{S \cdot \Delta T \cdot La}{k_l \cdot T_{sat}} \right)^{0.745} \left(\frac{\rho_v}{\rho_l} \right)^{0.581} \text{Pr}^{0.533} \right]^{1/0.255} \\
 [40] & \\
 S &= C_2 \left(\frac{\rho_l c_{pl}}{\rho_v h_{fg}} T_{sat} \right)^{1.25} La \cdot F \cdot h_{lo} / k_l \\
 La &= \sqrt{\frac{2\sigma}{g(\rho_l - \rho_v)}} \\
 C_1 &= 1.35; C_2 = 3.3 \times 10^{-5}
 \end{aligned}$$

Table 6. Summary of existing heat transfer coefficient correlations

In small channels, the contribution of force convective heat transfer normally occurs later than it does in conventional channels due to the high contribution of nucleate boiling. Therefore, the enhancement factor F , which describes the increase in the convective heat transfer when the vapor quality increases, should be physically evaluated again. Chen [43] first introduced the enhanced factor F as the function of Lockhart-Martinelli parameter X_{tt} , $F = fn(X_{tt})$. Zhang et al. [44], later, took the flow condition effect in the enhanced factor into account. They introduced the relationship $F = fn(\phi_f^2)$, where (ϕ_f^2) is a general form proposed by Chisholm [18], as shown in Eq. (11). The values of the Chisholm parameter, C , are 20, 12, 10, and 5 corresponding to the four flow conditions of liquid and vapor: turbulent-turbulent (tt), laminar-turbulent (vt), turbulent-laminar (tv) and laminar-laminar (vv). However, as seen in the evaluation of existing heat transfer correlation above, the correlation of Zhang et al. [44] shows a large deviation with the present data. Hence, the factor F needs to reform to fit in the data.

Choi et al. [6] modified the enhancement factor F as a function of (ϕ_f^2) , $F = fn(\phi_f^2)$, where (ϕ_f^2) is obtained from Eq. (11) - (13). The value of C in study of Choi et al. [6] is calculated by an interpolation of the Chisholm parameter with thresholds of $\text{Re} = 1000$ and $\text{Re} = 2000$ for the laminar and turbulent flows, respectively. On the other hand, the enhancement factor F must be reduced to 1 for pure liquid or pure vapor, and be greater than 1 within the two-phase regime. Hence, using a regression method, the formula of F is satisfied as follows:

$$F = \text{MAX}(0.5\phi_f, 1) \tag{16}$$

A new factor F is shown in Fig. 12.

Cooper [45] developed a correlation that used a large nucleate boiling data bank. Kew and Cornwell [32] and Jung et al. [46] showed that the Cooper [45] pool boiling correlation best predicted their experimental data. Therefore, the prediction of the nucleate boiling heat transfer for the present experimental data used Cooper [45], which is a pool boiling correlation developed based on an extensive study,

$$h = 55 p_r^{0.12} (-0.4343 \ln p_r)^{-0.55} M^{-0.5} q^{0.67} \tag{17}$$

To account for the suppression of the nucleate boiling when vapor quality increases, Chen [43] defined the nucleate boiling suppression factor S , which is the ratio of mean superheat temperature, $\Delta T_{e,r}$, to the wall superheat temperature, ΔT_{sat} . Jung et al. [38] introduced the suppression factor N as the function of X_{tt} and boiling number, Bo , to take into account the strong effect of nucleate boiling in flow boiling. On the other hand, to consider the effect of flow conditions, the Lockhart – Martinelli parameter X_{tt} is replaced by the two-phase frictional multiplier, ϕ_f^2 . Using the regression program and the experimental data, a new nucleate boiling suppression factor was proposed by Choi et al. [6]. It is as follows:

$$S = 181.458 (\phi_f^2)^{0.002} Bo^{0.816} \tag{18}$$

The new heat transfer coefficient correlation is developed using 461 data points. Fig. 13 shows the comparison of the experimental heat transfer coefficient and the predicted one. The new correlation archives a good prediction with a mean deviation of 9.93% and an average deviation of -2.42%. When the C factor of the Chisholm [18] method is used to obtain ϕ_f^2 for equations (11) and (16), the heat transfer coefficient also showed a good comparison mean deviation of 14.40%.

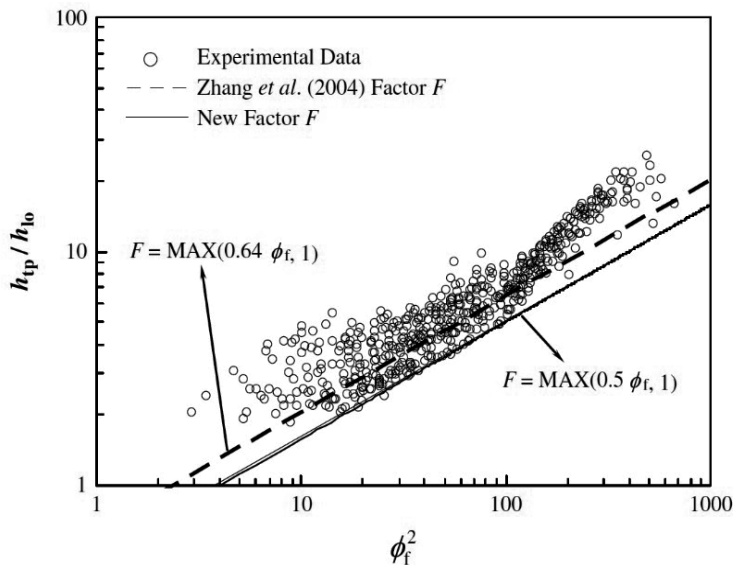


Figure 12. Two-phase heat transfer multiplier as a function of ϕ_f^2

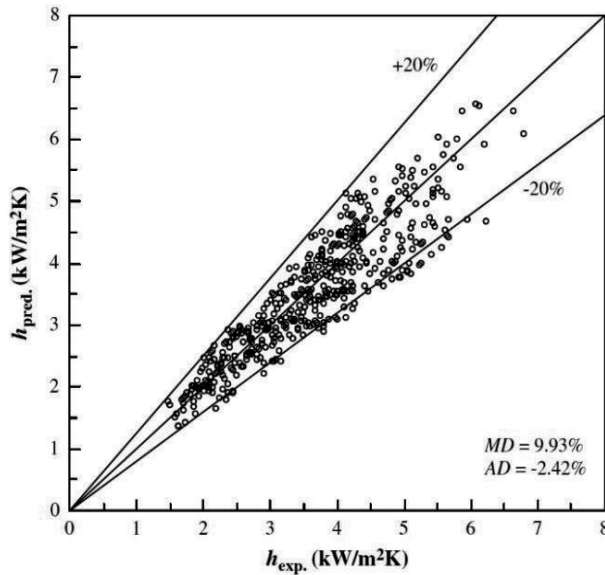


Figure 13. Comparison of the experimental and predicted heat transfer coefficients using the new developed correlation

5. Concluding remarks

This chapter demonstrated the convective boiling pressure drop and heat transfer experiments of propane in horizontal minichannels. The content is summarized as follows:

1. The experimental pressure drop of propane was well predicted by the models proposed by Mishima and Hibiki [19], Friedel [20] and Chang et al. [21]
2. The pressure drop increases with the increase of mass and heat fluxes, and the decrease in the inner tube diameter and saturation temperature. The experimental results illustrated that pressure drop is a function of the mass flux, the tube diameter, the surface tension, the density, and the viscosity.
3. A new pressure drop correlation was developed on the basis of the Lockhart–Martinelli model. The correlation was defined as a function of the two-phase Reynolds number, Re_{tp} , and the two-phase Weber number, We_{tp} . In addition, a new factor C was developed using a regression method with a mean and average deviation of 10.84% and 1.08%, respectively.
4. The effects of mass flux, heat flux, inner tube diameter, and saturation temperature on the heat transfer coefficient of propane were observed. The heat transfer coefficient increases with the decrease in the inner tube diameter and the increase in saturation temperature.

5. The heat transfer coefficient correlations proposed by Shah [37] and Tran et al. [35] show an accurate prediction with the current heat transfer coefficient experimental data.
6. The geometric effect of the small tube and flow condition must be considered to develop a new heat transfer coefficient correlation. The development of the enhanced factor F for the convective boiling contribution, and the suppression of factor S for nucleate boiling suppression factor have been also clearly evaluated with the consideration of laminar and turbulent flows. A new boiling heat transfer coefficient correlation that is based on a superposition model for propane in minichannels was demonstrated with 9.93% mean deviation and -2.42% average deviation.

Nomenclature

A: Area (m²)

AD: Average deviation, $AD = \left(\frac{1}{n} \right) \sum_1^n ((dp_{\text{pred}} - dp_{\text{exp}}) \times 100 / dp_{\text{exp}})$

Bo: Boiling number, $Bo = \frac{q}{G i_{\text{fg}}}$

C: Chisholm parameter

c_p: Specific heat (kJ kg⁻¹ K⁻¹)

D: Diameter (m)

f: Friction factor

G: Mass flux (kg m⁻² s⁻¹)

g: Acceleration due to gravity (m s⁻²)

h: Heat transfer coefficient (kW m⁻²K⁻¹)

i: Enthalpy (kJ kg⁻¹)

L: Tube Length (m)

MD: Mean deviation, $MD = \left(\frac{1}{n} \right) \sum_1^n |((dp_{\text{pred}} - dp_{\text{exp}}) \times 100 / dp_{\text{exp}})|$

M: Molecular weight (kg kmol⁻¹)

n: Number of data

p: Pressure (kPa)

Q: Electric power (kW)

q: Heat flux (kW m⁻²)

Re: Reynolds number, $Re = \frac{GD}{\mu}$

T: Temperature (K)

\dot{m} : Mass flow rate (kg s^{-1})

X: Lockhart-Martinelli parameter

x: Vapor quality

z: Length (m)

Greek letters

α : Void fraction

Δi : The enthalpy rise across the tube (kJ kg^{-1})

μ : Dynamic viscosity (N s m^{-2})

ρ : Density (kg m^{-3})

σ : Surface tension (N m^{-1})

ϕ^2 : Two-phase frictional multiplier

ΔT : Wall super heat (K)

Gradients and differences

(dp/dz) : Pressure gradient ($\text{N m}^{-2} \text{m}^{-1}$)

$(dp/dz F)$: Pressure gradient due to friction ($\text{N m}^{-2} \text{m}^{-1}$)

Subscripts

crit : Critical point

exp: Experimental value

f: Saturated liquid

fi: Inlet liquid

g: Saturated vapor

i: Inner tube

lo: Liquid only

o: Outlet tube

pb: Pool boiling

pred: Prediction value

r: Reduced

sat: Saturation

sc: Subcooled

t: Turbulent

tp: Two-phase

v: Laminar

w: Wall

wi: Inside tube wall

Acknowledgements

This research was supported by the Basic Science Research Program through the National Research Foundation of Korea (NRF) funded by the Ministry of Education (NRF-2013R1A1A2013476).

Author details

Jong-Taek Oh^{1*}, Kwang-Il Choi¹ and Nguyen-Ba Chien²

*Address all correspondence to: ohjt@chonnam.ac.kr

1 The Department of Refrigeration and Air Conditioning Engineering, Chonnam National University 50 Daehak-ro, Yeosu, Chonnam, Republic of Korea

2 Graduate school, Chonnam National University, 50 Daehak-ro, Yeosu, Chonnam, Republic of Korea

References

- [1] Calm, J. (2008). The next generation of refrigerants – Historical review, considerations, and outlook. *International Journal of Refrigeration*, 31 (7), 1123–1133.
- [2] Palm, B. (2007). Refrigeration systems with minimum charge of refrigerant. *Applied Thermal Engineering*, 27(10), 1693–1701.
- [3] S.S. Bertsch, E.A. Groll, S.V. Garimella, Review and comparative analysis of studies on saturated flow boiling in small channels, *Nanoscale Microscale Thermophys. Eng.* 12 (3) (2008) 187–227.

- [4] V. Dupont, J.R. Thome, Evaporation in microchannels: influence of the channel diameter on heat transfer, *Microfluid Nanofluid* 1 (2005) 119–127.
- [5] Blanco Castro, J., Urchueguía, J., Corberán, J. M., & González, J. (2005). Optimized design of a heat exchanger for an air-to-water reversible heat pump working with propane (R290) as refrigerant: Modelling analysis and experimental observations. *Applied Thermal Engineering*, 25(14-15), 2450–2462.
- [6] Choi, K.-I., Pamitran, a. S., Oh, J.-T., & Saito, K. (2009). Pressure drop and heat transfer during two-phase flow vaporization of propane in horizontal smooth minichannels. *International Journal of Refrigeration*, 32(5), 837–845. doi:10.1016/j.ijrefrig.2008.12.005
- [7] Fernando, P., Palm, B., Ameel, T., Lundqvist, P., & Granryd, E. (2008). A minichannel aluminium tube heat exchanger – Part II: Evaporator performance with propane. *International Journal of Refrigeration*, 31(4), 681–695. doi:10.1016/j.ijrefrig.2008.02.012
- [8] Fernando, P., Palm, B., Lundqvist, P., & Granryd, E. (2004). Propane heat pump with low refrigerant charge: design and laboratory tests. *International Journal of Refrigeration*, 27(7), 761–773.
- [9] Mastrullo, R., Mauro, A.W., Menna, L., & Vanoli, G.P. (2014). Replacement of R404A with propane in a light commercial vertical freezer: A parametric study of performances for different system architectures. *Energy Conversion and Management*, 82, 54–60. doi:10.1016/j.enconman.2014.02.069
- [10] Steiner, D., 1993. VDI-Warmeatlas (VDI Heat Atlas) chapter Hbb. In: Verein Deutscher Ingenieure, editor. VDI- €Gesellschaft Verfahrenstechnik und Chemieingenieurwesen (GCF), Translator: J.W. Fullarton, Dusseldorf.
- [11] Premoli, A., Francesco, D., Prina, A., 1971. A dimensionless correlation for determining the density of two-phase mixtures. *Lo Termotecnica* 25, 17–26.
- [12] Chisholm, D., 1972. An equation for velocity ratio in two-phase flow. *NEL Report*, 535.
- [13] Zhao, Y., Molki, M., Ohadi, M. M., Dessiatoun, S.V., 2000. Flow boiling of CO₂ in microchannels. *ASHRAE Trans*, 437–445. DA-00-2-1.
- [14] Yoon, S.H., Cho, E.S., Hwang, Y.W., Kim, M.S., Min, K., Kim, Y., 2004. Characteristics of evaporative heat transfer and pressure drop of carbon dioxide and correlation development. *Int. J. Refrigeration* 27, 111–119.
- [15] Park, C.Y., Hrnjak, P.S., 2007. CO₂ and R410A flow boiling heat transfer, pressure drop, and flow pattern at low temperatures in a horizontal smooth tube. *Int. J. Refrigeration* 30, 166–178.
- [16] Oh, H.K., Ku, H.G., Roh, G.S., Son, C.H., Park, S.J., 2008. Flow boiling heat transfer characteristics of carbon dioxide in a horizontal tube. *Appl. Therm. Eng.* 28, 1022–1030.

- [17] Cho, J.M., Kim, M.S., 2007. Experimental studies on the evaporative heat transfer and pressure drop of CO₂ in smooth and micro-fin tubes of the diameters of 5 and 9.52 mm. *Int. J. Refrigeration* 30, 986–994.
- [18] Chisholm, D., 1967. A theoretical basis for the Lockhart–Martinelli correlation for two-phase flow. *Int. J. Heat Mass Transfer* 10, 1767–1778.
- [19] Mishima, K., Hibiki, T., 1996. Some characteristics of air–water two-phase flow in small diameter vertical tubes. *Int. J. Multiphase Flow* 22, 703–712.
- [20] Friedel, L. Improved friction pressure drop correlations for horizontal and vertical two-phase pipe flow. In: the European Two-phase Flow Group Meeting, Paper E2, June 1979, Ispra, Italy.
- [21] Chang, Y.J., Chiang, S.K., Chung, T.W., Wang, C.C., 2000. Two-phase frictional characteristics of R-410A and air-water in a 5 mm smooth tube. *ASHRAE Trans*, 792–797. DA-00-11-3.
- [22] Cicchitti, A., Lombardi, C., Silvestri, M., Soldaini, G., Zavalluilli, R., 1960. Two-phase cooling experiments pressure drop, heat transfer, and burn out measurement. *Energia Nucl.* 7 (6), 407–425.
- [23] McAdams, W.H., 1954. *Heat Transmission*, third ed. McGraw-Hill, New York.
- [24] Beattie, D.R.H., Whalley, P.B., 1982. A simple two-phase flow frictional pressure drop calculation method. *Int. J. Multiphase Flow* 8, 83–87.
- [25] Dukler, A.E., Wicks III, M., Cleveland, R.G., 1964. Frictional pressure drop in two-phase flow: B. An approach through similarity analysis. *AIChE J.* 10 (1), 44–51.
- [26] Lockhart, R.W., Martinelli, R.C., 1949. Proposed correlation of data for isothermal two-phase, two-component flow in pipes. *Chem. Eng. Prog.* 45, 39–48.
- [27] Chisholm, D., 1983. *Two-Phase Flow in Pipelines and Heat Exchangers*. Longman, New York.
- [28] Zhang, M., Webb, R.L., 2001. Correlation of two-phase friction for refrigerants in small-diameter tubes. *Exp. Therm. Fluid Sci.* 25, 131–139.
- [29] Chen, I.Y., Yang, K.S., Chang, Y.J., Wang, C.C., 2001. Two-phase pressure drop of air–water and R-410A in small horizontal tubes. *Int. J. Multiphase Flow* 27, 1293–1299.
- [30] Kawahara, A., Chung, P.M.Y., Kawaji, M., 2002. Investigation of two-phase flow pattern, void fraction and pressure drop in a minichannel. *Int. J. Multiphase Flow* 28, 1411–1435.
- [31] Tran, T.N., Chyu, M.C., Wambsganss, M.W., France, D.M., 2000. Two-phase pressure drop of refrigerants during flow boiling in small channels: an experimental investigation and correlation development. *Int. J. Multiphase Flow* 26, 1739–1754.

- [32] Kew, P.A., Cornwell, K., 1997. Correlations for the prediction of boiling heat transfer in small-diameter channels. *Appl. Therm. Eng.* 17 (8–10), 705–715.
- [33] Lazarek, G.M., Black, S.H., 1982. Evaporative heat transfer, pressure drop and critical heat flux in a small diameter vertical tube with R-113. *Int. J. Heat Mass Transfer* 25, 945–960.
- [34] Wambsganss, M.W., France, D.M., Jendrzejczyk, J.A., Tran, T.N., 1993. Boiling heat transfer in a horizontal small-diameter tube. *J. Heat Transfer* 115, 963–975.
- [35] Tran, T.N., Wambsganss, M.W., France, D.M., 1996. Small circular- and rectangular-channel boiling with two refrigerants. *Int. J. Multiphase Flow* 22 (3), 485–498.
- [36] Bao, Z.Y., Fletcher, D.F., Haynes, B.S., 2000. Flow boiling heat transfer of freon R11 and HCFC123 in narrow passages. *Int. J. Heat Mass Transfer* 43, 3347–3358.
- [37] Shah, M.M., 1978. Chart correlation for saturated boiling heat transfer: equations and further study. *ASHRAE Trans* 2673, 185–196.
- [38] Jung, D.S., McLinden, M., Radermacher, R., Didion, D., 1989. A study of flow boiling heat transfer with refrigerant mixtures. *Int. J. Heat Mass Transfer* 32 (9), 1751–1764.
- [39] Gungor, K.E., Winterton, H.S., 1987. Simplified general correlation for saturated flow boiling and comparisons of correlations with data. *Chem. Eng. Res.* 65, 148–156.
- [40] Takamatsu, H., Momoki, S., Fujii, T., 1993. A correlation for forced convective boiling heat transfer of a non azeotropic refrigerant mixture of HCFC22/CFC114 in a horizontal smooth tube. *Int. J. Heat Mass Transfer* 36 (14), 3555–3563.
- [41] Kandlikar, S.G., Steinke, M.E., 2003. Predicting heat transfer during flow boiling in minichannels and microchannels. *ASHRAE Trans*, 667–676. CH-03-13-1.
- [42] Wattelet, J.P., Chato, J.C., Souza, A.L., Christoffersen, B.R., 1994. Evaporative characteristics of R-12, R-134a, and a mixture at low mass fluxes. *ASHRAE Trans*, 603–615. 94-2-1.
- [43] Chen, J.C., 1966. A correlation for boiling heat transfer to saturated fluids in convective flow. *Ind. Eng. Chem. Process Des. Dev.* 5, 322–329.
- [44] Zhang, W., Hibiki, T., Mishima, K., 2004. Correlation for flow boiling heat transfer in mini-channels. *Int. J. Heat Mass Transfer* 47, 5749–5763.
- [45] Cooper, M.G., 1984. Heat flow rates in saturated nucleate pool boiling—a wide-ranging examination using reduced properties. In: *Advances in Heat Transfer*, vol. 16. Academic Press, pp. 157–239.
- [46] Jung, D., Kim, Y., Ko, Y., Song, K., 2003. Nucleate boiling heat transfer coefficients of pure halogenated refrigerants. *Int. J. Refrigeration* 26, 240–248.

Effect of Depth Length on Mixing in a Double-Diffusive Convection Two-Layer System

Hideo Kawahara

Additional information is available at the end of the chapter

<http://dx.doi.org/10.5772/60954>

1. Introduction

With the rapid development of industrial technologies within recent years, development of multi-function, high-performance materials that can survive harsh conditions is in demand. In regards to the materials manufacturing processes that accompany coagulation, it has been indicated that multilayer convection cell formation and amalgamation occurs due to double diffusive convection, and that this may exert an influence on material quality [1, 2]. When manufacturing this kind of material, solute elimination occurs on the coagulation interface during the multi-component solution coagulation process, and double diffusive convection occurs due to the gradient between temperature and concentration in the droplet phase. It is thought that multilayer cell structure formation and destruction occur due to this phenomenon in the droplet phase, and that this exerts a major influence over crystal growth speeds and material quality. However, many relevant details remain unexplained. As the phenomenon of convection cell amalgamation in particular is complex, the phenomenon of convection between low- and high-concentration layers has come to be considered as a system using experiments and mathematical simulations [3 - 10]. Bergman et al. [5] measured the speed of material passing through the diffusion interface at convection cell amalgamation and between convection cells. Subsequently, Nishimura et al. [7, 8] made broad-ranging changes to control parameters, and proposed a correlational formula for these issues. Hyun et al. [10] considered the amalgamation process in detail using 2-dimensional mathematical calculations, and showed that high-frequency component fluctuation occurs at the average Nu number.

Convection cell amalgamation is governed by the diffusion interface, where major gradients in concentration are present. As both thermally unstable diffusive-type double diffusive convection and opposing, shear flows due to thermal convection co-exist in interface areas according to calculation results by Hyun et al. [10], it is anticipated that interface instability

can easily occur in these circumstances. Recently, Tanny et al. [9] focused on interface regions and investigated 2-dimensional structures using the Schlieren method. The team also reported that when initial buoyancy is low and thermal Rayleigh number is high, vortex arrays form above and below the interface, and convection cell amalgamation time is shortened. Considered in light of vortex structure, this phenomenon is thought to occur primarily due to shear current instability. However, while traditional research also leads us to anticipate interface instability due to double diffusive convection, characteristics of diffusive-type double diffusive convection in shear currents remain unknown.

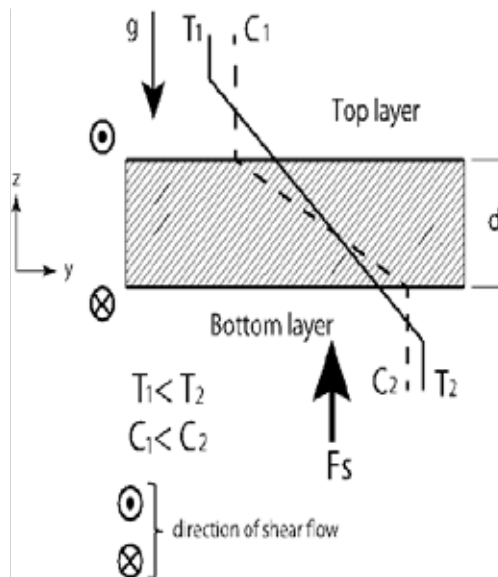


Figure 1. Diffusive interface between the convective cell

As shown in Fig. 1, diffusion interface between convection cells is stable in terms of concentration in a gravitational field, but is thermally unstable due to the presence of a vertical temperature differential. Accordingly, it is clear that it takes the aforementioned diffusive state. It has been previously confirmed that non-flowing diffusive interfaces fall into oscillating modality. This is explained via the diffusive interface shown in Fig. 2. As heat diffusion is much faster than material diffusion, high-concentration lower fluid bodies rise due to thermal buoyancy. Afterwards, the fluid body is cooled rapidly while maintaining its concentration, and then proceeds to descend due to reversed buoyancy. The repeated occurrence of this phenomenon at the interface is known as oscillation modality. The diffusive interface between convection cells shown in Fig. 1 contains shear currents due to thermal convection caused by horizontal temperature gradients above and below the interface. As it is possible for 3-dimensional structures to form due to the presence of shear currents and the occurrence of oscillation modality at the interface in this sort of situation, a detailed investigation is seen as necessary. In actuality, Chen et al. [11] have reported 3-dimensional structures in cases of finger-type interfaces coexisting with shear currents.

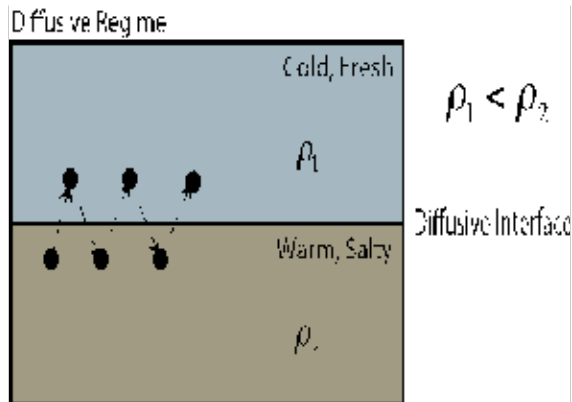


Figure 2. Oscillatory modes

In order to investigate 3-dimensional structures in diffusive interfaces in this research, 3-dimensional mathematical calculations were conducted for diffusive interfaces occurring in an aqueous solution with density stratification into a linear state, which is heated and cooled as a system from both sides in a rectangular container. In addition, the computational domain in the direction of depth is changed, and the mixing process of each convection layer was examined.

2. Numerical analysis

2.1. Mathematical model

The model equations to describe the double diffusive natural convection consist of the continuity, the Navier-Stokes, the energy and the concentration equations in dimensionless forms as follows:

$$\nabla \cdot V = 0 \tag{1}$$

$$\frac{\partial V}{\partial \tau} + (V \cdot \nabla)V = -\nabla P + \text{Pr} \cdot \nabla^2 V + \text{Pr} \cdot \text{Ra}(\theta - N \cdot C) \kappa \tag{2}$$

$$\frac{\partial \theta}{\partial \tau} + (V \cdot \nabla)\theta = \nabla^2 \theta \tag{3}$$

$$\frac{\partial \theta}{\partial \tau} + (V \cdot \nabla)C = \frac{\nabla^2}{Le} \tag{4}$$

Dimensionless parameters Pr, Ra, Le, N and A are defined as follows:

$$Pr = \frac{\nu}{\kappa}, Ra = \frac{g \cdot \alpha (T_{hot} - T_{cold}) b^3}{\kappa \cdot \nu}$$

$$Le = \frac{\kappa}{D}, N = \frac{\beta (C_{max} - C_{min})}{\alpha (T_{hot} - T_{cold})}, A = \frac{h}{b}$$
(5)

Here, the dimensionless variables are defined as follows:

$$X = x/b, Y = y/b, Z = z/b$$

$$U = u \cdot b/\kappa', V = v \cdot b/\kappa', W = w \cdot b/\kappa'$$

$$\tau = t \cdot \kappa/b^2, P = p \cdot b^2/(\rho \cdot \kappa^2)$$

$$\theta = \frac{T - T_{cold}}{T_{hot} - T_{cold}}, C = \frac{C - C_{min}}{C_{max} - C_{min}}$$
(6)

2.2. Boundary conditions

The boundary conditions in dimensionless form are illustrated in Fig.3. In the computational domain (see Fig.2), the aspect ratio is 1.25 and length of the direction of depth (Z) examined three kinds (1.0, 1.5 and 2.0). The initial temperature in the system is 0.0 and the initial concentration is linear profile: $C=f(Y)$

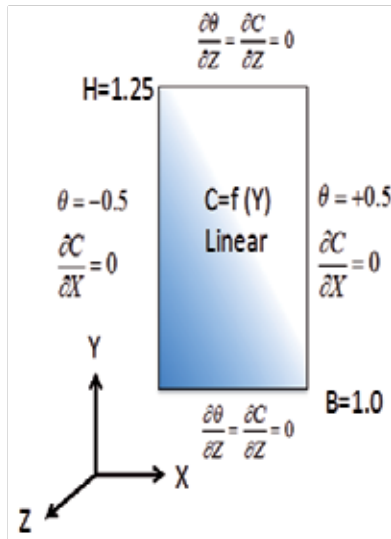


Figure 3. Boundary conditions

$$\begin{aligned}
 &\text{at } X = 0, U = V = W = 0, \theta = -0.5, \frac{\partial C}{\partial X} = 0 \\
 &\text{at } X = 1, U = V = W = 0, \theta = +0.5, \frac{\partial C}{\partial X} = 0 \\
 &\text{at } Y = 0, U = V = W = 0, \frac{\partial \theta}{\partial Z}, \frac{\partial C}{\partial Z} = 0 \\
 &\text{at } Y = 1.25, U = V = W = 0, \frac{\partial \theta}{\partial Y}, \frac{\partial C}{\partial Z} = 0 \\
 &\text{at } Z = 0, U = V = W = 0, \frac{\partial \theta}{\partial Y}, \frac{\partial C}{\partial Y} = 0 \\
 &\text{at } Z = 1.0, 1.5, 2.0, U = V = W = 0, \frac{\partial \theta}{\partial Y}, \frac{\partial C}{\partial Y} = 0
 \end{aligned}$$

2.3. Computation method

A fine difference method was employed to solve the model equations numerically. The calculation algorithm of pressure terms is the HSMAC method. To solve the mathematical model we developed a home-made code based on the HSMAC method [12,13] that utilizes the finite differences approximation: second order central finite differences for the viscous terms, third order up-wind finite differences (UTOPIA) [14] for the convective terms, and first order forward finite differences for the time derivative.

Details of the numerical algorithm are given next. The discrete form of eq. (2) is

$$\frac{m(\tilde{v}_x)_{i,j,k}^{n+1} - m(\tilde{v}_x)_{i,j,k}^n}{\Delta \tau} = \frac{m(\tilde{p})_{i,j,k}^{n+1} - m(\tilde{p})_{i+1,j,k}^{n+1}}{\Delta \tilde{x}} + (DSFX)_{i,j,k}^n \tag{7}$$

$$\frac{m(\tilde{v}_y)_{i,j,k}^{n+1} - m(\tilde{v}_y)_{i,j,k}^n}{\Delta \tau} = \frac{m(\tilde{p})_{i,j,k}^{n+1} - m(\tilde{p})_{i+1,j,k}^{n+1}}{\Delta \tilde{y}} + (DSFY)_{i,j,k}^n \tag{8}$$

$$\frac{m(\tilde{v}_z)_{i,j,k}^{n+1} - m(\tilde{v}_z)_{i,j,k}^n}{\Delta \tau} = \frac{m(\tilde{p})_{i,j,k}^{n+1} - m(\tilde{p})_{i+1,j,k}^{n+1}}{\Delta \tilde{z}} + (DSFZ)_{i,j,k}^n \tag{9}$$

$$\frac{\theta_{i,j,k}^{n+1} - \theta_{i,j,k}^n}{\Delta \tau} = (DSEN)_{i,j,k}^n \tag{10}$$

Here n is the time step and m is the iteration index. $DSFX$, $DSFY$, $DSFZ$ and $DSEN$ stand for the convection and viscous terms. The grid nodes have the indices (i, j, k) in X , Y and Z directions, respectively.

The mass balance (1) provides an equation for pressure. Introducing the discrete derivative

$$D_{i,j,k}^{n+1} = \frac{(\tilde{v}_x)_{i,j,k}^{n+1} - (\tilde{v}_x)_{i-1,j,k}^{n+1}}{\Delta\tilde{x}} + \frac{(\tilde{v}_y)_{i,j,k}^{n+1} - (\tilde{v}_y)_{i,j-1,k}^{n+1}}{\Delta\tilde{y}} + \frac{(\tilde{v}_z)_{i,j,k}^{n+1} - (\tilde{v}_z)_{i,j,k-1}^{n+1}}{\Delta\tilde{z}} \quad (11)$$

The grid pressure $\tilde{P}_{i,j,k}$ may be calculated by Newton method

$${}^{m+1}(\tilde{p})_{i,j,k}^{n+1} = {}^m(\tilde{p})_{i,j,k}^{n+1} - {}^m D_{i,j,k}^{n+1} \left[\frac{\partial D_{i,j,k}^{n+1}}{\partial \tilde{p}_{i,j,k}} \right]^{-1} = {}^m(\tilde{p})_{i,j,k}^{n+1} + \delta(\tilde{p})_{i,j,k}^{n+1} \quad (12)$$

The velocity is given by

$${}^{m+1}\tilde{v}_{x(i,j,k)}^{n+1} = {}^m\tilde{v}_{x(i,j,k)}^{n+1} + \left(\frac{\partial \tilde{v}_{x(i,j,k)}}{\partial \tilde{p}_{(i,j,k)}} \right)^{n+1} \delta \tilde{p}_{x(i,j,k)}^{n+1} \quad (13)$$

$${}^{m+1}\tilde{v}_{y(i,j,k)}^{n+1} = {}^m\tilde{v}_{y(i,j,k)}^{n+1} + \left(\frac{\partial \tilde{v}_{y(i,j,k)}}{\partial \tilde{p}_{(i,j,k)}} \right)^{n+1} \delta \tilde{p}_{y(i,j,k)}^{n+1} \quad (14)$$

$${}^{m+1}\tilde{v}_{z(i,j,k)}^{n+1} = {}^m\tilde{v}_{z(i,j,k)}^{n+1} + \left(\frac{\partial \tilde{v}_{z(i,j,k)}}{\partial \tilde{p}_{(i,j,k)}} \right)^{n+1} \delta \tilde{p}_{z(i,j,k)}^{n+1} \quad (15)$$

The calculation procedure is then:

1. Use eqs. (7), (8),(9) to compute the velocities $\{ {}^{m+1}(\tilde{v}_x)_{i,j,k}^{n+1}, {}^{m+1}(\tilde{v}_y)_{i,j,k}^{n+1}, {}^{m+1}(\tilde{v}_z)_{i,j,k}^{n+1} \}$ for ${}^{m+1}\tilde{p}^{n+1} = {}^m\tilde{p}^n$.
2. Repeat the calculation until ${}^{m+1}D^{n+1} \leq \varepsilon$ is satisfied, eq. (10)-(15) [in this study $\varepsilon = 10^{-3}$]; report $(\tilde{v}_x)^{n+1}, (\tilde{v}_y)^{n+1}, (\tilde{v}_z)^{n+1}, \tilde{p}^{n+1}$.
3. Calculate θ^{n+1} using eq. (10).
4. Repeat the cycle 1-3, until the final time.

The third order upwind scheme (Utopia scheme) for the inertial terms of Eqs. (2)-(4) was applied to the calculation. The local Nu number on the hot wall was calculated from a Taylor series for the temperature field and the average Nu number was computed by integration over the hot wall. The time step width $\Delta\tau$ was 1×10^{-6} .

2.4. Computational meshes

Figure 4 indicates computational domain ($Z=1.0, 1.5, 2.0$). The computational meshes used the uniform grid, and the finite difference grid points in the X-, Y- and Z-directions were $80 \times 100 \times 80$, $80 \times 100 \times 120$, $80 \times 100 \times 160$.

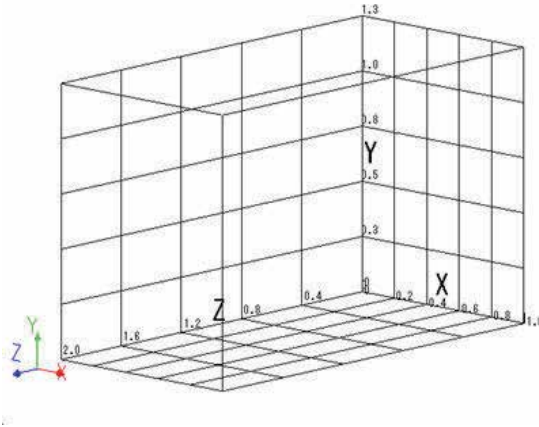


Figure 4. Computational domain

3. Result and discussion

3.1. Overall system behaviour

Figure 5 shows change over time to flow distribution, temperature distribution, and concentration distribution for an X–Y plane at system depth coordinates $Z=0.5$. As density is stratified linearly under initial concentration conditions in these calculations, density strata interface behavior shows major changes over a short time when compared to standard density stratification. At $\tau=0.002$ (Fig. 5 (a)), immediately after calculation starts, currents appear in the previously-still solution, and a large-scale vortex rotating in a counter-clockwise direction is present near the center. Accompanying this, vortices form at opposed upper and lower corners of the system. As heating and cooling is conducted from left and right wall surfaces, influence on temperature distribution gradually becomes apparent in the solution. The initial linear state of concentration distribution strata can be confirmed as decaying from the system's central region. At $\tau=0.005$ (Fig. 5 (b)), the vortex near the center decays, and an inclined interface appears in contrast near the center. This formation is shaped largely in parallel to concentration and flow distributions, and heating and cooling areas from wall areas spread toward the center. Concentration distribution changes in a form similar to temperature distribution, and a concentration plume forms near the interface. Each condition becomes pronounced at $\tau=0.008$ (Fig. 5 (c)). Of the multiple plumes formed along concentration distribution lines in Fig. 3

(b), one plume is present in both the upper and lower high- and low-concentration sides. At $\tau=0.015$ (Fig. 5 (d)), currents have become extremely complex and 3-dimensional. In terms of temperature distribution, a higher temperature stratum is present at the top, and a low temperature stratum is present at the bottom. Furthermore, the inclined interface becomes vertical in terms of concentration distribution, disorder is present near the interface, and an unstable state can be seen.

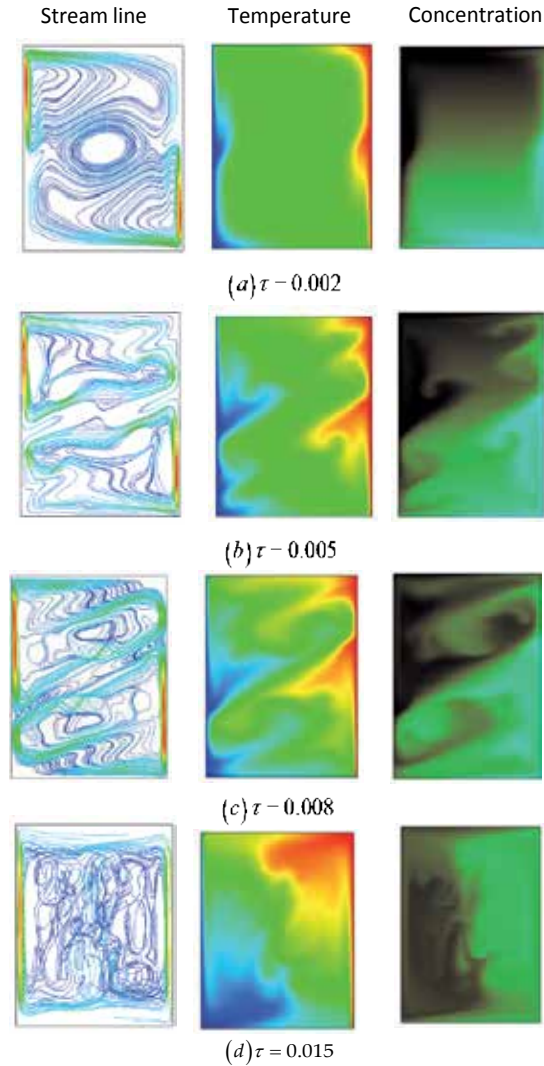


Figure 5. Velocity vector, concentration and temperature distribution for $Z=2.0$ in depth length at $Z=0.5$.

3.2. Heat transfer characteristics

Figure 6 shows the variation of the average Nu number in the heated wall. Furthermore, during the figure show $Z=1.0, 1.5,$ and 2.0 results. Overall changes in the Nu number are different with

pure convection as shown in Figure 6, uneven distribution. Minimum Nu number (position 1) to transition from thermal to thermal convection is less than pure convection. It is in due to the vertical density stratification. Then the Nu number increased with time and repeat the development layer, Nu number refers to the maximum value (position 2). However, for changing vertical from horizontal surface as shown in Fig. 5 (d), from heated wall heat transfer of cooling wall will be suppressed. As a result the Nu number is reduced again. Since then each layer blends Nu number increases again. And completely mixed, Nu number indicating steady-state value.

Note changes in the depth direction Z : increases the value of Z , and minimum value of the Nu number is even smaller. Also the Nu Max value has not been observed difference. The Nu number becomes a steady state value of time becomes shorter with increasing Z .

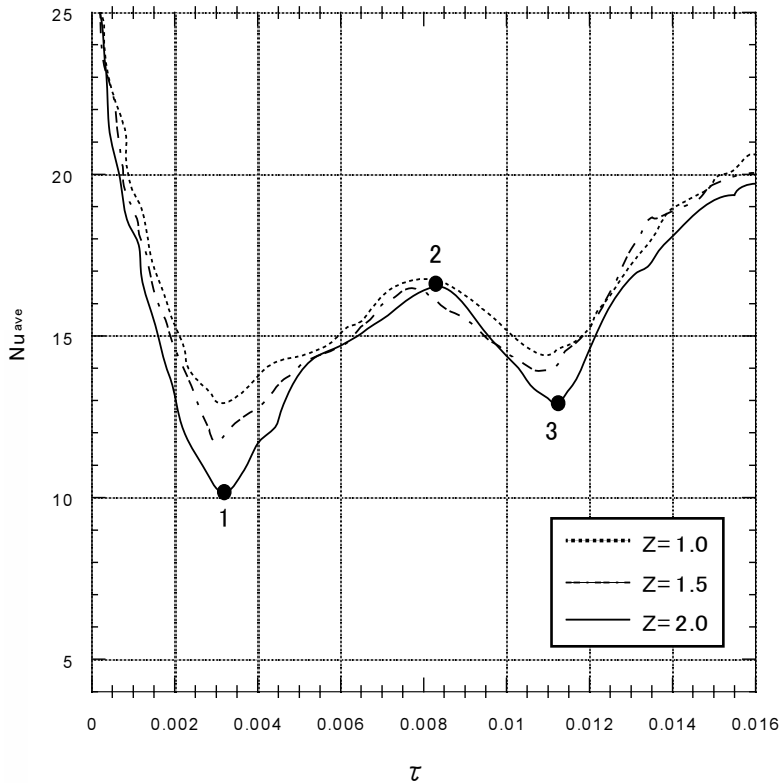


Figure 6. Average Nu number on the hot wall with time for $Z=1.0, 1.5$ and 2.0 in depth length

3.3. Influence of computational domain (depth length: Z)

Figure 7 shows $\tau=0.01$ at depths of $Z=1.0, 1.5,$ and 2.0 for X - Y plane ($Z=0.5$) and Y - Z plane ($X=0.5$) and a 3-dimensional contour diagram of concentration. Overall concentration structure

near the interface can be confirmed as symmetrical along vertical and horizontal axes. For X–Y plane concentration distribution of $1.0 \times 1.25 \times 1.0$ (Fig. 7 (a)), the interface is inclined and interface between high and low concentrations is extended near the center. When Z is increased, it is clear that high and low concentration interface extension increases further near the center as shown in Fig. 7 (b) and (c). On the Y–Z plane, the same patterns form horizontally and vertically at the center as Z rises. In the 3-dimensional contour diagram, at $1.0 \times 1.25 \times 1.0$ (Fig. 7 (a)), a concentration distribution with significant curvature appears near the center of the interface. Additionally, concentration distribution is unstable vertically along the Y axis. When Z is increased even further, the curved interface near the center disappears, and the center changes to an extremely smooth interface as shown in Fig. 7 (b) and (c). Disorder near the center decreases in Y axis vertical concentrations as Z increases.

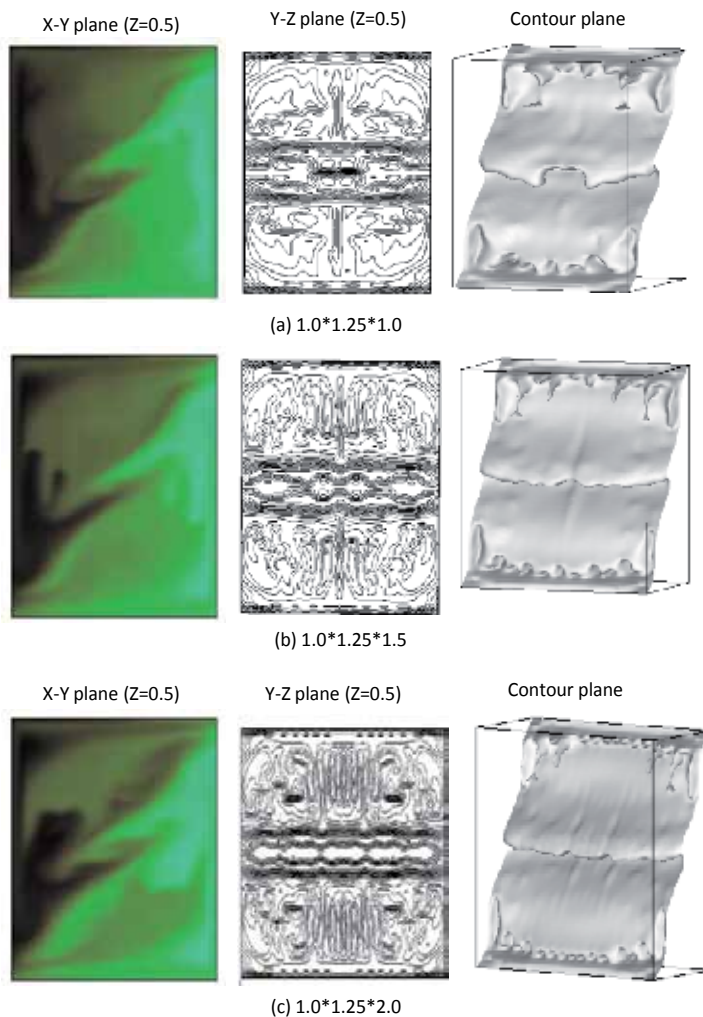


Figure 7. Concentration profile at $\tau = 0.01$

Similarly, Figure 8 shows the result of the concentration distribution in the $\tau=0.015$. Overall concentration distribution, as can be seen in the interface of the X-Y plane than in Figure 5, has the left and right opposite slope. In addition, the interface near it changes to a very complex structure. Further, when Z is large, as can be seen in the contour diagram, toward the center of the interface ($Z=0.5$) from the wall direction ($X=0, 1.0$) unevenness appeared on the structure of the interface, resulting in three-dimensional structure.

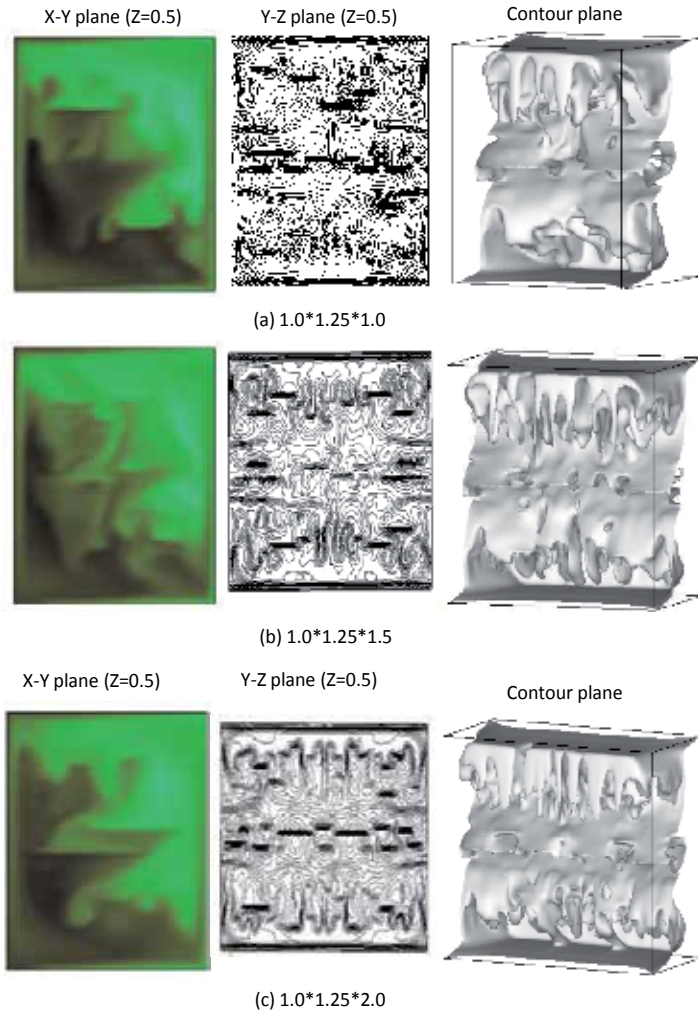


Figure 8. Concentration profile at $\tau=0.015$

4. Conclusions

We studied three-dimensional numerical calculations of double-diffusive convection in a rectangular parallelepiped enclosure filled with salt-stratified fluid under a horizontal

temperature difference for realistic values of parameters ($A=1.25$, $Ra=2.7 \times 10^7$, $N=0.882$, $Pr=7.15$ for an NaCl-H₂O system). The initial salt concentration linear profile was examined.

Three-dimensional numerical result with a high spatial resolution can capture the fine structures such as salt fingers and traveling plumes. In the linear profile, near the interface, vertical motion is dominant due to salt fingers in each layer. In addition, when the computational domain changes, it has a big influence on the behaviour of plume that appears on the diffusive interface. As a result, the mixing state of the entire fraction is greatly different.

Nomenclature

A	aspect ratio $=h/b$
b	width of the system m
B	dimensionless width of the system
C	dimensionless concentration $= (c - c_{\min}) / (c_{\max} - c_{\min})$
c	concentration kgm^{-3}
c_{\max}	initial maximum concentration (initial concentration in a linear profile) kgm^{-3}
c_{\min}	initial minimum concentration (initial concentration in a linear profile) kgm^{-3}
D	diffusion coefficient m^2s^{-1}
g	acceleration due to gravity ms^{-2}
h	height of the system m
H	dimensionless height of the system
Le	Lewis number $= \kappa/D$
N	buoyancy ratio $= \beta(c_{\max} - c_{\min}) / \{\alpha(T_{\text{hot}} - T_{\text{cold}})\}$
Nu_{ave}	average Nusselt number
p	pressure Pa
P	dimensionless pressure
Pr	Prandtl number $= \nu/k$
Ra	Rayleigh number $= g \cdot \alpha(T_{\text{hot}} - T_{\text{cold}}) \cdot b^3 / (\kappa \cdot \nu)$
T	temperature K
T_{cold}	temperature on the cold wall K
T_{hot}	temperature on the hot wall K
t	time s
U, V, W	dimensionless velocity

X, Y, W	dimensionless coordinate
<i>Greek symbols</i>	
α	volumetric coefficient of thermal expansion K^{-1}
β	volumetric coefficient of expansion with concentration m^3kg^{-1}
$\Delta\tau$	dimensionless time step
θ	dimensionless temperature $= (T - T_{cold}) / (T_{hot} - T_{cold})$
κ	Thermal diffusivity m^2s^{-1}
ν	Kinematic viscosity m^2s^{-1}
ρ	Density kgm^{-3}
τ	dimensionless time

Author details

Hideo Kawahara

Address all correspondence to: kawahara@s.oshima-k.ac.jp

National Institute of technology, Oshima College, Japan

References

- [1] Huppert, H.E., "The fluid mechanics of solidification", J. Fluid Mech., Vol.212 p. 209-240
- [2] Nishimura, T., "Double diffusive convection in solidification process", Kagaku-kougaku, Vol.61, p.924-927
- [3] Beckermann, C., Viskanta, R., "An experimental study of solidification of binary mixtures with double-diffusive convection in the liquid, Chem. Eng. Comm., Vol.85, p. 135-156
- [4] Nishimura, T., Imoto, T., Wakamatsu, M., "Layer merging during solidification of supereutectic NH_4Cl-H_2O system, Int. J. Heat Mass Transfer, Vol.41, p.3669-3674
- [5] Bergman T.L., Ungun, A., "A note on lateral heating in a double-diffusive system, J. Fluid Mech., Vol. 194, p.175-186
- [6] Paul, H., Bergman, T.L., "Polari graphic measurement of liquid-phase species distributions, Exp. Thermal and Fluid Sci., Vol. 10, p.519-524

- [7] Nishimura, T., Ogata, Y., Sakura, S., Morega, Al.M, "Interfacial breakdown of double-diffusive convective layers by a horizontal temperature gradient, *Int. J. Heat Mass Transfer*, Vol.42, p.1479-1489
- [8] Nishimura, T., Sakura, S., Ogata, Y, "Mass transfer through the diffusive interface in a two-layer salt-stratified system under a horizontal temperature gradient," *Chem. Eng. Sci.*, Vol.55, p.5301-5309
- [9] Tanny, J., Yakubov, B., "Experimental study of a double-diffusive two-layer system in a laterally heated enclosure", *Int. J. Heat Mass Transfer*, Vol.42, p.3619-3629
- [10] Hyun, M.T., Bergman, T.L., "Direct simulation of double-diffusive layered convection", *ASME J. Heat Transfer*, Vol.117, p.334-339
- [11] Chen, C.F. and Chen, F., "Salt-finger convection generated by lateral heating of a solute gradient", *J.Fluid Mech.*, Vol.352, p.161-176
- [12] R. Peyret, T.D. Taylor, *Computational methods for fluid flow*, *Springer Series in Computational Physics*, Springer Verlag, NY (1990).
- [13] H. Kawahara, Al.M. Morega and M.Morega, "A highly simplified mark and cell (HSMAC) scheme for the study of convection heat transfer in electroconductive fluids", *Rev. Roum. Sci. Techn.-Electrotechn. Et Energ.*, 54, 1, p.67-76, 2009
- [14] T. Tagawa, H. Ozoe, "Enhancement of heat transfer rate by application of a static magnetic field during natural convection of liquid metal in a cube," *J. Heat Transfer*, 119, 265-271, 1997.

Heat Transfer and Entropy

Heinz Herwig and Christoph Redecker

Additional information is available at the end of the chapter

<http://dx.doi.org/10.5772/60610>

1. Introduction

When you read a standard textbook on thermodynamics (like [1-3]) as one of the most fundamental formulae you will find

$$\delta Q = T dS \quad (1)$$

indicating that the (process) quantity heat (δQ) is obviously closely linked to the (state) quantity entropy (dS), here both written as infinitesimal quantities.

If, however, you do the same with a standard textbook on heat transfer (like [4] with 1024 pages or [5] with 1107 pages), you will find entropy neither in the index of these books, nor in the text.

There may be two reasons for that: Either entropy has turned out to be irrelevant for a heat transfer analysis or entropy is ignored deliberately in the heat transfer community in spite of its relevance. What is true is a yet open question and can only be answered when thermodynamic considerations are taken into account.

In thermodynamics the relevance of entropy with respect to heat transfer is beyond any controversy, it is the heat transfer community that has to be persuaded of its relevance. This can best be done by showing the advantages of including entropy in a heat transfer analysis as well as showing the disadvantages one has to face when entropy is ignored.

2. A thermodynamic view on heat transfer

2.1. General considerations

Engineers, using the phrase “heat transfer”, would not be bothered by the view that heat is moved across the boundary of a system and then stored in it, increasing its heat content.

This line of argument, however, violates at least two principles of thermodynamics and misses the crucial point. From a thermodynamics point of view heat is a process quantity that describes a certain way by which energy can be transferred across the boundary of a system. And of course this quantity cannot be stored, only the energy moved by it can be stored.

And the crucial point is: Transferring energy as heat into a system is fundamentally different from doing the same by work. The energy transferred in form of heat and work, though it may be the same amount, has a very different quality once it is part of the energy of the system. To put it in a simple and not yet precise form for the moment: It is not only the amount of energy that counts in energy transfer processes (like heat transfer) but also the quality of the energy and the change in quality during the transfer process. If that is true, there must be a measure for the quality and its potential degradation in energy transfer processes. This is where entropy comes in and plays a crucial role – even and also in heat transfer considerations.

From the very clear principle of energy conservation (thermodynamically formulated as the first law of thermodynamics) we know that energy given as primary energy never gets lost when used in technical devices but finally ends up as part of the internal energy of the ambient. Then, however, it is of no use anymore. Obviously energy has a certain potential that can get lost on the way from being primary energy to being part of the internal energy of the ambient.

In thermodynamics there is a useful definition by which the quality of an energy can be characterized which was first proposed in [6]. This definition primarily refers to an energy which is subject to transfer processes either by work or by heat. According to this definition energy is composed of two parts, *exergy* and *anergy*. Within this concept exergy is the precious part of the energy. It is that part which can be used by work until it is part of the internal energy of the ambient. Sometimes exergy is also called *available work*. The remaining part of the energy is called anergy. According to the second law of thermodynamics exergy can get lost (can be converted to anergy) in irreversible processes but never can be generated. Any transfer of energy by work or by heat thus can either preserve the exergy part of the energy in a reversible process or reduce it in an irreversible one.

As far as heat transfer is concerned there are two aspects that are important: The first is the amount of energy transferred by heat and the second is the amount of exergy lost in this (heat) transfer process. Ignoring entropy means that only the first aspect can be accounted for. For a complete characterization of a heat transfer process both aspects have to be accounted for, i.e. two physical quantities have to be specified. They can be

- the heat flux $\dot{q} = \delta \dot{Q} / dA$
- a characteristic temperature difference ΔT

In a heat transfer process both quantities are independent of each other because a certain amount of energy (\dot{q}) can be transferred with a different decrease of quality, i.e. with a different degree of irreversibility (ΔT). Here ΔT is an indirect measure of the quality decrease of the energy in the transfer process since $\Delta T = 0$ is the reversible limit of an irreversible process with $\Delta T > 0$. When two independent quantities are required then two nondimensional parameters are needed in the context of describing heat transfer processes nondimensionally. In section 3

it will be discussed what is missing when the Nusselt number Nu alone is used in order to characterize a heat transfer process.

In thermodynamics the two aspects of energy transfer and its devaluation by irreversible processes are quantified by introducing the entropy and its generation in the course of irreversible processes. In this context entropy is a measure of the structure of the system storing the energy under consideration, i.e. energy can be stored in a more or less ordered way. This again can be expressed in terms of exergy versus energy of the energy transferred and stored.

2.2. Change of entropy in energy transfer processes

For most considerations the absolute value of entropy is not of interest but its change during a certain process like a heat transfer process. This change of entropy in a transfer process generally is twofold:

- i. Transfer - change of entropy in a reversible process,
- ii. Generation - change of entropy when the transfer process is not reversible, i.e. irreversible.

In a real (irreversible) process the change of entropy thus always is the sum of both, i.e. (i) + (ii).

For a heat transfer process between two temperature levels T_a and T_b the two parts (i) and (ii) are

$$d_i \dot{S} = \frac{\delta \dot{Q}}{(T_a + T_b)/2} \quad (2)$$

$$d_g \dot{S} = \delta \dot{Q} \left(\frac{1}{T_a} - \frac{1}{T_b} \right) = \delta \dot{Q} \frac{T_a - T_b}{T_a T_b} = \delta \dot{Q} \frac{\Delta T}{T_a T_b} \quad (3)$$

Equation (2) corresponds to eq. (1) in the introduction, now in terms of rates for a continuous process. Equation (3) states that entropy generation leads to an increase of entropy when the energy is transferred from one system (a) with high temperature (i.e. low entropy) to another system (b) with low temperature (i.e. high entropy). Thus the overall change of entropy in such a process is

$$d\dot{S} = d_i \dot{S} + d_g \dot{S} \quad (4)$$

In figure 1 such a process is illustrated for the convective heat transfer from a flow in system (a) with \dot{m}_a to a flow in system (b) with \dot{m}_b . The wall between both flows is diabatic, walls to the ambient are adiabatic.

The generation-change of entropy in eq. (3) strictly speaking is an approximation only. It is based on the assumption that in (a) and in (b) the real temperature distributions can be approximated by their (constant) mean values and that the temperature drop from (a) to (b) completely happens in the wall between both systems, see figure 1 for an illustration of this approximation. In section 4 the real temperature distribution is accounted for in order to determine the generation-change of entropy without approximation.

Though it is not the topic of this chapter it should be mentioned what (i) and (ii) are for an energy transfer by work:

$$d_t \dot{S} = 0 \tag{5}$$

$$d_g \dot{S} = \delta\Phi/T \tag{6}$$

with $\delta\Phi$ as dissipation rate of mechanical energy in the flow field involved in the transfer process. That always $d_t \dot{S} = 0$ holds for a work transfer of energy shows the fundamental difference of the two ways to transfer energy, i.e. by heat or by work, c.f. eq. (2) for the energy transfer by heat.

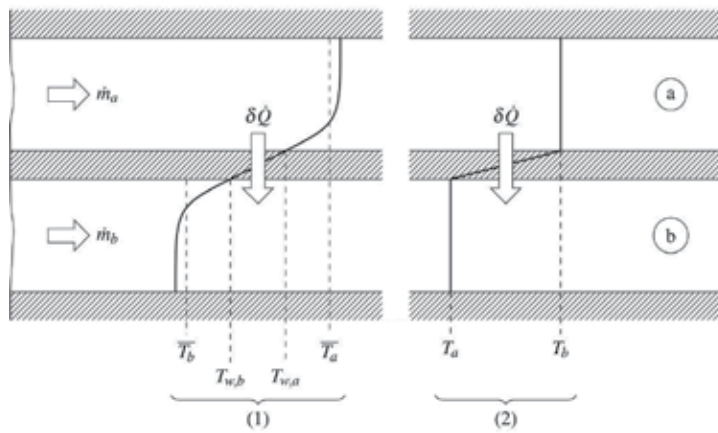


Figure 1. Convective heat transfer from a flow in (a) to a flow in (b) over a surface element dA (1) Real temperature distribution (2) Mean temperature model

2.3. Energy devaluation in a heat transfer process and the entropic potential concept

When in an energy transfer process exergy gets lost the “value” of the energy is reduced, since exergy as the precious part of the energy is reduced. This is called *energy devaluation* during a transfer process and is immediately linked to the generation-change of entropy, c.f. eq. (3).

Exergy lost and entropy generated are interrelated by the so-called Gouy-Stodola theorem, see for example [7]. It reads

$$d\dot{E}_l^e = T_\infty d\dot{S}_g \quad (7)$$

Here T_∞ is the ambient temperature and \dot{E}_l^e is the loss of the exergy rate \dot{E}^e of the energy rate \dot{E} , after subdividing \dot{E} into an exergy and an anergy part, \dot{E}^e and \dot{E}^a , respectively.

For a single transfer operation indicated by i then there is the finite exergy loss

$$\dot{E}_{l,i}^e = T_\infty \dot{S}_{g,i} \quad (8)$$

with $\dot{S}_{g,i}$ as entropy generation in the transfer operation i . This entropy generation can and should be seen in the context of those devaluations of the energy transfer rate \dot{E} that happened prior to the transfer operation i and that will happen afterwards. This idea takes into account that a certain energy (rate) always starts as primary energy being exergy as a whole and finally ends up as part of the internal energy of the ambient, then being anergy as a whole. In [8] this has been described as the “devaluation chain” with respect to the energy transfer rate \dot{E} with the process i being one link of this chain.

For the sum of all single transfer operations that completely devaluates the energy from 100% exergy to 100% anergy then

$$\dot{E}_l^e = \dot{E} = T_\infty \dot{S}_g \quad (9)$$

holds. Here \dot{S}_g is the overall entropy generation (rate), i.e. the entropy increase of the ambient, when \dot{E} becomes part of its internal energy.

In [8] this quantity is called the *entropic potential*:

$$\dot{S}_g = \frac{\dot{E}}{T_\infty} \quad (10)$$

of the energy \dot{E} involved in an energy (here: heat) transfer process. Taking this as a reference quantity the so-called energy devaluation number

$$N_i \equiv \frac{\dot{S}_{g,i}}{\dot{S}_g} = \frac{T_\infty \dot{S}_{g,i}}{\dot{E}} \quad (11)$$

indicates how much of the entropic potential of the energy is used in a certain transfer process i with $N_i=0$ for a reversible process. Examples will be given afterwards.

3. An engineering view on heat transfer

As mentioned before, engineers trained to solve heat transfer problems with books like [4] care little or not at all about entropy. They characterize heat transfer situations by the heat transfer coefficient

$$h = \frac{\dot{q}_w}{\Delta T} \quad (12)$$

or in a more systematic way by the Nusselt number

$$\text{Nu} = \frac{\dot{q}_w L}{k \Delta T} = h \frac{L}{k} \quad (13)$$

In both cases \dot{q}_w and ΔT are combined within one assessment quantity so that the two independent aspects of heat transfer

- the amount, associated with \dot{q}_w and
- the change of quality, associated with ΔT

are not captured separately. A second assessment quantity is required for a comprehensive characterization of a heat transfer situation. This can be the energy devaluation number N_i according to eq. (11).

When N_i accounts for the quality of heat transfer the Nusselt number Nu covers the quantitative aspect in the following sense. Often either ΔT or \dot{q}_w are prescribed as a thermal boundary condition. Then the Nusselt number quantifies the heat transfer by providing the heat flux that occurs or the temperature difference that is required, respectively. Both are quantitative aspects leaving the question about the quality still open. This then is addressed by the energy devaluation number N_i .

Since the Nusselt number Nu is well established in the heat transfer community, but the energy devaluation number N_i is not, N_i will be further explained with respect to its physical background in the following section.

4. The physics behind the energy devaluation number

According to Fourier's law of heat conduction, see for example [4] or [9],

$$\delta \vec{Q} = -k(\text{grad } T) \, dA \quad (14)$$

i.e. a heat flux occurs along the (negative) gradient of temperature. The energy transferred in this way reduces its exergy part because this exergy part is

$$\dot{Q}^e = \eta_c \dot{Q} \tag{15}$$

with the Carnot factor

$$\eta_c = 1 - \frac{T_\infty}{T} \tag{16}$$

Here again T_∞ is the ambient temperature, so that the exergy part of \dot{Q} once its temperature level T has reached the ambient temperature, is zero.

This permanent exergy loss when heat transfer occurs with $\text{grad}T > 0$ (irreversible heat transfer) according to the Gouy-Stodola theorem (7) is accompanied by entropy generation which here can be written as

$$\dot{S}_g^m = \frac{k}{T^2} (\text{grad } T)^2 \tag{17}$$

or after integrating the local entropy generation rate \dot{S}_g^m as

$$d_g \dot{S} = \frac{k}{T^2} (\text{grad } T)^2 dV \tag{18}$$

which in Cartesian coordinates reads

$$d_g \dot{S} = \frac{k}{T^2} \left[\left(\frac{\partial T}{\partial x} \right)^2 + \left(\frac{\partial T}{\partial y} \right)^2 + \left(\frac{\partial T}{\partial z} \right)^2 \right] dV \tag{19}$$

Note that this eq. (19) reduces to eq. (3) when there is a linear temperature distribution in x - direction only so that $\partial T / \partial x = \Delta T / \Delta x$, $dV = dA \Delta x$ and $\partial \dot{Q} = -k(\Delta T / \Delta x) dA$.

Comparing eqs. (3) and (19) shows that

$$\dot{S}_g = \int d_g \dot{S} \tag{20}$$

in the mean temperature model according to eq. (3) and figure 1(2) is an integration with respect to $\delta \dot{Q}$ while with the real temperature distribution according to eq. (19) and figure 1 (1) it is an integration with respect to the volume accounting for the local entropy generation rate.

In both cases $\dot{S}_{g,i}$ is determined which is the overall entropy generation due to heat conduction in a transfer process i . The energy devaluation number refers this to the entropic potential of \dot{Q} , i.e. to \dot{Q}/T_{∞} , so that

$$N_i = \frac{k T_{\infty}}{\dot{Q}} \int_V \frac{1}{T^2} \left[\left(\frac{\partial T}{\partial x} \right)^2 + \left(\frac{\partial T}{\partial y} \right)^2 + \left(\frac{\partial T}{\partial z} \right)^2 \right] dV \quad (21)$$

is that percentage used of the entropic potential of the energy \dot{E} which in a process i is transferred as heat \dot{Q} . Note that part of the entropic potential has been used already on the way of \dot{E} starting as primary energy to the situation in which it is transferred as heat and that the remaining part of the entropic potential after the heat transfer process i can be used in subsequent energy transfer processes. This may illustrate why it is important to see a certain transfer process i in the context of the overall devaluation chain of an energy starting as primary energy and ending as part of the internal energy of the ambient, for more details of this concept see [8].

5. Convective heat transfer

Often convective heat transfer occurs in technical applications like power plants and heating or cooling systems. Then a second energy flux is involved which is the flow work rate that is needed to maintain the flow into which or out of which the heat transfer occurs. This energy flux applied as work is pure exergy which gets lost in the dissipation process during the convective heat transfer.

5.1. Losses due to dissipation of mechanical energy

In fluid mechanics losses in a flow field usually are characterized by a drag coefficient c_D for external flows and a head loss coefficient K for internal flows, which are a nondimensional drag force F_D and a nondimensional pressure loss Δp , respectively. In table 1 both definitions are shown together with an alternative approach based on the entropy generation rate $\dot{S}_{g,D}$ due to the dissipation of mechanical energy (index: D). For details of this alternative approach see [10]. Since both coefficients, c_D and K , account for the dissipation rate in the flow field and according to eq. (6) $\delta\dot{\Phi} = T d_g \dot{S}$ the dissipation of mechanical energy corresponds to the loss of exergy only when $T = T_{\infty}$, c.f. eq. (7). Whenever the flow occurs on a temperature level which is not that of the ambient temperature T_{∞} , c_D and K account for the dissipation but not for the lost exergy in the flow.

Then a second coefficient is needed which best is defined as an *exergy destruction number* N^E analogous to the energy devaluation number, eq. (11), i.e.

$$N^E = \frac{T_\infty \dot{S}_{g,D}}{\dot{E}} \quad (22)$$

	conventional approach	alternative approach
external flow	$c_D = \frac{F_D}{\frac{\rho}{2} u_\infty^2 A}$	$c_D = \frac{T}{\frac{\rho}{2} u_\infty^3 A} \dot{S}_{g,D}$
internal flow	$K = \frac{\Delta p}{\frac{\rho}{2} u_m^2}$	$K = \frac{T}{\frac{\rho}{2} u_m^3 A} \dot{S}_{g,D}$

Table 1. Drag and head loss coefficients; conventional and alternative definitions, from [10]. u_∞ : free-stream velocity, u_m : cross-section averaged velocity

which for an external flow with $\dot{E} = \frac{u_\infty^2}{2} \dot{m} = \frac{\rho}{2} u_\infty^3 A$ is (c.f. table 1):

$$N^E = \frac{T_\infty}{T} c_D \text{ (exergy destruction number)} \quad (23)$$

and for an internal flow with $\dot{E} = \frac{u_m^2}{2} \dot{m} = \frac{\rho}{2} u_m^3 A$ is (c.f. table 1):

$$N^E = \frac{T_\infty}{T} K \text{ (exergy destruction number)} \quad (24)$$

Note that N^E is not an energy devaluation number in the sense of its definition in eq. (11) because the reference quantity \dot{E} in eq. (22) is not an energy transfer rate (that might be devaluated during the transfer process). Instead it is the kinetic energy involved in the convective process. It serves as a reference quantity for the flow work required to maintain the flow.

Different from N_i according to eq. (11), for which by definition always $0 \leq N_i \leq 1$ holds, N^E is not restricted to this range. For example $N^E = 3$ for an internal flow means that the exergy loss (exergy destructed) during this process is three times higher than the kinetic energy involved in the convective process. Note that it is not the kinetic energy that is devaluated but the energy that enters the system as flow work, being pure exergy at the beginning and partly or totally converted to energy by the dissipation process.

5.2. Assessing convective heat transfer

Since both energies in a convective heat transfer process (flow work needed and thermal energy transferred) are subjected to devaluation they should both be accounted for when a convective heat transfer process is assessed, for example for the purpose of its optimization.

In terms of losses what counts is the lost exergy in both energies that are involved in the convective heat transfer process. These exergy losses are characterized by the corresponding entropy generation rates $\dot{S}_{g,i}$ in eq. (11) and $\dot{S}_{g,D}$ in eq. (22). They can be added to provide the overall entropy generation rate in a convective heat transfer process and serve as a target quantity in an optimization procedure. This is a reasonable criterion for all those cases in which the exergy part of energy transfer process counts like for a power cycle. In such a process exergy lost ahead of the turbine cannot be converted to mechanical energy in the turbine and thus reduces the efficiency of the power cycle.

When the entropy generation rates should be determined from detailed numerical solutions of a convective heat transfer process, $\dot{S}_{g,i}$ follows from eqs. (19), (20) while \dot{S}_g due to dissipation is determined by

$$\dot{S}_g = \int d_g \dot{S} \quad (\text{exergy destruction number}) \quad (25)$$

with

$$d_g \dot{S} = \frac{\mu}{T} \left(2 \left[\left(\frac{\partial u}{\partial x} \right)^2 + \left(\frac{\partial u}{\partial y} \right)^2 + \left(\frac{\partial u}{\partial z} \right)^2 \right] + \left(\frac{\partial u}{\partial y} + \frac{\partial v}{\partial x} \right)^2 + \left(\frac{\partial u}{\partial z} + \frac{\partial w}{\partial x} \right)^2 + \left(\frac{\partial v}{\partial z} + \frac{\partial w}{\partial y} \right)^2 \right) dV \quad (26)$$

When the flow is turbulent, $d_g \dot{S}$ according to eqs. (19) and (26) are adequate only for a direct numerical simulation (DNS) approach with respect to the turbulence, as for the example shown in [11]. Since DNS solutions with their extraordinary computational demand cannot be used for solving technical problems, the time-averaged equations (Reynolds-averaged Navier-Stokes: RANS) are solved instead. Then, also $d_g \dot{S}$ has to be time averaged, leading to:

$$d_g \dot{S}_C = d_g \dot{S}_{\bar{C}} + d_g \dot{S}'_C \quad (27)$$

and

$$d_g \dot{S}_D = d_g \dot{S}_{\bar{D}} + d_g \dot{S}'_D \quad (28)$$

with $d_g \dot{S}_{\bar{C}}$ and $d_g \dot{S}_{\bar{D}}$ for the entropy generation in the time-averaged temperature and velocity field as well as $d_g \dot{S}'_C$ and $d_g \dot{S}'_D$ for the time averaged contributions of the corresponding fluctuating parts.

All four parts are

$$d_g \dot{S}_{\bar{c}} = \frac{k}{T^2} \left[\left(\frac{\partial \bar{T}}{\partial x} \right)^2 + \left(\frac{\partial \bar{T}}{\partial y} \right)^2 + \left(\frac{\partial \bar{T}}{\partial z} \right)^2 \right] dV \quad (29)$$

$$d_g \dot{S}_{c'} = \frac{k}{T^2} \left[\overline{\left(\frac{\partial T'}{\partial x} \right)^2} + \overline{\left(\frac{\partial T'}{\partial y} \right)^2} + \overline{\left(\frac{\partial T'}{\partial z} \right)^2} \right] dV \quad (30)$$

$$d_g \dot{S}_{\bar{D}} = \frac{\mu}{T} \left[2 \left[\overline{\left(\frac{\partial \bar{u}}{\partial x} \right)^2} + \overline{\left(\frac{\partial \bar{u}}{\partial y} \right)^2} + \overline{\left(\frac{\partial \bar{u}}{\partial z} \right)^2} \right] + \overline{\left(\frac{\partial \bar{u}}{\partial y} + \frac{\partial \bar{v}}{\partial x} \right)^2} + \overline{\left(\frac{\partial \bar{u}}{\partial z} + \frac{\partial \bar{w}}{\partial x} \right)^2} + \overline{\left(\frac{\partial \bar{v}}{\partial z} + \frac{\partial \bar{w}}{\partial y} \right)^2} \right] dV \quad (31)$$

$$d_g \dot{S}_{D'} = \frac{\mu}{T} \left[2 \left[\overline{\left(\frac{\partial u'}{\partial x} \right)^2} + \overline{\left(\frac{\partial u'}{\partial y} \right)^2} + \overline{\left(\frac{\partial u'}{\partial z} \right)^2} \right] + \overline{\left(\frac{\partial u'}{\partial y} + \frac{\partial v'}{\partial x} \right)^2} + \overline{\left(\frac{\partial u'}{\partial z} + \frac{\partial w'}{\partial x} \right)^2} + \overline{\left(\frac{\partial v'}{\partial z} + \frac{\partial w'}{\partial y} \right)^2} \right] dV \quad (32)$$

with the results for a turbulent flow field from RANS equations, $d_g \dot{S}_{\bar{c}}$ and $d_g \dot{S}_{\bar{D}}$ can be determined, but not $d_g \dot{S}_{c'}$ and $d_g \dot{S}_{D'}$. For these terms turbulence models are needed, as for examples discussed in [12].

5.3. Nondimensional parameters

When the whole process of a convective heat transfer should be assessed (comprising the exergy loss in the temperature and in the flow field) that again should be done by means of nondimensional parameters. The nondimensional parameters introduced so far are:

- *Nusselt number* Nu / eq. (13), indicating the strength of heat transfer versus its irreversibility;
- *Energy devaluation number* N_i / eq. (11), indicating the loss of entropic potential of the transferred energy;
- *Head loss coefficient* K / table 1, indicating the dissipation rate in the flow field;
- *Exergy destruction number* N^E / eq. (24), indicating the loss of exergy in the flow field.

If now the overall exergy loss for a convective heat transfer process is of interest this basically is the sum of the effects covered by N_i and N^E . Since both parameters are not nondimensionalized in the same way, however, they cannot simply be added. Note that N_i refers to the transferred energy which for the convective heat transfer is \dot{Q} , whereas in N^E the kinetic energy of the fluid flow is used as a reference quantity.

For an overall assessment of a convective heat transfer process we now refer the sum of the exergy losses (in the temperature and in the flow field) to the exergy transferred in the process, which is $\eta_c \dot{Q}$, c.f. eq. (15), and thus introduce the

$$\text{overall exergy loss number : } \hat{N}^E = \frac{T_\infty (\dot{S}_{g,C} + \dot{S}_{g,D})}{\eta_c \dot{Q}} \quad (33)$$

With the help of eq. (33) it can be decided whether the increase of the Nusselt number by a certain technique to improve the heat transfer, like adding turbulence promoters, roughening of the wall or simply increasing the flow rate, is beneficial from the perspective of exergy conservation. When \hat{N}^E is decreased, more available work is left and the increase of Nu is beneficial.

Since a device with a small \hat{N}^E obviously is more efficient than one with a larger \hat{N}^E , an

$$\text{overall efficiency factor : } \hat{N}_E = 1 - \hat{N}^E \quad (34)$$

was introduced in [13] which is $\hat{\eta}_E = 1$ for a perfect (thermodynamically reversible) process without any exergy loss and $\hat{\eta}_E = 0$ for a process in which all exergy gets lost because it is converted to energy.

6. Examples

Two examples will be given in which the parameters that were introduced above will be used in order to characterize the heat transfer situation. With these examples it should become obvious that entropy and/or its generation should not be ignored when heat transfer processes are considered in practical industrial applications.

6.1. Fully developed pipe flow with heat transfer

This simple example may illustrate how important it is to account for entropy generation which is the crucial aspect in the *energy devaluation number* N_i according to its definition (11).

What usually can be found as the characterization of the heat transfer performance of a fully developed pipe flow is the Nusselt number Nu. Let's assume it is $Nu = 100$ and it occurs on the

upper temperature level of a power cycle, i.e. ahead of the turbine of this energy conversion device. Let's also assume that this heat transfer situation with $Nu = 100$ and a heat flux $\dot{q}_w = 10^3 \text{ W/m}^2$ on a length $L = 0,1 \text{ m}$ occurs in two different power cycles:

- A steam power cycle (SPC) with water as the working fluid and an upper temperature level $T_{m,u} = 900 \text{ K}$.
- An organic Rankine cycle (ORC) with ammonia NH_3 as working fluid and an upper temperature level $T_{m,u} = 400 \text{ K}$.

When in both cycles Nu , \dot{q}_w and L are the same, the temperature difference ΔT in Nu according to eq. (13) is larger by a factor 2.6 for ammonia compared to water. This is due to the different values of the thermal conductivity k of water (at $T_{m,u} = 900 \text{ K}$ and $p = 250 \text{ bar}$) and ammonia (at $T_{m,u} = 400 \text{ K}$ and $p = 25 \text{ bar}$), assuming typical values for the temperature and pressure levels in both cycles.

For a further comparison note that the energy devaluation number according to eq. (11) in this case with $d_g \dot{S}_i$ according to eq. (3) and integrated to obtain

$$\dot{S}_{g,i} = \dot{Q}_{w,i} \left(\frac{1}{T_w} - \frac{1}{T_{m,u}} \right) \approx \dot{Q}_{w,i} \frac{\Delta T}{T_{m,u}^2} \quad (35)$$

with $\dot{E} = \dot{Q}_w$ is

$$N_i = \frac{T_\infty \Delta T}{T_{m,u}^2} \quad (36)$$

Table 2 shows the *energy devaluation number* N_i for both cases according to this approximation. It shows that only 0.37 % of the entropic potential is used for the heat transfer in the SPC-case, but almost 5% in the ORC-case "though" both heat transfer situations have the same Nusselt number $Nu = 100$ and the same amount of energy is transferred. Note that only that part of the entropic potential that is not yet used is available for further use after the process under consideration.

Cycle/fluid	$\frac{k}{\text{W/mK}}$	$\frac{T_\infty}{\text{K}}$	$\frac{T_{m,u}}{\text{K}}$	$\frac{\Delta T}{\text{K}}$	N_i
SPC/water	0.1	300	900	10	0.0037
ORC/ammonia	0.038	300	400	26	0.049

Table 2. Heat transfer with $Nu = 100$, $\dot{q}_w = 10^3 \frac{\text{W}}{\text{m}^2}$, $L = 0.1 \text{ m}$ in two different power cycles

6.2. Using CFD to assess a heat exchanger

In the previous example, two similar processes at two different temperature levels were considered. Such a pipe flow with heat transfer is part of the heat transfer situation illustrated in figure 1: the cold side (b) is heated.

In the second example computational fluid dynamics (CFD) is used to assess the heating of a fluid in a passage within a plate heat exchanger, trying to find the best point of operation for the device. We will first describe the device and how it is modeled, and then discuss the results and how to use them. Further details can be found in [14].

6.2.1. Geometry of the device

Plate heat exchangers are made of corrugated plates which are arranged in a plate stack, forming channels between the plates. The plates are designed in such a way that two fluids are separated from each other on their way through adjacent channels.

Depending on the plate corrugation the channels have constantly changing cross sections, but there is a repeating geometric pattern. Figure 2 (left) shows part of a plate with such a pattern; in this case it is a symmetric fish-bone pattern with a sinusoidal corrugation (see figure 2, right).

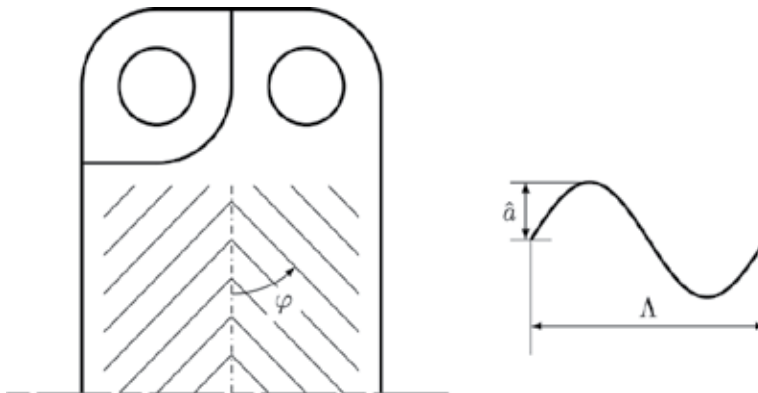


Figure 2. Heat exchanger plate geometry: the plate has a symmetric fishbone pattern with the corrugation angle φ , amplitude \hat{a} and period Λ ; c.f. [15]

6.2.2. Modeling of the device

The first simplification made in order to facilitate the simulations is that the plate (and therefore the heat exchanger) is assumed to have an infinite length. Thus effects on the flow caused by the inlet or outlet areas can be neglected: the flow is hydraulically developed. This has two consequences:

- the channel can be modeled as an endlessly repeating stripe of finite length, see figure 3 (a),
- only half of the channel must be simulated, see figure 3 (b).

The resulting domain geometry is shown in figure 4.

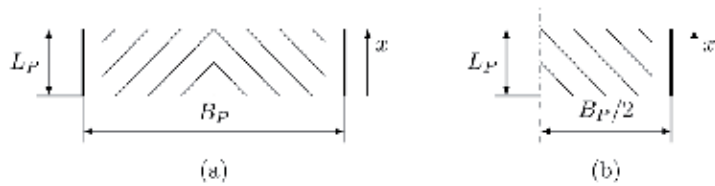


Figure 3. Simplified geometry of the heat exchanger: (a) symmetric stripe; (b) solution domain due to the symmetry assumption.



Figure 4. view of the simulated plate heat exchanger stripe.

The second simplification made here is that the heat exchanger is operated with a balanced counter-flow: The capacity flow rate $\dot{m}c_p$ is the same on the hot and the cold side, so that the temperature difference between them as well as the heat flux \dot{q}_w are the same at every point between the inlet and the outlet.

6.2.3. Boundary conditions

Based on the assumptions made above, periodic boundary conditions can be applied to the flow field in main flow direction x (see figure 3). The boundary condition applied with respect to the pressure field is a so-called “fan” boundary condition that sets a constant pressure drop between the inlet and outlet patch. In the symmetry plane a symmetry boundary condition is imposed, and no-slip boundary conditions hold at all walls.

The temperature field has a fan boundary condition with a positive temperature difference ΔT_{io} between the inlet and the outlet patch. This results in a heating of the fluid as it passes through the simulated passage. The boundary condition used for the top and bottom walls is a linearly increasing temperature profile in mean flow direction. The increase in temperature $\Delta T_{\omega,io}$ is the same as ΔT_{io} . Together, these two boundary conditions model the balanced counter-flow configuration of the heat exchanger. A zero-gradient boundary condition is used for the gasket, which is modeled as an adiabatic wall.

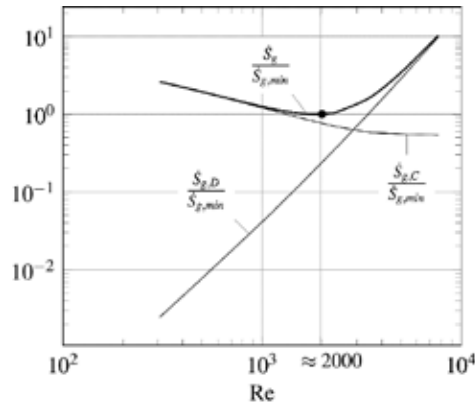


Figure 5. Overall entropy generation rate \dot{S}_g , entropy generation rate due to dissipation $\dot{S}_{g,D}$ and entropy generation rate due to conduction $\dot{S}_{g,C}$ (normalized with the minimum entropy generation rate at $Re \approx 2000$) at varying Reynolds numbers, for the simulated heat exchanger passage.

Changing the pressure drop leads to different mean flow velocities. In order to keep the heat flux \dot{q}_w fixed, it was necessary to adjust the temperature difference between inlet and outlet ($\Delta T_{w,i0} = \Delta T_{i0} = \dot{q}_w A / \dot{m}c_p$) accordingly.

6.2.4. Simulation results

The results obtained from CFD simulations give access to the velocity, pressure and temperature fields u , p and T . They can be used to calculate the heat transfer coefficient and the head loss coefficient for the convective heat transfer under consideration.

Calculating the pressure and velocity fields is the computationally expensive part of the simulation. When all fluid properties are assumed to be constant, i.e. pressure and temperature independent, the temperature field can even be modeled as a passive scalar, which comes at very little computational cost. The four parts of the entropy generation ($\dot{S}_{g,\bar{c}}$, $\dot{S}_{g,C}$, $\dot{S}_{g,\bar{D}}$, $\dot{S}_{g,D}$, see eqs. (29) to (32) in section 5.2.) are post-processing quantities: they can be obtained from the u -, p - and T -fields without solving further differential equations. This is beneficial for the assessment of a certain process operating on different temperature levels.

The entropy generation rates due to dissipation, conduction and the sum of both are shown in figure 5 for different Reynolds numbers. For increasing Reynolds numbers, $\dot{S}_{g,D}$ increases, while $\dot{S}_{g,C}$ decreases. An optimal point of operation can be identified at about $Re = 2000$. The same optimum can be identified in figure 6 for the energy devaluation number of the heat exchanger, N_{he} , since in eq. (11) the heat flux, wall area and ambient temperature are the same for all calculations.

Note that the curves for $\dot{S}_{g,C}$ and $\dot{S}_{g,D}$ in figure 5 are almost straight lines, especially for higher Reynolds numbers. Therefore only two simulations are necessary in order to roughly estimate

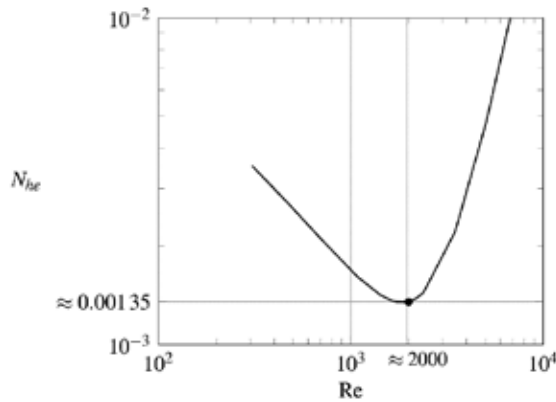


Figure 6. Energy devaluation number N_{he} for the simulated plate heat exchanger passage.

an optimum point of operation. From the two straight lines for $\dot{S}_{g,C}$ and $\dot{S}_{g,D}$ the sum of both results as a curve with the minimum at the optimal Reynolds number.

As mentioned before the entropy generation is a post-processing quantity. This can be leveraged to assess the simulated heat transfer situation at different temperature levels. If the overall change in temperature between inlet and outlet is not too large, an approximation can be done by simply scaling the results accordingly. The entropy generation due to dissipation $\dot{S}_{g,D,new}$ at the temperature level T_{new} is (compared to the entropy generation in an existing simulation result) $\dot{S}_{g,D,new} / \dot{S}_{g,D,sim} = T_{sim} / T_{new}$. If the new temperature level is higher, $\dot{S}_{g,D,new}$ will be smaller than $\dot{S}_{g,D,sim}$. Similarly, for entropy generation due to conduction, the relationship is $\dot{S}_{g,C,new} / \dot{S}_{g,C,sim} = (T_{sim} / T_{new})^2$. Again, if the new temperature level is higher, $\dot{S}_{g,C,new}$ will be smaller than $\dot{S}_{g,C,sim}$. The optimum point of operation shifts to a lower Reynolds number (see figure 7), because the effect of a temperature level change on $\dot{S}_{g,C}$ is larger than the effect on $\dot{S}_{g,D}$.

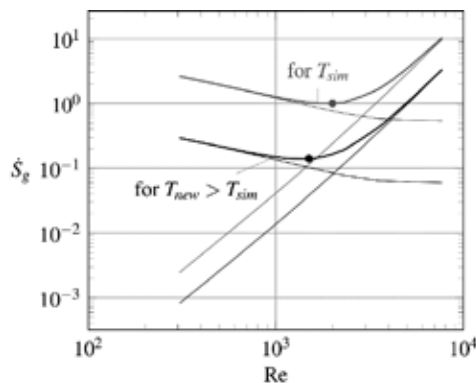


Figure 7. Entropy generation rates for a heat transfer at different temperature levels. For higher temperatures, the optimum point of operation shifts to lower Reynolds numbers.

7. Conclusions

Despite its apparently low popularity, entropy generation is a crucial aspect of every heat transfer process. Every real technical process includes the generation of entropy, which at some point has to be discharged to the ambient. It has been shown that every energy flow has an entropic potential, which is the amount of entropy that can be discharged to the ambient along with the energy flow. It therefore sets the limit for all wanted processes associated with this energy flow. Based on this, the *energy devaluation number* has been introduced, which quantifies the part of the entropic potential which is lost in a transfer process. The *energy devaluation number* is applicable to all processes in which energy is transferred and is recommended for their assessment especially with regard to sustainability.

In the examples it has also been shown how different heat transfer situations can be compared with each other. Such comparisons can be made on very different levels, reaching from system assessment (i.e. to compare different systems) to more detailed studies regarding the optimization of subsystems which are part of an overall heat transfer system. It has also been shown how existing simulation results can be reused at different temperature levels, effectively lowering the cost of CFD simulations.

Author details

Heinz Herwig and Christoph Redecker

*Address all correspondence to: h.herwig@tuhh.de

Institute for Thermo-Fluid Dynamics, Hamburg University of Technology, Germany

References

- [1] Moran, H. & Shapiro, H.. *Fundamentals of engineer thermodynamics*, 5th edn. New York: John Wiley & Sons; 2003
- [2] Baehr, H. & Kabelac, S. *Thermodynamik*, 14th edn. Berlin, Heidelberg, New York: Springer Verlag; 2009.
- [3] Herwig, H. & Kautz, C. *Technische Thermodynamik*. München: Pearson Studium; 2007.
- [4] Incropera, F., DeWitt, D., Bergmann, T. Lavine, A. *Fundamentals of heat and mass transfer*, 6th edn. New York: John Wiley & Sons; 2006.
- [5] Nellis, G. & Klein, S. *Heat transfer*. Cambridge: Cambridge University Press; 2009.

- [6] Rant, Z. (1956). Exergie, ein neues Wort fuer technische Arbeitsfaehigkeit. *Forschung im Ingenieurwesen* 1956;22 36-39.
- [7] Bejan, A. *Entropy Generation through Heat and Fluid Flow*. New York: John Wiley & Sons; 1982.
- [8] Wenterodt, T. & Herwig, H. The Entropic Potential Concept: A New Way to Look at Energy Transfer Operations, *Entropy* 2014;16 2071 – 2084.
- [9] Herwig, H. & Moschallski, A. *Wärmeübertragung*, 3rd. edn. Wiesbaden: Springer Vieweg; 2014.
- [10] Herwig, H. & Schmandt, B. How to Determine Losses in a Flow Field: A Paradigm Shift Towards the Second Law analysis, *Entropy* 2014;16 2959 – 2989.
- [11] Kis, P. & Herwig, H. A Critical Analysis of the Thermodynamic Model for Turbulent Forced Convection in a Plane channel Based on DNS Results. *Int. J. of Computational Fluid Dynamics* 2011;25 387-399.
- [12] Kock F. & Herwig, H. Local Entropy Production in Turbulent Shear Flows: A High Reynolds Number Model with Wall Functions, *Int. J. Heat Mass Transfer* 2004;47 2205 – 2215.
- [13] Herwig, H. & Wenterodt, T. Heat transfer and its assessment. In: Belmiloudi, A. (ed.) *Heat Transfer - Theoretical Analysis, Experimental Investigations and Industrial Systems* Rijeka: InTech; 2011. p437-452.
- [14] Redecker, C. Herwig, H. Calculating and assessing complex convective heat transfer problems: The CFD-SLA approach. In: *Proceedings of the International Heat Transfer Conference, IHTC-15, 10-15 August 2014, Kyoto, Japan*.
- [15] VDI e.v. *VDI-Wärmeatlas*, 11th edn. Wiesbaden: Springer Vieweg; 2013.

Analytical and Experimental Investigation

Modeling and Design of Plate Heat Exchanger

Fábio A.S. Mota, E.P. Carvalho and
Mauro A.S.S. Ravagnani

Additional information is available at the end of the chapter

<http://dx.doi.org/10.5772/60885>

1. Introduction

Heat exchangers are devices used to transfer energy between two fluids at different temperatures. They improve energy efficiency, because the energy already within the system can be transferred to another part of the process, instead of just being pumped out and wasted. In the new era of sustainability, the growing urgency to save energy and reduce overall environmental impacts has placed greater emphasis on the use of heat exchangers with better thermal efficiency. In this new scenario, the plate heat exchanger can play an important role.

A plate heat exchanger is a compact type of heat exchanger that uses a series of thin plates to transfer heat between two fluids. There are four main types of PHE: gasketed, brazed, welded, and semi-welded. The plate-and-frame or gasketed plate heat exchanger essentially consists of a pack of thin rectangular plates sealed around the edges by gaskets and held together in a frame (Figure 1). Plate heat exchangers were first introduced in 1923 for milk pasteurization applications, but are now used in many applications in the chemical, petroleum, HVAC, refrigeration, dairy, pharmaceutical, beverage, liquid food and health care sectors. This is due to the unique advantages of PHEs, such as flexible thermal design (plates can be simply added or removed to meet different heat duty or processing requirements), ease of cleaning to maintain strict hygiene conditions, good temperature control (necessary in cryogenic applications), and better heat transfer performance.

2. Mechanical characteristics

A PHE consists of a pack of thin rectangular plates with portholes, through which two fluid streams flow, where heat transfer takes place. Other components are a frame plate (fixed plate),



Figure 1. Typical plate heat exchangers [1].

a pressure plate (movable plate), upper and lower bars and screws for compressing the pack of plates (Figure 2). An individual plate heat exchanger can hold up to 700 plates. When the package of plates is compressed, the holes in the corners of the plates form continuous tunnels or manifolds through which fluids pass, traversing the plate pack and exiting the equipment. The spaces between the thin heat exchanger plates form narrow channels that are alternately traversed by hot and cold fluids, and provide little resistance to heat transfer.

2.1. Thermal plates and gaskets

The most important and most expensive part of a PHE is its thermal plates, which are made of metal, metal alloy, or even special graphite materials, depending on the application. Stainless steel, titanium, nickel, aluminum, incoloy, hastelloy, monel, and tantalum are some examples commonly found in industrial applications. The plates may be flat, but in most applications have corrugations that exert a strong influence on the thermal-hydraulic performance of the device. Some of the main types of plates are shown in Figure 3, although the majority of modern PHEs employ chevron plate types. The channels formed between adjacent plates impose a swirling motion to the fluids, as can be seen in Figure 4. The chevron angle is reversed in adjacent sheets, so that when the plates are tightened, the corrugations provide numerous points of contact that support the equipment. The sealing of the plates is achieved by gaskets fitted at their ends. The gaskets are typically molded elastomers, selected based on their fluid compatibility and conditions of temperature and pressure. Multi-pass arrangements can be implemented, depending on the arrangement of the gaskets between the plates. Butyl or nitrile rubbers are the materials generally used in the manufacture of the gaskets.

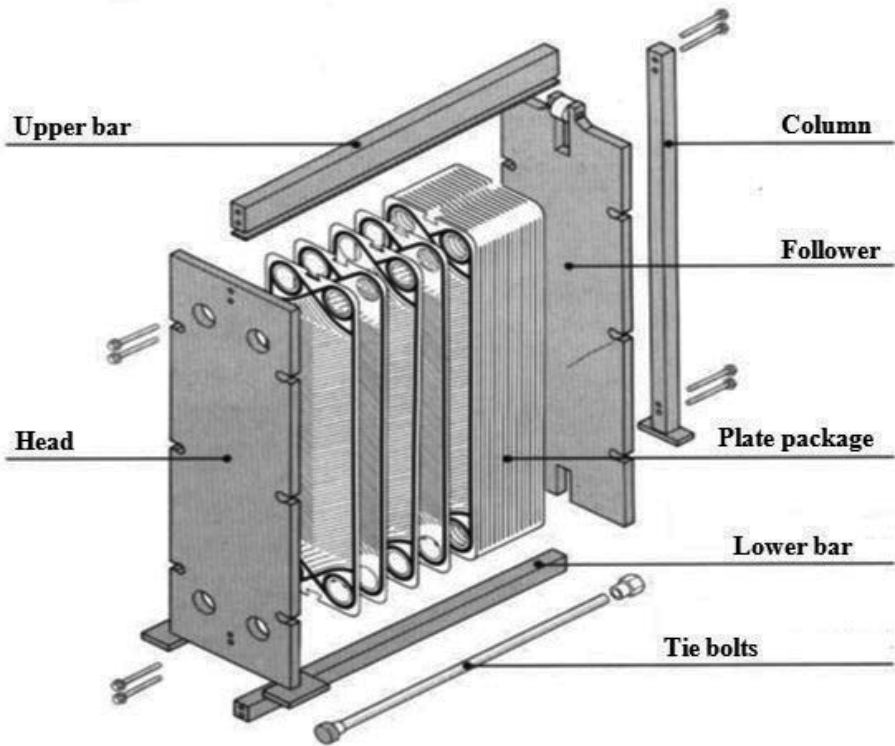


Figure 2. Exploded View of a Plate Heat Exchanger [2].

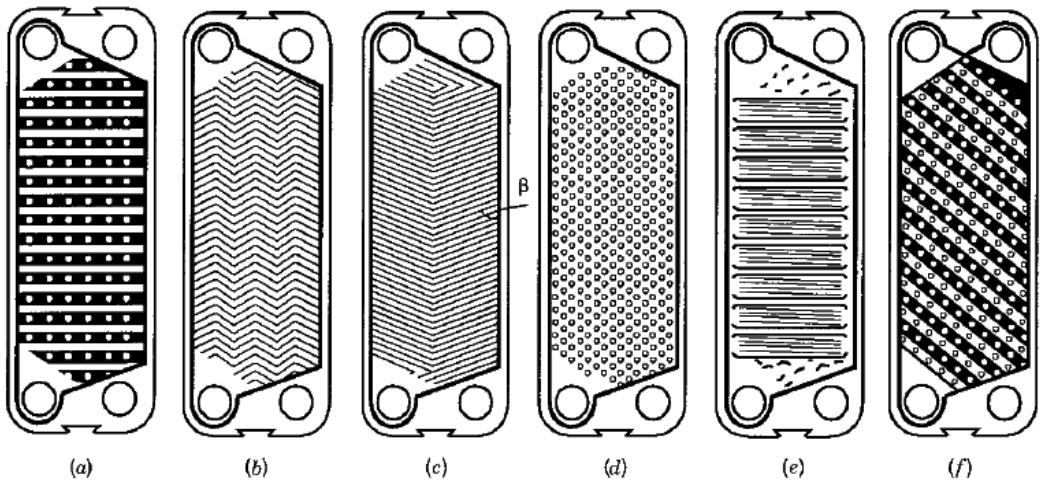


Figure 3. Typical categories of plate corrugations. (a) washboard, (b) zigzag, (c) chevron or herringbone, (d) protrusions and depressions (e) washboard with secondary corrugations, (f) oblique washboard [3].



Figure 4. Turbulent flow in PHE channels [4].

2.2. Design characteristics

This section presents some of the main advantages and disadvantages of a PHE, compared to shell-and-tube heat exchangers.

Advantages

Flexibility: Simple disassembly enables the adaptation of PHEs to new process requirements by simply adding or removing plates, or rearranging the number of passes. Moreover, the variety of patterns of plate corrugations available, together with the possibility of using combinations of them in the same PHE, means that various conformations of the unit can be tested during optimization procedures.

Good temperature control: Due to the narrow channels formed between adjacent plates, only a small volume of fluid is contained in a PHE. The device therefore responds rapidly to changes in process conditions, with short lag times, so that the temperatures are readily controllable. This is important when high temperatures must be avoided. Furthermore, the shape of the channels reduces the possibility of stagnant zones (dead space) and areas of overheating.

Low manufacturing cost: As the plates are only pressed (or glued) together, rather than welded, PHE production can be relatively inexpensive. Special materials may be used to manufacture the plates in order to make them more resistant to corrosion and/or chemical reactions.

Efficient heat transfer: The corrugations of the plates and the small hydraulic diameter enhance the formation of turbulent flow, so that high rates of heat transfer can be obtained for the fluids. Consequently, up to 90% of the heat can be recovered, compared to only 50% in the case of shell-and-tube heat exchangers.

Compactness: The high thermal effectiveness of PHEs means that they have a very small footprint. For the same area of heat transfer, PHEs can often occupy 80% less floor space (sometimes 10 times less), compared to shell-and-tube heat exchangers (Figure 5).

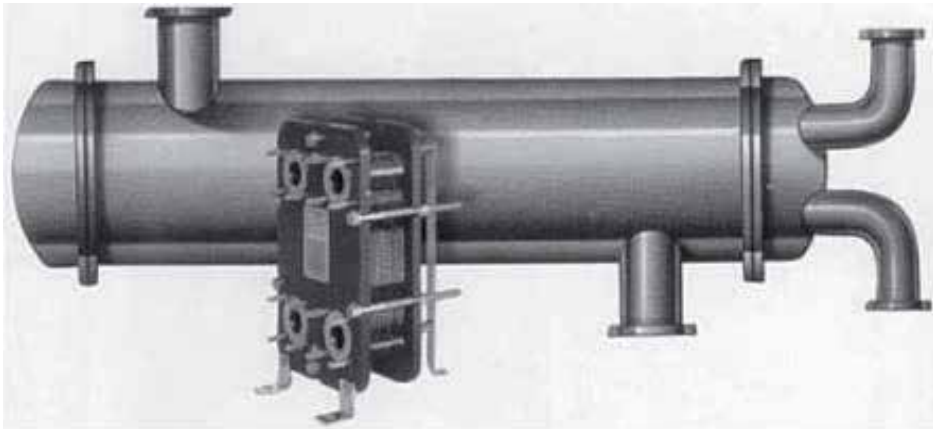


Figure 5. Illustration of the typical size difference between a PHE and a shell-and-tube heat exchanger for a given heat load [5].

Reduced fouling: Reduced fouling results from the combination of high turbulence and a short fluid residence time. The scale factors for PHEs can be up to ten times lower than for shell-and-tube heat exchangers.

Ease of inspection and cleaning: Since the PHE components can be separated, it is possible to clean and inspect all the parts that are exposed to fluids. This feature is essential in the food processing and pharmaceutical industries.

Easy leak detection: The gaskets have vents (Figure 6) that prevent fluids from mixing in the case of a failure, which also facilitate locating leaks.

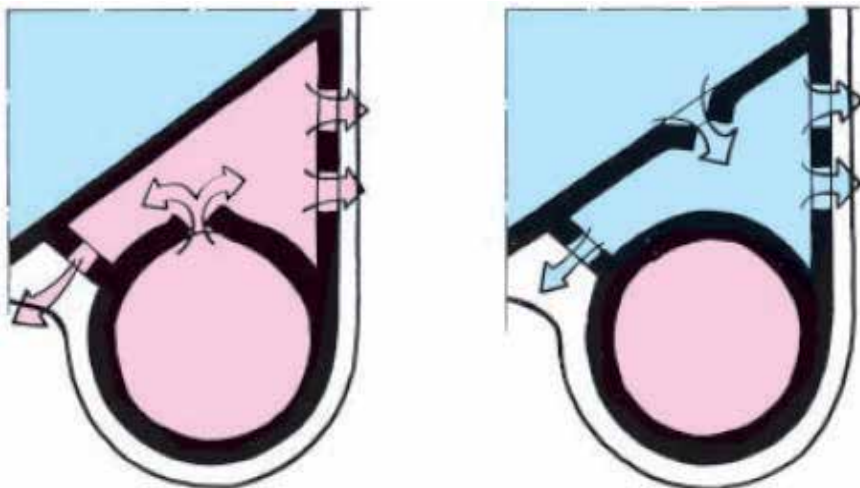


Figure 6. Vents in gaskets to detect possible leaks [4].

Drawbacks

Temperature and pressure limitations: An important limitation of PHEs is related to the plate gaskets. Pressures and temperatures exceeding 25 atm and 160 °C, respectively, are not tolerated because they can cause the standard gaskets to leak. However, gaskets made of special materials can withstand temperatures up to 400 °C, and it is possible to weld or braze the plates to each other in order to operate under more severe conditions. This would have the additional advantages of increasing the operational limits, as well as the possibility of working with corrosive fluids, because it would eliminate the need for gaskets. However, the PHE would lose its major advantages of flexibility and ease of cleaning, and the equipment would become more expensive.

High pressure drop: Because of the corrugated plates and the small flow space between them, the pressure drop due to friction is high, which increases pumping costs. The pressure drop can be reduced by increasing the number of passages per pass and splitting the flow into a greater number of channels. This diminishes the flow velocity within the channel, hence reducing the friction factor. However, the convective heat transfer coefficient is also reduced, decreasing the effectiveness of the heat exchanger.

Phase change: In special cases, PHEs can be used in condensation or evaporation operations, but are not recommended for gases and vapors due to the limited space within the channels and pressure limitations.

Types of fluids: The processing of fluids that are highly viscous or contain fibrous material is not recommended because of the high associated pressure drop and flow distribution problems within the PHE. Compatibility between the fluid and the gasket material should also be considered. Highly flammable or toxic fluids must be avoided due to the possibility of leakage.

Leakage: Friction between the metal plates can cause wear and the formation of small holes that are difficult to locate. As a precaution, it is advisable to pressurize the process fluid so that there is less risk of contamination in the event of leakage from a plate.

2.3. Arrangement of a plate heat exchanger

The simplest types of arrangements of plate heat exchangers are those in which both fluids make just one pass, so there is no change in direction of the streams. These are known as 1-1 single-pass arrangements, and there are two types: countercurrent and concurrent. A great advantage of the single-pass arrangement is that the fluid inlets and outlets can be installed in the fixed plate, making it easy to open the equipment for maintenance and cleaning, without disturbing the pipework. This is the most widely used single-pass design, known as the U-arrangement. There is also a single-pass Z-arrangement, where there is input and output of fluids through both end plates (Figure 7).

Countercurrent flow, where the streams flow in opposite directions, is usually preferred due to the achievement of higher thermal efficiency, compared to concurrent flow, where the streams flow in the same direction. Multi-pass arrangements can also be employed to enhance the heat

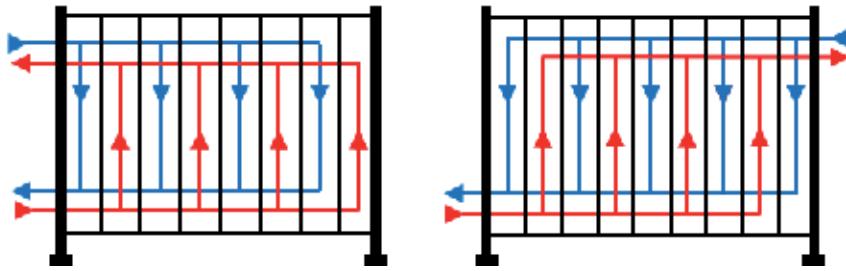


Figure 7. Arrangements of a simple-pass PHE. (a) U-arrangement and (b) Z-arrangement.

transfer or flow velocity of the streams, and are usually required when there is a substantial difference between the flow rates of the streams (Figure 8).

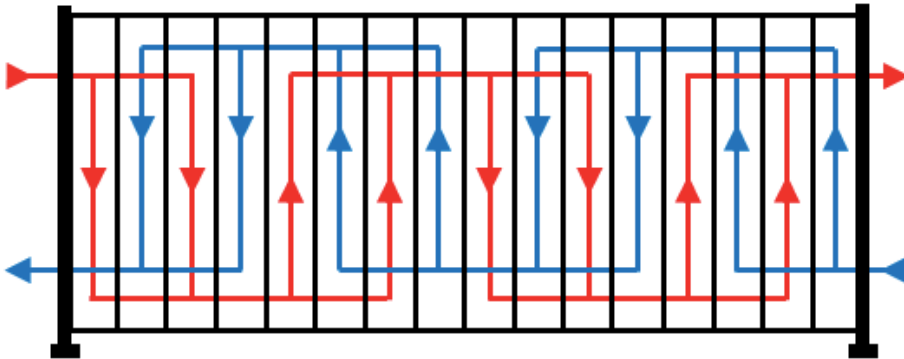


Figure 8. Multi-pass PHE.

There are five parameters that can be used to characterize the PHE configuration [6]: N_C , P^I , P^{II} , ϕ , Y_h and Y_f .

Number of channels (N_C): The space between two adjacent plates is a channel. The end plates are not considered, so the number of channels of a PHE is the number of plates minus one. The odd-numbered channels belong to side I, and the even-numbered ones belong to side II (Figure 9). The number of channels in each side are N_C^I and N_C^{II} .

Number of passes (P): This is the number of changes of direction of a determined stream inside the plate pack, plus one. P^I and P^{II} are the number of passes in each side.

Hot fluid location (Y_h): It is a binary parameter that assigns the fluids to the PHE sides. If $Y_h = 1$ the hot fluid occupies side I while if $Y_h = 0$ the hot fluid occupies side II.

Feed connection (ϕ): Feed side I is arbitrarily set at $\eta = 0$ as presented in Figure 9. The parameter ϕ represents the relative position of side II. Figure 9 illustrates all possibilities of connection. The parameter η is defined as $\eta = x / L_p$.

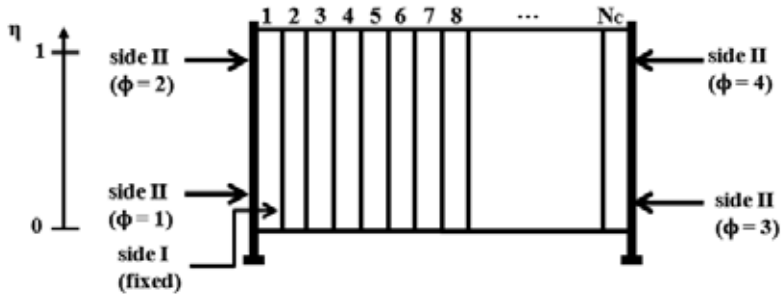


Figure 9. Feed connection of a PHE.

The plates of a PHE can provide vertical or diagonal flow, depending on the arrangement of the gaskets. For vertical flow, the inlet and outlet of a given stream are located on the same side of the heat exchanger, whereas for diagonal flow they are on opposite sides. Assembly of the plate pack involves alternating between the “A” and “B” plates for the respective flows. Mounting of the plate pack in vertical flow mode only requires an appropriate gasket configuration, because the A and B arrangements are equivalent (they are rotated by 180°, as shown in Figure 10a). This is not possible in the case of diagonal flow, which requires both types of mounting plate (Figure 10b). To identify each type of flow, Gut (2003) considered the binary parameter Y_f ($Y_f = 1$ for diagonal flow and $Y_f = 0$ for vertical flow). Poor flow distribution is more likely to occur in the array of vertical flow [7].

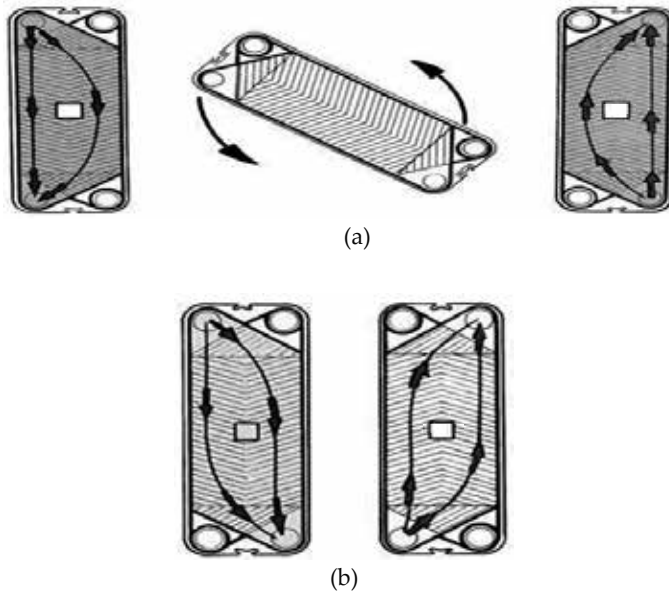


Figure 10. (a). Vertical flow plate [9]. (b). Diagonal flow plate [9].

3. Mathematical modeling

Due to the large number of plate types and pass arrangements, there are many possible configurations of a particular PHE design. As a result, a number of mathematical modeling approaches have been proposed for the calculation of performance. Two different modeling approaches are described below.

3.1. Model 1

A mathematical model was developed to simulate the general configuration of a PHE operating under steady state conditions, characterized using six different parameters [6]. In this model, the parameters considered are the number of channels, the number of passes for each side, the fluid locations, the feed connection locations, and the type of channel flow. The following assumptions are made:

- The PHE operates at steady state;
- The main flow is divided equally among the channels that make up each pass;
- The velocity profile in the channels is flat (plug flow);
- Perfect mixture in the end of each pass;
- There are no heat losses to the environment;
- There are no phase change;
- There is no heat transfer in the direction of flow, either in the fluids or in the plates, so heat transfer only occurs in the direction perpendicular to the flow;
- The physical properties of the fluids remain constant throughout the process.

The last assumption listed above implies an overall heat transfer coefficient U constant throughout the process, which is quite reasonable for compact heat exchangers operating without phase change [10]. In the absence of this consideration, the energy balance in the channels would result in a nonlinear system of ordinary first order differential equations, which would make the simulation much more complex. It has also been found that the results obtained assuming a constant overall heat transfer coefficient are very close to those found without such a restriction [6]. Thus, this assumption is not a limiting factor for the evaluation of a PHE.

Applying the energy conservation law to a given volume of control of a generic channel i with dimensions W_p , δx and b (Figure 11) and neglecting variations of kinetic and potential energy, the enthalpy change of the fluid passing through the volume is equal to the net heat exchanged by the two adjacent channels. This can be described by a system of differential equations:

$$\frac{d\theta_1}{d\eta} = s_1 \alpha^I (\theta_2 - \theta_1) \quad (1)$$

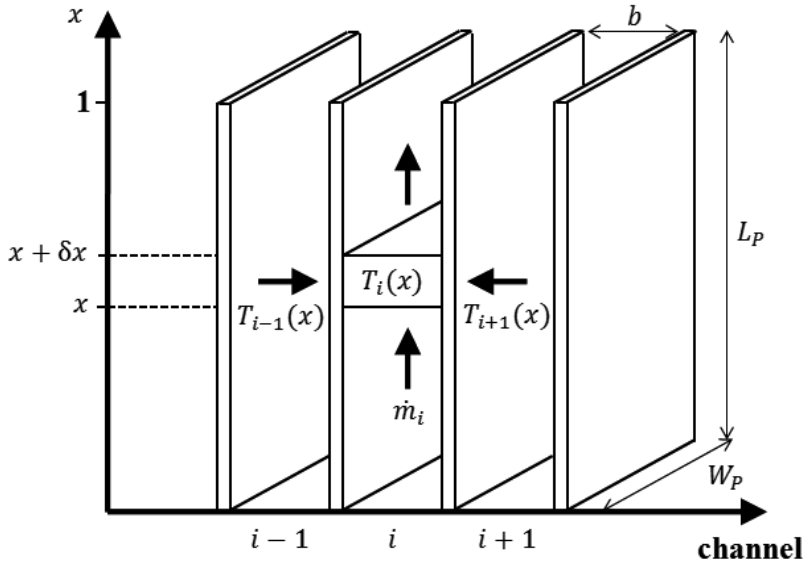


Figure 11. Scheme of a fluid control volume

$$\frac{d\theta_1}{d\eta} = s_i \alpha^{side(i)} (\theta_{i-1} + 2\theta_i + \theta_{i+1}) side(i) = \{I, II\} \tag{2}$$

$$\frac{d\theta_1}{d\eta} = s_i \alpha^{side(N_c)} (\theta_{N_c-1} - \theta_{N_c}) side(N_c) = \{I, II\} \tag{3}$$

where s_i is a constant that represents the flow direction in the channels ($s = 1$ for upward flow and $s = -1$ for downward flow); θ is the adimensional temperature:

$$\theta = \frac{T_i - T_{cold,in}}{T_{hot,in} - T_{cold,in}} \tag{4}$$

and

$$\alpha^I = \frac{A_p U N^I}{\dot{M}^I c_p^I}, \quad \alpha^{II} = \frac{A_p U N^{II}}{\dot{M}^{II} c_p^{II}} \tag{5}$$

A_p is the plate area, U is the overall heat transfer coefficient, N is the number of channels per pass, \dot{M} is the mass flow and c_p is the specific heat.

This system of linear differential equations can be written in the matrix form as:

$$\frac{d\bar{\theta}}{d\eta} = \bar{M} \cdot \bar{\theta} \tag{6}$$

where

$$\bar{M} = \begin{bmatrix} -d_1 & +d_1 & 0 & 0 & \dots & 0 \\ +d_2 & -2d_2 & +d_2 & 0 & \dots & 0 \\ 0 & +d_3 & -2d_3 & +d_3 & \vdots & \\ \vdots & & & & & 0 \\ 0 & \dots & 0 & +d_{N_C-1} & -2d_{N_C-1} & +d_{N_C-1} \\ 0 & \dots & 0 & 0 & +d_{N_C} & -d_{N_C} \end{bmatrix}$$

$$d_i = \begin{cases} s_i \alpha^I & \text{if } i \text{ is odd} \\ s_i \alpha^{II} & \text{if } i \text{ is even} \end{cases} \quad i = 1, \dots, N_C$$

The boundary conditions, which are dependent on the PHE configuration, can be divided into three different categories:

1. *Fluid inlet temperature:* In the channels of the first pass, the fluid inlet temperature is the fluid feed temperature.

$$\theta_i(\eta) = \theta_{fluid,in} \quad i \in \text{first pass} \tag{7}$$

2. *Change of pass temperature:* The temperature at the beginning of the channels of a particular pass is equal to the arithmetic average of the temperatures in the channels of the previous pass.

$$\theta_i(\eta) = \frac{1}{N} \sum_{\substack{j \in \text{previous} \\ \text{pass}}}^N \theta_j(\eta) \quad i \in \text{new pass} \tag{8}$$

3. *Fluid outlet temperature:* The outlet temperature of the fluid is the arithmetic average of the outlet temperatures of the channels of the last pass.

$$\theta_{fluid,out}(\eta) = \frac{1}{N} \sum_{\substack{j \in \text{last} \\ \text{pass}}}^N \theta_j(\eta) \tag{9}$$

The analytical solution is given by Eq. (10), where λ_i and \bar{z}_i are, respectively, the eigenvalues and eigenvectors of matrix \bar{M} :

$$\bar{\theta}(\eta) = \sum_{i=1}^{N_c} c_i \bar{z}_i e^{\lambda_i \eta} \tag{10}$$

Application of Eq. (10) in the boundary condition equations for the fluid inlet and change of pass enables the creation of a linear system of N_c equations for c_i variables. After solving the linear system, the outlet temperatures can be determined by the use of the outlet boundary conditions, hence enabling the thermal effectiveness to be determined.

Example: Creation of the linear system of N_c equations:

In order to illustrate the generation of the linear system, a PHE containing 7 thermal plates (or 8 channels), with the cold fluid making two passes and the hot fluid making one pass, is shown in Figure 12.

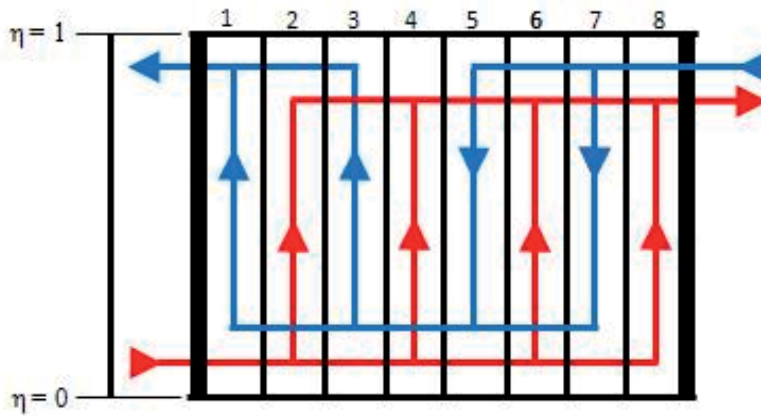


Figure 12. PHE streams.

Applying Eq. (10), the following analytical solution can be achieved:

$$\bar{\theta}(\eta) = c_1 \begin{bmatrix} z_{1,1} \\ z_{2,1} \\ \vdots \\ z_{8,1} \end{bmatrix} e^{\lambda_1 \eta} + c_2 \begin{bmatrix} z_{1,2} \\ z_{2,2} \\ \vdots \\ z_{8,2} \end{bmatrix} e^{\lambda_2 \eta} + \dots + c_8 \begin{bmatrix} z_{1,8} \\ z_{2,8} \\ \vdots \\ z_{8,8} \end{bmatrix} e^{\lambda_8 \eta}$$

Using the boundary condition equations (7) and (8) for all the channels of the PHE under investigation, the equations presented in Table 1 are generated.

Cold fluid	Hot fluid
$\theta_1(\eta=0)=[\theta_5(\eta=0) + \theta_7(\eta=0)]/2$	$\theta_2(\eta=1)=\theta_{hot,in}=1$
$\theta_3(\eta=0)=[\theta_5(\eta=0) + \theta_7(\eta=0)]/2$	$\theta_4(\eta=1)=\theta_{hot,in}=1$
$\theta_5(\eta=1)=\theta_{cold,in}=0$	$\theta_6(\eta=1)=\theta_{hot,in}=1$
$\theta_7(\eta=1)=\theta_{cold,in}=0$	$\theta_8(\eta=1)=\theta_{hot,in}=1$

Table 1. Boundary condition equations.

These equations can be written in the following way:

$$\begin{aligned} \theta_1(\eta=0) - [\theta_5(\eta=0) + \theta_7(\eta=0)]/2 &= 0 \\ \theta_2(\eta=1) &= 1 \\ \theta_3(\eta=0) - [\theta_5(\eta=0) + \theta_7(\eta=0)]/2 &= 0 \\ \theta_4(\eta=1) &= 1 \\ \theta_5(\eta=1) &= 0 \\ \theta_6(\eta=1) &= 1 \\ \theta_7(\eta=1) &= 0 \\ \theta_8(\eta=1) &= 1 \end{aligned}$$

To achieve the matrix form is Eq. (10) is applied to the linear system:

$$\bar{A} \cdot \bar{C} = \bar{B} \tag{11}$$

where

\bar{A} = eigenvalues and eigenvectors matrix

\bar{C} = c_i 's coefficients vector

\bar{B} = binary vector

where

$$\begin{aligned} B_i &= 0 \text{ if } B_i = \theta_{hot,in} \quad i \in \text{first pass} \\ B_i &= 1 \text{ if } B_i = \theta_{cold,in} \quad i \in \text{first pass} \\ B_i &= 0 \text{ if } B_i = \theta_i(\eta) - \frac{1}{N} \sum_{j \in \text{previous pass}}^N \theta_j(\eta) \end{aligned}$$

3.2. Model 2

The assumption is made that any multi-pass PHE with a sufficiently large number of plates (so that end effects and inter-pass plates can be neglected) can be reduced to an arrangement consisting of assemblies of single-pass PHEs [11]. This enables the development of closed-form equations for effectiveness, as a function of the ratio between the heat capacities of the fluids and the number of transfer units, for the arrangements 1-1, 2-1, 2-2, 3-1, 3-2, 3-3, 4-1, 4-2, 4-3, and 4-4 (Table 2). In other words, most multi-pass plate heat exchangers can be represented by simple combinations of pure countercurrent and concurrent exchangers, so that a multi-pass PHE is therefore equivalent to combinations of smaller single-pass exchangers (Figure 13).

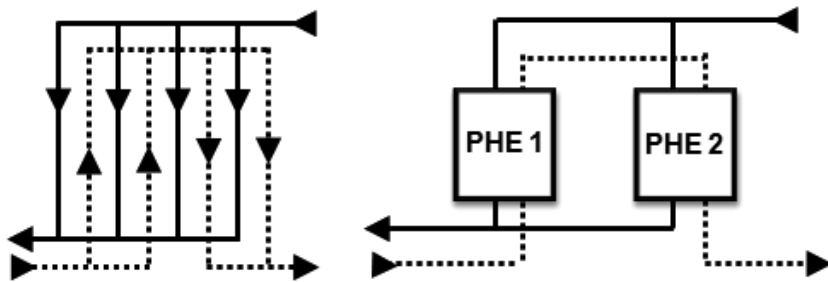
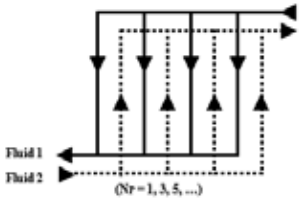
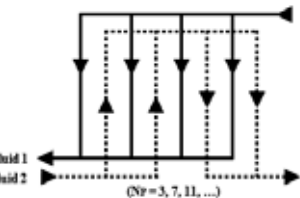
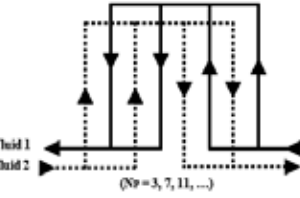
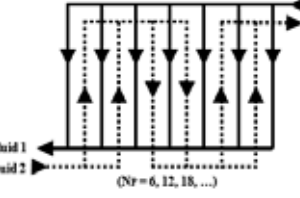
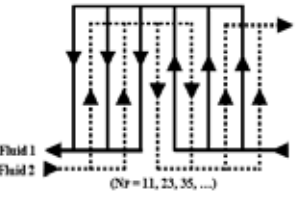


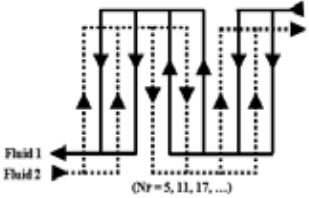
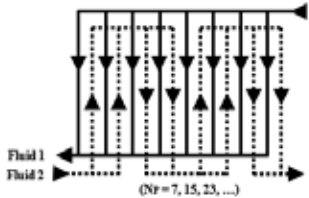
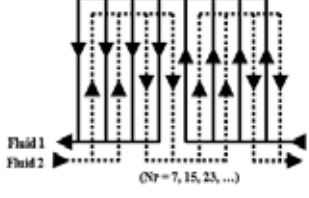
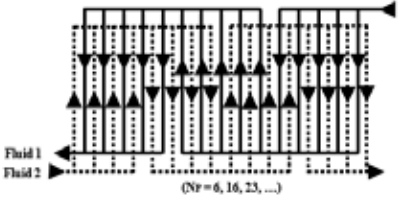
Figure 13. Equivalent configurations.

The assumptions considered are the same as in the first mathematical model. The derived formulas are only valid for PHEs with numbers of thermal plates sufficiently large that the end effects can be neglected. This condition can be satisfied, depending on the required degree of accuracy. For example, a minimum of 19 plates is recommended for an inaccuracy of up to 2.5% [12]. Elsewhere, a minimum of 40 thermal plates was used [11, 13]. In the formulas, P_{CC} and P_p are the thermal effectiveness for the countercurrent and concurrent flows, respectively, given by:

$$P_{CC}(NTU_1, R_1) = \begin{cases} \frac{1 - e^{-NTU_1(1-R_1)}}{1 - R_1 e^{-NTU_1(1-R_1)}} & \text{se } R_1 \neq 1 \\ \frac{NTU_1}{NTU_1 + 1} & \text{se } R_1 = 1 \end{cases} \quad (12)$$

$$P_p(NTU_1, R_1) = \frac{1 - e^{-NTU_1(1+R_1)}}{1 + R_1} \quad (13)$$

Formulas	Arrangements
<p>Arrangement 111</p> $P_1 = P_{CC}$ <p>where:</p> $P_{CC} = P_{CC}(NTU_1, R_1)$	 <p>(Nr = 1, 3, 5, ...)</p>
<p>Arrangement 211</p> $P_1 = \frac{1}{2} \left[P_{CC} + P_p - \frac{1}{2} (P_p P_{CC} R_1) \right]$ <p>where:</p> $P_{CC} = P_{CC}(NTU_1, R_1)$ $P_p = P_p(NTU_1, R_1/2)$	 <p>(Nr = 3, 7, 11, ...)</p>
<p>Arrangement 221</p> $P_1 = P_{CC}$ <p>where:</p> $P_{CC} = P_{CC}(NTU_1, R_1)$	 <p>(Nr = 3, 7, 11, ...)</p>
<p>Arrangement 311</p> $P_1 = \frac{1}{3} \left[P_{B,1} + P_{A,1} \left(1 - \frac{P_{B,1} R_1}{3} \right) \left(2 - \frac{P_{A,1} R_1}{3} \right) \right]$ <p>where:</p> $P_{A,1} = P_{CC}$ $P_{B,1} = P_p$ $P_{CC} = P_{CC}(NTU_1, R_1/3)$ $P_p = P_p(NTU_1, R_1/3)$	 <p>(Nr = 6, 12, 18, ...)</p>
<p>Arrangement 321</p> $P_1 = \frac{1}{R_1} (a + 0, 5b + 0, 5c + d)$ <p>where:</p> $a = \frac{2R_1 e^2 f^2 - 2ef - f^2}{2R_1 e^2 f^2 - e^2 - f^2 - 2ef + e + f}$ $b = \frac{a(e-1)}{f}, \quad c = \frac{(1-a)}{e}$ $d = R_1 e^2 c - R_1 e + R_1 - c/2$ $e = \frac{1}{(\frac{2}{3} R_1 P_{CC})}, \quad f = \frac{1}{(\frac{2}{3} R_1 P_p)}$ $P_{CC} = P_{CC}(NTU_1/2, 2R_1/3)$ $P_p = P_p(NTU_1/2, 2R_1/3)$	 <p>(Nr = 11, 23, 35, ...)</p>

Formulas	Arrangements
<p>Arrangement 331</p> $P_1 = P_{CC}$ <p>where:</p> $P_{CC} = P_{CC}(NTU_1, R_1)$	
<p>Arrangement 411</p> $P_1 = P_1 - \frac{P_1^2 R_1}{4}$ <p>where:</p> $P_1 = \frac{1}{2} \left(P_{CC} + P_P - \frac{R_1 P_{CC} P_P}{4} \right)$ $P_{CC} = P_{CC}(NTU_1, R_1/4)$ $P_P = P_P(NTU_1, R_1/4)$	
<p>Arrangement 421</p> $P_1 = P_1 - \frac{P_1(1-P_1)(1-P_1 R_1)}{1-P_1^2 R_1}$ <p>where:</p> $P_1 = \frac{1}{2} \left(P_{CC} + P_P - \frac{P_{CC} P_P R_1}{2} \right)$ $P_{CC} = P_{CC}(NTU_1/2, R_1/2)$ $P_P = P_P(NTU_1/2, R_1/2)$	
<p>Arrangement 431</p> $P_1 = A + \frac{[BD(1-G) + BQE]}{[(1-G)(1-E) - QS]}$ <p>where:</p> $A = \frac{1}{4}(3P_{CC} + P_P - rP_{CC}P_P)$ $B = 1 - A$ $D = \frac{1}{6}(1 - rP_{CC})(3P_{CC} + 3P_P - 2rP_{CC}P_P - rP_P^2)$ $E = \frac{1}{12}(1 - rP_{CC})(3 - 2rP_{CC} - rP_P)(P_{CC} + 3P_P - rP_{CC}P_P - 2rP_P^2)$ $G = \frac{r}{6}[(P_{CC}^2 + 3P_P^2) + P_{CC}P_P(3 - rP_{CC} - 2rP_P)]$ $H = \frac{r}{6}[3P_{CC}^2 + P_P^2 + P_{CC}P_P(3 - 2rP_{CC} - rP_P)]$ $Q = 1 - \frac{(P_{CC} + P_P)}{2} + \frac{rP_{CC}P_P}{3}$ $S = \frac{ErP_{CC}}{1 - rP_{CC}} + \frac{rP_P}{12}(P_{CC} + 3P_P - rP_P)(P_{CC} + 2P_P)$ $r = \frac{3R_1}{4}$ $P_{CC} = P_{CC}(NTU_1/3, r)$ $P_P = P_P(NTU_1/3, r)$	

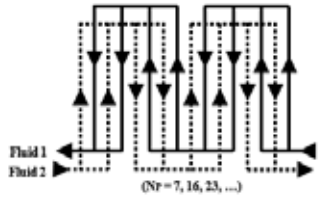
Formulas	Arrangements
<p>Arrangement 441</p> <p>$P_1 = P_{CC}$</p> <p>where:</p> <p>$P_{CC} = P_{CC}(NTU_1, R_1)$</p>	 <p>(NP = 7, 16, 23, ...)</p>

Table 2. Closed formulas for multi-pass arrangement [11]

4. Design of a plate heat exchanger

4.1. Basic equations for the design of a plate heat exchanger

The methodology employed for the design of a PHE is the same as for the design of a tubular heat exchanger. The equations given in the present chapter are appropriate for the chevron type plates that are used in most industrial applications.

4.1.1. Parameters of a chevron plate

The main dimensions of a *chevron* plate are shown in Figure 14. The corrugation angle, β , usually varies between extremes of 25° and 65° and is largely responsible for the pressure drop and heat transfer in the channels.

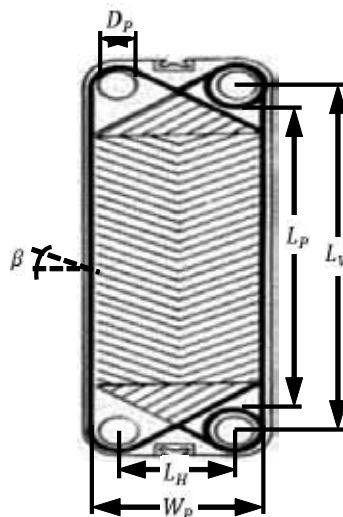


Figure 14. Parameters of a chevron plate.

The corrugations must be taken into account in calculating the total heat transfer area of a plate (effective heat transfer area):

$$A_p = \Phi \cdot W_p \cdot L_p \quad (14)$$

where

A_p = plate effective heat transfer area

Φ = plate area enlargement factor (range between 1.15 and 1.25)

W_p = plate width

L_p = plate length

The enlargement factor of the plate is the ratio between the plate effective heat transfer area, A_p and the designed area (product of length and width $W_p \cdot L_p$), and lies between 1.15 and 1.25. The plate length L_p and the plate width W_p can be estimated by the orifices distances. L_V , L_H , and the port diameter D_p are given by Eq. (15) and Eq. (16) [5].

$$L_p \approx L_V - D_p \quad (15)$$

$$W_p \approx L_H + D_p \quad (16)$$

For the effective heat transfer area, the hydraulic diameter of the channel is given by the equivalent diameter, D_e , which is given by:

$$D_e = \frac{2b}{\Phi} \quad (17)$$

where b is the channel average thickness.

4.1.2. Heat transfer in the plates

The heat transfer area is expressed as the global design equation:

$$Q = UA\Delta T_M \quad (18)$$

where U is the overall heat transfer coefficient, A is the total area of heat transfer and ΔT_M is the effective mean temperature difference, which is a function of the inlet and outlet fluid

temperatures, the specific heat, and the configuration of the exchanger. The total area of heat transfer can be given by:

$$A = N_p A_p \quad (19)$$

where N_p is the number of plates. The end plates, which do not exchange heat, are not taken into account in determining the area. The inner plates are usually called thermal plates in order to distinguish them from the adiabatic end plates. The overall heat transfer coefficient can be determined by:

$$U = \frac{1}{\frac{1}{h_{hot}} + \frac{t_p}{k_p} + \frac{1}{h_{cold}} + R_{f,cold} + R_{f,hot}} \quad (20)$$

where

h_{hot} = convective heat transfer coefficient of the hot fluid

h_{cold} = convective heat transfer coefficient of the cold fluid

t_p = plate thickness

k_p = plate thermal conductivity

$R_{f,hot}$ = fouling factor of the hot fluid

$R_{f,cold}$ = fouling factor of the cold fluid

The convective heat transfer coefficient, h , depends on the fluid properties, fluid velocity, and plate geometry.

4.1.3. Design methods

There are two main approaches used in the design of PHEs, namely the log-mean temperature difference and the thermal effectiveness methods. For the first method, the rate of heat transfer is given by:

$$Q = UA(F\Delta T_{lm}) \quad (21)$$

where ΔT_{lm} is the log-mean temperature difference, given by Eq. (22) and F is the log-mean temperature difference correction factor.

$$\Delta T_{lm} = \frac{\Delta T_1 - \Delta T_2}{\ln(\Delta T_1 / \Delta T_2)} \quad (22)$$

Where

$$\Delta T_1 = \begin{cases} T_{hot,in} - T_{cold,out} & \text{if countercurrent} \\ T_{hot,in} - T_{cold,in} & \text{if concurrent} \end{cases}$$

$$\Delta T_2 = \begin{cases} T_{hot,out} - T_{cold,in} & \text{if countercurrent} \\ T_{hot,out} - T_{cold,out} & \text{if concurrent} \end{cases}$$

The correction factor is a function of the heat exchanger configuration and the dimensionless parameters R and P_C . For purely countercurrent or concurrent (single-pass) arrangements, the correction factor is equal to one, while for multi-pass arrangements, it is always less than one. However, because the end channels of the PHE only exchange heat with one adjacent channel, different to the inner channels that exchange heat with two adjacent channels, purely countercurrent or concurrent flow is only achieved in two extreme situations. These are:

- i. when the PHE has only one thermal plate, so that only two channels are formed by the end plates and the thermal plate, with each stream flowing through one channel;
- ii. when the number of thermal plates is sufficiently large that the edge effect can be neglected.

The adimensional parameters R e P_C are defined as:

$$R = \frac{T_{hot,in} - T_{hot,out}}{T_{cold,out} - T_{cold,in}} = \frac{(\dot{M}c_p)_{cold}}{(\dot{M}c_p)_{hot}} \quad (23)$$

$$P_C = \frac{T_{cold,out} - T_{cold,in}}{T_{hot,in} - T_{cold,in}} = \frac{\Delta T_{cold}}{\Delta T_{max}} \quad (24)$$

The second method provides a definition of heat exchanger effectiveness in terms of the ratio between the actual heat transfer and the maximum possible heat transfer, as shown in Eq. (25):

$$E = \frac{Q}{Q_{max}} \quad (25)$$

The actual heat transfer can be achieved by an energy balance:

$$Q = (\dot{M}c_p)_{hot} (T_{hot,in} - T_{hot,out}) \quad (26)$$

$$Q = (\dot{M}c_p)_{cold} (T_{cold,out} - T_{cold,in}) \quad (27)$$

Thermodynamically, Q_{max} represents the heat transfer that would be obtained in a pure countercurrent heat exchanger with infinite area. This can be expressed by:

$$Q_{max} = (\dot{M}c_p)_{min} \Delta T_{max} \quad (28)$$

Using Eqs. (26), (27) and (28), the PHE effectiveness can be calculated as the ratio of temperatures:

$$E = \begin{cases} \frac{\Delta T_{hot}}{\Delta T_{max}} & \text{if } R > 1 \\ \frac{\Delta T_{cold}}{\Delta T_{max}} & \text{if } R < 1 \end{cases} \quad (29)$$

The effectiveness depends on the PHE configuration, the heat capacity rate ratio (R), and the number of transfer units (NTU). The NTU is a dimensionless parameter that can be considered as a factor for the size of the heat exchanger, defined as:

$$NTU = \frac{UA}{(\dot{M}c_p)_{min}} \quad (30)$$

4.1.4. Pressure drop in a plate heat exchanger

The pressure drop is an important parameter that needs to be considered in the design and optimization of a plate heat exchanger. In any process, it should be kept as close as possible to the design value, with a tolerance range established according to the available pumping power. In a PHE, the pressure drop is the sum of three contributions:

1. Pressure drop across the channels of the corrugated plates.
2. Pressure drop due to the elevation change (due to gravity).
3. Pressure drop associated with the distribution ducts.

The pressure drop in the manifolds and ports should be kept as low as possible, because it is a waste of energy, has no influence on the heat transfer process, and can decrease the uniformity of the flow distribution in the channels. It is recommended to keep this loss lower than 10% of the available pressure drop, although in some cases it can exceed 30% [3].

$$\Delta P = \frac{2fL_v PG_c^2}{\rho D_e} + 1,4 \frac{G_p^2}{2\rho} + \rho g L_v \quad (31)$$

where f is the Fanning factor, given by Eq. (33), P is the number of passes and G_p is the fluid mass velocity in the port, given by the ratio of the mass flow, \dot{M} , and the flow cross-sectional area, $\pi D_p^2/4$.

$$G_p = \frac{4\dot{M}}{\pi D_p^2} \quad (32)$$

$$f = \frac{K_p}{Re^m} \quad (33)$$

The values for K_p and m are presented in Table 3 as function of the Reynolds number for some β values.

4.1.5. Experimental heat transfer and friction correlations for the chevron plate PHE

Due to the wide range of plate designs, there are various parameters and correlations available for calculations of heat transfer and pressure drop. Despite extensive research, there is still no generalized model. There are only certain specific correlations for features such as flow patterns, parameters of the plates, and fluid viscosity, with each correlation being limited to its application range. In this chapter, the correlation described in [14] was used.

$$Nu = C_h (Re)^n (Pr)^{1/3} \left(\frac{\mu}{\mu_w} \right)^{0.17} \quad (34)$$

where μ_w is the viscosity evaluated at the wall temperature and the dimensionless parameters Nusselt number (Nu), Reynolds number (Re) and Prandtl number (Pr) can be defined as:

$$Nu = \frac{hD_e}{k}, \quad Re = \frac{G_c D_e}{\mu}, \quad Pr = \frac{c_p \mu}{k} \quad (35)$$

In Reynolds number equation, G_c is the mass flow per channel and may be defined as the ratio between the mass velocity per channel \dot{m} and the cross sectional area of the flow channel (bW_p):

$$G_c = \frac{\dot{m}}{bW_p} \quad (36)$$

The constants C_h and n , which depend on the flow characteristics and the chevron angle, are given in Table 3.

4.2. Optimization

Any industrial process, whether at the project level or at the operational level, has aspects that can be enhanced. In general, the optimization of an industrial process aims to increase profits and/or minimize costs. Heat exchangers are designed for different applications, so there can be multiple optimization criteria, such as minimum initial and operational costs, minimum volume or area of heat transfer, and minimum weight (important for space applications).

β	Heat transfer			Pressure drop		
	Re	C_h	n	Re	K_p	m
$\leq 30^\circ$	≤ 10	0.718	0.349	≤ 10	50.000	1.000
	> 10	0.348	0.663	10 - 100	19.400	0.589
				> 100	2.990	0.183
45°	< 10	0.718	0.349	< 15	47.000	1.000
	10 - 100	0.400	0.598	15 - 300	18.290	0.652
	> 100	0.300	0.663	> 300	1.441	0.206
50°	< 20	0.630	0.333	< 20	34.000	1.000
	20 - 300	0.291	0.591	20 - 300	11.250	0.631
	> 300	0.130	0.732	> 300	0.772	0.161
60°	< 20	0.562	0.326	< 40	24.000	1.000
	20 - 200	0.306	0.529	40 - 00	3.240	0.457
	> 400	0.108	0.703	> 400	0.760	0.215
$\geq 65^\circ$	< 20	0.562	0.326	< 50	24.000	1.000
	20 - 500	0.331	0.503	50 - 500	2.800	0.451
	> 500	0.087	0.718	> 500	0.639	0.213

Table 3. Constants for the heat transfer and pressure drop calculation in a PHE with chevron plates [14]

The optimization problem is formulated in such a way that the best combination of the parameters of a given PHE minimizes the number of plates. The optimization method used is based on screening [15], where for a given type of plate, the number of thermal plates is the objective function that has to be minimized. In order to avoid impossible or non-optimal solutions, certain inequality constraints are employed. An algorithm has been proposed in a screening method that uses MATLAB for optimization of a PHE, considering the plate type as the optimization variable [16]. For each type of plate, local optimal configurations are found (if they exist) that employ the fewest plates. Comparison of all the local optima then gives a global optimum.

5. Formulation of the optimization problem

Minimize:

$$N_p = f(N_c, P^I, P^{II}, \phi, Y_h, \text{plate type}) \quad (37)$$

Subject to:

$$N_c^{min} \leq N_c \leq N_c^{max} \quad (38)$$

$$\Delta P_{hot} \leq \Delta P_{hot}^{max} \quad (39)$$

$$\Delta P_{cold} \leq \Delta P_{cold}^{max} \quad (40)$$

$$v_{hot} \geq v_{hot}^{min} \quad (41)$$

$$v_{cold} \geq v_{cold}^{min} \quad (42)$$

$$E^{min} \leq E \leq E^{max} \quad (43)$$

If closed-form model is considered, as the closed-form equations are limited for some number of passes, there are two more constraints:

$$P^I \leq P^{I,max} \text{ if using closed - form model} \quad (44)$$

$$P^{II} \leq P^{II,max} \text{ if using closed - form model} \quad (45)$$

Depending on the equipment model, the number of plates can vary between 3 and 700. The first constraint (38) is imposed according to the PHE capacity. Constraints (39) and (40) can also be imposed, depending on the available pumping power. The velocity constraints are usually imposed in order to avoid dead spaces or air bubbles inside the set of plates. In practice, velocities less than 0.1 m/s are not used [5].

The optimization problem is solved by successively evaluating the constraints, reducing the number of configurations until the optimal set (OS) is found (if it exists). The screening process begins with the identification of an initial set (IS) of possible configurations, considering the channel limits. A reduced set (RS) is generated by considering the velocity and pressure drop constraints. The constraint of thermal effectiveness is then applied to the RS, in increasing order of the number of channels. Configurations with the smallest number of channels form the local optima set. The global optimum can therefore be found by comparing all the local optima. It is important to point out that the global optimum configuration may have a larger total heat transfer area. However, it is usually more economical to use a smaller number of large plates than a greater number of small plates [17]. The optimization algorithm is described in Table 4.

In Step 5, both methods can be used. The model using algebraic equations has the limitation of only being applicable to PHEs that are sufficiently large not to be affected by end channels and channels between adjacent passes. Industrial PHEs generally possess more than 40 thermal plates, although the limitation of the number of passes can still be a drawback. The major advantage of the model using differential equations is its general applicability to any configuration, without having to derive a specific closed-form equation for each configuration.

Steps	Mathematical relations	Comments
Step 1: Input data for each type of plate.		PHE dimensions, fluids physical properties, mass flow rate and inlet temperature of both streams, constraints.
Step 2: Verification of the number of plates constraint. The initial set of configurations (IS) is determined.	$\bar{N}_C = N_C^{min} : N_C^{max}$	The vector \bar{N}_C is generated with all possible number of channels.
Step 2.1: For each element of the vector \bar{N}_C , all possible number of passes for sides I and II are computed.	$N_C^I = \frac{2N_C + 1 + (-1)^{N_C+1}}{4}$ $N_C^{II} = \frac{2N_C - 1 + (-1)^{N_C}}{4}$ $P \leq P^{max} \text{ if using closed-form model}$	They are integer divisors of the number of channels of the corresponding side. If one is using closed-form equations, the number of passes constraint must be considered.
Step 3: Verification of the hydraulic constraints. The reduced set of configurations (RS) is determined.	$\Delta P_{fluid} \leq \Delta P_{fluid}^{max}$ $v_{fluid} \geq v_{fluid}^{min}$	Fluid velocity and pressure drop constrains are verified.
Step 3.1 Take $Y_h = 0$ and check the following constraints.	$P_{cold}^I = P^I$ and $P_{hot}^{II} = P^{II}$.	Cold fluid flows in the side I and the hot fluid in the side II.
Step 3.1.1 Verification of the velocity constraint for the fluid in side I.	$v_{cold}^I = \frac{G_{cold}^I}{P_{cold}}$	Cold fluid velocity v_{cold}^I is calculated, in a decreasing order of the possible number of passes of a given element of \bar{N}_C . If v_{cold}^I achieves the minimum

Steps	Mathematical relations	Comments
		allowable value, it is not necessary to evaluate configurations with smaller number of passes.
Step 3.1.2 Verification of the pressure drop constraint in side I Eq. (31)		The cold fluid pressure drop is calculated, ΔP_{cold}^I , in a crescent order of the possible number of passes of a given element of \bar{N}_C . If ΔP_{cold}^I achieves the maximum allowable value, it is not necessary to evaluate configurations with greater number of passes.
Step 3.1.3 Verification of the velocity constraint for the fluid in side II.	$v_{hot}^{II} = \frac{G_{C,hot}^{II}}{\rho_{hot}}$	Analogous to Step 3.1.1.
Step 3.1.4 Verification of the pressure drop constraint in side II. Eq. (31)		Analogous to Step 3.1.2.
Stage 3.2 Take $Y_h = 1$ and do the same as Stage 3.1.	$P_{cold}^{II} = P^{II}$ and $P_{hot}^I = P^I$	Analogous to stage 3.1.
Stage 3.3: Combination of the configuration parameters.	$[N_C P^I P^{II} Y_h \phi]$	For $Y_h = 0$ and $Y_h = 1$, the number of passes selected for the sides I and II of the PHE is combined.
Step 4: Calculate the effectiveness in pure countercurrent flow, E_{CC} .	$E_{CC} = \begin{cases} \frac{1 - e^{-NTU(1-C_r)}}{1 - C_r e^{-NTU(1-C_r)}} & \text{if } C_r < 1 \\ \frac{NTU}{NTU + 1} & \text{if } C_r = 1 \end{cases}$	If $E_{CC} < E^{min}$, these configurations can be discarded.
Step 5: Verification of the thermal effectiveness constraint. The local optimal set of configurations (OS) is determined.	$E^{min} \leq E \leq E^{max}$	The selected configurations in Step 4 are simulated in a crescent order of the number of channels to find the possible local optimum set (OS). The remaining configurations do not need to be simulated. Both modeling can be used.
Step 6: Find global optimum.		By comparing all local optima, the global optimum is found.

Table 4. Optimization algorithm.

However, a drawback is the highly complex implementation of the simulation algorithm (see Table 5), in contrast to the second model, which is very simple.

Steps	Equations and tables	Comments
Step 1. Tri-diagonal matrix coefficients are computed.	$d_{(i)} = s_{(i)} \alpha^{(I \text{ or } II)}$ and Table 7	As $s_{(i)}$ depends on the configuration of the PHE, it can be calculated by means of an algorithm.
Step 2. Tri-diagonal matrix construction.	Eq. (6)	
Step 3. Eigenvalues and eigenvectors are computed.		If one is using Matlab, one can use build-in functions.
Step 4. Linear system generation.	$\bar{A} \bar{C} = \bar{B}$ and Table 6	The boundary condition equations in algorithmic form of inlet fluids and change of pass are used.
Step 4.1. Generation of eigenvalues and eigenvectors matrix, \bar{A} , and the binary vector, \bar{B}^I .	$\bar{A} = \bar{A}^I + \bar{A}^{II}$ $\bar{B} = \bar{B}^I + \bar{B}^{II}$	The resulting matrices are the sum of the matrices of both sides of the PHE.
Step 5. Determination of c_i 's coefficients by solving the linear system.	$\bar{C} = \bar{B}^* \bar{A}^{-1}$	
Step 6. Determination of the output dimensionless temperatures.	Table 6	The boundary condition of output fluid in algorithmic form is used.
Step 7. Computation of thermal effectiveness.	$E = \begin{cases} E^I = \frac{N^I}{\alpha^I} \max\left(\frac{\alpha^I}{N^I}, \frac{\alpha^{II}}{N^{II}}\right) \theta_{in} - \theta_{out} ^I \\ E^{II} = \frac{N^{II}}{\alpha^{II}} \max\left(\frac{\alpha^I}{N^I}, \frac{\alpha^{II}}{N^{II}}\right) \theta_{in} - \theta_{out} ^{II} \end{cases}$	It may be obtained considering any side of the PHE, because the energy conservation is obeyed only if $E = E^I = E^{II}$.

Table 5. Simulation algorithm.

5.1. Simulation algorithm for the model using differential equations

For the development of this algorithm, the boundary conditions equations are used in the algorithm form described previously [6] (see Table 6). The simulation algorithm is applied separately for each value of ϕ separately. The algorithm is presented below.

6. Case study

A case study was used to test the developed algorithm and compare the two mathematical models. Data were taken from examples presented in [18]. A cold water stream exchanges heat with a hot water stream of process. As the closed-form equations only consider configurations with a maximum of 4 passes for each fluid, a case was chosen in which the reduced set only had configurations with less than 4 passes for each stream. Table 8 presents the data used. Only one type of plate was considered.

The RS was obtained by applying the optimization algorithm up to Step 3. The optimal set was found by applying Step 5. As only one type of plate was considered, the local optimum was

also the global optimum. The same optimal set was found with both approaches: two heat exchanger configurations with 144 channels and a 3-2 asymmetric pass arrangement (as presented in Table 9).

Boundary conditions for side I.	Fluid inlet	Fluid outlet
	For $n = 1$ to $n = N^I$ $\theta_{2n-1}(\eta = 0) = \theta_{in}^I$ end	$\theta_{out}^I = \frac{1}{N^I} \sum_{i=1}^{N^I} \theta_{2(p^I-1)N^I+2i-1} \left(\eta = \frac{(-1)^{p^I+1} + 1}{2} \right)$
	Change of pass	
	for $p = 2$ to $p = P^I$ for $n = 1$ to $n = N^I$ $\theta_{2(p-1)N^I+2n-1} \left(\eta = \frac{(-1)^p + 1}{2} \right) = \frac{1}{N^I} \sum_{i=1}^{N^I} \theta_{2(p-2)N^I+2i-1} \left(\eta = \frac{(-1)^p + 1}{2} \right)$ end end	
Boundary conditions for side II ($\phi = 1$).	Fluid inlet	Fluid outlet
	for $n = 1$ to $n = N^{II}$ $\theta_{2n}(\eta = 0) = \theta_{in}^{II}$ end	$\theta_{out}^{II} = \frac{1}{N^{II}} \sum_{i=1}^{N^{II}} \theta_{2(p^{II}-1)N^{II}+2i} \left(\eta = \frac{(-1)^{p^{II}+1} + 1}{2} \right)$
	Change of pass	
	for $p = 2$ to $p = P^{II}$ for $n = 1$ to $n = N^{II}$ $\theta_{2(p-1)N^{II}+2n} \left(\eta = \frac{(-1)^p + 1}{2} \right) = \frac{1}{N^{II}} \sum_{i=1}^{N^{II}} \theta_{2(p-2)N^{II}+2i} \left(\eta = \frac{(-1)^p + 1}{2} \right)$ end end	
Boundary conditions for side II ($\phi = 2$).	Fluid inlet	Fluid outlet
	for $n = 1$ to $n = N^I$ $\theta_{2n}(\eta = 1) = \theta_{in}^{II}$ end	$\theta_{out}^{II} = \frac{1}{N^{II}} \sum_{i=1}^{N^{II}} \theta_{2(p^{II}-1)N^{II}+2i} \left(\eta = \frac{(-1)^{p^{II}} + 1}{2} \right)$
	Change of pass	
	for $p = 2$ to $p = P^I$ for $n = 1$ to $n = N^I$ $\theta_{2(p-1)N^I+2n} \left(\eta = \frac{(-1)^{p+1} + 1}{2} \right) = \frac{1}{N^{II}} \sum_{i=1}^{N^{II}} \theta_{2(p-2)N^I+2i} \left(\eta = \frac{(-1)^{p+1} + 1}{2} \right)$ end end	
Boundary conditions for side II ($\phi = 3$).	Fluid inlet	Fluid outlet
	for $n = 1$ to $n = N^I$ $\theta_{2(p^{II}-1)N^I+2n}(\eta = 0) = \theta_{in}^{II}$ end	$\theta_{out}^{II} = \frac{1}{N^{II}} \sum_{i=1}^{N^{II}} \theta_{2i} \left(\eta = \frac{(-1)^{p^{II}+1} + 1}{2} \right)$
	Change of pass	
	for $p = 2$ to $p = P^I$ for $n = 1$ to $n = N^I$ $\theta_{2(p-2)N^I+2n} \left(\eta = \frac{(-1)^{p^{II}+p} + 1}{2} \right) = \frac{1}{N^{II}} \sum_{i=1}^{N^{II}} \theta_{2(p-1)N^I+2i} \left(\eta = \frac{(-1)^{p^{II}+p} + 1}{2} \right)$ end end	
Boundary conditions for side II ($\phi = 4$).	Fluid inlet	Fluid outlet
	for $n = 1$ to $n = N^I$ $\theta_{2(p^{II}-1)N^I+2n}(\eta = 1) = \theta_{in}^{II}$ end	$\theta_{out}^{II} = \frac{1}{N^{II}} \sum_{i=1}^{N^{II}} \theta_{2i} \left(\eta = \frac{(-1)^{p^{II}} + 1}{2} \right)$
	Change of pass	
	for $p = 2$ to $p = P^I$ for $n = 1$ to $n = N^I$ $\theta_{2(p-1)N^I+2n} \left(\eta = \frac{(-1)^{p^{II}+p+1} + 1}{2} \right) = \frac{1}{N^{II}} \sum_{i=1}^{N^{II}} \theta_{2(p-1)N^I+2i} \left(\eta = \frac{(-1)^{p^{II}+p+1} + 1}{2} \right)$ end end	

Table 6. Boundary conditions [6].

Side I	<pre> forp = 2 to p = P^I forn = 1 to n = N^I i = 2(p - 1)N^I + 2n - 1 s_i = (-1)^{p+1} end end </pre>
Side II	<pre> forp = 2 to p = P^I forn = 1 to n = N^I i = 2(p - 1)N^I + 2n - 1 if ϕ = 1: s_i = (-1)^{p+1} if ϕ = 1: s_i = (-1)^p if ϕ = 1: s_i = (-1)^{P^{II}+p} if ϕ = 1: s_i = (-1)^{P^{II}+p+1} end end </pre>

Table 7. Algorithm to define the flow direction [6].

Plate characteristics	
$L_p = 1.38 \text{ m}$	$\beta = 50^\circ$
$W_p = 0.535 \text{ m}$	$\Phi = 1.15$
$b = 3.7 \text{ mm}$	$t_p = 0.6 \text{ mm}$
$D_p = 150 \text{ mm}$	$k_p = 17 \text{ W/m}\cdot\text{K}$
Process-water	Cooling-water
$T_{in,hot} = 87.0 \text{ }^\circ\text{C}$	$T_{in,cold} = 20.0 \text{ }^\circ\text{C}$
$\dot{M}_{hot} = 26.0 \text{ kg/s}$	$\dot{M}_{cold} = 62.5 \text{ kg/s}$
Constraints	
$80 \leq N_C \leq 150$	$E^{min} = 90\%$
$10 \leq \Delta P_{hot} \leq 20 \text{ psi}$	$0 \leq \Delta P_{cold} \leq 25 \text{ psi}$
$v_{hot}^{min} = 0.0 \text{ m/s}$	$v_{cold}^{min} = 0.6 \text{ m/s}$

Table 8. Example data

It can be seen from the Tables that the simulations using the two models resulted in values that were very close. It is important to point out that the closed-form equations are only applicable when the end effects can be neglected (in the present case, when the number of thermal plates was greater than 40).

#	N_C	P^I	P^{II}	Y_h	E (differential equation model)				E (closed-form model)			
					$\phi=1$	$\phi=2$	$\phi=3$	$\phi=4$	$\phi=1$	$\phi=2$	$\phi=3$	$\phi=4$
1	80	1	2	0	80.1	80.3	80.3	80.1	80.4	80.4	80.4	80.4
2	80	2	1	1	80.3	80.1	80.3	80.1	80.4	80.4	80.4	80.4
3	81	1	2	0	80.3	80.3	80.3	80.3	80.6	80.6	80.6	80.6
4	83	2	1	1	80.5	80.5	80.5	80.5	80.8	80.8	80.8	80.8
5	84	1	2	0	80.5	80.8	80.8	80.5	80.9	80.9	80.9	80.9
6	84	2	1	1	80.8	80.5	80.8	80.5	80.9	80.9	80.9	80.9
7	85	1	2	0	80.8	80.8	80.8	80.8	81.0	81.0	81.0	81.0
8	87	2	1	1	80.9	80.9	80.9	80.9	81.2	81.2	81.2	81.2
9	88	1	2	0	80.9	81.2	81.2	80.9	81.3	81.3	81.3	81.3
10	88	2	1	1	81.2	80.9	81.2	80.9	81.3	81.3	81.3	81.3
11	89	1	2	0	81.2	81.2	81.2	81.2	81.4	81.4	81.4	81.4
12	91	2	1	1	81.4	81.4	81.4	81.4	81.6	81.6	81.6	81.6
13	92	1	2	0	81.3	81.6	81.6	81.3	81.7	81.7	81.7	81.7
14	92	2	1	1	81.6	81.3	81.6	81.3	81.7	81.7	81.7	81.7
15	93	1	2	0	81.6	81.6	81.6	81.6	81.8	81.8	81.8	81.8
16	95	2	1	1	81.7	81.7	81.7	81.7	82.0	82.0	82.0	82.0
17	96	1	2	0	81.7	81.9	81.9	81.7	82.1	82.1	82.1	82.1
18	96	2	1	1	81.9	81.7	81.9	81.7	82.1	82.1	82.1	82.1
19	97	1	2	0	81.9	81.9	81.9	81.9	82.2	82.2	82.2	82.2
20	144	2	3	0	71.8	71.7	92.8	92.9	71.8	71.8	93.0	93.0
21	144	3	2	1	71.7	71.8	92.8	92.9	71.8	71.8	93.0	93.0
22	149	3	2	1	71.7	71.7	93.0	93.0	71.7	71.7	93.2	93.2

■ Optimal configurations

Table 9. Thermal effectiveness of RS for both mathematical models

7. Conclusions

In this chapter it was presented the development of two models for the design and optimization of plate heat exchangers. Both mathematical models were used to accomplish the heat exchanger design simulations. These methods use differential equations and closed-form equations based on the notion that a multi-pass PHE can be reduced to an arrangement consisting of assemblies of single-pass PHEs.

As a case study, an example obtained from the literature was used. The optimal sets were the same for both approaches, and agreement was achieved between the effectiveness values. The model using algebraic equations has the limitation of only being applicable to PHEs sufficiently large not to be affected by end channels and channels between adjacent passes. However, industrial PHEs generally possess more than 40 thermal plates. The major advantage of using this model is its general applicability to any configuration, without having to derive a specific closed-form equation for each configuration. However, its drawback is the highly complex implementation of the simulation algorithm, unlike the second approach, which is very simple.

Nomenclature

A	Effective plate heat transfer area (m ²)
A_p	Plate effective area, m ²
$\frac{=}{A}$	Eigenvalues and eigenvectors matrix
b	Average thickness channel, m
\bar{B}	Binary vector
c_p	Specific heat, J/kg·K
C_r	Heat capacity ratio
\bar{C}	c_i coefficients vector
D_e	Equivalent diameter of the channel(m)
D_p	Port diameter of the plate(m)
E	Exchanger effectiveness, %
E_{CC}	Thermal effectiveness in purely countercurrent flow (%)
f	Fanning factor
g	Gravitational acceleration (m/s ²)
G_C	Channel mass velocity (kg/m ² s)
G_p	Port mass velocity (kg/m ² s)
IS	Initial set of configurations
k	Thermal conductivity(W/mK)
k_p	Plate thermal conductivity, W/m·K
L_p	Plate length, m
L_H	Horizontal port distance (m)
L_V	Vertical port distance (m)

\dot{m}	mass velocity per channel (kg/s)
\dot{M}	Mass flow rate, kg/s
\tilde{M}	Tri-diagonal matrix
N	Number of channels per pass
N_C	Number of channels
N_P	Number of plates
NTU	Number of transfer units
Nu	Nusselt number
OS	Optimal set of configurations
P	Number of passes
P_C	Temperature effectiveness
Pr	Prandtl number
Q	Heat transfer rate(J/s)
R	Heat capacity rate ratio
R_f	Fouling factor, K/W
Re	Reynolds number
RS	Reduced set of configurations
s_i	Binary parameter for flow direction
t_p	Plate thickness, m
U	Overall heat transfer coefficient, W/m ² ·K
v	Fluid velocity inside channels, m/s
W_P	Plate width, m
Y_h	Binary parameter for hot fluid location
Y_f	Binary parameter for type of channel flow
z_i	Eigenvector of the tri-diagonal matrix

Greek symbols

α	Heat transfer coefficient
β	Chevron corrugation inclination angle, degrees
ΔP	Pressure drop, Pa
ΔT_{lm}	Log-mean temperature difference (K)

ΔT_M	Effective mean temperature difference (K)
η	Normalized plate length
θ	Dimensionless fluid temperature
λ	Eigenvalue of the tri-diagonal matrix
μ	viscosity (Pa.s)
μ_w	Viscosity at wall temperature (Pa.s)
ρ	density (kg/m ³)
Φ	Enlargement factor of the plate area
ϕ	Parameter for feed connections position

Subscripts

<i>cold</i>	Cold fluid
CC	Countercurrent
<i>hot</i>	Hot fluid
<i>i</i>	Generic element
<i>in</i>	Inlet
<i>j</i>	Generic element
<i>out</i>	Outlet

Superscripts

I	Odd channels of the heat exchanger
II	Even channels of the heat exchanger
<i>max</i>	Maximum
<i>min</i>	Minimum

Author details

Fábio A.S. Mota^{1,2}, E.P. Carvalho² and Mauro A.S.S. Ravagnani^{2*}

*Address all correspondence to: ravag@deq.uem.br

1 National Institute for Space Research, São José dos Campos, SP, Brazil

2 Chemical Engineering Graduate Program - State University of Maringá, Maringá, PR, Brazil

References

- [1] Alfa Laval. Canada. Plate Heat Exchanger: A Product Catalogue for Comfort Heating and Cooling. Available in <[http://www. pagincorporated.com](http://www.pagincorporated.com)>. (Accessed 20 October 2010).
- [2] Sondex. Louisville. Plate Type Heat Exchangers: Operation & Maintenance Manual. Availble in <<http://www.sondex-usa.com>>. (Accessed 26April 2011).
- [3] Shah, R. K.; Sekulic, D. P. Fundamentals of Heat Exchanger Design. New Jersey: John Wiley & Sons, Inc. 2003. Page 24.
- [4] Taco. Craston. Plate Heat Exchanger: Operational and Maintenance Manual. Available in <<http://www.taco-hvac.com>>. (Accessed 18 May 2011).
- [5] Kakaç S., Liu H., Heat Exchanger: Selection, Rating and Thermal Design, 2ed. Boca Raton: CRC Press, 2002.
- [6] J. A. W. Gut, J. M Pinto, Modeling of Plate Heat Exchangers with Generalized Configurations. Int. J. Heat Mass Transfer 2003; 46:2571-2585.
- [7] Kho, T. Effect of Flow Distribution on Scale Formation in Plate Heat Exchangers. Thesis (PhD) – University of Surrey, Surrey, UK, 1998.
- [8] Wang L., Sundén B., Manglik R. M., *Plate Heat Exchangers: Design, Applications and Performance*, Ashurst Lodge: WIT Press, 2007, pp. 27-39.
- [9] Alfa Laval. Canada. Plate Heat Exchanger: Operational and Maintenance Manual. Available in <<http://www.schaufcompany.com>>. Accessed: 18 May 2011.
- [10] Lienhard IV, J. H.; Lienhard V, J. H. A Heat Transfer Textbook. 3ed. Cambridge: Phlogiston Press, 2004. Page 103.
- [11] Kandlikar, S. G.; Shah, R.K. Asymptotic Effectiveness-NTU Formulas for Multipass Plate Heat Exchangers. Journal of Heat Transfer, v.111, p.314-321, 1989.
- [12] Heggs, P. J. e Scheidat, H. J. Thermal Performance of Plate Heat Exchangers with Flow Maldistribution. Compact Heat Exchangers for Power and Process Industries, ed. R. K. Shah, T. M. Rudy, J. M. Robertson, e K. M. Hostetler, HTD, vol.201, ASME, New York, p.621-626, 1996.
- [13] Shah, R. K.; Kandlikar, S. G. The Influence of the Number of Thermal Plates on Plate Heat Exchanger Performance. In: MURTHY, M.V.K. et al. (Ed.) Current Research in Heat and Mass Transfer. New York: HemisTCPre P.C., 1988, p.227-241.
- [14] Kumar, H. The Plate Heat Exchanger: Construction and Design. 1st UK National Conference of Heat Transfer. n.86, p.1275-1286, 1984.
- [15] Gut J. A. W., Pinto J. M, Optimal Configuration Design for Plate Heat Exchangers. Int. J. Heat Mass Transfer 2004; 47:4833-4848.

- [16] Mota F. A. S., Ravagnani M. A. S. S., Carvalho E. P., Optimal Design of Plate Heat Exchangers. *Applied Thermal Engineering* 2014;63:33-39. 2013.
- [17] Hewitt, G. F.; Shires, G.L.; Bott, T.R. *Process Heat Transfer*. Boca Raton: CRC Press, 1994.
- [18] Gut, J. A. W.; *Configurações Ótimas de Trocadores de Calor a Placas*. 2003. 244p. Tese (Doutorado) – Escola Politécnica, Universidade de São Paulo, São Paulo, 2003.

Modelling of Global Heat Transfer by Local Cooling in Fusion Plasmas

Mikhail Tokar

Additional information is available at the end of the chapter

<http://dx.doi.org/10.5772/60642>

1. Introduction

Global reaction on very localized but intensive disturbances is a problem of interest for diverse physical media and systems. In devices for magnetic nuclear fusion such conditions arise, e.g., if a significant inflow of neutral particles, either of the working hydrogen isotopes or of impurities, enter the plasma. These inflows can occur both spontaneously and be created deliberately. Even particles enter the plasma through spots with dimensions much smaller than those of the plasma boundary their density is so high that the local plasma can be perturbed very substantially. One of the most important channels for perturbations is the local cooling of the plasma through the energy losses on the excitation and ionization of inflowing neutral particles. Although such distortions are triggered very locally, they can spread in the plasma far from the position of their origin. Thus, the heat conduction along magnetic surfaces towards the region, where the plasma is directly cooled down by intruding particles, may decrease the temperature in remote plasma. The drop of the pressure, induced by cooling in the neutral cloud, triggers plasma flow resulting in a reduction of the plasma density far away from the perturbation source. If neutral particles are injected for diagnostic purposes [1] it is desirable to keep distortions in the plasma as small as possible, to get trustful information about the original plasma state. In other cases, e.g., by a massive gas injection (MGI) [2], used to mitigate plasma disruptions in Tokamak devices [3], the impact has to be maximized. Generally, the changes induced in the plasma parameters are determined both by the duration of the injection and by the number of injected particles. Depending on the application type these characteristics change in extremely broad ranges. Thus by laser-induced ablation spectroscopy, LIAS [4], an intense laser pulse irradiates a small part of the device wall during an extremely short time in the nanosecond-range. By measuring the intensity of impurity line emission in the plasma one can assess the amount of particles emitted by the radiation, normally of the order of 10^{16-17} , and judge about the wall composition. This diagnostics is designed as a passive non-invasive one and negligible

modifications in the background plasma are expected by LIAS. In MGI experiments up to 10^{23-24} impurity neutral particles are injected through valves if special magnetic coils record precursors of a disruption. This results in a strong cooling of the whole plasma through radiation during several *ms* and the generation of relativistic electrons, being extremely dangerous for the wall, can be avoided. Besides a deliberate injection strong localized sources of neutrals can arise in fusion plasmas spontaneously, often if some critical phenomena, limiting the discharge performance, develop. For example at the so called "density limit" where the confinement of energy in the plasma deteriorates suddenly by approaching to some critical density [5], inflows of neutrals from certain wall spots increase tremendously. Multifaceted asymmetric radiation from the edge (MARFE) is a prominent example of such phenomena [6].

Understanding, modelling and prediction of the behaviour of plasmas affected by intense localized inflows of neutral particles is of importance for designing of injection systems and for controlling of conditions critical for performance. This is, however, a very demanding task, including a self-consistent description of non-linear processes of extremely different scales in time and space, from *ns* and *mm* till *s* and *km*, respectively. A consistent approach has to be based on time-dependent three-dimensional simulations. Presently there are, however, principal limitations to perform such calculations, mostly because various physical mechanisms are non-linearly interrelated and parallelization of time-dependent calculations is impracticable. Estimates [7] show that a realization of such a comprehensive approach to obtain reasonably accurate solutions during a time shorter than a year is still out of possibilities even of the most modern computers. To overcome technical problems outlined and to obtain an approximate but accurate enough model for the phenomena in question a new reduced approach has been elaborated [7-9]. It is based on reduction of three-dimensional fluid transport equations for particle, parallel momentum and energy transfer for all neutral and charged components of the plasma to a set of one-dimensional equations describing the time variation of the radial profiles for several parameters characterizing 3-D solutions although crudely but exhaustively enough.

For impurity spreading from a localized source it takes into account that the cross-sections by magnetic surfaces of the regions occupied by different neutral and charged species represent nested shells with dimensions increasing with the particle charge. This approach, named "shell model" [7, 8], allows assessing the characteristic density of the species and dimensions of their shells along and across magnetic field lines. By comparing with direct numerical solutions [8, 9], the approximations done in the "shell model" have been proven to be sufficiently accurate. By describing the main plasma components, a two zone approximation (TZA) has been elaborated presuming the separation of magnetic surfaces into cooled and hot zones. In the former one the energy is dissipated in direct interactions with injected particles, and the latter one is cooled down by the transfer, predominantly with the parallel heat conduction, to the cooled zone [9]. The radial profiles of the temperatures of plasma components in both zones are governed by one-dimensional heat balance equations interrelated non-linearly through the heat and particle fluxes between zones. A firm determination of these fluxes on the basis of two-dimensional transport equations [10] tremendously slows down numerical calculations. Therefore an assessment on the basis of a minimum entropy production principle [11] has been utilized in the TZA approach [9, 12]. It allows to relate analytically the heat fluxes between cooled and hot zones with the average temperatures in the zones. In addition to extreme savings in the

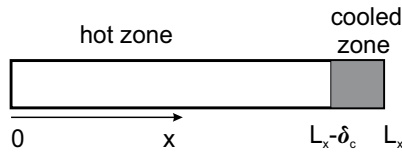


Figure 1. One-dimensional plasma stripe with an intense heat sink llocalized in the small segment of the stripe $L_x - \delta_c \leq x \leq L_x$.

CPU time, this approach allows to implement straightforwardly the so called heat flux limit [13], restricting the heat flux to a fraction of the free-streaming one if the temperature decay length becomes small compared to the mean free path length of electrons. The present paper is mostly devoted to a sophisticated test of the models being on the ground of the TZA, by comparing its predictions with the results of direct numerical solutions in one- and two-dimensional configurations. As examples for application the plasma edge cooling by argon MGI into JET and plasma distortions by LIAS in TEXTOR are modelled and the results of calculations are compared with the experimental data.

2. One-dimensional configuration

2.1. Numerical solution

Our consideration begins with a one-dimensional model for the transport in a plasma stripe along the magnetic field oriented in the direction x , as it is shown in figure 1. This situation is typical for the scrape-off layer (SOL) in a limiter tokamak like TEXTOR [14]. We consider the reaction of the whole plasma stripe on a cooling which is suddenly initiated at time $t = 0$ in a small fraction of the stripe through, e.g., energy losses on the excitation of injected impurity. The plasma is characterized by the temperature $T(t, x)$ and the deviation of T from its initial homogeneous level T_0 is governed by the following heat conduction equation

$$1.5\partial_t T - \partial_x (\chi \partial_x T) = \nu_h (T_0 - T) - \nu_l E_l \tag{1}$$

Here $\chi = \kappa/n$, with n being the plasma density and κ the heat conduction of plasma electrons; the latter is assumed here in the Spitzer-Härm approximation [15], i.e. $\kappa = A_e T^{2.5}$ with $A_e = 10^{20} eV^{-2.5} cm^{-1} s^{-1}$; the former term on the right hand side (rhs) is the heat source, maintaining $T(t < 0, x) = T_0$ in a steady equilibrium; the latter term is the localized energy loss activated at $t \geq 0$ in the region $L_x - \delta_c \leq x \leq L_x$ with $\delta_c \ll L_x$; this is assumed dependent on the electron temperature, $\nu_l = \nu_0 \exp(-E_l/T)$, to take into account that the excitation rate drops sharply if the electron temperature reduces below the excitation energy E_l of injected particles. The boundary condition correspond zero heat conduction through the borders of the computation domain, $\partial_x T(t, x = 0) = \partial_x T(t, x = L_x) = 0$.

Henceforth the temperature profile is characterized by its values averaged over the hot, $0 \leq x \leq L_x - \delta_c$, and cooled, $L_x - \delta_c \leq x \leq L_x$, zones of the plasma stripe:

$$\langle T \rangle_h = \int_0^{L_x - \delta_c} T(t, x) \frac{dx}{L_x - \delta_c}, \quad \langle T \rangle_c = \int_{L_x - \delta_c}^{L_x} T(t, x) \frac{dx}{\delta_c} \tag{2}$$

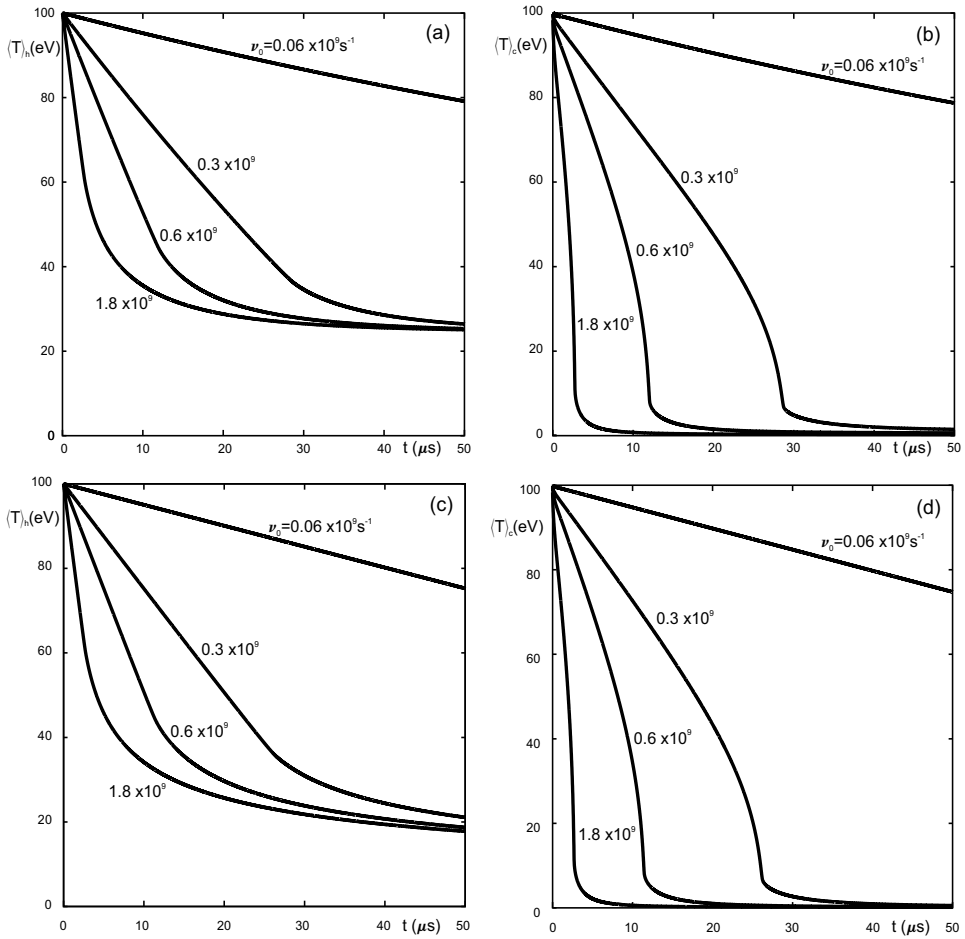


Figure 2. The time evolution of the temperature values averaged over the hot (a,c) and cooled (b,d) zones, computed by solving equation (1) numerically for $\nu_h = 10^4 s^{-1}$ (a,b) and $\nu_h = 10^2 s^{-1}$ (c,d), with different cooling rates ν_0 .

Figure 2 demonstrates the time variation of $\langle T \rangle_{h,c}$ computed by solving equation (1) with numerical methods outlined in Ref.[16], for different combinations of the parameters ν_h and ν_0 ; other parameters involved into the problem are typical for the SOL plasma in TEXTOR with injected carbon impurity: $L_x = 10m$, $\delta_c = 0.1m$ and $E_l = 1.26eV$. The main conclusion from these results is the existence for sufficiently large ν_0 of phase with sudden acceleration in the temperature drop in the cooled zone. This fact is related to a cooling instability predicted in references [17, 18] on the basis of zero-dimensional models and discussed deeper below.

2.2. Two-zone approximation

As it was claimed above the main aim of the present study is to develop reduced models to describe global impacts of local cooling in *three-dimensional* configurations. This would give a possibility to model phenomena in question without direct 3-D non-stationary calculations, being presently out of possibilities of even the most modern computers. An important

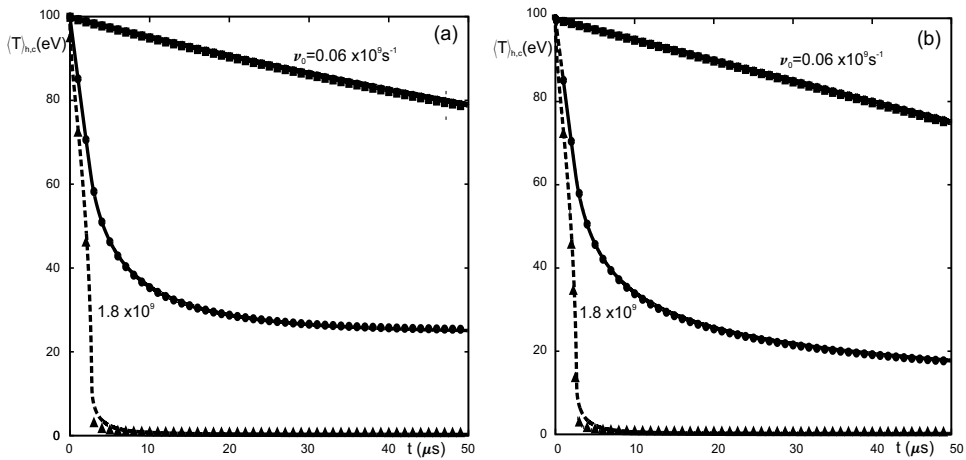


Figure 3. The time evolution of the temperature values averaged over the hot (solid curves, crosses and circles) and cooled (dashed curves, boxes and triangles) zones, computed by solving equation (1) numerically (curves) and by using TZA equations (symbols) for $\nu_h = 10^4 \text{s}^{-1}$ (a) and $\nu_h = 10^2 \text{s}^{-1}$ (b), with different cooling rates ν_0 .

element of this complex of models is a two-zone approximation (TZA) of the transport on magnetic surfaces. The latter is dominated by transfer along magnetic field lines and therefore it is instructive to start with elaborating of such an approximation in the one-dimensional case. By integrating equation (1) over the hot and cooled zones we get the following ODE, governing the time evolution of $\langle T \rangle_h$ and $\langle T \rangle_c$:

$$1.5\partial_t \langle T \rangle_h + \frac{q_{hc}}{n(L_x - \delta_c)} = \nu_h (T_0 - \langle T \rangle_h), \quad (3)$$

$$1.5\partial_t \langle T \rangle_c - \frac{q_{hc}}{n\delta_c} = \nu_h (T_0 - \langle T \rangle_c) - \langle \nu \rangle_c E_I \quad (4)$$

Here q_{hc} is the density of the heat flux conducted from the hot zone to the cooled one. To assess this approximately we apply approaches developed in reference [19] and proceed from equation (1) in the form:

$$\partial_x (\chi \partial_x T) = Q \quad (5)$$

with the term Q combining all other contributions in equation (1) besides the heat conduction one. The main assumption of the two-zone approximation is: in both zones Q can be approximated by some *a priori* unknown functions of time, $Q_h(t)$ and $Q_c(t)$, respectively, being **independent** of x . Under this assumption equation (5) can be analytically integrated for $\chi \sim T^\beta$. By exploiting the continuity of T and $\partial_x T$ at the zone interface, we get:

$$T(t, 0 \leq x \leq L_x - \delta_c) = T_h(t) \phi_h \left(\xi \equiv \frac{x}{L_x - \delta_c} \right) \quad (6)$$

$$T(t, L_x - \delta_c \leq x \leq L_x) = T_c(t) \phi_c \left(\xi \equiv \frac{L_x - x}{\delta_c} \right) \quad (7)$$

where $T_h \equiv T(t, x = 0)$, $T_c \equiv T(t, x = L_x)$ and the functions ϕ_h and ϕ_c of $0 \leq \xi \leq 1$ are given by the relations:

$$\phi_h = \left[1 - (1 - \theta^{\beta+1}) \left(1 - \frac{\delta_c}{L_x} \right) \xi^2 \right]^{1/(\beta+1)}, \quad \phi_c = \left[1 + (1/\theta^{\beta+1} - 1) \frac{\delta_c}{L_x} \xi^2 \right]^{1/(\beta+1)} \quad (8)$$

with $\theta = T_c/T_h$. The temperatures at the stripe edges, T_h and T_c , have to be related to $\langle T \rangle_h$ and $\langle T \rangle_c$ according to the definitions (2). With the profiles obtained above we get

$$T_{h,c} = \langle T \rangle_{h,c} / \langle \phi \rangle_{h,c}$$

and θ is determined from the transcendent equation

$$\theta = \frac{\langle T \rangle_c \langle \phi \rangle_h(\theta)}{\langle T \rangle_h \langle \phi \rangle_c(\theta)}$$

Finally, for the Stirzer-Härm formula for the heat conduction, with $\beta = 2.5$:

$$q_{hc} = \frac{4A_e}{7} \frac{T_h^{3.5} - T_c^{3.5}}{L_x} \quad (9)$$

In figure 3 we compare the time variation of $\langle T \rangle_h$ and $\langle T \rangle_c$ calculated from equations (3) and (4) with those found by direct numerical integration of equation (1). The agreement between two approaches is nearly perfect, both for low and for high level of the cooling. Thus the relation (9) for the heat outflow from the hot zone to the cooled one provides a firm basis to describe local and global heat transfer induced by a strongly localized cooling. By concluding this subsection we discuss shortly the phenomenon of cooling instability. It develops since the heat conduction influx into the cooled zone becomes saturated with reducing $\langle T \rangle_c$, see equation (9), and cannot compete with the local cooling there if ν_0 is large enough. The existence of a threshold for cooling instability is demonstrated in figure 4 by the time variation of $\langle T \rangle_c$ computed in the TZA for different magnitudes of ν_0 : there is a characteristic change in the behaviour of the cooled zone temperature occurring by a slight change of ν_0 in the range $7.2 - 7.8 \times 10^7 \text{s}^{-1}$.

2.3. Assessment of other approximations

Consider now the role of physical effects neglected in equation (1): heat transfer by electron-ion coulomb collisions, particle convection caused by the pressure drop in the cooled plasma zone, the induced change in the plasma density, etc. For this purpose we use now the following system of equations, describing the evolution of the electron and ion temperature T_e and T_i , respectively:

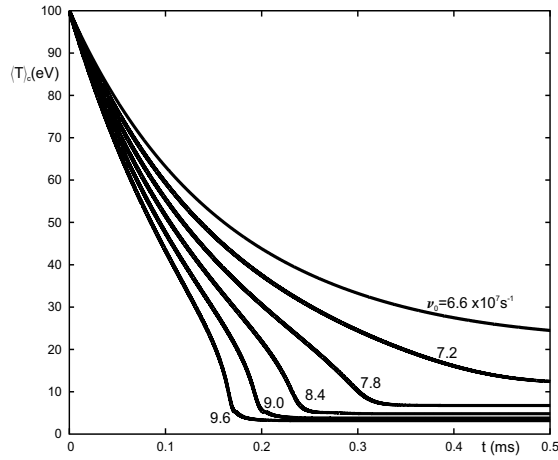


Figure 4. The time evolution of the temperature value averaged over the cooled zone and computed with slightly different cooling rates ν_0 in the vicinity of the cooling instability threshold.

$$1.5\partial_t P_e + \partial_x (2.5\Gamma T_e - \kappa_e \partial_x T_e) = n\nu_h (T_0 - T_e) - Q_{ei} - \nu_I n E_I \quad (10)$$

$$1.5\partial_t P_i + \partial_x (2.5\Gamma T_i - \kappa_i \partial_x T_i) = n\nu_h (T_0 - T_i) + Q_{ei} \quad (11)$$

where $P_{e,i} = nT_{e,i}$ are the pressures of the plasma components, $Q_{ei} = \frac{3m_e}{m_i} \frac{n}{\tau_{ei}} (T_e - T_i)$ is collisional heat exchange between electrons and ions, with m_e and m_i being the electron and ion masses, correspondingly, and $\tau_{ei} \sim T_e^{1.5}/n$ the time between electron-ion coulomb collisions. The plasma density n and the particle flux density Γ are governed by particle continuity and momentum conservation equations:

$$\partial_t n + \partial_x \Gamma = \nu_n (n_0 - n) \quad (12)$$

$$\partial_t \Gamma + \partial_x \left(\frac{\Gamma^2}{n} + n \frac{T_e + T_i}{m_i} \right) = -\nu_I \Gamma \quad (13)$$

with the terms in the rhs of equations (12) and (13) ensuring the stability of the stationary state with $n = n_0$ and $\Gamma = 0$ before the initiation of the local cooling. The boundary conditions to equations (12) and (13) correspond to the impenetrability of the stripe borders for particles, $\Gamma(t, x = 0) = \Gamma(t, x = L_x) = 0$.

The TZA for the system of equations (10)-(13) follows from the averaging of them over the hot and cooled zones:

$$1.5\partial_t \langle P_e \rangle_h + \frac{q_{hc,e}}{L_x - \delta_c} = \nu_h \langle \langle n \rangle_h T_0 - \langle P_e \rangle_h \rangle - \frac{3m_e}{m_i} \left\langle \frac{n}{\tau_{ei}} (T_e - T_i) \right\rangle_h \quad (14)$$

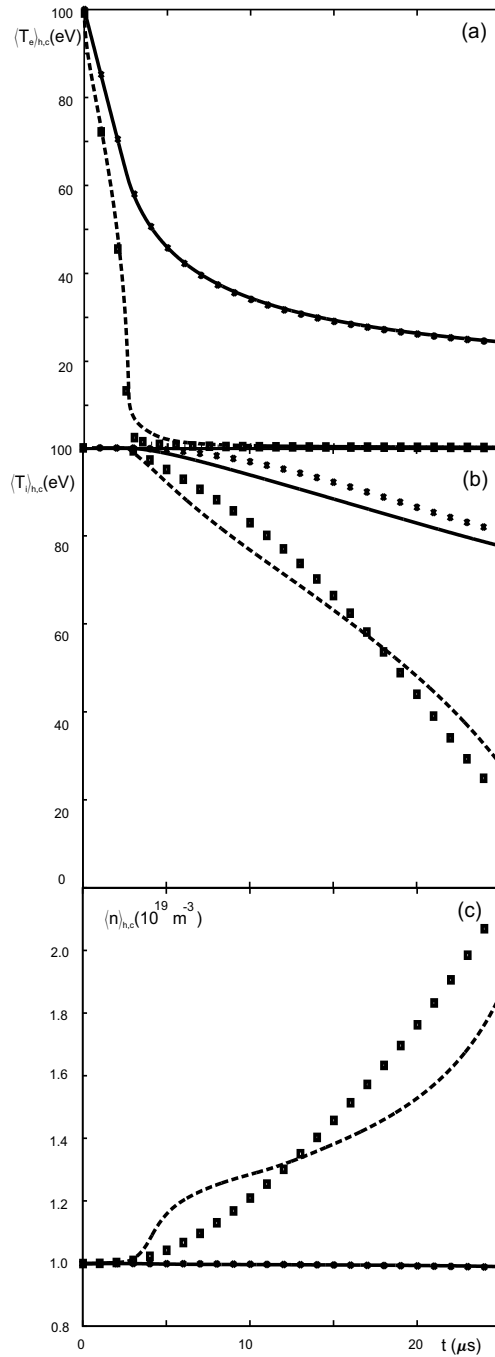


Figure 5. The time evolution of the plasma parameters averaged over the hot (solid curves and stars) and cooled (dashed curves and boxes) zones computed numerically (curves) and with TZA equations (symbols) for $\nu_{hi} = 10^2 \text{s}^{-1}$ and $\nu_0 = 1.8 \times 10^9 \text{s}^{-1}$: electron temperature (a), ion temperature (b) and plasma density (c).

$$1.5\partial_t \langle P_e \rangle_c - \frac{q_{hc,e}}{\delta_c} = \nu_h (\langle n \rangle_c T_0 - \langle P_e \rangle_c) - \frac{3m_e}{m_i} \left\langle \frac{n}{\tau_{ei}} (T_e - T_i) \right\rangle_c - \langle \nu_1 n \rangle_c E_l \quad (15)$$

$$1.5\partial_t \langle P_i \rangle_h + \frac{q_{hc,i}}{L_x - \delta_c} = \nu_h (\langle n \rangle_h T_0 - \langle P_i \rangle_h) + \frac{3m_e}{m_i} \left\langle \frac{n}{\tau_{ei}} (T_e - T_i) \right\rangle_h \quad (16)$$

$$1.5\partial_t \langle P_i \rangle_c - \frac{q_{hc,i}}{\delta_c} = \nu_h (\langle n \rangle_c T_0 - \langle P_i \rangle_c) + \frac{3m_e}{m_i} \left\langle \frac{n}{\tau_{ei}} (T_e - T_i) \right\rangle_c \quad (17)$$

$$\partial_t \langle n \rangle_h + \frac{\Gamma_{hc}}{L_x - \delta_c} = \nu_n (n_0 - \langle n \rangle_h) \quad (18)$$

$$\partial_t \langle n \rangle_c - \frac{\Gamma_{hc}}{\delta_c} = \nu_n (n_0 - \langle n \rangle_c) \quad (19)$$

$$\partial_t \langle \Gamma \rangle + \frac{P_{ec} + P_{ic} - P_{eh} - P_{ih}}{m_i L_x} = -\nu_\Gamma \langle \Gamma \rangle \quad (20)$$

where Γ_{hc} is the density of the particle outflow from hot to cooled zone and $\langle \Gamma \rangle = \int_0^{L_x} \Gamma(t, x) \frac{dx}{L_x}$. To relate the parameters at the zone edges, $f_{h,c,hc'}$ with those averaged over zones, $\langle f \rangle_{h,c'}$ we apply an approximate approach similar to that outlined in the previous section. We start by relating $\langle \Gamma \rangle$ and $\Gamma_{hc} = \Gamma(t, x = L_x - \delta_c)$. For this purpose equation (12) is represented as $\partial_x \Gamma = S$ where the source/sink term S is assumed as **independent** of x in each of the zones. With zero boundary conditions at $x = 0, L_x$ this results in:

$$\begin{aligned} \Gamma(0 \leq x \leq L_x - \delta_c) &= \Gamma_{hc} x / (L_x - \delta_c) \\ \Gamma(L_x - \delta_c \leq x \leq L_x) &= \Gamma_{hc} (L_x - x) / \delta_c \end{aligned}$$

and $\Gamma_{hc} = 2 \langle \Gamma \rangle$. Equation (13) is represented as $\partial_x [n(T_e + T_i)] = F$. The term on the rhs is mostly determined by the flux density Γ and the x -dependence of F in the zones is the same as in the relations above. Straightforward calculations result in the following density profile:

$$\begin{aligned} n(0 \leq x \leq L_x - \delta_c) &= n_h \frac{T_{eh} + T_{ih}}{T_e + T_i} (1 - \varphi_h) + n_c \frac{T_{ec} + T_{ic}}{T_e + T_i} \varphi_h \\ n(L_x - \delta_c \leq x \leq L_x) &= n_h \frac{T_{eh} + T_{ih}}{T_e + T_i} \varphi_c + n_c \frac{T_{ec} + T_{ic}}{T_e + T_i} (1 - \varphi_c) \end{aligned}$$

where $\varphi_h \left(\xi = \frac{x}{L_x - \delta_c} \right) = \left(1 - \frac{\delta_c}{L_x} \right) \xi^2$ and $\varphi_c \left(\xi = \frac{L_x - x}{\delta_c} \right) = \frac{\delta_c}{L_x} \xi^2$. With relations (6) and (7) assumed for the temperature profiles of electrons and ions we get:

$$n_h = \frac{\langle n \rangle_h \left(\mu_c^0 - \frac{\delta_c}{L_x} \mu_c^2 \right) - \langle n \rangle_c \frac{T_{ec} + T_{ic}}{T_{eh} + T_{ih}} \left(1 - \frac{\delta_c}{L_x} \right) \mu_h^2}{(\mu_h^0 - \mu_h^2) \mu_c^0 + \frac{\delta_c}{L_x} (\mu_h^2 \mu_c^0 - \mu_h^0 \mu_c^2)}$$

$$n_c = \frac{\langle n \rangle_c \left[\mu_h^0 - \left(1 - \frac{\delta_c}{L_x} \right) \mu_h^2 \right] - \langle n \rangle_h \frac{T_{eh} + T_{ih}}{T_{ec} + T_{ic}} \frac{\delta_c}{L_x} \mu_c^2}{(\mu_h^0 - \mu_h^2) \mu_c^0 + \frac{\delta_c}{L_x} (\mu_h^2 \mu_c^0 - \mu_h^0 \mu_c^2)}$$

where

$$\mu_h^0 = \int_0^1 \frac{T_{eh} + T_{ih}}{T_{eh} \phi_{eh} + T_{ih} \phi_{ih}} d\zeta, \quad \mu_c^0 = \int_0^1 \frac{T_{ec} + T_{ic}}{T_{ec} \phi_{ec} + T_{ic} \phi_{ic}} d\zeta,$$

$$\mu_h^2 = \int_0^1 \frac{T_{eh} + T_{ih}}{T_{eh} \phi_{eh} + T_{ih} \phi_{ih}} \zeta^2 d\zeta, \quad \mu_c^2 = \int_0^1 \frac{T_{ec} + T_{ic}}{T_{ec} \phi_{ec} + T_{ic} \phi_{ic}} \zeta^2 d\zeta.$$

Finally, for the pressures of the plasma components we obtain:

$$\langle P_{e,i} \rangle_h = (P_{eh} + P_{ih}) \left(\eta_{e,ih}^0 - \eta_{e,ih}^2 \right) + (P_{ec} + P_{ic}) \eta_{e,ih}^2,$$

$$\langle P_{e,i} \rangle_c = (P_{ec} + P_{ic}) \left(\eta_{e,ic}^0 - \eta_{e,ic}^2 \right) + (P_{eh} + P_{ih}) \eta_{e,ic}^2$$

with

$$\eta_{e,ih}^0 = \int_0^1 \frac{d\zeta}{1 + \frac{T_{i,eh} \phi_{i,eh}}{T_{e,ih} \phi_{e,ih}}}, \quad \eta_{e,ic}^0 = \int_0^1 \frac{d\zeta}{1 + \frac{T_{i,ec} \phi_{i,ec}}{T_{e,ic} \phi_{e,ic}}},$$

and

$$\eta_{e,ih}^2 = \left(1 - \frac{\delta_c}{L_x} \right) \int_0^1 \frac{\zeta^2 d\zeta}{1 + \frac{T_{i,eh} \phi_{i,eh}}{T_{e,ih} \phi_{e,ih}}}, \quad \eta_{e,ic}^2 = \frac{\delta_c}{L_x} \int_0^1 \frac{\zeta^2 d\zeta}{1 + \frac{T_{i,ec} \phi_{i,ec}}{T_{e,ic} \phi_{e,ic}}}$$

The ion heat conduction has the same temperature dependence as the electron one, $\kappa_i = A_i T_i^{2.5}$, but A_i is by the factor $\sqrt{m_e/m_i} \approx 0.016$ for deuterium plasmas smaller than A_e . Therefore the ion temperature, being reduced in the cooled zone by collisions with electrons cannot drop in the hot zone so fast as the electron one. Through $e-i$ collisions in the hot area this may slow down the drop of $\langle T_e \rangle_h$. However due to smallness of the mass ratio m_e/m_i coulomb collisions are very ineffective for the heat transfer between the plasma components. This confirmed by the results of calculations presented in figure 5 and by comparing them with those in figure 3. Again, the agreement between the time evolutions of $\langle T_e \rangle_h$ and $\langle T_e \rangle_c$ computed by direct numerical integration of equations (10)-(13) and that

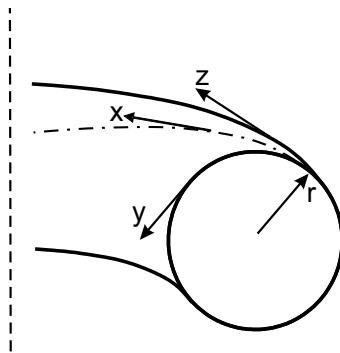


Figure 6. The tokamak geometry: x is the direction of the magnetic field whose lines of force create a closed magnetic surface of the minor radius r . All physical quantities are periodic in the toroidal and poloidal directions, z and y , correspondingly.

found from TZA equations (14)-(20) is nearly perfect. The results for $\langle T_i \rangle_h$, $\langle T_i \rangle_c$, $\langle n \rangle_h$ and $\langle n \rangle_c$ are less satisfactory, but also in this case the difference between the exact and TZA solutions is tolerable and does not exceed 20 %.

3. Two-dimensional configuration

In this section we consider transport along closed magnetic surfaces in fusion devices to a small cooled area on the surface and generalize the TZA on this case.

3.1. 2-D heat conduction equation for heat transport on a closed magnetic surface

In magnetic fusion devices, e.g., tokamaks, electric currents, flowing both in external coils and inside the plasma, produce magnetic field components both in the toroidal and poloidal directions and lines of force generate closed nested magnetic surfaces, see figure 6. The charged plasma constituents, i.e. electrons, deuterium-tritium and impurity ions, are magnetized. This allows to confine them inside the plasma volume during times exceeding by many orders of magnitude those spent by particles, moving with their thermal velocities, to wrap magnetic surfaces very tightly. Due to this fact the temperatures of the plasma components are normally very homogeneous on the surfaces. However, if there is a very localized position where plasma is suddenly cooled down, the temperatures may become strongly inhomogeneous and it is of interest to know how promptly the whole surface will get cold in response to the local distortion. Even under the dominance of heat transfer along field lines the heat conduction to the locally cooled area cannot be straightforwardly described by a one-dimensional equation (1). This is because the majority of magnetic surfaces is non-resonant so that a field line does not close on itself and makes infinite number of turns around the surface before two points on the line come infinitesimally close each other. Thus, the coordinate x along the magnetic field is not periodic and no boundary conditions can be imposed for equation (1). Nonetheless, one can introduce two periodic coordinates on the torus: z , aligned along the toroidal direction, and y - along the poloidal one. The periods for this coordinates are $L_z = 2\pi R$ and $L_y = 2\pi r$, respectively, with r and R being the minor and major radius of the toroidal surface. In the coordinates z and y equation (1) has the following form:

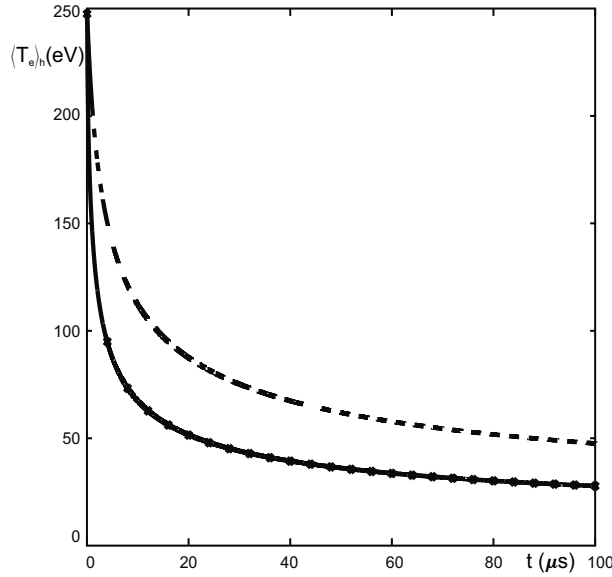


Figure 7. The time evolution after the start of MGI of the electron temperature averaged over the hot zone on the JET separatrix, computed with Spitzer-Härm formula for heat conduction for $v_h = 10^2 \text{s}^{-1}$ the solid curve has been obtained by solving equation (21) numerically, the dashed curve and symbols - by using TZA equations (22)-(24) without and with the correction of Sc in equation (24), respectively.

$$1.5\partial_t T - \cos^2 \psi \partial_z (\chi \partial_z T) - \sin^2 \psi \partial_y (\chi \partial_y T) - \sin \psi \cos \psi [\partial_y (\chi \partial_z T) + \partial_z (\chi \partial_y T)] = v_h (T_0 - T) - \nu_l E_l \quad (21)$$

where $\psi \ll 1$ is the inclination angle of the magnetic field to the toroidal direction z . The last cooling term is localized in the area $|L_z/2 - z|, |L_y/2 - y| \leq \delta_c/2$. By discretizing the derivatives with respect of one of coordinates, e.g., y , one reduces equation (21) to a set of one-dimensional PDE, similar to equation (1), which are solved by the same numerical approach. To construct a TZA for equation (21) we start again from equation (1). The only difference to the one-dimensional situation is that in the present case one does not know *a priori* the length L_x of the field line connecting the cooled zone with the hot rest of the surface. In reference [12] this is estimated by employing a principle of minimum entropy production [11]. By neglecting viscous and friction forces, the volume density of the entropy production rate is given as $\chi (\partial_l \ln T)^2$ [20]. For fixed $T_{h,c}$ the total entropy production rate in the parallel stripe is $\Theta \approx \delta_c q_{hc}$ with the heat flux density from hot to the cooled zone q_{hc} given by equation (9). Thus Θ is decreasing with increasing L_x and approaches its minimum when L_x reaches its maximum value corresponding to a parallel stripe covering tightly the whole magnetic surface. This corresponds to $L_x = L_z L_y / (2\delta_c) = S_s / (2\sqrt{S_c})$, where $S_s = 4\pi^2 r R$ is the total area of the magnetic surface and $S_c = \delta_c^2$ the area of the cooled zone. For the time evolution of the temperature values averaged over the hot and cooled zones on the magnetic surface we get:

$$1.5\partial_t \langle T \rangle_h + \frac{Q_{hc}}{n(S_s - S_c)} = v_h (T_0 - \langle T \rangle_h) \quad (22)$$

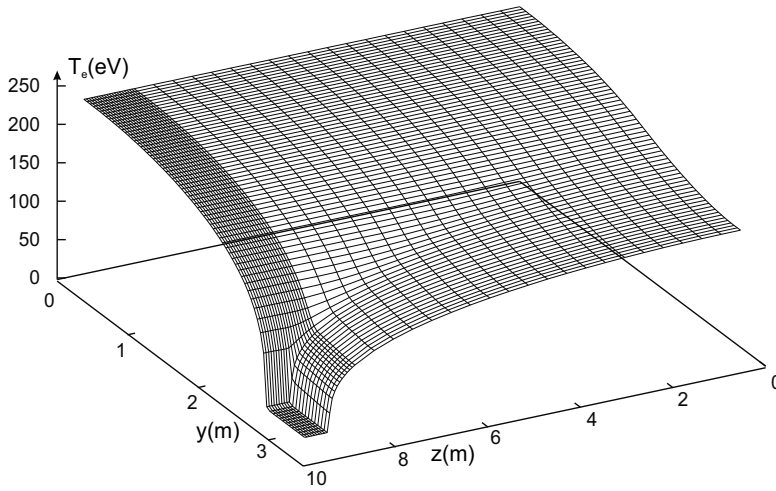


Figure 8. The calculated two-dimensional profile of the electron temperature at $t = 0.3\mu s$

$$1.5\partial_t \langle T \rangle_c - \frac{Q_{hc}}{nS_c} = v_h (T_0 - \langle T \rangle_c) - \langle v_l \rangle_c E_t \quad (23)$$

with the total heat outflow to the cooled zone:

$$Q_{hc} = \frac{16A_e S_c}{7 S_s} (T_h^{3.5} - T_c^{3.5}) \quad (24)$$

As an example of applications to 2-D configurations we consider experiments with massive gas injection into the tokamak JET to mitigate plasma disruptions [21, 22]. Calculations have been performed for the conditions on the magnetic separatrix between the confined plasma region and the SOL, with $R = 3m$ and $r = 1m$, the initial values of the electron temperature and density as in the shot 77808 with MGI into the H-mode plasma [22]: $n_0 = 10^{19}m^{-3}$ and $T_0 = 250eV$; the cooled area is a square with a side of $1m$, i.e. $S_c \approx 0.01S_s$, where the density of argon atoms is increased instantaneously up to $2 \times 10^{24}m^{-3}$. Curves in figure 7 represent the computed time evolution of the electron temperature values averaged over the hot zone found by solving 2-D equation (21) and 0-D TZA-equations (22)-(24). There is a noticeable difference between the results of both approaches, much larger than in the one-dimensional case discussed in the previous section. The cause of this discrepancy can be understood by looking on the calculated two-dimensional profile of the electron temperature displayed in figure 8. One can see that there is a very sharp gradient of the temperature at the border of the cooled zone, corresponding to $L_T \equiv |T/\partial_x T| \ll \delta_c$. For the heat conduction $\kappa \sim T^\beta$ the TZA approach predicts $L_T \geq \delta_c (\beta + 1) / 2$ at this position, i.e. $L_T \geq 7\delta_c / 4$ for the Spitzer-Härm approximation used above. This means that the area of the cooled zone is actually reduced in the TZA compared with that following from 2-D calculations. One can improve TZA predictions by increasing S_c in equation (24). Indeed, the TZA results obtained for the cooled zone enlarged by a factor of 4 are presented in figure 7 with stars and agree with 2-D calculations very good. As a rule of thumb one can estimate the enhancement factor for S_c in equation (24) as $1 + (\beta + 1)^2 / 4$.

3.2. Heat flux limit

Calculations in the previous section predict that after the initiation of the localized cooling the whole magnetic surface is cooled down during a time shorter than $10\mu s$. This is in a striking disagreement with the experimental data showing that such a global cooling requires at least half a millisecond. A possible cause for this discrepancy may be rooted in the fact that the Spitzer-Härm formula κ_{SH} has been used for the electron heat conduction. This approximation is deduced in the limit of a very small mean free path length between coulomb collisions for thermal particles, λ_{th} , compared to the characteristic dimension for the temperature change L_T ; it results in the heat flux density $q_e = q_{SH} \equiv -\kappa_{SH}\partial_x T$. Since $\kappa_{SH} \sim T^{5/2}$ the heat conduction increases very fast with rising temperature. However, $\lambda_{th} \sim T^2$ for coulomb collisions of charged particles. Thus, the SH-approximation can be violated in the case of strong local cooling where the temperature in the cooled zone drops much faster than that in the hot one and a region with strong temperature gradient arises. Actually, the SH-approximation is violated already if the free path of particles carrying heat, λ_{hcp} , exceeds L_T . The energy of such particles is by an order of magnitude larger than T and $\lambda_{hcp} \approx 100\lambda_{th}$. In a collision-less limit, $\lambda_{hcp} \gg L_T$, heat is transported because more hotter particles escape from the region in question compared to colder particles entering it. This would lead to a free-streaming heat flux with the density $q_e = q_{FS} \simeq nT^{3/2}/\sqrt{m}$ [23, 24]. However, interpretation of laser fusion experiments [13] and experiments with heating of magnetic islands in TEXTOR [25, 26] led to the conclusion that for electrons this heat flux level is strongly reduced by the so called heat flux limit (HFL) factor, $0.02 \leq \zeta_{HFL} \leq 0.1$. Two physical mechanisms can explain such a strong reduction of q_e . First, non-local effects in collision-less plasma reduce the perturbation in the distribution function caused by the temperature gradient and resulting in heat conduction [27]. Second, light electrons are braked by the ambipolar electric field, arising because heavy ions lag behind electrons and a charge separation is induced [24]. A smooth transition between collisional and collision-less limits can be described by the formula [13], $q_e = \zeta_{HFL}q_{FS}q_{SH} / (\zeta_{HFL}q_{FS} + q_{SH})$, and resulting in

$$\kappa_e \approx \kappa_{HFL} = \frac{\kappa_{SH}}{1 + \lambda_{hcp}/L_T} \quad (25)$$

The dependence of κ_e in equation (25) on the temperature gradient makes the procedure of numerical integration of equation (1) very unstable. This is extremely exaggerated by the fact that q_e becomes actually independent of the temperature gradient for $\lambda_{hcp} \gg L_T$, i.e., the heat flow is convective and the heat conduction equation (1) becomes actually an equation of the first order. Therefore, often the relation (25) is approximated by a simple decrease of κ_{SH} . Here for rough estimates we assume $L_T \approx L_x$. For the parameters on the JET separatrix we get $L_x \approx 55m \ll \lambda_{hcp} \approx 6250m$, and equation (25) provides $\chi = \kappa/n \approx 10^9 m^{-1} s^1$. Thus, the characteristic time for cooling of the magnetic surface $t_{cool} \approx L_x^2/\chi \approx 0.3ms$, in good agreement with the experiment [21, 22], especially by taking into account that the electron temperature and χ are reducing as the cooling progresses. Another argument for the relevance of the equation (25) is the fact that for $\lambda_{hcp} \gg L_T$ it provides $\chi \sim \sqrt{T}$ and, thus, t_{cool} depends weakly on the experimental conditions. This agrees with the experimental observation [21, 22] showing that t_{cool} is practically the same for the magnetic surfaces with the initial temperatures of $250eV$ and $400eV$. For $\kappa_e \approx \kappa_{SH}$ this would result in t_{cool} differing by a factor of 3.

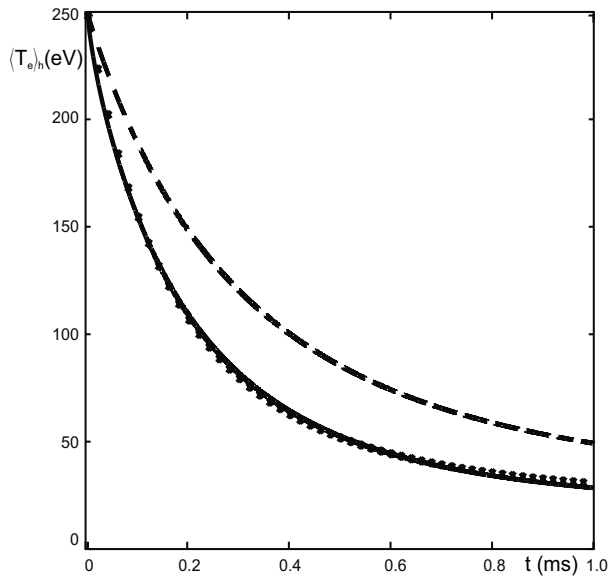


Figure 9. The time evolution after the start of MGI of the electron temperature averaged over the hot zone on the JET separatrix, computed with the heat flux limit for $\nu_h = 10^2 s^{-1}$; the solid curve has been obtained by solving equation (21) numerically, the dashed curve and symbols - by using TZA equations (22)-(24) without and with the correction of Sc in equation (24), respectively.

To generalize the TZA by including the HFL, we estimate λ_{hcp} at $\hat{T} = (T_h + T_c) / 2$ and assume $1/L_T = (T_h - T_c) / L_x / \hat{T}$. This results in $\lambda_{hcp} / L_T = 0.05 (T_h^2 - T_c^2) / (nL_x)$, where the temperatures are measured in electron-volts, plasma density - in $10^{19} m^{-3}$ and L_x - in m . Since now $\kappa \sim \sqrt{T}$, one would expect that a significantly smaller, compared to the temperature dependence of $\kappa_{SH} \sim T^{5/2}$, increase of the cooled zone area in the TZA approach is necessary to reproduce well the 2-D calculations. Figure 9 shows the time evolution of the $\langle T \rangle_h$ calculated for the conditions at the JET separatrix, by taking into account the approximate assessment above for the heat flux limit. One can see that both 2-D and corrected TZA approaches reproduce well the found experimentally [21, 22] characteristic time of 0.5ms for the temperature drop far from the cooled area.

4. Three-dimensional configuration

4.1. Basic equations

The TZA elaborated in previous sections for 1-D and 2-D situations provides a basis for modelling with reasonable accuracy and CPU time of the global response on a local cooling in a three-dimensional case, e.g., by injection of impurities into a tokamak plasma. The 3-D heat transport equation for electrons has the form:

$$\begin{aligned} \partial_t (1.5n_e T_e) + \partial_r (r q_r) / r - \cos^2 \psi \partial_z (\kappa_{||} \partial_z T_e) - \sin^2 \psi \partial_y (\kappa_{||} \partial_y T_e) \\ - \sin \psi \cos \psi \left[\partial_y (\kappa_{||} \partial_z T_e) + \partial_z (\kappa_{||} \partial_y T_e) \right] = Q_h - Q_{loss} \end{aligned} \quad (26)$$

Here we take into account that in fusion devices the electron density n_e varies with the third coordinate, the minor radius r of magnetic surfaces, and the parallel heat conduction of electrons, $\kappa_{||}$, is used in this equation instead of the heat conductivity $\chi = \kappa/n$ used in equation (1). The heat flux density across the magnetic surfaces includes both conduction and convection contributions:

$$q_r = -\kappa_r \partial_r T_e + 1.5 \Gamma_r T_e$$

where κ_r and Γ_r are the heat conduction and density of the electron flux in the radial direction; Q_h is the density of heating power due to different mechanisms, such as Ohmic dissipation of the plasma current, energetic neutral beams, radio-frequency electromagnetic waves, etc.; henceforth the r -dependences of κ_r , Γ_r and Q_h are prescribed and assumed constant in time. The localized cooling is described by the term Q_{loss} . Before its initiation at $t = 0$ the quasi-stationary state is maintained by the balance of heating and radial heat outflow toward the plasma edge. In the SOL region, $r_s \leq r \leq r_w$, where r_s is the radius of the last closed magnetic surface (LCMS) and r_w that of the device wall, the heat is additionally lost along the magnetic field lines to limiter or divertor target plates. The boundary conditions to equation (26) are imposed at the plasma axis, $r = 0$, where $\partial_r T = 0$, and at the wall, $r = r_w$, where the so called e -folding length δ_T is fixed and $\partial_r T = -T/\delta_T$.

By deducing the TZA-equations for $\langle T \rangle_{h,c}(t, r)$ we have to take into account a possible variation of the cooled and hot zone areas, S_c and $S_h = S_s - S_c$, respectively, with t and r . The averaging of equation (26) over the zones results in:

$$\begin{aligned} \partial_t (1.5 S_h n_e \langle T_e \rangle_h) + S_h \partial_r [r (-\kappa_r \partial_r \langle T_e \rangle_h + 1.5 \Gamma_r \langle T_e \rangle_h)] / r = \\ = S_h (Q_h - Q_{SOL}) - Q_{hc} \end{aligned} \quad (27)$$

$$\begin{aligned} \partial_t (1.5 S_c \langle n_e T_e \rangle_c) + S_c \partial_r [r (-\kappa_r \partial_r \langle T_e \rangle_c + 1.5 \Gamma_r \langle T_e \rangle_c)] / r = \\ = S_c (Q_h - Q_{SOL}) - W_{loss} \end{aligned} \quad (28)$$

where Q_{SOL} is non-zero for $r_s \leq r$ and gives the heat loss to the target plates, see reference [28]; the heat outflow to the cooled zone is computed by taking into account the heat flux limit and the correction due to smoothing in the TZA of the temperature gradient at the border between zones:

$$Q_{hc} = 4A_e \frac{T_h^{3.5} - T_c^{3.5}}{\frac{S_s}{S_c} + 0.1 \frac{T_h^2 - T_c^2}{n \delta_c}} \quad (29)$$

the plasma density in the hot zone is assumed unchanged, but if the local cooling is caused by the injection of neutral particles, n_e may be modified in the cooled one due to the ionization of these particles; W_{loss} is the integral of the loss term Q_{loss} over the cooled zone.

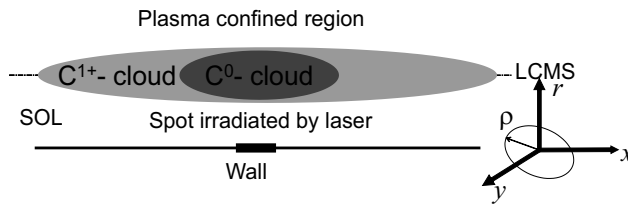


Figure 10. Spreading in the plasma of impurity (carbon) particles released from the wall by LIAS.

4.2. Example of application: Plasma distortion by laser-induced ablation spectroscopy

Laser-based diagnostics have been proposed to measure and monitor *in situ* the composition of layers on plasma facing components (PFC) [4]. By laser-induced ablation spectroscopy (LIAS) a short, in nanosecond-range, intense laser pulse is directed at the PFC during a plasma discharge. Particles of the PFC material, released into the plasma, are excited and ionized by electrons. By measuring the intensity of impurity line radiation, one can assess the amount of particles emitted and judge about the wall composition. To interpret LIAS measurements local plasma parameters, especially the electron density and temperature, have to be known. Normally the parameters, measured somewhere at the plasma edge before the LIAS application, are used. However, processes with particles released from the wall may lead to significant disturbances in the plasma: the energy loss on the particle excitation leads to reduction of the electron temperature, the delivery of new electrons by the ionization - to the increase of their density. An assessment of such perturbations is of importance for quantitative interpretation of measurements [29].

Consider the spreading of carbon particles released by the laser pulse from the wall, see figure 10. The penetration depth of these species is usually significantly smaller than the radius r_w of the wall element in question. Therefore, it is convenient to use an orthogonal coordinate system with the axes r , directed from the plasma to the injection spot, x and y , being tangential to the magnetic surface and oriented parallel and perpendicular to field lines, respectively, see figure 10. The velocity distribution of neutral particles is identical in the directions x and y and the distribution function can be characterized by its dependence on the velocity components V_r and V_ρ in a cylindrical reference system with axes r and $\rho = \sqrt{x^2 + y^2}$. At the wall the fraction of such particles in the total density n_0 of neutrals is $f(V_r, V_\rho) dV_r dV_\rho$, where the distribution function $f(V_r, V_\rho)$ is assumed as a Maxwellian one at the temperature T_0 with respect to V_ρ and a one-side Maxwellian, shifted with the drift velocity V_m , for V_r [30]:

$$f(V_r, V_\rho) = \frac{4V_\rho}{\sqrt{\pi} [1 + \operatorname{erf}(V_m/V_{th})] V_{th}^3} \exp \left[-\frac{(V_r + V_m)^2 + V_\rho^2}{V_{th}^2} \right] \quad (30)$$

Here $V_{th} = \sqrt{2T_0/m}$, with m being the particle mass, and the form-factor arises due to the normalization $\int_{-\infty}^0 dV_r \int_0^\infty f(V_r, V_\rho) dV_\rho = 1$. The density dn_0 of neutrals with the velocity components in the ranges dV_r and dV_ρ is determined from the continuity equation:

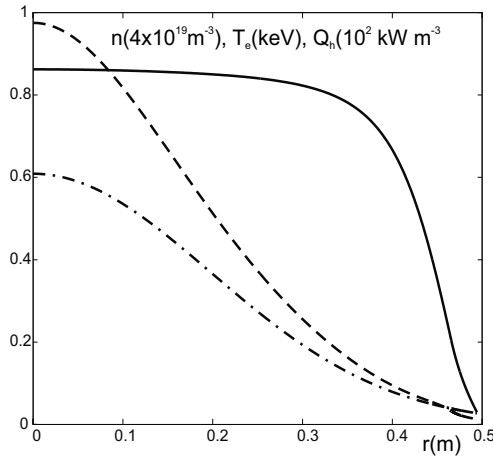


Figure 11. The radial profiles of the electron density (solid curve), temperature (dashed curve) and heating power density (dash-dotted curve) used by the modelling of the spreading process of carbon particles released by LIAS.

$$\partial_t dn_0 + V_r \partial_r dn_0 + (V_r / \rho) \times \partial_\rho (\rho dn_0) = -k_{ion}^0 n_e dn_0 \tag{31}$$

where k_{ion}^0 is the ionization rate coefficient. An approximate solution of equation (31) is searched for in the form:

$$dn_0(t, r, \rho) = d\eta_0(t, r) \times \exp \left[-\rho^2 / \lambda^2(t, r) \right] \tag{32}$$

This form of the solution mimics the fact that on each magnetic surface the density of injected neutral particles is localized in some vicinity of the ejection position and decays to zero far from this due to ionization.

Introduce new dependent variables:

$$\begin{aligned} dN_0(t, r) &= \int_0^\infty dn_0 2\pi\rho d\rho = \pi\lambda^2 d\eta_0 \\ d\Lambda_0(t, r) &= \int_0^\infty dn_0 2\pi\rho^2 d\rho = \frac{\sqrt{\pi}}{2} \lambda dN_0 \end{aligned} \tag{33}$$

Equations for $dN_0(t, r)$ and $d\Lambda_0(t, r)$ follow from the integration of equation (31) with respect to ρ with the weights $2\pi\rho$ and $2\pi\rho^2$, respectively, and with dn_0 substituted in the form (32):

$$\begin{aligned} \partial_t dN_0 + V_r \partial_r dN_0 &= -k_{ion}^0 n_e dN_0 \\ \partial_t d\Lambda_0 + V_r \partial_r d\Lambda_0 &= V_\rho dN_0 - k_{ion}^0 n_e d\Lambda_0 \end{aligned} \tag{34}$$

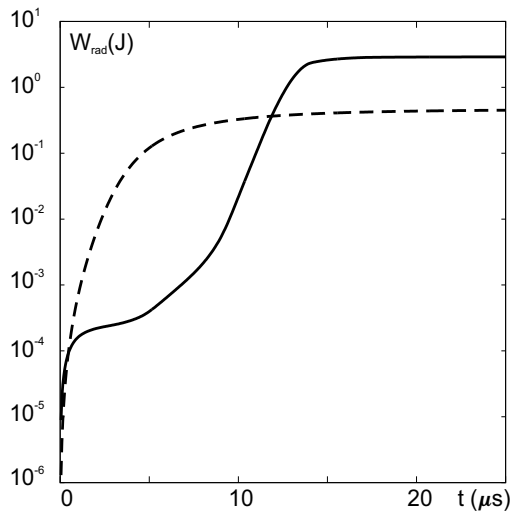


Figure 12. Time evolution of the cumulative energy radiated by C^+ ions calculated with (solid curve) and without (dashed curve) taking into account the plasma distortion by LIAS.

The boundary conditions at the wall take into account that no particles are released after the irradiation pulse, i.e. $dN_0(t > 0, r_w) = d\Lambda_0(t > 0, r_w) = 0$, since the release occurs during a time by orders of magnitude shorter than a typical time step τ in calculations. The latter has to be, however, chosen so that the distance $s = \tau |V_r|$ covered by particles in the radial direction during one time step is significantly smaller than their free path before collisions with electrons. In such a case the actual initial radial profile of dn_0 is of no importance. Here we assume that at $t = 0$ all particles fill homogeneously the first shell, $r_w - h \leq r \leq r_w$, but practically the same results are obtained for other assumptions, e.g. for the initial density profile decaying exponentially with s assumed as the e -folding length; along the wall the source region is localized in the irradiated spot with the radius ρ_0 . For the variables dN_0 and $d\Lambda_0$ this results in the following initial conditions:

$$dN_0(0, r_w - h \leq r) = \frac{N_{tot}}{h} f(V_r, V_\rho) dV_r dV_\rho; \quad d\Lambda_0(0, r) = \frac{\sqrt{\pi}}{2} \rho_0 dN_0(0, r)$$

where N_{tot} is the total amount of injected particles. With known $dN_0(t, r)$ and $d\Lambda_0(t, r)$ one can obtain the original parameters characterizing the local density of neutrals:

$$d\eta_0(t, r) = \frac{(dN_0)^3}{(d\Lambda_0)^2}; \quad \lambda(t, r) = \frac{2}{\sqrt{\pi}} \frac{d\Lambda_0}{dN_0} \quad (35)$$

The ρ -profile of the total density of neutral particles is approximated analogously to the relation (32)

$$n_0(t, r, \rho) = \eta_0(t, r) \times \exp \left[-\rho^2 / \lambda_0^2(t, r) \right] \quad (36)$$

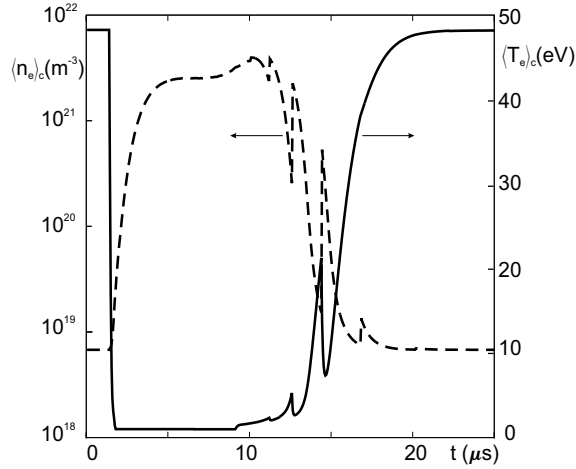


Figure 13. Calculated time evolution of the electron temperature (solid curve) and density (dashed curve) induced by LIAS in the cooled zone at the last closed magnetic surface.

where the maximum density $\eta_0(t, r) = \int d\eta_0(V_r, V_\rho)$ and the radius of the localization region is defined by conserving the total number of particles on the magnetic surface, $N_0(t, r) = \int dN_0(V_r, V_\rho)$:

$$\lambda_0(t, r) = \sqrt{\frac{N_0(t, r)}{\pi\eta_0(t, r)}} \quad (37)$$

The area of the cooled zone is assumed henceforth to be equal to:

$$S_c(t, r) = \pi\lambda_0^2(t, r) \quad (38)$$

The characteristic time for LIAS is of $10\mu\text{s}$. According to figures 5b,c it is too short for a noticeable reaction of the main ions and their density n_i is considered as unperturbed. The electron density n_e may be, however, significantly distorted by the generation of new electrons through the ionization of impurity neutrals; due to the plasma quasi-neutrality one has $n_e = n_i + n_1$. Here n_1 is the density of singly charged impurity ions assessed by solving fluid transport equations:

$$\partial_t n_1 + \partial_r \Gamma_{1r} + \partial_x \Gamma_{1x} = k_{ion}^0 n_e n_0 - k_{ion}^1 n_e n_1 \quad (39)$$

$$\begin{aligned} \partial_t \Gamma_{1,x} + \partial_r (\Gamma_{1r} \Gamma_{1,x} / n_1) + \partial_x (\Gamma_{1,x} \Gamma_{1,x} / n_1 + n_1 T_1 / m) = \\ = -k_{ion}^1 n_e \Gamma_{1,x} + e n_1 E_x / m_I \end{aligned} \quad (40)$$

where Γ_{1x} and Γ_{1r} are the components of the impurity ion flux density along the magnetic field and in the radial direction, respectively, m_I is the ion mass and the parallel electric field

E_x is determined from the electron force balance

$$en_e E_x = -\partial_x(n_e T_e)$$

In this study, by solving equations (39) and (40), we apply the ‘shell’ approximation, see references [7, 8], to find the profiles of n_1 and $\Gamma_{1,x}$ along the magnetic field. Due to the rapid decay of the plasma distortion induced by the outburst of impurity neutrals the temperatures of the main and impurity ions do not change noticeably, and only the change of the electron temperature is modelled by solving the TZA equations (27)-(29). The energy losses due to inelastic collisions with impurity species is assessed as

$$W_{loss} = \langle n_e \rangle_c \sum_{j=0,1} N_j \left(L_c^j + k_{ion}^j E_{ion}^j \right)$$

where $N_1(t, r)$ is the total numbers of impurity singly charged species on the magnetic surface per unit length in the direction r , provided by the ‘shell’ model for impurity spreading; L_c^j and E_{ion}^j are the cooling rate and the ionization energy of the species, respectively [31]. Calculations have been performed for the conditions of LIAS in Ohmic TEXTOR discharges, see reference [4] and the radial profiles of the plasma parameters before the LIAS application are presented in figure 11. The laser radiation has been concentrated on a wall spot with fine grain graphite bulk material of 0.15cm^2 area and $\rho_0 \approx 0.22\text{cm}$; typically $N_{tot} \sim 10^{17}$ carbon atoms were released per pulse. Time of flight measurements are well interpreted by the velocity distribution (30) with $T_0 \approx 1.5\text{eV}$ and $V_m \approx 8.7\text{km s}^{-1}$. The results of LIAS are normally quantified by measuring the total radiation emitted by C^+ species with a particular wave length [4]. To calculate this one has to apply a firm collision-radiation model that is out of scope of the present study. In figure 12 we display the cumulative energy radiated till time t by singly charged carbon ions, W_{rad} , calculated without and with the plasma reaction taken into account. One can see that in the latter case the rise of W_{rad} is significantly delayed but the overall emitted energy is much higher. The delay is explained by the plasma cooling through losses on radiation and ionization of impurity neutrals and significant decrease of the ion excitation rate; the larger cumulative ion radiation - by the increased electron density and growth of the ion cooling rate L_c^1 as the temperature in the cold zone recovers due to the heat transfer from the hot zone. The time variation of $\langle n_e \rangle_c$ and $\langle T_e \rangle_c$ at $r = r_s = 0.465$ is shown in figure 13. The results presented show that by interpreting the LIAS measurements one has to take into account distortions in the plasma parameters induced by the diagnostic itself.

5. Conclusion

Very localized injection of neutral particles of the working gas and impurities routinely happens in fusion devices, both in deliberate and accident ways. For example, by using laser-based diagnostics the particles resided in thin surface layer on the wall are released within a short intense bunch. In the plasma they are excited by electrons, emit light and, by measuring this, one can assess the total number of particles ejected and, thus, judge about the wall composition. Puffing of the working gas for the plasma density

control is also done through inlets of much smaller dimensions than that of the wall. The time variation and three-dimensionality of the problem in question requires normally the application of extremely time demanding modelling tools. In the present paper we elaborate a two zone approximation, an approach which allows to reduce the problem to solving of one-dimensional equations, describing the time evolution of the radial profiles of the electron temperature values averaged over the cooled and hot zone, where energy is dissipated in direct interactions with injected particles and transferred to the cooled zone with parallel heat conduction, respectively. The elaborated TZA approach is tested by comparing its predictions with numerical solution of heat conduction equation in one- and two-dimensional configurations. In the latter case both numerical solutions and TZA demonstrate the importance of the heat flux limit by interpreting the edge plasma cooling caused by a massive gas injection in the JET tokamak. As an example of applications for realistic three-dimensional configurations the penetration of carbon atoms released into a TEXTOR deuterium plasma by a short laser pulse is modelled. It is demonstrated that for a firm interpretation of measurements with the laser-based LIAS diagnostics one has to take into account the modifications induced in the plasma by impurity particles released.

Author details

Mikhail Tokar

Institute for Energy and Climate Research - Plasma Physics, Research Centre Jülich, Germany

References

- [1] McCormick K, Fiedler S, Kocsis G, Schweinzer J, Zoletnik S. Edge density measurements with a fast Li beam probe in tokamak and stellarator experiments. *Fusion Engineering and Design* 1997; 34-35 125-134.
- [2] Hollmann EM, Jernigan TC, Groth M, et al. Measurements of impurity and heat dynamics during noble gas jet-initiated fast plasma shutdown for disruption mitigation in DIII-D. *Nuclear Fusion* 2005; 45(9) 1046-55.
- [3] Wesson J. *Tokamaks*. Third edition. Oxford: Clarendon Press; 2004.
- [4] Philipps V, Malaquias A, Hakola A, et al. Development of laser-based techniques for in situ characterization of the first wall in ITER and future fusion devices. *Nuclear Fusion* 2013; 53(9) 093002.
- [5] Greenwald M. Density limits in toroidal plasmas. *Plasma Physics and Controlled Fusion* 2002; 44(8) R27-R80.
- [6] de Vries PC, Rapp J, Schüller FC, Tokar MZ. Influence of Recycling on the Density Limit in TEXTOR-94. *Physical Review Letters* 1998; 80(16) 3519-22.
- [7] Tokar MZ, Koltunov M. 'Shell' model for impurity spreading from a localized source. *Nuclear Fusion* 2013; 53(9) 093014.

- [8] Tokar MZ, Koltunov M. "Shell" approach to modelling of impurity spreading from localized sources in plasma. *International Journal of Modelling, Simulation, and Scientific Computing* 2014; 5(1) 1441005.
- [9] Tokar MZ. Quasi-three-dimensional modelling of penetration and influence of impurity in plasma. *Plasma Physics and Controlled Fusion*, in press.
- [10] Tokar MZ, Koltunov M. Modelling of the plasma global response to a local cooling. *Plasma Physics and Controlled Fusion* 2013; 55(4) 045013.
- [11] Prigogine I *Introduction to Thermodynamics of Irreversible Processes*, 2nd ed. New York: Interscience; 1961.
- [12] Tokar MZ, Koltunov M. A simplified, numerically verified model for the global plasma reaction on a local cooling. *Physics of Plasmas* 2013; 20(10) 102502.
- [13] Malone RC, McCrory RL, Morse RL. Indications of Strongly Flux-Limited Electron Thermal Conduction in Laser-Target Experiments. *Physical Review Letters* 1975; 34(12) 721-24.
- [14] TEXTOR Team, ALT-I Group et al. Plasma-wall interaction and plasma performance in textor - A review. *Journal of Nuclear Materials* 1987; 145-147 3-14.
- [15] Spitzer L, Härm R. Transport Phenomena in a Completely Ionized Gas. *Physical Review* 1953; 89(5) 977-981.
- [16] Tokar MZ. Numerical modelling of transport barrier formation. *Journal of Computational Physics* 2010; 229(7) 2625-2633.
- [17] Koltunov M, Tokar MZ. Modification of local plasma parameters by impurity injection. *Plasma Physics and Controlled Fusion* 2011; 53(6) 065015.
- [18] Tokar MZ, Koltunov M. Modelling of non-stationary local response on impurity penetration into plasma. *Physics of Plasmas* 2012; 19(4) 042502.
- [19] Kantorowitsch LW, Krylow WI. *Approximate methods of higher analysis*. New York: Interscience Publishers Inc.; 1958.
- [20] Braginskii SI. Transport Processes in a Plasma. In: Leontovich MA. (ed.) *Reviews of Plasma physics* V1. New York: Consultants Bureau; 1965. p205-304.
- [21] Lehnen M, Alonso A, Arnoux G, et al. First experiments on massive gas injection at JET - consequences for disruption mitigation in JET and ITER. In: Mateev M, Benova E. (eds.) *Proceedings of 36th European Physical Society Conference on Plasma Physics*, June 29 - July 3 2009, Sofia, Bulgaria. European Physical Society; 2009. pO2.001.
- [22] Lehnen M, Alonso A, Arnoux G, et al. Disruption mitigation by massive gas injection in JET. *Nuclear Fusion* 2011; 51(12) 123010.
- [23] Rechester AB, Rosenbluth MN. Electron heat transport in a tokamak with destroyed magnetic surfaces. *Physical Review Letters* 1978; 40(1) 38-41.

- [24] Harvey RW, McCoy MG, Hsu JY, Mirin AA. Electron dynamics associated with stochastic magnetic and ambipolar electric fields. *Physical Review Letters* 1981; 47(18) 102-5.
- [25] Classen IGJ, Westerhof E, Domier CW, et al. Effect of heating on the suppression of tearing modes in tokamaks. *Physical Review Letters* 2007; 98(3) 035001.
- [26] Tokar MZ, Gupta A. Elucidation of the heat-flux limit from magnetic-island heating. *Physical Review Letters* 2007; 99(22) 225001.
- [27] Epperlein EM, Short RW. Nonlocal heat transport effects on the filamentation of light in plasmas. *Physics of Fluids B* ; 4(7) 2211-2216.
- [28] Stangeby PC. *The Plasma Boundary of Magnetic Fusion Devices*. Bristol and Philadelphia: Institute of Physics Publishing; 2000. p187.
- [29] Tokar MZ, Gierse N, Huber A, Philipps V, Samm U. Model for plasma distortion by laser-induced ablation spectroscopy. 41st European Physical Society Conference on Plasma Physics, June 23 - 27 2014, Berlin, Germany. <http://ocs.ciemat.es/EPS2014ABS/html/author.html>
- [30] Konomi I, Motohiro T, Kobayashi T, Asaoka T. Considerations on the determining factors of the angular distribution of emitted particles by laser ablation. *Applied Surface Science* 2010; 256(3) 4959-65.
- [31] Suno H, Kato T. Cross section database for carbon atoms and ions: Electron-impact ionization, excitation, and charge exchange in collisions with hydrogen atoms. *Atomic Data and Nuclear Data Tables* 2006; 92(1) 407-455.

Modeling and Simulation of Heat Transfer Phenomena

Muhammad Musaddique Ali Rafique

Additional information is available at the end of the chapter

<http://dx.doi.org/10.5772/61029>

1. Introduction to modeling and simulation of heat transfer

“Heat transfer is a discipline of thermal engineering that concerns the generation, use, conversion, and exchange of thermal energy and/or heat between physical systems. Heat transfer is classified into various mechanisms, such as heat conduction, convection, thermal radiation, and transfer of energy by phase changes. Engineers also consider the transfer of mass of differing chemical species, either cold or hot, to achieve heat transfer. While these mechanisms have distinct characteristics, they often occur simultaneously in the same system” [1].

In recent times, numerical modeling and simulation techniques have been increasingly applied to the problems of heat transfer. Various studies have been carried out utilizing the basic techniques and their modifications and/or customized variants to customize, operate, test, evaluate, optimize and judge the performance of experimental systems and actual engineering problems. Problems particularly related to engineering issues in the fields of energy [2], oil and gas, metallurgy [3], chemical, process and reaction engineering, fuel cell technologies, manufacturing technologies [2], nanotechnology [4, 5], and aerospace have been extensively studied.

This chapter enlists, describes, explains and elaborates with examples these techniques as applied to problems and practical scenarios of heat transfer.

2. Basic techniques of modeling and simulation

Modeling and simulation, like any other field of science and technology has some certain basic techniques using which all practices are carried out. These are the foundation stones on which the building of modeling and simulation practices and procedures is built.

2.1. Introduction

Various techniques have evolved in modeling and simulation since its inception [6] for the solution of technical and engineering problems, ranging from ancient Roman military techniques to classical analog methods to modern Runge – Kutta method and Monte Carlo techniques. [7]. The history of modeling and simulation dates back to ancient times. It was first used by ancient Romans to simulate the actual war conditions in areas of peace to train its soldiers to fight in areas where they have never been. These war games were based upon very well and adequately designed models. Later, techniques of modeling and simulation were used by artists and scientists to test their designs of statuary or edifices during the age of the Renaissance (1200 – 1600 C.E). The renowned Leonardo da Vinci, extensively made use of techniques of modeling and simulation to test and validate his models in art, military, and civil works. [7]. Chess, also known as the world's first war game and its evolution in to a computer game is a result of rigorous use of techniques of modeling and simulation [8]. Similarly, war games (a technique of modeling and simulation) were used in Europe (Prussia, modern-day northeastern Germany) and same was used by Army Corps of Engineers in the United States [9]. In technical fields, the first successful use is reported in the production and use of "Link Flight Simulator", which was patented in 1929 by the American Edward Link. [10]. SAGE – semi, automated ground environment (1949);, MEW – Microwave early warning (1950) [11]; "Whirlwind", MIT, *Cape Cod System* (1953) were also important milestones in modeling and simulation. Ranging from days of the Cold War to the war in Iraq (1991), more advanced techniques were used to develop more realistic and real-world-scenario war games. Following this increasingly well designed simulation centers were opened at various universities and institutions in the United States and the world to better research the areas of modeling and simulation, develop new models, improve existing ones, and develop applications, as a result of which various new techniques/methods of modeling and simulation were formulated [11].

2.2. Energy minimization

Energy minimization (also called energy optimization or geometry optimization) methods are numerical procedures for finding a minimum on the potential energy surface/state starting from a higher energy initial structure/state [1, 14]. These are extensively used in chemistry, mathematics, computer science, image processing, biology, metallurgical engineering, materials science, mechanical engineering, chemical engineering, electrical engineering etc. to find the stable/equilibrium states of molecules, solids, and items. Extensive studies have been carried out in various fields making use of energy minimization techniques to formulate models highlighting the importance, significance, and use of this method in modeling and simulation and solution of engineering problems.

Levitt [12] used energy minimization to formulate solutions of protein folding. The potential energy functions used are detailed and include terms that allow bond stretching, bond angle bending, bond twisting, van der Waals' forces, and hydrogen bonds. A unique feature of the methods used includes easy approach for restrained energy minimization work (including all terms) to anneal the conformations and reduce their energies further. The methods used were very versatile and were proposed to be applicable for building models of protein conforma-

tions that have low energy values and obey a wide variety of restraints. Recently, Micheletti and Maritan, [13] also used energy minimization methods to formulate solutions of protein design. They went a step further in their approach, and defined actual real-world scenarios and formulated alternative design strategies based upon correct treatment of free energy. Sutton [14] presented the use of energy minimization methods to determine the solution of atomic structures and solute concentration profiles at defects in elemental solids and substitutional alloys as a function of temperature. He used mean field approximation, rewrote free energy, used Einstein models and auto-correlation approximation and showed that the better statistical averaging of the auto-correlation approximation leads to better temperature – and concentration – dependent pair interactions. His formula was fairly simple and effective. Lwin [15] used spreadsheets to solve chemical equilibrium problems by Gibbs energy minimization.

Similarly, Olga Veksler during her PhD thesis at Cornell University [16] presented the use of energy minimization techniques in computer vision problems. She developed algorithms for several important classes of energy functions incorporating everywhere smooth, piecewise constant and piecewise smooth priors. These algorithms primarily rely on graph cuts as an optimization technique. For a certain everywhere smooth prior, an algorithm based on finding the exact minimum by computing a single graph cut was developed. For piecewise smooth priors, two approximate iterative algorithms, computing several graph cuts at each iteration, were developed and for certain piecewise constant prior, same algorithms were used along with a new one which finds a local minimum in yet another move space. The approach was quite effective on image restoration, stereo, and motion. [16]. Similar studies were carried out later as well to further test and evaluate energy minimization in computer vision [17, 19]. Nikolova [20] explained the use of energy minimization methods in the field of image analysis and processing. Onofrio and Tubaro applied the same to the problem of three-dimensional (3D) face recognition [21]. Standard [22] explained the use of energy minimization to determine the states for a molecule in chemistry; he explained that the geometry of molecule is changed in a stepwise fashion so that the energy is reduced to lowest minimum.

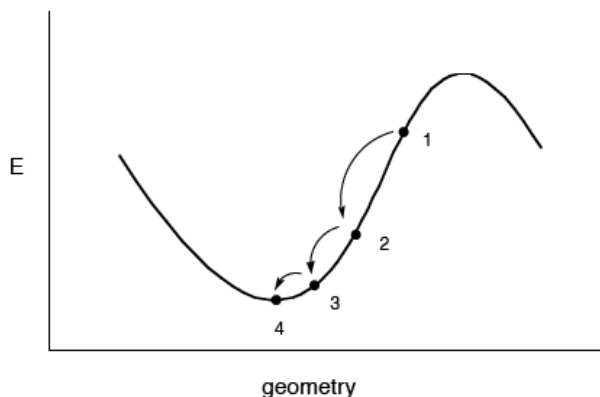


Figure 1. Graphical representation of energy minimization process [22]

Figure 1 shows energy minimization process for a molecule in steps. “Most energy minimization methods proceed by determining the energy and the slope of the function at point 1. If the slope is positive, it is an indication that the coordinate is too large (as for point 1). If the slope is negative, then the coordinate is too small. The numerical minimization technique then adjusts the coordinate; if the slope is positive, the value of the coordinate is reduced as shown by point 2. The energy and the slope are again calculated for point 2. If the slope is zero, a minimum has been reached. If the slope is still positive, then the coordinate is reduced further, as shown for point 3, until a minimum is obtained”. [22]

There are other methods for actually varying the geometry to find the minimum [22]. Many of these, which are used to find a minimum on the potential energy surface of a molecule, use an iterative formula to work in a step wise fashion. These are all based on formulas of the following type:

$$x_{new} = x_{old} + correction \quad (1)$$

where, x_{new} is value of the geometry at the next step, x_{old} is geometry at the current step, and *correction* is some adjustment made to the geometry.

2.2.1. Newton Raphson method

“The Newton-Raphson method is the most computationally expensive per step of all the methods utilized to perform energy minimization. It is based on Taylor series expansion of the potential energy surface at the current geometry” [22]. The equation for updating the geometry is a modification of eq. [1]:

$$x_{new} = x_{old} - \frac{E'(x_{old})}{E''(x_{old})}. \quad (2)$$

The correction term depends on both the first derivative (also called the slope or gradient) of the potential energy surface at the current geometry and also on the second derivative (also called the curvature). The Newton Raphson method involves fewest steps to reach the minimum.

2.2.2. Steepest descent method

This is a method which relies on an approximation. In this method, the second derivative is assumed to be a constant.

$$x_{new} = x_{old} - \gamma E'(x_{old}) \quad (3)$$

where γ is a constant. In this method, the gradient at each point is again calculated. Because of the approximation, it is not efficient, so more steps are required to find the minimum. [22]

2.2.3. Conjugate gradient method

“In this method, the gradients of the current geometry are first computed. Then, the direction of the largest gradient is determined. The geometry is minimized along this one direction (this is called a line search). Then, a direction orthogonal to the first one is selected (a ‘conjugate’ direction). The geometry is minimized along this direction. This continues until the geometry is optimized in all the directions”. [22]

2.2.4. Simplex method

In the Simplex Method, the energies at the initial geometry and two neighboring geometries on the potential energy surface are calculated (points A, B, and C in Fig. 2).

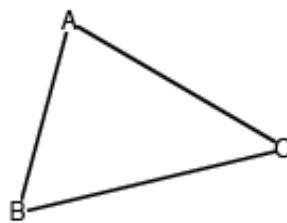


Figure 2. Schematic of Simplex Method implementation (three points)

“The point with the highest energy of the three is noted. Then, this point is reflected through the line segment connected to the other two (to move away from the region of high energy). For example, if the energy of point A is the highest out of the three points A, B, and C, then A is reflected through line segment BC to produce point D.” (Fig. 3)

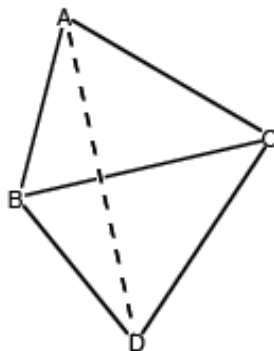


Figure 3. Simplex Method (four points)

“In the next step, the two original lowest energy points (B and C) along with the new point D are analyzed. The highest energy point of these is selected, and that point is reflected through the line segment connecting the other two. The process continues until a minimum is located” [22]. As a result, it is the least expensive in CPU time per step. However, it often requires the most steps.

2.3. Molecular Dynamics (MD) simulations

Molecular dynamics (MD) is a technique in which physical movements of atoms and molecules is simulated using computers. In this the atoms and molecules are allowed to interact for a period of time, giving a view of the motion of the atoms. MD simulation circumvents the problem of finding the properties of complex molecular systems by using numerical methods. In the most common version, the trajectories of molecules and atoms are determined by numerically solving Newton's equations of motion for a system of interacting particles [1, 23]. This is one of the two main families of simulation techniques [23]. The results of molecular dynamics simulation can be used in various fields such as thermodynamics, biology, chemistry, materials science and engineering, statistical mechanics and nanotechnology [1, 24, 25].

van Gunsteren, [26] explained in detail about methodology, applications and prospective of molecular dynamics in chemistry. He effectively explained molecular dynamics in terms of choosing unavoidable assumptions, approximations and simplifications of the molecular model and computational procedure such that their contributions to the overall inaccuracy are of comparable size, without affecting – significantly the property of interest. *“He further postulated and argued that the aim of computer simulation of molecular systems is to compute macroscopic behavior from microscopic interactions giving the reason that the main contributions a microscopic consideration can offer are (1) the understanding and (2) interpretation of experimental results, (3) semi – quantitative estimates of experimental results, and (4) the capability to interpolate or extrapolate experimental data into regions that are only difficultly accessible in the laboratory”* [26]. His methodology was good, accurate and in detail for explaining molecular dynamics. A similar study is also conducted by McKenzie [27]. Karplus and McCammon [28] extensively reviewed the use of molecular dynamics as applied to biomolecules. Their study encompasses all aspects of application of computational techniques for solving structure, folding, internal motion, conformational changes, etc., of biomolecules and problems. A similar study was carried by Kovalskyy et al. [29] in which they used molecular dynamics for the study of structural stability of HIV – 1 Protease under physiological conditions.

Kupka [30] applied molecular dynamics in computer-based graphic accelerators. He proposed an algorithm consisting of CPU and GPU parts, The CPU part is responsible for streams preparations and running kernel functions from the GPU part, while the GPU part consists of two kernels and one reduce function.

A very nice study about molecular dynamics simulation for heat transfer problems is given by Maruyama [31]. He also applied MD simulations to the problem of heat conduction of finite length single walled-carbon nanotubes [32]. The measured thermal conductivity did not converge to a finite value with increase in tube length up to 404 nm, but an interesting power law relation was observed.

Wang and Xu applied MD techniques to problems of heat transfer and phase change during laser matter interaction [33]. They irradiated argon crystal by a picoseconds pulsed laser and investigated the phenomena using molecular dynamics simulations. Result reveals transition region, superheating, and rapid movement of solid-liquid interface and vapors during phase

change. Lin and Hu [34] applied the same techniques to the problems of ablation and bio heat transfer in bimolecular systems and biotissues and developed a new model.

Krivtsov, [35] discussed the problems of heat conductivity in monocrystalline materials with defects via molecular dynamics simulation. *“It was shown that in ideal monocrystals the heat conductivity is not described by the classical conductivity theory. For the crystals with defects for the big enough specimens the conductivity obeys the classical relations and the coefficient (β) describing the heat conductivity is calculated. The dependence of the heat conductivity on the defect density, number of particles in the specimen, and dimension of the space is investigated”* [35]. The obtained dependencies increase with time: almost linear in two dimensional (2D) cases and nonlinear in one-dimensional (1D) and (3D) (with positive time derivative in 1D case, and with negative time derivative in 3D case).

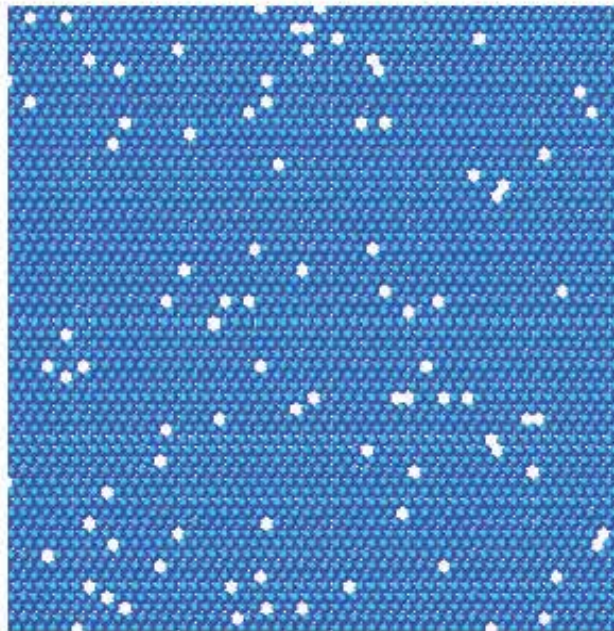


Figure 4. An element of 2D monocrystal with predefined distribution of defects.[35]

He also applied the same technique for determining and simulating the mechanical properties of polycrystals as well earlier. [36]. Recently, Steinhäuser applied molecular dynamics simulation technique to various condensed matter forms [37]. He showed how semi flexibility or stiffness of polymers can be included in the potentials describing the interactions of particles in proteins and biomolecules. For ceramics he modeled the brittle failure behavior of a typical ceramic and simulated explicitly the set-up of corresponding high-speed impact experiments. It was shown that this multiscale particle model reproduces the macroscopic physics of shock wave propagation in brittle materials very well while at the same time allowing for a resolution of the material on the microscale.

2.4. Monte Carlo (MC) simulations

Monte Carlo (MC) methods/simulations are a set of simulation techniques that rely on repeated random sampling to compute their results. They are often used in computer simulations of physical and mathematical systems. These are also used to complement theoretical derivations. Monte Carlo methods are especially useful for simulating systems with many coupled degrees of freedom, such as fluids, disordered materials, strongly coupled solids, and cellular structures. They are widely used in business (calculation of risk), mathematics, (evaluate multidimensional definite integrals), Space exploration, and oil exploration (predictions of failures, cost overruns and schedule overruns) [1, 38].

Howell [39] explained in detail the use of Monte Carlo method in radiative heat transfer problems. He used the method for computations of complex geometries, configurations, and exchange factors, inverse design, packed beds, and fiber layers, etc., and also explained the use of related algorithms (READ, REM, Markov Chains, etc.). A similar study was also conducted by Zeeb [40] and Kersch (1993) [41]. Modest [42] used various implementations of the backward Monte Carlo method for problems with arbitrary radiation sources. His focus area was backward Monte Carlo simulation. He included small collimated beams, point sources, etc., in media of arbitrary optical thickness and solved radiative heat transfer equation with specified internal source and boundary intensity.

Frijns et al. [43] used Monte Carlo simulation to discuss and solve problems of heat transfer in micro and nanochannels. They proposed and utilized a combination algorithm of Monte Carlo and molecular dynamics simulation to argue about its effectiveness.

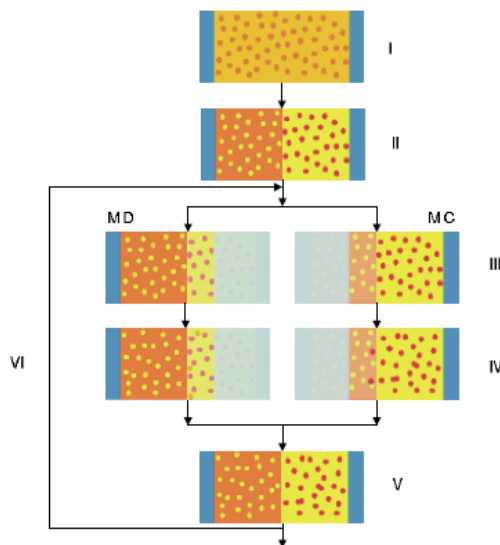


Figure 5. Schematic view of the coupling algorithm. Left: MD steps; right: MC steps. The particles that have been assigned to molecular dynamics have a light color, whereas the MC particles are dark [43]

Steps of performing simulation are: I) define an initial condition. II) Assign particles to MD or MC part. III) Distribute over MD and MC codes. IV) Compute new positions and velocities. V) Update the particles in the buffer layer. VI) Start over with step III.

An extensive use of Monte Carlo in gas flow problems is explained by Wang and co-workers [44, 45, 46]. They used direct simulation MC for simulation of gas flows in MEMS devices. They examined orifice and corner flow using modified DSMC codes and showed that the channel geometry significantly affects the micro gas flow [44]. For orifice flow, the flow separation occurred at very small Reynolds numbers while in corner flow, no flow separation occurred even with a high driving pressure. The results were found to have good agreement with continuum theory and existing experimental data. In a later study, they used the same methods to discuss and solve the problem of gas mixing in micro channels [45]. Very high Knudsen numbers were used. The simulation results show that the wall characteristics have little effect on the mixing length. The mixing length is nearly inversely proportional to the gas temperature. The dimensionless mixing coefficient is proportional to the Mach number and inversely proportional to the Knudsen number. They also extended the use of their codes to heat transfer and gas flow problems in vacuum-packaged MEMS devices [46] and found to have good results in explaining the heat transfer and gas flow behavior on chip surfaces.

2.5. Langevin dynamics

Langevin dynamics is an approach to the mathematical modeling of the dynamics of molecular systems. The approach is characterized by the use of simplified models while accounting for omitted degrees of freedom by the use of stochastic differential equations. [1]. In philosophy, the Langevin equation is a stochastic differential equation in which two force terms have been added to Newton's second law to approximate the effects of neglected degrees of freedom. One term represents a frictional force, the other a *random* force [47]. They are used in biology, chemistry, engineering, etc, to formulate solutions of complex problems. Antonie [48] used LD methods to investigate influence of confinement on protein folding. He used MATLAB to formulate code of equation developed using LD methods. The model developed and then its programming was found effective. A similar type of study was also conducted by Lange et al [49].

Quigley [50] discussed the advantages of using LD in constant pressure extended systems and showed it to be effective technique for simulating the equilibrium isobaric–isothermal ensemble. They analyzed canonical ensemble, Hoover ensemble, and Parrinello–Rahman ensemble and showed that despite the presence of intrinsic probability gradients in this system, a Langevin dynamics approach samples the extended phase space in the correct fashion. Wu, Li and Nies [51] applied Langevin dynamics method to the problem of cross-linking into polymer networks. Commercially available software package GROMACS 4.0 was used for simulation. Their study revealed that cross-linking is associated with effects such as changes in thermodynamic stability of reacting mixture or the presence of nanoparticles. This also facilitated the study of macromolecules.

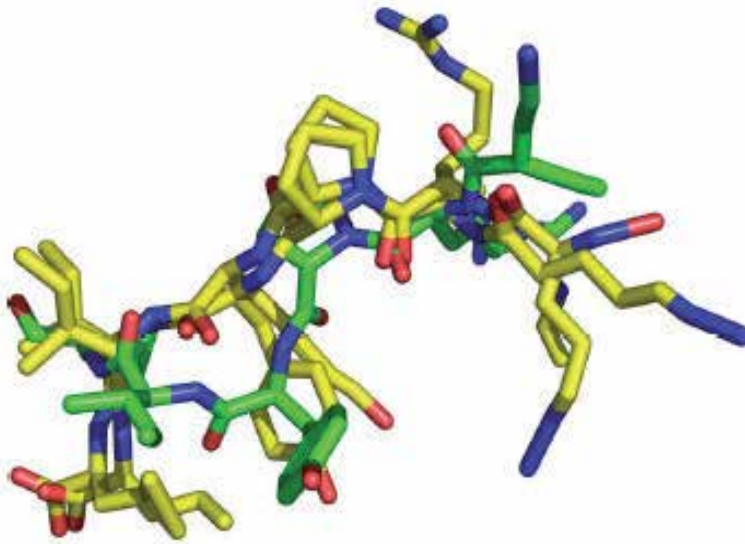


Figure 6. “Overlay of average neurotensin structures. The relative orientation of the structures minimizes the RMSD between the C_α atoms. The green structure is obtained from state A, and the two yellow structures are obtained from state B. The parts of the side chains that were overly distorted due to the averaging were removed. The N terminus is oriented towards the upper right corner”. [49]

2.6. Normal mode (harmonic) analysis

Normal mode (harmonic) analysis is a method of simulation in which the characteristic vibrations of an energy-minimized system and the corresponding frequencies are determined assuming its energy function is harmonic in all degrees of freedom. Normal mode analysis is less expensive than MD simulation, but requires much more memory [52]. These are extensively used in science and engineering to model, simulate and solve engineering problems. Magyari [53] used this method to examine the convection model of the fully developed flow in a differentially heated vertical slot with open to capped ends. He found that the method is quite transparent and has algebraic and computational efficiency. It is shown that dimensionless temperature field and the velocity field scaled by the Grashof number are characterized by only two physical parameters; also, capped slot is an ideal heat transfer device. Schuyler et al., [54] used the same method to C_α – based elastic network model (C_α – NMA) of protein analysis and “present a new coarse grained rigid body based analysis (cluster NMA). This new cluster NMA represents a protein as a collection of rigid bodies interconnected with harmonic potentials. This produces reduced degree of freedom (DOF) equations of motion (EOMs), which even in the case of large structures enable the computation of normal modes to be done on a desktop PC” [54]. This new cluster NMA proved to be very effective for protein analysis. Similar type of studies have been done by Hinson [55] in France and showed that normal mode analysis is advantageous as no sampling is required, enables fast calculations and is simple to use. However, it suffers from the drawback of exhibiting inaccuracies in certain cases and is limited to single-well potentials and thus offers no possibility to study conformational transitions explicitly.

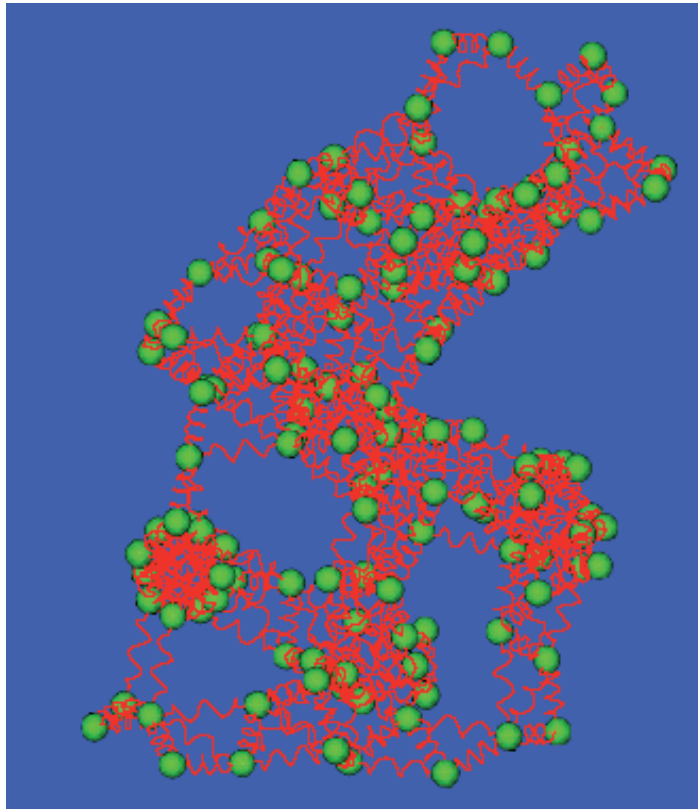


Figure 7. Elastic network model [55]

2.7. Stimulated annealing

“Simulated annealing (SA) is a random-search technique which exploits an analogy between the way in which a metal cools and freezes into a minimum energy crystalline structure (the annealing process) and the search for a minimum in a more general system; it forms the basis of an optimization technique for combinatorial and other problems” [56]. It has attracted significant attention as suitable for optimization problems of large scale, especially ones where a desired global extremum is hidden among many, poorer, local extrema. The method has proved effective in solving problems such as traveling salesman problem in N cities, designing complex integrated circuits, etc. In the latter case it has proved effective in arranging several hundred thousand circuit elements on a tiny silicon substrate in an optimized way so as to avoid/minimize interference among their connecting wires. *“SA’s major advantage over other methods is an ability to avoid becoming trapped in local minima. The algorithm employs a random search which not only accepts changes that decrease the objective function (assuming a minimization problem), but also some changes that increase it”* [57].

3. Modeling and simulation of heat transfer — Applications

Modeling and simulation of heat transfer phenomena is the subject matter of various recent studies in many technical and/or engineering applications. It has helped a great deal in operation, achieving enhanced results, increasing efficiency, and optimizing processes. It is one of the basic engineering techniques used in analysis of engineering problems/processes during initial steps/stages of design. This section highlights this significance of heat transfer in various engineering applications via modeling and simulation approach.

3.1. Introduction

Heat transfer analysis has made its distinct position among engineering analyses carried out for any technical/engineering problem/application at first hand. Providing initial data, it paves the way for in-depth analysis and incursion into the problem solving technical intimacies. Its use has gained more importance and popularity especially after the introduction of computer/simulation techniques [2, 3]. Ironically, its use started in complex engineering problems such as determining the heat transfer profile of single crystal turbine blades, determining heat transfer coefficients for material(s) in tube and shells heat exchangers for measuring and enhancing process efficiency [3] and then extended to simpler situation and scenarios.

3.2. Modelling & simulation of heat transfer in process industry

Process industry is one of the major industries that utilise heat transfer and thermodynamic studies to operate and optimize its processes. Equipment such as Heat Exchangers, Boilers, Evaporators, Dryers, Condensers, Ovens, Reboilers, etc., rely and heavily make use of heat transfer studies for their optimum and efficient operation. Several tools such as FLUENT, Modelica, FEMLAB, APROS (Powerful dynamic simulation), BALAS (Conceptual process design), ChemSheet (Process Chemistry), KilnSimu (Rotary Kiln Simulator), etc., are being frequently used to model and simulate the process engineering parameters of different units/unit operations [58].

3.2.1. Boilers

Heat transfer of boilers is extensively studied as it helps immensely in finding the parameters and determining the process efficiency of equipment as well as suggesting its design improvement. Bordbar and Hyppänen [59] explained the use of modeling for problem of radiation heat transfer in a boiler furnace. Temperature and heat flux within the furnace and on the heat surfaces was investigated. They used CFD method for solving velocity field of combusted fuel from the burner using some empirical equations and found that use of CFD on the model developed conforms to measured data and greatly helps in achieving the results.

Earlier, Zeeb [60] used the Monte Carlo method to study the same problem in axisymmetric furnace and got good results. Gómez, Fueyo and Díez, used the same CFD method to solve a model for the calculation of “*shell-side flow and the shell-side, tube-side and tube-wall, thermal fields, and of the shell-tube heat-exchange in convective zone of power station 350 MW boiler. The model allows*

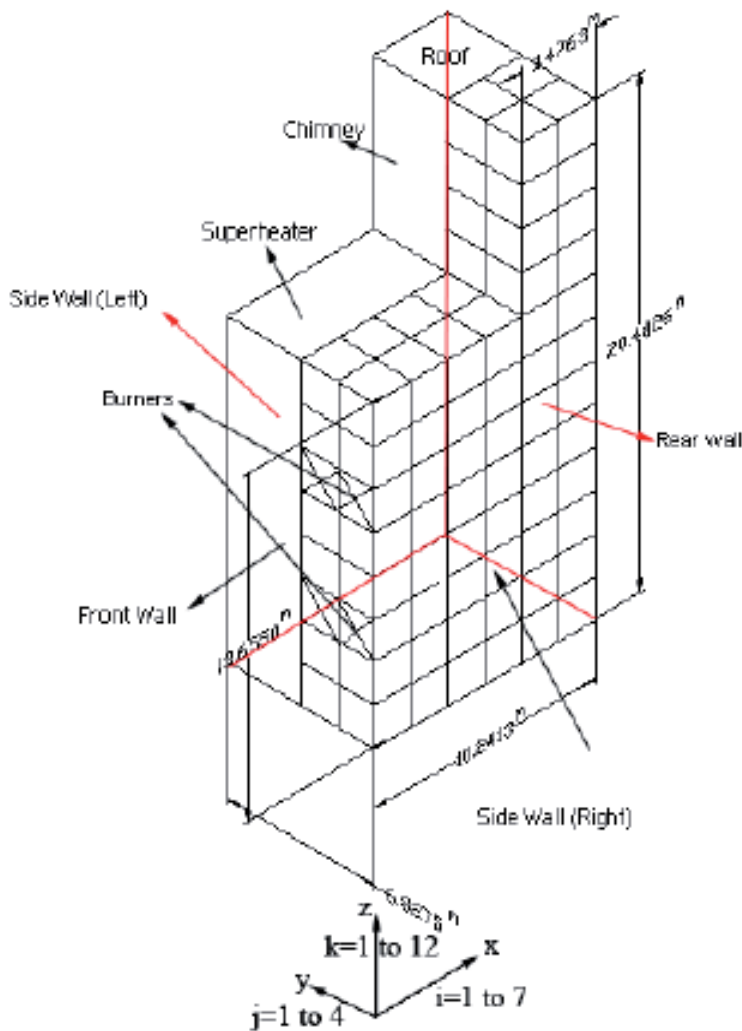


Figure 8. An illustration of our simplified model of the furnace, The names that we used of different parts of the furnace with the volume and surface zones, the position of the burners in the front and rear walls. [59]

for several arbitrarily-interconnected heat-exchanging elements to be simulated in a flexible manner. The model has been validated with the simulations of a real power-station convective zone for different loads, and the agreement between calculated and plant data has been satisfactory" [61]. Sørensen et al. [62] used modeling and simulations to check, measure, optimize, and improve the performance of a fire tube boiler. Model covers effect of flue gas and the water-/steam sides. Various sub-models form final "overall model for the complete boiler. Sub models have been defined for the furnace, the convection zone (split in 2: a zone submerged in water and a zone covered by steam), a model for the material in the boiler (the steel) and 2 models for resp. the water/steam zone (the boiling)

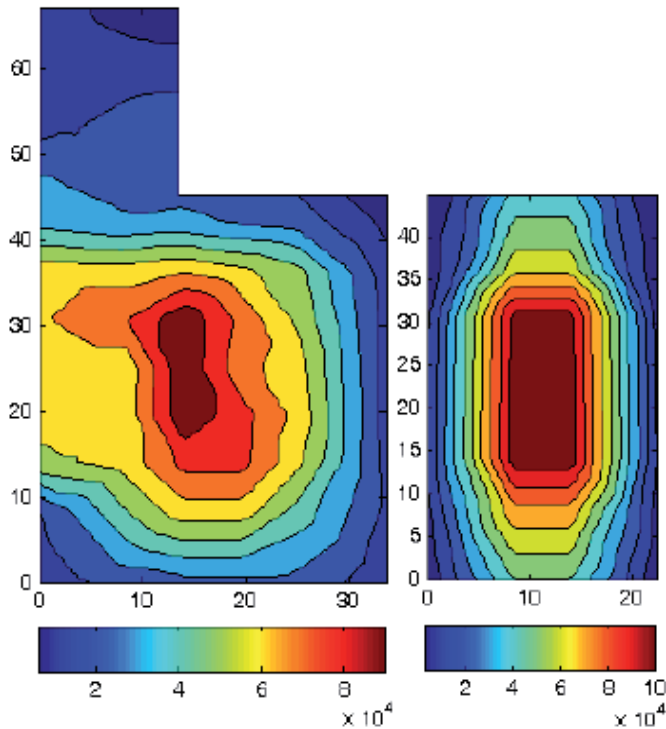


Figure 9. (a) Radiative heat flux distribution on the front wall of the furnace (Btu / ft^2hr). (b) Radiative heat flux distribution on the side wall of the furnace (Btu / ft^2hr). [59]

and the steam. The dynamic model has been developed as a number of Differential-Algebraic-Equation systems (DAE). Subsequently MATLAB/Simulink has been applied for carrying out the simulations" [62]. A full-scale experiment was carried out to verify the simulated results and they are found to be in good agreement. In a similar study [63], modeling and simulation was applied for optimizing the dynamic performance of water tube boiler installed on board ship Coral Princess.

In this study, the object function to be optimized takes the weight of the boiler and its dynamic capability into account. "The dynamic model for simulating boiler performance consists of a model for the flue gas side, a model for the evaporator circuit and a model for the drum. The dynamic model has been developed for the purpose of determining boiler material temperatures and heat transfer from the flue gas side to the water-/steam side in order to simulate the circulation in the evaporator circuit and hereby the water level fluctuations in the drum" [63]. As in previous study, DAE is used to develop and MATLAB is used to simulate the model. The results are found to be in good agreement with experimental data.



Figure 10. Coral Princess at sea and boiler installed on ship [63]

3.2.2. Heat exchanger

Heat transfer and its modeling and simulation for heat exchangers have been nicely reported in various excellent studies. Dafe., [64] presented the use of FLUENT for CFD codes used to

solve problems of heat transfer in plate heat exchangers. The work was carried out to determine the effect of channel geometry and flow conditions on the heat transfer. Two PHE's, one with wave geometry and the other with chevron design were studied. Temperature of the wall was kept constant, water was used as the working fluid, and the mass flow rate varied to study the effect of Reynolds number. Simulated Reynolds number range is 100 – 25, 600.

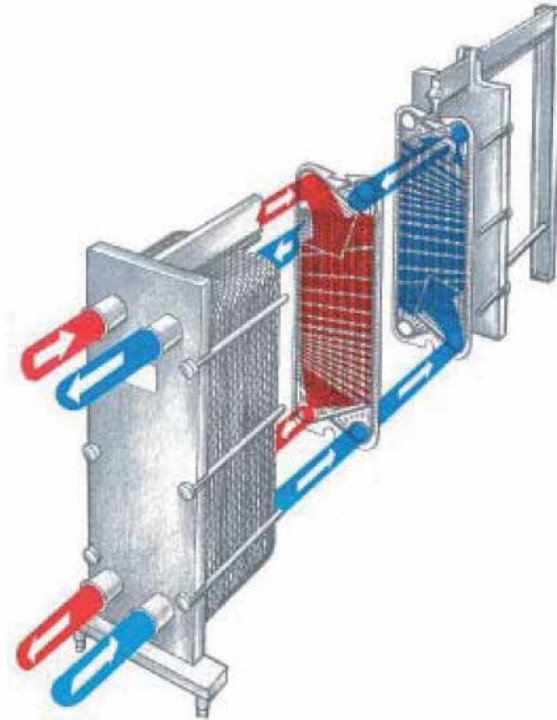


Figure 11. Plate Heat Exchanger [64]

It was efficiently shown that choice of PHE geometry is a strong function of application. Convective design is shown to give better convective properties for low Reynolds number applications while at higher Reynolds numbers chevron design gives better convective properties. Tomas et al., [65] described the use of object-oriented heat exchanger models for simulation of fluid property transitions. The models were written in Modelica. Three models were developed and employed, namely, Model 1: instantaneous property change; Model 2: Ideally mixed volume; Model 3: Transition port delay. Simulations showed that Model 3 is the best for determining computational performance as well as affording flexibility in fluid dispersion modeling. Othman, et al. [66] used CFD as a tool in solving and analyzing problems of heat transfer in shell and tube heat exchanger. Gambit 2.4 was used as tool for simulation. Same experimental parameters at constant mass flow rate of cold water varying with mass flow rate at 0.0151 kg/s, 0.0161 kg/s and 0.0168 kg/s of hot water were used. The CFD model is validated by comparison to the experimental results within 15% error.

3.2.3. Condensers

Heat transfer in condensers is vastly discussed and has been in practice since long for solving efficiency problems and determining process parameters. Various research and industrial studies have explained the use and application of heat transfer via modeling for condensers. Corberan and Melon [67] developed a model to predict the behavior of the finned tube condenser and evaporators that work with R-134a. For simulation of evaporator and condenser, many of the phase change heat transfer coefficient correlations are considered and the most recommended correlations are used. The experimental study to validate the model has been carried out in a small air-conditioning unit with cross-flow air refrigerant type heat exchangers. The model is capable of predicting the heat transfer of an evaporator or condenser with accuracy of $\pm 5\%$ in the studied range. Qureshi et al. [68] developed a mathematical model of evaporative fluid coolers and evaporative condensers to perform a comprehensive design and rating analysis. A fouling model was used to investigate the risk based thermal performance of evaporative heat exchangers. It is solved by Engineering Equation Solver (EES). It showed *“that thermal effectiveness of the evaporative heat exchangers degrades significantly with time indicating that, for a low risk level ($p < 0.01$), there is about 66.7% decrease in effectiveness for the given fouling model. Furthermore, it is noted that there is about 4.7% increase in outlet process fluid temperature of the evaporative fluid cooler. A parametric study was also performed to evaluate the effect of elevation and mass flow rate ratio on typical performance parameters such as effectiveness for rating calculations”* [68]. The model was well validated by experimental results. Acunha Jr et al. [69] further discussed this problem using FLUENT. They studied the air and water behavior inside an evaporative condenser operating with ammonia as the refrigerant fluid. The *“air flow is modeled as a continuous phase using the Eulerian approach while the droplets water flow is modeled as a disperse phase with Lagrangian approach. The coupling between pressure and velocity fields is performed by the SIMPLE algorithm. The pressure, velocity and temperature fields are used to perform qualitative analyses to identify functional aspects of the condenser, while the temperature and the relative humidity evolution contributed to verify the agreement between the results obtained with the numerical model and those presented by equipment manufacturer”* [69]. It was shown that use of deflectors with different angles along the air inlet may attenuate the effects caused by vortex in the entrance region, and hence improve the heat transfer in tubes located immediately above this. Overall results were found to be in good agreement. Lee et al., [70] in a recent study reported the use of modeling and simulation for heat transfer related problems in a simple shell and tube condenser for a longitude baffles for a moderately high temperature heat pump. A simulation method was developed and used to carry out size determination and performance rating of S&T condenser. A good agreement is observed between computed values and experimental data. The deviation (CV) is within 3.16% for size estimation and is within 1.02% for performance rating.

3.2.4. Ovens

Therdthai, et al. [71] used 3D CFD modeling and simulation for the determination of temperature profiles and airflow patterns in continuous oven used for baking process. It was used to

predict dynamic responses during continuous baking process. "According to the simulation results, the heat supply could be reduced whereas the airflow volume should be increased. With this modification, the weight loss of bread was reported to be reduced by 1.4% with an acceptable crust color and a completed baking as indicated by its internal temperature" [71]. Flick et al. [72] used modeling for determining heat transfer and fluid flow inside pressure cooker. A 3D CFD code was developed and is used to reproduce the experimentally observed trends and some experimentally difficult to characterize phenomena (fluid flow).

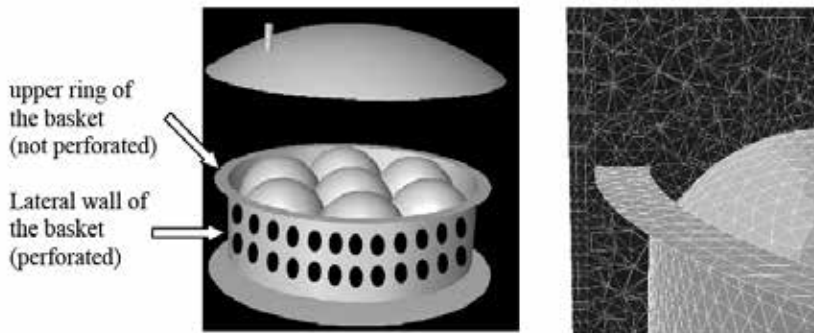


Figure 12. Geometry and mesh of pressure cooker [72]

Further aim of the work is to use numerical simulation for the choice of operating conditions and equipment design which was achieved nicely. Similarly, Sargolzaei et al. [73] applied 1D finite difference and 3D computational fluid dynamic models on the hamburger cooking process. Three different oven temperatures (114, 152, 204°C) and three different pressures (20, 332, 570 pa) were selected and nine experiments were performed. An optimum oven temperature in the range of 114°C to 204°C was proposed. Effect of oven temperature on weight loss is more than pressure. Decreasing oven temperature and increasing cooking time can increase uniformity of temperature distribution in the hamburger, and therefore, microbial safety will increase as well as product quality. The CFD-predicted results were in good agreement with the experimental results than the finite difference (FD) ones. But finite difference model was more economical due to longer time needed for CFD model to simulate (about 1 h). Several other authors used CFD codes for modeling and simulation of heat transfer problems in ovens and found them to be very effective in predicting the results and optimizing process. [74, 75]

3.3. Modeling and simulation of heat transfer in manufacturing industry

Heat transfer studies have also been extensively carried out in manufacturing engineering processes. The models developed, their simulations, and data generated from them have helped immensely in defining process parameters and increasing process efficiencies. Processes such as Casting, Welding, Machining, Powder Metallurgy, Forging, Rolling, Extrusion, Plastics forming have been extensively studied by heat transfer models to improve and

optimize their performances. Various commercially available general – purpose and custom built software have been used to perform simulations.

3.3.1. Castings

Heat transfer and its modeling and simulation approach have been extensively applied to foundry technology and processes. Determination of time of solidification, prediction of solidification pattern and structure, improvement of gating system, furnace and mold design are the most important areas in which heat transfer has been applied. Sabau et al. [76] presented heat transfer analysis of direct chill (DC) cast process of ingot using boundary conditions. *“Heat transfer phenomena such as (a) direct contact of liquid metal and mold, (b) air gap between mold and ingot surface, (c) water cooling on rolling and end faces of the ingot, (d) ingot contact with the bottom block, and (e) water intrusion between the bottom block and ingot were analyzed. Data on solid fraction and temperature evolution were compared at points located on the end face for the two cases in which heat transfer conditions (a) were assumed to be the same on both ingot faces, and (b) were assumed to be different on the two ingot faces and in the corner. Small differences in solid fraction were observed while temperature distribution showed significant differences when more appropriate heat transfer boundary conditions were used on the end face and corner regions”* [76]. Rafique et al. [77] applied modeling and simulation to the problem of heat transfer during solidification of liquid metal in investment casting mold using C++. A mathematical model was developed using standard transport equations incorporating all heat transfer coefficients to calculate the time for solidification of metal in casting and computer simulation of the model was carried out in C++ to validate the model.

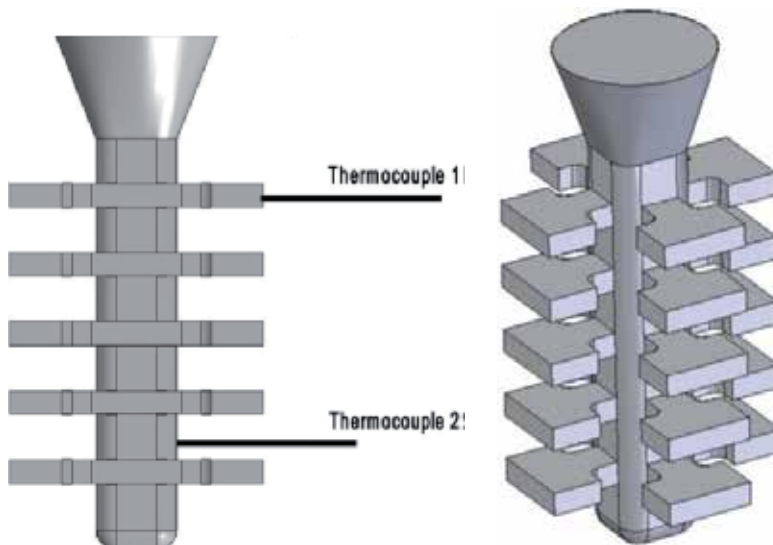


Figure 13. Investment casting tree a) with thermocouples b) schematic [77]

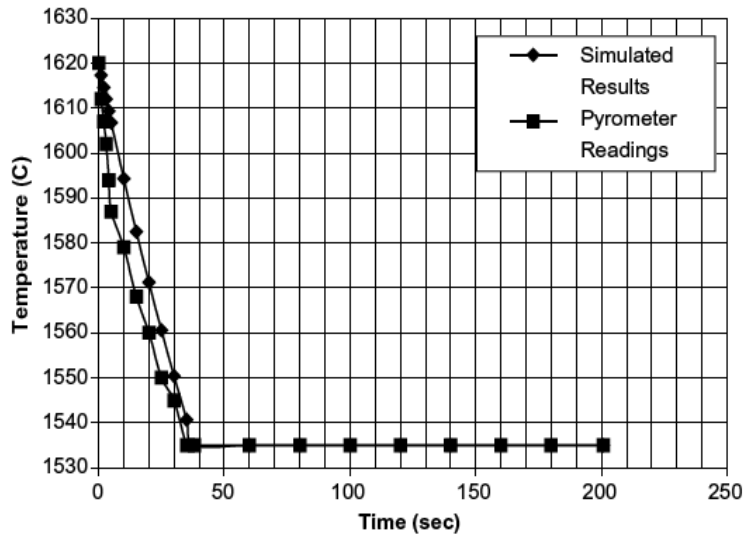


Figure 14. Effect of time on metal temperature (simulated and measured from pyrometer) [77]

The computed results were found in good agreement with experimental data paving the way for process operation, optimization and improvement. Ramírez-López et al. [78] discussed the problem of heat transfer and modeled it using C++ in continuous casting process. “The algorithms developed to calculate billet temperatures, involve the solutions of the corresponding equations for the heat removal conditions such as radiation, forced convection, and conduction according to the billet position through the CCP. This is done by a simultaneous comparison with the kinematics model. A finite difference method (Crank-Nicholson) is applied to solve the two-dimensional computational array (2D model). Enthalpy (H_i, J) and temperature (T_i, J) in every node are updated at each step time” [78]. The results are compared with the surface temperature of three steel casters under different operating conditions and found to be in good agreement. Hardin et al. [79] developed a 3D simulation model for continuous steel slab caster. The temperature predictions are validated using pyrometer data from an operating caster. The stress simulation is based on a visco-plastic constitutive equation for steel, where the semi-solid mush is treated as a compressible porous medium. The stress predictions show regions in the slab where hot tears and cracks are likely to form.

3.3.2. Welding

The application of heat transfer phenomena on welding and joining processes have been studied to check, determine and ascertain its effect on welding process, weld design, determination of weld structure and effect of process control parameters on weld formation. Hu et al. [80] described heat and mass transfer during gas metal arc welding using a unified comprehensive model. Based on this, a thorough investigation of the plasma arc characteristics during the gas metal arc welding process was conducted incorporating all parameters such as

interactive coupling between arc plasma; melting of the electrode; droplet formation, detachment, transfer, and impingement onto the work piece; and weld pool dynamics. The assumed Gaussian distributions of the arc pressure, current and heat flux at the weld pool surface in the traditional models were shown not to be representative of the real distributions in the welding process. In the second part of this study [81], the transient melt-flow velocity and temperature distributions in the droplet and in the weld pool were calculated. They simulated the crater formation in weld pool as well as the solidification process in the electrode and in the weld pool after the current were turned off. The predicted droplet flight trajectory is in good agreement with published data. Takemori et. al. [82] studied the numerical simulation of the heat transfer on the compressor during the welding process. It is used to determinate housing and internal components temperatures of the compressor during the sealing welding. A lumped parameter model was used to study various welding variables initially. After that, the best welding process was analyzed in detail using a numerical solution of a 3D transient model. All the monitored temperatures during the simulation were found very close to the temperatures measured experimentally, thus validating the model. Daha, et al. [83] discussed the problem of heat transfer in keyhole plasma arc welding of dissimilar steel joints (2205 – A36) using 3D heat transfer and fluid flow model. An adaptive heat source is proposed as a heat source model for performing a non-linear transient thermal analysis. Temperature profiles and solidified weld pool geometry are presented for three different welding heat input. The reversed bugle shape parameters are proposed to successfully explain the observations. The model was also applied to keyhole plasma welding of 6.8 mm thick similar 2205 duplex stainless steel joint for validation. The simulation results were found in good agreement with independently obtained experimental data.

3.3.3. *Machining*

Machining processes have been studied by heat transfer methods and their use has increased lately with the introduction of modeling and simulation techniques. Their use has made easier the defining process, determining its parameters, driving its efficiency and optimization. Processes such as facing, turning, milling, shaping, groughing, honing have been modeled to investigate effect of process itself, material, lubricant, etc. as a function of heat transfer process. Åkerström [84] discussed the problem of heat transfer associated with thermo-mechanical forming of thin boron steel sheets into ultra-high strength components via modeling and simulation. The objective is to predict the shape accuracy, thickness distribution, and hardness distribution of the final component with high accuracy. Method based on multiple overlapping continuous cooling and compression experiments (MOCCCT) in combination with inverse modeling (mechanical response) and a model based on combined nucleation and growth rate equations (austenite decomposition) was developed and used. FE – code LS – DYNA was used for simulating these models. The results were compared for forming force, thickness distribution, hardness distribution, and shape accuracy/springback with experimental values and found to be in good agreement. Iqbal et al [85] discussed the problem of interface heat transfer coefficient for finite element modeling of high-speed machining. They used an improved heat transfer coefficient for heat generation and frictional contact, derived from an experimental setup, consisting of an uncoated cemented carbide pin rubbing against a steel workpiece while

the latter was rotated at speeds similar to the cutting tests. This “pin-on disc” set-up had temperature and force monitoring equipment attached to it for measurements. Results show that the estimated interface heat transfer coefficient decreases at low rubbing speeds and then becomes approximately constant for high rubbing speeds. At these low rubbing speeds, the estimated values show a dependence on temperature. Interface heat transfer coefficient for a range of rubbing speeds of the dry sliding process is produced from modeling and simulation results and found to be in good agreement with experimental values. In a similar study [86], they used and developed a Lagrangian finite element code DEFORM 2D for studying same phenomena and found it to be useful. Ma et al. [87] discussed and applied FE analysis on thermal characteristics of Lathe Motorized Spindle. The structure feature of the spindle was introduced defining two major internal heat sources of motorized spindle with the aim to calculate the heat transfer coefficients of the major components of the lathe spindle. *“A 2D temperature field model has been developed with finite element method. Based on it, the temperature field and temperature rises of the spindle have been simulated and the reasonability of temperature distribution of the spindle unit has also been discussed. The results yielded reference for evaluating the thermal behavior of the high speed NC motorized spindle and proved to be effective practically”.* [87]

3.3.4. Forming processes

Forming processes, in general, such as rolling, forging, extrusion have been vastly studied by heat transfer methods and their modeling and simulation. This comprises the main area of heat transfer application in metal forming industry and processes related to it. These studies have revealed in great detail the discrepancies (defect formation and its causes, energy inefficiency, etc.) in processes and helped increase their efficiency and optimization. Behrens [88] discussed the modeling and simulation of friction and heat transfer models in hot forging processes. Two representative forging tests were carried out; the forming load and surface temperature distribution were recorded incorporating effects such as prevailing normal stress and shear yield stress of the workpiece material, the temperature and surface roughness of the tool and workpiece as well as the relative sliding velocity. By means of these data, the models were appropriately extended and adjusted using the software FORGE ®.

The application of the extended models allows for a more accurate description of the interaction at the contact interface and delivers more realistic results. Rabbah et al. [89] explained the use of modeling and simulation of heat transfer along a cold rolling system. *“They used a semi analytical solution for the work roll subjected to predict transient thermal profiles of work rolls with multiple cooling / heating zones. It was derived from the heat balance equation using the finite difference method and Runge-Kutta method. Numerical simulations are based on both recursive calculation methods and iterative methods”* [89]. The model suggested is used for the numerical simulations in rolling using the work roll temperature distribution within a very short computing time. The thermal profile development depends primarily on the cooling water flow. Thus, the cooling conditions (fluid temperature) and the corresponding heat transfer coefficients are very important in the model adjustment process. The objective of the study was the development of a control law to reduce to the maximum the deformations of both the strip and the work rolls which was simulated efficiently. Parvizian et al. [90] discussed the modeling and

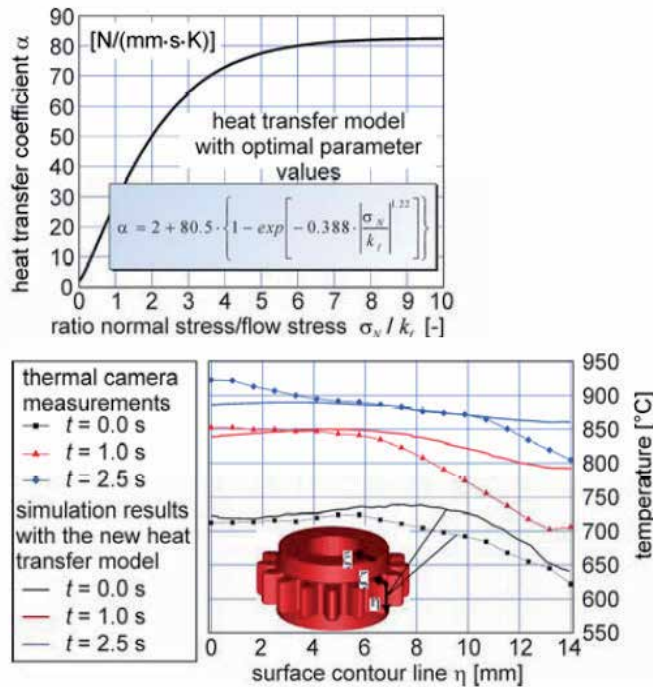


Figure 15. Finite element results based on the developed method [88]

simulation of aluminum alloys during extrusion, cooling and further forming processes. Individual steps are combined into multi-stage processes in order to optimize the production process as a whole. “A number of aspects of the structural simulation as well as that of extrusion as a thermomechanical process are considered. These aspects include contact and adaptive mesh refinement, heat transfer inside the billet, heat transfer between the workpiece and the container, frictional dissipation, mechanical energy and surface radiation” [90]. Commercial finite-element program ABAQUS and an external remeshing software incorporate the effects of python scripting and mesh refinement respectively. The achieved results were in good agreement.

3.4. Modeling and simulation of heat transfer in defense applications

Application of heat transfer phenomena in defense applications such as determination of efficiency of engines, their design and material design, performance, and selection; determination of heat transfer profiles of guns, barrels and shells; design and selection of suitable high-performance materials (composite structures and their design), etc., has been a major field of study. Many excellent studies explain in detail the application of heat transfer principles and their simulation approaches as applied to defense applications. Wu et al. [91] explained the phenomena of heat transfer in a 155 mm compound gun barrel cooled by midwall cooling

channels. *“Finite element analysis (FEA) method was employed to validate the results obtained by theoretical analyses. The present study showed: (1) natural air cooling is ineffective for transferring the heat out of the barrel because the combined convection and radiation heat transfer coefficient is relatively small; (2) forced midwall cooling has great heat extraction capability and is able to keep the chamber temperature below the cook-off temperature by increasing the heat transfer coefficient; (3) an optimal flow rate should be selected to balance the cooling efficiency and the pressure loss”* [91]. A similar study conducted by Mishra et al. described an accurate modeling of gun barrel temperature variation over time to assess wear and the number of shot fires needed to reach cook-off. *“Using lumped parameter methods, an internal ballistics code was developed to compute heat transfer to the gun barrel for given ammunition parameters. Subsequently the finite element method was employed to model gun barrel temperature history (temperature variation over time). Simulations were performed for a burst of nine shots and the results were found to match satisfactorily to the corresponding experimental measurements”* [92]. An important and unique advantage of the developed scheme is that it easily couples internal ballistics simulations with the finite element methods and also accurately calculates gun barrel temperature history and wear calculations. Sutar et al. explained unsteady heat transfer in externally heated Magnesium Thermic reduction reactor. *“Simulations were carried out using Anuprva, a computational fluid dynamics (CFD) and heat transfer solver to study the temperature profiles inside the reactor including its lining. The results are studied for both preheating and reaction stage which gives an idea about the reaction temperature and molten mass inside the reactor proving present study’s significance for correct design of reactor thereby preventing nuclear radiation to the surroundings”* [93]. Numerous other studies review the use of modeling and simulation techniques for heat transfer analysis in military, defense as well as strategic applications [63, 76, 94 – 96].

3.5. Modeling and simulation of heat transfer in energy applications

Heat transfer via modeling and simulation has been rigorously applied in energy applications (energy generation and production methods) for process identification, operation, improvement and optimization. It has been applied in all areas of energy methods (source tapping, method determination and generation of power from source, conversion of power to energy and its distribution, etc.) and all field of energy generation and production (thermal, hydal, wind, geothermal, solar, fuel cell, nuclear, etc.) and has generated excellent results coupled with capital saving. Schimon et al. [97] modeled and simulated different components of power plant and associated heat transfer phenomena using Modelica. The heat transfer for the heat exchanger component was modeled by calculating the heat transfer coefficient in dependency on the flow velocity of the medium in the pipes. Dymola (a Modelica based tool) was used to perform simulations. The models were realized with time domain differential equations and algebraic equations. Bandyopadhyay [98] presented modeling and simulation of heat transfer phenomena in solar thermal power plants. Models developed were based on the fundamental conservation algebraic equations along with phenomenological laws and simple representative equipment characteristics whose simulations were carried out. Different detailed equipment characteristics including thermal stresses, time variations of components etc. were incorporated in the developed models and then were simulated for control and optimization. Ramousse et al. [99] presented a fuel cell model that takes into account heat transfer in MEA

and bipolar plates along with gas diffusion in the porous electrodes, water diffusion, and electro-osmotic transport through the polymeric membrane. Heat and mass transfer phenomena in the cell are combined with “coupled charge and mass transfers in the electrodes, considered porous to construct the model. The results show that thermal gradients in the MEA could lead to thermal stresses at high current densities. The feeding gas temperature influence on the cell temperature is also important” [99] and shown to bear significance on overall cell performance. Yuan et. al [100] extended the use of modeling and simulation to similar problems in PEMFC and SOFC. They further used modeling and simulation and predicted convective heat transfer and pressure drop in flow ducts of fuel and the oxidant.

3.6. Modeling and simulation of heat transfer in miscellaneous applications

Apart from the above branches, heat transfer and its modeling and simulation is also applied in various other fields of engineering and technology such as electronics, environmental engineering, biomaterials and biomedical engineering, etc., to take advantage of process modeling, operation, and optimization. Guérin et al. [101] used finite volume approach to model and simulate the heat transfers between the different environmental elements to synthesize realistic winter sceneries. They simulated snow fall over the ground, as well as the conductive, convective, and radiative thermal transfers according to the variations of air and dew point temperatures, the amount of snow, cloud cover, and day-night cycles.

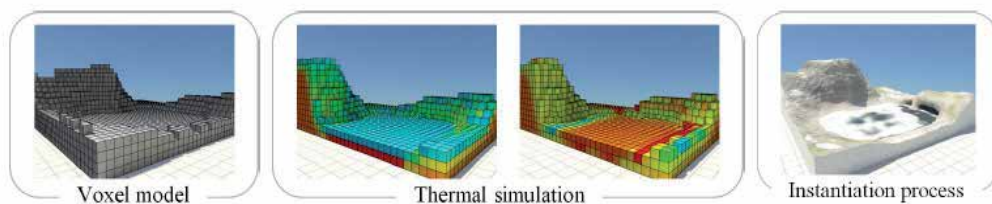


Figure 16. Synthetic overview of winter scenery generation process (high altitude partially frozen lake) [101]

The model also takes into account the phase changes such as snow melting into water or water freezing into ice and yielded good results and inferences. Lakatoš et. al. (2006) [102] used FEMLAB to simulate heat transfer and electromagnetic fields for the development of protected microcomputer prototypes. Heat field was extended and simulated from heat sources inside a monitor case along with electromagnetic fields in electronic systems. The temperature dependence on time was interpreted along with value of steady temperature. Elwassif et. al. developed and used a bio heat transfer model for getting information on the thermal effects of DBS using finite element models to investigate the magnitude and spatial distribution of DBS-induced temperature changes. “The parameters investigated include stimulation waveform, lead selection, brain tissue electrical and thermal conductivities, blood perfusion, metabolic heat generation during the stimulation and lead thermal conductivity/heat dissipation through the electrode.” [103]. It was shown that depending on stimulation/tissue parameters, temperature of surrounding tissue is increased by to 0.8°C in clinical DBS protocols.

4. Conclusions

Heat transfer studies comprise an important part of engineering analysis for any system ranging from automotive to process to energy applications. These are first hand analyses in any engineering problem/application related directly and/or indirectly with heat. Lately, modeling and simulation techniques and use of high-speed computers have greatly facilitated the thermal and heat transfer related analysis. More and more models are being developed, tested and used to ease out the calculations involved in the process also yielding direct results and even predicting future trends and auxiliary data. The present chapter deal with and explained in detail this field of engineering in a rational and practical way. Modeling and simulation of heat transfer phenomena as developed and applied is presented in various engineering applications. New and novel processes (investment casting, numerical machining, fuel cell technologies etc.) have also been discussed. The chapter draws attention to the use of modeling and simulation techniques and use of simulation packages (C++, MATLAB ® SIMULINK ®, Modelica, FLUENT, SolidCAST, COMSOL Packages, etc.) for solving heat transfer related problems of conventional and advanced processes, at the same time encouraging the reader to develop his/her own models for specific engineering problem/application.

Author details

Muhammad Musaddique Ali Rafique

Address all correspondence to: mrafique001@ikasle.ehu.es

Interdisciplinary Research Center in Biomedical Materials (IRCBM), COMSATS Institute of Information Technology, Lahore Campus, Raiwind, Lahore, Pakistan

References

- [1] Wikipedia, the free encyclopedia, Accessed April 17, 2012.
- [2] Subramanian, K., et al. *Mathematical modeling and simulation of reciprocating compressors – a review of literature*, Math Model ApplComput. 2010, 1, 81–96.
- [3] Rohde, J and Jeppsson, A, “*Literature review of heat treatment simulations with respect to phase transformation, residual stresses and distortion*,” Scandinavian Journal of Metallurgy, 2000, 29(2), 47-62.
- [4] Poulidakos, D., Arcidiacono, S., and Maruyama, S., *Molecular dynamics simulations in nanoscale heat transfer: a review*. Microsc Thermophysic Engin 7, 2003, 181-206.

- [5] Zhuomin Zhang, *Nanotechnology Heat Transfer*, 1st Edition, McGraw Hill Education EMEA, Berkshire, UK, 2007
- [6] Åström, K. J. et al. *Evolution of Continuous-Time Modeling and Simulation*, The 12th European Simulation Multiconference, ESM'98, June 16–19, 1998, Manchester, UK
- [7] Sokolowski, J. A., and Banks, C. M., (Eds.), *Principles of Modeling and Simulation: A Multidisciplinary Approach*, John Wiley & Sons, Inc., N. Y., 2009
- [8] IBM Research — Deep Blue Available at <http://www.research.ibm.com/deepblue/watch/html/c.shtml> Accessed 2008 Jan 2
- [9] Young J. P. *History and Bibliography of War Gaming*. Department of the Army; Bethesda, Maryland, 1957.
- [10] Link Simulation & Training. Available at <http://www.link.com/history.html> Accessed 2008 Jan 2.
- [11] Ören TI. (2005 — Invited Tutorial). Toward the Body of Knowledge of Modeling and Simulation (M & SBOK), In Proceedings of I/ITSEC (Interservice/Industry Training, Simulation Conference); 2005 Nov 28 – Dec 1; Orlando, FL. pp. 1 – 19.
- [12] Levitt, M., *Protein folding by restrained energy minimization and molecular dynamics*, J. Mol. Biol. (1983) 170, 723-764
- [13] Micheletti, C. and Maritan, A., *A study of energy minimization techniques applied to protein design*, <http://arxiv.org/abs/cond-mat/9808154v1> Aug 14, 1998
- [14] Sutton, A. P. et al., *Direct free energy minimization methods: Application to grain boundaries*, New methods for modeling processes within solids and at their surfaces, Philosop Transact: Physic Sci and Engin, (1992) 341, (1661), pp. 233-245
- [15] Lwin, Y., *Chemical equilibrium by Gibbs energy minimization on spreadsheets*, Int J Engin Ed. 2000, 16 (4): 335 – 339.
- [16] Veksler, O., *Efficient Graph Based Energy Minimization Method in Compute Vision*, PhD Thesis, Cornell University, Ithaca, N. Y, 1999.
- [17] Boykov, Y., Veksler, O., and Zabih, R., *Fast approximate energy minimization via graph Cuts*, IEEE Transactions on Pattern Analysis and Machine Intelligence, 2001, 23 (11).
- [18] Szeliski1, R. et al. *A Comparative Study of Energy Minimization Methods for Markov Random Fields*, In A. Leonardis, H. Bischof, and A. Prinz (Eds.): ECCV 2006, Part II, LNCS 3952, © Springer-Verlag Berlin Heidelberg 2006, pp. 16–29.
- [19] Kim, J., Kolmogorov, V. and Zabih, R., *Visual correspondence using energy minimization and mutual information*, Proceedings of the Ninth IEEE International Conference on Computer Vision (ICCV 2003) 2-Volume Set (2003)
- [20] Nikolova, M., *Energy minimization methods*, In Otmar Scherzer (Eds.), *Handbook of Mathematical Methods in Imaging*, 1st edition, Springer (2011).

- [21] Onofrio, D. and Tubaro, S., *A model based energy minimization method for 3D face recognition*, 2005 IEEE International Conference on Multimedia and Expo, (ICME 2005) pp. 1274-1277, 2005.
- [22] Standard, J. M., *Energy minimization methods*, Chemistry 380.37, Department of chemistry handouts, Illinois State University, (2011)
- [23] Allen, M. P. *Introduction to Molecular Dynamics Simulation, computational soft matter: from synthetic polymers to proteins*, Lecture Notes, N. Attig, K Binder, H Grubmuller, K Kremer (Eds.), John von Neumann Institute for Computing, Julich, NIC Series, Vol. 23, ISBN 3-00-012641-4, (2004) pp. 1-28.
- [24] *Principles and Engineering Applications of Molecular Dynamics Simulations*, Course 151-0267-00L, ETH Zurich, Switzerland, 2011.
- [25] Hedman, F., *Algorithms for Molecular Dynamics Simulations – Advancing the Computational Horizon*, PhD Thesis, Stockholms Universitet, Stockholm, Sweden, (2006).
- [26] van Gunsteren, W. F. et al., *Computer simulation of molecular dynamics: methodology, applications, and perspectives in chemistry*, Anger Chem Lnr Ed Engl (1990) 29, 992-1023.
- [27] McKenzie, M. *Computational Chemistry Molecular Dynamics: Programming to Production*, Presentation, HPC, Louisiana State University, (2011).
- [28] Karplus, M., and McCammon, J. A., *Molecular dynamics simulations of biomolecules*, Natur Struct Biol., 2002, 9, 646 – 652.
- [29] Kovalskyy, D. et al. *A Molecular dynamics study of the structural stability of HIV-1 protease under physiological conditions: the role of Na⁺ Ions in stabilizing the active site*, Proteins: Struct, Funct, and Bioinform (2005), 58: 450–458.
- [30] Kupka, S. "Molecular Dynamics on Graphics Accelerators". Central European Seminar on Computer Graphics for Students 2006.
- [31] Maruyama, S., *Molecular dynamics method For microscale heat transfer*, In W. J. Minkowycz and E. M. Sparrow (Eds.), *Advances in Numerical Heat Transfer*, Vol. 2, Taylor & Francis, New York, Chap. 6, pp. 189-226..
- [32] Maruyama, S. *A molecular dynamics simulation of heat conduction of finite length single walled carbon nanotubes*, Microscale Thermophysi Engin, (2003) 7:41–50.
- [33] Xinwei Wang and Xianfan Xu, *Molecular Dynamics Simulation of Heat Transfer and Phase Change During Laser Material Interaction*, J of Heat Transf, Transac ASME, April 2002, Vol. 124.
- [34] David T.W. Lin and Yuh-Chung Hu, *A Molecular Dynamics Study of Thermal Ablation*, Proceedings of the 1st IEEE International Conference on Nano/Micro Engineered and Molecular Systems January 18, 21, 2006, Zhuhai, China

- [35] Krivtsov, A. M., et al., *Molecular dynamics investigation of heat conductivity in monocrystalline materials with defects*, Proceedings of XXXV International Summer School-Conference APM2007, 264 – 276.
- [36] Krivtsov, A. M., et al. *Molecular dynamics simulation of mechanical properties for polycrystalline materials*, Mater Phys Mech (2001), 3, 45-51.
- [37] Steinhäuser, O. M. *Introduction to molecular dynamics simulations: applications in hard and soft condensed matter physics*, In: Lichang Wang (Ed.), *Molecular Dynamics – Studies of Synthetic and Biological Macromolecules*, ISBN 978-953-51-0444-5, Intech Publishers, 2012
- [38] Wittwer, J.W., "Monte Carlo Simulation Basics" From *Vertex42.com*, June 1, 2004, <http://www.vertex42.com/ExcelArticles/mc/MonteCarloSimulation.html>
- [39] Howell, J. R., The Monte Carlo method in radiative heat transfer, *J of Heat Transfer, Transactions of ASME*, 1998, 120, 548 – 560.
- [40] Zeeb, C. N., *Performance and Accuracy Enhancement of Radiative Heat Transfer Modeling via Monte Carlo*, Colorado State University, Fort Collins, Colorado, Fall 2002.
- [41] Kersch, A., et al., IMA Reprint Series # 1110, March 1993.
- [42] Modest, M. F. *Backward Monte Carlo simulations in radiative heat transfer*, *J. Heat Transfer*, 2013, 125 (1), 57.
- [43] Frijns, A. J. H., Nedea, S. V. and van Steenhoven, A. A., *Molecular dynamics and Monte Carlo simulations for heat transfer in micro- and nanochannels*, *I J Multiscale Comput Engin*, 2006, 4(3), 391–397.
- [44] Wang, M., et al. *Simulations for gas flows in microgeometries using the direct simulation Monte Carlo method*, *Int J Heat Flu Flow* 2004, 25 975–985.
- [45] Wang, M., et al. *Gas mixing in microchannels using the direct simulation Monte Carlo method*, *Int J Heat Mass Transf.* 2006, 49 1696–1702.
- [46] Liu, H., et al. *Monte Carlo simulations of gas flow and heat transfer in vacuum packaged MEMS devices*, *Appl Thermal Engin*, 2007, 27, 323 – 329.
- [47] http://cmm.info.nih.gov/intro_simulation/node24.html Accessed June 2, 2012
- [48] Antonie, O. *Langevin dynamics of protein folding: influence of confinement*, Masters Degree Project, Scuola Internazionale Superiore di Studi Avanzati, SISSA, Trieste, Italy (2007)
- [49] Lange, O. F., and Grubmüllera, H. *Collective Langevin dynamics of conformational motions in proteins*, *J Chem Phys* 2006, 124, 214903 DOI: 10.1063/1.2199530
- [50] Quigley, D., and Probert, M. I. J., *Langevin dynamics in constant pressure extended systems*, *J Chem Phys*, 2004, 120, 11432 doi: 10.1063/1.1755657

- [51] Rongliang Wu, Ting Li and Erik Nies *Langevin dynamics simulation of chain crosslinking into polymer networks*, *Macromol Theory Simul.* 2012, 21, DOI: 10.1002/mats.201100088
- [52] http://cmm.info.nih.gov/intro_simulation/node26.html Accessed June 8, 2012
- [53] Magyari, E. Normal mode analysis of the fully developed free convection flow in a vertical slot with open to capped ends, *Heat Mass Transf* 2007 43:827–832, DOI 10.1007/s00231-006-0162-2
- [54] Schuyler, A. D., et al., *Normal mode analysis of proteins: a comparison of rigid cluster modes with C_α coarse graining*, *J Mol Graphics Model* 2004, 22, 183–193
- [55] <http://dirac.cnrs-orleans.fr/plone/Members/hinsen> Accessed June 29, 2012
- [56] Busetti, F. (2003). Simulated annealing overview. 2003 163.18.62.64/wisdom/Simulated%20annealing%20overview.pdf, Accessed June 29, 2012.
- [57] Press, W. H., Flannery, B. P., Teukolsky, S. A., and Vetterling, W. T. *Numerical recipes in FORTRAN 77: The art of scientific computing, Ch – 10*, The Cambridge University Press, 1986 – 1992
- [58] *Modeling and Simulation for Process Industry*, VTT Technical Research Centre of Finland, Vuorimiehentie 3, Espoo P.O.Box 1000, FI-02044 VTT, Finland
- [59] Bordbar, M. H., and Hyppänen, T, *Modeling of radiation heat transfer in a Boiler Furnace*, *Adv. Studies Theor. Phys.*, 2007, 1 (12), 571 – 584.
- [60] Zeeb, C. N., *Two dimensional Radiative Heat Transfer in Combustion Gases via Monte Carlo*, Thesis, Colorado State University, Fort Collins, Colorado (1996).
- [61] Gómez, A., Fueyo, N., Díez, L. I., *Modelling and simulation of fluid-flow and heat transfer in the convective zone of a power-generation boiler* *Appl Thermal Engin* 2008, 28, 5-6, 532.
- [62] Sørensen, K., et al. *Modeling and simulating fire tube boiler performance* The 44th Conference on Simulation and Modelling, Västerås, Sweden, September 18-19 2003.
- [63] Sørensen, K., et al. *Modeling, simulating and optimizing boiler heating surfaces and evaporator circuits* The 44th Conference on Simulation and Modelling, Västerås, Sweden, September 18-19 2003.
- [64] Dafe, E., *Numerical Simulation of Heat Transfer and Pressure Drop in Plate Heat Exchangers Using Fluent as CFD Tool*, Master Degree Thesis, ISRN: BTH – AMT- EX – 2008/D – 11 – SE, Department of Mechanical Engineering, Blekinge Institute of technology, Karlskrona, Sweden, 2008.
- [65] Skoglund, T., et al. *Dynamic object-oriented heat exchanger models for simulation of fluid property transitions*, *Int J Heat Mass Transf* 2006, 49, 2291–2303.
- [66] Othman, K. H., et al. *CFD Simulation of Heat Transfer in Shell and Tube Heat Exchanger*, Bachelor Degree Thesis, Faculty of Chemical and Natural Resource Engineering, Universiti Malaysia Pahang, Malaysia, 2009

- [67] Corberan, J.M. and Melon, M.G., *Modeling of plate finned tube evaporators and condensers working with R134a*, Int. J. Refrig 1998 21 (4) 273-284.
- [68] Qureshi, B. A., et al., *A comprehensive design and rating study of evaporative coolers and condensers. Part I. Performance evaluation*, Int J of Refrig 2006, 29, 645–658
- [69] Acunha, Jr., A. C., et al. *Numerical simulation of air – water flows in an evaporative condenser*, Engenharia Térmica (Therm Engin), June 2009, 8, (01) 24-30.
- [70] Tzong-Shing Lee and Jhen-Wei Mai. *Modeling and simulation of the heat transfer behaviour of a shell-and-tube condenser for a moderately high-temperature heat pump*, In Dr. Animul Ahsan (Ed.), Two Phase Flow, Phase Change and Numerical Modeling, ISBN: 978-953-307-584-6, InTech, Austria (2011).
- [71] Therdthai, N., et al., *Three-dimensional CFD modelling and simulation of the temperature profiles and airflow patterns during a continuous industrial baking process*, J Food Engin, 2004, 65 (4) 599 – 608.
- [72] Flick, D., et al. *Modeling heat transfer and fluid flow inside a pressure cooker*, The 17th European Symposium on Computer Aided Process Engineering – ESCAPE17, 2007.
- [73] Sargolzaei, J., et al. *Modeling and Simulation of Hamburger Cooking Process Using Finite Difference and CFD Methods*. Int. J. Ind. Chem., 2011, 2 (1) 52-62.
- [74] Hussain, S., et al. *2-dimensional CFD Simulation of the air flow inside a lemang oven*, Int J of Engin Sci Technol, 2011, 3 (9), 7103 – 7107.
- [75] Rek, Z., et al. *Application of CFD Simulation in the development of new generation heating oven*, Strojniški vestnik – J Mech Engin 2012 58 (2) 134-144.
- [76] Sabau, et al. *Heat Transfer Boundary conditions for the numerical simulation of the DC casting process*. In Alton T. Tabereaux (Ed.) Light Metals TMS (The Minerals, Metals & Materials Society), 2004.
- [77] Rafique, M. M. A., et al., *Modeling and Simulation of heat transfer phenomena during investment casting*, I J Heat Mass Transf 2009, 52, 2132–2139.
- [78] Ramírez-López, A., et al., *Simulation of heat transfer in steel billets during continuous casting*, Int J Min, Metall Mater, August 2010, 17 (4) DOI: 10.1007/s12613-010-0333-5
- [79] Hardin, R., et al. *Three dimensional Simulation of heat transfer and stresses in a steel slab caster* Proceedings of the 4th International Conference on Modeling and Simulation of Metallurgical Processes in Steelmaking, Paper No. STSI-71, Steel Institute VDEh, Düsseldorf, Germany, 2011.
- [80] Hu, J., et al., *Heat and mass transfer in gas metal arc welding. Part I: The arc*, International Journal of Heat and Mass Transfer 50 (2007) 833–846
- [81] Hu, J., et al., *Heat and mass transfer in gas metal arc welding. Part I: The metal*, Int J Heat Mass Transf 2007, 50, 808–820.

- [82] Takemori, C. K., et al., *Numerical Simulation of Transient Heat Transfer During Welding Process*, International Compressor Engineering Conference at Purdue, July 12-15, 2010.
- [83] Daha, M. A., et al., *Numerical modeling of heat transfer and fluid flow in keyhole plasma arc welding of dissimilar steel joints*. Int. J. of Engin. Sci. and Technol (IJEST) February 2012, 4(02), 506 -518.
- [84] Åkerström, P., *Modeling and Simulation of Hot Stamping*, Doctoral Thesis, Department of Applied Physics and Mechanical Engineering, Division of Solid Mechanics, Luleå University of Technology 2006 30, ISSN: 1402-1544, ISRN: LTU – DT – 06/30 – SE
- [85] Iqbal, S. A., *An investigative study of the interface heat transfer coefficient for FE modeling of high speed machining*. Proc. IMechE: J. Engin Manufact, 2008, 222 Part B, 1405 -1416.
- [86] Iqbal, S. A., et al., *A Sensitivity Study Of The Effects Of Interface Heat Transfer Coefficient On FE Modeling Of Machining Process For A Wide Range Of Cutting Speeds*, The 6th International Conference on Manufacturing Research (ICMR08) Brunel University, UK, 9-11th September 2008.
- [87] Ma., P., et al., *Finite element analysis on thermal characteristics of lathe motorized spindle*, Adv Materi Res, 2011, 311 – 313 2434 – 2439.
- [88] Behrens, B. –A., et al., *Numerical and experimental investigations on the extension of friction and heat transfer models for an improved simulation of hot forging processes*, Int J of Materi Forming, 2009, 2, 1, 121 – 124 DOI: 10.1007/s12289-009-0618-2
- [89] Rabbah, N., et. al. *Modeling and simulation of the heat transfer along a cold rolling system*, Lat Am Appl Res, 2009 39, 79 – 83.
- [90] Parvizian, F., et al., *Application of adaptive method in thermomechanical modeling and simulation of extrusion of aluminum alloys*, The 8th. World Congress on Computational Mechanics (WCCM8), 5th European Congress on Computational Methods in Applied Sciences and Engineering (ECCOMAS 2008), June 30 –July 5, 2008, Venice, Italy
- [91] Wu, B., et al, *Heat transfer in a 155 mm compound gun barrel with full length integral mid-wall cooling channels*, Appl Therm Engin 2008, 28, 881–888.
- [92] Mishra, A., et al., *A Novel Scheme for Computing Gun Barrel Temperature History and Its Experimental Validation*, J Pressure Vessel Technol 2012, 132, (2012), 061202 – 1 – 061202 – 6
- [93] Sutar, H., et al., *Computational simulation of unsteady state heat transfer in externally heated magnesio thermic reduction reactor: an overview*, Int J Chem Engin and Appli, June 2011, 2(3).
- [94] Qingyan, Xu., et al. *Progress on modeling and simulation of directional solidification of superalloy turbine blade casting* China Foundry, 2012, 9(1).

- [95] Morrison, C., et al., *Modeling Heat Transfer in the Space Shuttle Thermal Protection System*, New Mexico Adventures in Supercomputing Challenge, Report (2004).
- [96] Sozer, E., et al. *Modeling of Fluid Dynamics and Heat Transfer through porous media for liquid rocket propulsion*, 43rd AIAA/ASME/SAE/ASEE Joint Propulsion Conference & Exhibit, 8, 11 July 2007, Cincinnati, OH.
- [97] Schimon, R., et al. *Simulation of components of thermal power plant*, The Modelica Association, Modelica, Sep 4 – 5th, 2006, 119 – 125.
- [98] Bandyopadhyay, S. *Modeling, Simulation and Optimization of Solar Thermal Power Plants*, Presentation, Indian Institute of Technology, Bombay, March 2008.
- [99] Ramousse, J., et al. *Modeling of heat, mass and charge transfer in a PEMFC single cell*, J Power Sources 2005, 145, 416 – 427.
- [100] Yuan, J., et. al, *On the heat and Mass Transfer Phenomena in PEMFC and SOFC and modeling approaches*, In B. Sundén & M. Faghri (Eds.) Transport Phenomena in Fuel Cells, Ch – 4, pp. 133-174, WIT Press, 2005 ISBN 1-85312-840-846.
- [101] Guérin, N. M. E., et al., Heat transfer simulation for modeling realistic winter scenarios, EUROGRAPHICS 2010 / T. Akenine-Möller and M. Zwicker, 2010 29 (2).
- [102] Lakatoš, J., et. al., *Simulation of heat transfer and electromagnetic fields of protected micro-computers*, Adv in Electrical and Electronic Engineering. 2006, 5 (3), 281-286.
- [103] Elwassif, M. M., et. al. Bio-heat transfer model of deep brain stimulation-induced temperature changes, J. Neural Engin. 2006, 3, 306–315.

Computer-Aided Determination of the Air-Side Heat Transfer Coefficient and Thermal Contact Resistance for a Fin-and-Tube Heat Exchanger

Jan Taler, Paweł Oćłoń, Dawid Taler and
Marzena Nowak-Oćłoń

Additional information is available at the end of the chapter

<http://dx.doi.org/10.5772/60647>

1. Introduction

Plate fin-and-tube heat exchangers with oval tubes attract the broad scientific interest due to its large thermal efficiency, significant heat transfer rate between the mediums and compact shape [1-10]. The heat exchangers of this type are widely used in industrial plants and installations, as air-coolers, convectors for home heating and waste heat recovery for gas turbines. The large thermal efficiency is achieved by using the external fins, fixed at the oval tubes of the heat exchanger [1-3]. Mostly, fin-and-tube heat exchangers operate in the cross-flow arrangements. A liquid (water or oil) flows through the tubular space of the heat exchanger, and gas (air, flue gas) flows across the intertubular space of the heat exchanger. Due to the use of external fins, a heat transfer rate increases when compared with tubes without fins. Moreover, the application of the oval tube shape reduces the pressure drop and improves heat transfer conditions on the gas side when compared to the circular shape [4-14, 17]. Since plate fin-and-tube heat exchangers operate in a cross-flow arrangement with the complex path of gas flow, hence in order to determine the velocity field and heat transfer characteristics, the numerical methods must be used [15-16, 18-25]. For the gas flow, with the use of the commercial CFD codes (ANSYS CFX [31], FLUENT), it is possible to calculate the local values of heat transfer coefficient. However, it is impossible to incorporate these values into the analytical formulas, which allow determining the overall heat transfer coefficient. These formulas are fundamental when designing cross-flow heat exchangers and use the average not local values of heat transfer coefficient. Therefore in this study authors present different methods for determination of the average heat transfer coefficient for gas flow in a plate fin-and-tube heat exchanger using the CFD simulations. The values of the heat transfer coefficient obtained using

the heat transfer formulas for the Nusselt number, determined with the CFD simulations, can be directly implemented in the thermal designing procedure of the cross-flow heat exchangers. The results of the numerical computations will be validated experimentally, using the procedures described in [14, 17, 20].

The numerical studies of the performance of plate fin-and-tube heat exchangers encounter difficulties in the proper prediction of the total gas side temperature difference. This problem occurs, because of the flow maldistribution of mediums flowing through the heat exchanger and thermal contact resistance between the fin and tube. The thermal contact resistance, which can significantly reduce the thermal performance of heat exchange apparatus, is difficult to determine [15, 19]. It is considerable when the oval tubes are inserted into the holes, which are stamped in metal strips. Then, the tubes are expanded to create the so-called interference fit. Since the gap exists between the fin and tube, the corrosion residuals can cumulate within the gap, leading to the decrease in heat transfer ability. It should be noted, that the direct investigation of thermal contact resistance is difficult to conduct. Therefore, the alternative methods are needed. This study discusses the alternative approach to determining the thermal contact resistance between fin and tube, based on the CFD simulation and experimental data. Moreover, the methods for determining the heat transfer coefficient correlations for the air side are also presented.

2. Test facility – fin-and-tube heat exchanger with oval tubes

Figure 1 presents the scheme of a car radiator, for which the heat transfer coefficients will be determined [19].

The heat exchanger is used for cooling the spark ignition engine with a cubic capacity equal to 1, 580 cm³. Hot water, which flows inside the aluminum tubes of the heat exchanger, is cooled down by the air flowing across the intertubular space.

The two-pass /two-row fin and tube heat exchanger is considered. The following characteristics are given:

- Total number of tubes: 38, including 20 tubes in the first pass and 18 tubes in the second
- The tube length is $L_t = 0.52$ m.
- The radiator width, height, and thickness is equal to 520 mm, 359 mm and 34 mm, respectively
- The aluminum ($k = 207$ W/(m K)) oval tubes of outer diameters $d_{min} = 6.35$ mm and $d_{max} = 11.82$ mm, respectively, with thickness of $\delta_t = 0.4$ mm are used
- Total number of plate fins (359 mm height, 34 mm width and 0.08 mm thickness) along the tube length is 520
- The fin pitches in the perpendicular and longitudinal directions to the air flow are as follows: $p_1=18.5$ mm $p_2=17$ mm (Fig. 2, [19])

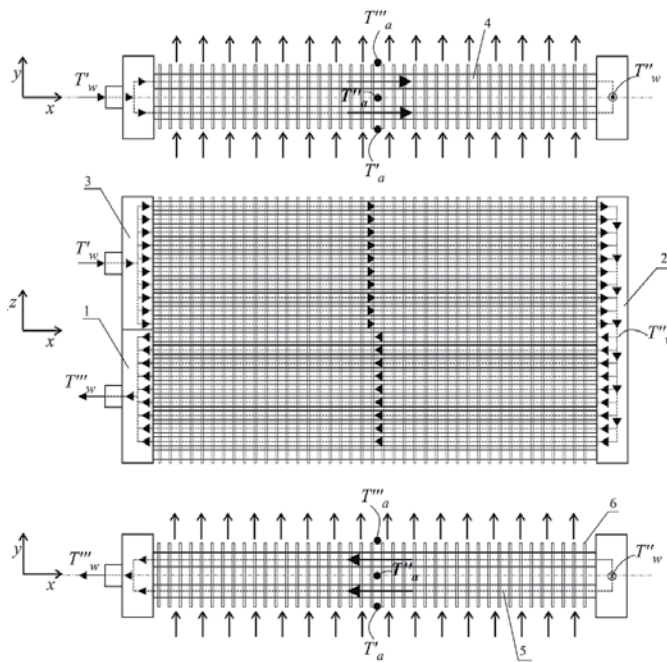


Figure 1. Flow scheme of two-row car radiator with two passes: 1 – inlet manifold, 2 – intermediate manifold, 3 – outlet manifold, 4 – second row of oval tubes, 5 – first row of oval tubes, 6 – plate fin.

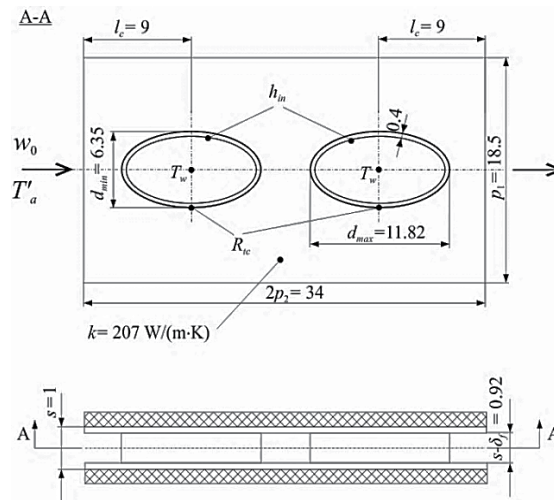


Figure 2. Scheme of the narrow air flow passage across the car radiator.

The path of the water flow is U-shaped, this means that the water reverses in the intermediate manifold. In the first pass (upper), the hot water with temperature T'_w flows from the inlet header (1) through the two rows of the oval tubes, with the length $L_t = 0.52$ m. Then, in the

intermediate header (2), the mixing of the water streams from the first (4) and second (5) row occurs. The intermediate temperature of the water is equal to T''_w . Next, the water reverses and flows into the two rows of the tubes located in the second (lower) pass. Finally, the liquid, cooled down to temperature T'''_w flows out of the heat exchanger through the outlet manifold (3). The air with inlet temperature T'_a flows in the normal direction to the both rows of the finned tubes. After the first and second row, air temperature is T''_a and T'''_a respectively (Fig. 1). The plate fins (6) are used to enhance the heat transfer from the air side.

For the CFD calculations presented in this paper (section 4), the flow in a narrow passage formed between two consecutive fins is considered.

3. Experimental methods of determining the air-side heat transfer coefficient in fin-and-tube heat exchanger

The experimental-numerical method for determining the average air-side heat transfer coefficient was described in details in ref. [14, 17]. Moreover, in ref. [17], the detailed list of measurement points, used in this work, is presented. The experimental-numerical method involves the performance tests of a car radiator (Fig. 1) and allows to obtain the formulas for the Nusselt number for the air and water flows. During the measurements the inlet and outlet air temperatures (T'_a and T'''_a), the inlet and outlet water temperatures (T'_w and T'''_w), the volumetric mass flow rate of water \dot{V}_w , and the inlet velocity of the air w_0 , are determined. The following change ranges of T'_a , T'''_a , \dot{V}_w , T'_w , T'''_w and w_0 were examined:

- $T'_a = 12.5 \text{ }^\circ\text{C} - 15 \text{ }^\circ\text{C}$,
- $T'''_a = 38.51 \text{ }^\circ\text{C} - 57.66 \text{ }^\circ\text{C}$,
- $\dot{V}_w = 865.8 \text{ dm}^3/\text{h} - 2186.40 \text{ dm}^3/\text{h}$,
- $T'_w = 61.0 \text{ }^\circ\text{C} - 71.08 \text{ }^\circ\text{C}$,
- $T'''_w = 49.58 \text{ }^\circ\text{C} - 63.83 \text{ }^\circ\text{C}$,
- $w_0 = 1 \text{ m/s} - 2.2 \text{ m/s}$.

The value of the experimental heat transfer coefficient $h_{a,i}^e$ for the air flow is determined based on the condition that the calculated outlet temperature $T_{w,i}^m(h_{a,i}^e)$ of water must be equal to the measured temperature $(T_{w,i}^m)^e$, where $i=1, \dots, n$ is the dataset number. The following non-linear algebraic equation must be solved for each dataset to determine $h_{a,i}^e$:

$$\left(T_{w,i}^m\right)^e - T_{w,i}^m\left(h_{a,i}^e\right) = 0, i = 1, \dots, n \quad (1)$$

where n is the number of datasets. This study employs the mathematical model of the heat exchanger developed in [11] to calculate the water outlet temperature $T_{w,i}^m$ as a function of the

heat transfer coefficient $h_{a,i}^e$. The heat transfer coefficient for the air flow $h_{a,i}^e$ is determined by searching for such a preset interval that makes the measured outlet temperature of water $(T_{w,i}^m)^e$ and the computed outlet temperature $T_{w,i}^c$ the same. The outlet water temperature $T_{w,i}^c(h_{a,i}^e)$ is calculated at each search step. Next, a specific form is adopted for the formula on the air-side Colburn factor $j_a = j_a(\text{Re}_a)$, with $m = 2$ unknown coefficients. The least squares method allows to determine the coefficients x_1, x_2 under the condition:

$$S_{min} = \sum_{i=1}^n \left[j_{a,i}^e - j_{a,i}(x_1, x_2) \right]^2 = \min, \quad m \leq n \quad (2)$$

where:

$$j_a = \text{Nu}_a / (\text{Re}_a \text{Pr}_a^{1/3}) \quad (3)$$

is the air Colburn factor and $\text{Pr}_a = \mu_a c_{pa} / k_a$ is the air Prandtl number. The $\text{Nu}_a = h_a d_h / k_a$ and $\text{Re}_a = w_{max} d_h / \nu_a$ are the air Nusselt and Reynolds numbers, respectively. The velocity w_{max} is the air velocity in the narrowest free flow cross-section A_{min} . The symbol $j_{a,i}^e$ is the experimentally determined Colburn factor, and $j_{a,i}$ is the j -factor calculated with the approximating function for the set value of the Reynolds number $\text{Re}_{a,i}$. The Colburn factor j_a is approximated by a power-law function:

$$j_a = x_1 \text{Re}_a^{x_2} \quad (4)$$

The unknown coefficients x_1 and x_2 are determined by the Levenberg-Marquardt method [35], using the Table-Curve program [36]. Combining Equations (3) and (4) one gets:

$$\text{Nu}_a = x_1 \text{Re}_a^{(1+x_2)} \text{Pr}_a^{1/3} \quad (5)$$

The w_{max} air velocity in the narrowest cross-section of flow A_{min} is defined as:

$$w_{max} = \frac{sp_1}{A_{min}} \left(\frac{\bar{T}_a + 273.15}{T'_a + 273.15} \right) w_0 \quad (6)$$

where A_{min} is

$$A_{min} = (s - \delta_f)(p_1 - d_{min}) \quad (7)$$

The equivalent diameter for the air flow passage d_h is [17, 18-19]:

$$d_h = \frac{4A_{min}L_t}{A_f + A_e}, \quad (8)$$

where the fin surface of a single passage A_f is:

$$A_f = 2 \cdot 2(p_1p_2 - A_{oval}) = (4p_1p_2 - \pi d_{min}d_{max}), \quad (9)$$

the tube external surface between two fins A_e is:

$$A_e = 2 \cdot P_o(s - \delta_f). \quad (10)$$

For the given parameters of the air-flow passage, the equivalent hydraulic diameter is $d_h = 0.00141$ m. The arithmetic average air temperature \bar{T}_a taken from the inlet air temperature T_a' and the outlet air temperature T_a'' is used to evaluate the thermal properties.

Air-side heat transfer correlations found in this chapter will be compared with the correlations of Kröger [37, 38].

The air-flow Nusselt number correlations, determined via the measurements, are listed in Table 1 [19, 20]. These correlations are paired with the water-flow heat transfer formulas, given in the literature [39- 41]. The correlations presented in Table 1 were employed to determine the outlet temperature of water $T_{w,i}''$ using the heat exchanger model [11].

The water flow criteria numbers are: $Nu_w = h_{in} d_t / k_w$ and $Re_w = w_w d_t / \nu_w$. The friction factor ξ is defined as:

$$\xi = \frac{1}{(1.82 \log Re_w - 1.64)^2} = \frac{1}{(0.79 \ln Re_w - 1.64)^2} \quad (11)$$

The mean water velocity in a single tube – w_w is calculated using the total volumetric flow rate \dot{V}_w as follows:

$$w_w = \dot{V}_w / (n_{tp} A_{w,in}), \quad (12)$$

where n_{tp} is the number of tubes in a single pass of the heat exchanger and $A_{w,in}$ is the cross-sectional area of the flow related to one tube.

No.	Correlation - experiment	Estimated parameters
1	$Nu_a = x_1 Re_a^{x_2} Pr_a^{1/3} \text{ (experiment)}$ $Nu_w = \frac{(\xi/8)(Re_w - 1000)Pr_w}{1 + 12.7\sqrt{(\xi/8)(Pr_w^{2/3} - 1)}} \left[1 + \left(\frac{d_t}{L_t} \right)^{2/3} \right]$ [39]	$S_{min} = 0.6678 \text{ K}^2$ $s_f = 0.1102 \text{ K}$ $x_1 = 0.1117 \pm 0.0024,$ $x_2 = 0.6469 \pm 0.0045$
2	$Nu_a = x_1 Re_a^{x_2} Pr_a^{1/3} \text{ (experiment)}$ $Nu_w = \frac{(\xi/8)(Re_w - 1000)Pr_w}{k_1 + 12.7\sqrt{(\xi/8)(Pr_w^{2/3} - 1)}} \left[1 + \left(\frac{d_t}{L_t} \right)^{2/3} \right]$ $k_1 = 1.07 + \frac{900}{Re_w} + \frac{0.63}{(1 + 10Pr_w)}$ [40]	$S_{min} = 1.2799 \text{ K}^2$ $s_f = 0.1540 \text{ K}$ $x_1 = 0.1309 \pm 0.00418,$ $x_2 = 0.6107 \pm 0.0559$
3	$Nu_a = x_1 Re_a^{x_2} Pr_a^{1/3} \text{ (experiment)}$ $Nu_w = \frac{(\xi/8)Re_w Pr_w}{1 + 8.7\sqrt{(\xi/8)(Pr_w - 1)}} \left[1 + \left(\frac{d_t}{L_t} \right)^{2/3} \right]$ [41]	$S_{min} = 1.4034 \text{ K}^2$ $s_f = 0.1569 \text{ K}$ $x_1 = 0.1212 \pm 0.0398,$ $x_2 = 0.6258 \pm 0.0595$
4	$Nu_a = x_1 Re_a^{x_2} Pr_a^{1/3} \text{ (experiment)}$ $Nu_w = \frac{\xi/8(Re_w - x_3)Pr_w}{1 + x_4(\xi/8)^{1/2}(Pr_w^{2/3} - 1)} \left[1 + \left(\frac{d_t}{L_t} \right)^{2/3} \right]$ [19]	$S_{min} = 1.2117 \text{ K}^2$ $s_f = 0.1496 \text{ K}$ $x_1 = 0.1012, x_2 = 0.6704$ $x_3 = 1404.4860, x_4 = 11.9166$

Table 1. Nusselt number formulas for the air flow Nu_a obtained from the measurements

The water-flow equivalent hydraulic diameter d_t is calculated as

$$d_t = \frac{4A_{w,in}}{P_{in}}, \tag{13}$$

where P_i denotes the oval perimeter (referred to inner tube wall). In this study, the water side hydraulic diameter d_t is 0.00706 m.

4. Determining of the air-side heat transfer coefficient using CFD simulations

The CFD simulations [32] were performed to model the heat and fluid flow processes in the air-flow passage, shown in Fig. 2. As a result, the air temperature and velocity are determined. Moreover, with the application of a conjugate heat transfer treatment, the wall temperature of fin and tube are calculated. A similar modeling approach for the gas flow in fin-and-tube heat exchangers was used in papers [15, 18-20]. The approach allows to simplify the computational

domain and reduce the computational costs. In this study, the CFD software ANSYS CFX - release 13.0 [31] was used. The phenomenon of air flow across the passage is complex e.g. flow is turbulent at the heat exchanger inlet and laminar between the fins. Hence, the SST turbulence model with Gamma-theta transitional turbulence formulation [33, 34] is used in computations. The model allows to study at the same time both the laminar and turbulent flows.

The element based finite volume method is used to discretize the differential governing equations. The coupled solver is used for the momentum and continuity equations. The Rhie-Chow interpolation scheme with the co-located grid is applied for pressure. The so-called "high resolution" scheme is used to discretize the convective terms [31].

Fig. 3 shows the discrete model and the applied boundary conditions. The model consists of three heat transfer domains: air (1), fin (2), and tube (3). The inlet boundary condition, where the values of air velocity w_0 and temperature T'_a are prescribed, is denoted as (I). At the outlet boundary (II) the pressure level was held constant at 1 bar. At the inner tube surface (III) the convective boundary condition is applied to model the heat transfer from the water to the tube wall. The water-side heat transfer coefficient h_{in} was determined from the experimental correlation for Nu_w given in Table 1. The bulk temperature of the water \bar{T}_w flowing through the tube is calculated as the arithmetic average of the measured temperatures: T'_w and T'''_w .

The thermal resistance between external tube surface and fin R_{tc} was set at location (IV). The symmetry boundary condition is applied at the location of (V) in Fig. 3.

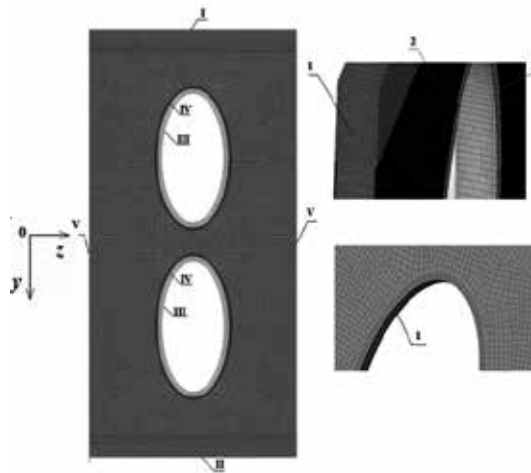


Figure 3. Flow passage studied during the computations: 1 – air, 2 – fin, 3 – tube; boundary conditions: I – inlet, II – outlet, III – convective surface, IV – solid \ solid interface (thermal contact resistance), V – symmetry.

The numerical mesh, shown in Fig. 3 was used in the computation (the number of nodes: 452917, the number of elements: 404560). The grid independence tests were performed for the mass averaged outlet air temperature. Refining this numerical model does not lead to the relative change in the obtained results more than 0.1 %. The global imbalance of mass,

momentum and energy equations were less than 0.1%. The boundary flow region computational accuracy was controlled by the so-called y^+ value which was less than 3 in the present computations.

The CFD simulation results, obtained for the following parameters: $w_0 = 0.8 \text{ m/s}$, $T'_a = 14.98 \text{ }^\circ\text{C}$, $h_w = 1512 \text{ W}/(\text{m}^2\cdot\text{K})$, $T_w = 73.85 \text{ }^\circ\text{C}$, $R_{tc} = 0 \text{ (m}^2\cdot\text{K)/W}$ are presented in Fig. 4 [19].

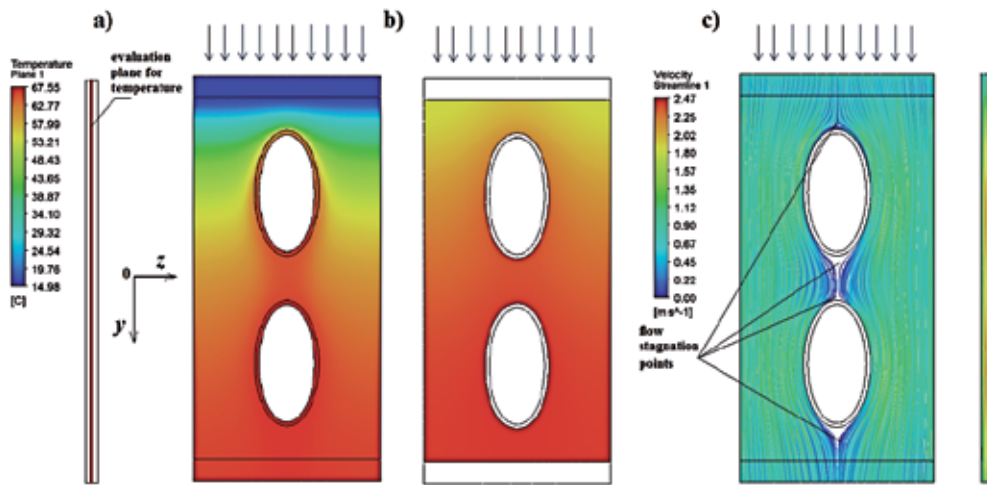


Figure 4. The results of test CFD simulation: a) air temperature distribution at the symmetry plane between two neighboring fins b) fin temperature c) air velocity distribution at the symmetry plane between two neighboring fins.

The temperature variations for the air and tube are shown in Fig. 4a. The air temperature is determined at the middle plane between fins. Figure 4b shows fin surface temperature while Figure 4c plots the air velocity distribution. The considerable increase of air temperature can be observed in the first tube row. The increase is larger compared to the second tube row (Fig. 4a). Also, the temperature difference between the fin surface and air is larger in the first row than in the second. Fig 4a and 4b reveals that the temperature difference between the fin surface and fluid is large in the entrance region, what in turn increases the heat flow rate. The efficient heat transfer at the inlet section is the main reason of the significant heat flow rate transferred from water to air in the first row of tubes.

In the existence of the low velocity region between the tubes along the symmetry plane, where the wake behind the upstream tube is bounded by the stagnation on the downstream one (Fig. 4c), the fin temperature (Fig. 4b) in the second tube row is high. Due to the recirculation zones the air entrapped in the vortices is heated almost up to the fin temperature (Fig. 4a). In this region the heat flow rate is close to zero, since the temperature difference between the fin surface and recirculating air is close to zero [19].

The presence of two dead-air zones near the tubes located in the second row decrease the heat flow rate from the second tube row to air. The average heat flux q at the outer tube surface on the length of one pitch s between two y coordinates: \bar{y}_n and \bar{y}_{n+1} (Fig. 5) can be calculated as [19]:

$$q(\bar{y}_{n+1/2}) = q\left(\frac{\bar{y}_n + \bar{y}_{n+1}}{2}\right) = \frac{\int_{A_o} q_o dA_o + \int_{A_c} q_c dA_c}{A_o + A_c} \Bigg|_{\bar{y}=\bar{y}_n}^{\bar{y}=\bar{y}_{n+1}} \quad (14)$$

with:

dA_o -the elemental surface area on the outer surface of the oval tube,

dA_c - the elemental surface area on the contact surface between fin and tube,

q_o - the heat flux from the outer tube surface to the air across the elemental surface dA_o ,

q_c - the heat flux from the outer tube surface to the fin base across the elemental surface dA_c ,

\bar{y} - the vertical distance from horizontal plane passing through the center of the oval tube to the elevation of the point situated on the tube outer surface.

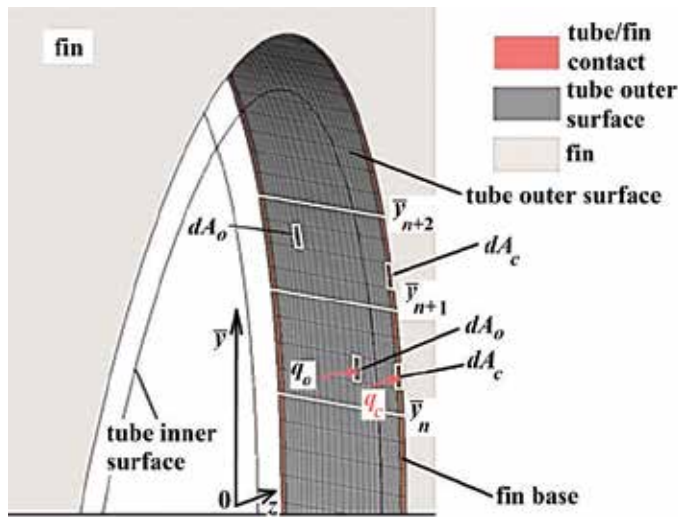


Figure 5. The outer surface of oval tube (grey elements) and the contact surface between fin and tube (red elements).

The variation of outer surface heat flux with the direction of air flow, is presented in form of dimensionless coordinate ξ ,

$$\xi = -\frac{2\bar{y}}{d_{\max}} \quad (15)$$

The symbol \bar{y} denotes a distance in the vertical direction between the horizontal plane passing through the oval gravity center '0' and the point located at the outer surface of the tube wall.

Figure 6 [19] shows the variation of the heat flux q with the dimensionless major radius ξ of the oval tube for the first and second tube rows.

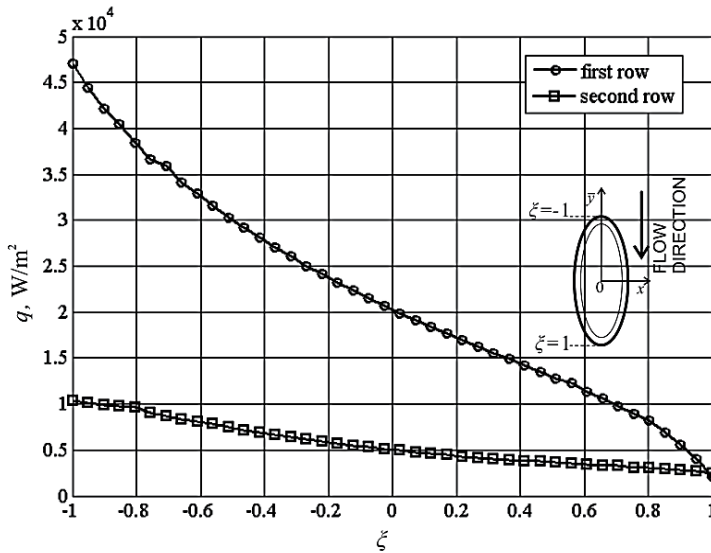


Figure 6. The variations of heat flux q on the outer surface of tube wall for the first and second row.

The heat flux q reaches its highest value equal to $q = 4.72 \cdot 10^4 \text{ W/m}^2$ in the first row at the inflow surface of the oval profile ($\xi = -1$), i.e. front stagnation point. In the area of the rear stagnation point ($\xi = 1$), the considerable heat flux decrease can be observed in both the first and second tube row. In the rear stagnation point on the tube in the first row, the heat flux is only $q = 2.04 \cdot 10^3 \text{ W/m}^2$.

The heat transfer is more efficient in the first row of tubes, than in the second. The mean (area-weighted) values of heat flux in the first and second tube row are: $\bar{q}_I = 2.19 \cdot 10^4 \text{ W/m}^2$ and $\bar{q}_{II} = 5.62 \cdot 10^3 \text{ W/m}^2$, respectively. Thus the average value falls almost four times.

In subsections, 4.1 and 4.2 two methods of determining the air-side heat transfer coefficient are presented. The first considers the application of the analytical model of fin-and-tube heat exchanger while the second allows determining the air-side heat transfer coefficient directly from CFD simulations.

4.1. Determination of the gas-side heat transfer coefficient using the analytical model of fin-and-tube heat exchanger and CFD simulation results

The CFD calculations allow to determine the temperature and heat flux distributions in heat transfer domains. It should be noted that the local and average heat transfer coefficients are difficult to determine due to the unclear definition of fluid bulk temperature. From the definition the local heat transfer coefficient is calculated as a ratio of the local heat flux and

difference between the fin surface temperature and air temperature (averaged in the referred flow cross-section). In the case that the average temperature of the air is calculated as the arithmetic mean of the inlet and outlet temperature, the fin surface temperature at the inlet section of a channel formed by the fins is lower than the air mean temperature and then the calculated local heat transfer coefficient can be negative. This is due to a large change in air temperature with the flow direction. Another possibility of determining the average heat transfer coefficient is to calculate first the local distribution of the heat transfer coefficient and then its average value. Nevertheless, this method encounters difficulties in evaluating the local mass-averaged temperature of the air (air bulk temperature) due to the different directions of air flow in the duct between the fins (in vicinity of flow stagnation zones).

A method for determining heat transfer coefficient [18], presented in this study, aims to avoid defining the bulk temperature of air, local or average for the entire flow passage. The method is appropriate for determining the average heat transfer coefficient using the analytical solution for the temperature distribution of air flowing through the two row fin-and-tube heat exchanger. The method is compatible with experimental predictions of heat transfer correlations.

The mean heat transfer coefficient on the air side is determined from the condition that the air temperature increase over two rows of tubes, is the same for the analytical method and for the CFD calculations (Fig. 7a) [19]. To compare the air temperature difference in the heat exchanger, the inlet and outlet air temperatures obtained from the CFD simulations should be mass weighted over the inlet and outlet cross-sections. From the comparison of the difference of the air mass averaged temperatures between the inlet and outlet cross-sections with analytical temperature difference, the average heat transfer coefficient on the air side is computed. The analytical model assumes that the air side heat transfer coefficient is constant. Fig. 7b depicts the positions of evaluation planes used in the CFD simulations to determine the mass-weighted air temperatures.

The average heat transfer coefficient h_a on the tube and fin surface is determined from the condition that the total mass average air temperature difference $\Delta \bar{T}_{to,CFD}$ computed using ANSYS CFX program is equal to the air temperature difference $\Delta T_{to}(R_{tc}, h_a)$ calculated from an analytical model

$$\Delta T_{to}(R_{tc} = 0, h_{a,CFD}) - \Delta \bar{T}_{to,CFD} = 0 \quad (16)$$

The total air temperature difference ΔT_{to} is

$$\Delta T_{to} = T_a''' - T_a' = \Delta T_I + \Delta T_{II} \quad (17)$$

where $\Delta T_I = T_a'' - T_a'$ and $\Delta T_{II} = T_a''' - T_a''$ is the air temperature increase over the first and second tube row, respectively (Fig. 7a).

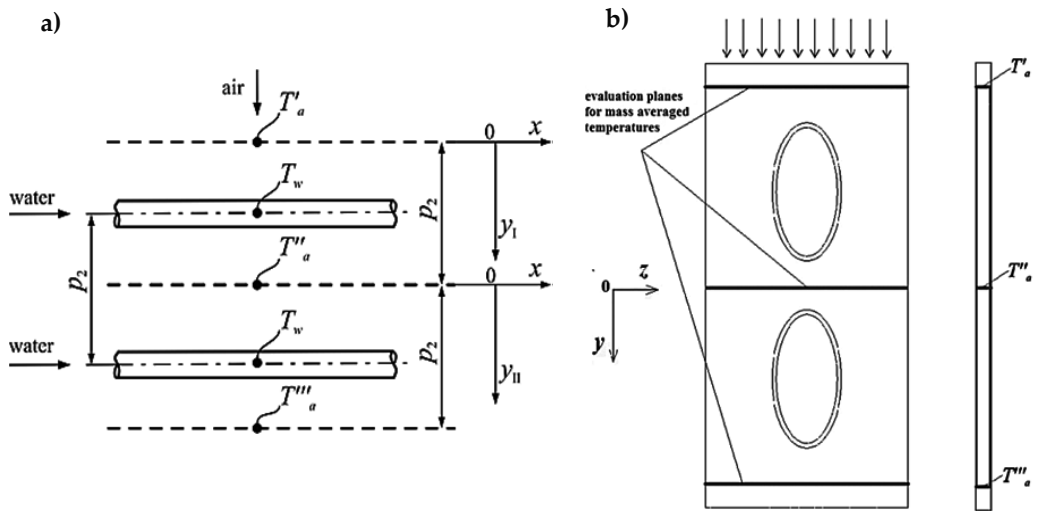


Figure 7. Cross flow heat exchanger with two rows of tubes: a) air flow passage used in analytical model, b) evaluation planes for mass averaged temperatures T'_a , T''_a , and T'''_a used in CFD simulations.

The average heat transfer coefficient h_a over two rows of tubes is calculated by solving equation (16). This study assumes the same water temperature T_w in the first and the second tube. This small temperature difference has insignificant influence on the average heat transfer coefficient h_a . Furthermore, the water temperatures are assumed as constant along the tube length. Under these assumptions, the following differential equations with appropriate boundary conditions describe the air temperature [19]

$$\frac{dT_a(y_1^+)}{dy_1^+} = N_a^I [T_w - T_a(y_1^+)] \quad (18)$$

$$T_a \Big|_{y_1^+=0} = T'_a \quad (19)$$

$$\frac{dT_a(y_{II}^+)}{dy_{II}^+} = N_a^{II} [T_w - T_a(y_{II}^+)] \quad (20)$$

$$T_a \Big|_{y_{II}^+=0} = T''_a \quad (21)$$

Solving the initial-boundary problems (18-19) and (20-21) yields

$$T_a(y_I^+) = T_w + (T'_a - T_w) e^{-N_a^I y_I^+} \tag{22}$$

$$T_a(y_{II}^+) = T_w + (T'_a - T_w) e^{-(N_a^I + N_a^{II}) y_{II}^+} \tag{23}$$

where

$$N_a^I = U_o^I A_o / (\dot{m}_a c_{pa}), \quad N_a^{II} = U_o^{II} A_o / (\dot{m}_a c_{pa})$$

The symbols \dot{m}_a and A denote the air mass flow rate and the outer surface area of the bare tube, respectively. The overall heat transfer coefficient referred to surface area A_o can be expressed as [15, 19-22]:

$$U_o = \frac{1}{\frac{A_o}{A_{in}} \frac{1}{h_{in}} + \frac{2A_o}{A_{in} + A_o} \frac{\delta_t}{k_t} + \frac{1}{h_a}} \tag{24}$$

with: A_{in} – area of the inner tube surface, δ_t - the thickness of tube wall, k_t - the thermal conductivity of the tube, h_{in} - the water side heat transfer coefficient. The equivalent air-side heat transfer coefficient \bar{h}_a referred to the tube outer surface area A_o is defined as:

$$\bar{h}_a = \frac{A_f \eta_f (R_{tc}, h_a) + A_e}{A_g} h_a \tag{25}$$

where [19]

$$\eta_f (R_{tc}, h_a) = \frac{(c_1 + c_3 R_{tc} + c_5 h_a + c_7 R_{tc}^2 + c_9 h_a^2 + c_{11} R_{tc} h_a)}{(1 + c_2 R_{tc} + c_4 h_a + c_6 R_{tc}^2 + c_8 h_a^2 + c_{10} R_{tc} h_a)} \tag{26}$$

The unknown coefficients in the function (26) were estimated by the Levenberg – Marquardt method using a commercial software Table Curve 3d version 4.0 [36]. The coefficients appearing in the function $\eta_f (R_{tc}, h_a)$ are shown in Table 2 [19].

The differences of air temperature over the first and second tube row can be calculated as follows

Coefficient	Value
c_1	0.999
c_2	3.100
c_3	4.850
c_4	$2.100 \cdot 10^{-3}$
c_5	9.626
c_6	-1625.550
c_7	-3192.846
c_8	-6.763
c_9	-2.013
c_{10}	221.620
c_{11}	$3.260 \cdot 10^{-3}$

Table 2. The coefficients of function $\eta_f (R_{tc}, h_a)$ given by expression (26) [19].

$$\Delta T_I = T_a \Big|_{y_I^+ = 1} - T_a \Big|_{y_I^+ = 0} = (T_w - T'_a) \left(1 - e^{-N_a^I} \right) \tag{27}$$

$$\Delta T_{II} = T_a \Big|_{y_{II}^+ = 1} - T_a \Big|_{y_{II}^+ = 0} = (T_w - T'_a) e^{-N_a^I} \left(1 - e^{-N_a^{II}} \right) \tag{28}$$

Assuming that the heat transfer coefficients in the first and second tube row are equal, i.e. $h_a^I = h_a^{II} = h_a$ and the water side heat transfer coefficient h_{in} is the same in both tubes results in the equality of the numbers of heat transfer units across the first and second row, i.e. $N_a = N_a^I = N_a^{II}$. Hence, the total temperature difference ΔT_{to} over two rows can be defined as

$$\Delta T_{to} = \Delta T_I + \Delta T_{II} = (T_w - T'_a) \left(1 - e^{-2N_a} \right) \tag{29}$$

The temperature difference ΔT_{to} given by expression (29) and Eq. (17) are nonlinear functions of the heat transfer coefficient h_a . Also, the overall heat transfer coefficient $U_o = U_o^I = U_o^{II}$ is a nonlinear function of \bar{h}_a which in turn depends on h_a . The expression (29) is used in Equation (16) to evaluate the heat transfer coefficient h_a while the temperature difference $\Delta \bar{T}_{to,CFD}$ obtained from the CFD simulations is assumed as a measured temperature difference.

4.2. Determination of the gas-side heat transfer coefficient directly from CFD simulations of fin-and-tube heat exchanger

The method of determining the average heat transfer coefficient directly from CFD simulation was presented in [20]. The average heat transfer coefficients can be calculated, based on the following relationship:

$$h_{avg,CFD} = \frac{Q}{A_t (\bar{T}_{wall} - T_\infty)}, \quad (30)$$

where the heat transfer rate, referenced to a single pitch, is:

$$Q = \dot{m} (i_{0,outlet} - i_{0,inlet}), \quad (31)$$

where \dot{m} denotes the mass flow rate of the air, $i_{0,outlet}$ and $i_{0,inlet}$ are the air static enthalpy calculated at the outlet and inlet of the flow passage, respectively. The total heat transfer area is calculated as:

$$A_t = A_f + A_e, \quad (32)$$

the area averaged wall temperature is defined as:

$$\bar{T}_{wall} = \frac{1}{A_t} \int_{A_t} T_{wall} dA, \quad (33)$$

the air bulk temperature T_∞ is calculated as the arithmetic mean temperature from the air inlet and outlet temperatures:

$$T_\infty = \bar{T}_a = 0.5(T'_a + T''_a). \quad (34)$$

Correlations for air-side heat transfer coefficient will be determined using both methods presented in this chapter. If the air temperature increase ($T''_a - T'_a$) is small then both procedures described in the sections 4.1 and 4.2 give the same results.

5. Results and discussion

5.1. The correlation on gas-side heat transfer coefficient obtained directly from CFD simulations

Table 3 lists the flow and heat transfer parameters studied during the performed computational cases [20]. Moreover the values of the computed outlet air temperature T''_a are given in Table 3.

Case	$w_0, m/s$	$T'_{av}, ^\circ C$	$h_{iw}, W/(m^2 K)$	$\bar{T}_w, ^\circ C$	$T''_{av}, ^\circ C$
1	1				62.59
2	1.2				61.44
3	1.4				60.14
4	1.6				58.71
5	1.8	14.98	4795	65	57.29
6	2				55.86
7	2.2				54.46
8	2.4				53.14
9	2.5				52.51
10	1				29.23
11	1.2				28.87
12	1.4				28.45
13	1.6				28.01
14	1.8	14.98	4795	30	27.56
15	2				27.13
16	2.2				26.70
17	2.4				26.30
18	2.5				26.11

Table 3. The list of the computational cases used in the CFD simulations and the values of inlet air velocity w_0 , inlet air temperature T'_{av} , the average heat transfer coefficient for water flow h_{iw} , average temperature of water \bar{T}_w and outlet temperature of the air T''_{av}

The determined values of the average heat transfer coefficients $h_{avg.CFD}$ are listed in Table 4 [20]. The computations were carried out for the mean water temperatures: $\bar{T}_w = 30\text{ }^\circ C$ and $\bar{T}_w = 65\text{ }^\circ C$, respectively, to demonstrate that the influence of the tube wall temperature on the determined air side heat transfer coefficients is insignificant. The maximum relative difference between the heat transfer coefficients for $\bar{T}_w = 30\text{ }^\circ C$ and $\bar{T}_w = 65\text{ }^\circ C$ does not exceed 2.9 %. These discrepancies are due to different temperature in the boundary layer, which in turn affects the value of thermal conductivity and kinematic viscosity of air, although the air side Prandtl number is 0.7 in both cases. A similar effect of wall temperature on the value of heat transfer coefficient on the air side can be expected in experimental studies [20].

Case no.	$w_0, m/s$	Q, W	$\bar{T}_{wall}, ^\circ C$	$\bar{T}_a = T_\infty, ^\circ C$	$h_{avg,CFD}, W/(m^2 K)$
1	1	0.8609	59.049	37.014	39.385
2	1.2	1.0089	58.059	36.521	47.121
3	1.4	1.1445	57.152	36.066	54.155
4	1.6	1.2678	56.321	35.651	60.347
5	1.8	1.3804	55.569	35.275	65.849
6	2	1.4806	54.865	34.922	70.589
7	2.2	1.575	54.247	34.614	74.774
8	2.4	1.6608	53.672	34.326	78.506
9	2.5	1.7007	53.403	34.191	80.204
10	1	0.2570	28.228	21.604	38.913
11	1.2	0.3010	27.938	21.459	46.399
12	1.4	0.3405	27.661	21.321	53.069
13	1.6	0.3765	27.416	21.198	58.935
14	1.8	0.4091	27.186	21.083	64.106
15	2	0.4392	26.989	20.985	68.628
16	2.2	0.4662	26.798	20.889	72.563
17	2.4	0.4913	26.625	20.803	76.083
18	2.5	0.5039	26.551	20.765	77.804

Table 4. The values of the heat transfer rate Q referenced to a single pitch, the area averaged wall temperature \bar{T}_{wall} , the bulk temperature of the air T_∞ and the average heat transfer coefficient $h_{avg,CFD}$ for the air flow, obtained for the computational cases listed in Table 1

The values of $h_{avg,CFD}$ obtained when $\bar{T}_w = 30^\circ C$ and $\bar{T}_w = 65^\circ C$ do not differ significantly for the same air velocity. Table 5 [20] lists the Nusselt number correlation obtained from CFD simulations.

No.	Correlation – CFD simulations	Estimated parameters
1	$Nu_a(T_\infty = 65^\circ C) = x_1 Re_a^{x_2} Pr_a^{1/3}$ $150 < Re_a < 400$ $Pr_a = 0.7$	$x_1 = 0.0674 \pm 0.00621$ $x_2 = 0.7152 \pm 0.0612$
2	$Nu_a(T_\infty = 30^\circ C) = x_1 Re_a^{x_2} Pr_a^{1/3}$ $150 < Re_a < 400$ $Pr_a = 0.7$	$x_1 = 0.0623 \pm 0.00574$ $x_2 = 0.7336 \pm 0.0703$

Table 5. Nusselt number formulas for the air flow Nu_a obtained from the CFD simulations based on the mean arithmetic temperatures of the air: $T_\infty = 65^\circ C$ and $T_\infty = 30^\circ C$

The air-flow Nusselt number correlations obtained from CFD simulations are compared with the experimental correlations listed in Table 1. Fig. 8 reveals that the correlations for the air-flow Nusselt number, determined via the CFD simulations, predicts slightly lower values than the one obtained via the measurements. The maximum percentage differences can be observed for $Re_a = 150$, where the values of the Nusselt number, obtained using the CFD simulations are from 10.1 % to 13.7% lower than those obtained from the measurements. For the largest value of Re_a ($Re_a = 400$) these differences are smaller: from 0.5 % to 8.4 % [20].

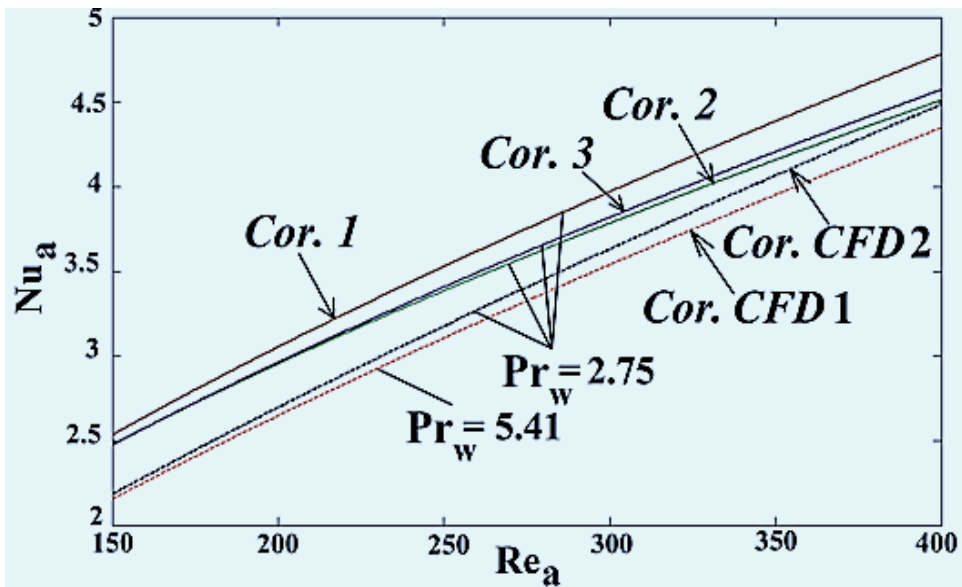


Figure 8. The values of the Nusselt number of the air Nu_a obtained for the Reynolds numbers $Re_a = 150 - 400$ and the Prandtl number $Pr_a = 0.7$, using the correlations listed in Table 1 (experimental correlations: Cor. 1 – Cor. 3) and in Table 5 (correlations based on CFD: Cor. CFD 1, Cor. CFD 2).

The values of the Prandtl numbers for the air and water: $Pr_a = 0.7$ and $Pr_w = 2.75$ are typical for air temperatures \bar{T}_a from 10 °C to 40 °C and for water temperature $\bar{T}_w = 65$ °C. Fig. 8 and Fig. 9 reveal that the experimental correlation 1 (see Table 1) predicts the largest values of the Nusselt number for the air flow if $Re_a > 150$ and for water flow if $Re_w > 10364$. Experimental correlation 2 predicts the lowest values of the Nusselt number for the air flow if $Re_a > 150$ and for water flow if $Re_w > 4000$. Experimental correlation 3 predicts slightly larger values of Nu_a if $Re_a > 150$ and the largest values of Nu_w if $Re_w < 10364$.

During the CFD simulations the idealistic heat transfer conditions were assumed: the constant inlet velocity and the perfect contact between the fin and the outer surface of tube wall. In a real fin-and-tube heat exchanger the maldistribution of air flow as well as the thermal contact resistance between the fin and tube [18, 19] can significantly influence the heat and momentum transfer. Furthermore, the maldistributions of water flow to the tubes of heat exchanger exists for these devices [21-23].The circumstances, mentioned above, explain why the Nusselt

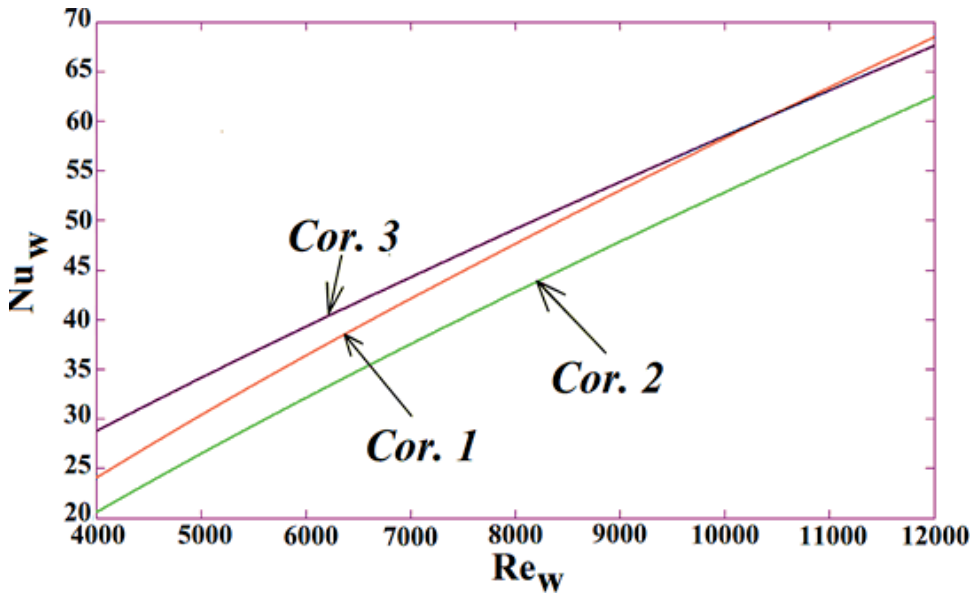


Figure 9. The values of the Nusselt number of water Nu_w obtained for the Reynolds numbers $Re_w = 4000 - 12000$ and the Prandtl number $Pr_w = 2.75$ using the correlations presented in Table 1.

number correlations obtained using CFD simulation differ slightly from the experimental correlations. The analytical-numerical approach for calculating the average thermal contact resistance for a studied fin-and-tube heat exchanger is presented in section 6.

5.2. The correlation on gas-side heat transfer coefficient obtained using fin-and-tube heat exchanger model and CFD simulations

Application of the proposed method is illustrated by the following data set[19]:

- air velocity w_0 in front of heat exchanger: 1 m/s – 2.5 m/s,
- air temperature before the heat exchanger $T'_a = 14.98$ °C,
- mean water temperature in the tubes $T_w = 68.3$ °C,
- water side heat transfer coefficient $h_{in} = 4793.95$ W/(m²·K).

The temperatures T'_a , T_w , and the heat transfer coefficient h_{in} were held constant, while the inlet air velocity w_0 was varied from $w_0 = 1$ m/s to $w_0 = 2.5$ m/s (Table 6). First, the CFD simulations were performed without including thermal contact resistance ($R_{tc} = 0$). Table 6 [19] lists the air temperature differences obtained from the CFD simulations, for the first and second tube rows ($\Delta \bar{T}_{I,CFD}$ and $\Delta \bar{T}_{II,CFD}$) as well as the total air temperature difference $\Delta \bar{T}_{to,CFD}$. The secant method was employed to solve the nonlinear algebraic equation (16) for the air-side heat transfer coefficient $h_{a,CFD}$. The values of $h_{a,CFD}$ and heat transfer coefficients $h_{a,me}$ obtained based on the experimental data (correlation 4 in Table 1), are shown in Table 7 [19].

$w_0, m/s$	$\Delta \bar{T}_{I,CFD}, ^\circ C$	$\Delta \bar{T}_{II,CFD}, ^\circ C$	$\Delta \bar{T}_{to,CFD}, ^\circ C$
1.0	41.26	6.37	47.63
1.2	39.03	7.84	46.87
1.4	36.80	9.00	45.80
1.6	34.71	9.84	44.55
1.8	32.79	10.44	43.23
2.0	31.04	10.82	41.86
2.2	29.47	11.05	40.52
2.5	27.39	11.19	38.58

Table 6. Temperature differences for the first and second row of tubes $\Delta \bar{T}_{I,CFD}$ and $\Delta \bar{T}_{II,CFD}$ and the total temperature difference $\Delta \bar{T}_{to,CFD}$ obtained using CFD simulations for different air inlet velocities w_0

$w_0, m/s$	Re_a	Pr_a	$j_a^{CFD}, -$	$h_{a,CFD}, W/(m^2 \cdot K)$	$h_{a,me}, W/(m^2 \cdot K)$
1.0	149.87	0.694	0.026233	67.54	52.31
1.2	180.01		0.026226	81.02	59.19
1.4	210.29		0.025386	91.49	65.68
1.6	240.70		0.024134	99.39	71.87
1.8	271.22		0.022781	105.53	77.81
2.0	301.86		0.021425	110.26	83.53
2.2	332.60		0.020175	114.20	89.06
2.5	378.86		0.018529	118.94	97.04

Table 7. Air-side heat transfer coefficient for entire heat exchanger obtained from CFD simulation: $h_{a,CFD}$ and experimental correlation $h_{a,me}$ (correlation 4 in Table 1) for different air inlet velocities w_0 .

The air-side Reynolds and Prandtl numbers (Re_a and Pr_a) were calculated as presented in section 3 for the experimental method. For the determined heat transfer coefficients $h_{a,CFD}$ the heat transfer correlations are derived as follows. First, the Colburn factor j_a is approximated using the power law function [20]

$$j_a = x_1 Re_a^{x_2} \tag{35}$$

where the Colburn factor j_a is defined as [19, 20]

$$j_a = Nu_a / (Re_a Pr_a^{1/3}) \tag{36}$$

Based on the heat transfer coefficients $h_{a,CFD}$ obtained from the solution of Equation (16), the Colburn factors (Table 7) $j_{a,i}^{CFD} = Nu_{a,i}^{CFD} / (Re_{a,i} Pr_{a,i}^{1/3})$, $i = 1, \dots, 8$, were calculated. The symbol $Nu_{a,i}^{CFD} = h_{a,CFD} \frac{d_h}{k_a}$ is the Nusselt number for i th data set CFD. The unknown coefficients x_1 and x_2 in the function (35) were determined using the least squares method. The coefficients x_1 and x_2 were selected to minimize the following sum of squares:

$$S = \sum_{i=1}^{n=8} \left(j_{a,i}^{CFD} - x_1 Re_{a,i}^{x_2} \right)^2 \tag{37}$$

The symbol n is the number of data sets shown in Table 7.

The coefficients x_1 and x_2 obtained using the least squares method for the data sets listed in Table 5 are: $x_1 = 0.188$ and $x_2 = -0.382$. To find the optimum values of x_1 and x_2 the Levenberg-Marquardt method was used [35]. The MATLAB R2012 curve fitting toolbox [42] was used for this purpose. Figure 10 [19] depicts the obtained correlation $j_a^{CFD}(Re_a)$, also the prediction bounds set at 95 % confidence level are presented.

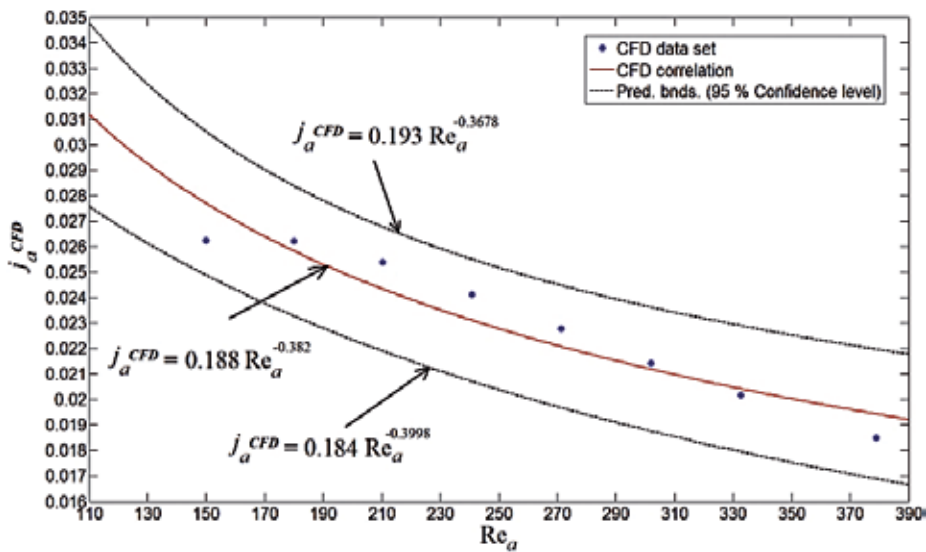


Figure 10. Correlation $j_a^{CFD}(Re_a) = 0.188 Re_a^{-0.382}$ - continuous line, and prediction bounds set at 95% confidence level - dashed line. The correlation was based on the CFD data set.

Fig. 10 reveals that the correlation $j_a(Re_a) = 0.1878 Re_a^{-0.382}$ predicts the values of Colburn factor j_a^{CFD} well for $Re_a \in (170, 390)$. The expression on the air side Nusselt number is obtained after rearranging Eq. (36)

$$Nu_a = x_1 Re_a^{(1+x_2)} Pr^{1/3} \tag{38}$$

The following formula for the air-side heat transfer coefficient was obtained after substituting the estimated coefficients x_1 and x_2 into the correlation (38),

$$h_{a,CFD} = \frac{k_a}{d_h} Nu_a = \frac{k_a}{d_h} 0.188 Re_a^{0.618} Pr_a^{1/3} \tag{39}$$

In ref. [37] similar correlations for continuous-fin and tube heat exchangers can be found. The correlation

$$h_a = \frac{k_a}{d_h} 0.174 Re_a^{0.613} Pr_a^{1/3} \tag{40}$$

obtained by Kröger [38] is similar to the correlation (39).

The thermal contact resistance exists between the tube and fin for some methods of attaching the fins on the tubes. It reduces the heat transfer rate between the fluids in the heat exchanger.

The correlation (39) leads to over-prediction of the heat transfer rate from the hot to the cold fluid, when the contact resistance occurs. The thermal contact resistance between the tube and the fin base will be determined by using the correlation (39) and the experimental results.

6. Estimation of the thermal contact resistance between the tube outer surface and fin base using CFD simulations and experimental data

The correlation for the air-side Nusselt number was derived based on: the experimental data and the CFD simulation. The values of the heat transfer coefficients obtained from the CFD simulation $h_{a,CFD}$ and from the experiment $h_{a,me}$ differ from each other (compare Table 1 and Table 7). The method based on the CFD simulation gives larger values of h_a in comparison to the experimental-numerical method (Table 7). The reason for this discrepancy is the thermal contact resistance between the fin and tube in the tested car radiator.

The air temperature increase across two tube rows $\Delta \bar{T}_{to,CFD}$ calculated using the heat transfer coefficient $h_{a,CFD}$ obtained from the CFD based method, is greater than the calculated temperature rise $\Delta \bar{T}_{to,me}$ obtained with the heat transfer coefficient $h_{a,me}$. The temperature differences $\Delta \bar{T}_{to,CFD}$ and $\Delta \bar{T}_{to,me}$ can be equal if a thermal contact resistance is included in the CFD simulations.

The air temperature difference $\Delta \bar{T}_{to,CFD}$ through the entire heat exchanger depends on the thermal contact resistance R_{tc} and air-side heat transfer coefficient h_a . To determine the thermal contact resistance R_{tc} , the nonlinear algebraic equation

$$\Delta \bar{T}_{to,CFD} (R_{tc}, h_{a,CFD}) - \Delta \bar{T}_{to,me} = 0 \tag{41}$$

was solved, for the given values of $h_{a,CFD}$, listed in Table 7. The value of the thermal contact resistance R_{tc} was so adjusted that Eq. (41) is satisfied. Equation (41) was solved using the Secant method. Note that the predicted value of total air temperature difference $\Delta T_{to,CFD}$ determined from Eq. (29) depends on fin-efficiency η_f which in turns depends on R_{tc} . Heat transfer coefficient $h_{a,CFD}$ is a function of air velocity w_0 and is independent of the thermal contact resistance R_{tc} . The heat transfer coefficient $h_{a,CFD}$ was calculated using the correlation (39).

Table 8 [19] lists the measurement data sets and the obtained values of thermal contact resistance.

Case	$w_0, m/s$	$T'_{a,} \text{ } ^\circ C$	$\Delta \bar{T}_{to,me} \text{ } ^\circ C$	$T_{w'} \text{ } ^\circ C$	$\dot{V}_w \text{ } , \text{ dm}^3/h$	$h_{in,} \text{ } W/(m^2K)$	$h_{a,CFD} \text{ } , \text{ } W/(m^2K)$	$R_{tc} \text{ } , \text{ } (m^2K)/W$
I	1.00	14.98	42.67	68.35	1,892.40	4,793.95	71.14	$4.45 \cdot 10^{-5}$
II	1.27	13.49	39.74	65.02	1,882.20	4,813.42	82.45	$3.27 \cdot 10^{-5}$
III	1.77	13.03	35.83	63.14	1,789.80	4,743.65	101.03	$2.42 \cdot 10^{-5}$
IV	2.20	12.69	31.83	61.24	1,788.00	4,739.78	115.34	$2.42 \cdot 10^{-5}$
							\bar{R}_{tc}	$3.16 \cdot 10^{-5}$

Table 8. Thermal contact resistance R_{tc} determined using experimental data sets and the heat transfer coefficient $h_{a,CFD}$ obtained from the CFD simulations

The mean value of thermal contact resistance, obtained for data set given in Table 8, is $\bar{R}_{tc} = 3.16 \cdot 10^{-5} (m^2K)/W$. To calculate the total air temperature differences $\Delta \bar{T}_{to,CFD}$ the \bar{R}_{tc} was included in the CFD model of heat exchanger.

Figure 11 presents the results of CFD simulations for computational cases listed in Table 8.

Equation (14) was used to determine the heat flux q variations at the outer surface of tube wall with dimensionless coordinate ξ . Fig. 12 presents the results for the first tube row and Fig 13 for the second tube row [19]. Additionally, the computed values of heat flux q for the thermal contact resistance $\bar{R}_{tc} = 0 (m^2 K)/W$ are compared with that obtained for $\bar{R}_{tc} = 3.16 \cdot 10^{-5} (m^2 K)/W$.

Fig 12 reveals that the thermal contact resistance significantly reduces heat flux through the finned outer surface of the tube. The influence of contact resistance on the average heat flux in the second row of tubes (Fig. 13) is smaller than in the first row of tubes (Fig. 12). The overall heat transfer rate decreases significantly if the thermal contact resistance exists because the largest amount of heat is transferred across the first row of tubes.

Table 9 [19] compares the temperature differences across the two rows of tubes computed using ANSYS CFX for the average thermal contact resistance $\bar{R}_{tc} = 3.16 \cdot 10^{-5} (m^2 K)/W$ with the

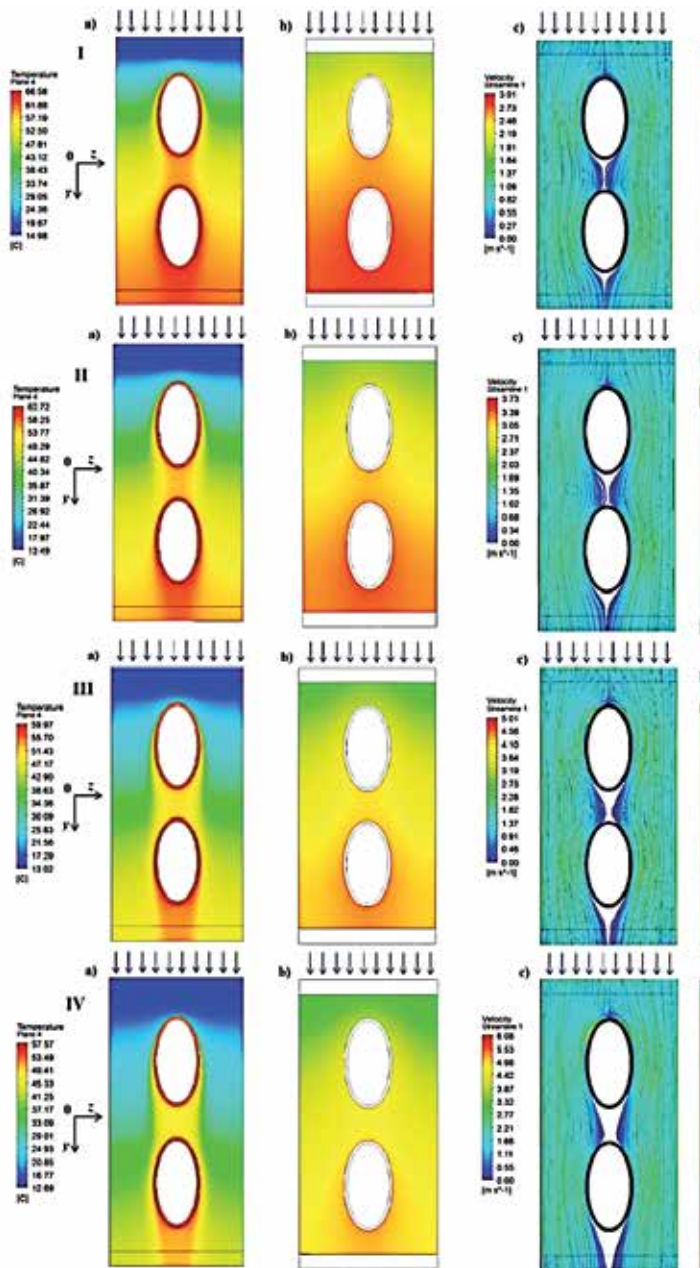


Figure 11. The results of CFD simulation for data sets I - IV listed in Table 8: a) temperature distribution in the air domain at the middle of flow passage, b) fin surface temperature, c) air velocity distribution at the middle of flow passage [19].

temperature differences obtained from the expression (29) for the experimentally determined heat transfer coefficient $h_{a,mc}$ (correlation 4, Table 1)

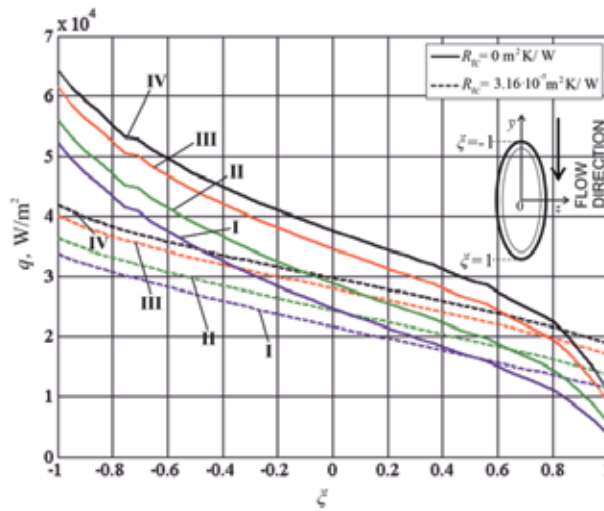


Figure 12. The distribution of heat flux q on the outer surface of tube wall for the first tube row, for computational cases I - IV listed in Table 8.

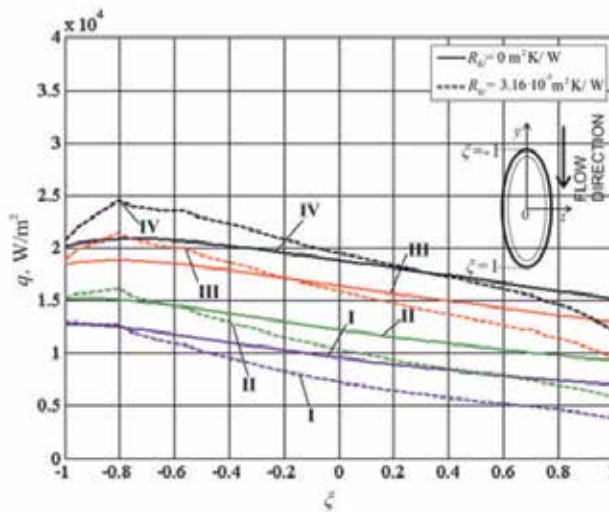


Figure 13. The distribution of heat flux q on the outer surface of tube wall for the second tube row, for computational cases I - IV listed in Table 8.

The relative temperature difference $|\varepsilon_a|$ between the obtained results, is calculated as:

$$|\varepsilon_a| = \left| \frac{\Delta \bar{T}_t - \Delta \bar{T}_{t,me}}{\Delta \bar{T}_{t,me}} \right| \cdot 100\%. \quad (42)$$

Case	$\Delta \bar{T}_{to,CFD}, ^\circ C$	$\Delta \bar{T}_{to,me}, ^\circ C$	$ \varepsilon_a , \%$
I	44.45	42.67	3.98
II	40.76	39.74	2.52
III	35.46	35.83	1.04
IV	31.16	31.83	2.15

Table 9. Air temperature differences $\Delta \bar{T}_{to,CFD}$ over two rows of tubes obtained using the CFD simulations with the thermal contact resistance $\bar{R}_{tc} = 3.16 \cdot 10^{-5} \text{ (m}^2 \text{ K)/W}$ and the temperature difference $\Delta \bar{T}_{to,me}$ obtained from Eq. (29) for the experimentally determined heat transfer coefficients $h_{a,me}$

The largest value of this difference was obtained for the case I - $|\varepsilon_a| = 3.98 \%$ (Table 9). For the other computational test cases, the value of $|\varepsilon_a|$ is less than 3 %. The performed calculations demonstrate the effectiveness of the method developed. The estimated contact resistance can be used in the calculation of equivalent heat transfer coefficient using (Eq. (25)) and in the analytical calculations of the heat transfer rate in the heat exchanger:

$$\dot{Q} = F A_o U_o \Delta T_{lm} \tag{43}$$

where the symbol F denotes the correction factor based on the logarithmic mean temperature difference ΔT_{lm} for a counter-current flow arrangement.

The method proposed for determining the air side heat transfer correlations based on the CFD computations, can easily account for the thermal contact resistance between the tube outer surface and fin bases. The method can also be used for heat exchangers with various tube shapes and other types of the fin to tube attachment as well as for different tube arrangements.

7. Conclusions

The experimental and CFD based methods for determining the air-side heat transfer coefficient, for fin-and-tube heat exchanger, are presented in this study. Two types of CFD based methods were described. The first one allows determining the air-side heat transfer coefficient directly from CFD simulations while the second employs the analytical model of fin-and-tube heat exchanger to determine the air-side heat transfer coefficient. The results obtained using these two methods were compared with the experimental data.

Moreover, the method for determination of the thermal contact resistance between the fin and tube was presented. The CFD simulations are appropriate for predicting heat transfer correlations for the plate fin and tube heat exchanger with tubes of various shapes and flow arrangements. Using the experimental data and CFD simulations, the thermal contact resistance between the fin base and tube was estimated. The fin efficiency appearing in the formula for the equivalent air side heat transfer coefficient is a function of the air side heat transfer

coefficient and the thermal contact resistance. The air-side heat transfer correlations are determined based on the CFD simulations. The heat transfer coefficients predicted from the CFD simulations were larger than those obtained experimentally, because in the CFD modeling the thermal contact resistance between the fin and tube was neglected. A new procedure for estimating the thermal contact resistance was developed to improve the accuracy of the heat exchanger calculation. When the value of mean thermal contact resistance, determined by the proposed method, is included in the CFD model, then the computed air temperature distributions show better agreement with measurements.

The computations presented in this study allows to draw the following conclusions. CFD modeling is an effective tool for flow and thermal design of plate fin-and-tube heat exchangers. and is an effective tool for finding heat transfer correlations in the newly designed heat exchangers. However, to obtain good agreement between the CFD modeling and experimental data, it is necessary to adjust some parameters of the CFD model using the experimental results. An example of such a parameter may be thermal contact resistance between the tube and the fin base.

Nomenclature

A ; area, m^2

A_{oval} ; area of oval cross-section, m^2

c_p ; specific heat at constant pressure, $J/(kg\ K)$

$c_1 - c_{11}$; coefficients of function $\eta_f(R_{tc}, h_a)$

d_h ; hydraulic diameter of narrow air flow passage, m

d_{min}, d_{max} ; minor/major oval axes, m

d_i ; hydraulic diameter of oval tube, m

F ; correction factor

h ; heat transfer coefficient, $W/(m^2K)$

\bar{h} ; enhanced heat transfer coefficient based on tube outer surface A_o , $W/(m^2K)$

j ; Colburn j-factor, $Nu/(Re\ Pr^{1/3})$

k ; thermal conductivity, $W/(mK)$

L_i ; tube length in car radiator, m

\dot{m} ; mass flow rate, kg/s

N ; number of transfer units

Nu ; Nusselt number

p_1 ; pitch of tubes in plane perpendicular to flow, m

p_2 ; pitch of tubes in direction of flow, m

P ; perimeter, m

Pr ; Prandtl number

R_{tc} ; mean thermal contact resistance between tube and fin, m^2K/W

Re ; Reynolds number

q ; heat flux, W/m^2

\bar{q}_I, \bar{q}_{II} average heat flux on the outer surface of tube in the first and second tube row, W/m^2

\dot{Q} ; heat flow, W

s ; thickness of air flow passage, m

T ; temperature, $^{\circ}C$

\bar{T}_a, \bar{T}_w mean temperature of air/water in heat exchanger, $^{\circ}C$

U ; overall heat transfer coefficient, $W/(m^2K)$

\dot{V} ; volumetric flow rate, dm^3/h

w ; velocity, m/s ;

w_0 ; air inlet velocity, m/s ;

w_{max} ; maximum air velocity in narrow flow passage, m/s ;

x, y, z ; Cartesian coordinates, m

\bar{y} distance, measured along the flow direction, between the oval gravity center and the point located at the outer surface of tube wall, m

x_i ; unknown coefficient

Greek symbols

δ ; thickness, m

ΔT ; air side temperature difference obtained using analytical model of heat exchanger, $^{\circ}C$

$\Delta \bar{T}$; air side temperature difference obtained from the CFD simulations, $^{\circ}C$

$|\varepsilon_a|$; relative change of the air temperature increase, %

η_f ; fin efficiency

μ ; dynamic viscosity, Ns/m^2

ν ; kinematic viscosity, m^2/s

ξ ; Darcy Weisbach friction factor

Subscripts

a; air

c; contact area

CFD; obtained using CFD based method

e; external surface of tube between fins

f; fin

g; external surface of tube without fins

in; inner

m; logarithmic mean temperature difference

me; measured temperature difference on air side

min minimum cross-section area for transversal air flow through the tube array

o; outer

t; tube

to; total air side temperature difference

w; water

I, II; first and second tube row, respectively

Superscripts

'; inlet

''; intermediate

'''; outlet

Author details

Jan Taler^{1*}, Paweł Ocioń², Dawid Taler³ and Marzena Nowak-Ocioń⁴

*Address all correspondence to: taler@mech.pk.edu.pl

1 Cracow University of Technology, Faculty of Mechanical Engineering, Institute of Thermal Power Engineering, Cracow, Poland

2 Cracow University of Technology, Faculty of Mechanical Engineering, Institute of Thermal Power Engineering, Cracow, Poland

3 Cracow University of Technology, Faculty of Environmental Engineering, Institute of Heat Transfer Engineering and Air Protection, Cracow, Poland

4 Cracow University of Technology, Faculty of Mechanical Engineering, Institute of Thermal Power Engineering, Cracow, Poland

References

- [1] Matos R. S., Vargas J. V. C., Laursen T. A., Bejan A., 2004: Optimally staggered finned circular and elliptic tubes in forced convection, *International Journal of Heat and Mass Transfer* 47(6-7): 1347–1359.
- [2] Jang J. Y., Yang J. Y., 1998: Experimental and Numerical Analysis of the Thermal-Hydraulic Characteristics of Elliptic Finned-Tube Heat Exchangers, *Heat Transfer Engineering* 19(4): 55-67.
- [3] Li. B., Feng B., He Y. L., Tao W.Q., 2006: Experimental study on friction factor and numerical simulation on flow and heat transfer in an alternating elliptical axis tube, *Applied Thermal Engineering*, 26(17–18): 2336–2344.
- [4] Nishiyama H., Ota T., Matsumo T., 1988: Heat Transfer and Flow around an Elliptic Cylinders in Tandem Arrangement, *JSME International Journal Series II*, Vol. 31: 410-419.
- [5] Khan M. G., Fartaj A., Ting D. S. K., 2004: An experimental characterization of cross-flow cooling of air via an in-line elliptical tube array, *International Journal of Heat and Fluid Flow* 25(4): 636–648.
- [6] Saboya F. E. M., Sparrow E. M., 1974: Local and Average Transfer Coefficients for One-Row Plate Fin and Tube Heat Exchanger Configurations, *Journal of Heat Transfer* 96(3): 265-272.
- [7] Saboya S. M., Saboya F. E. M., 1981: Transfer Coefficients for Plate Fin and Elliptical Tube Heat Exchangers, *Proceedings of the VI Brazilian Congress of Mechanical Engineering*, pp. 153-162.
- [8] Bordallo S. N., Saboya F. E. M., 1999: Pressure Drop Coefficients for Elliptic and Circular Sections in One, Two and Three-Row Arrangements of Plate Fin and Tube Heat Exchangers, *Journal of the Brazilian Society of Mechanical Sciences* 21(4): 600-610.
- [9] Idem S., Jacobi A. M., Goldchmidt V. W., 1990: Heat Transfer Characterization of a Finned-Tube Heat Exchanger (with and without Condensation). *Journal of Heat Transfer, Transaction of the ASME*, 112(1): pp. 64-70.

- [10] Hong K. T., Webb R. L., 1996: Calculation of Fin Efficiency for Wet and Dry Fins, *HVAC&R Research* 2(1): 27 -41.
- [11] Taler D., 2002: *Theoretical and experimental analysis of heat exchangers with extended surfaces*, Polish Academy of Science publishing press, ISBN 83-915470-1-9, Poland.
- [12] Zilio C., Cecchinato L., Corradi M., Schiochet G., 2007: An Assessment of Heat Transfer through Fins in a Fin-and-Tube Gas Cooler for Transcritical Carbon Dioxide Cycles, *HVAC&R Research* 13(3): 457-469.
- [13] Taler D., 2004: Determination of heat transfer correlations for plate-fin-and-tube heat exchangers, *Heat and Mass Transfer*, Vol. 40: 809-822.
- [14] Taler D., 2007a: Experimental and numerical predictions of the heat transfer correlations in the cross-flow plate fin and tube heat exchangers, *Archives of Thermodynamics* 28(2): 3-18.
- [15] Taler D., 2007b: Effect of thermal contact resistance on the heat transfer in plate finned tube heat exchangers, ECI Symposium Series, Volume RP5: *Proceedings of 7th International Conference on Heat Exchanger Fouling and Cleaning – Challenges and Opportunities*, pp. 362-371, H Müller-Steinhagen, M. R. Malayeri, P. Watkinson (Eds.), Engineering Conferences International, Tomar, Portugal.
- [16] Taler D., 2009: *Dynamics of Tube Heat Exchangers* (in Polish), Monograph 193, AGH University of Science and Technology Press, ISSN 0867-6631, Cracow, Poland.
- [17] Taler D., 2013: Experimental determination of correlations for average heat transfer coefficients in heat exchangers on both fluid sides, *Heat and Mass Transfer*, Vol. 49. 1125-1139.
- [18] Taler, D., Cebula, A., 2010: A new method for determination of thermal contact resistance of a fin-to-tube attachment in plate fin-and-tube heat exchangers, *Chemical and Process Engineering* 31(4): 839-855.
- [19] Taler D., Ocloń P., Thermal contact resistance in plate fin-and-tube heat exchangers, determined by experimental data and CFD simulations, *International Journal of Thermal Sciences*, Volume 84, October 2014, Pages 309-322.
- [20] Taler D., Ocloń P., Determination of heat transfer formulas for gas flow in fin-and-tube heat exchanger with oval tubes using CFD simulations, *Chemical Engineering and Processing: Process Intensification*, Volume 83, September 2014, Pages 1-11.
- [21] Łopata S, Ocloń P (2010) *Investigation of the flow conditions in a high-performance heat exchanger*, *Arch Thermodyn* 31(3):37–53.
- [22] Łopata S, Ocloń P (2012) *Analysis of operating conditions for high performance heat exchanger with the finned elliptical tube*, *Rynek Energii* 5(102):112–124.

- [23] Łopata S, Ocloń P (2012) Modelling and optimizing operating conditions of heat exchanger with finned elliptical tubes. In: Hector Juarez L (ed) *Fluid dynamics, computational modeling and applications*, InTech, pp 327–356. ISBN:978-953-51-0052-2, Rijeka.
- [24] Ocloń P, Łopata S, Nowak M (2013) Comparative study of conjugate gradient algorithms performance on the example of steady-state axisymmetric heat transfer problem. *Arch Thermodyn* 34(3):15–44.
- [25] Ocloń P, Łopata S, Nowak M, Benim AC (2014) Numerical study on the effect of inner tube fouling on the thermal performance of high-temperature fin-and-tube heat exchanger. *Prog Comput Fluid Dyn* (accepted for print)
- [26] Taler J., Taler D., Sobota T., Cebula A., 2012: Theoretical and Experimental Study of Flow and Heat Transfer in a Tube Bank, in V. M. Pertowa (Ed), *Advances in Engineering Research*, Vol. 1, Nova Science Publishers Inc., pp. 1-56, New York.
- [27] He Y., Tao Y., Tao W., 2008, : Numerical study on the performance of wavy fin heat exchangers with different elliptic tube patterns, *Progress in Computational Fluid Dynamics, An Int. J.* 8 (7/8): 510 – 517.
- [28] Wu Z., Ding G., Wang K., Fukaya M., 2008a: An Extension of a Steady-State Model for Fin-and-Tube Heat Exchangers to Include Those Using Capillary Tubes for Flow Control, *HVAC&R Research*, 14(1): 85-101.
- [29] Liu L., Fan Y., Ling X., Peng H., 2013: Flow and heat transfer characteristics of finned tube with internal and external fins in air cooler for waste heat recovery of gas-fired boiler system, *Chemical Engineering and Processing: Process Intensification*, 74: 142-152.
- [30] Li. B., Feng B., He Y. L., Tao W.Q., 2006: Experimental study on friction factor and numerical simulation on flow and heat transfer in an alternating elliptical axis tube, *Applied Thermal Engineering*, 26(17–18): 2336–2344.
- [31] ANSYS CFX, 2009: Solver Theory Guide r12, ANSYS Inc.
- [32] Chung T. J., 2010: *Computational Fluid Dynamics 2nd ed.*, ISBN 978-0521769693, Cambridge University Press, USA.
- [33] Menter, F. R., 1993: Zonal Two Equation $k-\omega$ Turbulence Models for Aerodynamic Flows, *AIAA Paper* 93-2906.
- [34] Langtry R. B., Menter F. R., 2005: Transition Modeling for General CFD Applications in Aeronautics, *AIAA paper*.
- [35] Seber G. A. F., Wild C. J., 1989: *Nonlinear Regression*, ISBN 978-0471617600, John Wiley & Sons, New York.
- [36] Table Curve, 2005: *Automated Curve Fitting Software*, AISN Software, Chicago.
- [37] T. Kuppan, *Heat exchanger design handbook*, 2nd ed., CRC Press – Taylor and Francis Group, 2013, Boca Raton.

- [38] D. G. Kröger, *Radiator characterization and optimization*, SAE Paper 840380, 1985, pp. 2.984 – 2.990.
- [39] Gnielinski, V., 1976: Neue Gleichungen für den Wärme- und den Stoffübergang in turbulent durchströmten Rohren und Kanälen, *Forschung im Ingenieurwesen* 41(1): 8-16.
- [40] Pietukhov B. S., Popov V. N., 1963: *Theoretical Calculations of Heat Transfer in Turbulent Flow in Tubes of an Incompressible Fluid with Variable Physical Properties*, High Temperature Institute Paper, 1(1), pp. 69-83 (in Russian).
- [41] Bejan A., 2003: Forced Convection: Internal Flows, Chapter 5 in *Heat Transfer Handbook*, Bejan A. Kraus S. (Eds.), ISBN 978-0-471-39015-2, Wiley, Hoboken.
- [42] MATLAB, 2013: MATLAB online documentation: <http://www.mathworks.com/help/matlab>, MathWorks

Heat Transfer Enhancement

Heat Transfer and Nanofluid Flow Through Different Geometries

S.N. Kazi and Hussein Togun

Additional information is available at the end of the chapter

<http://dx.doi.org/10.5772/61075>

1. Introduction

The use of annular passages in application engineering extends through such areas as heat exchangers, gas turbines, cooling of nuclear reactor and some operation industries, cementing operations, formation fracturing, and flow of lubricants in journal bearing and pressure bushings, as well as those applications found in the form of horizontal or vertical directions. Therefore, many researchers have studied fluid flow and heat transfer in annular passages in horizontal and vertical directions for different types of fluid used in varied applications. Thus, investigations that deal with different fluids, for example air, water, oil, gas, etc., are included in this study. Regarding annular passages, there are two types; in concentric annular passages, the position of the inner pipe is in the center of the outer pipe/passage, and in eccentric annular, the position of the inner pipe is not in the center of the outer passage.

Enhancement of heat transfer has been widely researched with different techniques in the last decades. Most researchers have studied the effect of changing the feature of geometry on heat transfer rate. The flow through an axisymmetric sudden expansion or contraction, over backward-facing or forward-facing steps and through ribbed channels, creates separation flow.

There are many experimental and numerical studies that have investigated the effect of separation flow on performance of heat transfer, using different configurations and boundary conditions. Most of these investigations were carried out for separation air flow, while a few were carried out for separation liquid flow in sudden expansion. In the last decade, researchers have used nanofluid in their studies to improve augmentation of heat transfer. Studies on heat transfer to nanofluid flow in sudden expansion, or over backward-facing and forward-facing steps, are very limited for the laminar range, and most have been numerical, the turbulent range of nanofluid flow has not yet been investigated. The main efforts toward studying

separation flow were carried out in the late 1950s. All of these efforts were performed experimentally using many flow visualization techniques, and they deal exclusively with turbulent or laminar flows. This chapter covers most of the investigations that have studied heat transfer and pressure drop of separation flow with fluid and nanofluid, in sudden expansion and backward-facing and forward-facing steps, as well as heat transfer and flow in annular pipes.

2. Nanofluid

Nanofluid is a mix of a base fluid and nanometer-sized particles called nanoparticles. The base fluid is commonly water, oil, and ethylene glycol, while there are different types of nanoparticles, including metals, carbides, oxides, and carbon nanotubes. There are several parameters that affect the performance of nanofluid, including the size and shape of the nanoparticles, concentration, base fluid, and if the nanoparticle type is metal or non-metal. For example, nanoparticle size has a significant impact on thermal conductivity; the small size of the nanoparticle leads to an increase in surface area, and therefore researchers have employed different types of nanofluids in different geometries to reach augmentation of heat transfer.

Nanofluid can be prepared by two methods. In summary, the first method creates nanoparticles with chemical or physical processes (e.g., evaporation and inert-gas condensation processing), and then disperses them into a host fluid. The second method includes production and dispersal of the nanoparticles directly into a host fluid.

3. Annular pipe

Earlier studies, which focused on forced, natural and mixed heat transfer to fluid flow in an annular passage, were carried out by Taylor [1], Dufinescz and Marcus [2], Zerban [3], Foust and Christian [4], Jakob and Rees [5], TEMA [6], Monrad and Pelton [7], Davis [8], Lorenzo and Anderson [9], Chen et al. [10], McMillan and Larson [11], Carpenter et al. [12], Bailey [13], Migushiva [14], Trefethen [15], MacLeod [16], Barrow [17], and Murakawa [18, 19]. They adopted numerical and experimental forms that investigated forced, natural and mixed heat transfer to fluid flow with vertical or horizontal annular passages and rotating or non-rotating flow for different boundary conditions, such as uniform heat flux or uniform temperature wall, for either inner pipe or outer pipe or both. They also used various types of fluids in their studies. These studies have generated various results, including the effects of the step ratio between the inner pipe and outer pipes, eccentricity, roughness of surfaces, type of fluid, and velocity of fluid in an annular passage on the heat transfer processes; in addition, the temperature profiles of fully developed flow, thermal stresses and thermal length in earlier studies also contributed to good understanding of these aspects.

Miller et al. [20] studied turbulent heat transfer to water flowing in an annulus with a heated inner pipe. They showed the effect of the space ratio, Reynolds number and heat flux on the enhancement of heat transfer, and obtained experimental results that were 20 % higher than

the calculated value obtained by using Colburn's equation for internal flow in pipes with an equivalent diameter. Quarmby and Anand [21, 22] conducted a study on turbulent heat transfer and fluid flow in a concentric annular passage with constant wall temperature and uniform heat flux. They observed that the values of the Nusselt number for boundary conditions of uniform heat flux are higher in comparison to that for boundary conditions of constant wall temperature.

Donne and Meerwald [23] have studied heat transfer and friction loss of turbulent flow of air in smooth annuli at high temperature. They measured subsonic turbulent flow of air in smooth annuli with diameter ratios of 1.99 and 1.38, with an inner pipe heated up to 1000°C. They obtained their Nusselt numbers as correlated with equation (1):

$$Nu_B = 0.018 \left(\frac{D_2}{D_1} \right)^{0.16} Re_B^{0.8} Pr_B^{0.4} \left(\frac{T_w}{T_E} \right)^{-0.2} \quad (1)$$

It was observed that the work of Petukhov and Roizen [24] correlated well with equation (1) at low temperature differences ($T_w/T_E \rightarrow 1$).

Also, the average Nusselt numbers at the inner pipe of the annulus are given by equation (2).

$$Nu_B = 0.0217 Re_B^{0.8} Pr_B^{0.4} \left(\frac{T_w}{T_E} \right)^{-0.2} \quad (2)$$

For experimental investigations, good agreement for circular tubes was obtained by Dalle Donne [25]. Dalle Donne presented experimental data with the correlating factor $A = (Nu_B / Re_B^{0.8} Pr_B^{0.4})_{TW/TB=1}$ with a ratio of diameter ($D1/D2$), and made comparisons with previous theories and experimental findings reported by Donne and Meerwald [23], Petukhov and Roizen [24], Wilson and Medwell [26], Kays and Leung [27], Deissler and Taylor [28], and Sheriff and Gumley [29].

Heikal and Hatton [30] presented predictions and measurements of fully developed turbulent non-axisymmetric flow and heat transfer in an annular channel by implementing the turbulence model. They showed good agreement with experimental data, especially for velocity profiles, friction factor and shear stress. They also showed best agreement between predicted and measured data when the ratio of circumferential to radial mass diffusivity of heat was maintained at a value of 2 over the whole cross section. Robinson and Walker [31] investigated to obtain the value of circumferential diffusion heat for turbulent flow in a symmetrical annular passage and compared the obtained results with theoretical solutions.

Stein and Begell [32] carried out investigations on turbulent water flow and heat transfer in internally heated annuli by implemented cosine and uniform lengthwise heat flux distributions. They computed 900 evaluates of local heat transfer coefficients of water flow with heated inner pipe. They observed no considerable effect of cosine heat flux distribution on the heat

transfer coefficients. Chen and Yu [33] also studied turbulent heat transfer to flowing liquid metals in concentric annular channels. They focused on the effect of variable heat flux and entrance region dimensions on the Nusselt number, and showed that the predicted Nusselt number agreed with the experimental value. Lee et al. [34] presented numerical results of heat transfer in fully developed flow by using the K - ϵ equation model in annular pipes with rectangular roughness. They obtained more improvement in the Nusselt number by using a curvature correlation model in comparison to the standard K - ϵ equation model. They also obtained a maximum value for the Nusselt number at the near reattachment point of the separated flow. The computational results have shown good agreement with previous investigations reported by Kang and Choi [35], Lee [36], and Hong et al. [37].

Ho and Lin [38] numerically investigated heat transfer to air–water flow in horizontal concentric and eccentric cylindrical annuli with constant heat flux at the outer wall and isothermal condition at the inner one. They observed that an increase of heat exchange transfer to air–water interface occurred at mixed boundary conditions. Ahn and Kim [39] performed an analytical and experimental study of heat transfer and fully developed fluid flow in rough annuli by using artificial roughness elements on the wall of the inner pipe or outer pipe or both. They obtained enhancement in the heat transfer coefficient due to the effect of the roughness element on turbulence enhancement.

Shahi et al. [40] performed a numerical study on natural convection heat transfer rate in vertical annular channels with nanofluid copper-water. By using a finite volume method with Fortran, the analysis of equations showed an increase in Nusselt number with the increase of solid concentration of nanofluid, and the maximum Nusselt number occurred as inclined angle of the annular channel was equal to zero degree. They validated their result by comparing values of the Nusselt number with Guj and Stella [41] and Davis and Thomas [42].

Mehrizi et al. [43] have numerically studied natural convection heat transfer to Copper (Cu)-water nanofluid flow in horizontal cylinder annuli with an inner triangular cylinder, using the Lattice Boltzmann method. They showed increased enhancement of heat transfer and stream functions with an increase in the volume fraction of nanoparticles and with the inner cylinder moving downward, while there was a decrease in the improvement of heat transfer with the inner cylinder moving horizontally. In contrast, Matin and Pop [44] presented a numerical study of the natural heat transfer to Cu-water nanofluid flow in a horizontal, eccentric annulus. They applied stream function vorticity formulation in the polar coordinate in order to obtain highly accurate results on the effect of eccentric and volume fraction of nanoparticles on the Prandtl number and the Nusselt number, and obtained good agreement with previous investigations. The enhancement of heat transfer for two-phase mixed convection of laminar Al_2O_3 nanofluid flow in an annulus with constant heat flux was numerically studied by Mokhtari et al. [45]. In their simulation, a three-dimensional finite volume method was used and the Brownian motions of nanoparticles were considered to calculate the effects of thermal conductivity and dynamic viscosity. The computational data indicated that the Nusselt number increased with an increase in the volume fraction of nanoparticles, but the friction factor was not affected.

4. Sudden expansion

The earliest investigations of flow in sudden expansion were carried out by Macango and Hung [46]. They obtained results that presented the streamlines and vorticity contour as functions of the Reynolds number. Also, they analyzed the dynamic interaction found between the main flow and captive eddy.

Durst et al. [47] have experimentally studied the flow visualization and laser-anemometry measurements of flow at the downstream of a plan 3:1 symmetric expansion in a duct with an aspect ratio of 9.2:1. The flow was found to be markedly dependent on Reynolds number, as strongly noticed in a three-dimensional study at well away from the channel corners at the lowest measurable velocities. The separation regions behind each step were of equal length at a Reynolds number of 56, which indicated that the symmetric velocity profiles existed from the expansion to a fully developed parabolic profile for the downstream, although there were substantial three-dimensional effects in the vicinity of the separation regions. Study of the velocity profiles shows good agreement with those obtained by solving the two-dimensional momentum equation. The data indicated that the two separation regions were of different lengths, leading to asymmetric velocity profiles at the Reynolds number of 114, whereas at the Reynolds number of 252, the third separation zone was found on one wall, downstream of the smaller of the two separation zones adjacent to the steps.

Afshin and Peter [48] have experimentally studied laminar water flow through confined annular channel with sudden expansion. They used particle image velocimetry (PIV) and refractive index matching (RIM) to measure velocity and length of separation, where they showed increase separation regions with increase of Reynolds number, and as shown in Figs. 1–3, they also obtained good agreement with the numerical result reported by Nag and Datta [49].

Guo et al. [50] conducted a numerical study on the effect of heating on corner recirculation zone (CRZ) in sudden expansion with gas flow. They noticed a decrease in the length of the corner recirculation zone as the heating gas flow increased in sudden expansion. Oliverira and Pinho [51] conducted a numerical study of pressure drop coefficient of laminar Newtonian flow through sudden expansion by using a finite volume method based on a second order differencing scheme. The numerical results indicate a decrease of local loss coefficient with an increase of (between 1 and 225 in the) Reynolds number, and it was also found that a correlation for local loss coefficient could be represented by equation 3.

$$C_1 = \frac{19.2}{Re^{0.93}} - 2.55 + 2.87 \log Re - 0.542 (\log Re)^2 \quad (3)$$

Chiang et al. [52] conducted a computational investigation on the effect of side wall on structure laminar incompressible fluid flow over a plane symmetric sudden expansion. In their analysis, 14 aspect ratios were used and were varied from 3 to 48, with $Re = 60$ for three-dimensional analysis and $Re = 60$ and 140 for two-dimensional analysis. The numerical results

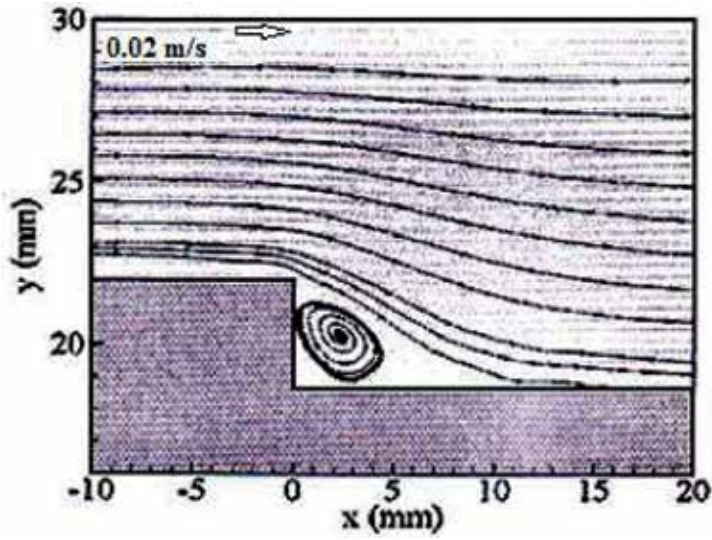


Figure 1. Measurements of velocity flow field at $Re=100$.

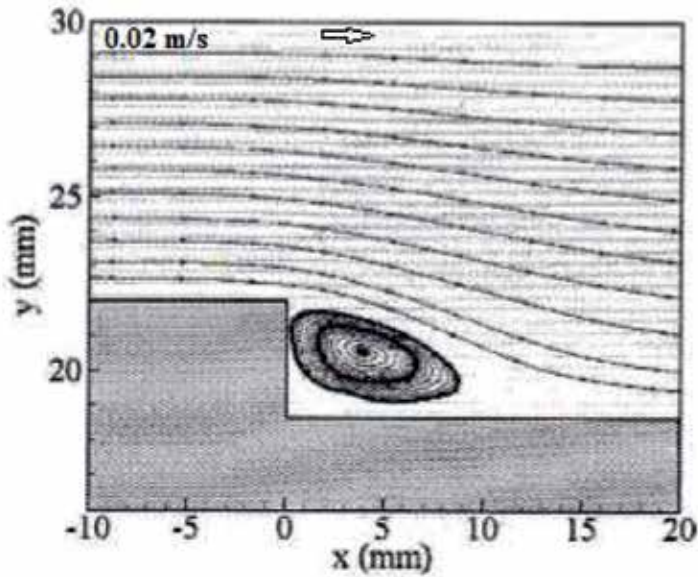


Figure 2. Measurements of velocity flow field at $Re=300$.

were in good agreement with the experimental results of Fearn et al. [53], whose experimental results indicated that symmetric flow occurred at $Re = 26$, while asymmetric flow happened at Re values up to 36. Oliveira has reported numerical simulations on viscoelastic liquid flow in symmetric sudden expansion [54]. The constitutive model follows FENE-MCR, employed in this simulation as three meshes with different sized cells, a Reynolds number ranging from

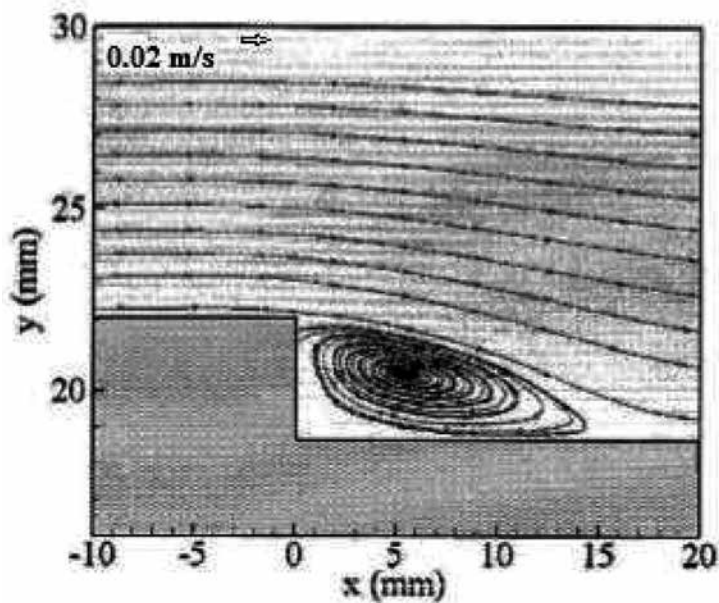


Figure 3. Measurements of velocity flow field at $Re=500$.

0 to 100 and an expansion ratio of 1:3. Due to asymmetric vortex shapes, a pitch-fork type bifurcation takes place beyond the critical Reynolds number ($Re_c = 64$), while it occurred at $Re_c=54$ with Newtonian fluid in the same expansion ratio. Hammad et al. [55] performed a numerical study of the laminar flow of non-Newtonian Herschel Bulkley fluid through axisymmetric sudden expansion. They used a finite difference method to solve governing fully elliptic momentum and continuity equations, and obtained the regime of laminar flow for a range of yield numbers, Reynolds number, and power-law index values, where the range of Re varied between 50 and 200, yielded numbers that varied between 0 and 2, and power-law index values varied between 0.6 and 1.2. They obtained significant dependence of the flow for large values of yield number only, while at lower yield number, the power law index value became effective with yield number on the flow field. They also found good agreement with Hammad [56] and available experimental results for reattachment length. Meanwhile, Miranda et al. [57] numerically studied the local loss coefficient for inelastic laminar fluids flow in axisymmetric sudden expansion by using the finite volume method, and the sudden expansion varied from 1 to 2.6. The authors showed that the local loss coefficient varied inversely with Reynolds number at low Re .

Numerous studies have adopted various models for analysis of heat transfer in separated flow with sudden expansion, and compared the obtained results with experimental data or with other numerical results. Cheing and Launder [58] performed a numerical study of turbulent heat transfer and flow in a separation region with an abrupt pipe expansion by using the standard $k-\epsilon$ model, and thus obtained good agreement with the experimental data of Zemanick and Dougall [59].

Gooray et al. [60] presented numerical calculations for heat transfer in recirculation flow over two-dimensional, rearward-facing steps and sudden pipe expansions by using the standard $k-\epsilon$ model and low-Reynolds number $k-\epsilon$ model. The Reynolds number ranged from 500-10,000 in the investigation. The authors applied two-dimensional back-step and pipe expansion geometries for numerical turbulent flow modeling, and compared the results with the experimental data of Zemanick and Dougall [50], Aung and Goldstein [61], and Sparrow and O'Brien [62]. The investigations considered herein have confirmed that the improved $k-\epsilon$ procedure is capable of providing an insight into complex phenomena having turbulent separated and reattachment flow with heat transfer.

The study of laminar nanofluid flow in sudden expansion is very limited and appears only in Santosh Christopher et al. [63], in a preformed numerical study on laminar Al_2O_3 , Ag, Cu, SiO_2 , and CuO nanofluid flow in sudden expansion. They used the same method as Kanna and Das [64] to solve sudden expansion flow and backward-facing flow with Reynolds numbers from 30 to 150 and volume fractions of 0.1, 0.2, and 0.5. The results showed a decrease in reattachment length of about 1.3% compared with the values obtained by Eiyad Abu-Nada [65], as shown in Fig. 4.

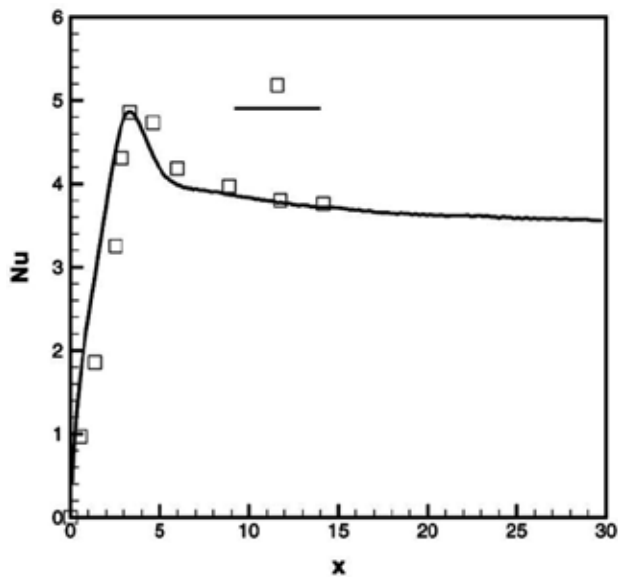


Figure 4. Comparison of Nusselt number for SiO_2 at $\text{Re} = 100$.

5. Backward-facing step

Armaly et al. [66] conducted experimental and theoretical experiments on the two-dimensional effect of the Reynolds number on reattachment length flow downstream of a backward-facing

step in a rectangular channel using laser Doppler measurement where the range of Reynolds number varied between 70 and 8000 and the aspect ratio was 1:36. The experimental result obtained agrees with data predicting increasing reattachment length with increasing Reynolds number.

Barton [67] used a particle phase model with Eulerian-Lagrangian to study laminar flows over backward-facing steps with a stream of hot particles. He focused his investigation on the effect of heat transfer and thermal characteristics on recirculation regions, and noticed that the streamlines in the separation region were ten times smaller than the streamlines in the free flow.

Lee and Matteescu [68] conducted an experimental and numerical study on two-dimensional air flows over a backward-facing step. They measured lengths of separation and reattachment on lower and upper duct by using a hot wire probe with an expansion ratio of 1.17 and 2 and Re below 3000. The numerical and experimental results agree with previous experimental data for separation and reattachment lengths and locations on the lower and upper wall of the duct.

Armaly et al. [69] adopted experimental measurements of velocity in three-dimensional laminar separated flows on backward-facing steps by using two components: laser Doppler velocimeter where the expansion ratio is 2.02, and Reynolds number ranging from 98.5 to 525. They showed an increase in the size of recirculation regions with increased Reynolds number, and the maximum location of the stream-wise velocity line component (u) is zero at the stepped wall with constant Reynolds number at the sidewall.

Barbosa et al. [70] conducted a numerical study of three-dimensional mixed laminar air flow over a horizontal backward step using the finite volume method. The bottom wall of a channel was heated with constant temperature and the other walls were adiabatic, the aspect ratio was equal to 4 and the range of Richardson number (Ri) varied between 0 and 3. The numerical results indicated a decrease in the size of the primary recirculation region with increase in Richardson number, and also moved the maximum value of the average Nusselt number. Li and Armaly [71] presented a numerical study of laminar mixed convection in a three-dimensional backward-facing step, where the full elliptic 3 coupled governing equation was solved using the finite volume method. They found that buoyancy force and temperature affect reattachment length.

The pioneer researchers who applied a large eddy simulation model for the analysis of turbulent heat transfer in separated flow over a backward-facing step are represented by Labbe et al. [72], Avancha and Pletcher [73], and Zouhaier et al. [74]. These researchers showed significant improvement of heat transfer rate in the recirculation zone and obtained trends of heat transfer coefficients that agreed with previous experimental data.

Numerical simulations for two-dimensional turbulent forced convection flows adjacent to backward-facing step were investigated by Chen et al. [75]. The researchers paid attention to the effects of step height on turbulent separated flow and heat transfer. They considered Reynolds number and duct height downstream from the constant step as $Re_0 = 28,000$ and $H = 0.19$ m, respectively. Heat flux was uniformly maintained at $q_w = 270$ W/m² at the stepped wall downstream from the step, while other adjacent walls were treated as adiabatic. The

velocity and temperature fields were calculated by using two equations at low Reynolds number and turbulence models. Results of Abe et al. [76, 77] showed that with the increase of step height, the peak values of the transverse velocity component reduces as shown in Fig. 5, while the maximum temperature becomes greater as the step height increases as shown in Fig. 6. Chen et al. also reported that the bulk temperature increases more rapidly with the increase of step height.

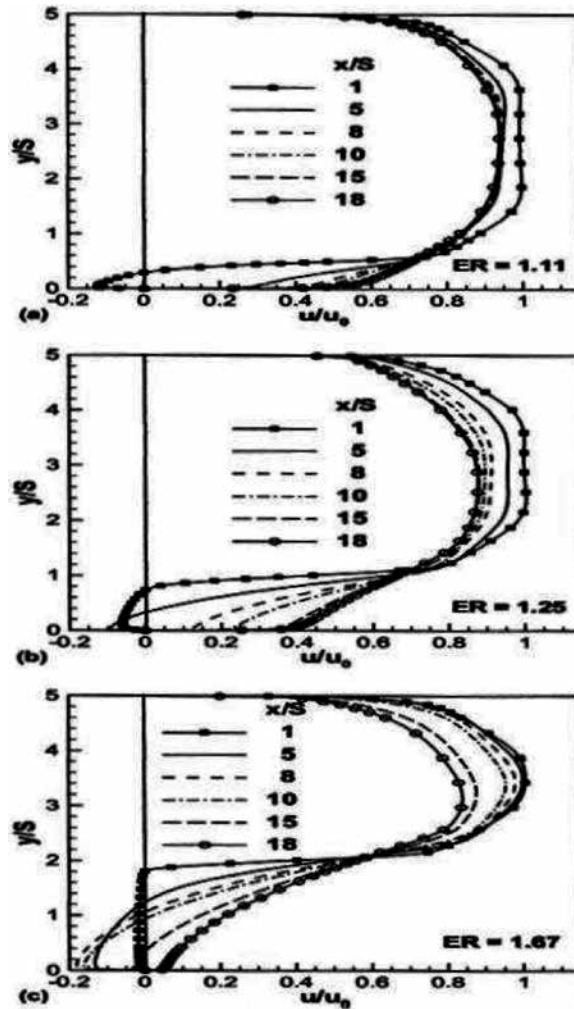


Figure 5. Distribution of the mean streamwise velocity component (u) at several x -planes.

Abu-Nada [65] can be considered a pioneer in the numerical study of heat transfer to nanofluid over a backward-facing step. The types of nanoparticles in this study are represented by Cu, Ag, Al_2O_3 , CuO, and TiO_2 , with volume fractions between 0.05 and 0.2 and Reynolds numbers ranging from 200 to 600. Momentum and energy equations were solved by using the finite

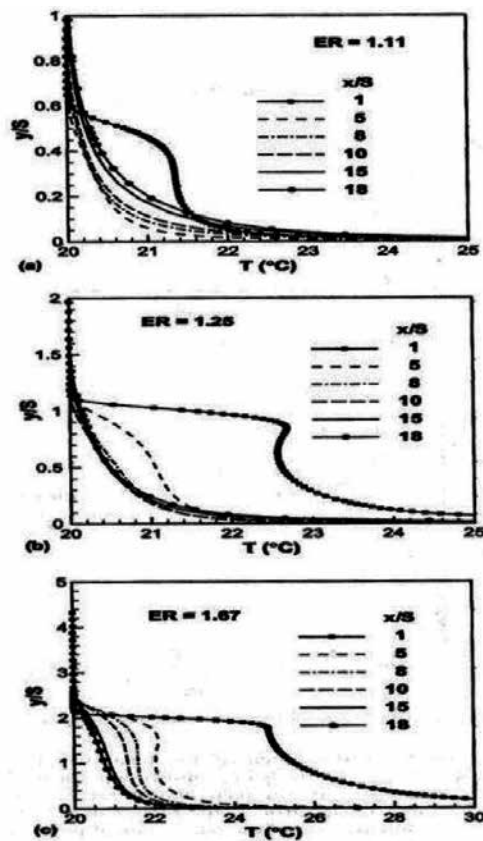


Figure 6. Distribution of the mean temperature at several x-planes.

volume method, and an increase in Nusselt number was observed at the top and bottom of the backward-facing step. Also, the investigations found high thermal conductivity of nanoparticles outside of recirculation zones. Later, Kherbeet et al. [78] presented a numerical investigation of heat transfer and laminar nanofluid flow over a micro-scale backward-facing step. The Reynolds numbers ranged from 0.01 to 0.5, nanoparticle types comprised Al_2O_3 , CuO , SiO_2 , and ZnO , and the expansion ratio was 2. An increasing Reynolds number and volume fraction seemed to lead to an increasing Nusselt number; the highest Nusselt number value was obtained with SiO_2 .

6. Forward-facing step

Stuer et al. [79] presented an experimental study of the laminar separation flow on forward-facing steps by using particle tracking velocimetry to get more information about separation phenomena. The experimental results obtained showed an increase in distance between the

breakthroughs in span at decreased Reynolds numbers, and they also noticed that the transverse direction of separation was slow compared with a short time scale.

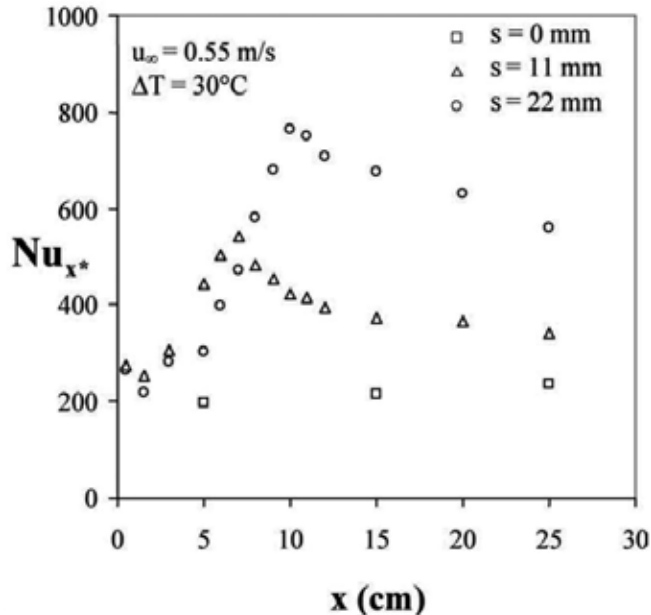


Figure 7. Local Nusselt number variation downstream of the step.

Abu-Mulawah et al. [80] have also reported on the effect of step height on turbulent mixed convection flows over a backward-facing step. Abu-Mulawah [81] noticed that the highest local Nusselt number at the reattachment region for the backward-facing and forward-facing steps in turbulent natural convection flow along a vertical flat plate.

The turbulent fluid flow and heat transfer of a mixed convection boundary-layer of air flowing over an isothermal two-dimensional, vertical forward step was experimentally investigated by Abu-Mulaweh [82]. He studied the effect of forward-facing step heights on local Nusselt number distribution, as shown in Fig. 7. The results indicate that the Nusselt number increases with the increase of step height, and the highest value is obtained at the reattachment region. The present results indicate that the increase of step height leads to an increase in the intensity of temperature fluctuations, the reattachment length transverse velocity fluctuations and the turbulence intensity of the stream.

7. Conclusion

Heat transfer and nanofluid flow through annular pipe over a backward-forward facing step has been presented in this chapter. The effect shape of geometry on thermal performance is clearly seen in experimentally and numerically studies in the literature. The results show that

heat transfer rate increases with an increase in step height and Reynolds number. More augmentation of heat transfer was found using nanofluid, due to an increase of heat transport in the fluid. The enhanced thermal conductivity and viscosity of nanofluids, as well as the random movement of nanoparticles, effect the increased enhancement of heat transfer and stream functions. Also, using nanofluids could offer a positive effect on the energy crisis that is happening in the world.

Acknowledgements

The authors gratefully acknowledge High Impact Research Grant UM.C/625/1/HIR/MOHE/ENG/45 and UMRG Grant RP012D-13AET, Faculty of Engineering, University of Malaya, Malaysia for support to conduct this research work.

Author details

S.N. Kazi^{1*} and Hussein Togun²

*Address all correspondence to: salimnewaz@um.edu.my

1 Department of Mechanical Engineering, Faculty of Engineering, University of Malaya, Kuala Lumpur, Malaysia

2 Department of Mechanical Engineering, University of Thi-Qar, Nassiriya, Iraq

References

- [1] Taylor, G. I. (1935) Distribution of velocity and temperature between concentric rotating cylinders. *Proceedings of the Royal Society of London*, A151, 494–418.
- [2] Dufinescz, M., Marcus, P. (1938) Heat transfer coefficients in annular spaces. M.Sc. Thesis, Carnegie Institute of Technology, Pittsburgh, PA.
- [3] Zerban, A. H. (1940) Clarification of heat transfer characteristics of fluids in annular passage. Ph.D. Thesis, University of Michigan, Ann Arbor, MI.
- [4] Foust, A. S., Christian, G. A. (1940) Non-boiling heat transfer coefficients in annuli. *Transactions of the American Institute of Chemical Engineers*, 36, 541–554.
- [5] Jakob, M., Rees, K. A. (1941) Heat transfer to a fluid in laminar flow through an annular space. *Transactions of the American Institute of Chemical Engineers*, 37, 619–648.

- [6] TEMA. Standards of tubular exchanger manufactures association. First edition, Inc. New York, 1941.
- [7] Monrad, C. C., Pelton, J. F. (1942) Heat transfer by convection in annular spaces. Transactions of the American Institute of Chemical Engineers, 38, 593–611.
- [8] Davis, E. S. (1943) Heat transfer and pressure drop in annuli. Transactions of American Society of Mechanical Engineers, 65, 755–760.
- [9] Lorenzo, B. de, Anderson, E. D. (1945) Heat transfer and pressure drop of liquids in double pipe fin tube exchangers. Transactions of the American Society of Mechanical Engineers, 67, 697–702.
- [10] Chen, C. Y., Hawkins, G. A., Solberg, H. L. (1946) Heat transfer in annuli. Transactions of the American Society of Mechanical Engineers, 68, 99–106.
- [11] McMillan, E. L., Larson, R. E. (1946) Annular heat transfer coefficient for turbulent flow. Transactions of the American Institute of Chemical Engineers, 41, 177–179.
- [12] Carpenter, F. G., Colburn, A. P., Schoenborn, E. M., Wurster, A. (1946) Heat transfer and friction of water in an annular space. Transactions of the American Institute of Chemical Engineers, 42, 165–187.
- [13] Bailey, R. V. (1950) Heat transfer to liquid metals in concentric annuli. Oak Ridge National Laboratory Report ORNL-521.
- [14] Migushiva, T. (1951) Analogy between fluid friction and heat transfer in annuli. General Discussion on heat transfer. IME and ASME, 191–192.
- [15] Trefethen, L. M. (1951) Liquid metal heat transfer in circular tubes and annuli. General discussion on heat transfer. Journal of IMechE, 436–438.
- [16] MacLeod, A. L. (1951) Liquid turbulence in a gas-liquid absorption system, Ph.D. Thesis, Carnegie Institute of Technology, Pittsburgh, PA.
- [17] Barrow, H. (1951) Fluid flow and heat transfer in an annulus with a heated core tube. General discussion on Heat Transfer. Journal of IMechE, 169, 1113–1124.
- [18] Murakawa, K. (1952) Analysis of temperature distribution in non isothermal laminar flow of pipes with annular space. Transactions of Japan Society of Mechanical Engineers, 18 (67), 43.
- [19] Murakawa, K. (1953) Heat transmission in laminar flow through pipes with annular space. Transactions of Japan Society of Mechanical Engineers, 88(10), 15.
- [20] Miller, P., Byrnes, J. J., Benforado, D. M. (1995) Heat transfer to water in an annulus. AIChE Journal, 1(4), 501–504.
- [21] Quarmby, A. (1967) Some measurements of turbulent heat transfer in the thermal entrance region of concentric annuli. International Journal of Heat and Mass Transfer, 10(3), 267–276. doi: [http://dx.doi.org/10.1016/0017-9310\(67\)90144-5](http://dx.doi.org/10.1016/0017-9310(67)90144-5).

- [22] Quarmby, A., Anand, R. K. (1970) Turbulent heat transfer in concentric annuli with constant wall temperatures. *Journal of Heat Transfer*, 92(1), 33–45.
- [23] Donne, M. D., Meerwald, E. (1973) Heat transfer and friction coefficients for turbulent flow of air in smooth annuli at high temperatures. *International Journal of Heat and Mass Transfer*, 16(4), 787–809. doi: [http://dx.doi.org/10.1016/0017-9310\(73\)90091-4](http://dx.doi.org/10.1016/0017-9310(73)90091-4).
- [24] Petukhov, B. S., Roizen, L. I. (1965) Heat exchange and friction resistance in pipes and channels of various geometrical shapes. *Heat and Mass Transfer I Nauka i Tekhnika Mink*.
- [25] Dalle Donne, M., Bowditch, F. H. (1963) Experimental local heat transfer and friction coefficients for subsonic laminar, transitional and turbulent flow of air or helium in a tube at high temperatures. *Dragon Project Report 184*.
- [26] Wilson, N. W., Medwell, J. O. (1968) An analysis of heat transfer for fully developed turbulent flow in concentric annuli. *Journal of Heat and Mass Transfer*, 90(1), 43–50.
- [27] Kays, W. M., Leung, E. Y. (1963) Heat transfer in annular passages—hydrodynamically developed turbulent flow with arbitrarily prescribed heat flux. *International Journal of Heat and Mass Transfer*, 6(7), 537–557. doi: [http://dx.doi.org/10.1016/0017-9310\(63\)90012-7](http://dx.doi.org/10.1016/0017-9310(63)90012-7).
- [28] Deissler, R. G., Taylor, M. F. (1955) Analysis of fully developed turbulent heat transfer and flow in an annulus with various eccentricities. *NACA-TN3451*.
- [29] Sheriff, N., Gumley, P. (1966) Heat-transfer and friction properties of surfaces with discrete roughnesses. *International Journal of Heat and Mass Transfer*, 9(12), 1297–1320. doi: [http://dx.doi.org/10.1016/0017-9310\(66\)90130-X](http://dx.doi.org/10.1016/0017-9310(66)90130-X).
- [30] Heikal, M. R. F., Hatton, A. P. (1978) Predictions and measurements of non-axisymmetric turbulent diffusion in an annular channel. *International Journal of Heat and Mass Transfer*, 21(7), 841–848. doi: [http://dx.doi.org/10.1016/0017-9310\(78\)90175-8](http://dx.doi.org/10.1016/0017-9310(78)90175-8).
- [31] Robinson, D. P., Walker, V. (1978) Mass transfer for turbulent flow in an annulus with non-axisymmetric boundary conditions. *International Journal of Heat and Mass Transfer*, 21(10), 1299–1308. doi: [http://dx.doi.org/10.1016/0017-9310\(78\)90021-2](http://dx.doi.org/10.1016/0017-9310(78)90021-2).
- [32] Stein, R. P., Begell, W. (1958) Heat transfer to water in turbulent flow in internally heated annuli. *AIChE Journal*, 4(2), 127–131. doi: 10.1002/aic.690040203.
- [33] Chen, J. C., Yu, W. S. (1970) Entrance region and variable heat flux effects in turbulent heat transfer to liquid metals flowing in concentric annuli. *International Journal of Heat and Mass Transfer*, 13(4), 667–680. doi: [http://dx.doi.org/10.1016/0017-9310\(70\)90041-4](http://dx.doi.org/10.1016/0017-9310(70)90041-4).
- [34] Lee, B. K., Cho, N. H., Choi, Y. D. (1988) Analysis of periodically fully developed turbulent flow and heat transfer by k- ϵ equation model in artificially roughened annu-

- lus. *International Journal of Heat and Mass Transfer*, 31(9), 1797–1806. doi: [http://dx.doi.org/10.1016/0017-9310\(88\)90194-9](http://dx.doi.org/10.1016/0017-9310(88)90194-9).
- [35] Kang, J. S., Choi, Y. D. (1985) Study on the effects of artificial roughness on the turbulent heat transfer of concentric annular pipes. *Journal of KSME*, 9(3), 335–344.
- [36] K. M., Lee. (1982) The experiment of turbulent heat transfer in annular pipe with artificial roughness. Master's Thesis, Korea University.
- [37] Hong, J. K., L. K. M., Choi, Y. D. (1983) Analysis of turbulent heat in a concentric annular pipe with artificial roughness. *Journal of KSME*, 7(3), 301–312.
- [38] Ho, C. J., Lin, Y. H. (1989) Thermal convection heat transfer of air/water layers enclosed in horizontal annuli with mixed boundary conditions. *Wärme und Stoffübertragung*, 24(4), 211–224. doi: 10.1007/bf01625497.
- [39] Ahn, S. W., Kim, K. C. (1998) Fully developed fluid flow and heat transfer in rough annuli. *International Communications in Heat and Mass Transfer*, 25(4), 501–510. doi: [http://dx.doi.org/10.1016/S0735-1933\(98\)00037-2](http://dx.doi.org/10.1016/S0735-1933(98)00037-2).
- [40] Shahi, M., Mahmoudi, A. H., Talebi, F. (2011) A numerical investigation of conjugated-natural convection heat transfer enhancement of a nanofluid in an annular tube driven by inner heat generating solid cylinder. *International Communications in Heat and Mass Transfer*, 38(4), 533–542. doi: <http://dx.doi.org/10.1016/j.icheatmasstransfer.2010.12.022>.
- [41] Guj, G., Stella, F. (1995) Natural convection in horizontal eccentric annuli: numerical study. *Numerical Heat Transfer, Part A: Applications*, 27(1), 89–105. doi: 10.1080/10407789508913690.
- [42] Davis, G., Thomas, R. W. (1969) Natural convection between concentric vertical cylinders. *Phys. Fluids*, 12, 198–207.
- [43] Mehrizi, A. A., Farhadi, M., Shayamehr, S. (2013) Natural convection flow of Cu-water nanofluid in horizontal cylindrical annuli with inner triangular cylinder using lattice Boltzmann method. *International Communications in Heat and Mass Transfer*, 44(0), 147–156. doi: <http://dx.doi.org/10.1016/j.icheatmasstransfer.2013.03.001>.
- [44] Habibi Matin, M., Pop, I. (2013) Natural convection flow and heat transfer in an eccentric annulus filled by Copper nanofluid. *International Journal of Heat and Mass Transfer*, 61(0), 353–364. doi: <http://dx.doi.org/10.1016/j.ijheatmasstransfer.2013.01.061>.
- [45] Mokhtari Moghari, R., Akbarinia, A., Shariat, M., Talebi, F., Laur, R. (2011) Two phase mixed convection Al_2O_3 -water nanofluid flow in an annulus. *International Journal of Multiphase Flow*, 37(6), 585–595. doi: <http://dx.doi.org/10.1016/j.ijmultiphaseflow.2011.03.008>.

- [46] Macagno, E. O., Hung, T. K. (1967) Computational and experimental study of a captive annular eddy, *Journal of Fluid Mechanics*, 28, 43–64.
- [47] Durst, F., Melling, A., Whitelaw, J. H. (1974) Low Reynolds number flow over a plane symmetric sudden expansion, *Journal of Fluid Mechanics*, 64(1), 111–128.
- [48] Afshin Goharzadeh, P. R. (2009) Experimental measurement of laminar axisymmetric flow through confined annular geometries with sudden inward expansion. *Journal of Fluids Engineering*, 131, 124501 (124504 pages).
- [49] Nag, D., Datta, A. (2007) On the eddy characteristics of laminar axisymmetric flows through confined annular geometries with inward expansion. *Proceedings of the Institution of Mechanical Engineers. Part C: Journal of Mechanical Science*, 221, 213–226.
- [50] Guo, Z.-Y., Li, D.-Y., Liang, X.-G. (1996) Thermal effect on the recirculation zone in sudden-expansion gas flows. *International Journal of Heat and Mass Transfer*, 39(13), 2619–2624. doi: [http://dx.doi.org/10.1016/0017-9310\(95\)00371-1](http://dx.doi.org/10.1016/0017-9310(95)00371-1).
- [51] Oliveira, P. J., Pinho, F. T. (1997) Pressure drop coefficient of laminar Newtonian flow in axisymmetric sudden expansions. *International Journal of Heat and Fluid Flow*, 18(5), 518–529. doi: [http://dx.doi.org/10.1016/S0142-727X\(97\)80010-0](http://dx.doi.org/10.1016/S0142-727X(97)80010-0).
- [52] Chiang, T. P., Sheu, T. W. H., Wang, S. K. (2000) Side wall effects on the structure of laminar flow over a plane-symmetric sudden expansion. *Computers and Fluids*, 29(5), 467–492. doi: [http://dx.doi.org/10.1016/S0045-7930\(99\)00018-3](http://dx.doi.org/10.1016/S0045-7930(99)00018-3).
- [53] Fearn, R. M., Mullin, T., Cliffe, K. A. (1990) Nonlinear flow phenomena in a symmetric sudden expansion. *Journal of Fluid Mechanics*, 211, 595–608. doi: 10.1017/S0022112090001707.
- [54] Oliveira, P. J. (2003) Asymmetric flows of viscoelastic fluids in symmetric planar expansion geometries. *Journal of Non-Newtonian Fluid Mechanics*, 114(1), 33–63. doi: [http://dx.doi.org/10.1016/S0377-0257\(03\)00117-4](http://dx.doi.org/10.1016/S0377-0257(03)00117-4).
- [55] Hammad, K. J., Vradis, G. C., Volkan Otugen, M. (2001) Laminar flow of a Hershel-Bulkley fluid over an axisymmetric sudden expansion. *Journal of Fluids Engineering*, 123, 588–594.
- [56] Hammad, K. J. (1998) Experimental and computational study of laminar axisymmetric recirculating flows of Newtonian and viscoplastic non-Newtonian fluids. Ph.D. Dissertation, Polytechnic University, New York.
- [57] Miranda, J. P., Pinho, F. T., Oliveira, P. J. (2003) Local loss coefficient in sudden expansion laminar flows of inelastic shear thinning fluids. 17th International Congress of Mechanical Engineering, November 10–14, 2003.

- [58] Chieng, C. C., Launder, B. E. (1980) On the calculation of turbulent heat transport downstream from an abrupt pipe expansion. *Numerical Heat Transfer*, 3(2), 189–207. doi: 10.1080/01495728008961754.
- [59] Zemanick, P. P., Dougall, R. S. (1970) Local heat transfer downstream of abrupt circular channel expansion. *Journal of Heat Transfer*, 92, 53–60.
- [60] Gooray, A. M., Watkins, C. B., Aung, W. A. (1985) Turbulent heat transfer computations for rearward-facing steps and sudden pipe expansions. *Journal of Heat Transfer*, 107, 70–76.
- [61] Aung, W. (1983) An experimental study of laminar heat transfer downstream of backstep. *Journal of Heat Transfer*, 105, 823–829.
- [62] Sparrow, E. M., Chuck, W. (1987) PC solutions for the heat transfer and fluid flow downstream of an abrupt asymmetric enlargement in a channel. *Numerical Heat Transfer*, 12, 19–40.
- [63] Santosh Christopher, D., Kanna, P. R., Madhusudhana, G. R., Venkumar, P., Mohamed, H. A. (2012) Numerical investigation of heat transfer from a two-dimensional sudden expansion flow using nanofluids. *Numerical Heat Transfer, Part A: Applications*, 61(7), 527–546. doi: 10.1080/10407782.2012.666933.
- [64] Kanna, P. R., Das, M. K. (2006) Heat transfer study of two-dimensional laminar incompressible wall jet over backward-facing step. *Numerical Heat Transfer, Part A: Applications*, 50(2), 165–187. doi: 10.1080/10407780500506857.
- [65] Abu-Nada, E. (2008) Application of nanofluids for heat transfer enhancement of separated flows encountered in a backward facing step. *International Journal of Heat and Fluid Flow*, 29(1), 242–249. doi: <http://dx.doi.org/10.1016/j.ijheatfluidflow.2007.07.001>.
- [66] Armaly, B. F., Durst, F., Pereira, J. C. F., Schönung, B. (1983) Experimental and theoretical investigation of backward-facing step flow. *Journal of Fluid Mechanics*, 127, 473–496.
- [67] Barton, I. E. (1997) Laminar flow over a backward-facing step with a stream of hot particles. *International Journal of Heat and Fluid Flow*, 18(4), 400–410.
- [68] Lee, T., Mateescu, D. (1998) Experimental and numerical investigation of 2-d backward-facing step flow. *Journal of Fluids and Structures*, 12(6), 703–716.
- [69] Armaly, B. F., Li, A., Nie, J. H. (2003) Measurements in three-dimensional laminar separated flow. *International Journal of Heat and Mass Transfer*, 46(19), 3573–3582. doi: [http://dx.doi.org/10.1016/S0017-9310\(03\)00153-4](http://dx.doi.org/10.1016/S0017-9310(03)00153-4).
- [70] Barbosa Saldana, J. G., Anand, N. K., Sarin, V. (2005) Numerical simulation of mixed convective flow over a three-dimensional horizontal backward facing-step. *Journal of Heat Transfer*, 127, 1027–1036.

- [71] Li, A., Armaly, B. F. (2000) Mixed convection adjacent to 3D backward facing step. Proceedings of the ASMEIMECE conference, ASME HTD366-2, New York, 51–58.
- [72] Labbe, O., Sagaut, P., Montreuil, E. (2002) Large-eddy simulation of heat transfer over a backward-facing-step. *Numerical Heat Transfer Part A*, 42, 73–90.
- [73] Avancha, R. V. R., Pletcher, R. H. (2002) Large eddy simulation of the turbulent flow past a backward-facing step with heat transfer and property variations. *International Journal of Heat and Fluid Flow*, 23(5), 601–614. doi: [http://dx.doi.org/10.1016/S0142-727X\(02\)00156-X](http://dx.doi.org/10.1016/S0142-727X(02)00156-X).
- [74] Mehrez, Z., Bouterra, M., El Cfsi, A., Belghith, A., Quere, P. (2009) The influence of the periodic disturbance on the local heat transfer in separated and reattached flow. *Heat and Mass Transfer*, 46(1), 107–112. doi: 10.1007/s00231-009-0548-z.
- [75] Chen, Y. T., Nie, J. H., Armaly, B. F., Hsieh, H. T. (2006) Turbulent separated convection flow adjacent to backward-facing step—effects of step height. *International Journal of Heat and Mass Transfer*, 49(19–20), 3670–3680. doi: <http://dx.doi.org/10.1016/j.ijheatmasstransfer.2006.02.024>.
- [76] Abe, K., Kondoh, T., Nagano, Y. (1994) A new turbulence model for predicting fluid flow and heat transfer in separating and reattaching flows—I. Flow field calculations. *International Journal of Heat and Mass Transfer*, 37(1), 139–151. doi: [http://dx.doi.org/10.1016/0017-9310\(94\)90168-6](http://dx.doi.org/10.1016/0017-9310(94)90168-6).
- [77] Abe, K., Kondoh, T., Nagano, Y. (1995) A new turbulence model for predicting fluid flow and heat transfer in separating and reattaching flows—II. Thermal field calculations. *International Journal of Heat and Mass Transfer*, 38(8), 1467–1481. doi: [http://dx.doi.org/10.1016/0017-9310\(94\)00252-Q](http://dx.doi.org/10.1016/0017-9310(94)00252-Q).
- [78] Kherbeet, A. S., Mohammed, H. A., Salman, B. H. (2012) The effect of nanofluids flow on mixed convection heat transfer over microscale backward-facing step. *International Journal of Heat and Mass Transfer*, 55(21–22), 5870–5881. doi: <http://dx.doi.org/10.1016/j.ijheatmasstransfer.2012.05.084>.
- [79] Stüer, H., Gyr, A., Kinzelbach, W. (1999) Laminar separation on a forward facing step. *European Journal of Mechanics – B/Fluids*, 18(4) 675–692.
- [80] Abu-Mulaweh, H. I., Chen, T. S., Armaly, B. F. (2002) Turbulent mixed convection flow over a backward-facing step—the effect of the step heights. *International Journal of Heat and Fluid Flow*, 23(6), 758–765.
- [81] Abu-Mulaweh, H. I. (2002) Effects of backward- and forward-facing steps on turbulent natural convection flow along a vertical flat plate. *International Journal of Thermal Sciences*, 41(4), 376–385.
- [82] Abu-Mulaweh, H. I. (2005) Turbulent mixed convection flow over a forward-facing step—the effect of step heights. *International Journal of Thermal Sciences*, 44(2), 155–162.

Evaluation of Solidification Times for Medium and High Carbon Steels Based upon Heat Transfer and Solidification Phenomena in the Continuous Casting of Blooms

Panagiotis Sismanis

Additional information is available at the end of the chapter

<http://dx.doi.org/10.5772/60706>

1. Introduction

The quest for billets and blooms production in the continuous casting of carbon steels with more stringent quality demands in internal soundness, free from surface defects, and internal porosity has increased the need for more insight in the appraisal of the phenomena associated with solidification under industrial conditions. Medium and high carbon steels cover a broad range of manufacturing products; nevertheless, the production of this type of material with a constant high percentage of prime-choice products remains a tough subject to analyze, understand, and more difficult to attain in practice. These carbon steels exhibit relatively low liquidus and solidus temperatures, with these values decreasing even further as carbon levels increase. It is understood that the blooms produced must be 100% crystallized (solid) at least before cutting to the delivered lengths is accomplished. It is realized that the larger the cross-section of the produced cast product the more time it requires in order to solidify completely. Big-sized cast products (or blooms) are more desirable for mainly two reasons: (a) large cross-sections are associated with large values of mass per unit length, hence, productivity is favored, and more important (b) large cross-sections are subject to larger values of area reduction once rolled, giving products with smaller possibility to quality degradation. On the other hand, the proper control of the cooling intensity in the secondary cooling zones (air-mist spray zones) upon the solidifying product in order to avoid surface/sub-surface defects in the unbending regions of the caster, places limitations on the casting speeds, and therefore productivities are not always at the desired levels. In practice, fundamental operation parameters like casting speed, casting temperature, and cooling-water consumption at the secondary (spray) zones

per produced mass of steel are among the most critical ones that the operator should keep in mind, once these have been analyzed, and their impact upon quality has been realized. Furthermore, from the early stages of medium and high-carbon steels casting, the operator has appreciated that it has been impossible to attain the high levels of productivity as with low and medium-low carbon steels without loss of internal quality. This is so because the low solidus temperatures that these grades exhibit become even lower in a dynamic way due to the local cooling rates that affect the solidification mechanism. Indeed, micro-segregation phenomena become more pronounced for these types of steels reducing even further the temperature at which the product becomes 100% solid, or in other terms, the solid fraction becomes one. There are some correlations for the solidus temperatures that unfortunately do not hold appreciably well, under varying cooling conditions, as it normally happens in the industrial continuous casting process. Nevertheless, the liquidus temperature is computed with great precision based upon the liquid-steel chemical analysis, and in this way, the industrial parameter known as superheat, which is the difference between the casting and liquidus temperatures, is calculated correctly; it is known that superheat is of paramount importance in the casting process. In this study, an attempt was carried out in order to shed some light into the effect of the various casting parameters upon the internal quality of the produced blooms in the continuous caster of Stomana, Pernik, Bulgaria. The biggest size of blooms produced currently in this caster is 300 x 250 mm x mm, and most medium and high-carbon grades are produced in this size. A heat transfer and a micro-segregation model were coupled and put into effect in order to facilitate the analysis of solidification along the caster length. Consequently, the solid fraction in the mushy zone, which is actually the intermediate zone between liquid and solid, was computed across a bloom section at any point along the caster, or in other words, from the meniscus level in the mold till the point of analysis. In addition to this, temperature and local-cooling rate distributions were also computed in a similar manner. Different operating conditions were fed into the simulation model in order to compute the required metallurgical lengths, or in other words, the effective cutting lengths that obeyed the unity solid fractions in the mushy zone along the centerline of a bloom.

2. Quality problems associated with internal soundness/central porosity

From the early times of the continuous casting for medium and high carbon steels, it has been realized that central porosity as a quality problem seems inevitable. Figure 1 shows a picture from a macro-etched high carbon bloom cross-section.

It is pointed out that for high carbon steels the tendency for central porosity generation is very large no matter how well liquid steel is treated, and how successful the casting process is performed. With time, the continuous casters manufacturers realized that this problem can be abided if electromagnetic stirring (EMS) was applied not only in the mold but in specific positions along the strand, mostly known as strand (S-EMS) and final (F-EMS) positions. F-EMS position is considered the position at which the mushy zone along the centerline becomes solid, or the position around the final solidification of the product. This is an effective technical solution to lessen the problem and is currently applied in some caster installations worldwide.



Figure 1. A macro etched cross-section from a 300 x 250 mm x mm bloom. The central porosity, which creates an internal-soundness quality problem, is apparent for this high-carbon cast product.

Another promising technical solution is the dynamic soft reduction, in which the part of the bloom which approaches final solidification is subject to a compressive force that slightly reduces its size in one direction but mechanically eliminates the central porosity problem. It is interesting to note that there are installations worldwide that currently apply both technical solutions for internal porosity minimization. However, no matter whether an installation applies one technical solution or another, it is really intriguing to try to figure out why and how this happens, and most importantly up to what extent, depending upon the various casting operating conditions. Without some knowledge upon this problem for a specific installation, one may not appreciate all the phenomena involved in, and maybe a definitive solution may not be successfully attained even after the installation of the discussed technical solutions. That is why it was decided to get some extra information on the subject before the installation of any technical solution might be applied at the Stomana bloom caster.

3. Literature review mostly oriented to quality problems for medium and high carbon steels

Superheat was one of the most fundamental factors recognized from the early years of continuous casting especially for medium and high carbon steels. In an early report [1], pilot plant tests were performed casting 150 x 150 mm x mm billets of high carbon steels. It was proven that at low superheats or even sub-liquidus casting temperatures, the centerline segregation was minimized. The electromagnetic stirring at the mold (M-EMS) exhibited some benefits, and the application of EMS at the strand (S) and final (F) stages of solidification started

being installed in some casters worldwide. In a study [2], it was found that the combination of EMS, that is, (S+F)-EMS for blooms and (M+S+F)-EMS for billets, is the most effective method for reducing macro-segregation among various EMS conditions, causing them to solidify more rapidly during the final stages of solidification, providing more finely distributed porosities and segregation spots along the central region. The optimum liquid pool thickness was found to decrease as the carbon content increased, which may be attributed to longer solidification times in the solid fraction range from $f_s = 0.3$ to 0.7. By gaining experience [3] in an actual caster installation, they concluded that a mold tube with a parabolic taper was proven good enough quality-wise for the continuous casting of medium and high carbon steels for carbon contents up to 0.55%. In another study [4], a coupled model was developed consisting of a cellular automaton scheme (CA) simulating the grain structure formation during solidification, and a finite difference scheme simulating the macroscopic heat transfer and solute transport in the continuous casting process. Columnar to equiaxed dendritic transition was effectively reproduced. The effect of superheat on the solidification structure was analyzed, verifying the empirical fact that increasing superheat the columnar dendritic growth increases against the equiaxed one. Under industrial conditions [5], S-EMS applied in the continuous casting of 150 x 150 mm x mm billets reduced centerline segregation up to a degree. However, increasing field intensity, deterioration upon the attained quality improvement was recorded. Some interesting fundamental research, as well as industrial achievements regarding medium and high carbon steels were presented in the recent European continuous casting conference [6-18], revealing the broad research and practice that may be developed in the field during the coming years. In Ref. [6], they used the liquid–solid interface energy as the main property in order to study the micro-segregation during solidification. They concluded that convection effects influenced micro-segregation behavior of the studied high carbon ($C \leq 0.7\%$), and high manganese steels. In another work [7], a 3D mathematical model was used to analyze the characteristics of magnetic field, flow field, and solidification of molten steel in the mold with electromagnetic stirring for a 260 x 300 mm x mm bloom. A dominant swirling motion at the transverse direction described the flow in the mold; the electromagnetic field was computed with similar values to those measured. They took under consideration the air-gap formation in the corners of the bloom adjacent to the mold. A summary of the actions taken to increase the productivity of Tenaris casters and to ensure high-quality standards in the produced round blooms for low, medium, and high carbon steels was presented in Ref. [8]. An in-house heat transfer model was developed to simulate the temperature distribution at various casting conditions. In addition to this, a rigid-viscoplastic model for simulating the thermal strain effects was developed to assess the potential risk of internal and surface cracks. Industrial practice was improved [9] in the field of high-carbon steel casting by the introduction of EMS not only in the mold, but in specific positions in the strand, and sometimes in the position of the final solidification front. Typical values for solid fraction along the central axis where the F-EMS is effective were found to be in the range of 0.1–0.4. Just for the sake of sense, comparing the findings between the published works [2] and [9] for the valid solid-fraction range for a successful F-EMS application, it is derived that depending upon a specific caster installation different approximations may yield to optimum solutions. In a recent monumental industrial installation [10], the excellent quality results in the production of –among others – medium and high carbon steels were successfully attained by a 2-strand vertical caster (in order to avoid extra strains from the bending/unbending of the strand, which are inevitable to customary

curved casters) for the production of big sections of blooms (up to 420 x 530 mm x mm). The caster managed to attain high quality results with the simultaneous application of a soft reduction system plus a moveable F-EMS system per strand. Chaotic phenomena seem to take place [11] in the continuous casting of steel billets, and specifically porosity chains seem to follow chaotic behavior along a cast billet. In other words, the chain of voids that are formed in the central zone along a billet and are generally coupled with segregation exhibit a spacing fluctuation in an erratic, random manner; stochastic modelling was applied on the basis of empirical time series in order to capture much of the dynamics. The lowering of the solidus temperature with respect to carbon-content increase for steels seems to be magnified by the boron effect [12]. Indeed, high Mn medium carbon steels with B higher than 40 ppm exhibit a very low solidification temperature at about 1140°C. In general, it has been verified that for high carbon steels ($C \leq 1\%$), the addition of B introduces the possibility of a retrograde melting phenomenon retaining liquid at temperatures around 1100°C. In actual practice, a proper secondary cooling scheme should be applied in order to minimize re-melting behavior. In a similar study [13], low and medium carbon boron-steels ($B \approx 30\text{--}40$ ppm) exhibit a sharp decrease of hot ductility at about 1100°C for a 0.7%Mn content. It was explained on the basis of BN formation after the initial MnS formation; castability is therefore reduced for these types of steels. The implementation of soft reduction at the Voestalpine Stahl Donawitz bloom caster for the continuous casting of high carbon (0.80–1.05%C) rounds exhibited positive quality results [14]. On the other hand, the EMS underlined the proper positioning limitations that made the implementation very difficult to attain reliable and reproducible quality results. Proper design can be successful in as far as quality results are concerned even for small radius casters. In a revamping case [15], good quality results were obtained in a relatively small radius (~5m) caster through multi-radius unbending. Furthermore, the addition of M-EMS, S-EMS, and F-EMS gave rise to the successful casting of medium and high carbon steels with billets cross-sections of 110 x 110 up to 160 x 160 mm x mm. Proper design by reducing roll pitch in the areas where soft reduction was applied and implementing EMS and proper secondary cooling led to the required quality improvements in the revamping of another caster [16] for the production of high carbon steels. The need for fundamental research is illustrated in the following two published works. In the first one [17], an in situ material characterization by bending (IMC-B) 3-point-bending test was developed to simulate crack formation that takes place during continuous casting for most carbon grades; after the test, the strains were calculated using a simulation model in ABAQUS. In the next work [18], it was explicitly verified that micro-segregation phenomena are of paramount importance in the calculation of the final solidification front in order to apply soft reduction efficiently; specifically, an error of about 40°C in the estimation of the solidus temperature may result in an uncertainty of about 1.2 m in the determination of the correct soft reduction point.

4. Micro-segregation effects

The liquidus temperature for a specific steel chemical analysis is calculated with very good accuracy. However, the correct calculation of the solidus temperature is not always that easy. Nevertheless, there are some formulas for the computation of the solidus temperature based upon the specific chemical analysis. One is given by equation (1) as presented in reference [19]:

$$T_s^* = 1535 - 200(\%C) - 12.3(\%Si) - 6.8(\%Mn) - 124.5(\%P) - 183.9(\%S) - 4.3(\%Ni) - 1.4(\%Cr) - 4.1(\%Al) \quad (1)$$

The Simple model [20] for micro-segregation gives a thorough fundamental analysis for the computation of both the liquidus and solidus temperatures. According to this, the computation of the liquidus temperature is given by equation (2) based on chemical analysis only:

$$T_L = 1536 - 78(\%C) - 7.6(\%Si) - 4.9(\%Mn) - 34.4(\%P) - 38(\%S) - 4.69(\%Ni) - 1.04(\%Cr) - 5.32(\%Cu) - 2.6(\%Mo) - 10.24(\%Ti) - 12.95(\%V) - 10.24(\%Nb) - 0.24(\%W) - 60(\%N) \quad (2)$$

However, for the computation of the solidus temperature the same model [20] requires more computational effort, as the solid fraction in the mushy zone (in which solid and liquid co-exist) depends not only upon temperature but local cooling-rates as well. This can be described as:

$$f_s = G(T, C_R) \quad (3)$$

The function G includes the whole logic of calculation depending upon the phase of crystallization, that is, γ , δ , and/or peritectic. Most medium-high and high carbon steels crystallize in the γ phase. Table 1 shows the salient species for the two chemical analyses that were used in this study belonging in the category of medium-high (MC), and high carbon (HC) steels.

Type	$T_L(^{\circ}C)$	$T_s(^{\circ}C)$	$T_s(^{\circ}C)$	C	Si	Mn	P	S	Cr	V
HC	1466	1366	1325	0.77	0.28	0.76	0.01	0.02	0.32	0.00
MC	1493	1435	1404	0.44	0.23	0.63	0.01	0.02	0.08	0.00

Table 1. Chemical analyses with computed values for the liquidus and solidus temperatures

Equation (2) was used for the calculation of the liquidus temperatures, and equation (1) for the solidus temperature T_s^* . Nevertheless, in order to have more uniform and comparable results, the solidus temperature T_s based on the simple model of micro-segregation analysis was computed at very low cooling rates (10^{-12} °C/sec) for both steel grades, respectively. Figures 2 and 3 illustrate the effect of micro-segregation upon the solidus temperature and show a form for function G at various levels of cooling rates. It is interesting to note that in both cases, the larger the cooling rate the lower the solidus temperature. On the other hand, the solidus temperatures that were computed by equation (1) are by far above the corresponding values computed by the micro-segregation analysis even at moderate local cooling rates. Furthermore, the biggest difference is computed at the lowest selected cooling rate (10^{-12} °C/s) for both cases; this extreme low value for the local cooling rate was adopted in order to simulate – as much as possible – the solidus temperature at infinite time of crystallization.

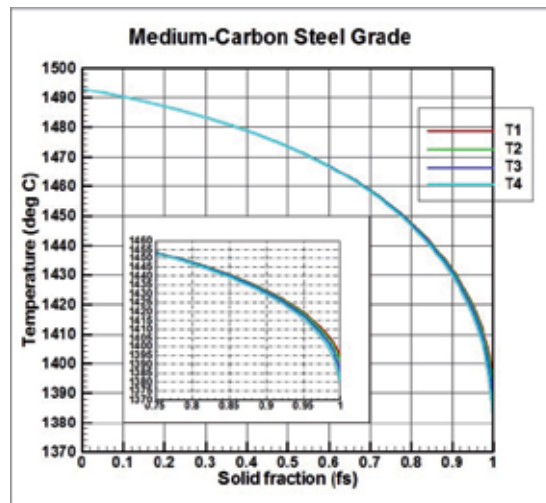


Figure 2. Micro-segregation results for the selected medium carbon steel at various levels of cooling rates: (T1) $C_R=0.01$ °C/s, $T_s=1394$ °C; (T2) $C_R=0.10$ °C/s, $T_s=1391$ °C; (T3) $C_R=1.0$ °C/s, $T_s=1385$ °C; (T4) $C_R=10.0$ °C/s, $T_s=1379$ °C.

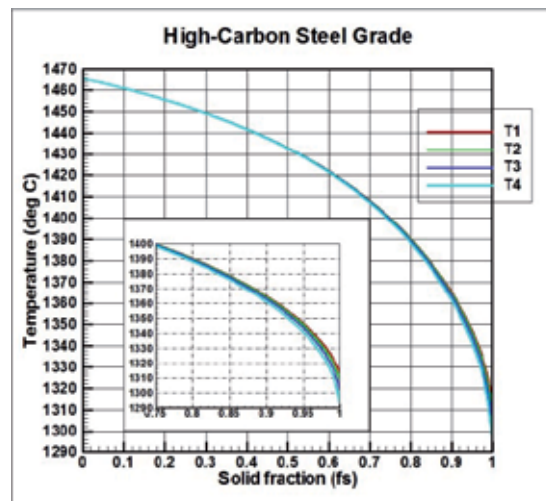


Figure 3. Micro-segregation results for the selected high carbon steel at various levels of cooling rates: (T1) $C_R=0.01$ °C/s, $T_s=1313$ °C; (T2) $C_R=0.10$ °C/s, $T_s=1308$ °C; (T3) $C_R=1.0$ °C/s, $T_s=1301$ °C; (T4) $C_R=10.0$ °C/s, $T_s=1292$ °C.

5. Heat-transfer mathematical approach

The general 3D heat-transfer equation that describes the temperature distribution inside the solidifying body is given by the following equation according to Refs. [21, 22]:

$$\rho C_p \frac{\partial T}{\partial t} = \nabla \cdot k \nabla T + S \quad (4)$$

The source term S may be considered [23] to be of the form:

$$S = S_c + S_p \cdot T \quad (5)$$

Furthermore, T is the temperature, and ρ , C_p , and k are the density, heat capacity, and thermal conductivity, respectively. The heat transfer equation in Cartesian coordinates may be written as:

$$\rho C_p \frac{\partial T}{\partial t} = \frac{\partial}{\partial x} \left(k \frac{\partial T}{\partial x} \right) + \frac{\partial}{\partial y} \left(k \frac{\partial T}{\partial y} \right) + S \quad (6)$$

The boundary conditions applied in order to solve (6) are as follows.

The heat flux in the mold was computed based on a recent treatment [7] that takes under consideration the air gap formation at the corners of the bloom, in conjunction with another older analysis [24] that came up with more precise heat-transfer coefficients in the mold. In the latter, the heat transfer coefficient at any position inside the mold is given by:

$$h_{m,z} = 1.35 \cdot 10^{-3} (1 - 0.8z) q_m \quad (7)$$

The heat flux at any position in the mold is given by:

$$q_z = a - b\sqrt{z}, \quad a = 2.680 \cdot 10^6, \quad b = 2.59578 \cdot 10^6, \quad 0 \leq z \leq L_m \quad (8)$$

Integrating (8), the average value for heat flux that is transferred through the walls of the mold is:

$$q_m = a - \left(\frac{2}{3} b \right) \sqrt{L_m} \quad (9)$$

Finally, the mold heat transfer coefficient was adjusted for the air-gap effect at the corners of the bloom [7], according to the following sets of equations:

$$h_{m,ag,z} = f_{corner} * h_{m,z}$$

$$f_{corner} = \begin{cases} 1.0 & 0 \leq z \leq 0.1L_m \\ 0.7 & 0.1L_m \leq z \leq 0.25L_m \text{ for the corner region(+), and 1.0 elsewhere} \\ 0.5 & 0.25L_m \leq z \leq L_m \text{ for the corner region(+), and 1.0 elsewhere} \\ (+) & \text{Corner region: } (a_g W_x) \text{ along x-axis, } (a_g W_y) \text{ along the y-axis} \end{cases} \quad (10)$$

This formulation reasonably neglects the effect of contact resistance between the solidified shell of steel and the copper mold; this is a valid approach for blooms and big sections

generally, as the soft shell bulges a bit and stays in contact with the copper mold in the central areas of the mold, retracting somewhat at the corners. Furthermore, this analysis was performed on similar sized sections (300 x 260 mm x mm) [7]. The heat fluxes due to water spraying and strand radiation in the secondary cooling zones were calculated using the following expressions:

$$\begin{aligned} q_s &= h_s \cdot (T - T_{w0}) \\ q_r &= h_r \cdot (T - T_{env}) \quad \text{with } h_r = \sigma \varepsilon \cdot \frac{T^4 - T_{env}^4}{T - T_{env}} \\ q_c &= h_c \cdot (T - T_{env}) \end{aligned} \quad (11)$$

where h_s , h_r , and h_c are the heat transfer coefficients for spray cooling, radiation, and convection, respectively, T_{w0} is the water temperature, T_{env} is the ambient temperature, σ is the Stefan-Boltzmann constant, and ε is the steel emissivity (considered equal to 0.8 in the present study). Natural convection was assumed to be the prevailing convective mechanism, as stagnant air-flow conditions were considered due to the low casting speeds of the strands applied in practice. The strand was assumed to be a long horizontal cylinder with an equivalent diameter of a circle having the same area with that of the cross-section of the bloom, and a correlation valid for a wide Rayleigh number range [25] was applied, written in an appropriate form [26]:

$$\sqrt{Nu_D} = 0.60 + 0.387 B^{1/6} \quad B = Ra_D \left[1 + \left(\frac{0.559}{Pr} \right)^{9/16} \right]^{16/9} \quad (10^{-5} < B < 10^{13}) \quad (12)$$

where Nu , Ra , and Pr are the dimensionless Nusselt, Rayleigh, and Prandtl numbers, respectively. In this way, h_c is calculated by means of the Nu_D number. It is worth mentioning, however, that the radiation effects are more pronounced than the convection ones in the continuous casting of steels. From various expressions proposed in the literature for the heat transfer coefficient in water-spray cooling systems, the following formula was applied as approaching the present casting conditions:

$$h_s = 1570 \cdot W^{0.55} \cdot \frac{1 - 0.0075T_{w0}}{4} \quad (13)$$

where W is the water flux for any secondary spray zone in liters/m²/sec, and h_s is in W/m²/K. At any point along the secondary zones (starting just below the mold) of the caster, the total heat flux q_{tot} is computed according to the following formula, taking into account that q_s may be zero at areas where no sprays are present:

$$q_{tot} = q_s + q_r + q_c \quad (14)$$

In mathematical terms, considering one quarter-section of the bloom assuming symmetry is valid, the aforementioned boundary conditions below mold can be written in compact form:

$$\begin{aligned}
 -k \frac{\partial T}{\partial x} &= \begin{cases} h_{m,ag,z}(T - T_{WF}) & \text{at } x = W_x, 0 \leq y \leq W_y, 0 \leq z \leq L_m \\ q_{tot} & \text{at } x = W_x, 0 \leq y \leq W_y, z > L_m \end{cases} \\
 -k \frac{\partial T}{\partial y} &= \begin{cases} h_{m,ag,z}(T - T_{WF}) & \text{at } y = W_y, 0 \leq x \leq W_x, 0 \leq z \leq L_m \\ q_{tot} & \text{at } y = W_y, 0 \leq x \leq W_x, z > L_m \end{cases}
 \end{aligned} \tag{15}$$

where z follows the casting direction starting from the meniscus level inside the mold; the mold has an effective length equal to L_m , and W_x and W_y are the half-width (as seen along the horizontal x -axis) and half-thickness (as seen along the vertical y -axis) of the bloom, respectively. Due to symmetry, the heat fluxes across the central planes are considered to be zero:

$$\begin{aligned}
 -k \frac{\partial T}{\partial x} &= 0 \quad \text{at } x = 0, 0 \leq y \leq W_y, z \geq 0 \\
 -k \frac{\partial T}{\partial y} &= 0 \quad \text{at } y = 0, 0 \leq x \leq W_x, z \geq 0
 \end{aligned} \tag{16}$$

Finally, the initial temperature of the pouring liquid steel is supposed to be the temperature of liquid steel in the tundish:

$$T = T_0 \quad \text{at } t = 0 \text{ (and } z = 0), 0 < x < W_x, 0 < y < W_y \tag{17}$$

The thermo-physical properties of carbon steels were obtained from an older published work [27], in which the properties were given as functions of carbon content for the liquid, mushy, solid, and transformation-temperature domain values; this also gave rise to the advantage of eliminating the source factor ($S=0$) by absorbing all transformation heats in the heat capacity values.

6. Numerical solution

This specific article is part of a series of published works with respect to the numerical solution of the heat transfer equation in 2D and 3D domains [28-30]. The strongly implicit method as practiced by Patankar [23] was applied. Although a grid of 200×200 nodal points was sufficient to stabilize results with a maximum error of 10^{-2}°C for each nodal point in the bloom quarter-section, a final grid of 400×400 nodal points was selected for the final computations. The selected time interval (Δt) was 0.25 sec, and the space intervals (Δx , Δy) were about 0.376 mm and 0.313 mm for the horizontal (x -axis) and vertical (y -axis) directions, respectively. Figure

4 depicts the domain (quarter-section) upon which the computations took place. This specific section was also cut in four sub-sections in order to exploit the 4-cores of a professional DELL laptop, Latitude E4310, with 8 GB RAM, operating under Windows 7 Professional. The Gauss–Seidel algorithm for the iterative solution of the matrix of equations was applied, as it was proven as a very suitable scheme for the solution of the temperature distribution putting into effect the OpenMP instruction set for parallel computation. Over-relaxation was applied for the fastest possible convergence; the over-relaxation parameter used was $\omega=1.870$, which has exhibited good results for these kinds of studies [28-32]. This specific piece of software was developed in GNU C++, version 4.8.1, supplied by TDM-GCC, and accessed through the open source, cross-platform IDE, Code::Blocks, version 13.12. Due to a very large number of data (~2–3 GB) stored in disk per run, a time span of about 30 minutes was required in order to cover the phenomena taking place top-to-bottom in the bloom caster. In summary, the main points of the computations included the following:

- Calculation of the temperature distribution inside a bloom cross-section at a specific location at the caster.
- Calculation of the local cooling-rates distribution at the same cross-section and position.
- Calculation of the solid fraction in the mushy zone at the same cross-section and position.

The dynamic computation of the solidus temperature (at the solid fraction value equal to 1, $f_s = 1$) defined the border of the new solidification front of the mushy zone.

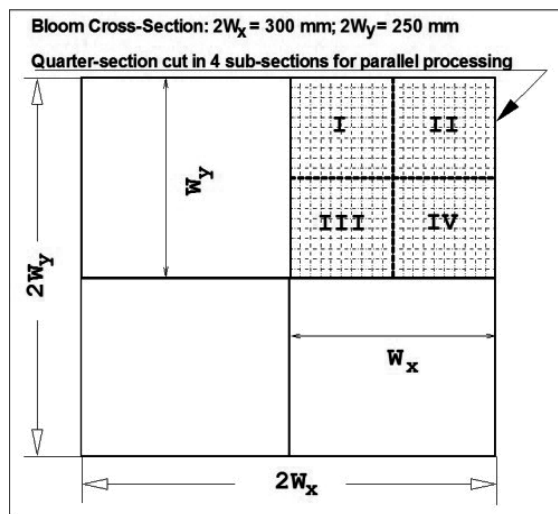


Figure 4. Illustration of the selected bloom quarter-section for the numerical solution of the 2D heat transfer equation. In roman numerals are depicted the four selected sub-sections upon which each CPU solved the temperature distribution using the Gauss-Seidel algorithm.

In this way, the computed results were stored in the disk and the system proceeded for the next time step; step-by-step the solidification front reached the center of the bloom. In average,

about 30–40 iterations per time step sufficed for convergence. The local cooling rates were computed at every nodal point, as follows:

$$C_R = (T|_{t+\Delta t} - T|_t) / \Delta t \quad (18)$$

7. Results and discussion

The Stomana bloom caster has a casting radius of 12 m, with M-EMS and no extra EMS or soft reduction along its four strands. Nevertheless, it is interesting to know the effect of critical casting parameters in order to maximize casting speed and hence, productivity, keeping the most attainable good internal porosity as much as possible. Consequently, the effect of parameters like U_c , SPH , ℓ_{pkg} , and a_g upon L_{SOL} was decided to be analyzed. Preliminary results showed that there were specific ranges of casting speeds U_c depending upon the selected steel grade; moving from MC to HC grades U_c should decrease, otherwise the required casting length for complete solidification L_{SOL} exceeded a lot the design value of the Stomana bloom caster that is close to 34 m. Figures 5 and 6 present typical computational results for the medium and high carbon steel grades selected at specific casting conditions. L_{SOL} values may vary a lot depending upon casting conditions and steel grades. For this reason, a reduced semi-factorial [33] computational experimental design was carried out in order to minimize the steps required to study the phenomenon.

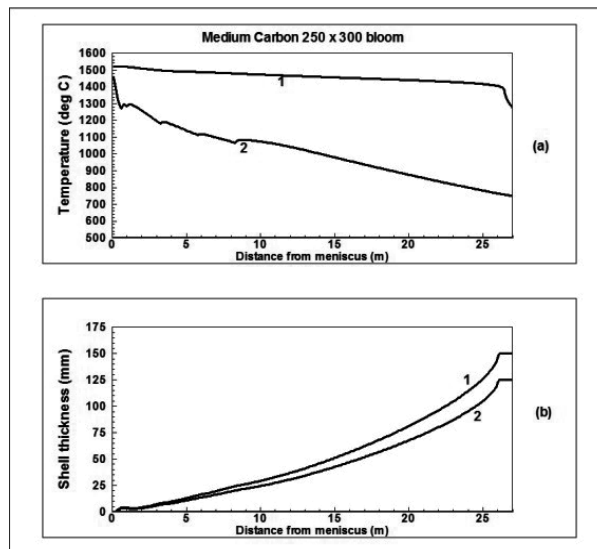


Figure 5. Casting results for the selected MC grade, for $U_c = 0.55$ m/min, $SPH = 30$ K, $\ell_{pkg} = 0.200$, $a_g = 12\%$. (a) Curves 1 and 2 show the centerline and surface temperatures, respectively. (b) Curves 1 and 2 show the shell thicknesses as they progress through the width (x-axis or horizontal direction) and the thickness (y-axis or vertical direction). The solidification or actual metallurgical length computed was 26.12 m. (Run no. 4, Table 2).

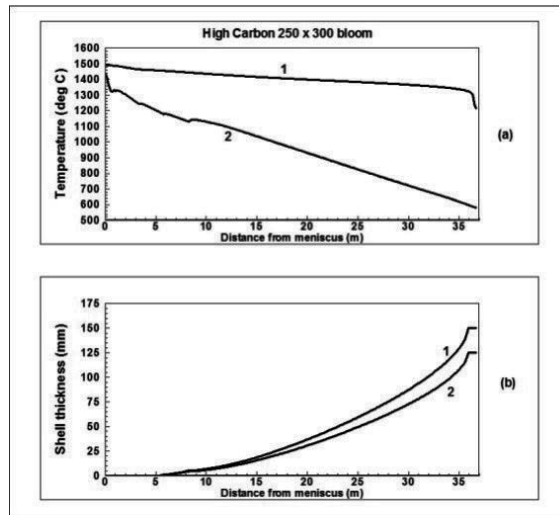


Figure 6. Casting results for the selected HC grade, for $U_c = 0.55$ m/min, $SPH = 30$ K, $\ell_{pkg} = 0.200$, $a_s = 12\%$. (a) Curves 1 and 2 show the centerline and surface temperatures, respectively. (b) Curves 1 and 2 show the shell thicknesses as they progress through the width (x-axis or horizontal direction) and the thickness (y-axis or vertical direction). The solidification or actual metallurgical length computed was 35.93 m. (Run no. 3, Table 2).

The adopted values for the casting parameters and the results for the required solidification lengths, for the MC and HC grades selected, are presented in Table 2. Initially it was designed for 12 cases; some more runs were added as of existing preliminary data (included in the statistical analysis).

The effect of air-gap formation upon the temperature distribution in the bloom corners was also verified in this study in accordance with a recent research work published in [7]. Specifically, Figure 7 depicts typical results revealing this important effect. Increasing the percentage of contact loss in the bloom corners due to air-gap formation inside the mold the exit-mold temperatures in the corners increase as well. On the other hand, a statistical analysis that was performed for the effect of the casting conditions upon the required solidification length for the two selected grades as presented in Table 2 showed that the air-gap formation inside the mold has no effect upon L_{SOL} . Probably this may be attributed to the fact that there is a lot of time for temperature re-distribution (soaking) due to conduction during the secondary cooling period, which is long enough as of the low casting speeds applied. Analysis of variance (ANOVA) was carried out using the R statistical package and the overall results are summarized in Table 3. Two things may be pointed out from the results presented in Table 3. First, similar behavior for the effects of the most critical factors upon the solidification length were found; in fact, an increase of 0.05 m/min upon casting speed seems to increase L_{SOL} by 2.4 m for MC, and by 3.2 m for HC, respectively. Similarly, an increase of 10°C upon superheat seems to increase L_{SOL} by 0.72 m for MC, and by 0.52 m for HC, respectively. The specific secondary water-cooling consumption has a negative effect for both grades, but unfortunately it cannot be increased appreciably due to potential surface defects on the blooms. Furthermore, the very good correlations deduced are attributed to the nature of the reduced semi-factorial design of runs that gave the maximum possible information to the ANOVA under the minimum number of tests.

Run no.	MC grade					HC grade				
	L_{sol} (m)	U_c (m/min)	SPH (K)	ℓ_{pkg} (liter/kg)	a_g (%)	L_{sol} (m)	U_c (m/min)	SPH (K)	ℓ_{pkg} (liter/kg)	a_g (%)
1	33.37	0.70	45	0.536	12	36.21	0.55	45	0.480	12
2	32.43	0.70	30	0.466	12	35.29	0.55	30	0.480	12
3	33.13	0.70	30	0.200	12	35.93	0.55	30	0.200	12
4	26.12	0.55	30	0.200	12	26.40	0.40	30	0.200	12
5	26.03	0.55	30	0.200	0	26.40	0.40	30	0.200	0
6	33.37	0.70	45	0.536	0	36.02	0.55	45	0.561	0
7	26.12	0.55	45	0.561	0	26.27	0.40	45	0.606	0
8	27.04	0.55	45	0.200	0	26.53	0.40	45	0.450	0
9	33.37	0.70	45	0.536	6	27.13	0.40	45	0.200	0
10	28.85	0.625	30	0.469	6	36.12	0.55	45	0.480	6
11	27.04	0.55	45	0.200	6	28.95	0.45	30	0.479	6
12	29.58	0.625	30	0.200	6	27.13	0.40	45	0.200	6
13	30.01	0.65	30	0.468	0	29.63	0.45	30	0.200	6
14	32.43	0.70	30	0.466	0	—	—	—	—	—

Table 2. Computational results for the effect of casting speed (U_c), superheat (SPH), specific secondary cooling-water consumption (ℓ_{pkg}), and air-gap percentage at the bloom corners (a_g) upon the required caster length for complete solidification (L_{sol}), for the two selected steel grades

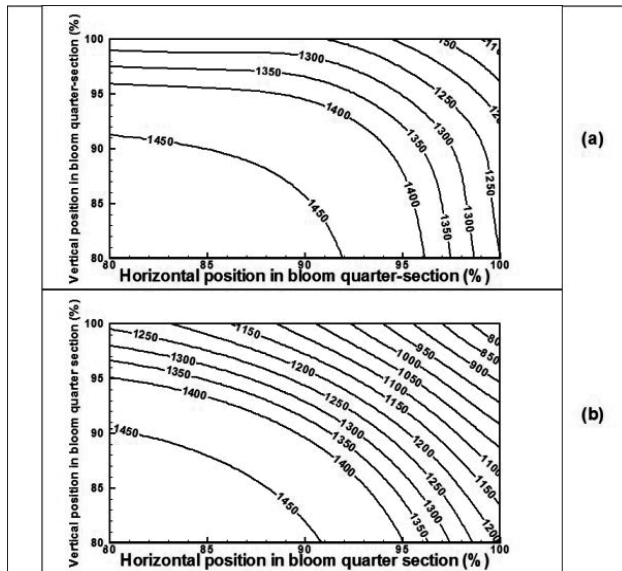


Figure 7. The effect of contact loss between the solidified shell and the mold upon the temperature distribution in the bloom corners, due to air-gap formation in these areas. The presented temperature distributions in the corner regions are from results obtained for MC steel cast at the following conditions: $U_c = 0.55$ m/min, SPH = 30 K, $\ell_{pkg} = 0.200$, case (a) $a_g = 12\%$ (Run no. 4, Table 2), case (b) $a_g = 0\%$ (Run no. 5, Table 2).

Factor	MC		HC	
	Regression coefficient	Statistical Significance	Regression coefficient	Statistical Significance
U_c	47.589	***	64.064	***
SPH	0.0716	***	0.052	***
ℓpkg	-2.636	***	-2.209	***
Intercept	-1.782	***	-0.383	***
Correlation coefficient	0.9997		0.9999	
Standard error of estimate	0.049		0.0545	
F-value	16770, on 3 and 10 DF		26920, on 3 and 9 DF	

Table 3. Linear regression and ANOVA results for the factors affecting the solidification length as performed using R

In this way, a regression formula of the form

$$L_{sol} = b_0 + b_1 * U_c + b_2 * SPH + b_3 * \ell pkg \tag{19}$$

is derived, where b 's are the regression coefficients (Table 3) for MC and HC, respectively.

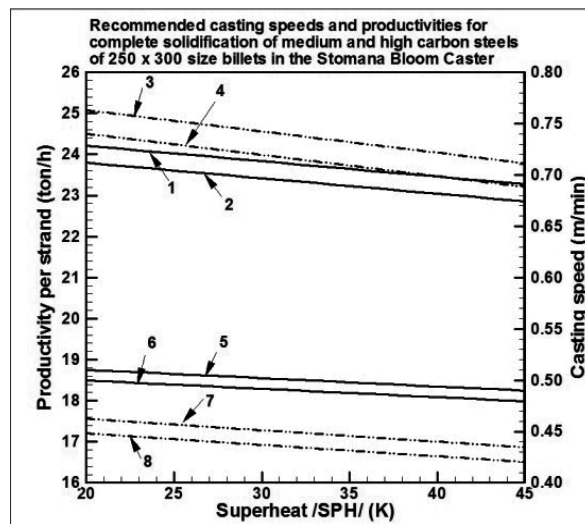


Figure 8. Casting speeds and productivities per strand in order to have complete solidification along the centerline at the point of cut-to-length products, for the selected MC and HC steels, and at various superheats. MC steel: Curves 1 and 3 represent the casting speed, and productivity for $\ell pkg = 0.5$, and 2 and 4 similar curves for $\ell pkg = 0.2$. HC steel: Curves 5 and 7 represent the casting speed and productivity for $\ell pkg = 0.5$, and 6 and 8 similar curves for $\ell pkg = 0.2$.

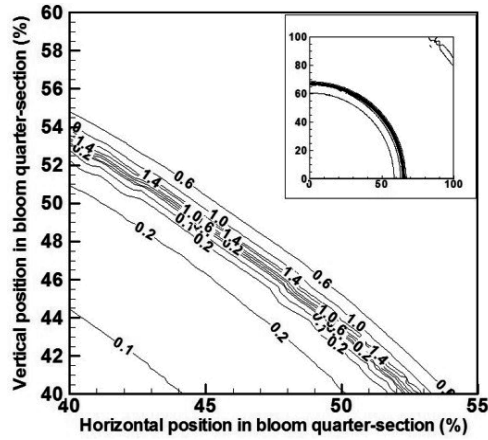


Figure 9. Typical local cooling-rate results as computed for the selected MC steel cast at the following conditions: $U_c = 0.70$ m/min, $SPH = 30$ K, $\ell_{pkg} = 0.200$, $a_s = 12\%$ (Run no. 3, Table 2). The results presented correspond to the time instance of 1710 sec, or equivalently, to a position of 19.95 m from the meniscus-level.

More than 99% statistical importance is signified by 3-stars (***) on Table 3, according to R. Figure 8 summarizes the results presented on Table 3 in graphical form. For practical purposes the maximum allowable caster length was considered to be 33 m (instead of 34 m that the Stomana caster actually is), introducing a small safety factor.

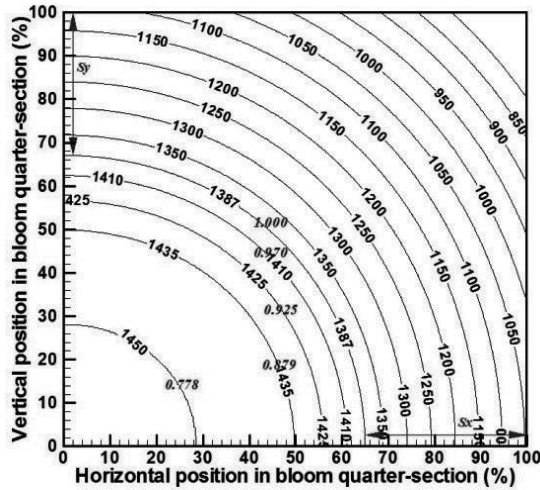


Figure 10. Temperature distribution inside a bloom section as computed for the selected MC steel cast at the following conditions: $U_c = 0.70$ m/min, $SPH = 30$ K, $\ell_{pkg} = 0.200$, $a_s = 12\%$ (Run no. 3, Table 2). The results presented correspond to the time instance of 1710 sec, or equivalently, to a position of 19.95 m from the meniscus-level. Some solid fraction values are also presented (in purple color).

Figures 9 and 10 illustrate results for the local-cooling rates and temperatures inside a bloom for the MC grade selected, under the same casting conditions at a specific location from the liquid-steel meniscus level in the mold. Figure 9 shows that there is a distribution of local cooling-rate values at any instance inside the bloom. For this case, a simple statistical analysis gave an average value $\mu = 0.205 \text{ }^\circ\text{C/s}$, a standard deviation $\sigma = 0.140$, and min and max values equal to 0 and 2.057, respectively. For this average value, the micro-segregation analysis gave a solidus temperature around 1389°C . This value is very close to the solidus temperature of 1387°C that the micro-segregation analysis gave for the computed cooling-rate conditions at the solidification front as depicted in Figure 10. The distances S_x and S_y show the corresponding shell thicknesses along the x and y axes. It is understood that the error would be tremendous if the shell thicknesses were computed based on the a priori solidus temperature ($T_s^* = 1435^\circ\text{C}$, Table 1) derived upon the chemical analysis only. Similar results are presented in Figures 11 and 12 for the HC grade selected.

Figure 11 depicts the local cooling rates inside a bloom section at about 24.98 m from the liquid steel meniscus level. In this case, the statistical analysis gave an average value for the local cooling rates of $\mu = 0.204 \text{ }^\circ\text{C/s}$, with a standard cooling rate of 0.074, and min and max values of 0 and 1.682, respectively. The local micro-segregation analysis gave a solidus temperature of 1307°C which is shown in Figure 12, and which is very close to the solidus temperature of 1306°C computed from the average cooling-rate of a section at the instance under discussion. One may wonder about the large error upon the estimate of the shell thickness if the whole analysis relied only upon the a priori calculated value ($T_s^* = 1366^\circ\text{C}$) based on the HC selected chemical analysis – an error of about 60°C in absolute value, erroneously concluding almost 100% solidification at a very premature time!

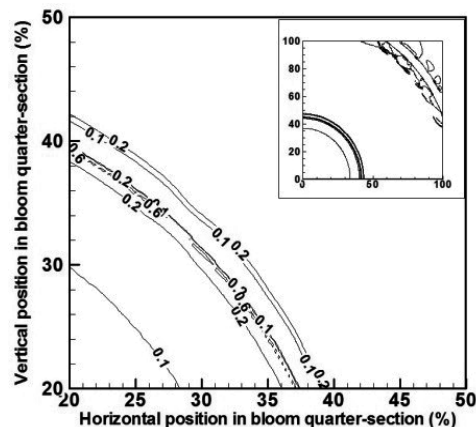


Figure 11. Typical local cooling-rates results as computed for the selected HC steel cast at the following conditions: $U_c = 0.45 \text{ m/min}$, $SPH = 30 \text{ K}$, $\ell_{pkg} = 0.200$, $a_s = 6\%$ (Run no. 13, Table 2). The results presented correspond to the time instance of 3330 sec, or equivalently, to a position of 24.98 m from the meniscus-level.

15 illustrates in graphical form that the local cooling rates remain as a distribution of values with an average value of $\mu = 0.230$ °C/sec, with a standard error of $\sigma = 0.073$, and min and max values of 0 and 1.729, respectively. Figure 16 depicts the temperature distribution inside the bloom section, defining the shell thicknesses along the x and y axes (S_x and S_y), at the computed solidus temperature of 1306°C.

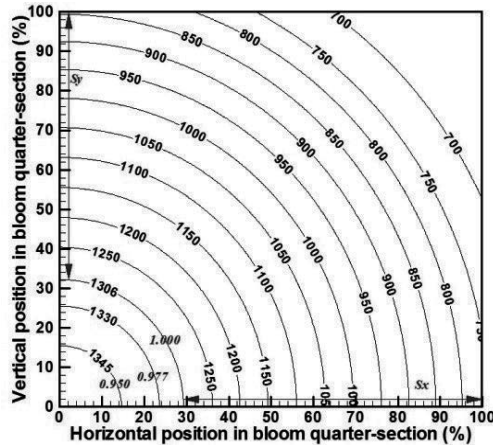


Figure 16. Temperature distribution inside a bloom section as computed for the selected HC steel cast at the following conditions: $U_r = 0.40$ m/min, $SPH = 45$ K, $\ell_{pkg} = 0.200$, $a_s = 0\%$ (Run no. 9, Table 2). The results presented correspond to the time instance of 3750 sec, or equivalently to a position of 25.0 m from the meniscus-level. Some solid fraction values are also presented (in purple color).

One last comment about the computed values of local cooling rates: once the shell formation has been created inside the mold, the average values of the local cooling rates are more or less stabilized to specific values. For example, for the cases presented in the Figures 9 through 16, the overall average values for the local cooling rates are about 0.234°C/s for the MC and 0.217°C/s for the HC, respectively. Supplying these values to the micro-segregation model, the values of 1389°C and 1306°C for the solidus temperatures of the MC and HC grades can be deduced, respectively. In this way, a priori calculated values for the solidus temperatures may be used with better precision in heat transfer applications that rely upon preselected values only.

The prediction of the grain size of the solidified metal structure as described in Ref. [27], together with the percentage of the equiaxed zone that may be formed depending on the prevailing heat-transfer conditions may be one part for future work; another part could be the analysis of thermal stress-strain phenomena that act upon the solidifying shell.

8. Conclusions

The installation of strand EMS has been decided for the Stomana caster. The target is to come up with blooms having better internal soundness than the one presented in Figure 1. However, some fundamental points are covered with the help of this study. Summarizing:

- The casting conditions with respect to the required casting length for complete solidification have been analyzed, and the effect upon expected productivity per grade is known.
- The appreciation of the solidification phenomena is impossible without coupling the micro-segregation analysis, especially for medium and high carbon grades. Once the S-EMS is installed, the specific range of critical solid fractions required for the proper performance of the stirrers can be linked with the operating conditions of the caster.
- The difficulty in predicting the solidus temperature at varying cooling conditions especially for high carbon steels has been illustrated. Nevertheless, a shortcut that can generate solidus temperatures to be used as a priori values in heat transfer models has been presented; it only takes some runs for the appropriate heat-transfer models to compute average values for the local cooling rates, which then may be fed to standalone micro-segregation models to calculate the corresponding solidus temperatures. Consequently, simple heat transfer models can simulate casting with less error in the involved solidification phenomena for medium and high carbon steels, by taking as input the solidus temperatures derived in the aforementioned manner.
- The great importance of heat transfer analysis on the domain of medium and high carbon solidification is proven once more. It is of paramount importance that mankind has this kind of tool for shedding light into similar type of complex industrial conditions.

Nomenclature

a_g ; Air gap factor. Percent of the bloom corner that lost contact to mold

C_p ; Heat capacity in J kg K^{-1}

f_s ; Solid fraction

h ; Heat transfer coefficient, in $\text{W m}^{-2} \text{K}^{-1}$

k ; Thermal conductivity, in $\text{W m}^{-1} \text{K}^{-1}$

L ; Length, in m

L_{sol} ; Required caster length for complete solidification, in m

ℓ_{pkg} ; Specific secondary cooling-water consumption, in liters of water/kg of steel

q ; Heat flux, in W m^{-2}

S, S_c ; Source term, constant term of S , in W m^{-3}

S_p ; Source term that compensates for the temperature dependence of S , in $\text{W m}^{-3} \text{K}^{-1}$

SPH ; Superheat, casting temperature – liquidus temperature, in $^{\circ}\text{C}$ or K

$t, \Delta t$; Time, time interval, in sec

T ; Temperature in a position inside the bloom, or at a nodal point, in $^{\circ}\text{C}$

T_L, T_S ; Liquidus, solidus temperature, in °C

U_c ; Casting speed, in m/min

W_x ; Half-width of the bloom, along the (horizontal) x-axis, in m

W_y ; Half-thickness of the bloom, along the (vertical) y-axis, in m

x, y, z ; Spatial coordinates, in m

$\Delta x, \Delta y$; Distance between adjacent nodal points along the x- and y-axis, respectively, in m

ε ; Emissivity

ρ ; Density, in kg m^{-3}

σ ; The Stefan–Boltzmann constant, which is equal to $5.67 \cdot 10^{-8} \text{ W m}^{-2} \text{ K}^{-4}$

ω ; Over-relaxation factor

Subscripts

0; Referring to an initial value

F, f; Fluid (WF referring to water as cooling fluid)

S, s; Surface, or solid

r, c; Radiation, convection

m; Average value, or referring to the mold

ag; Air gap is considered

Acknowledgements

The author is grateful to the top-management of Sidenor SA for the continuous support upon these types of studies, as well as for the permission of publishing this piece of work. My continuous gratitude and respect to Professor Rabi Baliga from the Mechanical Engineering Department of McGill University, Montreal, Canada, who introduced me to the field of computational fluid-flow and heat transfer should also be acknowledged.

Author details

Panagiotis Sismanis

Address all correspondence to: psismanis@sidenor.vionet.gr

Sidenor SA, Greece

References

- [1] Henderson S., Scholes A., Clarke B.D. Continuous Casting of High-Carbon steels in Billet and Bloom Sections at Sub-Liquidus Temperatures. Technical Steel Research, Final Report, EUR 13623 EN, Belgium, 1991.
- [2] Oh K.S., Chang Y.W. Macrosegregation Behavior in Continuously Cast High Carbon Steel Blooms and Billets at the Final Stage of Solidification in Combination Stirring. *ISIJ Intl*, Vol. 35, No. 7, 1995, pp. 866-875.
- [3] Chowaniek F. Quality Improvement of Continuously Cast Round Billets. *METAL-URGIJA*, Vol. 47, No. 3, 2008, pp. 191-193.
- [4] Luo S., Zhu M., Louhenkilpi S. Numerical Simulation of Solidification Structure of High Carbon Steel in Continuous Casting using Cellular Automaton Method. *ISIJ Intl*, Vol. 52, No. 5, 2012, pp. 823-830.
- [5] Cibulka J., Bocek D., Huczala T., Cupek J. Possibilities of S-EMS utilization for the Improvement of Central Segregation in Continuously Cast Billets in Conditions of TŽ. *Journal of Achievements in Materials and Manufacturing Engineering*, Vol. 55, No. 2, December 2012.
- [6] Rezende J., Schankies C., Alves C., Huettenmeister D., Senk D. Phase-Field Investigation of the Influence of the Solid-Liquid Interface Energy, Chemical Composition and Forced Convection on the Dendrite Growth Morphology for High Manganese Steels. In: 8th European Continuous Casting Conference and Symposium in Numerical & Physical Modeling, ASMET, 23-26 June 2014, Graz, Austria, pp. 124-132.
- [7] Wang Y., Yang Z., Zhang X., Wang B., Liu Q. 3D Numerical Simulation of Flow and Solidification of Molten Steel in Bloom Continuous Casting Mold with Electromagnetic Stirring. In: 8th European Continuous Casting Conference and Symposium in Numerical & Physical Modeling, ASMET, 23-26 June 2014, Graz, Austria, pp. 144-158.
- [8] Vazquez M., Poltarak G., Ferro S., Campos A., Cicutti C. Application of Mathematical Models to Optimize Operating Conditions during the Continuous Casting of Round Bars. In: 8th European Continuous Casting Conference and Symposium in Numerical & Physical Modeling, ASMET, 23-26 June 2014, Graz, Austria, pp. 179-188.
- [9] Sgro A., Rinaldi M., Kunstreich S., Yves D. Recent Danieli Experiences for Electromagnetic Stirrer Optimization in Round Blooms Continuous Casting. In: 8th European Continuous Casting Conference and Symposium in Numerical & Physical Modeling, ASMET, 23-26 June 2014, Graz, Austria, pp. 1454-1461.
- [10] Sgro A., Rinaldi M., Accardo G. A New Benchmark in Special Steel Casting: New Twin-Strand Vertical Caster at POSCO Specialty Steel, Korea. In: 8th European Con-

- tinuous Casting Conference and Symposium in Numerical & Physical Modeling, ASMET, 23-26 June 2014, Graz, Austria, pp. 338-346.
- [11] Tacke K-H. Irregular and Fluctuating Phenomena in Continuous Casting. In: 8th European Continuous Casting Conference and Symposium in Numerical & Physical Modeling, ASMET, 23-26 June 2014, Graz, Austria, pp. 699-708.
- [12] Alvarez de Toledo G., Komenda J., Stewart B., Brune T., Frisk K. Influence of Composition and Continuous Casting Parameters on the Cracking of B-Micro-alloyed High Mn Steel Grades. In: 8th European Continuous Casting Conference and Symposium in Numerical & Physical Modeling, ASMET, 23-26 June 2014, Graz, Austria, pp. 709-718.
- [13] Brune T., Haberl F., Senk D. Hot-Ductility and Precipitation Behavior of Boron in Nb-V-Ti Micro-alloyed Steels for CC. In: 8th European Continuous Casting Conference and Symposium in Numerical & Physical Modeling, ASMET, 23-26 June 2014, Graz, Austria, pp. 719-728.
- [14] Rauter W., Reiter J., Srienc K., Brandl W., Erker M., Huemer K., Mair A. Soft Reduction at a Round Bloom Caster: Implementation and Results. In: 8th European Continuous Casting Conference and Symposium in Numerical & Physical Modeling, ASMET, 23-26 June 2014, Graz, Austria, pp. 811-820.
- [15] Angelini L., Guerra F., Persi C., Straffelini G., Botelho P. Quality Improvement of the Acciaierie di Calvisano CCM through the EM Multi-Stirring Technology: Preliminary Results. In: 8th European Continuous Casting Conference and Symposium in Numerical & Physical Modeling, ASMET, 23-26 June 2014, Graz, Austria, pp. 821-830.
- [16] Chen M-H., Lu C-Y., Lin K-J., Kao C-L., Huang S-Y., Tsai M-F., Kuo A-N. Central Segregation Improvement of High Carbon Steels at CSC #3 Bloom Caster. In: 8th European Continuous Casting Conference and Symposium in Numerical & Physical Modeling, ASMET, 23-26 June 2014, Graz, Austria, pp. 831-838.
- [17] Krajewski P., Krobath R., Bernhard C., Miettinen J., Louhenkilpi S., Ilie S., Schaden T. A Novel Approach for the Simulation of Surface Cracks Formation in Continuous Casting. In: 8th European Continuous Casting Conference and Symposium in Numerical & Physical Modeling, ASMET, 23-26 June 2014, Graz, Austria, pp. 1160-1169.
- [18] Hahn S., Schaden T. DynaPhase: Online Calculation of Thermodynamic Properties during Continuous Casting. In: 8th European Continuous Casting Conference and Symposium in Numerical & Physical Modeling, ASMET, 23-26 June 2014, Graz, Austria, pp. 1170-1180.
- [19] Thomas B.G., Samarasekera I.V., Brimacombe J.K. Mathematical Modeling of the Thermal Processing of Steel Ingots: Part I. Heat Flow Model. *Metallurgical Transactions B*, Vol. 18B, 1987, pp. 119-130.

- [20] Won Y-M., Thomas B.G. Simple Model of Micro-segregation During Solidification of Steels. *Metallurgical Transactions A*, Vol. 32A, 2001, pp. 1755-1767.
- [21] Carslaw H.S., Jaeger J.C. *Conduction of Heat in Solids*. Oxford University Press, New York, 1986.
- [22] Incropera F.P., DeWitt D.P. *Fundamentals of Heat Transfer*. John Wiley & Sons, New York, 1981.
- [23] Patankar S.V. *Numerical Heat Transfer and Fluid Flow*. Hemisphere Publishing Corporation, Washington, 1980.
- [24] Yoon U-S., Bang I-W., Rhee J-H., Kim S-Y., Lee J-D., Oh K-H. Analysis of Mold Level Hunching by Unsteady Bulging during Thin Slab Casting. *ISIJ International*, Vol. 42, No.10, 2002, pp. 1103-1111.
- [25] Churchill S.W., Chu H.H.S. Correlating Equations for Laminar and Turbulent Free Convection from a Horizontal Cylinder. *Int. J. Heat Mass Transfer*, Vol.18, 1975, pp. 1049-1053.
- [26] Burmeister L.C. *Convective Heat Transfer*. John Wiley & Sons, 1983, p. 551.
- [27] Cabrera-Marrero J.M., Carreno-Galindo V., Morales R.D., Chavez-Alcala F. Macro-Micro Modeling of the Dendritic Microstructure of Steel Billets by Continuous Casting. *ISIJ International*, Vol. 38, No. 8, 1998, pp. 812-821.
- [28] Sismanis P. Heat Transfer Analysis of Special Reinforced NSC-Columns under Severe Fire Conditions. *International Journal of Materials Research*, Vol. 101, March 2010, DOI 10.3139/146.110290, pp. 417-430.
- [29] Sismanis P. Modeling Solidification Phenomena in the Continuous Casting of Carbon Steels. In: Amimul Ahsan (ed.). *Two Phase Flow, Phase Change and Numerical Modeling*. Rijeka: InTech; 2011. p.121-148. Available from by <http://www.intechopen.com/books/two-phase-flow-phase-change-and-numerical-modeling/modeling-solidification-phenomena-in-the-continuous-casting-of-carbon-steels> (accessed 21 August 2014).
- [30] Sismanis P. The Effect of Local Cooling Rates upon Solidification Phenomena in the Continuous Casting of Carbon Steels. In: 8th European Continuous Casting Conference and Symposium in Numerical & Physical Modeling, ASMET, 23-26 June 2014, Graz, Austria, pp. 1462-1471.
- [31] Anderson D.A., Tannehill J.C., Pletcher R.H. *Computational Fluid Mechanics and Heat Transfer*. Hemisphere Publishing Corporation. Washington. 1984.
- [32] James M., Smith G.M., Wolford J.C. *Applied Numerical Methods for Digital Computation with FORTRAN and CSMP*. Harper & Row Publishers. New York. 1977.
- [33] Montgomery D.C. *Design and Analysis of Experiments*. 2nd ed., John Wiley, New York, 1984.

Convective Heat Transfer to Sisko Fluid over a Nonlinear Radially Stretching Sheet

Masood Khan, Asif Munir and Azeem Shahzad

Additional information is available at the end of the chapter

<http://dx.doi.org/10.5772/60799>

1. Introduction

Over the past several decades, the Navier-Stokes equations have been studied frequently in the literature. This is due to the fact that the use of the Newtonian fluid model in numerous industrial applications to predict the behavior of many real fluids has been adopted. However, there are many materials of industrial importance (e.g. polymeric liquids, molten plastics, lubricating oils, drilling muds, biological fluids, food products, personal care products, paints, greases and so forth) are non-Newtonian. That is, they might exhibit dramatic deviation from Newtonian behavior and display a range of non-Newtonian characteristics. A few points of non-Newtonian characteristic are the ability of the fluid to exhibit relaxation and retardation, shear dependent viscosity, shear thinning or shear thickening, yield stress, viscoelasticity and many more. Thus, it has been now well recognized in technology and industrial applications that non-Newtonian fluids are more appropriate than the Newtonian fluid. Consequently, the theory of non-Newtonian fluids has become an active field of research for the last few years.

Unlike, the Newtonian fluid, it is very difficult to provide a universal constitutive model for non-Newtonian fluids as they possess very complex structure. However, there are some classes of fluids that cannot be classified as Newtonian or purely non-Newtonian such as water-borne coating etc. This situation demands some more general models which can be utilized for analysis of both Newtonian and non-Newtonian behaviors. For this purpose, some models have been proposed in the literature including generalized Newtonian fluids. The Sisko fluid model [1] is a subclass of the generalized Newtonian fluids which is considered as the most appropriate model for lubricating oils and greases [2]. The Sisko fluid model is of much importance due to its adequate description of a few non-Newtonian fluids over the most important range of shear rates. The appropriateness of the Sisko fluid model has been successfully extended to the shear thinning rheological behavior of concentrated non-

Newtonian slurries [3]. The three parameters Sisko fluid model, which can be considered as a generalized power-law model that includes Newtonian component, has not been given due attention in spite of its diverse industrial applications. A representative sample of the recent literature on the Sisko fluid is provided by references [4-10].

Investigations of the boundary layer flow and heat transfer of non-Newtonian fluids over a stretching surface are important due to immense applications in engineering and science. A great number of investigations concern the boundary layer behavior on a stretching surface. Many manufacturing processes involve the cooling of continuous sheets. To be more specific, examples of such applications are wire drawing, hot rolling, drawing of plastic films, paper production, and glass fiber etc. In all these situations, study of the flow and heat transfer is of significant importance as the quality of the final products depends to the large extent on the skin friction and heat transfer rate at the surface. In view of these, the boundary layer flows and heat transfer over a stretching surface have been studied extensively by many researchers. Crane [11] was first to investigate the boundary layer flow of a viscous fluid over a stretching sheet when the sheet is stretched in its own plane with velocity varies linearly with the distance from a fixed point on the sheet. Dutta *et al.* [12] examined the heat transfer in a viscous fluid over a stretching surface with uniform heat flux. Later on, this problem was extended by Chen and Char [13] by considering the variable heat flux. Grubka and Bobba [14] analyzed the heat transfer over a stretching surface by considering the non-isothermal wall that is varying as a power-law with the distance. Cortell [15] investigated the flow and heat transfer of a viscous fluid over nonlinear stretching sheet by considering the constant surface temperature and prescribed surface temperature. It seems that Schowalter [16] was the first who has obtained the similarity solutions for the boundary layer flow for power-law pseudoplastic fluids. Howel *et al.* [17] considered the laminar flow and heat transfer of a power-law fluid over a stretching sheet. Hassanien *et al.* [18] investigated the heat transfer to a power-law fluid flow over a non-isothermal stretching sheet. Abel *et al.* [19] studied the flow and heat transfer of a power-law fluid over a stretching sheet with variable thermal conductivity and non-uniform heat source. Prasad and Vajravelu [20] analyzed the heat transfer of a power-law fluid over a non-isothermal stretching sheet. Khan and Shahzad [21,22] have considered the boundary layer theory of the Sisko fluid over the planer and radially stretching sheets and found the analytic solutions; however, they only considered the integral values of the power-law index in their flow problems. The integral values of the power-law index are inadequate to completely comprehend the shear thinning and shear thickening effects of the Sisko fluid. Moreover, a literature survey also indicates that no work has so far been available with regards to heat transfer to Sisko fluid flow over a stretching sheet in presence of viscous dissipation.

The objective of this chapter is to analyze the flow and heat transfer characteristics of Sisko fluid over a radially stretching sheet with the stretching velocity cr^s in the presence of viscous dissipation. In the present work we have spanned the value of the power-law index from highly shear thinning to shear thickening Sisko fluid ($0.2 \leq n \leq 1.9$). The modeled partial differential equations are reduced to a system of nonlinear ordinary differential equations using the appropriate transformations. The resulting equations are then solved numerically by implicit finite difference method in the domain $[0, \infty)$. The numerical results for the velocity and

temperature fields are graphically depicted and effects of the relevant parameters are discussed in detail. In addition, the skin friction coefficient and the local Nusselt number for different values of the pertaining parameters are given in tabulated form. Moreover, numerical results are compared with exact solutions as special cases of the problem. Furthermore, the present results for the velocity field are also validated by comparison with the previous pertinent literature.

2. Governing equations

This section comprises the governing equations and the rheological model for the steady two-dimensional flow and heat transfer of an incompressible and inelastic fluid Sisko fluid in the cylindrical polar coordinates. To derive the governing equations we make use of fundamental laws of fluid mechanics, namely conservations of mass, linear momentum and energy, including the viscous dissipation

$$\nabla \cdot \mathbf{V} = 0, \tag{1}$$

$$\rho(\mathbf{V} \cdot \nabla)\mathbf{V} = -\nabla p_1 + \nabla \cdot \mathbf{S}, \tag{2}$$

$$\rho c_p(\mathbf{V} \cdot \nabla)T = -\nabla \cdot \mathbf{q} + \mathbf{S} \cdot \mathbf{L}. \tag{3}$$

In the above equations \mathbf{V} is the velocity vector, ρ the density of fluid, c_p the specific heat at constant pressure, p_1 the pressure, T the temperature, \mathbf{S} the extra stress tensor and \mathbf{q} the heat flux given by

$$\mathbf{q} = -\kappa(\nabla T), \tag{4}$$

where κ is the thermal conductivity of the fluid and ∇ the gradient operator.

The extra stress tensor \mathbf{S} for an incompressible fluid obeys the Sisko rheological model. This model mathematically can be expressed as [4]

$$\mathbf{S} = \left[a + b \left| \sqrt{\frac{1}{2} \text{tr} (\mathbf{A}_1^2)} \right|^{n-1} \right] \mathbf{A}_1, \tag{5}$$

where \mathbf{A}_1 is the rate of deformation tensor or the first Rivlin-Erickson tensor defined as

$$\mathbf{A}_1 = \mathbf{L} + \mathbf{L}^T, \quad \mathbf{L} = \nabla \mathbf{V}, \tag{6}$$

with a the dynamic viscosity, b the Sisko fluid parameter or the flow consistency index, ($n \geq 0$) the power-law index or the flow behavior index (a non-negative real number) and \mathbf{T} stands for transpose.

The quantity

$$\mu_{\text{eff}} = \left[a + b \left| \sqrt{\frac{1}{2} \text{tr}(\mathbf{A}_1^2)} \right|^{n-1} \right], \quad (7)$$

represents an apparent or effective viscosity as a function of the shear rate. If $a=0$ and $n=1$ (or $b=0$) the equations for Newtonian fluid, $a=0$ for the power-law model and $n=0$ with b as yield stress for the Bingham plastic model are obtained.

For the steady two-dimensional axisymmetric flow, we assume the velocity, temperature and stress fields of the form

$$\mathbf{V} = [u(r, z), 0, w(r, z)], \quad T = T(r, z), \quad \mathbf{S} = \mathbf{S}(r, z), \quad (8)$$

when (r, z) denotes the cylindrical polar coordinates along the sheet and vertical to it, u and w the velocity components in the r - and z - directions, respectively.

The steady two-dimensional and incompressible equations of motion (2) including conservation of mass (1) and thermal energy (3) can be written as

$$\frac{\partial u}{\partial r} + \frac{u}{r} + \frac{\partial w}{\partial z} = 0, \quad (9)$$

$$\rho \left(u \frac{\partial u}{\partial r} + w \frac{\partial u}{\partial z} \right) = -\frac{\partial p_1}{\partial r} + \frac{\partial S_{rr}}{\partial r} + \frac{\partial S_{rz}}{\partial z} + \frac{S_{rr} - S_{\phi\phi}}{r}, \quad (10)$$

$$\rho \left(u \frac{\partial w}{\partial r} + w \frac{\partial w}{\partial z} \right) = -\frac{\partial p_1}{\partial z} + \frac{1}{r} \frac{\partial}{\partial r} (r S_{rz}) + \frac{\partial S_{zz}}{\partial z}, \quad (11)$$

$$\begin{aligned} \rho c_p \left(u \frac{\partial T}{\partial r} + w \frac{\partial T}{\partial z} \right) &= \kappa \left(\frac{1}{r} \frac{\partial}{\partial r} \left(r \frac{\partial T}{\partial r} \right) + \frac{\partial^2 T}{\partial z^2} \right) + a \left[2 \left(\frac{\partial u}{\partial r} \right)^2 + \left(\frac{\partial u}{\partial z} \right)^2 + 2 \frac{\partial u}{\partial z} \frac{\partial w}{\partial r} + 2 \frac{\partial w}{\partial z} \frac{\partial w}{\partial r} + 2 \frac{u^2}{r^2} \right] \\ &+ b \left[2 \left(\frac{\partial u}{\partial r} \right)^2 + \left(\frac{\partial u}{\partial z} \right)^2 + 2 \frac{\partial u}{\partial z} \frac{\partial w}{\partial r} + 2 \frac{\partial w}{\partial z} \frac{\partial w}{\partial r} + 2 \frac{u^2}{r^2} \right] \left| \sqrt{\frac{1}{2} \text{tr} \mathbf{A}_1^2} \right|^{n-1}, \end{aligned} \quad (12)$$

where

$$\frac{1}{2} \text{tr}(\mathbf{A}_1^2) = 2 \left(\frac{\partial u}{\partial r} \right)^2 + 2 \left(\frac{\partial w}{\partial z} \right)^2 + 2 \left(\frac{\partial u}{\partial z} \right)^2 + \frac{\partial u}{\partial z} \frac{\partial w}{\partial r} + 2 \frac{u^2}{r^2}. \quad (13)$$

In view of Eq. (8) the stress components are inserted into the equations of motion and the usual boundary layer approximations are made, the equations of motion characterizing the steady boundary layer flow and heat transfer take the form

$$\rho \left(u \frac{\partial u}{\partial r} + w \frac{\partial u}{\partial z} \right) = -\frac{\partial p_1}{\partial r} + a \frac{\partial^2 u}{\partial z^2} + b \frac{\partial}{\partial z} \left(\left| \frac{\partial u}{\partial z} \right|^{n-1} \frac{\partial u}{\partial z} \right), \quad (14)$$

$$0 = -\frac{\partial p_1}{\partial z} \quad (15)$$

$$u \frac{\partial T}{\partial r} + w \frac{\partial T}{\partial z} = \alpha \frac{\partial^2 T}{\partial z^2} + a \left(\frac{\partial u}{\partial z} \right)^2 + b \left(\frac{\partial u}{\partial z} \right)^2 \left| \frac{\partial u}{\partial z} \right|^{n-1}, \quad (16)$$

where $\alpha = \frac{\kappa}{\rho c_p}$ is the thermal diffusivity with κ as the thermal conductivity.

3. Mathematical formulation

3.1. Flow analysis

Consider the steady, two-dimensional and incompressible flow of Sisko fluid over a nonlinear radially stretching sheet. The fluid is confined in the region $z > 0$, and flow is induced due to stretching of the sheet along the radial direction with velocity $U_w = cr^s$ with c and s are positive real numbers pertaining to stretching of the sheet. We assume that the constant temperature of the sheet is T_w , while T_∞ is the uniform ambient fluid temperature with $T_w > T_\infty$. For mathematical modeling we take the cylindrical polar coordinate system (r, ϕ, z) . Due to the rotational symmetry, all the physical quantities are independent of θ . Note that if the streamwise velocity component u increases with the distance z from the moving surface, the velocity gradient and therefore the shear rate are positive; however, if u decreases with increasing z the velocity gradient and therefore shear rate are negative. In the present problem within the boundary layer the shear rate is assumed to be negative since the streamwise velocity component u decreases monotonically with increasing z from the moving boundary (stretching sheet). Thus, under these assumptions, the flow is governed by the following equation:

$$\rho \left(u \frac{\partial u}{\partial r} + w \frac{\partial u}{\partial z} \right) = a \frac{\partial^2 u}{\partial z^2} - b \frac{\partial}{\partial z} \left(-\frac{\partial u}{\partial z} \right)^n. \quad (17)$$

The boundary conditions associated to flow field are

$$u = cr^s, w = 0 \text{ at } z = 0, \quad (18)$$

$$u \rightarrow 0 \text{ as } z \rightarrow \infty. \quad (19)$$

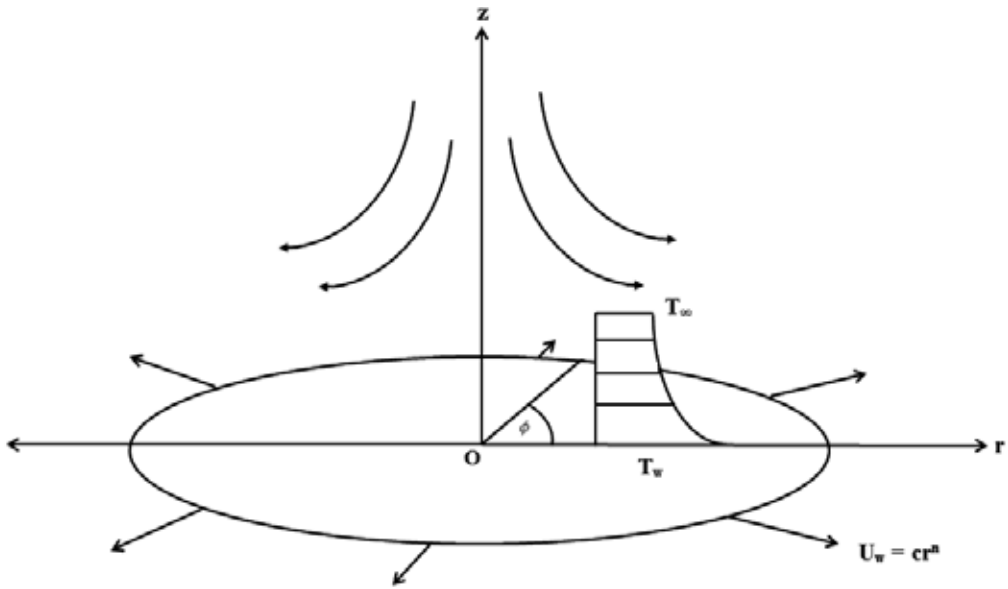


Figure 1. Physical model and coordinate system.

We define the following variables

$$\eta = \frac{z}{r} \text{Re}_b^{\frac{1}{n+1}} \text{ and } \psi(r, z) = -r^2 U \text{Re}_b^{\frac{-1}{n+1}} f(\eta), \tag{20}$$

where $\psi(r, z)$ is the Stokes stream function defined by $u = -\frac{1}{r} \frac{\partial \psi}{\partial z}$ and $w = \frac{1}{r} \frac{\partial \psi}{\partial r}$ giving

$$u = U f'(\eta) \text{ and } w = -U \text{Re}_b^{\frac{-1}{n+1}} \left[\frac{s(2n-1) + n + 2}{n + 1} f(\eta) - \frac{s(n-2) + 1}{n + 1} \eta f'(\eta) \right]. \tag{21}$$

On employing the above transformations, Eqs. (17) to (19) take the form [21]

$$A f''' + n(-f'')^{n-1} f''' + \left(\frac{s(2n-1) + n + 2}{n + 1} \right) f f'' - s(f')^2 = 0, \tag{22}$$

$$f(0) = 0, \quad f'(0) = 1, \quad f'(\infty) = 0, \tag{23}$$

where prime denotes differentiation with respect to η and

$$\text{Re}_a = \rho r U / a, \quad \text{Re}_b = \rho r^n U^{2-n} / b \text{ and } A = \text{Re}_b^{\frac{2}{n+1}} / \text{Re}_a \tag{24}$$

The physical quantity of major interest is the local skin friction coefficient and is given by [21]

$$\frac{1}{2} \text{Re}_b^{-\frac{1}{n+1}} C_f = Af''(0) - [-f''(0)]^n. \quad (25)$$

3.2. Heat transfer analysis

In the assumption of boundary layer flow, the energy equation for the non-Newtonian Sisko fluid taking into account the viscous dissipation effects and neglecting the heat generation effects for the temperature field $T = T(r, z)$ is

$$u \frac{\partial T}{\partial r} + w \frac{\partial T}{\partial z} = \alpha \frac{\partial^2 T}{\partial z^2} + \frac{1}{\rho c_p} \left[a \left(\frac{\partial u}{\partial z} \right)^2 + b \left(-\frac{\partial u}{\partial z} \right)^{n+1} \right]. \quad (26)$$

The corresponding thermal boundary conditions are

$$T = T_w \text{ at } z = 0, \quad (27)$$

$$T \rightarrow T_\infty \text{ as } z \rightarrow \infty. \quad (28)$$

Using the transformations (20) the above problem reduces to

$$\theta'' + \text{Pr} \frac{s(2n-1) + (n+2)}{n+1} f\theta' + Br(f'')^2 + \text{Pr} Ec(-f'')^{n+1} = 0, \quad (29)$$

$$\theta(0) = 1, \text{ and } \theta \rightarrow 0 \text{ as } \eta \rightarrow \infty, \quad (30)$$

where $\theta(\eta) = \frac{T - T_\infty}{T_w - T_\infty}$, $Br = \frac{aU^2}{\kappa(T_w - T_\infty)}$ the Brinkman number, $Ec = \frac{U^2}{c_p(T_w - T_\infty)}$ the Eckert number and $\text{Pr} = \frac{\rho U R}{\alpha} \frac{-2}{n+1}$ the generalized Prandtl number.

The local Nusselt number Nu_r at the wall is defined as

$$Nu_r = \left. \frac{rq_w}{\kappa(T_w - T_\infty)} \right|_{z=0}, \quad (31)$$

where the wall heat flux at the wall is $q_w = -\kappa \left(\frac{\partial T}{\partial z} \right) \Big|_{z=0}$, which by virtue of Eq. (31) reduces to

$$\text{Re}_b^{-1/n+1} Nu_r = -\theta'(0). \quad (32)$$

4. Solution procedure

The two point boundary value problems comprising Eqs. (22) and (29) along with the associated boundary conditions are solved by implicit finite difference scheme along with Keller box scheme. To implement the scheme, Eqs. (22) and (29) are written as a system of first-order differential equations in η as follows:

$$f' = p, \tag{33}$$

$$p' = q, \tag{34}$$

$$Aq' + n(-q)^{n-1}q' + Dfq - sp^2 = 0, \tag{35}$$

$$\theta' = t, \tag{36}$$

$$t' + Pr Ec(-q)^{n+1} + Pr Dft + Brq^2 = 0, \tag{37}$$

where $D = \frac{s(2n-1) + (n+2)}{n+1}$.

The boundary conditions in terms of new variable are written as

$$f(0) = 0, p(0) = 1 \text{ and } \theta(0) = 1, \tag{38}$$

$$p \rightarrow 0 \text{ and } \theta \rightarrow 0 \text{ as } \eta \rightarrow \infty. \tag{39}$$

The functions and their derivatives are approximated by central difference at the midpoint $\eta_{j-\frac{1}{2}}$ of the segment $\eta_{j-1}\eta_j$, where $j=1, 2, \dots, N$.

$$\eta_0 = 0, \eta_j = \eta_{j-1} + h_j, \eta_N = \eta_\infty. \tag{40}$$

Using the finite difference approximations equations (33) to (37) can be written as

$$f_j - f_{j-1} - h_j p_{j-1/2} = 0, \tag{41}$$

$$p_j - p_{j-1} - h_j q_{j-1/2} = 0, \tag{42}$$

$$A(q_j - q_{j-1}) + nh_j(-q_{j-1/2})^{n-1}(q_j - q_{j-1}) - sh_j(p_{j-1/2})^2 + Dh_j f_{j-1/2} q_{j-1/2} = 0 \tag{43}$$

$$\theta_j - \theta_{j-1} - h_j t_{j-1/2} = 0, \tag{44}$$

$$(t_j - t_{j-1}) + \text{Pr} \text{Ech}_j (-q_{j-1/2})^{n+1} (q_j - q_{j-1}) + \text{Br} h_j (q_{j-1/2})^2 + D \text{Pr} h_j f_{j-1/2} t_{j-1/2} = 0, \tag{45}$$

where $j=1, 2, 3, \dots, N$, $f_{j-1/2} = \frac{f_j + f_{j-1}}{2}$, $p_{j-1/2} = \frac{p_j + p_{j-1}}{2}$, $q_{j-1/2} = \frac{q_j + q_{j-1}}{2}$, and $t_{j-1/2} = \frac{t_j + t_{j-1}}{2}$.

Boundary conditions (38) and (39) are written as

$$f_0 = 0, p_0 = 1, \theta_0 = 1, \tag{46}$$

$$p_N = 0 \text{ and } \theta_N = 0. \tag{47}$$

Eqs. (41) to (45) are system of nonlinear equations and these equations are linearized employing the Newton's method and using the expressions:

$$f_j^{(k+1)} = f_j^{(k)} + \delta f_j^{(k)}, p_j^{(k+1)} = p_j^{(k)} + \delta p_j^{(k)}, q_j^{(k+1)} = q_j^{(k)} + \delta q_j^{(k)},$$

$$\theta_j^{(k+1)} = \theta_j^{(k)} + \delta \theta_j^{(k)}, t_j^{(k+1)} = t_j^{(k)} + \delta t_j^{(k)}, \tag{48}$$

where $k=1, 2, 3, \dots$

Putting the left hand side of the above expressions into Eqs. (41) to (45) and dropping the quadratic terms in $\delta f^{(k)}$, $\delta p^{(k)}$, $\delta q^{(k)}$, $\delta \theta^{(k)}$ and $\delta t^{(k)}$, the following linear equations are obtained:

$$\delta f_j - \delta f_{j-1} - h_j \delta p_{j-1/2} = (r_1)_{j-1/2}, \tag{49}$$

$$(\xi_1)_j \delta q_j + (\xi_2)_j \delta q_{j-1} + (\xi_3)_j \delta f_j + (\xi_4)_j \delta f_{j-1} +$$

$$(\xi_5)_j \delta p_j + (\xi_6)_j \delta p_{j-1} + (\xi_7)_j \delta \theta_j + (\xi_8)_j \delta \theta_{j-1} = (r_2)_{j-1/2}, \tag{50}$$

$$(\eta_1)_j \delta z_j + (\eta_2)_j \delta z_{j-1} + (\eta_3)_j \delta f_j + (\eta_4)_j \delta f_{j-1} +$$

$$(\eta_5)_j \delta p_j + (\eta_6)_j \delta p_{j-1} + (\eta_7)_j \delta \theta_j + (\eta_8)_j \delta \theta_{j-1} = (r_3)_{j-1/2}, \tag{51}$$

$$\delta p_j - \delta p_{j-1} - h_j \delta q_{j-1/2} = (r_4)_{j-1/2}, \tag{52}$$

$$\delta \theta_j - \delta \theta_{j-1} - h_j \delta t_{j-1/2} = (r_5)_{j-1/2}, \tag{53}$$

where

$$\xi_1 = \left[A - n(n-1) \left(\frac{q_j - q_{j-1}}{2} \right) (-q_{j-1/2})^{n-2} + n(-q_{j-1/2})^{n-1} + \frac{Dh_j}{2} f_{j-1/2} \right], \tag{54}$$

$$\xi_2 = \left[-A - n(n-1) \left(\frac{q_j - q_{j-1}}{2} \right) (-q_{j-1/2})^{n-2} + n(-q_{j-1/2})^{n-1} + \frac{Dh_j}{2} f_{j-1/2} \right], \tag{55}$$

$$\xi_3 = \xi_4 = \frac{Dh_j}{2} q_{j-1/2}, \quad \xi_5 = \xi_6 = -sh_j p_{j-1/2}, \quad \xi_7 = \xi_8 = 0, \tag{56}$$

and

$$\eta_1 = 1 + \frac{DPr}{2} h_j f_{j-1/2}, \quad \eta_2 = \eta_1 - 2, \quad \eta_3 = \eta_4 = \frac{DPr}{2} h_j t_{j-1/2}, \tag{57}$$

$$\eta_5 = \eta_6 = Brh_j q_{j-1/2} - \frac{Pr Ec}{2} (n+1) h_j (-q_{j-1/2})^n. \tag{58}$$

The right hand sides of Eqs. (49) to (53) are given by

$$r_1 = -(f_j - f_{j-1}) + h_j p_{j-1/2}, \tag{59}$$

$$r_2 = -\left[A(q_j - q_{j-1}) + Dh_j f_{j-1/2} q_{j-1/2} - sh_j p_{j-1/2}^2 \right] - n(q_j - q_{j-1})(-q_{j-1/2})^{n-1}, \tag{60}$$

$$r_3 = -\left[(t_j - t_{j-1}) + DPr h_j f_{j-1/2} t_{j-1/2} + Brh_j q_{j-1/2}^2 + Pr Ec (-q_{j-1/2})^{n+1} \right], \tag{61}$$

$$r_4 = -(p_j - p_{j-1}) + h_j q_{j-1/2}, \quad r_5 = -(t_j - t_{j-1}) + h_j t_{j-1/2}. \tag{62}$$

The boundary conditions (46) and (47) become

$$\delta f_0 = 0, \delta p_0 = 0, \delta q_0 = 0, \delta \theta_0 = 0, \delta q_N = 0 \text{ and } \delta \theta_N = 0. \quad (63)$$

The linearized Eqs. (49) to (53) can be solved by using block elimination method as outlined by Na [23]. The iterative procedure is stopped when the difference in computing the velocity and temperature in the next iteration is less than 10^{-5} . The present method is unconditionally stable and has second-order accuracy.

5. Exact solutions for particular cases

It is pertinent to mention that Eq. (22) has simple exact solution to special cases, namely (i) $n=0$ and $s=1$ [22] and (ii) $n=1$ and $s=3$ [24]. For case (i), with $Br=Ec=0$, Eq. (29) reduces to

$$\theta'' + Pr f \theta' = 0. \quad (64)$$

The exact solution to Eq. (64) in terms of the incomplete Gamma function, satisfying boundary conditions (30), is

$$\theta(\eta) = \frac{\Gamma(\frac{Pr}{\beta^2}, 0) - \Gamma(\frac{Pr}{\beta^2}, \frac{Pr}{\beta^2} e^{-\beta\eta})}{\Gamma(\frac{Pr}{\beta^2}, 0) - \Gamma(\frac{Pr}{\beta^2}, \frac{Pr}{\beta^2})}, \quad (65)$$

where $\beta = \frac{1}{\sqrt{A}}$ and $\Gamma(\cdot)$ is the incomplete Gamma function.

For case (ii), with $Br=Ec=0$, Eq. (29) reduces to

$$\theta'' + 3Pr f \theta' = 0. \quad (66)$$

Here the exact solution of Eq. (66) in terms of incomplete Gamma function, satisfying boundary conditions (30), is

$$\theta(\eta) = \frac{\Gamma(\frac{3Pr}{\alpha^2}, 0) - \Gamma(\frac{3Pr}{\alpha^2}, \frac{3Pr}{\alpha^2} e^{-\alpha\eta})}{\Gamma(\frac{3Pr}{\alpha^2}, 0) - \Gamma(\frac{3Pr}{\alpha^2}, \frac{3Pr}{\alpha^2})}, \quad (67)$$

where $\alpha = \frac{\sqrt{3}}{\sqrt{1+A}}$.

6. Validation of numerical results

The validation of present results is essential to check the credibility of the numerical solution methodology. The presently computed results are compared with the exact solutions obtained for some limiting cases of the problem. Figures 2 and 3 compare these results, and an excellent correspondence is seen to exist between the two sets of data. In addition, table 1 shows the comparison values of the local skin friction coefficient with those reported by of Khan and Shahzad [22]. It is seen that the comparison is in very good agreement, and thus gives us confidence to the accuracy of the numerical results.

7. Results and discussion

The main focus of the present chapter is to study the flow and heat transfer characteristics of a Sisko fluid over a nonlinear radially stretching sheet. To obtain physical insight of the flow and heat transfer, Eqs. (22) and (29) subject to boundary conditions (23) and (30) are solved numerically and the results are illustrated graphically. During the ensuing discussion, the assumption of incompressibility and isotropy of fluid is implicit. The influence of the flow behavior index n , the material parameter A , stretching parameter s , and Eckert number Ec on flow and heat transfer is the main interest of the study. Further, the effect of variation of Prandtl number Pr on heat transfer is also analyzed in depth. A comparison amongst the flow and heat transfer aspects of the Bingham, Newtonian, and Sisko fluids is also precisely depicted. Moreover, the flow and heat transfer characteristics are also discussed in terms of the local skin friction coefficient and local Nusselt number.

Figure 4 depicts the influence of the power-law index n on the velocity profile for pseudo-plastic ($n < 1$) and dilatant ($n > 1$) regimes for nonlinearly stretching sheet. The lower is the value of n , greater is the degree of shear thinning. Figure 4(a) shows that the velocity profile and momentum boundary layer thickness decrease with an increase in the value of the power-law index n , owing to increase in apparent viscosity. The shear thickening behavior ($n > 1$) is illustrated in figure 4(b). This figure reveals that as the value of the power-law index n is progressively incremented, the velocity profile and the corresponding momentum boundary layer thickness decrease due to gradual strengthening of viscous effects.

The heat transfer aspects of the Sisko fluid over a constant surface temperature stretching sheet for shear thinning ($n < 1$) and thickening ($n > 1$) fluids for different values of the power-law index n with nonlinear stretching is illustrated in figure 5. Figure 5(a) depicts that the temperature profile and thermal boundary layer reduce with incrementing the value of the power-law index n . The effect on the temperature profile is marginalized when the power-law index approaches unity. Figure 5(b) reveals that the power-law index n does not affect the temperature profile strongly for $n > 1$. However, a slight decrease in the thermal boundary layer thickness is observed.

The stretching parameter s affects the temperature distribution and thermal boundary layer due to the influence of momentum transfer. Its effect on heat transfer is illustrated in figures

6 (a-c). For the power-law index ($n < 1$), stretching parameter s does not affect the heat transfer in the Sisko fluid very strongly. The thermal boundary layer thickness increases when value of s is incremented progressively (figure 6(a)). Although, for $n = 1$, the effect of s on the temperature profile is significant and a contrary behavior is noticed as figure 6(b) elucidates. Figure 6(c) represents the temperature profiles for $n = 1.5$. The temperature profile seems to decrease as value of the stretching parameter is incremented. Moreover, it is also noticed that larger the value of the power-law index n the more is decrease in the temperature profile.

The effect of the material parameter A on the temperature profile for nonlinear stretching is presented through figures 7(a-c). These figures also make a comparison amongst the temperature profiles of the Newtonian fluid ($A = 0$ and $n = 1$) and the power-law fluid ($A = 0$ and $n \neq 1$) with those of the Sisko fluid ($A \neq 0$ and $n \neq 0$). Qualitatively, figures 7(a-c) reveal that the temperature profile and the corresponding thermal boundary layer thickness reduce in each case with increasing value of the material parameter A .

The Prandtl number Pr of a fluid plays a significant role in forced convective heat transfer. Figures 8(a,b) present its effect on heat transfer to Sisko fluid for pseudo-plastic ($n < 1$) and dilatant ($n > 1$) regimes. These figures depict that the Pr affects the heat transfer process strongly by thinning the thermal boundary layer thickness. It in turn augments the heat transfer at the wall. The augmentation can be ascribed to the enhanced momentum diffusivity for larger Prandtl number. The temperature profile is slightly lower for fluids with shear thickening behavior than that of the shear thinning, for the same Prandtl number.

Eckert number Ec measures the transformation of kinetic energy into heat by viscous dissipation. The variation of temperature with increasing Ec is given in figures 9(a,b). Figure 9(a) describes the effect of increasing Ec on highly shear thinning ($n = 0.2$) and moderately shear thinning ($n = 0.6$) Sisko fluids. These figures clearly elucidate that the temperature profile increases with increasing Ec . Further the strongly shear thinning fluids are dominantly affected by Ec as compared to that of the moderately shear thinning regime. Figure 9(b) describes the same phenomenon for shear thickening fluid ($n > 1$), but here the effects are less prominent.

Figures 10(a,b) compare the velocity and temperature profiles of the Bingham ($n = 0$ and $A \neq 0$) and Newtonian ($n = 1$ and $A = 0$) fluids with those of the Sisko fluid ($n \neq 0$ and $A \neq 0$). While sketching figure 10(a), the value of material parameter A is adjusted at 1.5. This figure clearly shows that for the particular value of variable η , the velocity profile of the Bingham fluid substantially higher than those of Newtonian and Sisko fluids. This figure also delineates that the velocity variation of the Bingham fluid approaches free stream velocity for larger values of η as compared to those the Newtonian and Sisko fluids. The temperature profiles of three different fluids are demonstrated in figure 10(b). The Bingham fluid shows larger thermal boundary layer thickness, whilst that of the Sisko fluid least, resulting better heat transfer. A wider variation in the concomitant heat transfer slopes at wall is observed in this figure, with least slope for the Bingham fluid, showing minimum heat transfer at the wall.

Adiabatic Eckert number Ec_a is a measure of direction of heat flux q_x ; the heat flows from heated sheet to fluid ($q_x > 0$), when $Ec < Ec_a$, and vice versa. Figures 11(a,b) shows a series of adiabatic Eckert numbers evaluated numerically for shear thinning ($n = 0.5$) and shear thick-

ening ($n=1.5$) Sisko fluids. It is clearly noticed from these figures that the adiabatic Eckert number increases at an accelerated pace for smaller values of Prandtl number. Further inspection of these figures reveal that the values of Ec_a decrease at a rapid rate for shear thinning fluid as compared to that of the shear thickening fluid.

Table 2 summarizes the overall trends of the skin friction coefficient for shear thinning and thickening fluids when the material parameter A , stretching parameter s and Eckert number Ec are varied. This table reveals that the value of the skin friction increases with each increment in the value of the material parameter A for linear as well as nonlinear stretching of the sheet, which results in increased drag to the Sisko fluid. The drag is slightly lower for the higher value of the power-law index. Further, this table also depicts the variation in the local Nusselt number with the increasing value of A for linear and nonlinear stretching. The Nusselt number shows improvement with each increment of A . It is also clear that the improvement is better for the power-law index $n > 1$. Moreover, a decrease in the local Nusselt number is observed with an increase in Ec . It is further noticed that the decrease in heat transfer from wall to fluid is about 24% for shear thinning and 13% for shear thickening fluids. Table 3 demonstrates the effects of the Prandtl number Pr on the local Nusselt number for different values of the power-law index n . An increase in the Prandtl number augments the Nusselt number at the sheet. Moreover, an increase in the Nusselt number is larger for fluids with medium power-law index n .

The stream function appearing in Eq. (20) is plotted in figure 12 for several values of ψ and different values of the power-law index n . The streamlines are symmetrical about the midway vertical axis, owing to the fact that sheet is being stretched radially by applying equal force in each direction. Moreover, the flow seems nearly straight down at large values of η (away from the sheet) and tends to horizontal at small values of η (vicinity of the stretching sheet). This figure further describes that the flow become identical for each value of the power-law index n close to the sheet.

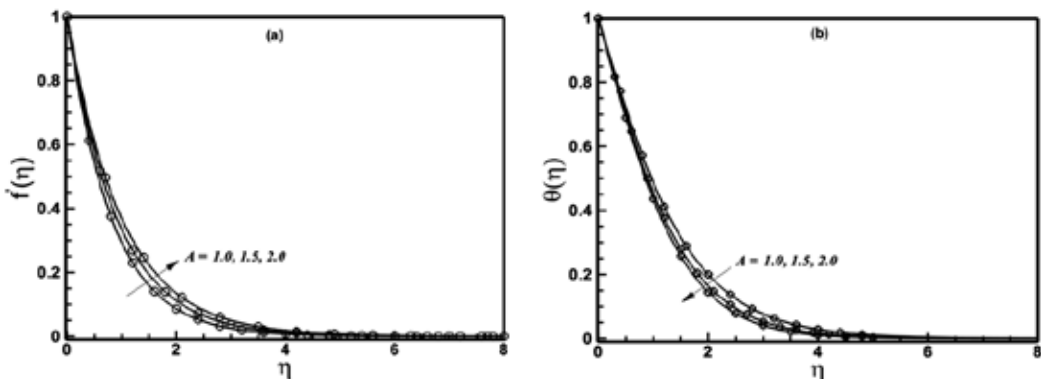


Figure 2. A comparison of the exact and numerical results (solid line exact results and open circles numerical results) when $n=0$ and $s=1$ are fixed.

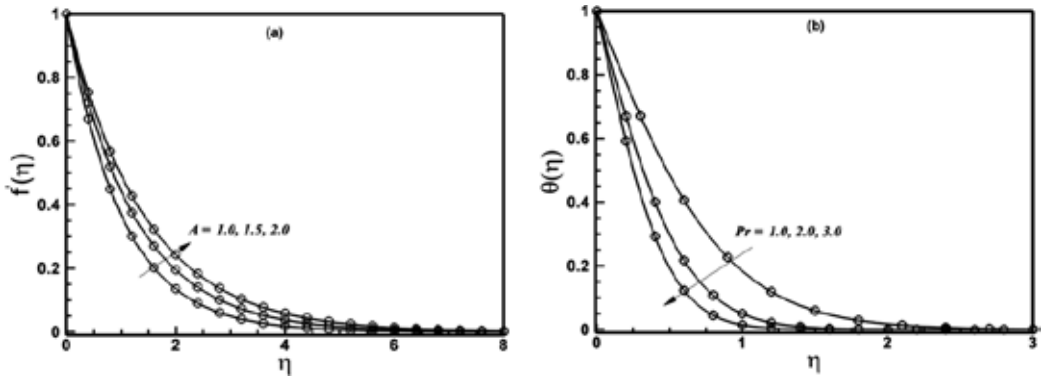


Figure 3. A comparison of the exact and numerical results (solid line exact results and open circles numerical results) when $n=1$ and $s=3$ are fixed.

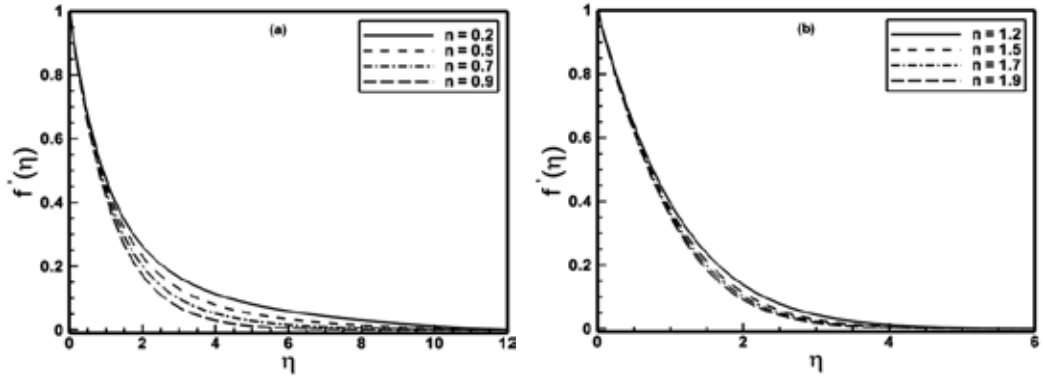


Figure 4. The velocity profile $f'(\eta)$ for different values of the power-law index n when $s=1.5$ and $A=1.5$ are fixed.

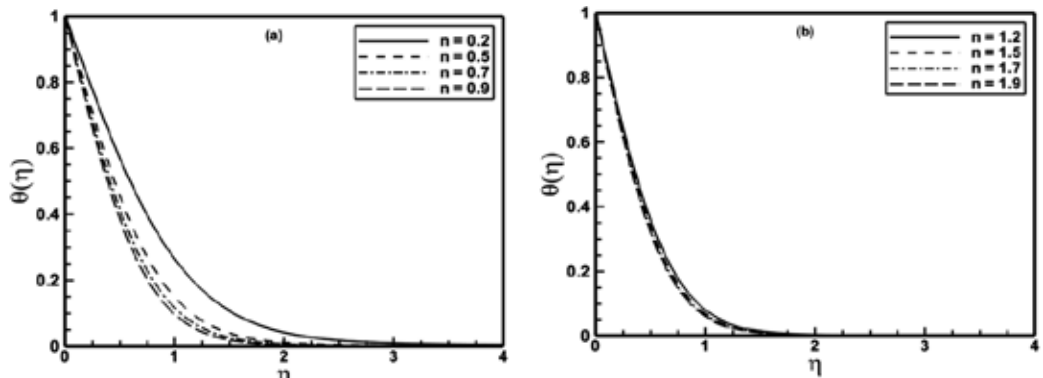


Figure 5. The temperature profile $\theta(\eta)$ for different values of the power-law index n when $s=1.5$, $A=1.5$, $Pr=2.0$, $Ec=0.1$ and $Br=0.1$ are fixed.

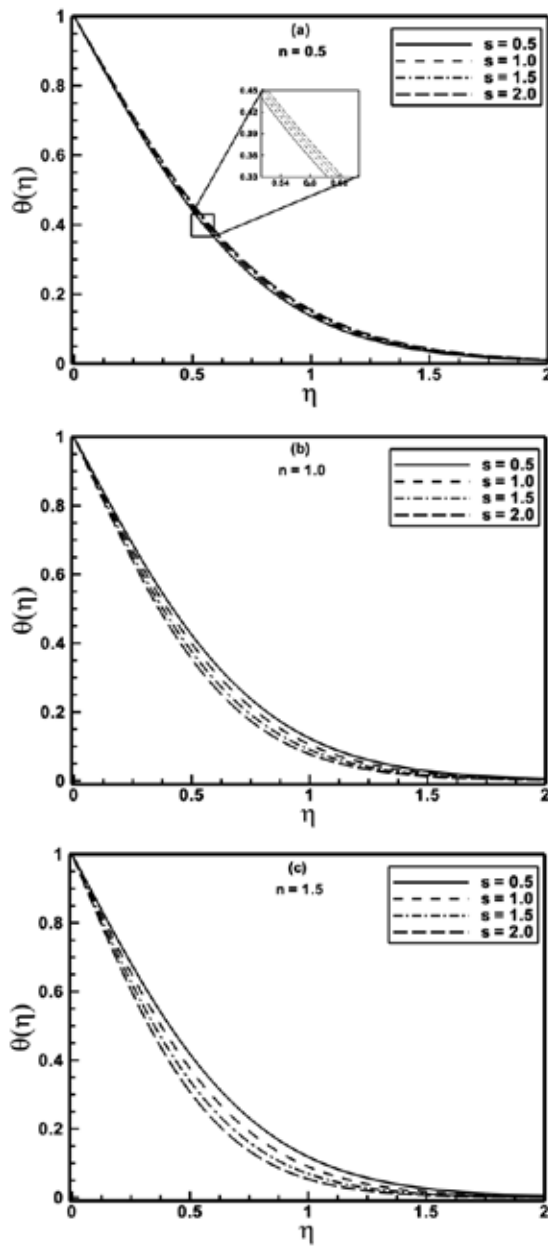


Figure 6. The temperature profile $\theta(\eta)$ for different values of the stretching parameter s when $A=1.5$, $Pr=2.0$, $Ec=0.1$ and $Br=0.1$ are fixed.

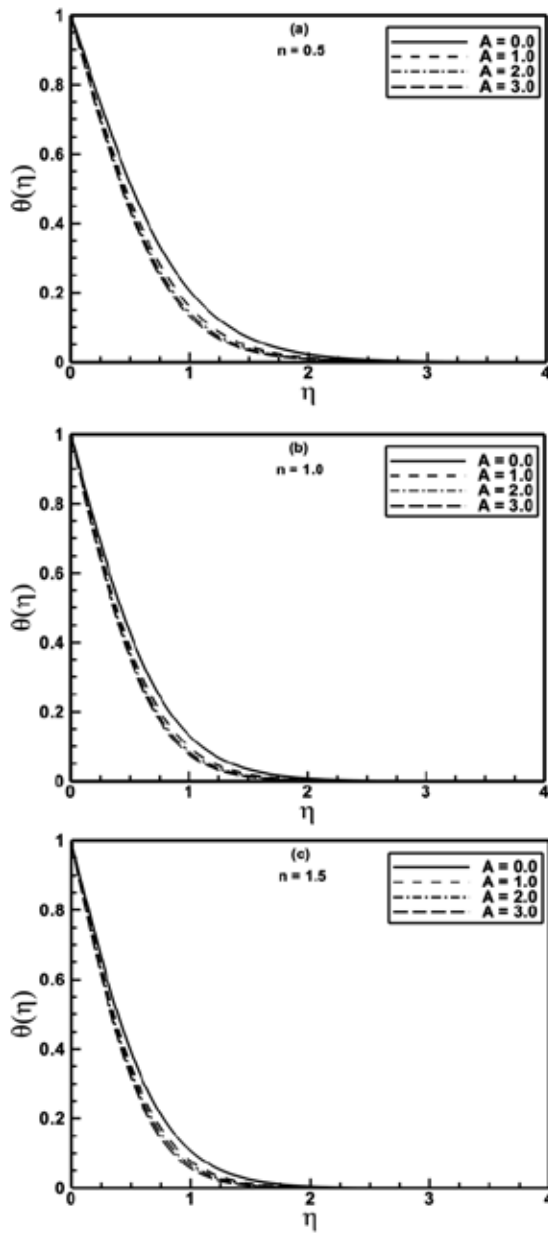


Figure 7. The temperature profile $\theta(\eta)$ for different values of the material parameter A when $s = 1.5$, $Pr = 2.0$, $Ec = 0.1$ and $Br = 0.1$ are fixed.

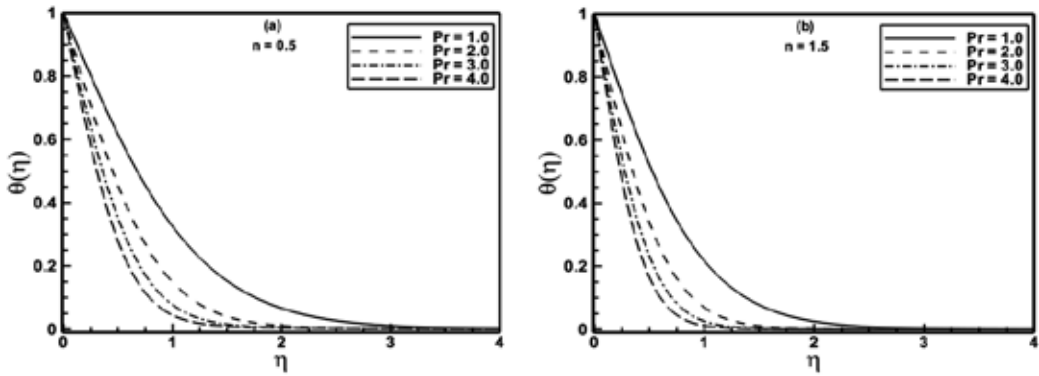


Figure 8. Temperature profile $\theta(\eta)$ for different values of the Prandtl number Pr when $s = A = 1.5$, and $Ec = Br = 0.1$ are fixed.

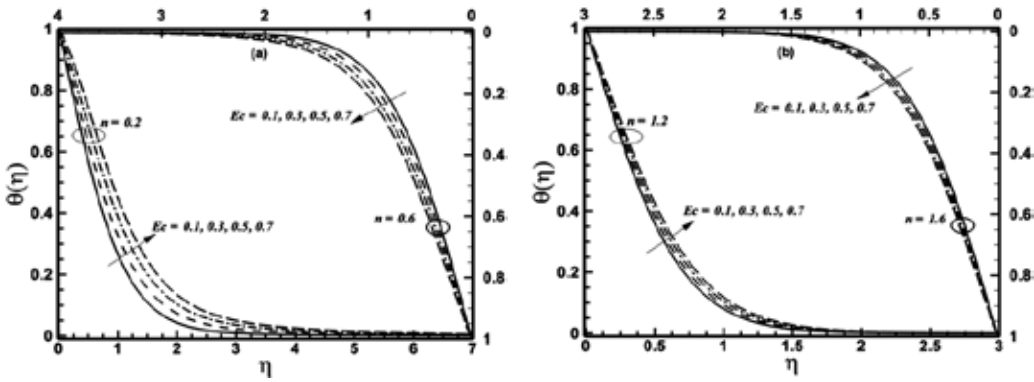


Figure 9. Temperature profiles $\theta(\eta)$ for different values of the Eckert number Ec when $s = 1.5$, $A = 1.5$, $Br = 0.1$, and $Pr = 2.0$ are fixed.

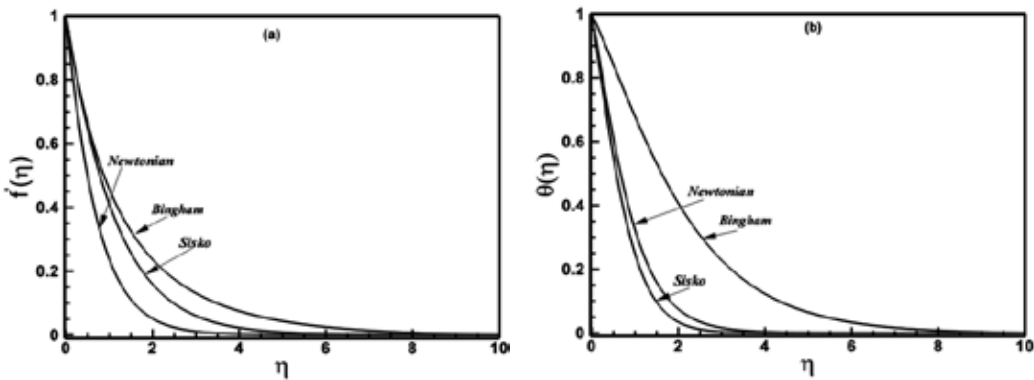


Figure 10. A comparison among the velocity and temperature profiles for different fluids when $s = 1.5$, $Ec = 0.1$, $Br = 0.1$, and $Pr = 2.0$ are fixed.

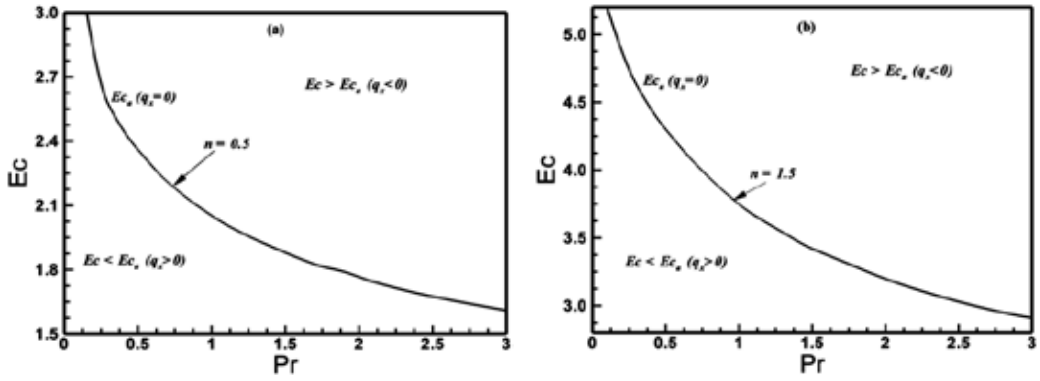


Figure 11. Adiabatic Eckert number E_{c_a} with variation of Prandtl number Pr when $s=1.5$, $Br=0.1$, and $A=1.0$ are fixed.

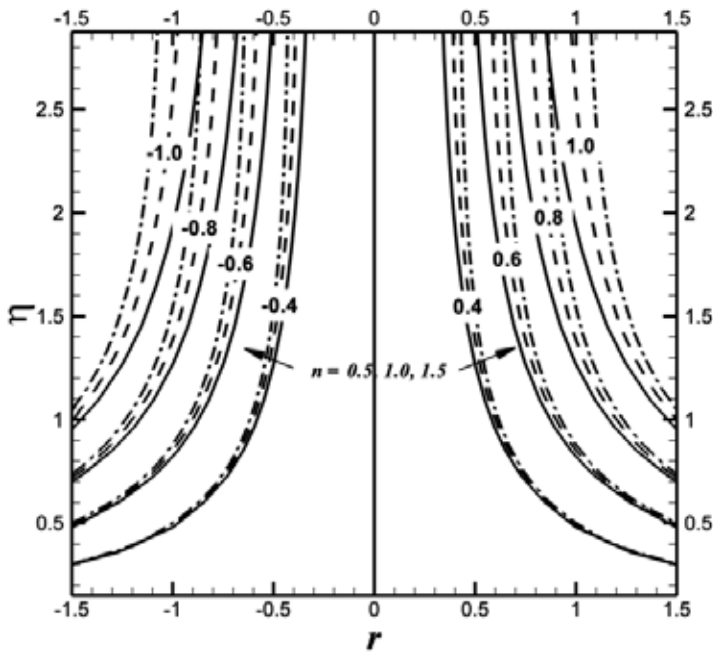


Figure 12. The streamlines for different values of the power-law index n when $s=1.5$ and $A=1.5$ are fixed.

		$\frac{1}{2}Re_b^{-\frac{1}{n+1}}C_f$			
		$n=1$		$n=2$	
A	s	Numerical results	HAM results	Numerical results	HAM results
0	1	-1.173721	-1.173721	-1.189598	-1.189567
1	1	-1.659892	-1.659891	-1.605002	-1.605010
2	1	-2.032953	-2.032945	-1.973087	-1.973092
3	1	-2.347441	-2.347451	-2.297733	-2.297713
1	2	-2.090755	-2.090753	-2.152145	-2.152153
1	3	-2.449490	-2.449491	-2.621176	-2.621182

Table 1. A tabulation of the local skin friction coefficient in terms of the comparison between the present results and the HAM results (ref. [22])

			$n=0.5$		$n=1.5$	
A	s	Ec	$\frac{1}{2}Re_b^{-\frac{1}{n+1}}C_f$	$Re_b^{-\frac{1}{n+1}}Nu_r$	$\frac{1}{2}Re_b^{-\frac{1}{n+1}}C_f$	$Re_b^{-\frac{1}{n+1}}Nu_r$
1.0	1.0	0.1	-1.1738050	-1.177395	-1.62676	-1.39104
2.0	1.0	0.1	-2.116299	-1.233161	-2.00146	-1.45209
3.0	1.0	0.1	-2.427310	-1.264815	-2.33186	-1.48665
1.0	2.0	0.1	-2.075148	-1.125830	-2.12359	-1.60519
2.0	2.0	0.1	-2.544792	-1.191590	-2.58828	-1.67792
3.0	2.0	0.1	-2.928524	-1.228861	-2.99557	-1.72052
1.5	1.5	0.1	-2.140943	-1.186123	-2.107053	-1.54061
1.5	1.5	0.3	-2.140943	-1.043431	-2.107053	-1.44104
1.5	1.5	0.5	-2.140943	-0.900738	-2.107053	-1.34148

Table 2. A tabulation of the local skin friction and the local Nusselt number.

		$Re_b^{-\frac{1}{n+1}}Nu_r$	
		$n=0.5$	$n=1.5$
	Pr		
	1	-0.789183	-1.019614
	2	-1.186123	-1.540612
	3	-1.487571	-1.935358
	4	-1.739727	-2.265692
	5	-1.960520	-2.555230

Table 3. A tabulation of the local Nusselt number for different values of Prandtl number when $s=1.5$ and $A=1.5$ are fixed.

8. Concluding remarks

In this chapter, a theoretical framework for analyzing the boundary layer flow and heat transfer with viscous dissipation to Sisko fluid over a nonlinear radially stretching sheet has been formulated. The governing partial differential equations were transformed into a system of nonlinear ordinary differential equations. The transformed ordinary differential equations were then solved numerically using implicit finite difference scheme along with Keller-box scheme. The results were presented graphically and the effects of the power-law index n , the material parameter A , the stretching parameter s , the Prandtl number Pr , and the Eckert number were discussed. It is pertinent to mention that the analysis in ref. [22] for velocity field was restricted to integer value of the power-law index n . However, the investigations in the present work were upgraded by adding the non-integral values of the power-law index n for the flow and temperature fields.

Our computations have indicated that the momentum and thermal boundary layers thickness were decreased by increasing the power-law index and the material parameter. Further it was noticed that the effects of the Prandtl and Eckert numbers on the temperature and thermal boundary layer were quite opposite. However, both the Prandtl and Eckert numbers were affected dominantly for shear thinning fluid as compared to that of the shear thickening fluid. Additionally, the Bingham fluid had the thickest momentum and thermal boundary layers as compared to those of the Sisko and Newtonian fluids.

Acknowledgements

This work has been supported by the Higher Education Commission (HEC) of Pakistan.

Author details

Masood Khan^{1*}, Asif Munir¹ and Azeem Shahzad²

*Address all correspondence to: mkhan@qau.edu.pk; mkhan_21@yahoo.com

¹ Department of Mathematics, Quaid-i-Azam University, Islamabad, Pakistan

² Department of Basic Sciences, University of Engineering and Technology, Taxila, Pakistan

References

- [1] Sisko, A.W., The flow of lubricating greases, *Industrial & Engineering Chemistry Research*, 50 (1958) 1789-1792.

- [2] Sisko, A.W., Capillary viscometer for non-Newtonian liquids, *J. Colloid Sci.*, 15 (1960) 89-96.
- [3] Turian, R.M., Ma, T.W., Hsu, F.L.G., and Sung, M.D., Flow of concentrated non-Newtonian slurries: 1, friction losses in laminar, turbulent and transition flow through straight pipe, *Int. J. Multiphase Flow*, 24 (1998) 225-242.
- [4] Siddiqui, A.M., Ahmad, M., and Ghori, Q.K., Thin film flow of non-Newtonian fluids on a moving belt, *Chaos, Solitons & Fractals*, 33 (2007) 1006-1016.
- [5] Siddiqui, A.M., Ansari, A.R., Ahamad, A., and Ahmad, N., On Taylor's scraping problem and flow of a Sisko fluid, *Math. Model. Anal.*, 14 (2009) 515-529.
- [6] Abelman, S., Hayat, T., and Momoniat, E., On the Rayleigh problem for a Sisko fluid in a rotating frame, *Appl. Math. Comput.*, 215 (2009) 2515-2520.
- [7] Momboundon, H.M., Khan, M., Hayat, T., and Mahomed, F.M., Reduction and solutions for magnetohydrodynamic flow of a Sisko fluid in a porous medium, *J. Porous Med.*, 12 (2009) 695-714.
- [8] Khan, M., Abbas Q., and Duru, K., Magnetohydrodynamic flow of a Sisko fluid in annular pipe: A numerical study, *Int. J. Numer. Methods Fluids*, 62 (2010) 1169-1180.
- [9] Khan, M. and Shahzad, A., Falkner-Skan boundary layer flow of a Sisko fluid, *Zeitschrift für Naturforschung A (ZNA)*, 67a (2012) 469-478.
- [10] Khan, M., Shahzad, A., Anjum, A., and Mahomed, F.M., Analytic approximate solutions for time dependent flow and heat transfer of a Sisko fluid, *Int. J. Numer. Method Heat Fluid Flow*, 24 (5) (2014) 1005-1019.
- [11] Crane, L.J., Flow past a stretching sheet, *Z. Angew. Math. Phys.*, 21 (1970) 645-647.
- [12] Dutta, B.K., Roy, P., and Gupta, A.S., Temperature field in flow over a stretching sheet with uniform heat flux, *Int. Commun. Heat Mass Transf.*, 28 (1985) 1234-1237.
- [13] Chen, C.K. and Char, M., Heat transfer on a continuous stretching surface with suction or blowing, *J. Math. Anal. Appl.*, 35 (1988) 568-580.
- [14] Grubka, L.J. and Bobba, K.M., Heat transfer characteristics of a continuous stretching surface with variable temperature, *ASME J. Heat Transf.*, 107 (1985) 248-250.
- [15] Cortell, R., Viscous flow and heat transfer over a nonlinearly stretching sheet, *Appl. Math. Comput.*, 184 (2007) 864-873.
- [16] Schowalter, W. R., The application of boundary layer theory to power-law pseudo-plastic fluids: similar solutions, *AIChE J.*, 6 (1960) 24-28.
- [17] Howel, T.G., Jeng, D.R., and Dewitt, K.J., Momentum and heat transfer on a continuous moving surface in a power-law fluid, *Int. J. Heat Mass Transf.*, 40 (1997) 1853-1861.

- [18] Hassanien, I.A., Abdullah, A.A., and Gorla, R.S.R., Flow and heat transfer in a power-law fluid over a non-isothermal stretching sheet, *Math. Comput. Model.*, 28 (1998) 105-116.
- [19] Abel, M.S., Datti, P.S., and Ahesha, N., Flow and heat transfer in a power-law fluid over a stretching sheet with variable thermal conductivity and non-uniform heat source, *Int. J. Heat Mass Transf.*, 52 (2009) 2902-2913.
- [20] Prasad, K.V. and Vajravelu, K., Heat transfer in the MHD flow of a power-law fluid over a non-isothermal stretching sheet, *Int. J. Heat Mass Transf.*, 52 (2009) 4956-4965.
- [21] Khan, M. and Shahzad, A., On boundary layer flow of Sisko fluid over stretching sheet, *Quaestiones Mathematicae*, 36 (2013) 137-151.
- [22] Khan, M. and Shahzad, A., On axisymmetric flow of Sisko fluid over a radially stretching sheet, *Int. J. Non-linear Mech.*, 47 (2012) 999-1007.
- [23] Na, T.Y., Computational Methods in Engineering Boundary Value Problems, *Academic Press, Inc. (London)* 1979.
- [24] Shahzad, A., Ali, R., and Khan M., On the exact solution for axisymmetric flow and heat transfer over a nonlinear radially stretching sheet, *Chin. Phys. Lett.*, 29 (2012) 084705.

Heat Transfer Applications

Resistive Electrothermal Sensors, Mechanism of Operation and Modelling

Heyd Rodolphe

Additional information is available at the end of the chapter

<http://dx.doi.org/10.5772/60888>

1. Introduction

The purpose of this chapter is to present the rich topic of resistive electrothermal sensors, from modelling to applications. Because of their manufacturing simplicity and ease of use, miniature resistive sensors are commonly used in many application fields, when the temperature or heat flux need to be measured. In flow metrology, the hot wires are commonly used to measure fast-changing flows for a wide range of velocities [2]. In biomedical instrumentation [3], due to their small size and the absence of moving parts, the resistive sensors can be used in vivo to accurately track real-time changes of blood flow and temperature.

In the present chapter we will focus on the study, the modelling and the applications of the most used resistive sensors, such as the resistance temperature detectors (RTD) made of a pure metal wire or a metallic thin film.

If on the one hand the electrical resistance of the sensor contains all the necessary information about its operating temperature, on the other hand it is essential that the sensor be traversed by an electric current in order to measure its resistance and then deduce its temperature. This electric current generates heat inside the sensor by the Joule effect and thus an unavoidable rise of its operating temperature. For the same values of the electrical parameters, this self-heating is more important as the sensor is small, and therefore this phenomenon is a major source of errors in the thermal measurements when using miniature resistive sensors. To quantify this deviation, sensors manufacturers usually measure a steady-state self-heating index (SHI) [4], that is only valid for one given operating temperature and one given surrounding environment, such as air or water for example.

Thus a realistic modelling of these sensors, based for example on electrothermal analogies [10] or on the use of thermal Laplace transfer functions [11], will allow to open new strategies

for a wider and a better use of these sensors in the fields of temperature or heat flux measurements, but also for the thermal characterization of materials. We will expose in this chapter a systemic approach, that includes simultaneously and in a single mathematical environment: a realistic modelling of the sensors and of their interactions with the system under study, both of them being described by partial differential equations (PDEs); the modeling of power, control and signal processing systems, described by electrical circuits and thus ordinary differential equations (ODEs).

2. Metallic resistive sensors

2.1. Presentation

The metallic resistive sensors, often called resistance temperature detectors (RTDs), are widely used, as well in the industry (automotive, medical, food) as in the academic laboratories, either in the form of a pure thin metal wire or as a thin film. The possible configurations are numerous (single wire, wire wound, duplex configuration, encapsulated flat film) but in all the cases, the underlying mechanisms of operation are based on the heat transfer between the metallic sensor and the surrounding media to be sensed.

We present here two base configurations: the single wire (Fig. 1a) and the thin encapsulated flat film (Fig. 1b). The former is frequently used to characterize fluid flows, as in the case of the hot wire anemometer [1, 2], but also to measure the thermal properties of solids [5, 6] and liquids [7]. The latter is widely used to measure the temperature.

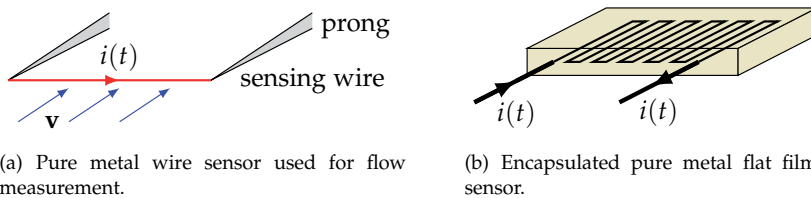


Figure 1. Two base configurations of metallic resistive sensors commonly used in the industry and laboratories. The characteristic lengths are of the order of millimeters, the widths and the diameters in the micrometer range or less.

2.2. Modelling

2.2.1. General hypothesis – Mathematical model

The operation of the metallic resistive sensors is generally limited to a relatively narrow temperature range near a given operating point, such that the physical characteristics of the constitutive materials of the sensor can usually be assumed to be constant during operation. As an example, these sensors are commonly used to measure variations of temperature with an extent of less than 100 K, in the vicinity of the room temperature. Under these conditions, the radiative heat transfer between the sensor and its environment can also be neglected or eventually linearized. Thus a linear model is very adequate to describe the most usual modes of operation of these kinds of electrothermal sensor. Without loss of generality of the study, it is furthermore assumed here that the physical quantities describing the system only depend of time and solely of one space variable, denoted x . In the most general case, the

system has to be considered as composite, as in the case of the figure 1b, thus we denote by $T_j(x, t)$ the temperature inside the j th layer and by $\delta T_j(x, t)$ its variations compared to the room temperature T_a . For each of the layers constituting the sensor, it is possible to write a local energy balance equation in the general form:

$$\mu_j c_j \partial_t [\delta T_j(x, t)] d\tau = k_j L_{x,j}(t) [\delta T_j(x, t)] d\tau + \dot{w}_j(x, t) d\tau \quad (1)$$

where μ_j , c_j and k_j are respectively the density, the specific heat and the thermal conductivity of the j th layer and $d\tau$ is an infinitesimal volume element of this layer. We denote by $L_{x,j}(t)$ a differential operator linear in x , time-dependent, acting on $\delta T_j(x, t)$, and whose expression will be given later, according to the geometry of the considered sensor. The volume density of internal heat, $\dot{w}_j(x, t)$, appearing in the equation (1), is due to the Joule effect and is different from zero only inside the conductive elements of the sensor where an electric current is flowing. The boundary conditions accompanying the equation (1) depend of the mode of operation of the metallic sensor, and will be specified later.

At this stage, no hypothesis has been made about the electrical resistance of the sensor. We consider here two situations:

- In the case where the electric current is flowing in the same direction as the temperature gradient (figure 1a), it is mandatory to take into account the dependence of the electrical resistance with the x position. If dx denotes the length of an infinitesimal portion of the j th conductive material, its infinitesimal electrical resistance $dR_j(x, t)$ can be written as:

$$dR_j(x, t) = r_j(x, t) dx \quad (2)$$

where $r_j(x, t)$ is the lineic resistance. The average resistance \bar{R}_j is then defined as $\bar{R}_j = \int_0^{\ell_j} r_j(x, t) dx$, with ℓ_j the active length of the j th conductive material. In this case, the internal heat source takes the following form: $\dot{w}_j(x, t) d\tau = i_j(t)^2 r_j(x, t) dx$.

- In the case where the electric current is flowing in a direction perpendicular to that of the temperature gradient (figure 1b), we suppose that the resistance of the j th conductive layer is uniform and given by $R_j(t) = \ell_j r_j(t)$. In this case, the internal heat source takes the following form: $\dot{w}_j(x, t) d\tau = i_j(t)^2 R_j(t) dx / \ell_j = i_j(t)^2 r_j(t) dx$.

In the vicinity of the ambient temperature, the lineic resistance of the metals commonly used in the formation of RTDs (such as Platinum, Nickel, Tungsten and even Silver), varies linearly with the temperature to a good approximation, making it possible to write this lineic resistance r_j as:

$$\begin{aligned} r_j(x, t) &= r_{j,\text{ref}} \left[1 + \alpha_j (T_j(x, t) - T_{\text{ref}}) \right] \\ &= r_{j,a} + \alpha_j r_{j,\text{ref}} \delta T_j(x, t) \end{aligned} \quad (3)$$

where α_j is the temperature coefficient of the metal considered, T_{ref} is a reference temperature (usually $T_{\text{ref}} = 273.15$ K), $r_{j,a}$ and $r_{j,\text{ref}}$ are the values of the lineic resistance, respectively at the temperatures $T = T_a$ and $T = T_{\text{ref}}$. Using the relation (3) and writing $d\tau = A_x dx$, it is now possible to rewrite the source term $\dot{w}_j(x, t) d\tau$ as:

$$\begin{aligned}\dot{w}_j(x, t) d\tau &= r_{j,a} i_j(t)^2 dx + \alpha_j r_{j,\text{ref}} i_j(t)^2 \delta T_j(x, t) dx \\ &= \dot{w}_{j,a}(t) d\tau + \alpha_j r_{j,\text{ref}} i_j(t)^2 \delta T_j(x, t) d\tau / A_x\end{aligned}\quad (4)$$

The local energy balance can now be proposed in a form to be solved:

$$\mu_j c_j \partial_t [\delta T_j(x, t)] = \left(k_j L_{x,j}(t) + \frac{\alpha_j r_{j,\text{ref}}}{A_x} i_j(t)^2 \right) [\delta T_j(x, t)] + \dot{w}_{j,a}(t) \quad (5)$$

The real-time mode of operation of the resistive sensor is obtained by solving the equations (5) for each layer. Depending on the time evolutions of both the electrical current $i_j(t)$ and of the boundary conditions, an analytical resolution of the equations (5) is unfortunately rarely possible. We will now discuss two possible ways to obtain a general solution of the differential equation describing the real-time evolution of the temperature inside the sensor: the method of Laplace transfer functions and an electrothermal analogy. Each of these methods presents some particular interests that will be exposed.

2.2.2. Transfer function approach – Inverse analysis

The resolution of the equations (5), by the approach in term of transfer functions, requires first of all be able to apply the Laplace transform to these equations. This is clearly impossible, firstly because of the time dependence of the $L_{x,j}(t)$ operator and secondly because of the term $i(t)^2$. However, in most cases considered in this study, we can decompose $L_{x,j}(t)$ in a stationary operator $L_{x,j}$ and a time-dependant part $a_{0,j}(t)$, independent of x :

$$L_{x,j}(t) = L_{x,j} + a_{0,j}(t) \quad (6)$$

It is thus possible to rewrite the equation (5) in the following form:

$$\mu_j c_j \partial_t [\delta T_j(x, t)] = k_j L_{x,j} [\delta T_j(x, t)] + a_j(t) \delta T_j(x, t) + \dot{w}_{j,a}(t) \quad (7)$$

where $a_j(t) = k_j a_{0,j}(t) + \alpha_j r_{j,\text{ref}} i_j(t)^2 / A_x$. Using the following change in function $\delta T_j(x, t) = f_j(t) u_j(x, t)$, and provided that $f_j(t) \neq 0 \forall t$, it is possible to transform the equation (7) in:

$$\mu_j c_j \partial_t [u_j(x, t)] = k_j L_{x,j} [u_j(x, t)] + \left[a_j(t) - \mu_j c_j \frac{f'_j(t)}{f_j(t)} \right] u_j(x, t) + \frac{\dot{w}_{j,a}(t)}{f_j(t)} \quad (8)$$

It is now possible to cancel the term $u_j(x, t)$ and thus obtain a differential equation with constant coefficients, provided to choose the function $f_j(t)$ such that $\mu_j c_j f_j'(t) / f_j(t) = a_j(t)$. It is also possible to write this condition as follows:

$$f_j(t) = f_j(0) \exp \int_0^t \frac{a_j(\tau)}{\mu_j c_j} d\tau \tag{9}$$

By choosing $f(0) = 1$, the differential equation (8) can finally be written in the form:

$$\mu_j c_j \partial_t [u_j(x, t)] = k_j L_{x,j} [u_j(x, t)] + \dot{w}_{j,a}(t) \exp \left[- \int_0^t \frac{a_j(\tau)}{\mu_j c_j} d\tau \right] \tag{10}$$

The differential equation (10) satisfied by $u_j(x, t)$ has constant coefficients, thus it is now possible to apply the Laplace transform. By noting $s_j(t) = \dot{w}_{j,a}(t) \exp \left[- \int_0^t \frac{a_j(\tau)}{\mu_j c_j} d\tau \right]$, $S_j(p) = \text{TL}[s_j(t)]$ and $U_j(x, p) = \text{TL}[u_j(x, t)]$, where TL is the Laplace transform and p is the Laplace variable, we obtain an ordinary differential equation (ODE) of the form:

$$\mu_j c_j (p U_j(x, p) - u_j(x, 0)) = k_j L_{x,j} [U_j(x, p)] + S_j(p) \tag{11}$$

Examples of resolution of (11) will be given in the next sections with different expressions of the linear operator $L_{x,j}$ and $S_j(p)$.

The main advantage of the present approach is to allow to write the response $\delta T_j(x, t)$ of the j th layer in term of a Laplace function transfer $H_j(x, p)$, deduced from the resolution of the ODE (11). This opens the route to the inverse analysis of thermal signals [8–10] and to new sensors exploitation [2], as it will be shown later in this study. Unfortunately this approach is limited to the description of the linear mode of operation of the RTDs.

2.2.3. Electrothermal analogy – SPICE modelling

The previous approach is limited to the case of linear differential operators $L_{x,j}$ and constant physical properties. If we need to investigate larger temperature variations than previously assumed, the hypotheses of constant physical properties and linear operator are no more valid and we need another approach to be able to describe extreme operating modes of the RTDs. We present now a modelling of the resistive sensor based on an electrothermal analogy deduced from the Godunov's scheme. Let's consider an infinitesimal volume of the j th layer, as represented in figure 2a. This infinitesimal system, which is assumed opaque and undeformable, is on the one hand subjected to various elementary heat flows: axial heat conduction $\dot{q}_{c,j}$, a lateral heat transfer $\dot{q}_{lat,j}$ which may for example include a conducto-convective transfer $\dot{q}_{cc,j}$ or a radiative transfer $\dot{q}_{r,j}$. On the other hand this infinitesimal system may be subjected to an internal heat source \dot{w}_j due to the Joule effect. Using the first law of thermodynamics, the energy balance of this infinitesimal system can be written as:

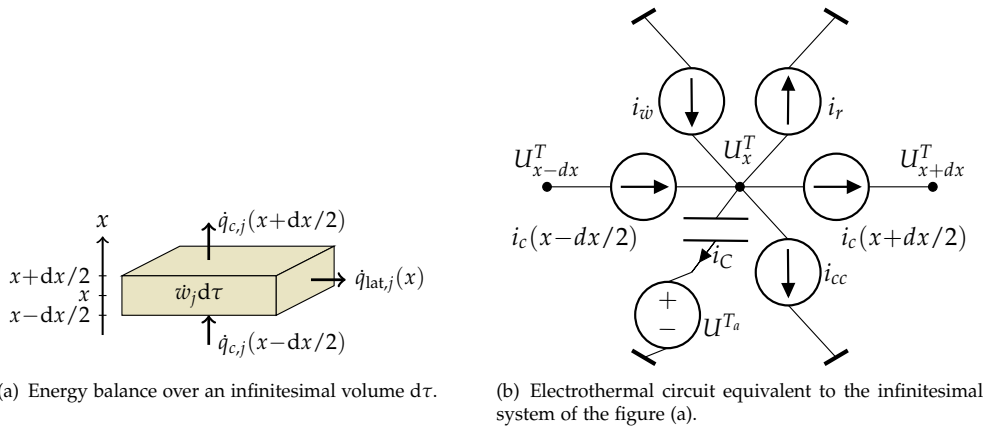


Figure 2. Balance of energy transfers inside an infinitesimal volume element $d\tau$ of the j th layer and electrothermal analogy.

$$\mu_j c_j \partial_t T_j(x, t) d\tau = \dot{w}_j(x, t) d\tau + \dot{q}_{c,j}(x - dx/2, t) + \dot{q}_{c,j}(x + dx/2, t) + \dot{q}_{lat,j}(x, t) \quad (12)$$

where the elementary heat fluxes are given by:

- $\dot{q}_{c,j}(x - dx/2) = -A_x(k_j \partial_x T_j)_{x-dx/2} = A_x j_{c,j}(x - dx/2)$ and $\dot{q}_{c,j}(x + dx/2) = A_x(k_j \partial_x T_j)_{x+dx/2} = -A_x j_{c,j}(x + dx/2)$. The partial derivative $(\partial_x T_j)_{x-dx/2}$ is approximated by $[T_j(x, t) - T_j(x - dx, t)]/dx$ and $(\partial_x T_j)_{x+dx/2}$ by $[T_j(x + dx, t) - T_j(x, t)]/dx$.
- The elementary lateral heat flux may take several forms, depending on the lateral boundary conditions. It may include for example:
 - a radiative term $\dot{q}_{r,j}(x) = -\sigma \epsilon_j [T_j^4(x, t) - T_a^4] A_{lat} = -j_{r,j}(x) A_{lat}$, where σ is the Stefan-Boltzmann constant, ϵ_j the emissivity of the material and A_{lat} the lateral area of exchange.
 - a conducto-convective term $\dot{q}_{cc,j}(x) = -h_j [T_j(x, t) - T_a] A_{lat} = -j_{cc,j}(x) A_{lat}$, where h_j is the Newton coefficient of exchange.

We now introduce the following unsteady electrothermal analogy, which consists in the associations shown in Table 1.

thermal quantity	temperature or temperature variations (K)	thermal capacity (J.K ⁻¹)	elementary heat flux (W)	internal heat source (W)
	T or δT	$\mu c d\tau$	jA	$\dot{w} d\tau$
electrical analogy	V^T or U^T	C	i	i_w
	potentiel or tension (V)	capacity (C.V ⁻¹ or F)	intensity (A)	intensity (A)

Table 1. Unsteady electrothermal analogy used to model RTDs.

By introducing the surface heat fluxes j , it is possible to rewrite the equation (12) as:

$$\begin{aligned} \mu_j c_j \partial_t T_j(x, t) d\tau = \dot{w}_j(x, t) d\tau + j_{c,j}(x - dx/2, t) A_x - j_{c,j}(x + dx/2, t) A_x \\ - j_{r,j}(x, t) A_{lat} - j_{cc,j}(x, t) A_{lat} \end{aligned} \quad (13)$$

Using the electrothermal analogy of the table 1, we can now rewrite an electrical version of the equation (13):

$$-C_j \partial_t U_j^T(x, t) + i_{w_j}(x, t) + i_{c,j}(x - dx/2, t) - i_{c,j}(x + dx/2, t) - i_{cc,j}(x, t) - i_{r,j}(x, t) = 0 \quad (14)$$

Recalling that the current charge of a capacitor is written as $i_C(t) = C \partial_t U$, we can see that the balance equation (14) is equivalent to the Kirchhoff's current law, applied to the node x of the portion of the electrothermal circuit represented in figure 2b:

$$-i_{C_j}(x, t) + i_{w_j}(x, t) + i_{c,j}(x - dx/2, t) - i_{c,j}(x + dx/2, t) - i_{cc,j}(x, t) - i_{r,j}(x, t) = 0 \quad (15)$$

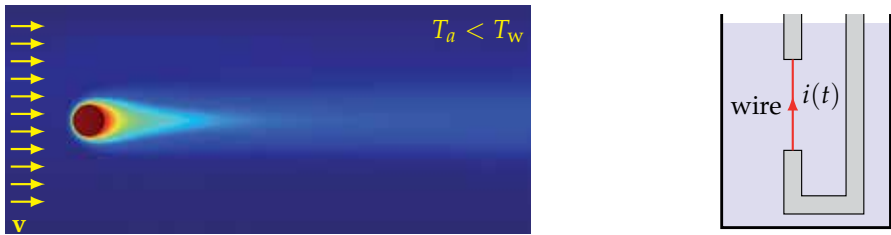
The controlled current sources, used in the electrothermal circuit of the figure 2b, are easily implemented in SPICE, allowing for a very complete systemic approach of the operation of the RTDs sensors, even in the case of extreme nonlinear conditions. Using this approach, it is possible to simulate the complete operation of the resistive sensor, from the heat transfer between the sensor and its environment to the instrumentation circuits. Unfortunately this analogy doesn't allow the same inverse analysis possibilities than those offered by the transfer function approach.

2.3. Resistive wire sensor

2.3.1. Presentation – Mathematical model

The hot-wire sensor is commonly used in anemometry and in flows characterization (HWA, see Fig. 3) as well as for the thermal characterization of fluids (THW, see Fig. 3b). This sensor is usually made of a metallic resistive wire with a diameter d of the order of a few microns and a length $\ell \gg d$, of the order of a few millimeters (Fig. 1a). This wire is heated by the Joule effect, due to the flow of an electric current of intensity $i(t)$ across the wire. The operating principle of this sensor is based on the balance between the energy supplied to the wire by the Joule heating and the energy lost by conduction, convection and radiation. The instantaneous average temperature $\bar{T}_w(t)$, that is reached by the heated wire, is an image of the flow velocity and thermal characteristics of the fluid, that are to be measured. In general, the wire temperature is determined via the measurement of its instantaneous electrical resistance $\bar{R}_w(t)$.

It is mainly the radial boundaries conditions, at $r = d/2$, that distinguish the two modes of operation of the single resistive wire sensor. In the domain of anemometry, the conducto-convective boundary conditions are considered, while in the domain of thermal characterization it is rather the conductive boundary conditions that are taken into account. In this last case the convection is considered as an obstacle to the measure, and should be minimized.



(a) HWA mode. Visualization of the temperature T_w of the hot wire and T_f of the fluid (atmospheric air is considered here), in a transverse plane $x = \text{cste}$. The temperature is calculated by the finite element technique using the code OpenFoam. v is the velocity of the fluid far away from the stationary wire.

(b) THW mode. Hot wire immersed in a fluid, for an utilization in thermal characterization mode.

Figure 3. Different modes of operation of a single metallic wire: (a) Hot Wire Anemometry (HWA) and (b) Transient Hot Wire method. The temperature of the fluid, far away from the wire, is denoted by T_a .

As the sensor is only made by one material, here $j = 1$ and T_w will denote the wire temperature. In the most general case, the temperature of the wire can be written in the form $T_w = T_w(r, \theta, x, t)$. However, we can examine the dependence of T_w with the different space variables. According to the resolution by finite element shown in Fig. 3 and due to the very small diameter of the wire, we can see that the temperature of the wire presents the axial symmetry and is independent of r . In conclusion we can suppose to a very good approximation that the temperature of the wire only depends on the axial variable x and the time t : $T_w = T_w(x, t)$. The characteristic diameter of the holders being substantially greater than the one of the sensitive wire, their electrical resistances are perfectly negligible compared to the electric resistance $R_w(t)$ of the wire, therefore only the latter is subjected to a significant temperature rise by the Joule effect. The supports must then be considered as cold heat sinks with a constant temperature, equal to that of the ambient temperature (or measurement temperature) T_a .

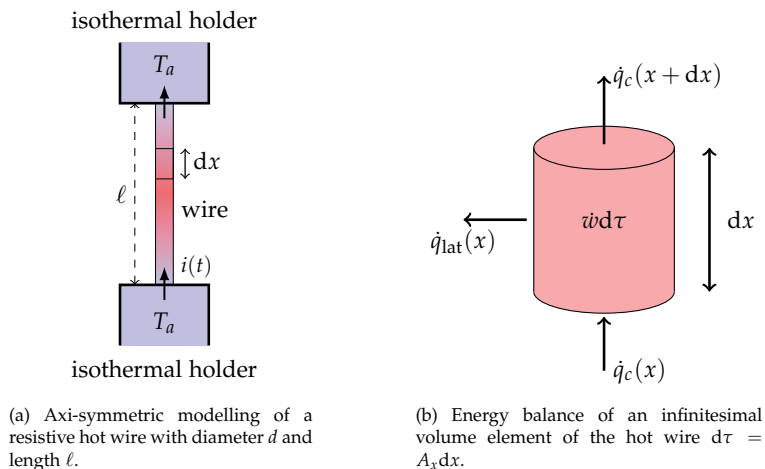


Figure 4. Axi-symmetric modelling of a single hot wire. The diameter d of the wire is much smaller than the one of the holders.

The energy balance of an infinitesimal volume element $d\tau$ of the hot wire is written in the general form (12), where $\dot{q}_{lat}(x)$ depends on the mode of operation of the sensor. For example:

- In the HWA mode: $\dot{q}_{lat}(x) = \dot{q}_r(x) + \dot{q}_{cc}(x)$;
- In the THW mode: $\dot{q}_{lat}(x) = \dot{q}_{cm}(x)$, where the letter m indicates that the conduction has to be considered in the surrounding medium and the radiative contribution is negligible;
- In a fuse mode: $\dot{q}_{lat}(x) \approx 0$.

2.3.2. Linear mode of operation – A new HWA method

2.3.2.1. HWA modelling

We focus here on the HWA modelling in the linear regime. In this case, the approach in terms of transfer functions will allow to propose a new method for the absolute measurement of the fluids flow velocity [2]. Under the assumptions of the linear regime, the balance equation (5) becomes in this case:

$$\mu_w c_w \partial_t [\delta T_w(x, t)] = \left(k_w \partial_{x^2} - h(v) \frac{\pi d}{A_x} - 4\sigma \epsilon_w T_a^3 \frac{\pi d}{A_x} + \frac{\alpha_w r_{w,ref}}{A_x} i(t)^2 \right) [\delta T_w(x, t)] + \dot{w}_a(t) \quad (16)$$

where $A_x = \pi d^2/4$, T_a is the temperature of the fluid far from the wire and is assumed constant, ϵ_w is the emissivity of the wire and $h(v)$ is the Newton coefficient of exchange, which value depends on the velocity amplitude v of the fluid far from the wire. We assume that the direction of the flow is perpendicular to the symmetry axis of the wire (see Fig. 3). It is also possible to introduce the Nusselt number Nu defined by $h(v) = k_f Nu(v)/d$, where k_f is the thermal conductivity of the fluid:

$$\mu_w c_w \partial_t [\delta T_w(x, t)] = \left(k_w \partial_{x^2} - Nu(v) \frac{\pi k_f}{A_x} - 4\sigma \epsilon_w T_a^3 \frac{\pi d}{A_x} + \frac{\alpha_w r_{w,ref}}{A_x} i(t)^2 \right) [\delta T_w(x, t)] + \dot{w}_a(t) \quad (17)$$

From the equation (17) we can identify the linear differential operator $L_{x,w}(t)$ of the equation (5) as:

$$L_{x,w}(t) = k_w \partial_{x^2} - Nu(v) \frac{\pi k_f}{A_x} - 4\sigma \epsilon_w T_a^3 \frac{\pi d}{A_x} \quad (18)$$

where the time dependence of $L_{x,w}(t)$ is generally due to the time variations of the speed v . We assume now that the speed v of the fluid is constant and that the variations δT_w of the temperature of the wire are small compared to $1/\alpha_w$ (which is of the order of 300 K). This last assumption allows to neglect the term $\alpha_w r_{w,ref} i(t)^2 \delta T_w(x, t)/A_x$ compared to the term $\dot{w}_a(t)$, assuming that $r_{w,ref} \approx r_{w,a}$, which is easy to realize. Under these assumptions, the equation (17) can be rewritten as:

$$\mu_w c_w \partial_t [\delta T_w(x, t)] = \left(k_w \partial_{x^2} - Nu(v) \frac{\pi k_f}{A_x} - 4\sigma \epsilon_w T_a^3 \frac{\pi d}{A_x} \right) [\delta T_w(x, t)] + \dot{w}_a(t) \quad (19)$$

The Laplace transform TL can now be directly applied to this equation. By denoting $\Theta_w(x, s) = \text{TL}[\delta T_w(x, t)]$ and $\dot{W}_a(s) = \text{TL}[\dot{w}_a(t)]$, we get the following ODE:

$$\mu_w c_w (s\Theta_w(x, s) - \delta T_w(x, 0)) = k_w \frac{d^2}{dx^2} \Theta_w(x, s) - \left(\text{Nu}(v) \frac{\pi k_f}{A_x} + 4\sigma \varepsilon_w T_a^3 \frac{\pi d}{A_x} \right) \Theta_w(x, s) + \dot{W}_a(s) \tag{20}$$

We assume the usual initial condition $\delta T_w(x, 0) = 0$ and isothermal boundary conditions $\delta T_w(x = \pm \ell/2, t) = 0$, recalling that the holders are supposed to be isothermal. Using this assumptions, the solution of (20) is given by:

$$\Theta_w(x, s) = \frac{\dot{W}(s)}{\beta + \frac{k_w}{\kappa_w} s} \left[1 - \frac{\cosh(\sqrt{s/\kappa_w + \beta/k_w} x)}{\cosh(\sqrt{s/\kappa_w + \beta/k_w} \ell/2)} \right] = H_w(x, s) \times \dot{W}(s) \tag{21}$$

where $\dot{W}(s) = \dot{W}_a(s)/\mu_w c_w = \kappa_w \dot{W}_a(s)/k_w = 4\kappa_w r_{w,a} \text{TL}[i(t)^2]/\pi d^2 k_w$, $x \in [-\ell/2, \ell/2]$ and $\beta = 4k_f \text{Nu}/d^2 + 16\sigma \varepsilon_w T_a^3/d$. The solution (21) has the form of the product of a transfer function $H_w(x, s)$ by an excitation signal $\dot{W}(s)$. Therefore, this approach allows to model the infinitesimal volume $d\tau$ of the hot wire, in the form of a linear system described by the transfer function $H_w(x, s)$, as shown in Fig. 5.

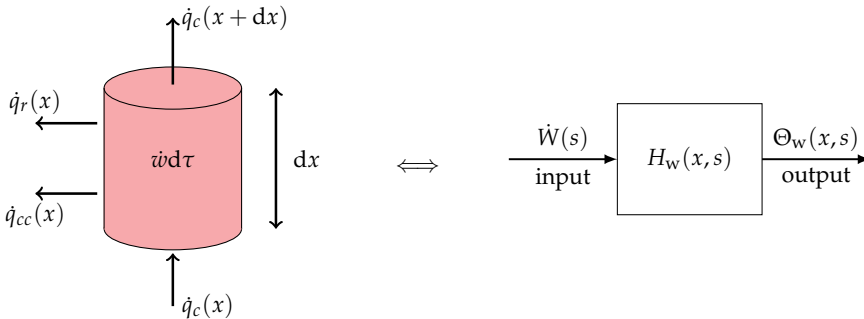


Figure 5. Linear modelling of an infinitesimal volume of the hot wire in HWA mode.

In practice, by measuring the resistance of the hot wire, one reaches the average temperature $\delta \bar{T}_w(t) = \bar{T}_w(t) - T_a$ of the wire rather than that of the sections of the wire. One can however obtain the expression of the average Laplace temperature $\bar{\Theta}_w(s)$ by using the average transfer function $\bar{H}_w(s)$ of the wire, defined by:

$$\bar{H}_w(s) = \frac{1}{\ell} \int_{-\ell/2}^{\ell/2} H_w(x, s) dx = \frac{1}{\beta + \frac{k_w}{\kappa_w} s} \left[1 - \frac{\tanh(\sqrt{s/\kappa_w + \beta/k_w} \ell/2)}{\sqrt{s/\kappa_w + \beta/k_w} \ell/2} \right] \tag{22}$$

The average temperature $\delta\bar{T}_w(t)$ of the whole wire is then calculated by the Laplace inversion of the product $\bar{H}_w(s) \times \dot{W}(s)$: $\delta\bar{T}_w(t) = \text{TL}^{-1}[\bar{H}_w(s) \times \dot{W}(s)]$.

2.3.2.2. A new HWA method

The analysis of the expression (22) shows that, in the case of the linear regime with small temperature variations, the average function transfer $\bar{H}_w(s)$ is independent of the excitation current $i(t)$ that flows through the wire, but depends only on the physical characteristics of the wire, of the fluid and of the flow. This observation is at the origin of a new absolute method of fluid flow characterization. Until now, the usual modes of operation of the hot wire anemometers consisted in measuring the amplitude of the average temperature of the wire, in response to a given flow velocity (or Nusselt number), using different forms of excitation currents. Previously, there were mainly two types of anemometers:

The constant current anemometer (CCA): schematically, the current intensity $i(t)$ through the wire is maintained constant (using an appropriate electrical circuit) and the variations of the wire temperature $\delta\bar{T}_w(t)$, induced by the changes in the flow velocity, are measured via the corresponding variations $\delta\bar{R}_w(t)$ of the resistance.

The constant temperature anemometer (CTA): in this case the average temperature of the wire is maintained constant (and thus the resistance is also maintained constant) by varying the intensity of the electrical current flowing through the wire, in response to the variations of the flow velocity.

The major drawback of these traditional utilization modes of the HWA is the need to calibrate the anemometer, since the amplitude of the temperature of the wire then depends directly on the amplitude of the excitation current. The new approach exposed here is very different¹ from the previous ones. By modelling the hot wire in terms of a Laplace transfer function, it is possible to easily examine the behavior of the wire in an domain that has not been yet visited: the frequency domain. We have plotted in Fig. 6 the evolution of the normalized imaginary part $\Im[\bar{H}_w/\bar{H}_w(0)]$ and the real part $\Re[\bar{H}_w/\bar{H}_w(0)]$ of the transfer function (22) in the Fourier space, by putting $s = 2i\pi\nu_w$, where ν_w is the frequency of the heat source. The modeled wire is supposed to be made of platinum, with a length $\ell = 10$ mm and a diameter $d = 50$ μm . The fluid considered here is the atmospheric air, flowing at room temperature with a velocity $v = 4$ $\text{m}\cdot\text{s}^{-1}$, corresponding to a Nusselt number $\text{Nu} = 2.1$.

As we can see from Fig. 6, the imaginary part of the transfer function shows a maximum value. The corresponding frequency $\nu_{w,m}$ depends only on the flow velocity, on the physical characteristics of the wire and of the fluid, but in any case not of the amplitude of the excitation, assuming that the wire is operating in its linear mode. Once the physical characteristics of the wire and the fluid are known, it becomes possible, using this new approach, to measure the velocity of the fluid in an absolute way, without the need of a prior calibration of the anemometer.

In order to experimentally access to the transfer function \bar{H}_w of the wire, the sensor has to be excited by an harmonic current $i(t) = \hat{I} \cos \omega t$ with a frequency $\nu = \omega/2\pi$, then we measure the corresponding harmonic variations of the temperature, at a frequency $\nu_w = 2\nu$.

¹ The usage that can be done of this new approach is also very different from the previous ones.

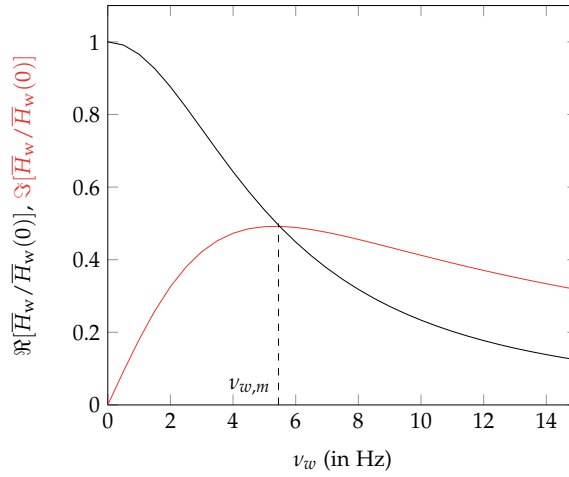


Figure 6. Evolution of the imaginary part $\Im[\bar{H}_w]$ and the real part $\Re[\bar{H}_w]$ of the transfer function (22) as a function of the frequency ν_w of the heat source, This example corresponds to the case of a platinum wire and atmospheric air at room temperature.

The Joule effect developed in the wire generates an averaged temperature oscillation $\delta\bar{T}_w(t)$ that contains a 2ω component written as $\delta\bar{T}_{2\omega}(t) = \Delta\hat{T}_{2\omega}^0(\nu) \cos 2\omega t + \Delta\hat{T}_{2\omega}^q(\nu) \sin 2\omega t$. Since the resistance of the wire is a known function of the temperature, the voltage drop $u(t) = \bar{R}_w(t)i(t)$ across the wire contains a 3ω component written as $u_{3\omega}(t) = \hat{U}_{3\omega}^0(\nu) \cos 3\omega t + \hat{U}_{3\omega}^q(\nu) \sin 3\omega t$. From equation (3) we can express the average resistance of the wire $\bar{R}_w(t)$ as:

$$\begin{aligned} \bar{R}_w(t) &= \int_{-\ell/2}^{\ell/2} r_w(x, t) dx \\ &= R_{w,a} + \alpha_w R_{w,\text{ref}} \delta\bar{T}_w(t) \\ &= R_{w,a} + \delta\bar{R}_w(t) \end{aligned} \tag{23}$$

The measurement of the harmonic variations $\delta\bar{T}_{2\omega}(t)$ of the temperature of the wire is achieved through the accurate measurement of the small harmonic component of the resistance variations $\delta\bar{R}_w(t)$.

There are mainly two kinds of circuits to achieve these measurements, the one that uses the classic Wheatstone bridge [2] and another one that uses a voltage divider (Fig. 7). This circuit must be balanced first, without any flowing, for each measurement temperature T_a , by ensuring that $R_g = R_{w,a}$ and thus $v(t) = 0$. Under flowing conditions, the use of two differential amplifiers allows to extract the informative signal $\Delta u(t) = u_1(t) - u_2(t)$ which is a function of $\delta\bar{T}_{2\omega}(t)$, the averaged harmonic temperature change of the line. The amplitude of $\Delta u(t)$ is very small in the linear regime and needs to be amplified by a factor $G \approx 1000$ using an instrumentation amplifier (IA). A dual phase synchronous detector (DPSD), adjusted to the third harmonic 3ω , allows to extract the amplitudes $\Delta\hat{T}_{2\omega}^0(\nu)$ and $\Delta\hat{T}_{2\omega}^q(\nu)$ from the voltage $v(t) = \alpha_w G \hat{I} R_{w,\text{ref}} \delta\bar{T}_w(t) \cos \omega t$ delivered by the circuit.

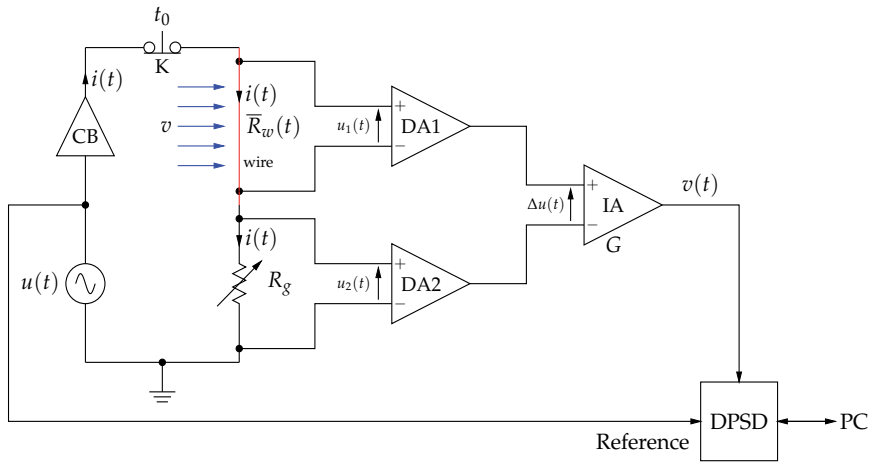


Figure 7. Circuit diagram of an experimental setup used for 3ω absolute anemometry. DPSD is a dual phase synchronous detector, that allows easy measurement of the 3ω harmonics real and imaginary parts. CB is a current buffer (LT1010), DA1 and DA2 are differential amplifiers (AMP03) and IA is an instrumentation amplifier (AD620). The DPSD, controlled by a PC, is operating in the frequency sweep mode and third harmonic detection.

Figure 8 compares the theoretical real part (dashed line) and imaginary part (continuous line) of the transfer function (22) to measurements (squares and circles) of the 2ω temperature amplitudes, at different excitation frequencies, in the case of air flowing at a speed $v = 4 \text{ m.s}^{-1}$ with ambient conditions, using a platinum wire of radius $25 \mu\text{m}$, length $\ell = 1 \text{ cm}$ and a current amplitude $\hat{I} = 10 \text{ mA}$. The results are plotted as a function of the frequency ν of the excitation current, that is half the heat source frequency: $\nu = \nu_w/2$.

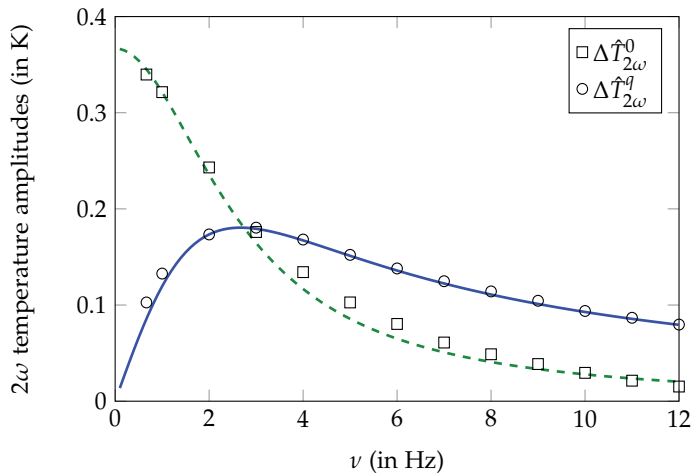


Figure 8. Experimental data (symbols) and theoretical results (lines) corresponding to the transfer function (22), with an air flow of speed $v = 4 \text{ m.s}^{-1}$, at ambient temperature and pressure. The results were obtained in the case of a platinum wire of length $\ell = 1 \text{ cm}$ and radius $d/2 = 25 \mu\text{m}$.

From the experimental results shown in Fig. 8, we found here $\nu_m^{\text{exp}} = 2.67$ Hz, which is very close to the theoretical value $\nu_m = 2.70$ Hz predicted by the function transfer of the wire Eq. (22), Fig. 6 and Fig. 8. Using this approach, we have repeated the measurements of ν_m^{exp} for different flow velocities v , and plotted the results as a function of v (Fig. 9).

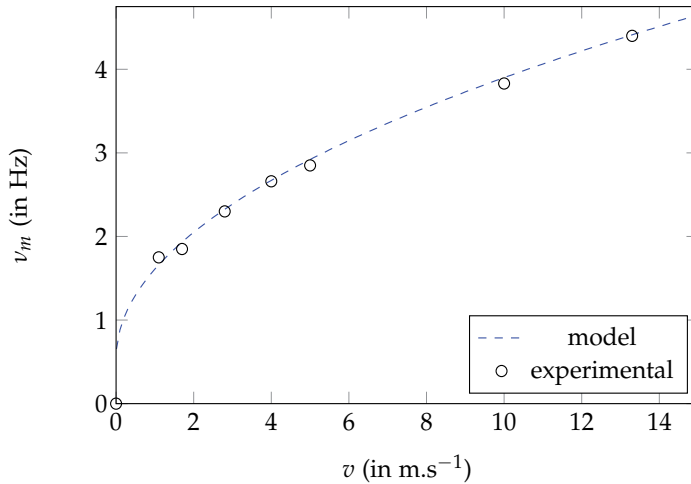


Figure 9. Absolute measurement of fluid velocity. The dashed line corresponds to the calculation of ν_m by using the averaged transfer function (22).

As it can be seen on the figure 9, there is a good correspondence between the experimental values of the frequencies ν_m and the theoretical values (dashed line) calculated from the averaged transfer function (22), and using the Churchill's correlation (24). These results show that it is possible to use this new approach in order to measure, in an absolute way, the Newton coefficient h or the Nusselt Number Nu and thus, by using an appropriate correlation, the flow velocity v .

2.3.2.3. Conclusion

The modelling of a single wire, operating in the linear mode, in terms of a Laplace transfer function, allows for a new approach of the use of such a sensor, based on a frequency description. A new absolute method of fluid flow characterization has thus been developed using this approach. This new approach is also very fruitful in the domain of fluid thermal properties characterization.

2.3.3. Non linear mode of operation – The electrothermal analogy

2.3.3.1. Presentation

The preceding approach is limited to the description of the linear mode of operation of the single wire. In the common case of large variations in the temperature of the sensor, as for example in the case of the classical CTA or CCA modes, another approach is necessary to be able to realistically describe the operation of the sensor. The electrothermal analogy exposed

in the paragraph 2.2.3, is an interesting approach to illustrate the mode of operation of the hot wire resistive sensor, in the most general configuration.

If Ox denotes the axis of symmetry of the wire, the electrical circuit of Fig. 2b allows to describe the mechanisms of the instantaneous heat transfers between an infinitesimal volume $d\tau$ of the wire and its environment, with $A_x = \pi d^2/4$, $A_{lat} = \pi d dx$ and the Newton coefficient h is given by the correlation of Churchill and Bernstein [12], which is known for its universality over a wide range of flow conditions:

$$h(v_\infty) = \frac{k_f}{2a_1} \left\{ 0.3 + \frac{0.62 \text{Re}^{1/2} \text{Pr}^{1/3}}{\left[1 + \left(\frac{0.4}{\text{Pr}}\right)^{2/3}\right]^{1/4}} \left[1 + \left(\frac{\text{Re}}{282000}\right)^{5/8}\right]^{4/5} \right\} \quad (24)$$

where $\text{Re} = dv/v_f$ and $\text{Pr} = \nu_f/\kappa_f$ are respectively the Reynolds and Prandtl numbers, ν_f is the kinematic viscosity, k_f the thermal conductivity and κ_f the thermal diffusivity of the fluid. This relation is valid as long as $\text{Pr} \times \text{Re} \geq 0.2$.

The wire is mathematically divided in N identical infinitesimal volumes, each of them being described by a circuit of the type 2b, that are connected in serial. Dirichlet boundary conditions are supposed at the extremities $x = \pm \ell/2$ of the system, due to the isothermal supports. The figure 10 shows such a modelling of the wire in term of the electrothermal analogy of table 1, for the elementary case where $N = 2$. Based on this circuit, a SPICE code allows to calculate the instantaneous voltages $U_i^T(t)$, analogous to the temperatures $T_i(t)$ of each elementary volume.

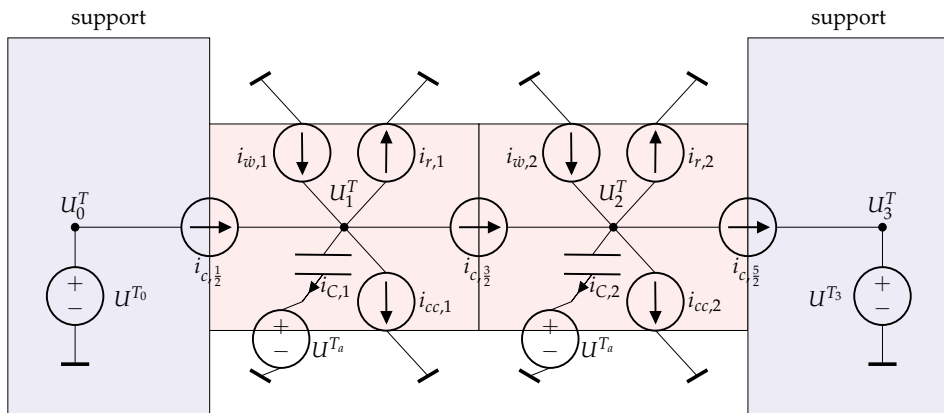


Figure 10. Electrothermal circuit equivalent to the hot wire sensor. For reasons of space and clarity, the model has been restricted to $N = 2$.

The simulated wire is supposed to be made of platinum, with a length $\ell = 1$ cm and a diameter $d = 10 \mu\text{m}$. Its resistance at room temperature is $R_{w,a} = 13.58 \Omega$. If for example we choose to impose a value of the resistance $\bar{R}_w = 22 \Omega$ by setting $R_1 = 22 \Omega$ in the CTA circuit, the average temperature of the wire should consequently be $\delta \bar{T}_w = 159.5$ K, whatever

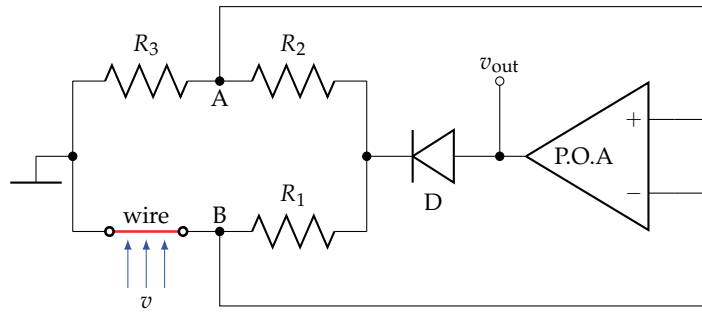


Figure 11. Elementary CTA circuit. D is a signal diode (1N4148), P.O.A is a power operational amplifier (OPA 548), $R_2 = R_3$ and are of the order of 1 k Ω . The value of R_1 is chosen in order to control the value of the resistance R_w of the wire and consequently its temperature \bar{T}_w . The output v_{out} is a function of the flow velocity v .

the velocity of the fluid around the wire. To test the quality of the present electrothermal analogy, we decide to impose important harmonic variations of the fluid velocity $v(t) = v_{c,0} + \hat{v} \cos \omega t$ where $\nu = \omega/2\pi = 10$ Hz, $v_{c,0} = 2.5 \text{ m}\cdot\text{s}^{-1}$ and $\hat{v} = 1.5 \text{ m}\cdot\text{s}^{-1}$, which means 60% in variations (Fig. 12). As we can see from the results of the simulation, the temperature of the wire is stabilized at around 0.2% of its average value, while its resistance is stabilized at 0.08% of its average value \bar{R}_w . We have also plotted in figure 13, the evolution of the output

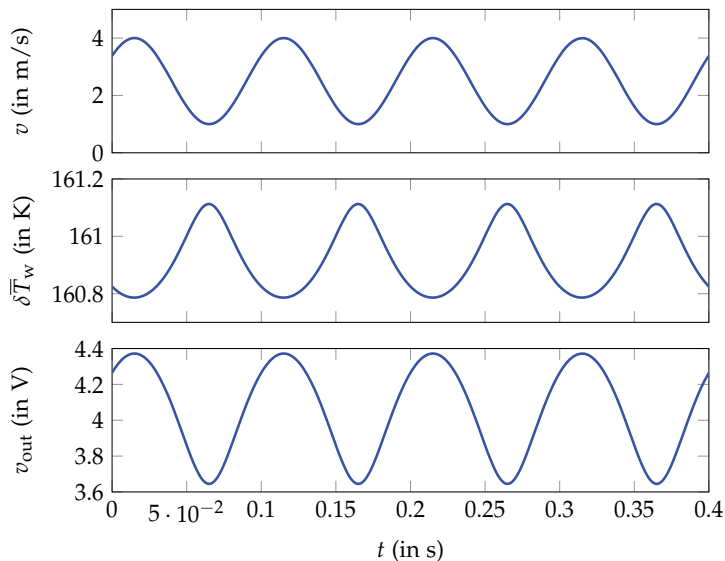


Figure 12. Results of the simulation of a CTA circuit, using an electrothermal analogy of a hot wire sensor.

v_{out} as a function of the velocity of the fluid v . This curve is typical of the evolution of the coefficient of transfer h with the fluid velocity v , showing once more the good adequacy of this approach with the description of the CTA mode. It is also possible to add some noise to the velocity v and thus to test the stability of the model. The obtained results, not reported here, show a very good behavior of the modelling in respect to the noise.

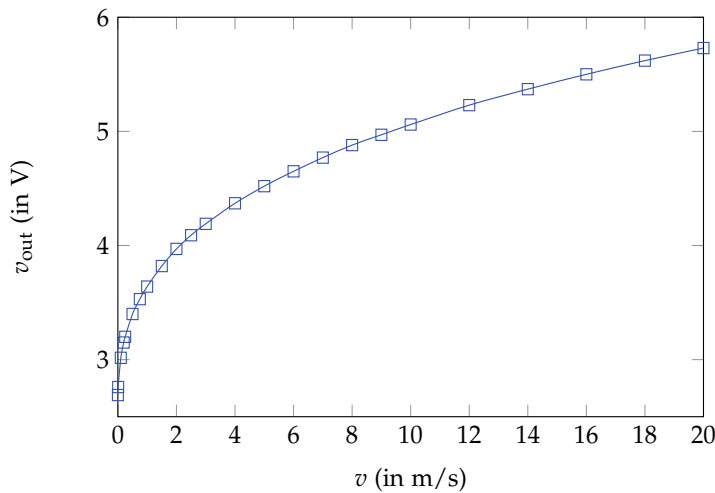


Figure 13. Results of the simulation of a CTA circuit, using an electrothermal analogy of a hot wire sensor.

2.3.3.2. Conclusion

The approach in term of an electrothermal analogy is a very powerful modelling tool, allowing to realistically describe the different modes of operation of a hot wire sensor. This opens the way to a systemic description of the whole system: sensor, control and signal processing electrical circuits. A Python script is available, upon request to the author (at the following address: rodolphe.heyd@cnrs-orleans.fr). It allows to generate a SPICE sub-circuit that is equivalent to the whole wire, with an arbitrary number N of infinitesimal volumes, under Dirichlet boundary conditions. SPICE scripts describing the operation of a CTA, based on the present modelling, are also available.

2.4. Resistive flat film sensor

2.4.1. Presentation – Mathematical model

The miniature thin-film resistive sensors (see Fig. 1) are very commonly used to measure the temperature, in many applications ranging from biomedical instrumentation to automotive industry or cooling systems for example. In most of the cases, the sensitive resistive film is protected by insulating shells and maintained on the system to study by an adhesion layer. These sensors are thus composite systems (see Fig. 14) and due to the heat conduction process through the different layers, the instantaneous operating temperature provided by the sensor can be different from that to be measured.

In order to take into account the influence of the different constitutive layers on the operation of the sensor, we first need to solve the problem of heat conduction through the sensor. As in the case of the single wire, we will first use the formalism of the Laplace transform. This allows us to provide an analytical expression of the distribution of the temperature in the system as a continuous function of the position and the time. This analytical approach also has the advantage to clearly identify the influence of the different physical parameters on the behavior of the system, thus facilitating its optimization for example. Moreover this

formalism allows to describe the thermal behavior of the composite system in terms of transfer functions [8, 10, 11], allowing inverse analysis.

In order to obtain a realistic modelling of the flat thin film sensor, we have to consider the conduction of heat through a thin composite slab (see Fig. 14) of finite thickness $L_2 + L_1 \approx 100$ to $500 \mu\text{m}$. The bottom layer (1) is frequently made of ceramic while the top layer (2) is usually a very thin passivation coating, made of glass. The thickness 2ϵ of the metallic film (h) is only a fraction of that of the coating layers and is of the order of 10 to 100 nm. The lateral dimensions a and b of the slab are frequently of the order of a few millimeters to a few centimeters. Therefore we can consider that the heat transfer inside this composite system is only axial. It is also possible to use flexible sensors, for which the sensing metallic film is protected by two polyimide layers for example.

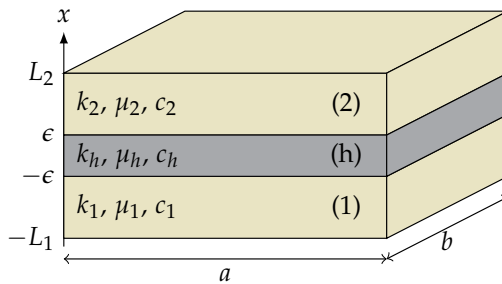


Figure 14. Composition of the composite slab considered in this study, with $L_j \ll a, b$ and $\epsilon \ll L_j$ where $j = 1, 2$.

We assume that the very thin metallic film has a high thermal conductivity k_h and is inserted between two insulating materials with thermal conductivity $k_j \ll k_h$, where $j = 1, 2$. The imperfect thermal contacts, between the very thin film and the insulating shells, are modeled by introducing thermal contact resistances. Because of the dimensions of the slab ($L_j \ll a, b$) and of the boundary conditions considered here, a planar invariance (no dependence in y and z) without in-plane temperature gradients is supposed. It follows that the temperature $T(x, t)$ of the slab is a function of x and t only, written as $T(x, t) = T_a + \delta T(x, t)$. At initial time $t = 0$, the whole system is supposed to be at thermal equilibrium with an uniform temperature T_a , therefore $\delta T(x, 0) = 0$. For time $t > 0$, we consider heat conduction through the whole system due both to the outermost boundary conditions, at $x = L_2$ and $x = -L_1$, and to internal heat sources supposed to be localized only inside the high conductivity film (h). This heat conduction induces temperature variations $\delta T_j(x, t)$ of the coatings that satisfy the following one-dimensional diffusion equations:

$$\partial_t [\delta T_j(x, t)] = \alpha_j \partial_{x^2} [\delta T_j(x, t)] \tag{25}$$

where $\alpha_j = k_j / \mu_j c_j$ is the thermal diffusivity, μ_j is the density and c_j is the specific heat of the corresponding coating, that are supposed constant in the linear approach considered here. Under these conditions, the differential operator $L_{x,j}(t)$ of equation (1) is simply written as $L_{x,j}(t) = \partial_{x^2}$, with $j \neq h$.

Moreover, due to the high value of the ratio k_h/k_j commonly encountered with resistive sensors, the temperature $T_h(x, t) = T_a + \delta T_h(x, t)$ of the high thermal conductivity film can be considered as uniform to a very good approximation. Numerical simulations, made with the finite element solver FlexPDE, show that in all the cases under study here, the spatial variations in the temperature $\delta T_h(x, t)$ are absolutely negligible: $1 - |\delta T_h(0, t)/\delta T_h(\pm\epsilon, t)| < 0.1\%$. Thus it is possible to consider that the temperature δT_h only depends on the time t . Therefore the energy balance of the highly conductive film can be written as:

$$2\epsilon ab\mu_h c_h \frac{d\delta T_h}{dt} = \dot{Q}_h + \dot{W}_h \tag{26}$$

where $\dot{W}_h(t)$ is the internal heat power due to the Joule effect and $\dot{Q}_h(t) = \dot{Q}_{h,\epsilon}(t) + \dot{Q}_{h,-\epsilon}(t)$ is the heat exchanged by unit time between the sensing film (h) and the insulating shell. The temperature uniformity of the highly conductive film and the introduction of the thermal contact resistances, allow us to write at $x = \pm\epsilon$:

$$\delta T_h(t) = \delta T_1(-\epsilon, t) - R_1^c \dot{Q}_{h,-\epsilon}/ab = \delta T_2(\epsilon, t) - R_2^c \dot{Q}_{h,\epsilon}/ab \tag{27}$$

where R_1^c and R_2^c are the thermal contact resistances respectively at $x = -\epsilon$ and $x = \epsilon$. Furthermore, the continuity of the heat fluxes at $x = \pm\epsilon$ leads to the following relations:

$$ab k_1 \left(\frac{\partial \delta T_1}{\partial z} \right)_{-\epsilon} = -\dot{Q}_{h,-\epsilon}(t) \text{ and } ab k_2 \left(\frac{\partial \delta T_2}{\partial z} \right)_{\epsilon} = \dot{Q}_{h,\epsilon}(t) \tag{28}$$

In the limit of a very thin conductive film that is considered here, $\epsilon \ll L_j$, it is possible to neglect the term $2\epsilon ab\mu_h c_h d\delta T_h/dt$ compared to \dot{Q}_h and \dot{W}_h . Thus we can write with a very good approximation:

$$\dot{W}_h(t) = - [\dot{Q}_{h,\epsilon}(t) + \dot{Q}_{h,-\epsilon}(t)] \tag{29}$$

In order to find the time evolutions of the temperatures δT_j and δT_h , we first apply the Laplace transform to the equations (25), (27), (28) and (29), we obtain:

$$sF_j = \alpha_j \partial_x^2 F_j \tag{30}$$

$$F_h(s) = F_1(-\epsilon, s) - R_1^c \dot{q}_{h,-\epsilon}(s) = F_2(\epsilon, s) - R_2^c \dot{q}_{h,\epsilon}(s) \tag{31}$$

$$k_1 (\partial_x F_1)_{-\epsilon} = -\dot{q}_{h,-\epsilon}(s) \text{ and } k_2 (\partial_x F_2)_{\epsilon} = \dot{q}_{h,\epsilon}(s) \tag{32}$$

$$\dot{w}_h(s) = - [\dot{q}_{h,\epsilon}(s) + \dot{q}_{h,-\epsilon}(s)] \tag{33}$$

where $F_j(x, s)$, $F_h(s)$, $\dot{w}_h(s)$ and $\dot{q}_{h,\pm\epsilon}(s)$ are the Laplace transforms respectively of $\delta T_j(x, t)$, $\delta T_h(t)$, $\dot{W}_h(t)/ab$ and $\dot{Q}_{h,\pm\epsilon}(t)/ab$. The solutions of the equations (30) can be written as:

$$F_j(x, s) = A_j(s)e^{\lambda_j x} + B_j(s)e^{-\lambda_j x} \tag{34}$$

where $\chi_j^2 = s/\alpha_j$. Using the continuity relations (31) and (32) ; the internal constraint (33) together with the outermost boundary conditions located at $x = -L_1$ and $x = L_2$, it is possible to find the expressions of the six unknowns $A_1(s)$, $A_2(s)$, $B_1(s)$, $B_2(s)$, $\dot{q}_{h,\epsilon}(s)$ and $\dot{q}_{h,-\epsilon}(s)$. Finally by reversing the relation (34), we can find the time evolution of the temperatures and heat fluxes at each point of the system, according to the boundary conditions and internal heat source considered.

2.4.2. Temperature sensor mode

2.4.2.1. Dirichlet boundary conditions and transfer function

In usual situations, the highly conductive film is the sensing element whose operating temperature $\delta T_h(t)$ is measured and controlled. We want to determine here the evolution of this temperature as a function of the outermost temperatures of the sensor: $\delta T_1(-L_1, t) = \delta T_1(t)$ and $\delta T_2(L_2, t) = \delta T_2(t)$. Applying the Laplace transform to these Dirichlet boundary conditions, we get:

$$F_1(-L_1, s) = X_1(s) \quad (35)$$

$$F_2(L_2, s) = X_2(s) \quad (36)$$

where X_1 and X_2 are the Laplace transforms respectively of $\delta T_1(t)$ and $\delta T_2(t)$.

In order to deduce the real-time evolution of $\delta T_h(t)$ from the knowledge of the boundary temperatures $\delta T_1(t)$ and $\delta T_2(t)$, we need first to find the relationship between $F_h(s)$, $X_1(s)$ and $X_2(s)$. To simplify the mathematical expressions further, without reducing the generality of this approach, the system is assumed to be symmetric according to the plane $x = 0$. Using the relations (31) to (36) we get the following expression:

$$F_h(s) = \dot{w}_h(s) \left[\frac{\tanh [(L - \epsilon)\sqrt{s/\alpha}]}{2k\sqrt{s/\alpha}} + \frac{R^c}{2} \right] + \frac{X_1(s) + X_2(s)}{2 \cosh [(L - \epsilon)\sqrt{s/\alpha}]} \quad (37)$$

where $L = L_j$, $\alpha = \alpha_j$, $k = k_j$ and $R^c = R_j^c$, with $j = 1, 2$. As mentioned earlier in this section, it may be important to be able to quantify the influence of the internal self-heating on the temperature measurements using thin-film resistive sensors. The expression (37) clearly answers this question by showing the influence of the boundary temperatures X_1 and X_2 separately from the influence of the internal heat source \dot{w}_h .

It is still possible in the present case, to describe the sensor in terms of a combination of two linear dynamical systems as shown in Fig. 15, where H_X and H_w are the Laplace transfer functions associated respectively with the outermost boundary temperatures and the internal heat source, and defined by:

$$H_X(s) = 1 / \cosh [(L - \epsilon)\sqrt{s/\alpha}] \quad (38)$$

$$H_w(s) = \frac{\tanh [(L - \epsilon)\sqrt{s/\alpha}]}{2k\sqrt{s/\alpha}} + \frac{R^c}{2} \quad (39)$$

The relation (37) can now be written as:

$$F_h(s) = H_w(s)\dot{w}_h(s) + H_X(s)\frac{X_1(s) + X_2(s)}{2} \quad (40)$$

$$= F_{hX}(s) + F_{hw}(s) \quad (41)$$

Returning to the real time space, the operating temperature of the sensor can thus be written as $\delta T_h(t) = \delta T_{hX}(t) + \delta T_{hw}(t)$, where $\delta T_{hX}(t)$ is the contribution due to the outermost temperatures of the sensor and $\delta T_{hw}(t)$ is the contribution due to the internal heat source.

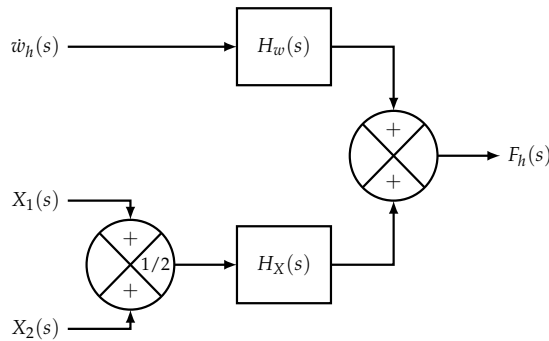


Figure 15. Description of the thin film sensor using a combination of two linear systems.

The inverse Laplace transform of the relation (37) must be computed now, in order to obtain the time variations of the temperature δT_h . Depending on the time evolutions of both the internal heat source and of the boundary temperatures, an analytical inversion of the Laplace transform $F_h(s)$ is not always possible. It is therefore essential to be able to reverse the function $F_h(s)$ in an approximate way, but with a sufficient accuracy to allow a precise description of the complete time evolution of the physical quantities, from the initial transient regime until the steady state.

There are usually several ways to calculate $\delta T_h(t)$ based on the relation (37). When the analytical expressions of the functions $\dot{w}_h(t)$, $\delta T_1(t)$ and $\delta T_2(t)$ are known, it is possible to resort to numerical Laplace transform inversion schemes [13–15]. However, this method becomes very difficult to apply when the temperatures $\delta T_1(t)$ and $\delta T_2(t)$ are known only as a set of discrete values provided for example by experimental records. Moreover, in the temperature measurement mode, these outermost temperatures are usually unknown or at the best partially known. We prefer to apply a method developed in [11], that uses the Padé digital filters. This approach presents the great advantages on the one hand to not require a Laplace inversion and on the other hand to allow to consider realistic situations, where the outermost temperatures and the source term are given for example by experimental records.

The first step of this method consists in approximating the Laplace transfer functions $H(s)$ by precise rational functions, obtained by using their Padé approximants, and expressed in the form:

$$H^{PA}(s) = \frac{H(0) + \sum_{k=1}^M b_k s^k}{1 + \sum_{k=1}^N a_k s^k} \tag{42}$$

where the coefficients $\{a_k, b_k\}$ are calculated analytically using the following equality [16]:

$$\left. \frac{d^k}{ds^k} H^{PA}(s) \right|_{s=0} = \left. \frac{d^k}{ds^k} H(s) \right|_{s=0}, \quad k = 1, 2, \dots, M + N \tag{43}$$

Next we determine the digital filter corresponding to $H(s)$ by applying the bilinear transformation $s = \frac{2}{T_e} \frac{Z-1}{Z+1}$, where T_e is an appropriate sampling period [17]. After some algebra manipulations, we obtain an approximated Z transfer function of the form:

$$H^{PA}(Z) = \frac{\sum_{k=0}^M A_k Z^{-k}}{1 + \sum_{k=1}^N B_k Z^{-k}} \tag{44}$$

where the coefficients (A_k, B_k) are expressed as a function of the sampling period T_e and coefficients (a_k, b_k) that are deduced from the relation (43). Finally we deduce from (44), a recursion formula that is easy to calculate using sampled quantities. To illustrate this process, we consider for example the situation where both faces of the sensor are submitted to the same temperature variations: $\delta T_1(t) = \delta T_2(t) = \delta T_X(t)$, $X_1(s) = X_2(s) = X(s)$ and $F_{hX}(s) = H_X(s)X(s)$, where $H_X(s)$ is given by (38). This is the case for example when the sensor is immersed at initial time $t = 0$ in a turbulent liquid or put in perfect thermal contact with a thermostat.

From the Padé Z transfer function $F_{hX}^{PA}(Z)$ we can deduce the recursion relation satisfied by the component T_{hX} of the sensing element temperature:

$$\delta T_{hX}(nT_e) = \sum_{k=0}^M A_k \delta T_X((n-k)T_e) - \sum_{k=1}^N B_k \delta T_{hX}((n-k)T_e) \tag{45}$$

The same procedure holds for the internal heat source contribution δT_{hw} :

$$\delta T_{hw}(nT_e) = \sum_{k=0}^M A'_k \delta \dot{w}_h((n-k)T_e) - \sum_{k=1}^N B'_k \delta T_{hw}((n-k)T_e) \tag{46}$$

where the coefficients (A'_k, B'_k) are deduced from the approximated Padé transfer function H_w^{PA} .

2.4.2.2. Influence of self-heating

To illustrate the benefit of the approach in terms of Laplace transfer functions, using the relation (37) together with the associated discrete digital Padé filters (45 and 46), we can compute the real-time evolution of the temperature $\delta T_h(t)$ in the case of a non-negligible contribution of the internal heat source. The results have been compared with those provided by the finite elements (FE) solver FlexPDE.

The physical characteristics of the thin film sensor considered in the following calculations are: $L = 30 \mu\text{m}$, $e = 1.0 \mu\text{m}$, $a = b = 1 \text{ mm}$, $k = 0.12 \text{ W.K}^{-1}.\text{m}^{-1}$, $\tau^{-1} = \alpha / (L - e)^2 = 89.1 \text{ Hz}$ and $R_{h,a} = 10 \Omega$. The influence of the thermal contact resistances has been taken into account using a typical value of $R^c = 2.0 \times 10^{-4} \text{ W}^{-1}.\text{m}^2.\text{K}$. The sampling period used with the digital Padé filters is chosen equal to $T_e = 0.05 / \tau$.

We consider first the case of a sudden variation of the boundary temperature $\delta T_X(t) = \delta T_X^m \Theta(t)$, together with a constant internal heat source $\dot{w}_h(t) = \dot{w}_h^m \Theta(t)$, where $\delta T_X^m = 1 \text{ K}$; $\dot{w}_h^m = 4 \times 10^3 \text{ W/m}^2$ and $\Theta(t)$ is the Heaviside step function. As shown in Fig. 16, the curve representing the real-time evolution of the temperature δT_h , calculated using the Padé digital filters, is nearly undistinguishable from that obtained using the FE solver (circles). The Fig. 16 shows that the relation (13) also presents the advantage, compared to the use of a FE solver, to allow for the calculation of the real-time contribution of the boundary temperatures δT_X separately from that of the internal heat source. In the particular case of a resistive sensor, this approach could permit a real time evaluation of the modelling of the influence of the self-heating on the accuracy of the outermost temperature measurements.

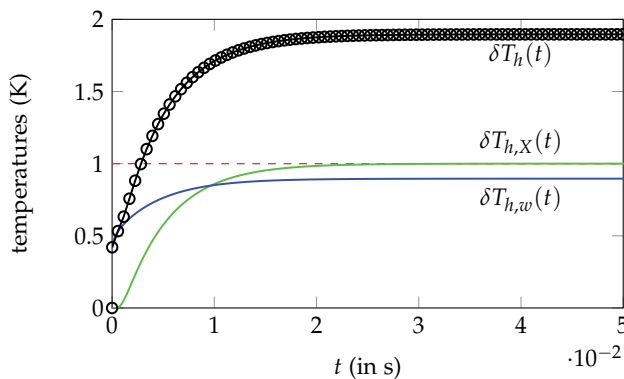


Figure 16. Time evolution of the operating temperature δT_h of a miniature thin film resistive sensor, in the case of a non-negligible contribution of the internal heat source, calculated by using Padé digital filters and a FE solver (circles). The curves show the decomposition of the operating temperature thanks to the transfer function approach: $\delta T_h = \delta T_{hX} + \delta T_{hw}$. The dashed line corresponds to the outermost temperature δT_X to be measured.

2.4.2.3. Inverse analysis

The direct analysis presented earlier is of a great interest in order to model the operation of the sensor but it is also very interesting to be able to process the thermal signal $\delta T_h(t)$ provided by the sensor in real time, in order for example to recover a precise estimate of the outermost temperatures, in spite of the self-heating. This is an inverse heat conduction

problem, where the influence of self-heating must be corrected. By rewriting the relation (37) as:

$$X(s) = H_X^{-1}(s)F_h(s) - H_X^{-1}(s)H_w(s)\dot{w}_h(s) \quad (47)$$

with $H_X^{-1} = 1/H_X$, it is now possible to determine the boundary temperature $\delta T_X(t)$ from the knowledge of $\delta T_h(t)$ and $\dot{w}_h(t) = \dot{W}_h(t)/ab$. We also use the method of the digital Padé filters to solve this inverse problem. It is possible to construct digital filters based on Padé approximants of the transfer functions $G_X = H_X^{-1}$ and $G_w = H_X^{-1}H_w$. These functions have a pathological behavior since they diverge when s diverges, so it is very unlikely to find some approximations of G_X and G_w by rational functions, that would allow for a stable resolution of this inverse problem. To overcome this difficulty, we approximate the functions G_f by the following rational functions, with f denoting X or w :

$$G_f^M(s) = \frac{G_f(0) + \sum_{k=1}^M b_k s^k}{1 + \sum_{k=1}^M a_k s^k} \quad (48)$$

where the b_k are the Padé coefficients of the function G_f , defined by the relation (43) with $N = 0$, but the a_k coefficients are chosen here in such a way that on the one hand $a_k \ll 1$ and on the other that the Routh–Hurwitz stability criterion is satisfied. With these choices, the rational function G_f^M allows for the stability of the inverse problem while being very close to the Padé approximant $G_f^{M,0}$ of G_f .

This inverse analysis is illustrated now by considering a situation where the outermost temperature $\delta T_X(t)$ is described by a square wave, the self-heating is considerable and the operating temperature $\delta T_h(t)$ is noisy, due for example to experimental conditions (Figure 17). The stability of the inverse Padé digital filter is not disturbed by the abrupt changes generated by the outermost temperature discontinuities and the Gaussian noise added to the exact operating temperature. If needed, the reconstructed outermost temperature can be filtered to smooth the unwanted residual noises. As can be seen on Fig. 17, the successive operations of inverse analysis and filtering allow for a good reconstruction (circles) of the outermost temperature $\delta T_X(t)$ (dashed line).

2.4.2.4. Extreme conditions

We have previously considered situations where the temperature variations were limited to only a few Kelvins (Fig. 16 and 17), thus the corresponding variations of the resistance R_h of the sensor can be neglected in the expression of the heat source term $\dot{w}_h(t) = R_h [\delta T_h(t)] i^2(t)/ab \approx R_{h,a} i^2(t)/ab$. This assumption is usually well verified in the domain of biomedical applications for example. However, this type of sensor can also be used in more extreme applications where the temperature variations are so large that the value of the resistance R_h can no more be considered as constant within the source term \dot{w}_h . The use of recursive filters offers the possibility to consider the problem of such extreme temperature variations, with only a few modifications of the preceding approach. Through

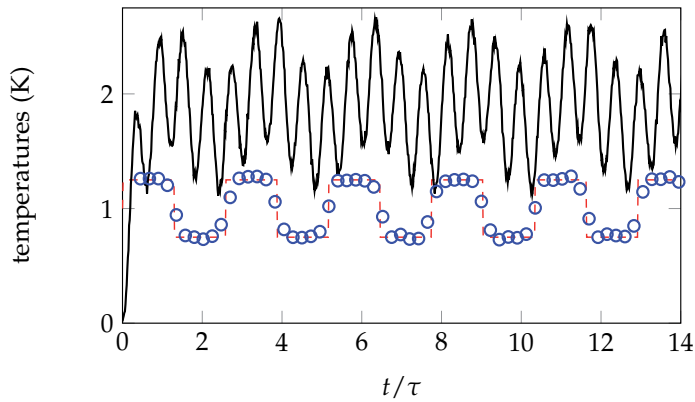


Figure 17. Time evolution of the operating temperature δT_h (solid line) in the case where the outermost temperature δT_X is a square wave (dashed line) and a Gaussian noise has been added to the operating temperature, with a 0 K mean value and a 0.03 K standard deviation value. The reconstructed δT_X is given by the circles.

the decomposition of the operating temperature as $\delta T_h = \delta T_{hX} + \delta T_{hw}$, we write first the source term \dot{w}_h as:

$$\dot{w}_h(t) = \dot{w}_h^0(t) [1 + \alpha_m (\delta T_{hX}(t) + \delta T_{hw}(t))] \quad (49)$$

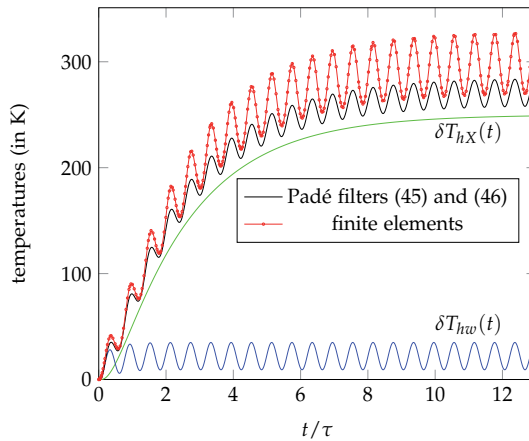
with $\dot{w}_h^0(t) = R_{h,a} i^2(t) / ab$ and $\alpha_m = \alpha_h R_{h,ref} / R_{h,a}$, where α_h is the temperature coefficient of the metallic film. Next we modify the recursion relation (46) in order to take into account the time evolutions of δT_{hX} and δT_{hw} :

$$\begin{aligned} \delta T_{hw}(nT_e) = & \sum_{k=0}^M A'_k \dot{w}_h^0((n-k)T_e) [1 + \alpha_m \delta T_{hX}((n-k)T_e) + \alpha_m \delta T_{hw}((n-k-1)T_e)] \\ & - \sum_{k=1}^N B'_k \delta T_{hw}((n-k)T_e) \end{aligned} \quad (50)$$

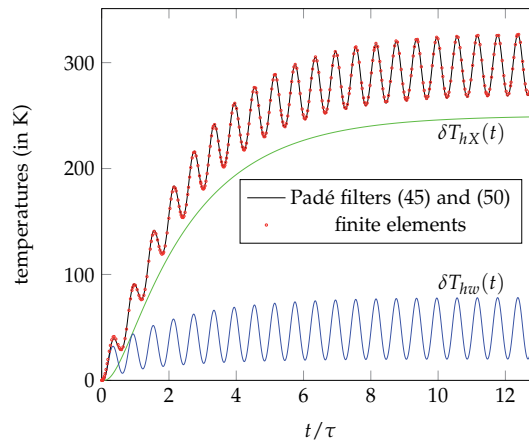
where the coefficients (A'_k, B'_k) are the same as those used in the relation (46) and $\delta T_{hX}((n-k)T_e)$ is still calculated using the relation (45), that must be solved first. Because of the recursive structure of (50), a small delay must be used in the expression of $\alpha_m \delta T_{hw}$.

To illustrate the efficiency of this approach, let's consider large outermost temperature variations $\delta T_X(t) = 250 \times (1 - \exp -t/\tau')$, together with a large contribution of the self-heating by using $R_{w,a} = 1000 \Omega$, $i(t) = 0.014 \sin(2\pi vt)$ and a thermal contact resistance $R^c = 2.0 \times 10^{-4} \text{ W}^{-1} \cdot \text{m}^2 \cdot \text{K}$.

Compared to the FEM results (dots) shown in the Figure 18a, the linear approach based on the recursion relation (46) gives very bad results in the present case. In contrast, we can see on Fig. 18b that the approach based on the modified recursion relation (50) gives excellent results (solid line), nearly undistinguishable from those found with a FEM solver. Another benefit of this approach is that the inversion relation (47) is still usable, even in the presence of this type of extreme temperature variations.



(a) Solution using the recursive filters (45) and (46). The results obtained here are very different from those obtained by finite element calculations (FEM).



(b) Solution using the recursive filters (45) and (50). The results are now very closed to those obtained by FEM.

Figure 18. Thin film resistive sensor modeled by using Padé filters in the case of important variations of the temperatures.

2.4.2.5. Mixed boundary conditions

We consider now the frequent case of mixed boundary conditions. We suppose that the heat flux obeys the Newton’s law of convective cooling at the position $x = L_2$: $-k_2(\partial_x T_2)_{L_2} = h(T_2 - T_a)_{L_2}$, where h is the convective heat transfer coefficient and T_a is the temperature of the fluid, far from the sensor. At the bottom surface $x = -L_1$, we assume that the outermost temperature is known, due to a perfect thermal contact of the sensor with a solid of temperature $T_1(t) = \delta T_1(t) + T_a$. By applying the Laplace transform to these boundary conditions, together with the relations (31) to (36) and using the same assumption of symmetry as in the preceding sections, it is still possible to write $F_h(s) = H_X(s)X(s) + H_w(s)\dot{w}_h(s)$, where $X(s)$ is the Laplace transform of $\delta T_1(t)$, $H_X(s)$ and $H_w(s)$ are given here by:

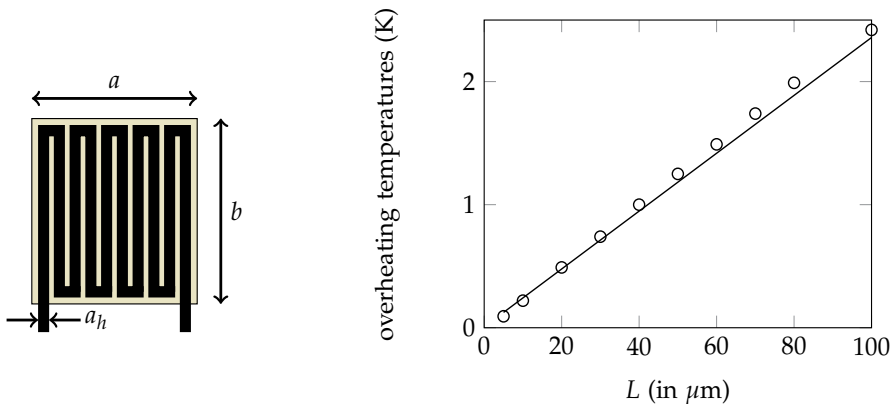
$$H_X(s) = \frac{h \sinh [(L - \epsilon)\sqrt{s/\alpha}] + k\sqrt{s/\alpha} \cosh [(L - \epsilon)\sqrt{s/\alpha}]}{h \sinh [2(L - \epsilon)\sqrt{s/\alpha}] + k\sqrt{s/\alpha} \cosh [2(L - \epsilon)\sqrt{s/\alpha}]} \quad (51)$$

and

$$H_w(s) = \frac{\sinh [(L - \epsilon)\sqrt{s/\alpha}]}{k\sqrt{s/\alpha}} \times H_X(s) \quad (52)$$

We focus now on the analysis of the influence of some physical parameters on the overheating temperature [18] $\Delta T = T_h - T_1 = \delta T_h - \delta T_1$, rather than on the inverse analysis in the case of self-heating, study that is very similar to the previous one.

Let's consider a constant internal heat source of a typical value $\dot{w}_h = 4 \times 10^3 \text{ W/m}^2$ and constant boundary conditions. From the study of the real-time evolution, obtained with the digital Padé filters deduced from transfer functions (51) and (52), we calculate the steady-state values of the overheating temperature of the thin film sensor previously described. These results are in good agreement with those provided by finite element calculations (FlexPDE solver) based on the geometric configuration illustrated by the Fig. 1b and 19a. The value of the operating temperature T_h has been considered at the center of the thin-film.



(a) Top view of the thin film sensor, $a = b = 1 \text{ mm}$ and $a_h = 95 \mu\text{m}$. The lateral sides are supposed thermally insulated. The thin-film heater (h) is encapsulated by an isolating coating of width $2(L - \epsilon) \approx 2L$.
 (b) Overheating temperature $\Delta T = T_h - T_1$ of the sensing film (h) as a function of the width L of the coating layers, $h = 100 \text{ W.m}^{-2}.\text{K}^{-1}$ and $\delta T_1 = 10 \text{ K}$.

Figure 19. Overheating study of the thin film sensor by using Laplace transfer functions.

The Fig. 19b shows a linear evolution of the steady-state overheating temperature within the considered range of values of the thickness L . As expected, the overheating temperature increases with the thickness of the insulating coating. The influence of other parameters (such as $h, \delta T_1, k, \mu$) can easily be studied in the same way with this method [11], at a fraction of the time needed with a FEM calculations, while having the advantage of an analytical approach.

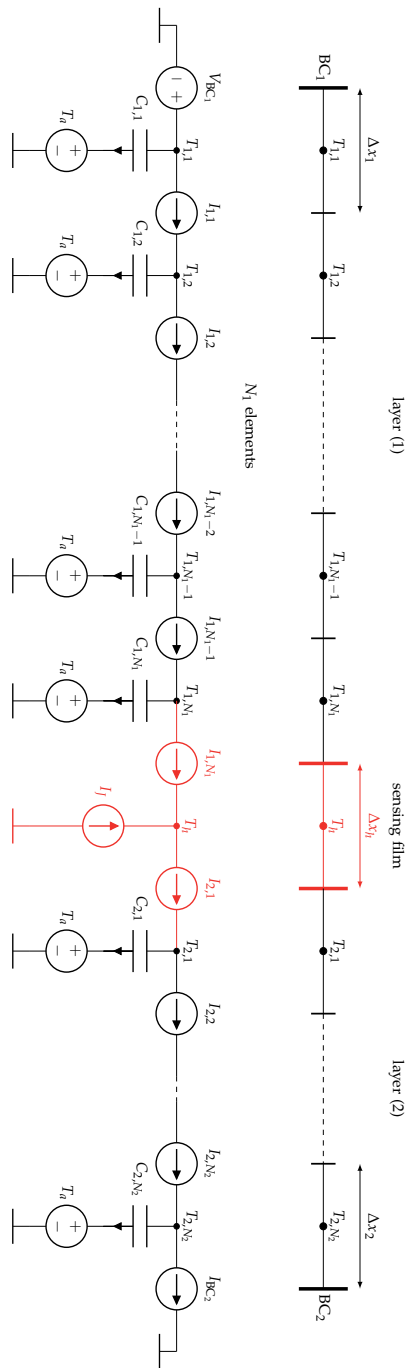


Figure 20. Electrothermal model equivalent to a non-symmetrical resistive thin film sensor. The boundary condition at $x = -L_1$ is of Dirichlet type, whereas the boundary condition at $x = L_2$ is of Robin type.

2.4.2.6. Electrothermal analogy

As in the case of the single wire sensor, an electrothermal analogy can be proposed in the case of the thin film sensor. It allows to easily consider the systemic modelling of nonlinear or non-symmetrical situations. Considering that the heat transfer through the lateral sides of the sensor is negligible compared to the parietal transfer, the general electrothermal analogy of paragraph 2.2.3 is formulated in the present case, as shown in Fig. 20. The boundary conditions considered in this example are the following: Dirichlet conditions at $x = -L_1$ and Robin (or mixed) conditions at $x = L_2$. This sub-circuit allows to simulate the operation mode considered in the paragraph 2.4.2.5.

Upon request to the author, a Python script is available, that allows the generation of a SPICE sub-circuit that is equivalent to the whole thin-film sensor, with an arbitrary number of infinitesimal volumes, under arbitrary boundary conditions.

3. Conclusion

We have exposed in this chapter two very rich and complementary approaches of the modelling of resistive electrothermal sensors. The first one uses the Laplace transform in order to allow a modelling of the sensor in terms of transfer functions. This opens the way to new modes of utilization of the electrothermal sensors, such as the absolute anemometry or thermal characterization of materials. This approach also allows to develop inverse analysis methods, in order for example to better consider and compensate the influence of the self-heating on the accuracy of thermal measurements using resistive sensors. The second approach exposed here uses an electrothermal analogy inspired from the Godunov scheme. It allows to consider more extreme situations than those considered by the transfer functions approach and also to envisage systemic approaches of the modes of operation of the resistive electrothermal sensors. This could be of great help to the designers of new instrumentation apparatus in the field of thermal measurement and materials and flow characterization. The same processes of modelling may be applied in the same way to the NTC resistive sensors made of semiconductors.

Author details

Rodolphe Heyd

ICMN UMR7374 CNRS/Orléans University, France

References

- [1] Bruun, H. Hot-Wire Anemometry, Principles and Signal Analysis. *Oxford University Press, New-York*, (1995).
- [2] Heyd, R., Hadaoui, A., Fliyou, M., Koumina, A., Ameziane, E., Outzourhit, A. and Saboungi, M. L. Development of absolute hot-wire anemometry by the 3ω method, *Review of Scientific Instruments* 81: 044901-1–044901-6, (2010).
- [3] Silvestri, S. and Schena, E. Micromachined flow sensors in biomedical applications. *Micromachines*. 3:225–243. (2012).

- [4] D'Aleo, F. P. and Prasser, H.-M. Design, calibration and testing of a thin film temperature gauge array for temperature and heat flux measurements in fluid mixing experiments, *Flow Measurement and Instrumentation*, 24:29–35, (2012).
- [5] Cahill, D. Thermal conductivity measurement from 30 to 750 K: the 3ω method, *Review of Scientific Instruments*, 61: 802, (1990).
- [6] Olson, B. W., Graham, S. and Chen, K. A practical extension of the 3ω method to multilayer structures, *Review of Scientific Instruments*, 76: 053901, (2005).
- [7] Lee, S.-M. Thermal conductivity measurement of fluids using the 3ω method, *Review of Scientific Instruments*, 80: 024901, (2009).
- [8] Feng, Z., Chen, J. and Zhang, Y. Real-time solution of heat conduction in a infinite slab for inverse analysis. *International Journal of Thermal Sciences*, 49:762–768, (2010).
- [9] Feng, Z., Chen, J., Zhang, Y. and Montgomery-Smith, S. Temperature and heat flux estimation from sampled transient sensor measurements, *International Journal of Thermal Sciences*, 49:2385–2390, (2010).
- [10] Heyd, R., Hadaoui, A. and Saboungi, M.-L. 1D analog behavioral Spice model for hot wire sensors in the continuum regime. *Sensors and Actuators A: Physical*, 174:9–15, (2012).
- [11] Heyd, R. Real-time heat conduction in a self-heated composite slab by padé filters. *International Journal of Heat and Mass Transfer*, 71:606–614, (2014).
- [12] Churchill, S. W. and Bernstein, M. *Journal of Heat Transfer*, 94:300, (1972).
- [13] Crump, K. S. Numerical inversion of Laplace transform using Fourier series approximation. *J. Assoc. Comput. Mach.*, 23:89–96, (1976).
- [14] Durbin, F. Numerical inversion of Laplace transforms: an efficient improvement to Dubner and Abate's method. *The Computer Journal*, 17(4):371–376, (1973).
- [15] Talbot, A. The accurate numerical inversion of Laplace transform. *J. inst. Maths. Applics.*, 23:97–120, (1979).
- [16] Baker, G. A. J. and Graves-Morris, P. Padé Approximants. *Cambridge University Press, New York, second edition*, (1996).
- [17] Ambardar, A. Analog and Digital Signal Processing. *Brooks/Cole, second edition*, (1999).
- [18] Kozlov, A. G. Analytical modelling of temperature distribution in resistive thin-film thermal sensors. *International Journal of Thermal Sciences*, 45:41–50, (2006).

Edited by Salim Newaz Kazi

In the wake of energy crisis due to rapid growth of industries, the efficient heat transfer could play a vital role in energy saving. Industries, household equipment, transportation, offices, etc., all are dependent on heat exchanging equipment. Considering this, the book has incorporated different chapters on heat transfer phenomena, analytical and experimental heat transfer investigations, heat transfer enhancement and applications.

Photo by nengredeye / iStock

IntechOpen

